Dissertation
submitted to the
Combined Faculties for the Natural Sciences and for Mathematics
of the Ruperto-Carola University of Heidelberg, Germany
for the degree of
Doctor of Natural Sciences

put forward by
Jan-Marcus Nasse, M.Sc.
born in Aalen

Oral examination:
May 15, 2019

Halogens in the coastal boundary layer of Antarctica

Referees: Prof. Dr. Ulrich Platt
Prof. Dr. Werner Aeschbach

Für Papa

"All the world loves a penguin: I think it is because in many respects they are like ourselves, and in some respects what we should like to be. Had we but half their physical courage none could stand against us. [...] Their little bodies are so full of curiosity that they have no room for fear. They like mountaineering, and joy-riding on ice-floes ..."

APSLEY CHERRY-GARRARD

member of Scott's Terra Nova expedition (1910-1913)
in *The Worst Journey in the World,* 1922

Zusammenfassung:

Reaktive Halogene haben großen Einfluss auf die atmosphärische Chemie in Polargebieten. Durch eine hohe Reaktivität verändern Halogenradikale die Oxidationskapazität der Atmosphäre und beeinflussen die chemischen Kreisläufe anderer Spurengase wie beispielsweise Ozon, Schwefelverbindungen, oder von gasförmigem, elementaren Quecksilber.
Diese Arbeit untersucht das Vorkommen von Halogenverbindungen und anderen Spurengasen in der atmosphärischen Grenzschicht über der antarktischen Küstenregion und analysiert die Freisetzung, den Einfluss und das weitere Verhalten von Chlor-, Brom-, und Jodverbindungen. Dazu wurde ein automatisiertes Messinstrument gebaut, das auf dem Prinzip der Langpfad-Differentiellen Optischen Absorptionsspektroskopie (LP-DOAS) beruht. Von Januar 2016 bis August 2018 wurde dieses erfolgreich auf der deutschen Antarktisstation Neumayer III betrieben. Dieser lange Datensatz wird in dieser Arbeit mit umfangreichen Beobachtungsdaten von der Station verknüpft.
Es konnte eine regelmäßige Präsenz von Brommonoxid (BrO) mit Mischungsverhältnissen von bis zu 111.2±0.7 ppt und ausgeprägten Tages- und Jahresgängen mit Aktivitätsmaxima in Frühjahr und Herbst nachgewiesen werden, die wesentlich durch die Dynamik von Sonneneinstrahlung und Atmsophäre bestimmt sind. Chlormonoxid (ClO) und Chlordioxid (OClO) wurden mit Mischungsverhältnissen bis zu 105±4 ppt beziehungsweise 7.7±0.8 ppt ebenfalls beobachtet. Atmosphärische Parameter legen eine zentrale Rolle lokaler Schneeoberflächen bei der Freisetzung von Chlor- und Bromverbindungen nahe. Jodmonoxid (IO) oberhalb der Nachweisgrenze wurde selten beobachtet bei höchstens 6.5±1.0 ppt. Der Einfluss von Kreuzreaktionen der Halogenverbindungen auf lokale Ozonkonzentrationen wurde abgeschätzt und stimmt sehr gut mit Messungen überein. Ein Jahresgang von Schwefeldioxid (SO_2) mit Mischungsverhältnissen bis zu 230±17 ppt konnte detektiert und durch den ozeanischen Schwefelkreislauf erklärt werden. Weiterhin wurde ein gleichzeitiges Auftreten von Partikelneubildung und erhöhten BrO Mischungsverhältnissen beobachtet.

Abstract:

Reactive halogens have a significant impact on atmospheric chemistry in the polar troposphere. Due to a high reactivity, halogen radicals change the oxidative capacity of the atmosphere and alter chemical cycles of other trace gases such as ozone, sulphur species, or gaseous elemental mercury.
This thesis investigates abundances of halogen and other trace gases in the boundary layer of coastal Antarctica and studies release, impact, and fate of chlorine, bromine, and iodine species. For this, an automated Long-Path Differential Optical Absorption Spectroscopy (LP-DOAS) instrument was developed and successfully operated on the German Antarctic Station Neumayer III for 32 months from January 2016 until August 2018. This extensive record of trace gas abundances is combined with a comprehensive set of ambient observations from the station.
A frequent presence of bromine monoxide (BrO) was detected with mixing ratios of up to 111.2±0.7 ppt and pronounced daily and annual cycles with activity maxima in spring and autumn, mostly driven by solar radiation and atmospheric dynamics. Chlorine monoxide (ClO) and chlorine dioxide (OClO) were equally detected with mixing ratios up to 105±4 ppt and 7.7±0.8 ppt respectively. Ambient observations indicate a central role of local snow surfaces for the release of both bromine and chlorine species. Iodine monoxide (IO) was rarely present with mixing ratios up to 6.5±1.0 ppt. The influence of cross halogen reactions on ozone mixing ratios was estimated and found in good agreement with observations. An annual cycle of SO2 mixing ratios up to 230±17 ppt was detected and could be attributed to the marine sulphur cycle. A coincidence of natural new particle formation events and elevated BrO mixing ratios was observed.

Contents

1
Introduction

The Arctic and Antarctica, Earth's polar regions, are lands of extremes. Inside the polar circles, solar radiation - ultimately the driving force of most physical, chemical, and biological processes on the planet - varies between constant presence and complete absence for weeks or even months at a time. With it, physical quantities like air temperature or wind speed reach values as extreme as in few other places on the globe making the polar regions one of the most hostile environments to life.

Extremes are also evident in the time scales encountered. While millions of square kilometres of ocean surface freeze and melt over the course of a year, with considerable transformations occurring on time scales as short as hours or days, the large ice sheets on Greenland and the Antarctic continent contain ice that is millions of years old (Voosen, 2017). Globally, Arctic and Antarctic are important factors in the global radiation budget, for large scale circulations in both the atmosphere and the oceans, and as reservoir of the bulk of all freshwater (Lemke et al., 2007).

For the atmosphere in polar regions, the interplay of these particular environmental conditions has a major impact on composition and chemical properties. This thesis investigates the abundance, release, chemistry, and influence of reactive trace gases containing halogens, which owe their presence in the polar atmosphere to this interplay.

From a chemical point of view, Earth's atmosphere is an oxidising medium (A. M. Thompson, 1992). The presence of radicals - highly reactive trace molecules - determines the fate of hundreds of compounds released into it and hence influences its composition on the trace gas level, below the major constituents molecular nitrogen, molecular oxygen, and argon. Globally, in the lower atmosphere hydroxyl (OH) and the closely related hydroperoxyl (HO_2) radicals play a central part in atmospheric chemistry and the former is sometimes referred to as the 'detergent of the atmosphere' (Crutzen, 1986).

A presence of halogen radicals can shift the role of dominant oxidants from hydrogen to halogen species. This change of the oxidative capacity of the atmosphere can influence various chemical cycles and drastically reduce the abundance of other trace gases.

A well known example of the impact of halogen radical chemistry is the destruction of stratospheric ozone by halogens that are photolytically released from chlorofluorocarbons (CFCs) and other man-made halogen compounds (Crutzen, 1974; Molina and Rowland, 1974). In catalytic reactions these compounds cause the yearly formation of the Antarctic ozone hole (Farman et al., 1985; Solomon et al., 1986).

In the polar troposphere halogen compounds containing bromine or chlorine originate from salty surfaces, either sea ice, snow on which sea salt has been deposited, or aerosols. Observed iodine species were found to most likely be of biogenic and inorganic marine origin (Saiz-Lopez and von Glasow, 2012). From halide laden surfaces, halogen compounds can be released into the atmosphere by different chemical mechanisms. One is the so-called *bromine explosion* (Platt and Janssen, 1995; Platt and Lehrer, 1996; Wennberg, 1999), a sequence of heterogeneous reactions by which bromine is autocatalytically released to the gas phase leading to an exponential increase of reactive bromine in the atmosphere.

This mechanism was proposed to explain regular observations of an episodic, almost complete destruction of tropospheric ozone in both hemispheres during the respective polar spring (Oltmans, 1981; Kreher et al., 1996) referred to as Ozone Depletion Event (ODE). The contemporaneous observation of filterable bromine (Barrie et al., 1988; Oltmans et al., 1989) and, soon after, the direct detection of bromine monoxide (BrO) confirmed the role of bromine chemistry (Hausmann and Platt, 1994). Since then, numerous studies have contributed more observational evidence and have increased the understanding of the role of halogen compounds in the polar boundary layer. In addition to bromine, iodine species were detected (Frieß et al., 2001; Saiz-Lopez et al., 2007a; Frieß et al., 2010) and chlorine chemistry has been observed (Pöhler et al., 2010; Buys et al., 2013; Zielcke, 2015).

Regarding halogen release pathways and surfaces relevant for activation processes, the research focus has been extended from specific surface types such as frost flowers on sea ice (Kaleschke, 2004) to snow packs on sea ice (Yang et al., 2008) and land (Pratt et al., 2013; Wren et al., 2013; S. Wang and Pratt, 2017; Custard et al., 2017; Peterson et al., 2018) as well as lofted snow during storms (Yang et al., 2008; A. E. Jones et al., 2009; Yang et al., 2010). Release mechanisms other than the heterogeneous reaction sequence of the bromine explosion have been investigated, in particular the release of dihalogens by photolytically produced OH on ice surfaces (Pratt et al., 2013; Custard et al., 2017). Recent observations of high mixing ratios of chlorine compounds have raised new questions since the current understanding of prevailing reaction pathways does not support a release through a 'chlorine explosion' (Liao et al., 2014; Zielcke, 2015; Custard et al., 2017).

In addition to the influence on tropospheric ozone, an important precursor for hydrogen radicals, halogen radical chemistry is relevant for the understanding of several other chemical cycles in the lower atmosphere. The oxidation of gaseous elemental mercury by bromine monoxide occurs in parallel with ozone depletions and can lead to an input of toxic mercury compounds into the biosphere (Angot et al., 2016). A presence of halogen radicals alters the marine sulphur cycle with consequences for the formation of aerosol particles and cloud condensation nuclei (von Glasow and Crutzen, 2004; Read et al., 2008; Chen et al., 2018). Also in new particle formation, a topic of very active research in both polar regions and atmospheric science in general, an influence of halogen chemistry is assumed (Kulmala et al., 2013; Weller et al., 2015; Abbatt et al., 2019). For palaeoclimatology based on ice core samples, an understanding of halogen chemistry is important due to its influence on reactive proxies such as nitrate (Wolff et al., 2007) and in recent years halides themselves have been investigated as potential proxies for past sea ice extent (Spolaor et al., 2013).

Despite intense research, many central aspects of polar halogen chemistry and its impact on other trace gases remain unclear. Topics of current research reach from the relevant properties and structure of surface layers of ice and aerosols (Bartels-Rausch et al., 2014) to the role of entire synoptic frontal systems in the activation of halogens and the impact of climate change on future halogen release rates (Blechschmidt et al., 2016).

Even though satellite observations and data from extensive long-term measurement programs in several locations are available, a lack of (representative) observations is still often cited as an important factor limiting the understanding of halogen chemsitry, in particular when atmospheric modelling is employed (Simpson et al., 2015; C. R. Thompson et al., 2017). Furthermore, the assessment of the impacts of polar halogens on other species such as nitrogen oxides (Bloss et al., 2010), mercury (Angot et al., 2016), or sulphur compounds formed from dimethyl sulfide (Chen et al., 2018) is affected by insufficient knowledge of typical mixing ratios of relevant species.

The main goal of this thesis is to contribute to a better understanding of atmospheric halogen chemistry in polar regions by extending the observational data base of halogen species and other relevant trace gases. This was achieved both in terms of the temporal coverage of atmospheric composition, and by extending the instrumental sensitivity to species many instruments so far deployed to the polar regions, cannot detect.

For this, a new, largely automated low maintenance Long-Path Differential Optical Absorption Spectroscopy (LP-DOAS) instrument was designed and built, based on recent improvements of the instrumental setup (Nasse et al., 2019). Compared to other spectroscopic instrument types that use scattered or reflected sunlight (e.g. Multi-Axis Differential Optical Absorption Spectroscopy (MAX-DOAS) or satellite sensors), LP-DOAS offers the advantage of being independent of sun levels due to the artificial light source employed. This enables the observation of night-time chemistry and mixing ratios during polar night. Additionally, it allows a detection of species absorbing in UV spectral ranges where passive instruments receive insufficient radiances due to absorption in the stratosphere.

The instrument was set up on the German Antarctic station Neumayer III (NM III) and successfully operated for 32 months from January 2016 until August 2018. While LP-DOAS instruments have long been used in polar environments, technical limitations so far prevented such extended observation periods. The available data set is the longest so far acquired with a LP-DOAS in polar regions. In combination with observations from the meteorological and the trace gas observatory of NM III station, it allows a detailed study of tropospheric halogen chemsitry.

The presented work consists of four parts. After this introduction an overview of the polar regions and relevant physical and chemical processes is given in Chapter 2. In the second part, the theory of Differential Optical Absorption Spectroscopy (DOAS), the main measurement method used in this work, is introduced in Chapter 3, followed by an overview of the available instrumentation at NM III in Chapter 4, including a detailed description and characterisation of the new LP-DOAS instrument. In the third part, the results of the 32 months of observations are discussed. In Chapter 6 relevant atmospheric parameters as well as measurements of non-halogen trace gases are examined before in Chapter 7 halogen observations are presented and discussed both on an (inter-) annual time scale and with selected case studies. The influence of inter-halogen reactions on ozone destruction is estimated and compared to observed mixing ratios, and a potential connection of elevated bromine monoxide mixing ratios to new particle formation events was investigated. In Chapter 8 conclusions are drawn and an outlook is given in Chapter 9.

2

Polar tropospheric halogen chemistry

Atmospheric composition is a vital factor for life on a planet. On Earth, the atmosphere plays central roles in the energy budget and for the transfer of mass as well as energy in the form of radiation and heat. Atmospheric gases are a prerequisite for respiration of plants and animals. Trace constituents of the atmosphere and changes of their concentration can have an enormous impact e.g. on the global energy budget or, for pollutants, on air quality.

The composition of the atmosphere and its temporal evolution is determined by physical and chemical processes affecting emission, transformation, and removal of gases and particles. This chapter introduces the polar regions and gives an overview of the Earth system compartments relevant to the processes studied in this thesis. Then an introduction to polar tropospheric chemistry in general and the role of halogens in particular will be given with a focus on Antarctica, before concluding with an overview of the impacts of halogen chemsitry.

2.1 The Polar Regions

The polar regions are commonly defined as the areas of the globe that lie within the respective polar circle (66.6° N and S) around the poles (Christopherson and Birkeland, 2015). The often synonymously used terms Arctic for the northern and Antarctica for the southern polar region are defined less clearly.

Owing its name to the ancient Greek ἀρκτικός (arktikós) for *northern, near the bear* derived from ἄρκτος (árktos - *bear*) referring either to the constellation of the big bear (*Ursa Major*) or the small bear (*Ursa Minor*) that contains the *Polaris* or North Star, the Arctic can be defined by climatic characteristics such as the 10°C isothermal i.e. the region where the average air temperature in July is below 10 °C. Another definition is based on the presence of permafrost soil. A vegetation based definition uses the tree line as a border, which coincides more or less with the 10°C summer isothermal (see left panel in Fig. 2.1; J. L. Murray et al., 1998). From an oceanographic point of view, the border between colder and less salty water masses from the Arctic, and warmer, saltier water from lower latitudes can be used. There are additional anthropogenic borders e.g. based

on the regions monitored by the Artic Monitoring and Assessment Program (AMAP), one working group of the Arctic Council, an intergovernmental organisation of Arctic countries.

For the Antarctic (from Greek ἀνταρκτικός (antarktikos) for *opposite of the north/the Arctic*), in addition to the polar circle, the Polar front (i.e. the border between the Polar and the Ferrel cell in global atmospheric circulation patterns) is used (Larsen et al., 2014). It has an equivalent border in the Southern ocean also called Polar front (formerly also Antarctic Convergence) where cold, north-ward flowing Antarctic waters meet warmer waters of the Subantarctic (Giglio and Johnson, 2016). Regarding anthropogenic borders, the Antarctic Treaty that regulates all activities on the continent uses 60° S as the boundary (but explicitly excludes the oceans, Article VI, *The Antarctic Treaty* 1959).

2.1.1 Geography

Geographically, Arctic and Antarctic are different. The centre of the Arctic is a relatively shallow ocean (depth up to 4000 m, J. L. Murray et al., 1998) that is surrounded by landmasses (see Fig.2.1, left map).

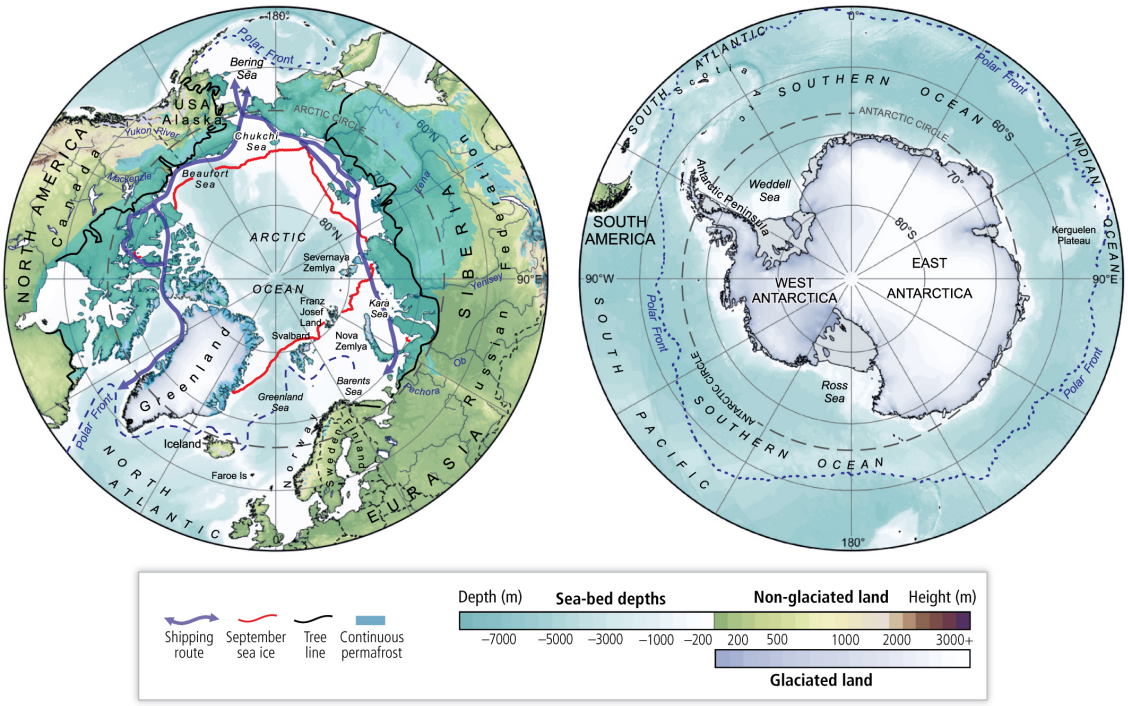

Figure 2.1: Location maps of the north and south polar regions (courtesy of P. Fretwell, British Antarctic Survey). (Figure 28-1 from Larsen et al., 2014)

It contains a number of islands and archipelagoes, most notably Greenland, Svalbard, Franz Josef land, Severnaya Zemlya, Novaya Zemlya, Victoria Island, Ellesmere Island, and Baffin island, which are largely covered by glacial ice or ice caps and sheets.

The orography of surrounding land masses varies from lowlands in the Russian Arctic to high mountain ranges in Alaska including the Denali (formerly Mount McKinley), with 6190 m the highest mountain in North America. The Arctic is home to several indigenous peoples (Huntington et al., 1998, see).

The Antarctic, in contrast (see right map in Fig. 2.1), is dominated by the Antarctic continent that from the South Pole extends northwards to 63.22°S on the Antarctic peninsula. It is surrounded by the Southern Ocean and the shortest distance to the closest neighbouring continent (South America) is about 800 km from the South Shetland Islands (120 km north of the peninsula) across the Drake passage. The lack of major orographic features around the continent leads to unimpeded circulation of ocean currents and low pressure systems, which dominate meteorological conditions in coastal Antarctica (see Chapter 6). Almost the entire continent is covered by ice sheets, which are divided by the Transantarctic Mountains into the East Antarctic Ice Sheet and the much smaller West Antarctic Ice Sheet. The average thickness of the ice is 2400 m with a maximum known thickness of 4776 m in *Terre Adélie* (69.9°S, 135.2°E) (Barry and Gan, 2011). The highest mountain is Mount Vinson (4892 m) at the base of the Antarctic peninsula.

Since its ratification in 1961, all human activities in Antarctica are regulated by *The Antarctic Treaty* (1959) that designates Antarctica as a place for exclusively peaceful purposes banning all military activities, promoting international cooperation in scientific research, and setting aside disputes over territorial claims. The treaty established a reporting and inspection system to ensure compliance and has 53 parties (Secretariat of the Antarctic Treaty, 2018). There are no indigenous inhabitants of the continent and the only "population" are scientists on permanently and temporarily manned research stations.

2.1.2 Radiation

A common feature of both Polar regions is the high variability of solar irradiation. Due to their location in high latitudes and the tilt of Earth's rotational axis, these regions are subject to a very pronounced annual cycle. For locations inside the respective polar circle (north of 66.57 °N or south of 66.57 °S), the Sun can be invisible for weeks and months during Polar night while being constantly above the horizon the almost equivalent time period.[1] Since solar energy is the driver for various physical (e.g. transport, phase changes), chemical (e.g. photochemistry), and biological processes (e.g. photosynthesis), many of these phenomena exhibit equally pronounced annual cycles.

In atmospheric chemistry, photolytic reactions play a central role (Sec. 2.3.1). The availability of solar radiation energetic enough to overcome molecular bonds determines the efficiency of numerous chemical cycles (Grannas et al., 2007, and references therin). Therefore, the ultra-violet (UV) spectral region ($100\,\text{nm} \leq \lambda \leq 400\,\text{nm}$ - see *ISO 21348* 2007, for definitions) is most important. The solar zenith angle (SZA), the position of the Sun above the horizon expressed in degree from the zenith- determines the magnitude of the irradiation throughout the day and the year, as well as the light path through the atmosphere. In combination with the stratospheric ozone layer, this influences the spectral distribution of photons available for photochemistry. Radiation with wavelengths shorter than 280 nm (UV-C) is completely absorbed by the ozone layer (Grannas et al., 2007, and references therin). UV-B radiation ($280 - 315\,\text{nm}$) can at least partly penetrate the ozone layer and is crucial e.g. for radical formation described in Sec. 2.3.1 below. However, higher SZAs, which are characteristic for Polar regions, increase the stratospheric portion of the light path through the atmosphere and hence increase the influence of ozone absorption. The availability of UV-B radiation therefore strongly depends on the SZA. UV-A radiation ($315 - 400\,\text{nm}$) is less dependent on SZA and stratospheric ozone.

The attenuation of radiation is partly offset by the high albedo of snow covered surfaces, which reflect incoming short-wave radiation back to the atmosphere. The spectrally averaged albedo is between 0.80 and 0.85 with 0.96-0.98 across the UV-visible spectral range (Grenfell et al., 1994; Grenfell and Perovich, 2004)) and dropping to 0.15 in the NIR. In Antarctica (and occasionally in the Arctic) also the springtime 'ozone hole' influences the amount of short-wave radiation reaching the surface (Madronich et al., 1995; Solomon et al., 2007). In the sea ice zone around the continent, spectrally averaged albedos vary between 0.87 for snow covered ice floes to 0.07 for open water (Brandt et al., 2005).

[1] **Excursion on Polar night and day:**
Polar day is longer than Polar night for a given location because times when the solar disk is only partly above the horizon are counted towards the day (i.e. sunrise and sunset are commonly defined as the upper edge of solar disk being on the horizon). For NM III at 70 ° 40‘ S, 8 ° 16‘ W this difference is 9 days with Polar night lasting 63 days and Polar day 72 days. Furthermore, atmospheric refraction seems to extend days and hence Polar day. Using common twilight definitions (e.g. US-Naval-Observatory, 2018) (civil twilight: center of the sun between 0 ° and 6 ° below the horizon, nautical twilight: sun between 6 ° and 12 °, astronomical twilight: sun 18 ° or more below the horizon) three somewhat stricter definitions of Polar night can be applied with civil Polar night being days when the sun never rises higher than 6 ° below the horizon and so on. Civil Polar night therefore only exist above 72.2 °. For NM III, this means that there are always periods of civil twilight around noon throughout the Polar night. Interestingly, Polar night in the Antarctic is slightly longer than in the Arctic because Earth is in aphelion during southern Polar night and therefore moves slower on its orbit around the Sun. This effect amounts to 4 days at NM III compared to the equivalent location in the northern hemisphere.

2.2 Earth system compartments relevant to halogen chemistry

A complementary approach to geographic categories, is the description of the polar regions from a climate system point of view. Among the five main compartments of the global climate system: lithosphere, biosphere, hydrosphere, cryosphere, and atmosphere (Planton, 2013), the latter two (and to some extent the hydrosphere) are relevant for the processes investigated in this thesis and will be discussed in following.

2.2.1 Cryosphere

The cryosphere comprises those areas of the Earth where a substantial fraction of available water is in a frozen state. Its components are snow covers, river and lake ice, sea ice, ice sheets (ice mass of continental extent), ice shelves, glaciers (ice mass constrained by local topography), ice caps (ice mass covering a limited land area), and frozen ground both on land (permafrost) and the ocean floor (Vaughan et al., 2013). Typical life times of the components vary between days to millennia (cf. Fig. 2.2). Among the parts of the cryosphere, sea ice and snow surfaces on sea ice, ice shelves, and ice sheets are particularly important for tropospheric halogen chemistry.

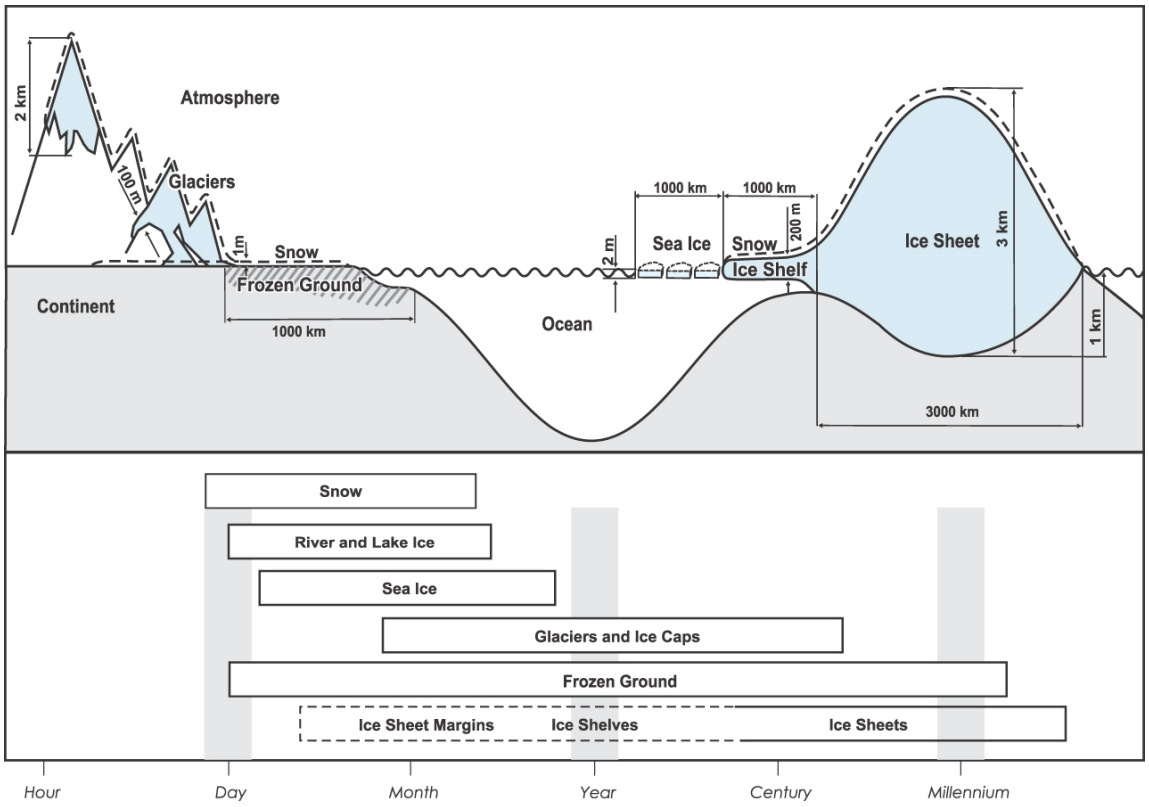

Figure 2.2: Components of the cryosphere and their time scales. (Figure 4.1. from Lemke et al., 2007)

Sea ice

Sea ice surfaces can be a direct source of atmospheric halogen compounds or serve as a source of halogen-containing (salty) aerosols (Rankin et al., 2002; Yang et al., 2008; Abbatt et al., 2012, , see Sec. 2.4.5).

Sea ice forms when the temperature of sea water drops below its freezing point (e.g. -1.86 °C for a typical salinity of 34 PSU (Practical Salinity Unit) - equivalent to $g\,kg^{-1}$ of water). As the salt ions contained in the sea water cannot be integrated in the ice crystals, they are expelled into brine (highly-concentrated solution of salt). This leads to a formation of microscopic brine pockets in the ice matrix rendering it porous and opaque compared to lake ice. Brine is also ejected from the bulk of the sea ice increasing sea water salinity at its base as well as creating layers of highly concentrated brine on its surface at the ice-atmosphere interface (Petrich and Eicken, 2017). Freshly formed sea ice has a C-shaped salinity profile with a bulk salinity of only 25% to 50% of the surrounding sea water (Vaughan et al., 2013) while salinity in brine and slush on the surface and at its base can exceed that of sea water by a factor of 2 (Ehn et al., 2007) to 3 (Rankin et al., 2002).

Where sea ice persists for more than a year (mostly in the Arctic, but also in the Weddell sea and in small patches along the Antarctic coast, see the February panel in Fig. 2.4), overall salinity decreases and surface melt water can flush the ice drastically reducing surface salinity (Petrich and Eicken, 2017).

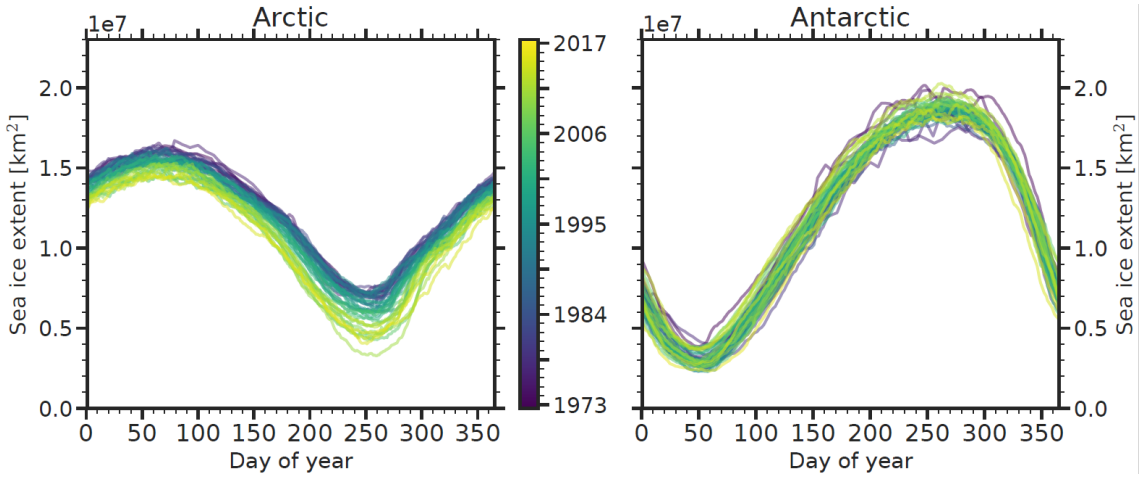

Figure 2.3: Sea ice extent in the Arctic and Antarctic from 1973 until 2017. Sea ice extent is defined as the total area with at least 15% ice concentration. Generated using data sets from different satellite sensors provided by the Sea ice remote sensing group of the University of Bremen (Spreen et al., 2008).

Sea ice forms as pack ice and grows through basal freezing. The thickness of individual pieces (ice floes) is determined by the energy balance at the surface and the heat provided by the ocean. The thicker a floe grows, the stronger it insulates its base from the cold air above (Petrich and Eicken, 2017). A snow cover on the ice drastically increases this insulation and generally has a higher albedo than sea ice (Grenfell and Perovich, 2004) further influencing the energy balance. High loads of snow on the other hand can lead to a flooding of ice floes creating a saturated and salty snow layer that forms snow ice upon (re-)freezing (Vaughan et al., 2013; Sturm and Massom, 2017).

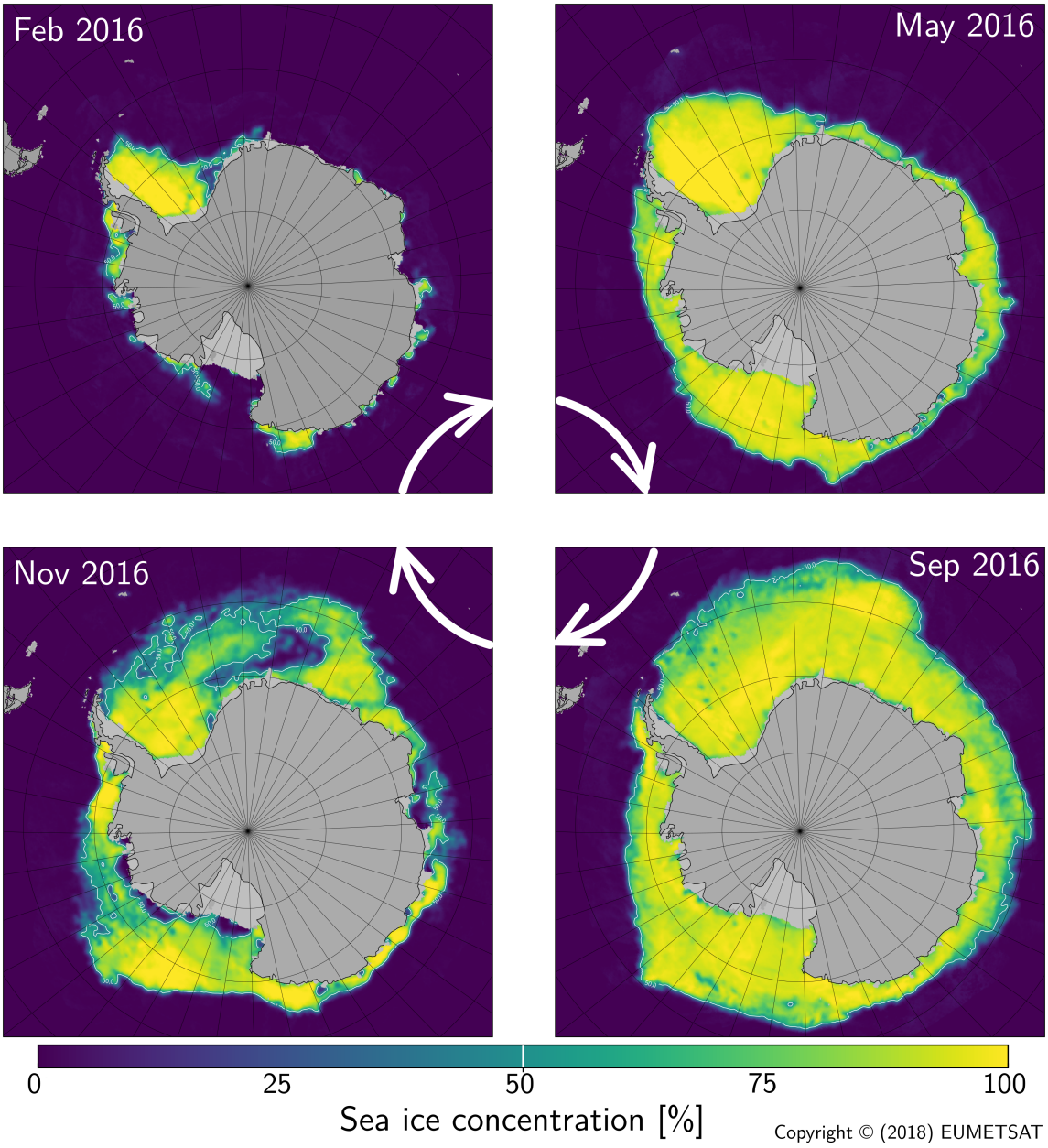

Figure 2.4: Sea ice concentration around Antarctica throughout the year. Data are plotted for the minimum extent (around mid-February), maximum extent (mid-September), and for the times in between (end of May and end of November). The white contour marks 50% concentration. Generated using Copernicus Climate Change Service information (2018), the EUMETSAT Ocean and Sea Ice Satellite Application Facility (2015) and *Panoply* by Schmunk (2018).

Ocean currents and wind sheer lead to dynamic changes of the sea ice thickness. In convergent sea ice motion, pressure ridges form and ice floes are rafted (pushed on top of each other). Divergent motions can break up floes and open up the sea ice creating so-called *leads*, where new ice can quickly form (Haas, 2017). The heat flux from the relatively warm ocean water also has implication for atmospheric dynamics (Anderson and Neff, 2008, see Sec. 2.2.2) and halogen chemistry (e.g. Abbatt et al., 2012, see Sec. 2.4).

In terms of sea ice thickness, Arctic and Antarctic are different. Whereas most ice in the Arctic is thicker than 2 m and a larger fraction survives the melting season,[2] in the Antarctic, only ice in the western Weddell sea and around the peninsula reaches comparable thicknesses and becomes multi-annual (see February panel of Fig. 2.4).

This difference can be explained by the geographic differences of the two polar regions (Haas, 2017). Since the Arctic is surrounded by land masses, it (1) receives a steady inflow of fresh water from rivers (about 10% of the world's river run-off). This cold freshwater sits stably on top of warmer, saltier ocean water reducing mixing and heat flux from below thus increasing basal freezing. Furthermore (2), the surrounding land masses lead to less snowfall over the Arctic reducing the insulating effect of snow. (3) The Arctic coasts also confine the sea ice motion leading to more deformation and (4) prevent a drift to lower latitudes hence making the ice on average older. As the probability of deformation events increases with age, this contributes to greater ice thicknesses. Sea ice around Antarctica in contrast, exhibits a net northerly drift into lower latitudes. Lastly (5), Arctic sea ice predominantly is located north of 70° N whereas Antarctic sea ice surrounds the large continent and extends as far as 55° S (see also September panel in Fig. 2.4).

Globally, at any time sea ice extent is between 16 and 26 million km^2 (calculated for 2017 with data from Spreen et al., 2008), which corresponds to 4.4 to 7.2% of the global ocean surface (or 3.1 to 5.1% of the surface of the Earth). Arctic and Antarctic sea ice have almost mirrored annual cycles with maxima in the Arctic at the beginning of March and minima in mid-September. Minimum sea ice extent in Antarctica is reached in mid-February and the maximum in mid- to end of September (see Fig. 2.3 and Fig. 2.4).

Surface snow

Snow in Polar regions exists on land, ice sheets, ice shelves, and on sea ice. Prerequisites for a snow cover are precipitation, temperatures low enough for the precipitation to deposit and survive as snow, and, for the sea ice region, a sufficient ice thickness to support the weight of the snow (Sturm and Massom, 2017).

In the atmosphere, ice particles that can grow into snow either form by homogeneous freezing of supercooled water droplets at temperatures below 235 K or heterogeneously at higher temperatures, triggered by suitable ice nucleation (IN) particles (e.g. Feldspar dust; B. J. Murray et al., 2012). There are several heterogeneous freezing mechanisms such as immersion freezing, when a droplet already contains one or several ice-active aerosol particles prior to cooling down, or impact freezing, when a supercooled droplet is impacted by an IN particle. For details on cloud microphysics, ice particle formation, and the processing mechanisms particles can undergo in clouds before falling as snow, the interested reader is referred to e.g. Pruppacher and Klett (2010) and B. J. Murray et al. (2012).

[2] As the clearly visible decline in sea ice extent in the Arctic in Fig. 2.3 shows, this fraction is currently decreasing quickly due the rapid warming of the Arctic induced by climate change. (Vaughan et al., 2013)

Gaseous or particulate contaminants originating from the atmosphere and incorporated in snow through heterogeneous freezing, scavenging mechanisms, or solution prior to freezing are the most important sources of impurities in surface snow (Bartels-Rausch et al., 2014). Adsorbed and dissolved impurities, and trapped aerosols can influence chemical reactions on snow surfaces as well as in the atmosphere above. The atmospheric processes leading to this take-up will not be discussed further here and the reader is referred to e.g. Barrie (1991), Dominé and Thibert (1995), and Pruppacher and Klett (2010). This section is confined to an overview of the physical properties of surface snow relevant for atmospheric chemistry. For a detailed discussion of this topic refer to the reviews by Dominé et al. (2008) and Bartels-Rausch et al. (2014). Chemical reactions involving snow surfaces will be covered in Sec. 2.3.

Relevant portions of the snow pack (i.e. the annually accumulated snow, Dominé and Shepson, 2002) are the *photic zone*, the depth to which light penetrates (about 20 cm) and the zone that is still ventilated by wind (50-100 cm) and following Dominé et al. (2008) will be referred to as *surface snow*. When snow is older than one year it is called *firn* and on glaciers, ice sheets, and ice shelves it is slowly transformed into ice through compression. At a depth of 60 to 100 m, pores in the firn close off with only bubbles of air remaining in the solid ice.

The physical properties of surface snow with importance for atmospheric chemistry are (1) snow density - the mass of ice(water) per unit volume of snow, (2) specific surface area (SSA) - the surface area of snow grains in contact with air per unit mass, (3) air permeability - a measure for the interstitial air flow that can be created by a pressure gradient. (4) the gas diffusion coefficient in snow - basically the gas diffusivity in air modified by the increase of path lengths in snow due to the pore structure, and (5) the availability of light inside the surface snow, which depends on its transmissivity and reflectivity. The e-folding depth in most snow packs is between 5 and 25 cm (for a detailed description of these quantities and typical values for different snow covers please refer to Dominé et al., 2008).

The relevance of snow for atmospheric chemistry lies in its property as 'a complex, multi-phase reactor' (Dominé et al., 2008). With its high porosity and hence relatively good accessibility for air flow, a large surface area where adsorption, dissolution and solid diffusion, or heterogeneous reactions (i.e. involving multiple phases) can take place (see Fig. 2.5), it can strongly influence the composition and chemistry of the overlying atmosphere (Dominé and Shepson, 2002). The high reflectivity of ice crystals furthermore provides sufficient radiation for photochemical reactions to take place in the interstitial air and on the ice surfaces in the photic zone of the surface snow. Impurities on the grain surfaces can be released to the interstitial air or can take part in surface reactions. At the same time, snow can act as a sink or reservoir for trace substances through adsorption and solution from air flowing through the snow pack. With regard to contaminants trapped inside the snow grains, it should however be noted that due to the slow solid diffusion in ice (e.g. $10^{-12}\,\mathrm{cm^2\,s^{-1}}$ for HCl, Thibert and Dominé, 1997), contaminants inside the snow grains and trace substances on its surface do not necessarily interact (Dominé et al., 2008).

Once deposited on a surface, surface snow is not a static system. The variation of environmental parameters like temperature, humidity, radiative heating and cooling, or temperature gradients (e.g. between sea ice surface below and the atmosphere above) lead to a constant redistribution of water molecules between snow grains and layers of the snow cover. This changes the size and shape of grains as well as properties like the density or

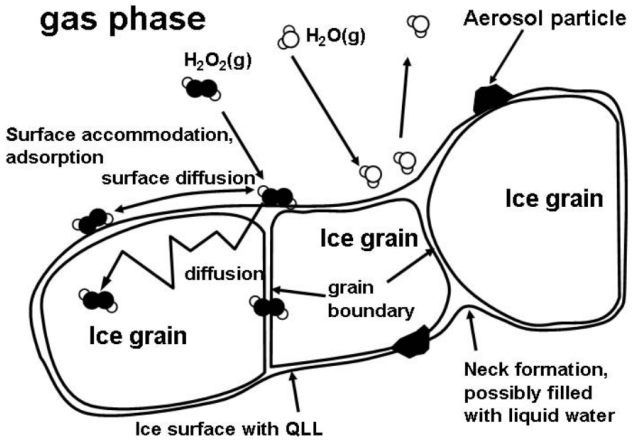

Figure 2.5: Potentially coexistent phases and reaction locations on snow grains using the example of H_2O_2. Reproduced from Dominé et al. (2008) under CC 3.0.

specific surface area of the surface snow and is referred to as *snow metamorphism* (Dominé and Shepson, 2002). Due to these dynamics, the air-snow interphase is a constantly changing environment where different phases can coexist. An important aspect for chemical reactions involving these surfaces are changes in the concentrations of impurities either through deposition or evaporation of water, or through effects like cryoconcentration (similar to the macroscopic increase of surface salinity in sea ice formation), or precipitation of complexes of dissolved substances when threshold temperatures are undershot (R. Sander et al., 2006; Abbatt et al., 2012; Bartels-Rausch et al., 2014). This complexity of surface snow and the fact that it is not readily accessible for measurements without disturbing it, still limit the understanding of physical and chemical processes (Dominé et al., 2008).

In this context, in particular the role of the surface layer of snow grains is still subject of an ongoing debate (Dominé et al., 2008; Bartels-Rausch et al., 2014). Several studies have demonstrated evidence for the existence of a thin surface layer of disordered molecules with a thickness of a few tens of nm (Dominé et al., 2008). As some of its properties appear to be liquid-like even down to temperatures around -20 °C, this layer is sometimes referred to as *Quasi Liquid Layer (QLL)*. In laboratory studies, reactions involving these surfaces successfully could be described using rate constants for liquid phase chemsitry and several observations and potential properties of this layer seem to explain observed phenomena (for halogen chemistry e.g. the possible existence of enhanced ion concentrations and reaction rates at the surface). Due to the analytical difficulties in natural snow, the role of this layer on chemical processes remains unclear (Dominé et al., 2008). Bartels-Rausch et al. (2014) stress the fact that a simple analogy of this layer to a (supercooled) liquid phase no longer can be supported by recent findings and that the disordered layer is a distinct phase in the surface snow system.

2.2.2 Atmosphere

The most common way to divide the vertical structure of the atmosphere and describe its properties is based on its temperature profile, which alternates between layers with negative and positive vertical temperature gradients.[3] The resulting layers are the troposphere that extends from the surface to about 8 to 18 km altitude depending on latitude. The stratosphere ranges from the tropopause, the top of the troposphere, to about 50 km. Here temperature increases with altitude due to molecular absorption (O_3 and O_2). The mesosphere where, similar the troposphere, the temperature gradient is negative, lies between $\approx$50 and 80 km and is topped by the thermosphere where temperatures increase beyond 1000 K and which extends to 500-1000 km altitude (Roedel and T. Wagner, 2011; Lutgens and Tarbuck, 2016).[4]

The pressure profile in the atmosphere is described by the barometric height formula:

$$p(z) = p_0 \cdot \exp\left(-\frac{g}{R}\left(\int_0^z \frac{M}{T}\mathrm{d}z'\right)\right) \approx p_0 \cdot \exp\left(-\frac{z}{z_0}\right) \tag{2.1}$$

where p is atmospheric pressure, z altitude, p_0 the surface pressure, M the average molar mass of air (M=28.97 g mol^{-1}), R the universal gas constant, and T the temperature of the atmosphere. For most purposes it is sufficient to use the second, approximated formulation with 'scale height' $z_0 \approx \frac{R \cdot T}{M \cdot g} \approx 8$ km (Roedel and T. Wagner, 2011).

Another useful concept is the potential temperature θ. It is the temperature an air parcel with pressure p would have when dry-adiabatically brought to normal pressure ($p_0 = 1013$ hPa).

$$\theta = T \cdot \left(\frac{p_0}{p}\right)^{\frac{R}{c_p}} \tag{2.2}$$

Here T is the temperature of the air parcel, p its pressure, and c_p the specific heat of air for constant pressure. The gradient $\frac{\mathrm{d}\theta}{\mathrm{d}z}$ is a measure for atmospheric stability. When $\frac{\partial\theta}{\partial z} > 0$ the atmosphere is in stable stratification, for $\frac{\mathrm{d}\theta}{\mathrm{d}z} = 0$ neutral, and for $\frac{\mathrm{d}\theta}{\mathrm{d}z} < 0$ it is unstable.

[3] Other divisions distinguish the neutrosphere (0 to $\approx$ 75 km) and ionosphere (above) based on the grade of ionisation through solar and cosmic radiation, or separate layers based on the dominating transport process - turbulent mixing in the turbo- or homosphere (up to $\approx$ 80-100 km) versus molecular diffusion in the heterosphere above (Roedel and T. Wagner, 2011; Lutgens and Tarbuck, 2016)

[4] Although the thermosphere is considered to be part of Earth's atmosphere, for legal purposes (national jurisdiction, aviation regulations) the von-Kármán line at 100 km altitude is used as border between atmosphere and space. It is the altitude where the speed to achieve lift equals the speed to orbit the planet. However, the altitude where this actually is the case and hence the definition of outer space has been under debate recently (Voosen, 2018).

The planetary boundary layer

The chemsitry investigated in this thesis involves surface-gas phase interactions in the lower troposphere close to the ground. The layer of the troposphere that is 'directly influenced by the presence of Earth's surface and responds to surface forcing with a time scale of an hour or less' (Stull, 1994) is referred to as *boundary layer*. Surface forcing can be the transfer of heat, momentum, and moisture (e.g. over open leads), or the emission of trace constituents, which in turn can affect the radiative balance of surface and atmosphere (Anderson and Neff, 2008). As Stull (1994) points out in his definition, the boundary layer does not necessarily have to be in equilibrium on the time scale of one hour but rather that 'alterations have begun'. In polar regions, dynamics and response of the boundary layer generally tends to be slower than in mid-latitudes (Neff et al., 2008).

In fluid dynamics there is a formal definition for the boundary layer of a fluid over a surface initially introduced by Prandtl (1905) for laminar flow (for Reynolds numbers $Re < 600$) and later extended to turbulent boundary layer flow, which applies to Earth's atmosphere (Re typically 10^5; Anderson and Neff, 2008). A detailed discussion of this is beyond the scope of this introduction and the interested reader is referred to (e.g. Anderson and Neff, 2008; Roedel and T. Wagner, 2011).

Qualitatively, the vertical mixing that forms the boundary layer can be caused by two different phenomena. It can be the result of (a) turbulence created by wind shear at the surface, which depends on wind speed and features such as the surface roughness or (b) through convection induced by a heating of the surface or the advection of a cold air mass over a warm surface (e.g. when cold air flows from the sea ice zone to the open ocean).

For the interpretation of atmospheric observations, there exist a number of practical definitions of the boundary layer linked to locally observable parameters or proxies (Anderson and Neff, 2008). A general approach is to define the top of the boundary layer as the height at which turbulence decreases to a small value compared to the surface. Then the effect of turbulent mixing on proxies like the potential temperature or humidity is investigated. In doing this, it has to be kept in mind that such proxies might be influenced by other phenomena. Potential temperature profiles for example can be disturbed by convective episode upstream (e.g. over leads) that are not accessible to local observations. Furthermore, there can be several mechanisms that induce the same situation e.g. a temperature profile that could be associated with a stable surface inversion, which in polar regions develops regularly under calm conditions due to surface cooling, could also be the result of warmer air being advected over colder air (Anderson and Neff, 2008).

Anderson and Neff (2008) identify five boundary layer types that can occur in polar regions.

- Neutral
  In this situation, there is neither convective nor stable temperature stratification ($\frac{\partial\theta}{\partial z} = 0$), hence buoyancy has no influence on turbulence and the mixing layer height h_z is only determined by upwind and local wind conditions. Above the boundary layer, the air is flowing along isobars balancing the local pressure gradient and the *Coriolis* force (geostrophic wind). Closer to the ground, surface friction modifies the flow creating the *Ekman* spiral (for details see Anderson and Neff, 2008; Roedel and T. Wagner, 2011). In this case, the top of the boundary layer is where the turbulence is close to zero and the wind direction is geostrophic.

- Convective
  When the temperature of the surface air layer exceeds that of the overlying air, convection occurs. This situation can be induced by absorption of short-wave radiation by the surface, an imbalance in long-wave radiation (e.g. when cloud covers prevent a radiative cooling of the surface), or when cold air is advected over a warm surface. In polar regions, it is mostly observed in summer when insolation peaks (see overview of radiation balance at NM III in Fig. 6.1). Air rises in thin plumes until it reaches thermal equilibrium with the surrounding atmosphere. For parametrisations of the mixing layer height h_z in this case, refer to Anderson and Neff (2008) and references therein.

- Moderately stable
  Most of the year, the polar boundary layer is stable - induced by a surface cooling due to small or absent energy uptake through absorption of short wave radiation (high surface albedos) and by radiative cooling through long wave radiation, which is facilitated by small water vapour concentrations in the atmosphere (see overview of radiation balance at NM III in Fig. 6.1). In contrast to the convective boundary layer, where the convection-driving temperature differences can disappear when convective mixing is too strong, for a stable boundary layer the stratification acts as a restoring force limiting vertical mixing by wind shear induced turbulence and hence energy transport to the surface. The balance between these two competing mechanisms can be expressed with the dimensionless *Richardson* number.

$$Ri = \frac{\frac{g}{T}\frac{\mathrm{d}\theta}{\mathrm{d}z}}{\left(\left(\frac{\mathrm{d}u}{\mathrm{d}z}\right)^2 + \left(\frac{\mathrm{d}v}{\mathrm{d}z}\right)^2\right)} \tag{2.3}$$

  where the numerator represents the influence of buoyancy and the denominator wind shear generated turbulence. g is the gravitational constant, T the absolute temperature, and u and v are the horizontal wind components. When Ri falls below 0.25, wind shear overcomes buoyancy and turbulence develops (Anderson and Neff, 2008). Based on this, the mixing layer height is defined as where this threshold is exceeded.

- Complex stable
  When wind speeds in a stable boundary layer are low enough, shear induced turbulence can be suppressed locally. This develops complex vertical structures that are still not well understood. This boundary layer type often occurs over flat terrain such as the ice shelf at NM III.

- Influenced by polynia or marginal ice zone
  This boundary layer type is the result of stable air advected over a warm surface, which induces convective mixing. This can occur over limited areas of open water in the sea ice zone (leads or polynias) in which case, the air can re-cool over ice surfaces downwind resulting in a residual well mixed layer in a section of a vertical profile of a proxy (e.g. θ). In the marginal ice zone, this type constitutes a transition boundary layer between the sea ice region with cold surfaces and the relatively warm open ocean.

Measurements in the boundary layer

Knowledge about the vertical structure, as well as vertical and horizontal dynamics of the boundary layer is important for the interpretation of trace gas mixing ratio time series measured close to the surface (Anderson and Neff, 2008). The temporal variation of the concentration C of a reactive species at a fixed height can be described by:

$$\frac{\mathrm{d}C}{\mathrm{d}t} = u \cdot \nabla C + \frac{\partial F}{\partial z} + P(t) - L(t) = u \cdot \nabla C + \frac{\partial}{\partial z}\left((K(z) + D)\frac{\partial C}{\partial z}\right) + P(t) - L(t) \quad (2.4)$$

where u is wind speed, F the vertical flux of C, $K(z)$ is the turbulent diffusivity and D the molecular diffusivity, which close to the surface becomes the dominant transport process. $P(t)$ and $L(t)$ are production and loss terms respectively. The expression states that the temporal variation of the observed concentration with time is the result of the advection of the spatial distribution of the species past the point of measurement, the flux divergence at the point of measurement (influenced by mixing), and, for a reactive species, production and loss.

The flux divergence can be reformulated with the definition of the flux as the product of the turbulent diffusivity and the vertical concentration gradient (see Anderson and Neff, 2008; Roedel and T. Wagner, 2011). If conditions allow the assumption that the distribution of C is horizontally homogeneous, which might be the case over the flat ice shelf at NM III (Anderson and Neff, 2008), the advection term might be neglected. The turbulent diffusivity can be measured (e.g. with sonic anemometers Neff et al., 2008) or estimated (e.g. A. E. Jones et al., 2001). To determine the vertical concentration gradient, contemporaneous (point) measurements at two altitudes are necessary.

There are several studies from Antarctica that report an anti-correlation between the mixing layer height h_z and the surface concentration of short-lived trace gas species (e.g. NO_x, respectively NO; Davis et al., 2004; Neff et al., 2008). The variations of C are then explained by the interplay of a surface production and the variable, low mixing height whose changes cause a variation of the available volume into which the trace gas is emitted. Whether this is the case strongly depends on the chemistry of the species with respect to source (only surface or additionally aerosols) and further fate (only decay or recycling mechanisms in the atmosphere). Anderson and Bauguitte (2007) argue that for very short lived gases with a pure surface source, the concentration can be independent of the depth of the boundary layer. Another situation where this correlation might not exist, is the advection of an airmass with different composition over the measurement site as discussed in e.g. Hausmann and Platt (1994), A. E. Jones et al. (2006), and Bottenheim and E. Chan (2006).

Transport from mid-latitudes

For atmospheric composition at a given (measurement) location, the influence of local and regional processes, and long range transport can vary. Due to their fundamental difference in terms of geography (see Sec. 2.1.1), Arctic and Antarctic experience a distinct difference in long-range transport from lower latitudes. For the Antarctic, the Southern ocean and efficient deposition removal in the circumpolar low pressure trough (see analysis of atmospheric conditions at NM III in Sec. 6.2 below) lead to a very reduced influence of continental and anthropogenic trace constituents and make the Antarctic troposphere very pristine (Chambers et al., 2018).

Both model studies (e.g. Stohl and Sodemann, 2010), and the analysis of proxies for terrestrial influence like ^{222}Rn (Chambers et al., 2018) show the relative isolation of the Antarctic troposphere. Transport to the continent occurs either by synoptic transport in the marine boundary layer or by subsiding tropospheric air that experienced continental influence upstream. Over the Antarctic plateau, another source of 'exterior' air can be intrusions of stratospheric air. Stohl and Sodemann (2010) find the probability of this occurring (up to 2% for 10 day periods) an order of magnitude higher at the South pole compared to coastal regions of Antarctica and the North pole.

For different regions of Antarctica they calculated the potential emission sensitivity (PES) of the boundary layer, i.e. the footprint area from where emissions could influence a point in the Antarctic boundary layer if removal processes on the way are not considered. They find a strong decrease in the PES field with increasing distance from the continent. Comparing Antarctic and Arctic, the influence of South America, Africa, and Australia on Antarctica is 1-2 orders of magnitude smaller than that of Eurasia and North America on the Arctic. The (small) influence of long-range transport from continental regions to Antarctica exhibits an annual cycle and is higher in winter than in summer. Similar results based on ^{222}Rn activity were found by Chambers et al. (2018).

The analysis of ^{222}Rn at NM III by Weller et al. (2014) gave somewhat inconclusive results. Proxy activity here is more dominated by local sources and tropospheric subsidence events than by long-range transport through the marine boundary layer. High wind speed episodes, for which long-range transport could be expected, were not linked to high proxy activity. As local source, open ocean emissions were identified. Weller et al. (2014) conclude that the annual ^{222}Rn cycle is clearly modulated by sea ice extent with a maximum proxy activity in February when sea ice reaches its minimum (see Sec. 2.2.1). A clear annual cycle of transport regimes, however, could not be identified which is agreement with König-Langlo et al. (1998) who find no general transport patterns for the troposphere at NM III except for the episodic influence of cyclones. A model based investigation of the catchment area of air masses arriving at NM III by Kottmeier and Fay (1998) identified the Southern ocean and the South Atlantic south of 50° S and in a sector from 60° W (north of the Falklands) to 30° E (about half way between South Africa and the Antarctic continent) as the main source region of air masses.

Aerosols

Aerosols are a suspension of fine solid or liquid particles in a gas (Seinfeld and Pandis, 2016). Globally, there is a wide variety of aerosol formation processes which is reflected in a great variation in size and composition. Typical aerosol diameters reach from around 10 nm up to 10 µm. Particles below 1 µm in diameter can have concentrations of several thousands per cm^{-3}, bigger particles are only found at concentrations of below 1 cm^{-3} (Seinfeld and Pandis, 2016). For chemical processes, aerosols are potentially important due to the high surface area they provide as a source and sink for trace gases, or for heterogeneous reactions.

In the atmosphere, aerosols evolve through a number of processes. Especially when particles are small they can coagulate within hours (Roedel and T. Wagner, 2011) with medium-sized particles forming larger ones. Interaction with the atmosphere can lead to size changes by condensation or evaporation of vapours. In clouds, aerosols can be processed (e.g. through uptake by ice particles or cloud droplets where they can act as ice nucleation particles - see Sec. 2.2.1). For halogen chemistry, multi-phase surface reactions on aerosols play an important role (Simpson et al., 2007; Abbatt et al., 2012).

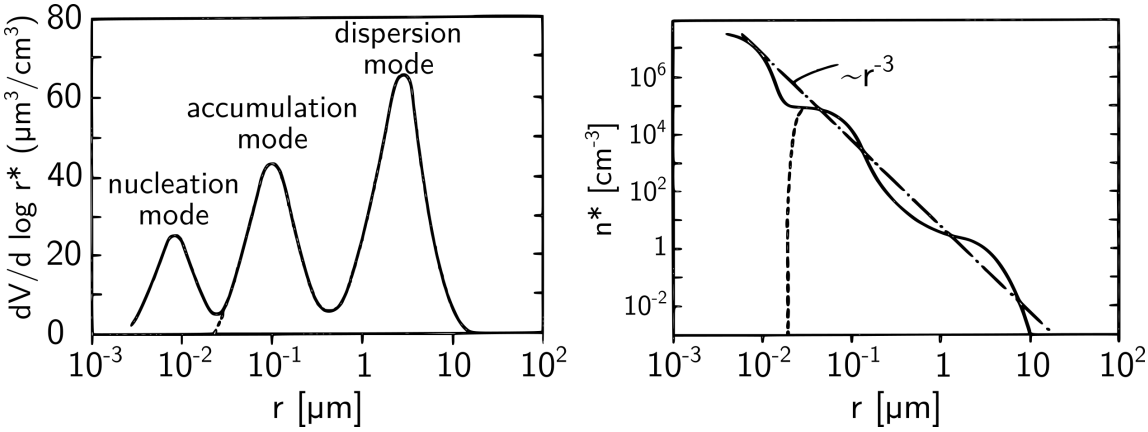

Figure 2.6: Volume and number distributions of atmospheric aerosols as a function of radius r. The left panel shows a tri-modal distribution of the aerosol volume per logarithmic radius interval. The right panel is a number density spectrum. Please note that a lognormal number density (n*=dN(r)/dlog r*) and with r* being a logarithmic radius interval is used. Since particles in the nucleation mode age rather quickly, this mode might not always be present. Then distributions follow the dashed lines. (adapted and translated from Roedel and T. Wagner, 2011, with permission from Springer Nature, 2019)

In general, aerosols can be attributed to three distinct modes (with respect to size and volume): (1) the nucleation mode - small particles that form from condensation of trace gases (secondary aerosols), (2) the dispersion mode - particles that were directly emitted (e.g. dust from the surface). Most ageing processes quickly increase the size of nucleation mode aerosols through condensation growth or coagulation leading to an intermediate accumulation mode (3). Exemplary distributions of all three modes as a function of number densities and volume are depicted in Fig. 2.6.

The pristine conditions of the Antarctic troposphere discussed in the previous section lead to a limited variability of aerosol origin and composition with the Southern ocean dominating the aerosol body (Weller et al., 2008). Hence biogenic sulphur from ocean emission and sea salt are the most important components. Analysis of aerosol composition

at NM III shows a distinct annual cycle of sea salt aerosols (determined from sodium ion concentrations) with a maximum contribution to aerosol composition (in weight percent) around 90% from April to October and about 50% between November and March. Non sea salt sulphate (nss-SO^{4-}) and methane sulphonate ($CH_3O_3S^-$) have a mirrored annual cycle that peaks at 36% in summer and falls to less than 6% in winter. Mineral dust accounts for 2 to 5% with no distinct annual cycle (Weller et al., 2008). The annual cycle of condensation particles (diameter > 3 nm) exhibits a maximum at around 800 cm^{-3} in February and a minimum around 100 cm^{-3} in July (Weller et al., 2011a).

The dominating sea salt aerosol generally is produced by bubble bursting over the ocean where evaporation of small water droplets leaves sea salt superseded in the atmosphere (cf. Roedel and T. Wagner, 2011). This aerosol production is increased by high surface wind speeds over the ocean. In polar regions, an alternative source of sea salt aerosols can be salty sea ice surfaces e.g. from erosion of so called *frost flowers* (Rankin et al., 2002) or salty snow on ice (Yang et al., 2008). Due to a fractionation effect in the highly concentrated brine layer at the surface of sea ice at temperatures below -8 °C (Jourdain et al., 2008), the sulphate to sodium ratio from sea salt aerosols originating from ice surfaces changes compared to ocean water (from about 0.25 to 0.07 through the precipitation of mirabilite - $Na_2SO_4{\cdot}H_2O$). This allows to analyse the source surface of sea salt aerosols. At NM III however, Weller et al. (2011b) could not identify a clear association of sea salt aerosol signature with the extent of sea ice around Antarctica and hence a clear attribution of aerosol source regions and surfaces throughout the year is not possible.

2.2.3 Atmosphere - cryosphere interactions

Cryosphere and atmosphere are a closely coupled system where the cryosphere is not merely a 'cap' that inhibits exchange of energy and mass between the surface and the atmosphere or acts as a sink for atmospheric species (Grannas et al., 2007). Processes in or on ice crystals rather have a major influence on the overlying atmosphere and depend on exchange between the two compartments. For this, the following two phenomena are particularly relevant.

Wind pumping

Wind pumping is the increased flow of air through surface snow crossing the snow-atmosphere boundary Anderson and Neff (2008). It can be induced by (a) pressure fluctuations around exposed surface features such as sastrugi (wave-like structures in the snow surface created by erosion and deposition of snow), (b) atmospheric internal gravity waves, and (c) by turbulence. Depending on snow properties such as porosity and permeability (see previous section), this can shorten air exchange times and increase snow-atmosphere interactions (both for release and deposition of trace species).

Drifting and blowing snow

When wind speeds are high enough, the shear stress of the wind can overcome gravitational and cohesive forces of snow particles and lift them into the air (Leonard et al., 2012). Depending on the wind speed, snow can be transported in a saltation mode with a vertical extent lower than 2 m, which is referred to as *drifting snow* (J. Turner and Pendlebury, 2004), or suspended in the lower atmosphere, which is called *blowing snow*. In the latter case, snow particles can reach altitudes of several hundred metres.

Threshold wind speeds for both phenomena strongly depend on snow availability and structure (size of grains and snow density), snow metamorphism rates, as well as the availability of liquid water inside the snow (Li and Pomeroy, 1997). The strong variability of environmental conditions in Antarctica means that these properties can be variable and have a distinct annual cycle (Amory et al., 2017).

For the onset of drifting snow in spring, Leonard et al. (2012) e.g. found threshold wind speeds at 10 m altitude between 5.6 - 7.2 $\mathrm{m\,s^{-1}}$. Li and Pomeroy (1997) report values between 4 - 11 $\mathrm{m\,s^{-1}}$ for dry snow and 7 - 14 $\mathrm{m\,s^{-1}}$ for wet snow, and König-Langlo and Loose (2007) report 6 - 12 $\mathrm{m\,s^{-1}}$ for NM III. Based on continuous ceilometer observations, blowing snow conditions at NM III are observed 36% of the time throughout the year with an inter-annual variability of 5% (Gossart et al., 2017). In line with that, König-Langlo and Loose (2007) report frequencies for drifting snow of 20% and blowing snow in another 20% of the time as observed on a three-hourly basis by the station meteorologists. The highest frequencies of drifting or blowing snow are attained in winter and early spring with close to 50% and a minimum of around 30% is reached in late summer.

Compared to surface snow, blowing snow potentially has an even larger surface area and particles are much better aspirated which leads to a faster equilibrium of their surfaces with the atmosphere (Anderson and Neff, 2008). With respect to halogen chemistry, release of reactive species during blowing episodes is reported to be an important mechanism leading to elevated mixing ratios of bromine monoxide in the boundary layer (A. E. Jones et al., 2009; Yang et al., 2008; Yang et al., 2010) in addition to the release under stable atmospheric conditions (see Sec 2.3).

2.3 Chemistry of the Polar boundary layer

As discussed in Sec. 2.2.2, the boundary layers in the Arctic and Antarctica, albeit both pristine compared to mid-latitudes, are different regarding the importance of lower latitude influence due to the distinct geographic characteristics of the two regions and the distance from the main sources of anthropogenic and natural pollutant emissions (e.g. from forest fires). The Arctic is subject to regular pollution episodes known as *Arctic haze* (see also Sec. 2.5.6) that, in addition to sulfate, particulate organic matter, or dust, contains the ozone precursors NO_x and VOCs (Law and Stohl, 2007).

Since observations for this work were only done in the Antarctic, the following discussion of boundary layer chemical processes will focus on very pristine Antarctica that can serve as a backdrop against which additional processes occurring in the Arctic can be compared. For discussions of the effects of pollutant export to the Arctic refer to e.g. Klonecki et al. (2003), Law and Stohl (2007), and Vinogradova and Ivanova (2018). Details on the influence of sub-arctic tundra and boreal forests are discussed e.g. in Myhre et al. (2007).

2.3.1 Atmospheric oxidation capacity and the role of radicals

Radicals are defined as molecular entities that posses an unpaired electron (Nič et al., 2009).[5] Their energetically unfavourable configuration makes them highly reactive and their abundance makes Earth's atmosphere oxidising (A. M. Thompson, 1992). Radicals react with most natural and anthropogenic pollutants causing their degradation and removal from the atmosphere. The most abundant oxidants, O_2 and O_3, have large bond strengths and only react with certain free radicals (Seinfeld and Pandis, 2016) examples of which will be discussed in 2.4.1 and 2.5.1.

Therefore globally, the photochemically produced hydroxyl radical (OH) is the primary oxidizing species (A. M. Thompson, 1992). Closely linked to OH is the hydroperoxyl radical HO_2 and collectively, both are referred to as HO_x. Other relevant radicals are organic peroxy radicals (RO_2), hydrogen peroxide (H_2O_2) or nitrogen oxides (NO, NO_2,NO_3) (Brasseur et al., 2003). The abundance and oxidative strength of the different radicals determine the 'oxidizing capacity' of the atmosphere (A. M. Thompson, 1992).

Sources and sinks of hydroxyl radicals

HO_x in the troposphere is primarily formed through photolysis of ozone followed by a reaction with water:

$$O_3 + h\nu \longrightarrow O_2 + O(^1D) \quad \text{(R 1)}$$

$$O(^1D) + H_2O \longrightarrow OH + OH \quad \text{(R 2)}$$

The photolysis of ozone (1) requires radiation with wavelengths of 300-320 nm or below. Since these wavelengths are strongly absorbed by the stratospheric ozone layer, the photolysis rate in turn depends on the amount of ozone in the atmosphere above and the path of the radiation through it, which is mainly determined by the SZA. Further reaction of OH with O_3 then yields HO_2 that in turn can react to H_2O_2:

$$OH + O_3 \longrightarrow HO_2 + O_2 \quad \text{(R 3)}$$

$$HO_2 + HO_2 \longrightarrow H_2O_2 + O_2 \quad \text{(R 4)}$$

OH then can be restored by reaction of HO_2 with NO or O_3 or photolysis of H_2O_2:

$$HO_2 + NO \longrightarrow OH + NO_2 \quad \text{(R 5)}$$

$$H_2O_2 + h\nu \longrightarrow OH + OH \quad \text{(R 6)}$$

$$HO_2 + O_3 \longrightarrow OH + 2\,O_2 \quad \text{(R 7)}$$

For the global OH budget of today's troposphere, the relative importance of reactions (R 2) and (R 5) to (R 7) for OH formation was estimated to be 42 %, 28 %, 11 %, and 11 % respectively (L. T. Murray et al., 2014).

[5] The term 'free radical' that previously was used to indicate the difference from a radical, which was the term used for a substituent group bound to a molecular entity, according to the International Union of Pure and Applied Chemistry (IUPAC) nomenclature to date is obsolete having been replaced by the term 'radical'.

Important sinks for OH are reactions with carbon-containing compounds:

$$\mathrm{CO} + \mathrm{OH} \longrightarrow \mathrm{CO_2} + \mathrm{H} \tag{R 8}$$
$$\mathrm{CH_4} + \mathrm{OH} \longrightarrow \mathrm{CH_3} + \mathrm{H_2O} \tag{R 9}$$
$$\mathrm{CH_3OOH} + \mathrm{OH} \longrightarrow \mathrm{H_2O} + \mathrm{CH_3O_2} \tag{R 10}$$

Further sinks are reactions with $\mathrm{HO_x}$ or molecular hydrogen:

$$\mathrm{HO_2} + \mathrm{OH} \longrightarrow \mathrm{H_2O} + \mathrm{O_2} \tag{R 11}$$
$$\mathrm{H_2} + \mathrm{OH} \longrightarrow \mathrm{H_2O} + \mathrm{H} \tag{R 12}$$

Reactions (R 8) to (R 12) are estimated to constitute 41 %, 14 %, 6.9 %, 4.9 %, and 4.2 % of OH sinks with 34.3 % of OH removal originating from other reactions (L. T. Murray et al., 2014). For a detailed discussion of these reaction cycles under different atmospheric conditions, e.g. under the high NO_x concentrations of a polluted environment or during pre-industrial times refer to Seinfeld and Pandis (2016) or Brasseur et al. (2003).

2.3.2 Tropospheric ozone

The formation of tropospheric ozone that is at the start of the radical formation processes discussed above, is the result of an interplay of $\mathrm{HO_X}$, odd nitrogen molecules $\mathrm{NO_X}$ ($\mathrm{NO} + \mathrm{NO_2}$) and volatile organic compounds (VOCs) (Seinfeld and Pandis, 2016).

Ozone formation

Ozone can form when $\mathrm{NO_2}$ is photolysed ($\lambda < 424\,\mathrm{nm}$):

$$\mathrm{NO_2} + h\nu \longrightarrow \mathrm{NO} + \mathrm{O}(^3P) \tag{R 13}$$
$$\mathrm{O}(^3P) + \mathrm{O_2} + \mathrm{M} \longrightarrow \mathrm{O_3} + \mathrm{M} \tag{R 14}$$

where 'M' in (R 14) denotes an air molecule required for momentum conservation. Ozone however, can restore $\mathrm{NO_2}$ through reaction with NO leading to no net production of $\mathrm{O_3}$:

$$\mathrm{O_3} + \mathrm{NO} \longrightarrow \mathrm{O_2} + \mathrm{NO_2} \tag{R 15}$$

Depending on solar radiation and presence of the different trace gases, NO and $\mathrm{NO_2}$ will reach a steady state called the *Leighton* ratio (Leighton, 1961):

$$L := \frac{[\mathrm{NO}]}{[\mathrm{NO_2}]} = \frac{j_{\mathrm{NO_2}}}{k_{\mathrm{NO+O_3}}[\mathrm{O_3}]} \tag{2.5}$$

When hydrocarbons such as methane ($\mathrm{CH_4}$) or CO and $\mathrm{HO_x}$ radicals are present, (R 6) can be replaced by a reaction of NO with $\mathrm{HO_2}$ or $\mathrm{RO_2}$ (where R denotes a hydrocarbon chain; $\mathrm{RO_2}$ can be formed by the reaction of a VOC with OH):

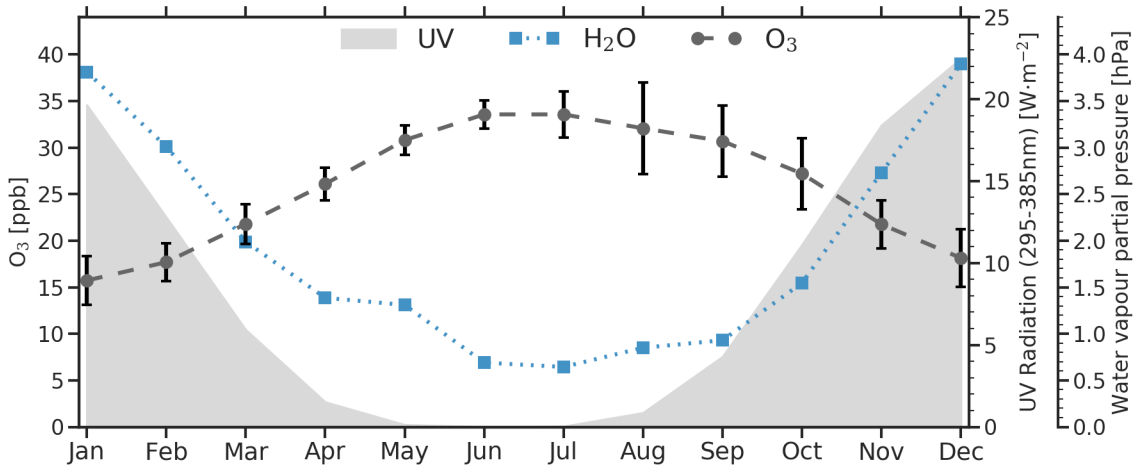

Figure 2.7: Monthly means of surface ozone mixing ratios at Neumayer III/Antarctica (cf. Sec. 4.1.3) including data from January 2016 until August 2018 (Weller, 2017; Weller, 2018a; Weller, 2019a). Error bars indicate the standard deviation. Radiation and water vapour partial pressure data are from NM III meteorological data (see Sec. 4.1.2 for complete list of references). The water vapour partial pressure was calculated according to W. Wagner and Pruß (2002).

$$\mathrm{OH} + \mathrm{RO_2} \longrightarrow \mathrm{HO_2} + \mathrm{RO} \qquad \text{(R 16)}$$

$$\mathrm{HO_2} + \mathrm{NO} \longrightarrow \mathrm{OH} + \mathrm{NO_2} \qquad \text{(R 17)}$$

This leads to a net production of ozone as long as sunlight and VOCs are available. When VOCs and NO_x are present in very high concentrations (as primary pollutants) - in urban environments e.g. from internal combustion engines where NO_x is the result of high temperatures and VOCs of incomplete combustion (Seinfeld and Pandis, 2016), ozone can be produced in high concentrations as a secondary pollutant - a phenomenon known as photochemical or Los Angeles smog (a blend of 'smoke' and 'fog').

The annual ozone cycle in Antarctica

Surface ozone mixing ratios in coastal Antarctica exhibit a very pronounced annual cycle. Figure 2.7 shows the monthly means and associated variations from NM III for the observation period covered in this thesis (the high resolution ozone mixing ratios containing the strong short term variations caused by halogen chemistry are shown in Fig. 6.10 (2017), data for 2016 and the part of 2018 considered in this thesis can be found in Chapter D in the appendix in Fig. D.30 and Fig. D.31). The highest values are reached in June-August and seasonal minima in December-February. The peak-to-peak amplitude is in the order of 20 ppb. This annual cycle has highest mixing ratios around 35 ppb and minima around 15 ppb (excluding short-term depletions) and is comparable to other coastal stations in Antarctica such as Halley VI or McMurdo (Helmig et al., 2007).

In comparison to the global scale, the lowest ozone mixing ratios are found in the remote marine boundary layer (e.g. 8-19 ppb at Samoa; Oltmans, 1981). Land masses on the other hand increase the potential for ozone formation. Background mixing ratios for low

altitude continental sites have been reported to be between 14-43 ppb (Vingarzan, 2004; Helmig et al., 2007). and is the result of different aspects of the Polar regions and its tropospheric chemistry.Levels at coastal polar stations therefore fall between purely marine and continental conditions.

The annual O_3 cycle at NM III is the result of different aspects of the Polar regions and its tropospheric chemistry. In clean air masses only small amounts of ozone precursors are available and sources are hence weak. Photolysis and subsequent reaction with water (reactions R 1 and R 2), and the reaction with OH radicals (R 3) are the most important ozone sinks. In higher latitudes, the importance of ozone photolysis (R 1) and formation of hydroxyl radicals through reaction with water (R 2) decreases because of the limited availability of radiation which strongly depends on SZA (see 2.1.2) and because colder air masses can only hold smaller concentrations of water vapour.

During the winter months, therefore the life time of ozone in Polar regions is the longest anywhere on Earth and can reach up to 100 days (Helmig et al., 2007). Increased photolysis during summer months leads to the annual minimum values during this time. In addition to the overall annual cycle, local variations in ozone mixing ratios are the result of synoptic transport, mixing of air masses from free troposphere (higher ozone than surface air for remote regions) and stratospheric intrusions, and natural photochemical processes in the boundary layer (Helmig et al., 2007; Legrand et al., 2016). The increased variation of ozone mixing ratios between July and November that is apparent in Fig. 2.7, is the result of halogen chemsitry and mechanisms are discussed in Sec. 2.4.1 below.

2.3.3 Nitrogen chemistry over snow

As discussed in Sec. 2.2.1, snow can be an efficient reactor releasing trace gases into the boundary layer. Relevant to ozone mixing ratios is the photolysis of nitrate deposited to snow that leads to elevated mixing ratios of NO_x and HONO in interstitial air of snow packs (Honrath et al., 1999; A. E. Jones et al., 1999; A. E. Jones et al., 2000) and to net fluxes into the boundary layer (A. E. Jones et al., 2001). The source of nitrogen compounds is photolysis ($\lambda < 345$ nm) of nitrate and nitrite originating from stratospheric air that subsequently have been deposited on the surface of snow grains. From there release into the gas phase via the following reactions (Grannas et al., 2007, and references therein): Reactions include:

$$NO_3^- + h\nu \xrightarrow{\text{aq}} NO_2 + O^- \quad \text{(R 18)}$$

$$NO_3^- + h\nu \xrightarrow{\text{aq}} NO_2^- + O(^3P) \quad \text{(R 19)}$$

The formation of NO_2 is favoured over that of nitrite by a factor of about 8 to 9. Nitrite that is formed can be photolysed in a further reaction forming NO:

$$NO_2^- + h\nu \xrightarrow{\text{aq}} NO + O^- \quad \text{(R 20)}$$

Nitrous acid can be formed either on the ice surface (R 21) and subsequently released to the gas phase.

$$NO_2^- + H^+ \xrightarrow{\text{aq}} HONO \quad \text{(R 21)}$$

The production of NO_x and HONO is driven by the annual cycle of insolation (R 18 to R 20). Isotopic analysis suggests that the origin of NO_3^- on the snow surfaces is stratospheric

NO_3^- that undergoes photochemistry in the troposphere before being deposited (Grannas et al., 2007). Highest mixing ratios of nitrogen compounds are found during summer at the South Pole with NO levels of up to 100 ppt (NO_x was calculated to be up to 330 ppt) (Davis et al., 2004). On ice shelves (NM III and Halley VI), considerably smaller mixing ratios, the lowest observed over ice covered surfaces, are present with peak NOx levels of a few 10 ppt (20-30 ppt of NO_2 and 10-15 ppt NO in air above the snow A. E. Jones et al., 1999; A. E. Jones et al., 2000; A. E. Jones et al., 2001). The difference in NO_x production between the interior of the Antarctic continent and the coast can be explained by longer insolation during summer and a higher probability of stratospheric air intrusions at the South Pole (see Sec. 2.2.2) and with it the advection of nitrate (NO_3). In the gas phase, this nitrogen species forms through reaction of NO_2 with ambient ozone and can react further to Dinitrogen pentaoxide (N_2O_5), which are both photolabile and potential night-time reservoirs of NO_x.

$$NO_2 + O_3 \longrightarrow NO_3 + O_3 \quad \text{(R 22)}$$

$$NO_2 + NO_3 + M \longrightarrow N_2O_5 + M \quad \text{(R 23)}$$

Higher NO_x mixing ratios usually lead to an increased O_3 production (R 13 and R 14 with reaction partners for R 16 being H_2O_2, CH_2O and CH_4, Helmig et al., 2008) and consequentially air masses arriving from the Antarctic plateau in summer are associated with higher ozone mixing ratios (Masclin et al., 2013; Legrand et al., 2016).

2.4 Halogens in the polar troposphere

Halogens are the elements of the seventh main chemical group in the periodic table. Naturally occurring are fluorine (F), chlorine (Cl), bromine (Br), and iodine (I). For tropospheric chemistry, only chlorine, bromine, and iodine are of importance. The hydrogen halide of fluorine (HF) has the highest bond strength of all halogens. It has a very long life time in the troposphere and therefore is not involved in chemical reactions here (in contrast to the stratosphere D. Jacob, 1999).

The chemistry of halogens in the troposphere became a focus of research in the mid-1980s when, shortly after the discovery of the Antarctic ozone hole in the stratosphere (Farman et al., 1985), from the high Arctic episodes of a virtually complete absence of tropospheric ozone were reported (Oltmans and Komhyr, 1986; Bottenheim et al., 1986). These episodes were termed Ozone Depletion Events (ODEs). An example for such an event during the observation period of this work can be found in Fig. 2.8.

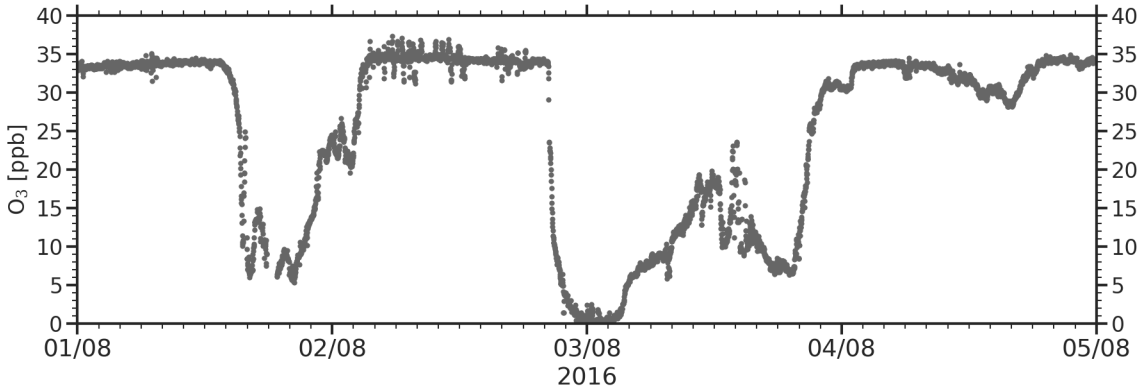

Figure 2.8: An ozone depletion episode at NM III. Data from the ozone monitor (Weller, 2017).

The influence of halogens on the stratosphere had been intensely studied in the previous decade even leading to a joint Nobel Prize in Chemistry in 1995 for Crutzen, Molina and Rowland (Crutzen, 1974; Molina and Rowland, 1974) for the explanation of stratospheric ozone depletion mechanisms; the role of halogens in the troposphere, however, was unclear. In the late 1980s Barrie et al. (1988) and Oltmans et al. (1989) reported an anti-correlation of ozone mixing ratios and 'filterable bromine' and a catalytic destruction mechanism involving Br and BrO (bromine monoxide) was proposed (e.g Barrie et al., 1988; Fan and D. J. Jacob, 1992; McConnell et al., 1992). Observations of BrO with a Long-Path DOAS then confirmed its role in ozone depletion (Hausmann and Platt, 1994; Hönninger and Platt, 2002) and Jobson et al. (1994) indirectly could infer an influence of chlorine. In the Antarctic, ODEs first were reported by Kreher et al. (1996) and Kreher et al. (1997) who also confirmed a presence of BrO (Kreher et al., 1996) and an intense research activity ensued.

Reviews summarising the respective state of knowledge exist by Platt (2000), Platt and Hönninger (2003), von Glasow and Crutzen (2003), Saiz-Lopez and von Glasow (2012), and Simpson et al. (2015). Articles specifically focussing on the polar troposphere were written by Simpson et al. (2007) and Abbatt et al. (2012); halogen chemistry is also covered in reviews on ice surface chemistry by Grannas et al. (2007) and Bartels-Rausch et al. (2014).

2.4.1 Halogen radical chemistry

The pivotal role of halogen chemistry in the polar troposphere has been underlined by numerous studies (e.g. Barrie et al., 1988; Finlayson-Pitts et al., 1990; Le Bras and Platt, 1995; Hönninger and Platt, 2002; A. E. Jones et al., 2009; Yang et al., 2010; Toyota et al., 2011; Cao et al., 2014; C. R. Thompson et al., 2015; Cao et al., 2016a). The partitioning of other species like that of NO_x also cannot be explained without considering halogen chemistry (Bauguitte et al., 2012). Based on the reviews by Simpson et al. (2007), Saiz-Lopez and von Glasow (2012), and Simpson et al. (2015), this section will give an overview of general reaction pathways halogens can undergo in the polar troposphere, and discuss release and removal mechanisms.

Photolytic properties

The absorption cross-sections of dihalogens are in the near-UV to VIS spectral range - peak absorptions around 300 nm (F_2), 330 nm (Cl_2), 415 nm (Br_2), and 530 nm (I_2). This leads to high photolysis rates in the troposphere resulting two halogen radicals (where X stands for F, Cl, Br, or I):

$$X_2 + h\nu \longrightarrow 2\,X \qquad \text{(R 24)}$$

For the same radiation conditions (sun in the zenith, 300 DU (dobson unit) ozone column and a surface albedo of 0.1), Tie (2003) calculated photolysis rates for dihalogens to be $0.0022\,s^{-1}$ (Cl_2), $0.032\,s^{-1}$ (Br_2), and $0.15\,s^{-1}$ (I_2) respectively which is about 50 (Cl_2) to more than 3000 (I_2) times that of the ozone photolysis (R 1) under the same conditions ($0.000045\,s^{-1}$). Due to the influence of ozone layer and the high SZAs typical for polar regions (see Sec. 2.1.2), this difference and the importance of halogens here is further increased.

Interaction with other trace gases

Reactions of halogens with ozone form a halogen oxide and reduce ozone.

$$X + O_3 \longrightarrow XO + O_2 \qquad \text{(R 25)}$$

Competing reactions are those with hydrocarbons (the hydrocarbon chain is denoted with R) in which the halogen atoms abstract a hydrogen atom.

$$X + RH \longrightarrow HX + R^{\bullet} \qquad \text{(R 26)}$$

Bond strengths of hydrogen halides decrease from HF over HCl and HBr to HI. Fluorine is reactive enough to abstract hydrogen from water which, in the troposphere, prevents it from participating in catalytic chemistry (Simpson et al., 2015, and references therin). Since the bond strength of HCl is comparable to that of C-H bonds, chlorine atoms can react with hydrocarbons such as methane. Bromine and iodine are less reactive with respect to hydrocarbons. Bromine can react with aldehydes (e.g. with formaldehyde: $k=7.8 \cdot 10^{-13}\,cm^3 \cdot molec^{-1} \cdot s^{-1}$ at -20 °C, R. Atkinson et al., 2007) and all halogens with ozone (R 25). After reaction with ozone, halogen atom radicals can be restored through photolysis (R 27).

$$XO + h\nu \longrightarrow X + O(^3P) \qquad \text{(R 27)}$$

For bromine monoxide and iodine monoxide, reaction with ozone (R 25) and photolysis have comparable reaction constants leading to a null-cycle. The ratio between the halogen atom and its oxide is determined by the actinic flux and ozone mixing ratios. At typical ozone values, for bromine, BrO is favoured whereas for iodine, the ratio is about unity (Simpson et al., 2015, and references therin). Photolysis of ClO is about 3 (BrO) to respectively 4 (IO) orders of magnitude slower which prevents a similar null-cycle (C. R. Thompson et al., 2015).

In reactions (R 25) and (R 27), the resulting radical continues to be a halogen compound whereas (R 26) results in a hydrocarbon radical and the halogen in a reservoir species with long lifetime.

The hydrocarbon radical typically reacts with O_2 to form a RO_2 radical which, through rearrangements or reaction, can yield a HO_x radical (Simpson et al., 2015, and references therin).

Self and cross halogen reactions

Halogen oxides undergo self reactions, which are an important prerequisite for ozone destruction. Dominant pathways depend on the halogen (see R. Atkinson et al., 2007, for relative importance and reaction constants).

$$\mathrm{XO} + \mathrm{XO} \longrightarrow \mathrm{X_2} + \mathrm{O_2} \quad \text{(R 28)}$$
$$\longrightarrow \mathrm{X} + \mathrm{X} + \mathrm{O_2} \quad \text{(R 29)}$$
$$\longrightarrow \mathrm{OXO} + \mathrm{X} \quad \text{(R 30)}$$
$$+ \mathrm{M} \longrightarrow \mathrm{X_2O_2} + \mathrm{M} \quad \text{(R 31)}$$

During the day, these reactions directly (R 29, R 30) or after a photolytic step (R 28) yield halogen atoms. Also the halogen dioxides resulting from (R 30) are readily photolysed - peak absorption around 350 nm (OClO), 530 nm (OBrO), and 550 nm (OIO). Efficiency and further fate of the product of (R 31) depends on the the halogen species. For bromine, this reaction pathway is negligible ($k=8.8 \cdot 10^{-32}\,\mathrm{cm^3 \cdot molec^{-1} \cdot s^{-1}}$, R. Atkinson et al., 2007). In the troposphere, the chlorine product of (R 31), Cl_2O_2, is thermally decomposed back to two ClO radicals (Saiz-Lopez and von Glasow, 2012). The formation of I_2O_2, however, is exothermic and can start a polymerisation, which was linked to new particle formation in mid-latitude coastal regions (Hoffmann et al., 2001). Here, high IO mixing ratios of biogenic origin have been observed (e.g Seitz et al., 2009; Commane et al., 2011; Saiz-Lopez et al., 2012). Recently, however, the addition iodic acid (HIO_3) rather than iodine oxides has been observed to govern particle growth (Sipilä et al., 2016).

During the night, X_2 and OXO can serve as reservoirs for halogens. All self reactions in the medium term preserve radicals and the formation of halogen atoms via this pathway is important for ozone destruction (Simpson et al., 2015, , see also Sec. 2.4.2).

When multiple halogen species are present, in addition to the self reactions, cross halogen reactions can proceed. These are about an order of magnitude faster than self reactions

(Saiz-Lopez and von Glasow, 2012) and increase ozone destruction.

$$\begin{aligned} XO + YO &\longrightarrow XY + O_2 && \text{(R 32)} \\ &\longrightarrow X + Y + O_2 && \text{(R 33)} \\ &\longrightarrow OXO + Y && \text{(R 34)} \\ &\longrightarrow XOO + Y \text{ (for X=Cl, Y=Br)} && \text{(R 35)} \\ + M &\longrightarrow OXOY + M && \text{(R 36)} \end{aligned}$$

Details on the relative importance of the pathways for the different reactions can be found R. Atkinson et al. (2007). For reaction (R 34), in the BrO + IO reaction, the formation of OIO is favoured, when BrO and ClO react, the formation of chlorine dioxide and its short lived isomer chlorine peroxide (R 35) are favoured, and for the reaction of ClO + IO, OClO is favoured (R. Atkinson et al., 2007).

2.4.2 Ozone destruction

A net destruction of ozone (see Fig. 2.8) only occurs, when the reaction of a halogen atom with ozone (R 25) is not followed by an ozone restoring reaction (e.g. via photolysis of the halogen monoxide (R 27) or a halogen dioxide (R 30, R 34, or R 35) followed by a reaction of the resulting oxygen atom with molecular oxygen (R 14). Self or cross reactions that form two halogen atoms (R 29 or R 33) or a dihalogen (R 28 or R 32) lead to a net ozone destruction.

Due to higher reactivities, destruction rates are drastically increased by cross halogen reactions (Simpson et al., 2007, and references therin). Another series of ozone destroying reactions are those of a halogen atom with ozone (R 25), followed by the reaction of the halogen oxide with hydroperoxyle (R 37) and the reactions restoring both the halogen atom and the hydroperoxyle (R 24, R 39, and R 40) or by reaction with OH or NO_2 (R 37, R 38 and R41 to R 45)

2.4.3 Reactions with other radicals

Halogen radical mixing ratios can be decreased by reaction with the hydroperoxyle radical HO_2 the product of which, HOX, is another reservoir of halogens.

$$XO + HO_2 \longrightarrow HOX + O_2 \qquad \text{(R 37)}$$

Reactivation can occur via photolysis creating two radicals:

$$HOX + h\nu \longrightarrow X + OH \qquad \text{(R 38)}$$

When followed by further reactions of the hydroxyl radical, hydroperoxyle radical can be formed again.

$$\begin{aligned} OH + CO &\longrightarrow CO_2 + H && \text{(R 39)} \\ H + O_2 + M &\longrightarrow HO_2 && \text{(R 40)} \end{aligned}$$

2.4.4 Reactions with nitrogen compounds

As discussed in Sec. 2.3.3, despite the remote location of polar regions, nitrogen chemistry over snow and ice surfaces is not negligible. In the Arctic, additionally long-range transport from mid-latitudes (with anthropogenic as well as natural sources like forest fires) can contribute to the nitrogen budget (Stohl, 2006; Law and Stohl, 2007; Custard et al., 2015). Potential reactions of halogens compounds with nitrogen species include (Cao et al., 2014; Custard et al., 2015):

$$\mathrm{XO} + \mathrm{NO} \longrightarrow \mathrm{X} + \mathrm{NO_2} \quad \text{(R 41)}$$

$$\mathrm{X} + \mathrm{NO_2} + \mathrm{M} \longrightarrow \mathrm{XNO_2} + \mathrm{M} \quad \text{(R 42)}$$

$$\mathrm{XO} + \mathrm{NO_2} \longrightarrow \mathrm{XONO_2} \quad \text{(R 43)}$$

In the atmosphere, the halogen nitrite (R 42) and halogen nitrate (R 43) can be photolysed when radiation is available (lifetimes in the range of minutes to several hours depending on the halogen species - see e.g. C. R. Thompson et al., 2015).

$$\mathrm{XNO_2} + h\nu \longrightarrow \mathrm{X} + \mathrm{NO} \quad \text{(R 44)}$$

$$\mathrm{XONO_2} + h\nu \longrightarrow \mathrm{X} + \mathrm{NO_3} \quad \text{(R 45)}$$

$$\mathrm{NO_3} + h\nu + \mathrm{O_2} \longrightarrow \mathrm{NO_2} + \mathrm{O_3} \quad \text{(R 46)}$$

Otherwise they are halogen reservoir gases and also can be taken up by surfaces (snow, ice, aerosol):

$$\mathrm{XONO_2} \longrightarrow \mathrm{XONO_{2(aq)}} \quad \text{(R 47)}$$

$$\mathrm{XONO_{2(aq)}} + \mathrm{H_2O} \longrightarrow \mathrm{HOX} + \mathrm{HNO_3} \quad \text{(R 48)}$$

The formation of additional reservoir gases such as $\mathrm{XONO_2}$ was found to impede the destruction of ozone by halogens through the decrease of active halogens, in particular where high NO_x levels were present (Custard et al., 2015; Zielcke, 2015). The uptake of halogen nitrates by surfaces on the other hand, can lead to a reactivation of halogens through heterogeneous surface reactions and an increased ozone depletion as will be discussed in the following section (Cao et al., 2014). The critical parameter in this mechanism is the uptake rate onto surfaces.

2.4.5 Halogen release mechanisms

All reactions presented so far activate or deactivate halogens, and the uptake of reservoir species (e.g. HX, HOX, $\mathrm{XONO_2}$) by surfaces decreases the mixing ratios of halogen compounds in the gas phase. For the observed influence of halogens on the atmosphere (e.g. during ODEs) to occur, reaction mechanisms that increase mixing ratios of (active) halogens in the atmosphere are required.

Bromine explosion

One such release mechanism is a heterogeneous cycle of reactions that was proposed soon after the observation of ODEs (Fan and D. J. Jacob, 1992; McConnell et al., 1992; Abbatt, 1994; Abbatt, 1995). It follows the uptake of hypobromous acid (HOBr) by a halide containing surface.

$$\mathrm{HOBr} + \mathrm{Br^-} + \mathrm{H^+} \xrightarrow{\mathrm{mp}} \mathrm{Br_2} + \mathrm{H_2O} \quad \text{(R 49)}$$

$$\mathrm{Br_2} + h\nu \longrightarrow 2\,\mathrm{Br} \quad \text{(R 50)}$$

$$\mathrm{Br} + \mathrm{O_3} \longrightarrow \mathrm{BrO} + \mathrm{O_2} \quad \text{(R 51)}$$

$$\mathrm{BrO} + \mathrm{HO_2} \longrightarrow \mathrm{HOBr} + \mathrm{O_2} \quad \text{(R 52)}$$

$$\text{net: } \mathrm{Br^-} + \mathrm{H^+} + \mathrm{HO_2} + \mathrm{O_3} + h\nu \xrightarrow{\mathrm{mp}} \mathrm{Br} + \mathrm{H_2O} + 2\,\mathrm{O_2}$$

In the aqueous phase/on the ice surface (or QLL), HOBr reacts with bromide to form molecular bromine (Br_2) which subsequently degasses to the atmosphere (R 49). There it can be photolysed if sufficient radiation is available (R 50). The bromine atoms react with ozone (R 51) and the resulting bromine monoxide with hydroperoxyl (R 52).

In total, the active bromine compound that is removed from the atmosphere by uptake of HOBr leads to a release of up to two active bromine atoms. In the process, bromide and a proton (acidity) in the surface layer and hydroperoxyle and ozone in the atmosphere are consumed. When more than 50% of active bromine compounds go through this series of reactions, the stock of active bromine in the atmosphere increases exponentially. Therefore, this heterogeneous reaction cycle was named *bromine explosion* (Platt and Janssen, 1995; Platt and Lehrer, 1996; Wennberg, 1999). Heterogeneous reactions of the bromine explosion as well as other mechanisms discussed in the following are also sketched in the box in Fig. 2.9.

For such an "explosion" to occur, three important factors for a sustained halogen release and ozone depletion can be identified:

(1) For a bromine explosion to start, ozone is required, both as a direct reaction partner in the release cycle (R 51), and as a source of HO_x radicals from photolysis (R 1 to R 3).

(2) The heterogeneous and surface reaction steps require a surface with a sufficient halide density. As will be discussed in Sec. 2.4.7 below, ice surfaces seem to be particularly suited due to the properties of the QLL and a potential cryoconcentration of halides at the surface (see Sec. 2.2.1, Abbatt et al., 2012; Bartels-Rausch et al., 2014; Simpson et al., 2015). Furthermore, an acidic surface is beneficial (R 49).

(3) The consumption of ozone and hydroperoxyl in the bromine explosion directly implies that the release stops as soon as ozone is entirely depleted since it serves as the 'fuel' of the reaction cycle. Regarding hydroperoxyl, the reaction of halogen atoms with hydrocarbons (R 26) and the resulting formation of secondary HO_x from the hydrocarbon radical $R^{\cdot}$ supports the bromine release (Simpson et al., 2015, and references therin).

(4) Low pH. Laboratory studies, in which the source of halides in the surface phase was assumed to be sea salt, confirmed the mechanism for liquid (Fickert et al., 1999) and then ice surfaces (Huff and Abbatt, 2000; Huff and Abbatt, 2002; Adams et al., 2002).

When in addition to bromide, chloride was present, which in sea water has an abundance that is about 650 times that of bromide, an additional (intermediate) reaction sequence was observed (e.g. Wren et al., 2013):

$$\mathrm{HOBr} + \mathrm{Cl^-} + \mathrm{H^+} \xrightarrow{\mathrm{mp}} \mathrm{BrCl} + \mathrm{H_2O} \qquad \text{(R 53)}$$

$$\mathrm{BrCl} + \mathrm{Br^-} \overset{\mathrm{aq}}{\rightleftharpoons} \mathrm{Br_2Cl^-} \qquad \text{(R 54)}$$

$$\mathrm{Br_2Cl^-} \overset{\mathrm{aq}}{\rightleftharpoons} \mathrm{Br_2} + \mathrm{Cl^-} \qquad \text{(R 55)}$$

$$\text{net: } \mathrm{HOBr} + \mathrm{Br^-} + \mathrm{H^+} \xrightarrow{\mathrm{mp}} \mathrm{Br_2} + \mathrm{H_2O}$$

Due to the higher abundance of chloride in the surface layer, HOBr here initially reacts with Cl^- and forms BrCl (R 53). This can either degas leading to a bromine and chlorine release. However, BrCl has a higher polarity than Br_2 and hence is expected to stay longer on the surface (Adams et al., 2002). Therefore, unless bromide is not strongly depleted compared to chloride, a reaction of BrCl with bromide with an intermediate trihalogen state (R 54) and a subsequent release of Br_2 (R 55) is the preferred reaction pathway.

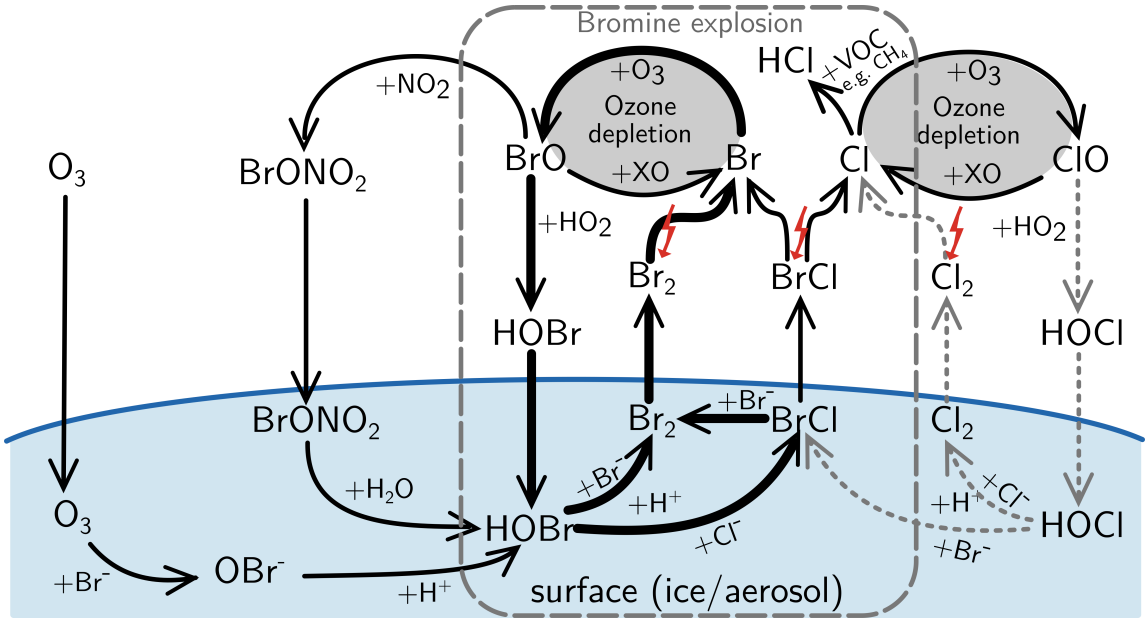

Figure 2.9: Reaction pathways of heterogeneous halogen release. The bromine explosion reactions are those inside the dashed-line box with bold arrows marking reactions that lead to an increase of bromine in the atmosphere. Photolysis is marked with a red arrow. Ozone depleting reaction cycles are highlighted in grey. Grey dotted arrows indicate reactions of chlorine equivalent to that of bromine as proposed in Wren et al. (2013). Due to the high reactivity of Cl with hydrocarbons this does not lead to an increase of active halogens in the gas phase (no chlorine explosion). On the left side, alternative pathways leading to formation of HOBr in the surface phase are shown (Oum et al., 1998b; Aguzzi and Rossi, 2002).

When indeed BrCl is released and photolysed, due to the high reactivity of chlorine with hydrocarbons (R 26) and the ubiquitous presence of e.g. methane, about 50% or more of chlorine reacts via this pathway (Platt et al., 2004; Simpson et al., 2015; C. R. Thompson

et al., 2015). Therefore, an equivalent 'explosion type' increase of reactive chlorine in the atmosphere is not expected. Nevertheless, laboratory studies with artificial snow (Wren et al., 2013) and field measurements (Custard et al., 2017) could detect a Cl_2 release and Liao et al. (2014) detected chlorine molecule mixing ratios of up to 400 ppt in the Arctic. Wren et al. (2013) conclude that a 'halogen explosion' explains their laboratory observations of Cl_2 (see reaction pathway sketched in grey in fig. 2.9). The atmospheric observations (Liao et al., 2014; Custard et al., 2017) resort to alternative release mechanisms for dihalogens that are discussed below.

Since iodine is a nutrient, it is consumed by the marine biosphere, and on the surfaces is not present in sufficient concentrations for a similar heterogeneous release to occur (Simpson et al., 2015, and references therin). Its sources and release mechanisms in polar regions are still unclear with one proposed being emission by under-ice algae similar to iodine chemistry observed in mid-latitude tidal zones (e.g. Commane et al., 2011). Observed mixing rations from ground and satellite, however, seem to require an inorganic source as typical fluxes of biogenic iodocarbons from the sea are not sufficient (Saiz-Lopez and von Glasow, 2012). A detailed discussion of this is beyond the scope of this chapter and the reader is referred to Saiz-Lopez and von Glasow (2012) and Saiz-Lopez et al. (2012).

Alternative release mechanisms

In addition to the heterogeneous reactions described above, there are a number of alternative pathways that might contribute to a release of dihalogens from surfaces. Most were proposed based on knowledge of stratospheric reaction pathways and many were only observed in controlled laboratory experiments. However, observations suggest, that a combination of mechanisms is required to explain halogen release occurring in the field (e.g. Pratt et al., 2013) - starting with the fact that a seed mixing ratio is required to start any release via the explosion mechanism.

Oum et al. (1998b) proposed a release via surface uptake of ozone. This mechanism recently was investigated by Artiglia et al. (2017) who confirmed it (with some clarification of the reactions dynamics). In contrast to the bromine explosion, this reaction does not require sunlight and hence could lead to a build-up of dihalogens during the night which are photolysed at sunrise.

$$O_3 \longrightarrow O_{3(aq)} \tag{R 56}$$

$$O_{3(aq)} + Br^- \xrightarrow{aq} OBr^- + O_2 \tag{R 57}$$

$$OBr^- + H^+ \xrightarrow{aq} HOBr \tag{R 58}$$

HOBr is then converted to Br_2 via reactions R 49 and R 50.

As already mentioned above, also the uptake of halogen nitrates can form HOBr in the surface layer.

$$BrONO_2 + H_2O \xrightarrow{aq} HOBr + HNO_3 \tag{R 45 revis.}$$

(R 59)

The subsequent release of dihalogens was first proposed by Aguzzi and Rossi (2002). Cao et al. (2014) showed in a modelling study that, if NO_x levels are not too high, this mechanism

can increase halogen release. Pratt et al. (2013) report it to contribute to the observed release of Br_2 in a field snow reaction chamber.

Both ozone uptake (R 56 to R 58), and $BrONO_2$ uptake (R 59 form HOBr in the surface layer. The release of bromine then follows the same steps as in the bromine explosion (see R 49 and R 52 or Fig. 2.9).

Another set of release pathways that does not lead to a formation of surface phase HOBr was proposed by George and Anastasio (2007) and Sjostedt and Abbatt (2008). It is initiated by a reaction of hydroxyl with a halide in the surface layer. Sjostedt and Abbatt (2008) initially investigated an uptake of OH. George and Anastasio (2007) and Abbatt et al. (2010) proposed a formation of OH within the surface layer through photolysis of a nitrate radical (NO_3^-),McConnell et al. (1992) through photolysis of a nitrite radical (NO_3^-) and George and Anastasio (2007) also used hydrogen peroxide (HOOH) in their samples. Once OH is present in the surface layer, a number of successive reactions leads to the formation of a dihalogen that passes into the gas phase. The following reactions can equally proceed for chlorine and a combination of both halogens (for details see Sjostedt and Abbatt, 2008)

$$OH + Br^- \overset{aq}{\rightleftharpoons} HOBr^- \quad (R\,60)$$

$$HOBr^- + H^+ \overset{aq}{\longrightarrow} Br + H_2O \quad (R\,61)$$

$$Br + Br^- \overset{aq}{\rightleftharpoons} {Br_2}^- \quad (R\,62)$$

$$2\,{Br_2}^- \overset{aq}{\longrightarrow} {Br_3}^- + Br^- \quad (R\,63)$$

$${Br_3}^- \overset{aq}{\longrightarrow} Br^- + Br_2 \quad (R\,64)$$

2.4.6 Overview of previous halogen observations

The number of available observations of tropospheric halogen chemistry depends on the species considered. This is due to constraints of the instrumentation with regard to the low detection limits necessary for trace gases with typical mixing ratios of a couple of ppt and high reactivities. For polar observations, the additional difficulties associated with measurement campaigns in remote regions with extreme environmental conditions have to be kept in mind. Table 2.1 shows selected results of ground-based polar observations with maximum mixing ratios for different species in both hemispheres, which might be compared to results of this thesis. For detailed lists of reported observations across all latitudes, refer to the review by Saiz-Lopez and von Glasow (2012). Additional observations, in particular from satellites, which cannot easily be compared to mixing ratios derived from ground-based instruments but give important insights into larger scale dynamics and importance of halogen release, will be briefly discussed in the following sections.

Halogen	Species		Location	max. mixing ratio [ppt]	Reference
Chlorine	ClO	Arc	Spitsbergen	39	Tuckermann et al. (1997)
			Alert	10	S. Wang and Pratt (2017)
		Ant	Scott Base	58	Zielcke (2015)
	OClO	Arc	Amundsen Gulf	24	Pöhler et al. (2010)
	Cl_2	Arc	Alert	400	Liao et al. (2014)
				20	S. Wang and Pratt (2017)
	BrCl	Arc	Alert	35	Foster (2001)
		Ant	Halley	6	Buys et al. (2013)
Bromine	BrO	Arc	Spitsbergen	30	Tuckermann et al. (1997)
			Amundsen Gulf	41	Pöhler et al. (2010)
			Utqiaġvik (Barrow)	36	Frieß et al. (2011)
			Greenland Summit	5	Stutz et al. (2011)
			Alert	30	S. Wang and Pratt (2017)
		Ant	Arrival Heights	30	Kreher et al. (1997)
			Neumayer	13*	Frieß et al. (2004)
			Halley	20	Saiz-Lopez et al. (2007a)
			Southern Ocean	50*	T. Wagner et al. (2007)
			Weddell sea	45	Zielcke (2015)
			Scott base	5	Zielcke (2015)
			Marambio	26	Prados-Roman et al. (2018)
			Belgrano	8	Prados-Roman et al. (2018)
	Br_2	Arc	Utqiaġvik (Barrow)	46	Liao et al. (2014)
			Alert	50	S. Wang and Pratt (2017)
		Ant	Halley	45	Buys et al. (2013)
	HOBr	Arc	Alert	260	G. Impey et al. (1999)
			Utqiaġvik (Barrow)	26	Liao et al. (2012)
Iodine	IO	Arc	Spitsbergen	<2.5**	Tuckermann et al. (1997)
			Hudson Bay	<1.5**	Hönninger et al. (2004)
			Hudson Bay	3.4	Mahajan et al. (2009)
			Alert	0.6	Zielcke (2015)
		Ant	Neumayer	10	Frieß et al. (2001) and Frieß et al. (2010)
			Halley	20	Saiz-Lopez et al. (2007a)
			Scott Base	0.7	Zielcke (2015)
			Weddell sea	0.6	Zielcke (2015)
	I_2	Ant	Weddell sea	12.4	H. M. Atkinson et al. (2012)

Table 2.1: Overview of selected observations of halogen species in polar regions. For a detailed overview please refer to Saiz-Lopez and von Glasow (2012). (*) These mixing ratios were determined from scattered light measurements and are based on assumptions about boundary layer structure and radiative transfer but were included here because of their observations location (at or on the way to NM III). (**) Values here indicate the level of detection.

Bromine

Among the three atmospherically relevant halogens, bromine species are the most observed and probably best understood. Except for a few early studies where a bromine signal was acquired on cellulose filters (Barrie et al., 1988) or gas chromatography was used (G. A. Impey et al., 1997), most reported observations either used optical techniques (in the majority of cases DOAS in one form or another, see Chapter 3) or Chemical Ionisation Mass Spectroscopy (CIMS). The latter technique is used both in field measurements (Liao et al., 2012; Buys et al., 2013; Pratt et al., 2013) where it yields point measurements (in contrast to most DOAS instruments) and in laboratory experiments (e.g. Abbatt et al., 2010; Wren et al., 2013). Even though the ionizing medium can limit the number of observable species, and, in particular for reactive trace gases, the influence of inlet and tubing of the mass spectrometer have to be considered carefully (Neuman et al., 2010; Liao et al., 2011), measurements with high sensitivities can be performed. Most reported observations of dihalogens are CIMS measurements with Br_2 values reported to be e.g. up to 46 ppt in Utqiaġvik(Barrow[6])/Alaska (Liao et al., 2012) or 45 ppt (Buys et al., 2013) at Halley/Antarctica. Equally, HOBr observations of 26 ppt at Utqiaġvik were observed with a CIMS (see tab. 2.1 for selected observations and Saiz-Lopez and von Glasow (2012) for a detailed overview).

The most comprehensive observation record of any bromine species is that of BrO (see Tab. 2.1 and Saiz-Lopez and von Glasow, 2012). Observations in both hemispheres range from a few ppt to peak values of around 30 to 45 ppt. In addition to ground based measurements with both DOAS and CIMS, BrO can be detected from airborne platforms (e.g. Peterson et al., 2017) and from satellite (e.g Platt and T. Wagner, 1998; A. Richter et al., 1998; Hollwedel et al., 2004; Schönhardt et al., 2012; Sihler et al., 2012). For instruments operating with scattered solar radiation (passive DOAS, see Chapter 3 for details), in many cases the reported quantity is a vertical column density. A conversion into mixing ratios that can be compared to ground-based measurements is not straight-forward and requires assumptions or knowledge about the radiative transport (see Sec. 4.3). Passive ground based instruments usually report tropospheric vertical columns that can be converted into (surface) mixing ratios with optimal estimation techniques (e.g. Frieß et al., 2004; T. Wagner et al., 2007, , see also short description in Sec. 4.3.2). Satellite observations typically indicate the total vertical BrO column, which includes a contribution from BrO in the stratosphere. Nevertheless, satellite maps of bromine monoxide enhancements (in the order of $1 \cdot 10^{14}$ molec·cm^{-2} over a background of $3 - 4 \cdot 10^{13}$ molec·cm^{-2}) allow to study the distribution and dynamics of air masses with active chemsitry on a regional scale and can give insight into the large scale impact of reactive halogens. Furthermore, methods exist to separate stratospheric and tropospheric BrO signals yielding tropospheric columns up to $5 \cdot 10^{13}$ molec·cm^{-2} (Sihler et al., 2012).

[6]The town was renamed in 2016 changing from Barrow to the Iñupiat name Utqiaġvik

Chlorine

Observational evidence of and hence knowledge about chlorine species in the polar troposphere is very limited. Indications of an involvement of halogen compounds in tropospheric halogen chemistry was reported early on (e.g. Jobson et al., 1994; Tuckermann et al., 1997) but there are only few direct detections of chlorine species. ClO absorption bands are below 300 nm, instruments that use scattered sunlight are not sensitive to it and OClO, which has absorption structures in the UV above 300 nm, is quickly photolysed. Tuckermann et al. (1997) report up to 30 ppt of ClO at Spitsbergen and Pöhler et al. (2010) could detect up to 24 ppt of OClO in the Amundsen Gulf in the Arctic. From the Antarctic, the only observation of ClO so far were up to 60 ppt at Scott base (Zielcke, 2015). CIMS measurements indicate an influence of chlorine chemistry in the Arctic with reported Cl_2 values from a few tens of ppt (Custard et al., 2017; S. Wang and Pratt, 2017) over about 90 ppt (C. R. Thompson et al., 2015) up to 400 ppt Liao et al. (2014). In Antarctica, Buys et al. (2013) reported BrCl mixing ratios up to 6 ppt. (X. Wang et al., 2018)

Iodine

For iodine in polar regions, there is an apparent disparity of observations between the hemispheres. In Antarctica, Frieß et al. (2001) first detected IO signals in zenith sky scattered light observations and attributed the IO presence to the boundary layer. Saiz-Lopez et al. (2007a) performed LP-DOAS measurements at Halley detecting average mixing ratios of 5 ppt with peaks up to 20 ppt during the sunlit period. From satellite observations, Saiz-Lopez et al. (2007b), Schönhardt et al. (2008), and Schönhardt et al. (2012) reported an IO signal both over the centre and coastal regions of the Antarctic continent with Weddell and Ross sea identified as 'hot spots' for iodine compounds. In another study, Frieß et al. (2010) deduced high mixing ratios of IO in interstitial air of the snowpack from measurements of light scattered by surface snow. During a ship-based campaign, H. M. Atkinson et al. (2012) detected high mixing ratios of I_2 which, however, could not be reconciled with a much lower IO presence. Zielcke (2015), however, investigated IO at Scott base at the edge of the Ross sea as well as during a cruise in the Weddell sea and could only detect mixing ratios of up to 0.5 ppt with occasional peaks of 1 ppt.

In the Arctic on the other hand, the only iodine observation above the detection limit is by Mahajan et al. (2009) with up to 3.4 ppt of IO in air masses originating from open leads in the sea ice. Neither Tuckermann et al. (1997) nor Pöhler et al. (2010) observed mixing ratios above their detection limits of 1-2.5 ppt and 0.3 to 2.5 ppt respectively. Zielcke (2015) detected an almost continuous presence of IO in data from Alert, Canada. Mixing ratios here were also around 0.5 ppt similar to observations from Antarctica.

2.4.7 Relevant environmental factors for halogen activation

Combining the current understanding of halogen heterogeneous reactions based on theoretical considerations and laboratory studies as well as field observations, critical factors for the release of reactive halogens can be identified.

Radiation

A key requirement for elevated halogen mixing ratios is sufficient radiation in order for the photolytic reactions of the different cycles discussed above to take place. On a daily time scale, solar radiation determines the partitioning between active and reservoir halogen species as well as between halogens and HO_x radicals. The reactions of the 'bromine explosion' cannot proceed without the photolysis of bromine molecules released from the surface (R 50). Therefore, also on an annual time scale, the presence of elevated halogen mixing ratios is governed by the solar radiation cycle with ODEs typically observed after the return of the Sun in the respective spring (Simpson et al., 2007; Simpson et al., 2015).

With regard to other release mechanisms that might provide an initial 'seed' mixing ratios of halogens, the role of radiation is less clear. The release of dihalogens through uptake or rather production of hydroxyl in the surface layer proposed and confirmed in laboratory experiments by McConnell et al. (1992), Sjostedt and Abbatt (2008), and Abbatt et al. (2010), requires radiation (either for the formation of OH radicals in the gas phase that can be taken up or for the photolysis of nitrite and nitrate).

Other mechanisms like the uptake of ozone (Oum et al., 1998b, R 56 to R 58) would not necessarily require a photolytic step, even though release then would only lead to a build-up of inactive/reservoir halogen species like bromine molecules, which then would be photolysed after sunrise. Observational evidence from natural snow chamber observations by Pratt et al. (2013) seem to support a release pathway via surface OH since radiation here was a prerequisite for dihalogen release, while ozone merely increased production but did not lead to a release in darkness (see Fig. 2.10). In a laboratory study with artificial snow, Wren et al. (2013) could confirm these observations.

Surface properties

Regarding the question which surfaces are relevant in heterogeneous halogen release, a number of different substrates namely sea ice, brine on sea ice, frost flowers on fresh sea ice, sea salt aerosols, salty surface snow, or blowing snow were discussed (Grannas et al., 2007; Simpson et al., 2015).

A high surface area seems to be beneficial and hence frost flowers, fragile structures forming from re-sublimating water vapour on very fresh sea ice with large surface to volume ratios for some time were suspected to preferentially release active halogens and be the source of sea salt aerosols (Rankin et al., 2002; Kaleschke, 2004). Indeed, Wren et al. (2013) observed higher dihalogen production rates when their artificial snow grains were smaller. Airmass trajectory analysis of field observations, however, could not established a clear link between halogen mixing ratios and a contact of air with frost flowers and they are no longer believed to be distinct from other halide containing surfaces (Abbatt et al., 2012; Simpson et al., 2015). Also their role in sea salt aerosol production is questioned by recent studies (Obbard et al., 2009; Roscoe et al., 2011; Yang et al., 2017).

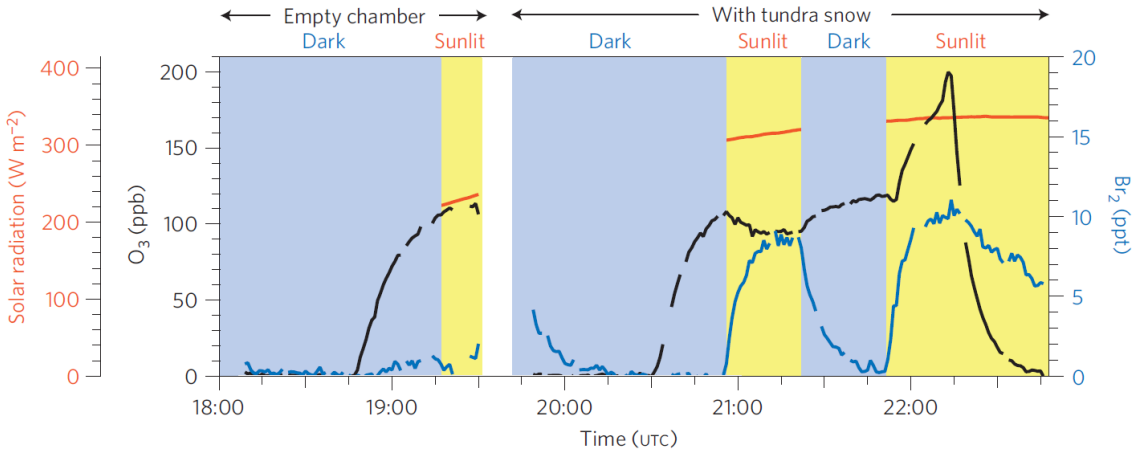

Figure 2.10: Results of a bromine release experiment by Pratt et al. (2013) in a snow chamber using natural tundra snow and an artificial light source. Br_2 (blue line) is released upon radiation (orange line and yellow portions of the plot). No release is observed when ozone is present but the sample is not irradiated (blue portions). Reproduced from Pratt et al. (2013) with permission from Springer Nature (2019).

The pH value on the surface of substrates was identified as a central property for halogen release. In the bromine explosion reaction scheme as well as in O_3 and OH mediated release mechanisms, protons in the surface layer are consumed. In their laboratory study, Wren et al. (2013) found that lower pH values lead to an increased halogen release, however at (bulk) pH values of their artificial snow grains much lower than would be expected to occur and has been measured in nature (Simpson et al., 2015, and references therin). Since surface pH of natural samples is not easily determined and instead often the pH of a melted sample is measured (e.g. Kalnajs and Avallone, 2006) this might hint to the importance of the surface layer (QLL) with distinctly different properties than the bulk.

Sea water naturally is alkaline and its pH is buffered by bicarbonate (HCO_3^-) and carbonate (CO_3^{2-}). For it to become acidic, first this buffer has to be overcome. This can happen when the ice surface cools below a temperature of -2 °C at which calcium-carbonate ($CaCO_3{\cdot}6H_2O$) reaches its solubility limit and precipitates removing the buffering carbonate (R. Sander et al., 2006). Acidity then can be increased e.g. by uptake of sulphuric acid which in the Arctic is advected from mid-latitudes. In the clean atmosphere of Antarctica, less acidity or acid precursors are available. Here, sulphuric acid originating from oceanic dimethyl sulphide emissions (see also Sec. 2.5.3) and nitric acid from surface snow nitrogen chemistry (see Sec. 2.3.3) could acidify surfaces. Modelling this, R. Sander et al. (2006) found that due to the limited availability of acidity in the Antarctic boundary layer, high aerosol concentrations and hence a large cumulative surface area could result in insufficient acidification of surfaces for halogen release to occur.

For the partitioning between the Br_2 and BrCl release, several studies found that the bromine to chlorine ratio on the surface has to be higher than in ocean water (1:650)(Simpson et al., 2007; Wren et al., 2013). One effect that could lead to this, is the precipitation of hydrohalite ($NaCl{\cdot}2H_2O$) that occurs below -21 °C and removes chloride. Another is the precipitation of mirabilite - $Na_2SO_4{\cdot}H_2O$ at 265 K, which removes Na^+ and SO^{2-} (Koop et al., 2000).

Atmospheric properties

Most observations of ODEs and elevated halogen activity are associated with calm meteorological conditions, low wind speeds, and a stable boundary layer induced by clear skies (T. Wagner et al., 2001; Frieß et al., 2004; A. E. Jones et al., 2006; Simpson et al., 2007; Saiz-Lopez and von Glasow, 2012). Under such conditions, temperatures are low enough for the precipitation processes in the surface layer to occur and the stable atmospheric conditions limit the removal of reactive trace gases from air above halide laden surfaces. For stations not directly located near or on the sea ice, reported wind speeds associated with ODEs tend to be higher since the trace gases need to be advected to the location of the observation (Hausmann and Platt, 1994; Hönninger and Platt, 2002; Simpson et al., 2007). As in the example of the ODE in Fig. 2.8, changes of mixing ratios tend to be very rapid (within few hours) which indicates a major influence of advection since chemical processes usually cannot deplete O_3 on such short time scales.

In addition to calm conditions, elevated bromine mixing ratios and ozone depletion have been observed under blowing snow conditions (see Sec. 2.2.3; A. E. Jones et al., 2009; Yang et al., 2010; Frieß et al., 2011) and satellite observations show that plumes of elevated BrO columns are associated with frontal systems where meteorological conditions leading to blowing snow are expected to occur (Begoin et al., 2010; Sihler, 2012; Blechschmidt et al., 2016).

2.5 Impacts of reactive halogen compounds

The presence of reactive halogen compounds in the polar boundary layer influences a number of other reaction cycles and has links to pollution phenomena, regional climate, and climate archives. An overview of these influences that briefly will be discussed in the following is also sketched in Fig. 2.11.

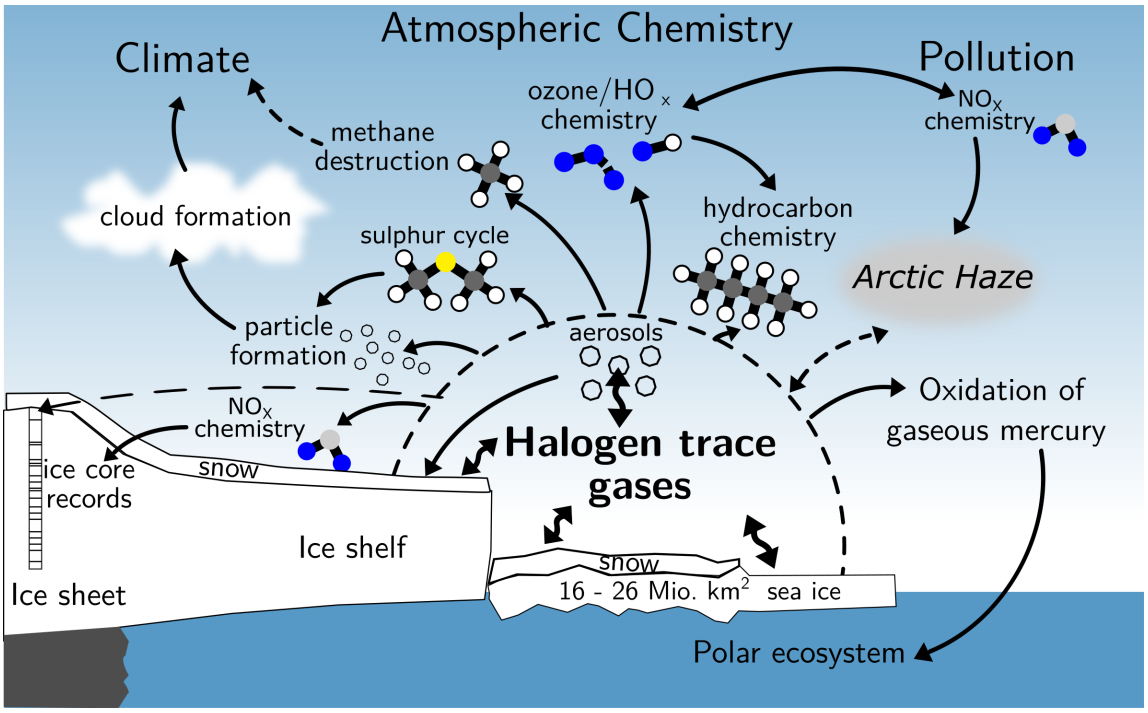

Figure 2.11: Impact of halogen chemistry on different chemical cycles in the polar boundary layer and links to (regional) climate and pollution phenomena. Unclear or weak connections are indicated with dashed lines.

2.5.1 Ozone and the oxidative capacity

Elevated mixing ratios of halogen compounds lead to a shift in the dominant, oxidising radical species from ozone related HO_x to halogen radicals (Simpson et al., 2015, and references therin). Even though release mechanisms like the bromine explosion do not increase the total number of radicals, halogen radicals have a higher reactivity than the replaced HO_x species. Furthermore, the reactivation of halogen compounds through photolysis requires radiation with lower energy photons compared to e.g. the photolysis of ozone. Both aspects make the boundary layer under halogen influence more oxidising. For an understanding of many chemical processes in polar regions (e.g. those in the following sections), the consideration of halogen chemistry therefore is essential.

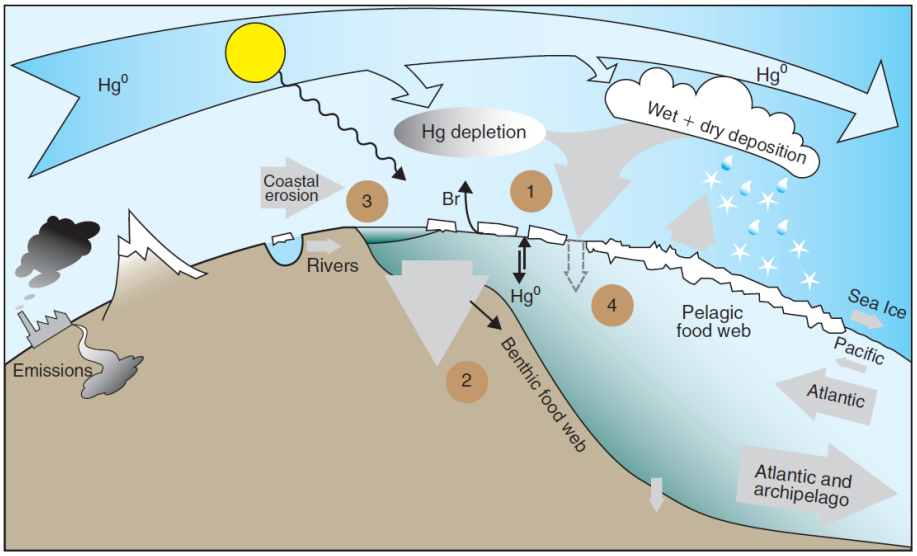

Figure 2.12: Input pathways of inorganic mercury into the polar regions. Reproduced from Douglas et al. (2012), adapted from Macdonald and Loseto (2010), with permission from CSIRO Publishing.

2.5.2 Mercury

Gaseous Elemental Mercury (GEM) is a contaminant that is present all around the globe, due to an atmospheric life time of about one year (Selin, 2009). It is emitted by natural processes (e.g. volcanic emissions) and several anthropogenic activities such as fossil fuel combustion (Dommergue et al., 2010; Angot et al., 2016). As a highly toxic compound, it can have adverse health impacts on humans and wildlife. When oxidised, GEM becomes very soluble and can be deposited onto surfaces. Through bromine radicals, this oxidation can occur very rapidly, which has been named Atmospheric Mercury Depletion Event (AMDE) similar to ODE (Dommergue et al., 2010; Mastromonaco et al., 2016). Such episodes also have been observed at NM III by Ebinghaus et al. (2002) and Temme et al. (2003).

Once deposited on surfaces, oxidised mercury can be reduced and re-emitted (studies from the Arctic suggest an emitted fraction of 60-80%; S. B. Brooks et al., 2006; Steen et al., 2009; Douglas et al., 2012) or, in aquatic environments, be processed to methylmercury. Since this bioactive compound is easily taken up by organisms but only hardly discharged, it can accumulate. Transfer between the subsequent levels of the food chain then can lead to high burdens in the higher trophic levels (biomagnification; Douglas et al., 2012).

The overall importance of deposition and uptake by ecosystems of mercury originating from AMDEs, however, so far is unclear. In the Arctic, rivers, and washout and deposition of un-oxidised mercury from the atmosphere probably provide much larger fluxes than AMDE-related mercury (Douglas et al., 2012; Obrist et al., 2017). In the Antarctic on the other hand, terrestrial influence is considerably smaller (e.g. no river run-off) and so the relative importance of chemsitry induced deposition might be larger. Up to now, however, the limited number of observations from Antarctica and an incomplete understanding of key processes (e.g. regarding the influence of different ice substrates) prevent a comprehensive assessment of the importance of tropospheric halogen chemistry on Antarctic mercury burdens (Dommergue et al., 2010; Angot et al., 2016).

2.5.3 Oceanic sulphur cycle

Over pristine areas of the oceans, sulphur aerosols are the dominating class of aerosols followed by sea salt aerosols (von Glasow and Crutzen, 2004). Droplets of sulphuric acid (H_2SO_4), which has a very low vapour pressure, can serve as Cloud Condensation Nuclei (CCN). The precursor substance that leads to the formation of these droplets is Dimethyl sulfide (DMS) - CH_3SCH_3 which is produced and emitted by phytoplankton (Dacey and Wakeham, 1986).

Once emitted into the atmosphere, there are two alternative oxidation reaction pathways DMS can undergo. Either by addition of an oxygen atom or by abstraction of a proton (von Glasow and Crutzen, 2004). Due to the negative activation energy of the addition path, it is preferred at lower temperatures and vice versa. For reactions of DMS with OH, the dominant radical when no halogens are present, an exemplary chain of abstraction reactions could be (for a detailed discussion see e.g. Barnes et al., 2006):

$$\begin{aligned} CH_3SCH_3 \xrightarrow{+OH} CH_3SCH_2 \xrightarrow{+O_2} CH_3SCH_2OO \xrightarrow{+NO} CH_3SCH_2O \xrightarrow{\text{therm decomp}} \\ \longrightarrow CH_3S \xrightarrow{+O_3} SO_2 \xrightarrow{+OH} SO_3 \xrightarrow{+H_2O} H_2SO_4 \end{aligned} \quad (R\,65)$$

Addition reactions on the other hand, can lead to the formation of dimethylsulfone ($DMSO_2$, R 66) or methylsulfinic acid (MSIA, R 67) via formation of dimethylsulfoxide (DMSO):

$$CH_3SCH_3 \xrightarrow{+OH} CH_3S(OH)CH_3 \xrightarrow{+O_2} CH_3SOCH_3 \xrightarrow{+OH/O_2} CH_3SO_2CH_3 \quad (R\,66)$$

$$CH_3SOCH_3 \xrightarrow{+OH} CH_3S(O)OH \quad (R\,67)$$

A reaction of DMS with BrO also initiates the addition sequence in reaction (R 66) and (R 67). This has been observed e.g. by Read et al. (2008). DMSO, $DMSO_2$, and MSIA (and a further product Methane sulfonic acid (MSA), which is frequently measured in aerosol composition studies) are preferentially taken up by existing aerosols or cloud droplets whereas sulphuric acid droplets resulting from the abstraction reactions (R 65) act as CCN leading to more and, due to growth competition, smaller droplet sizes (von Glasow and Crutzen, 2004).

Since the droplet size distribution of clouds determines their optical properties, namely the albedo, the addition reactions and hence a presence of BrO can lead to clouds with larger droplets and hence lower albedo compared to the abstraction pathway. In addition to this "first indirect albedo effect" (von Glasow and Crutzen, 2004), larger cloud droplets and clouds consisting of these droplets have shorter atmospheric life times leading to a faster removal which constitutes a "second indirect albedo effect".

Since cloud albedos over the dark ocean have a considerable impact on the radiative balance, this influence of halogen chemistry on clouds constitutes a potential link to (regional) climate. Modelling studies for the remote marine boundary layer outside the polar regions where BrO mixing ratios are much lower than during ODE periods find that the reduction of CCN production from DMS can reach up to 30% (Breider et al., 2014).

2.5.4 Volatile organic compounds

A presence of active chlorine (and to a lesser extent bromine atoms) in the atmosphere has an impact on hydrocarbons (Simpson et al., 2015, iodine reactions with hydrocarbon are negligible). This has been used to confirm halogen presence and influence on polar boundary layers with hydrocarbon clocks i.e. comparing mixing ratios of hydrocarbons with different reactivities with a radical and hence with different life times in the presence of a particular radical species (Jobson et al., 1994; Gilman et al., 2010). Jobson et al. (1994) observed that light hydrocarbon mixing ratios are quickly reduced during ODEs and the reduction of life times from an OH dominated chemistry to periods with elevated chlorine mixing ratio was found to be substantial (e.g. for propane down from $\approx$ 14 days in an OH dominated atmosphere to $\approx$ 8 h when chlorine atoms are present). Taking the example of the important greenhouse gas methane, Platt et al. (2004) estimated that while decreases in methane through reaction with chlorine atoms are small and the global contribution of chlorine chemistry to methane removal is only 3.3%, the isotope signal favouring the removal of ^{12}C methane over ^{13}C induced by reaction with OH is reduced.

In a model study by C. R. Thompson et al. (2015) based on an observation period of 7 days in March 2009 in Utqiaġvik (Barrow)- Alaska with Cl_2 mixing ratios of up to 100 ppt (and corresponding ClO values of about 15 ppt), for days without ODEs 63% of chlorine atoms react with Volatile Organic Compound (VOC)s and another 9% with oxidised VOCs (OVOCs) leaving only 27% to the reaction with ozone. When ozone is depleted (<5 ppb), these percentages increase to 78% (VOCs) and 22% (OVOCs) respectively. The influence of the recently observed high chlorine abundance (Liao et al., 2014) on hydrocarbons (e.g. in terms of reductions of (regional) atmospheric life times) has yet to be studied.

2.5.5 Climate records and halogens as sea ice proxies

The link between nitrogen chemistry and ozone production (R 13 to R 15,Sec. 2.3.3) and the importance of ozone for the oxidative capacity of the atmosphere makes the nitrate signal in ice cores an interesting proxy for chemical conditions in the atmosphere of the past (e.g. Röthlisberger et al., 2002; Wolff et al., 2007). Due to their high reactivity, the influence of active halogens has to be taken into account when reactive trace gases such as nitrogen compounds are used as proxies for past climate.

Recently, bromide and iodide signals from ice cores themselves were proposed as new proxies by Spolaor et al. (2013). The analysis of snow and ice samples from the Arctic and Antarctica showed an annual cycle of bromide in ice cores. The highest signal occurred in spring when most ODEs are observed, sea ice extent is largest and the bromine release is believed to be largest. A second peak was detected at the end of the respective summer (Spolaor et al., 2014). This was interpreted as the result of bromine deposition at the end of the photoactive period in the boundary layer.

Due to the importance of sea ice surfaces for bromine release, the goal of these investigations is to link the bromide signal to sea ice extent and age of the sea ice exploiting the fact that sea ice salinity and hence halogen release decreases with ice age (Spolaor et al., 2013). This seems to be supported by bromide minima during glacials (on average older sea ice and greater distance of core site from chemically active marginal sea ice zone) and maxima during inter-glacials (less multi-year sea ice and more first year sea ice with a greater release potential). However, comparison studies of shallow ice and firn cores with

satellite observations of reactive halogens show that the relation between ice core signals and e.g. sea ice extent is not unambiguous and seems to depend on location of the considered site and local transport patterns (Spolaor et al., 2014; Spolaor et al., 2016b; Spolaor et al., 2016a; Vallelonga et al., 2017).

2.5.6 New particle formation and Arctic haze

In mid-latitudes, in particular above algae fields in tidal zones, the formation of ultrafine particles through polymerisation of iodine compounds (briefly discussed in Sec. 2.4.1) is a regular phenomenon (Saiz-Lopez et al., 2012, and references therin). New particle formation (NPF) in general starts with a clustering of gaseous precursors (e.g. sulphuric acid) followed by particle growth.

In the pristine Antarctic boundary layer, where, for lack of local sources, precursors generally would be expected to originate from the marine boundary layer, NPF has been observed at several sites e.g. at the Finnish station Aboa 73.03° S, 12.40° W about 130 km from the coast (and 350 km south-west of NM III) by Koponen (2003), Asmi et al. (2010), and Kyrö et al. (2013), in the interior of the continent at Dome C (75.1° S, 123.32° E) by Järvinen et al. (2013), on a ship-based campaign from Hobart, Tasmania to Casey Station (66.28° S, 110.53° E) by Humphries et al. (2015), and at NM III by Weller et al. (2015).

The understanding of these events and the precursors governing the NPF is still incomplete. At Aboa, organics emitted by bacteria from melting ponds was identified as the most likely cause of NPF (Kyrö et al., 2013). At NM III, observations could be explained by a nucleation initiated by sulphuric acid, the cause for further growth of particles, however, was interpreted to be driven by another, yet unidentified gaseous precursor. Finally, Humphries et al. (2015) observed a decrease in ambient ozone and an increase in oxidised mercury coincident with a NPF event. They could not identify the oxidant causing the mercury oxidation but ruled out IO related nucleation due to insufficient mixing ratios and hypothesised that nucleation could be initiated by clusters of oxidised mercury potentially in combination with sulphuric acid.

In the Arctic, the recurring phenomenon of an increase of aerosol particles reducing visibility and affecting the radiation budget was regularly observed by pilots since the 1950s (Greenaway, 1950) and is referred to as *Arctic haze*. It is a transport related effect that is modulated by the extent of the polar front in the atmosphere. As it expands further south in winter, it allows a transport of pollution related particles from Eurasia and North America under the "Arctic Dome" (Barrie, 1986; Sihler et al., 2012; Abbatt et al., 2018). In summer, this dome is smaller and prevents an intrusion of pollutants leading to an annual cycle with a higher frequency of Arctic have episodes in winter. The influence of halogen chemistry on Arctic haze and vice versa is not yet clear. Some observations found a negative correlation between ozone and accumulation mode particles ($r \approx 0.7\,\mu m$ - see Fig. 2.6) which was interpreted as a potential influence of HBr in the growth of advected Arctic haze sulphate aerosols by uptake (Simpson et al., 2007, and references therin). Increased NO_x chemistry on the other hand might influence halogen release either by increasing it via uptake and conversion of $BrONO_2$ (R 59) or compete with release and ozone depletion via reduction of halogen oxides (R 41) (Cao et al., 2014).

3
Differential Optical Absorption Spectroscopy

The measurement of (reactive) trace gases in the atmosphere requires suitable instrumentation adapted to abundance and physicochemical properties of the target species. When e.g. small variations of a high background concentration are considered as for the green house gases carbon dioxide or methane, a very high relative accuracy is required. However, due to the comparably high inertness of these gases, mixing ratios in suitable containers are stable and samples can be stored for later analysis.

For the highly reactive halogen compounds investigated in this thesis however, the presence of surfaces (e.g. in the form of instrument tubing or the walls of a sample container) or changes of environmental parameters such as the actinic flux (see Sec. 2.1.2) can quickly alter mixing ratios through chemical reactions. Measurements therefore have to be performed promptly and the interference with the air sample has to be minimized or avoided altogether as in contact-free techniques. Furthermore, the typical mixing ratios of halogen species of only a few ppt require a high sensitivity and the large variety of trace gases present at these mixing ratios a sufficient selectivity.

DOAS is a measurement technique that allows the simultaneous detection of several trace gas species with such a high selectivity. It is commonly contact-free and most realisations can be classified as a remote sensing technique [1]. Depending on the molecule considered, currently achievable sensitivities allow the detection of mixing ratios in the ppb to ppt range. After a brief introduction of absorption spectroscopy, this chapter will discuss the DOAS measurement principle and the general implications of its instrumental realisation. It is based on the comprehensive introduction to DOAS and example applications that can be found in Platt and Stutz (2008) and in references therein.

[1] One exception are Cavity-Enhanced Differential Optical Absorption Spectroscopy (CE-DOAS) instruments that additionally do no longer qualify as contact-free when used with a closed optical path

3.1 Absorption Spectroscopy

Absorption spectroscopy relies on the measurement of electromagnetic radiation that travels through matter as a function of the wavelength λ. Different materials possess characteristic absorption cross sections $\sigma(\lambda)$. The attenuation $\mathrm{d}I$ of the spectral radiance $I(\lambda)$ that passes through a medium containing an absorber, is proportional to the current spectral radiance $I(\lambda)$, the concentration c of the absorber, its cross-section $\sigma(\lambda)$, and the layer thickness $\mathrm{d}l$. This relationship is known as the *Beer-Lambert* (or sometimes *Beer-Lambert-Bouguer*) law and can be written, in integrated form as:

$$I(\lambda) = I_0(\lambda) \cdot \exp(-\sigma(\lambda) \cdot c \cdot L) \tag{3.1}$$

where $I_0(\lambda)$ is the initial spectral radiance and L the total distance travelled in the medium. Comparing the initial and final radiances, the optical thickness τ of a sample can be determined:

$$\tau(\lambda) = \ln\left(\frac{I_0(\lambda)}{I(\lambda)}\right) = \sigma(\lambda) \cdot c \cdot L \tag{3.2}$$

This allows to calculate the concentration c of the absorber in the sample, if the absorption cross-section $\sigma(\lambda)$ and the sample length L traversed by the radiation are known and the ratio of $I_0(\lambda)$ and $I(\lambda)$ can be determined. For a measurement where the medium of interest can be introduced and removed from a light path (e.g. gas in a cell between a light source and a spectrometer) or the signal diverted to directly reach the detector ($L = 0$), the application of this relationship is simple to realise.

Absorption spectroscopic measurements in the open atmosphere, however, are much more complicated by the fact that here the absorbing medium (i.e. the gas) cannot be removed in a simple way and hence $I_0(\lambda)$ is difficult to determine. Furthermore, other processes such as scattering or refraction influence the radiation propagating through the atmosphere and there is typically more than one absorber present.

One early approach to apply spectroscopy for atmospheric measurements despite the difficulty of determining $I_0(\lambda)$ was proposed by Dobson and Harrison (1926) and consisted of comparing radiances at two wavelengths λ_1 and λ_2 where the cross-section of the absorber of interest $\sigma(\lambda_1)$ is sufficiently different from $\sigma(\lambda_2)$. This allowed the measurement of the total ozone column and instruments operating with this principle were central in discovering the Antarctic ozone hole (Farman et al., 1985) and are still in operation today (e.g. on the British Antarctic station Halley VI).

While the Dobson photospectrometer avoids the problem of the initial radiance, its selectivity is still limited even when more than one wavelength pair is used for the measurement. The DOAS principle (Perner et al., 1976; Platt et al., 1979; Platt and Perner, 1980; Platt and Perner, 1983), greatly improves this by taking into account continuous spectral intervals.

3.2 Attenuation of radiation in the atmosphere

To correctly describe radiation transport in the atmosphere, a number of effects other than absorption have to be considered. The radiative transfer equation that contains these effects is a continuity equation for radiative energy passing through a medium in a distinct direction and hence contains sink and source terms. Sinks are the aforementioned absorption and scattering, which will be discussed in detail below. Source terms in the radiative transfer equation consist of scattering (e.g. into a considered direction), thermal emission, and aerosol fluorescence (Platt et al., 2007). Depending on the spectral range and the particular application, a simplified description of the radiative transport is sufficient.

For the ultraviolet radiation (UV) to visble radition (VIS) wavelength range, which was used for measurements in this thesis, the thermal emission by molecules with typical atmospheric temperatures can be neglected. Aerosol fluorescence can be omitted as well. For the scattering source term, an important criterion is the spatial extent of the propagating radiation. For active remote sensing applications, the small field of view of instruments warrants the *narrow beam* approximation (Platt et al., 2007). In order for scattering to be a source, light that was scattered out of the path from light source to the instrument/observer would have to be scattered a second time into the direction of the (narrow) beam and in that beam a third time and exactly into the original direction of the radiation, which has a very low probability.

With the remaining (sink) terms of the radiative transport equation, the attenuation of radiation with an initial radiance $I_0(\lambda)$ recorded by an instrument, is described by the following equation, which basically is the *Beer-Lambert* law (Eq. 3.1) amended to incorporate the additional effects:

$$I(\lambda) = I_0(\lambda) \cdot \exp\left(- \int_0^L \sum_j (\sigma_j(\lambda, p(l), T(l)) \cdot c_j(l)) + \epsilon_\mathrm{R}(\lambda, l) + \epsilon_\mathrm{M}(\lambda, l) \, \mathrm{d}l \right) + N_\mathrm{p}(\lambda) \quad (3.3)$$

For molecular absorption, there are typically several species j whose combined absorption has to be accounted for in a particular spectral range. Their absorption cross-sections σ_j, which depend on temperature and pressure, and their distribution and hence their concentration c_j can vary along the light path. This is particularly relevant for radiation traversing the atmosphere vertically. Absorption therefore has to be integrated along the light path.

In addition to absorption, scattering of light has to be included. In the description of scattering processes in the atmosphere, the ratio of the dimension d of the scatterers to wavelength λ of the radiation is crucial. For atmospheric molecules, where for UV-VIS radiation $d \ll \lambda$, different molecular scattering mechanisms exist. As a first approximation elastic *Rayleigh*-scattering (Strutt (Lord Rayleigh), 1881; Strutt (Lord Rayleigh), 1899) and inelastic *vibrational Raman*-scattering (Raman and Krishnan, 1928) can be distinguished. In detail, Rayleigh-scattering consists of the two inelastic mechanisms *rotational Raman-* and *Rayleigh-Brillouin* scattering of which the latter has an elastic component (for details on the different processes see Young, 1981; Witschas, 2012).

Depending on the DOAS application, molecular scattering has to be considered in more or less detail. For scattered sun light applications like MAX-DOAS (see Sec. 4.3 for a description), the filling in of *Fraunhofer* lines by rotational Raman-scattering, known

as the *Ring* effect (Grainger and Ring, 1962) is important and recently Lampel et al. (2015a) showed that also vibrational Raman-scattering can influence DOAS observations of scattered sunlight. For the extinction by molecular scattering in Eq. 3.5, from Rayleigh's theory a wavelength dependence of the Rayleigh extinction coefficient, $\epsilon_{\mathrm{R}} \propto \lambda^{-4}$ can be derived.

When $d \geq \lambda$, which for UV-VIS radiation applies to aerosols or particles like ice crystals or water droplets, scattering can be approximated by *Mie* theory (Mie, 1908; Mishchenko et al., 1999). ϵ_{M} describes the scattering influence of spherical scatterers. Since aerosols and particle often are not spherical (e.g. ice crystals have platelet or column-like shapes), approximations like effective scattering cross-sections are used. The Mie extinction coefficient in Eq. 3.3 is also wavelength dependent: $\epsilon_{\mathrm{M}} \propto \lambda^{-\alpha}$ where the *Ångström coefficient* α usually varies between 0.5 and 2.5 (Ångström, 1929; Ångström, 1930) depending on shape- and size-distribution of the aerosols with typical values for α between 1 and 1.5 (Roedel and T. Wagner, 2011).

Photon shot noise

The *photon shot noise* $N_{\mathrm{p}}(\lambda)$ (introduced by Schottky, 1918) is a consequence of the discretisation of the electromagnetic field in the form of photons. It is an inevitable noise contribution of all real light sources and hence a fundamental limit for the accuracy that can be achieved when using radiation as measurement signal. Even for a detector with perfect quantum efficiency (i.e. the conversion of photons into photo-electrons) the number of detected photons fluctuates because the radiation arrives as discrete photons whose emission from the light source underlies quantum fluctuations (Mandel and Wolf, 2008) (when the quantum efficiency of the detector si smaller than unity, the effective photon noise is further increased). This fluctuation is *Poisson*-distributed and the signal to noise ratio R_{SN} for this effect depends on the square root of the number n of detected photons.

$$R_{\mathrm{SN}} = \frac{n}{\sqrt{n}} = \frac{n}{N_{\mathrm{p}}} \tag{3.4}$$

3.3 The DOAS principle

For radiation that traverses the atmosphere, both molecular absorption and Rayleigh- and Mie-scattering influence $I(\lambda)$ and concentrations c_j can no longer be determined through the ratio of $I(\lambda)$ and $I_0(\lambda)$ as in classical absorption spectroscopy (Eq. 3.2). The basic idea of DOAS is to separate the different attenuation mechanisms according to spectral characteristics. Molecular scattering ϵ_{R}, Mie scattering ϵ_{M} only have a weak wavelength dependence. The effect of suitable molecular absorbers can be separated in a broadband influence ($\mathrm{B}(\lambda)$) and a narrow band influence on the signal. Suitable in this case means that there are components $\sigma'_j(\lambda)$ of the absorption cross-sections $\sigma_j(\lambda)$ that sufficiently vary in strength with wavelength compared to the broadband effects of scattering. Structured cross-sections from ro-vibrational molecular transitions such as in BrO or SO_2 are very good examples (Fleischmann and Burrows, 2002; Bogumil et al., 2003).

Based on this separation, Eq. 3.3 can be written as follows:

$$I(\lambda) = I_0(\lambda) \cdot \overbrace{\exp\left(-\int_0^L \sum_j \sigma'_j(\lambda, p(l), T(l)) \cdot c_j(l)\ \mathrm{d}l\right)}^{\text{Narrow-band attenuation}} \cdot \underbrace{\exp\left(-\int_0^L \sum_j (\sigma_{\mathrm{B},j}(\lambda, p(l), T(l)) \cdot c_j(l)) + \epsilon_R(\lambda, l) + \epsilon_M(\lambda, l)\ \mathrm{d}l\right)}_{\text{Broad-band attenuation B}(\lambda)} + \underbrace{N_\mathrm{p}(\lambda)}_{\text{Photon shot noise}} \tag{3.5}$$

Here, the first component describes the strongly wavelength-dependent, *differential* part of the absorption with a cross-section σ'_j. The second incorporates broad band effects of (1) molecular absorption $\sigma_{\mathrm{B},j}(\lambda)$, (2) molecular scattering ϵ_R, and (3) aerosol and particle scattering ϵ_M. Both exponentials contain the concentrations $c_j(l)$ of absorbers, but in the first, narrow-band term, they only depend on molecular absorption.

The different spectral characteristics of narrowband and broadband terms in Eq. 3.5 allow to reduce the determination of c_j to the analysis of a differential absorption by removing or modelling the broad band extinction as will be shown in the following section. The ro-vibrational energy transitions are a characteristic property of the respective molecule j. Therefore, determining atmospheric concentrations based on differential absorption is a highly specific way to distinguish different species. This also brings the advantage that a correct measurement of absolute radiances no longer is necessary, since only the depth of narrow-band absorption features but not their absolute influence on radiance is required for the analysis. With $\mathrm{B}(\lambda)$ for the broadband term Eq. 3.5 becomes:

$$I(\lambda) = I_0(\lambda) \cdot B(\lambda) \cdot \exp\left(-\int_0^L \sum_j \sigma'_j(\lambda, p(l), T(l)) \cdot c_j(l)\ \mathrm{d}l\right) \tag{3.6}$$

The absorption cross-sections $\sigma_j(\lambda)$ are usually determined in preceding laboratory studies. A large collection of reference cross-sections can be found e.g. in the MPI-Mainz UV/Vis spectral atlas (Keller-Rudek et al., 2013).

The quantities that are directly determined with DOAS instruments are the column densities S_j of the concentration distributions c_j along the light path L. The column density is defined as:

$$S_j = \int_0^L c_j(l)\,\mathrm{d}l = \bar{c}_j \cdot L = \frac{\tau_j}{\sigma_j} \tag{3.7}$$

When the light path L is known, an average concentration $\bar{c}_j$ along the light path can be determined.

3.4 Instrumental implementation

When the DOAS principle is applied for a measurement, in addition to the atmospheric effects such as scattering and absorption, the influence of the instrument that is used to record and quantify the measurement signal has to be considered.

3.4.1 Instrumental effects

For a real measurement, Eq. 3.6 has to be amended to incorporate these effects. Using Eq. 3.7 it becomes:

$$I(\lambda) = \left[I_0(\lambda) \cdot B(\lambda) \cdot \exp\left(-\int_0^L \sum_j \sigma'_j(\lambda, p(l), T(l)) \cdot c_j(l)\, \mathrm{d}l \right) + N'_\mathrm{p} \right] \cdot A(\lambda) + X(\lambda) \quad (3.8)$$

The different components that collect, transmit and record the signal that eventually reaches its detector can alter its spectral distribution (e.g. through a wavelength dependent transmissivity of optical components) which is incorporated in the factor $A(\lambda)$.

The component $X(\lambda)$ incorporates several effects that add noise to the recorded signal. It includes (1) thermal noise which is the result of the thermally induced creation of a electron-hole pair in the detector not associated with an absorbed photon. this signal is referred to as *dark current* and depends on the temperature of the detector. To reduce it, detectors (or entire spectrometers) are typically cooled. To correct for the remaining dark current, the operation temperature of the detector is kept as stable as possible (see characterisation of the dark current of the LP-DOAS setup used in this thesis and discussion of temperature regulation in Sec. 4.2.6).

Another component of $X(\lambda)$ is (2) electronic or readout noise associated with the conversion of the charges of the photo-electrons into a digital signal. This requires the transfer of photo-electrons to an amplifier, the determination of the voltage created by these electrons, conversion of this voltage in the Analog-to-digital converter in a computer read-able signal and the conversion into a count number. Determining the charge created in one pixel is only possible with a finite accuracy.

Additionally, a constant offset signal is added before A/D conversion to prevent negative signals which would reduce the dynamic range. This offset can also vary (see characterisation of offset for CCD in the LP-DOAS of this thesis in Sec. 4.2.6).

Lastly, $X(\lambda)$ includes (3) spectrometer stray-light, the recording of photons from other spectral regions than the one considered in the measurement. This is typically caused by unwanted reflections inside the spectrometer. There are several methods to reduce stray-light which are discussed in Sec. 4.2.2 (see also Nasse et al., 2019).

3.4.2 Spectrometer resolution

In DOAS applications, the radiation that carries the absorption signal after traversing the probed air mass is collected and spectrally analysed. This is typically done with a grating spectrometer in combination with a light detecting element like a photodiode array or a CCD (e.g. Platt et al., 1979; Platt and Perner, 1980; Platt et al., 1980; Hausmann and Platt, 1994; Commane et al., 2011; Stutz et al., 2011) but not limited to it.

Since all spectrometers have a finite resolution $\frac{\Delta\lambda}{\lambda}$ that, for grating spectrometers, is determined by (1) the width of the entrance slit, (2) the focal length, and (3) the grating properties i.e. the number of grooves per mm, the spectral radiance $I(\lambda)$ is modified by the measurement process. Mathematically, this is described by a convolution of $I(\lambda)$ with an instrument function H that represents the influence of the spectrometer:

$$I^*(\lambda) = (I * H)(\lambda) = \int I(\lambda') \cdot H(\lambda - \lambda')\, \mathrm{d}\lambda' \tag{3.9}$$

With the influence of the instrument, Eq. 3.6 becomes:

$$I^*(\lambda) = \int I_0(\lambda') \cdot B(\lambda') \cdot \exp\left(-\sum_j \sigma'_j(\lambda') \cdot S_j\right) \cdot H(\lambda - \lambda')\, \mathrm{d}\lambda' \tag{3.10}$$

The convolution in Eq. 3.9, for practical applications can be simplified to only consider a spectral area $\pm\Delta\lambda$ around $H(\lambda - \lambda')$ (Platt and Stutz, 2008). Assuming furthermore that the initial spectral radiance $I_0(\lambda)$ is spectrally smooth, which means that light source structures are broader than the resolution of the instrument, $I_0(\lambda')$ and $B(\lambda')$ can be excluded from the convolution giving:

$$I^*(\lambda) = I_0(\lambda) \cdot B(\lambda) \cdot \int_{-\Delta\lambda}^{+\Delta\lambda} \exp\left(-\sum_j \sigma'_j(\lambda') \cdot S_j\right) \cdot H(\lambda - \lambda')\, \mathrm{d}\lambda' \tag{3.11}$$

The optical density $\tau(\lambda)$ (Eq. 3.2) then is a sum of the logarithms of the broadband attenuation $B(\lambda)$ and the narrowband attenuation. To determine the atmospheric concentrations of absorbers j, this expression has to solved for S_j.

$$\tau(\lambda) = \ln\left(\frac{I^*(\lambda)}{I_0(\lambda)}\right) = \cdot \ln(B(\lambda)) + \ln\left[\int_{-\Delta\lambda}^{+\Delta\lambda} \exp\left(-\underbrace{\sum_j \sigma'_j(\lambda') \cdot S_j}_{\tau'(\lambda')}\right) \cdot H(\lambda - \lambda')\, \mathrm{d}\lambda'\right] \tag{3.12}$$

If the differential optical density $\tau'(\lambda')$ is small (i.e. < 0.1; Platt and Stutz, 2008), the slant columns S_j can be extracted from the logarithm using two approximations for the logarithm and the exponential.

$$\ln(x) \approx x - 1 \quad \text{for} \quad 1 - \epsilon < x < 1 + \epsilon \quad \epsilon < 0.1 \tag{3.13}$$

$$\exp(x) \approx 1 + x \quad \text{for} \quad -\epsilon < x < \epsilon \quad \epsilon < 0.1 \tag{3.14}$$

This is shown in detail in Platt and Stutz (2008, p. 163 ff) and yields a linearised expression for Eq. 3.10:

$$\tau(\lambda) = \ln\left(\frac{I^*(\lambda)}{I_0(\lambda)}\right) \approx \ln(B(\lambda)) + \sum_j \frac{S_j}{\alpha_j} \cdot \ln\left[\int_{-\Delta\lambda}^{\Delta\lambda} \exp\left(-\sigma'_j(\lambda') \cdot \alpha_j\right) \cdot H(\lambda - \lambda')\, \mathrm{d}\lambda'\right] \tag{3.15}$$

$$= \ln(B(\lambda)) + \sum_j \frac{S_j}{\alpha_j} \cdot \Lambda^*_j(\lambda) \tag{3.16}$$

In this form, the logarithm of the ratio of $I^*(\lambda)$ and $I_0(\lambda)$ is expressed as a sum the broadband effects and exponentials of the differential literature absorption cross-sections that are adapted to the instrumental resolution by convolution with $H(\lambda - \lambda')$ and scaled by the column densities S_j. α_j is a scaling factor in column density units resulting from the linearisation. For optically thin absorbers, $\alpha_j = 1$. When an absorber no longer is optically thin, the linearisation of the DOAS problem only is valid for $\alpha_j \neq 1$ and the analysis has to be performed iteratively starting with the calculation the exponential with an expected column density that then iteratively is updated by the results of the analysis (see Platt and Stutz, 2008, for details).

For LP-DOAS systems, the DOAS technique mainly used in this thesis, the assumption regarding the smooth spectral properties of the light source usually is fulfilled. Furthermore, the optical densities of the absorbers investigated fulfils the second condition for the linearisation in Eq. 3.15. Details on the mathematical treatment of DOAS systems where one or both of these conditions no longer hold, are discussed in detail in Platt and Stutz (2008).

3.4.3 Spectral discretisation

The spectral distribution of the light refracted in the spectrometer is quantified by a detector element like a photodiode array (Stutz and Platt, 1997) or a CCD array yielding a discrete spectrum of $I^*(\lambda)$. It consists of n values corresponding to the n pixels or channels of the detector.

Due to its finite extent, each detector pixel i records light from a wavelength interval $\lambda(i)$ (wavelength at one edge of the pixel) to $\lambda(i+1)$ (wavelength at the other edge of the pixel). The width of this interval is determined by the resolution of the spectrometer and the dimension of the single pixel. The channel-wavelength attribution to determine $\lambda(i)$ is required for all DOAS analysis and is determined using a calibration with a spectrum with known emission features (often the line spectra of gas discharge lamps) or highly structured Fraunhofer lines in solar radiation spectra. It can be expressed by a polynomial of the order l where the 0th order indicates the wavelength of the first channel, the 1st order the dispersion and higher orders correct for non-linear dispersion effects:

$$\lambda(i) = \sum_{k=0}^{l} \gamma_k \cdot i^k \tag{3.17}$$

With this attribution, a channel i of the detector receives the following radiance:

$$I^+(i) = \int_{\lambda(i)}^{\lambda(i+1)} I^*(\lambda')\, d\lambda' \tag{3.18}$$

This yields to the discretised form of Eq. 3.16, that now has to be solved .

$$\tau^+(i) = \ln\left(\frac{I^{+*}(i)}{I_0^+(i)}\right) = \ln(B^+(i)) + \sum_j \frac{S_j}{\alpha_j} \cdot \Lambda_j^+(i) \tag{3.19}$$

3.5 The fitting process

The solution of Eq. 3.19 can be achieved in different ways. On way is to remove broad band contributions from the equation through high-pass filtering. Alternatively, the optical density can be described by a model $F(i)$.

$$\tau^+(i) = \ln\left(\frac{I^+(i)}{I_0^+(i)}\right) = F(i) \tag{3.20}$$

To account for broad band attenuation, the model contains a polynomial $P_q(i)$ is a polynomial of degree q:

$$F(i) = P_q(i) + \sum_{j=1}^{m} \frac{S_j}{\alpha_j} \cdot \Lambda_j^+(i) = \sum_{p=0}^{q} a_p \cdot i^p + \sum_{j=1}^{m} \frac{S_j}{\alpha_j} \cdot \Lambda_j^+(i) \tag{3.21}$$

The factors $\Lambda_j^+(i)$ are calculated based on literature cross-sections. An effect that has to be considered here, is the potential wavelength misalignment of reference spectra $\Lambda_j^+(i)$ and the measured atmospheric spectra $I^+(i)$ and $I_0^+(i)$. Reasons for this can be (1) thermal changes in the spectrometer, (2) for a turnable grating inaccuracy of the grating position compared to the calibration, (3) an inaccurate channel-wavelength calibration, or (4) the wavelength calibration of literature cross-sections might be inaccurate (Platt and Stutz, 2008).

Such a misalignment can introduce residual structures that limit the accuracy of DOAS measurements. Therefore, an alignment of $I^+(i)$ and $\Lambda_j^+(i)$ has to be included in the fitting procedure by shifting and/or squeezing the different references $\Lambda_j^+(i)$. The result are modified reference spectra, that depend on parameters $d_{j,k}$:

$$F(i) = \sum_{p=0}^{q} a_p \cdot i^p + \sum_{j=1}^{m} \frac{S_j}{\alpha_j} \cdot \Lambda_j^+(d_{j,0}, d_{j,1}, ...)(i) \tag{3.22}$$

These parameters indicate the modifications of the reference spectra $\Lambda_j^+(i)$ - $d_{j,0}$, for instance, determines the shift, $d_{j,1}$ is a linear squeeze or stretch, $d_{j,2}$ would be a quadratic squeeze/stretch and so on. The alignment of $\Lambda_j^+(i)$ and hence the parameters $d_{j,k}$ are determined in a non-linear fit of $F(i)$ to $\tau+(i)$ (Eq. 3.20) where parameters S_j and a_p are kept constant. For the overall fitting process, this means that two different fitting

procedures are alternated. With an initial set of prescribed values for $d_{j,1}$, in a first step parameters S_j and a_p are determined in a linear least-squares fit (e.g. Bevington, 1969). Then a non-linear fit, in many DOAS fitting software packages a *Levenberg-Marquardt* fit (Levenberg, 1944; Marquardt, 1963), estimates the non-linear parameters $d_{j,k}$ (see also Stutz and Platt, 1996, for a description the DOAS analysis procedure). With updated values $d^1_{j,k}$, then the linear fit is called again. In this fitting process, the difference χ between model function and $\tau'(i)$ is minimized.

$$\chi^2 = \sum_{i=0}^{n^*} \Big(\tau^+(i) - F(i)\Big)^2 \tag{3.23}$$

The fit is aborted when the change of χ between two iterations is smaller then a preselected limit. Other criteria are exceeding of a maximum number of iterations or when the non-linear fitting step becomes unstable.

Since real measurements are affected by noise (the photon noise omitted above is a fundamental limit, other sources of noise will be discussed in Sec. 3.6 below), the difference between $\tau'(i)$ and $F(i)$ can never vanish. As a criterion for the quality of a fit, the residual spectrum $R(i)$ can be defined as:

$$R(i) = \tau^+(i) - F(i) \tag{3.24}$$

Ideally, this residual spectrum only contains statistical noise. When systematic structures appear in the residual spectrum, this can indicate effects limiting the accuracy of the measurement (e.g. an absorber not accounted for in $F(i)$ or narrowband spectral structures caused by the instrument, see fibre modes in Sec. 4.2.3). As a measure to asses fit quality in an entire data set where not each individual residual spectrum can be inspected, statistics of the Root Mean Square (RMS) of the residual spectra can be used.

3.6 Errors and accuracy

3.6.1 Error estimation

The linear and non-linear fitting methods described in the previous section can yield the statistical errors Δa_p (polynomial) and ΔS_j (coefficients) from the linear fit and $\Delta d_{j,k}$ (shift and squeeze) from the non-linear fit respectively. For this, three conditions have to be fulfilled. (1) Pixel irradiance errors must have a finite variance, (2) irradiance errors of individual pixels must be independent and (3) the systematic error of the pixel irradiance must be zero (Stutz and Platt, 1996). Since the polynomial only is a by-product of the DOAS analysis, Δa_p are of no further interest.

The errors ΔS_j can be directly calculated as they follow from the covariance matrix of the linear fit that yield a single and unambiguous solution, which is the best result for the fit provided that shift and squeeze parameters $d_{j,k}$ were determined correctly. The errors of the non-linear Levenberg-Marquardt algorithm cannot be determined but are estimates based on further assumptions (Cunningham, 1993; Stutz and Platt, 1996). The determination of both types of errors is implemented in the DOASIS software package (Kraus, 2006) used in this thesis.

Estimating the combined errors of linear and non-linear fits

The shift and squeeze errors $\Delta d_{j,k}$ are not independent from ΔS_j and furthermore the error $\Delta d_{j,k}$ of one trace gas j propagates to the error $\Delta S_{j'}$ of another trace gas j' (Platt and Stutz, 2008). Since for this dependency no explicit relation for estimating the total error exists, Stutz and Platt (1996) proposed a method based on the artificial test spectra that adds a contribution of $\Delta d_{j,k}$ to ΔS_j. This has to be performed each time after linear and non-linear fits are finished and is not implemented in the fitting routine in DOASIS. The investigations of the contribution of $\Delta d_{j,k}$ to the total error $\Delta S_{\mathrm{tot},j'}$ of the coefficients S_j showed variations between 1% and 50% depending on the absorber. These experiments were done with a fit scenario with four absorbers that all could be shifted and squeezed independently and the resulting contribution of $\Delta d_{j,k}$ is the cumulative result of all shift errors. The influence of the non-linear errors on the total error then was estimated by calculating two sets of reference spectra Λ'_j with a modified channel-wavelength attribution accounting for the shift and squeeze uncertainty by quadratically summing errors $\Delta d_{j,k}$ determined in a previous fit. With these reference sets $\Lambda'^{,+}_j$ and $\Lambda'^{,-}_j$, two linear fits were performed yielding changed coefficients S^+_j and S^-_j from which the influence of the alignment errors $\Delta d_{j,k}$ on the total errors was estimated.

In the fits for this thesis, the same shift and squeeze parameters were used for all references (thus effectively linking them to each other assuming that the wavelength calibrations of the different references do not differ). The order of the corrections was limited to shift and linear squeezing/stretching. The non-linear fitting step therefore yields $d_{j,0} \pm \Delta d_{j,0}$ (shift) and $d_{j,1} \pm \Delta d_{j,1}$ (linear squeeze). With these non-linear and the linear coefficients a_p and S_j, $d_{j,0}$, and the respective errors, for the non-linear error estimation, the linear fit was repeated with fixed shift and squeeze parameters $d_{j,k,\mathrm{opt}}$ altered by their respective errors $\Delta d_{j,k,\mathrm{opt}}$.

$$F(i) = \sum_{p=0}^{q} a_p \cdot i^p + \sum_{j=1}^{m} S_j \cdot \Lambda^+_j(d_{j,0,\mathrm{opt}} \pm \Delta d_{j,0,\mathrm{opt}}, d_{j,1,\mathrm{opt}} \pm \Delta d_{j,1,\mathrm{opt}})(i) \tag{3.25}$$

With one shift and one squeeze parameter for all references, there are four combinations of fixed parameters $d_{j,k,\mathrm{opt}} \pm \Delta d_{j,k,\mathrm{opt}}$ yielding four coefficients for S_j: S^{++}_j, S^{+-}_j, S^{-+}_j, and S^{--}_j. As contribution of the alignment uncertainty $\Delta d_{j,k}$ to the total coefficient error $\Delta S_{j,\mathrm{tot}}$ the standard deviation of these coefficients is calculated:

$$\Delta S_{j,\mathrm{align}} = \sqrt{\frac{\sum_{n=1}^{4} \left(S^{xx_n}_j - \overline{S^{xx}_j} \right)^2}{4}} \tag{3.26}$$

where xx stands for the different combinations of fixed alignment parameters. Assuming that the errors of the linear fit and the contribution from the alignment uncertainty are independent, the total error of the slant columns is then calculated by quadratically adding both:

$$\Delta S_{j,\mathrm{tot}} = \sqrt{(\Delta S_j)^2 + (\Delta S_{j,\mathrm{align}})^2} \tag{3.27}$$

The relative influence of the non-linear error on the total error determined with this approach varied between 0.7% and 168% for the different absorbers (cf. Tab. 5.2). These results are discussed in Sec. 5.2.

Influence of residual structures

Often in DOAS fits, the residual of a fit contains structures other than pure noise. These can be the result of unaccounted or unknown absorbers but can also be instrumental artefacts that occur at random (Stutz and Platt, 1996). In contrast to pure noise spectra where the signals of individual pixels are independent, this is no longer true for these systematic structures. Therefore assumption (2) discussed above no longer is fulfilled and the real errors are larger than based on the statistical estimate.

When analysing atmospheric measurements where the real mixing ratios of trace gases are unknown, the determination of the true errors is difficult. Several studies have estimated this effect using artificial spectra and Monte Carlo techniques (e.g. Stutz and Platt, 1996; Hausmann et al., 1999). Stutz and Platt (1996) found that errors of both linear and non-linear fit errors are underestimated by a factor c_{D} of just over 1 up to 5 depending on the width of the spectral structures resolved by the instrument and the degree of correlation between adjacent pixels. Hausmann et al. (1999) report that errors typically are underestimated by a factor of $c_{\mathrm{D}} = 2$ - 5.

For selected absorbers, in this work the correction factor and the resulting detection limit was determined by analysing the scatter of mixing ratios for periods when it could be assumed that an absorber was not present in the atmosphere. This follows the approach in Tuckermann et al. (1997) and Alicke et al. (2002) and relies on an understanding of the daily cycle of the respective absorber. Only highly reactive radicals with short atmospheric life times were considered for which an atmospheric presence either requires solar radiation (BrO, ClO, IO) or the absence of it (OClO, OIO, OBrO, I_2, Br_2, and NO_3). For BrO, ClO, and IO mixing ratios are expected quickly decline after sunset (see details on halogen chemistry in Sec. 2.4). The other trace gases on the other hand, are expected to be absent when irradiations are sufficiently high. Details on the analysis of the correction factor c_{D} for these absorbers is given in Sec. 5.2.4. For all other species evaluated in this thesis, a dependence factor c_{D} of 3 was adopted.
In summary, the total error is:

$$\Delta S_{j,\mathrm{tot}} = (\underbrace{(\Delta S_j)^2}_{\substack{\text{Linear}\\ \text{error}}} + \underbrace{(\Delta S_{j,\mathrm{align}})^2}_{\substack{\text{influence of}\\ \text{shift/squeeze}\\ \text{uncertainty}}})^{\frac{1}{2}} \cdot \underbrace{c_{\mathrm{D}}}_{\substack{\text{Correction of}\\ \text{pixel}\\ \text{correlation}}} \tag{3.28}$$

3.6.2 Detection limit

The detection limit is defined as the smallest slant column or mixing ratio of an absorber that can be positively discerned in the spectral analysis. In accordance with the recommendations by the International Union of Pure and Applied Chemistry (IUPAC), a 3-σ criterion was applied for the detection limits in this thesis (Nič et al., 2009).

4
Instrumentation at Neumayer III

The basis of this thesis is a data set that was acquired over a period of 32 months from January 2016 to August 2018 on the German Antarctic station NM III. The central time series of trace gas mixing ratios was recorded by a LP-DOAS instrument that was purpose-built for these observations. It was deployed in a first campaign during the Antarctic summer season 2015/16 and measurements started on January 10th 2016. In January 2017, the instrument underwent detailed maintenance and minor improvements of the setup based on experiences during the first year of operation were realised. After the second year of operation, the trace gas observatory (see Sec. 4.1.3) had to be elevated to counterbalance snow accumulation. After this, the setup had to be re-aligned. Simultaneously, another major maintenance routine was performed. Measurements continued until August 10th 2018 when a fault of the light source ended the observations.

Between the maintenance campaigns, the instrument was supervised by the air-chemists of the successive wintering crews of NM III station as well as a remote connection to the instrument via satellite internet link to the station's network.

In addition to the observations with the LP-DOAS instrument, this thesis makes use of data sets that are routinely acquired by the trace gas (Sec. 4.1.3) and the meteorological (Sec. 4.1.3) observatories of NM III station. All data are made available on the public data base *PANGAEA - Data Publisher for Earth & Environmental Science* 2018. Furthermore, LP-DOAS observations are compared to co-located MAX-DOAS observations (Sec. 4.3) that are performed and evaluated by Frieß (2018) since 2001.

This chapter first describes NM III station, its surroundings, the two observatories relevant for the investigations in this thesis, and the measurements performed there (Sec. 4.1). In Sec. 4.2, the principle of LP-DOAS measurements is introduced and the new LP-DOAS setup, its measurement routine and the technical performance throughout the observation period are discussed in detail. Section 4.3 gives a brief introduction to MAX-DOAS observations, profile retrieval, and the co-located measurements at NM III.

4.1 Neumayer III station and its observatories

As the name suggests, *Neumayer III station* is the third Antarctic station on its site and is operated by Alfred Wegener Institute - Helmholtz centre for polar and marine research on behalf of the Federal Republic of Germany.[1] The two previous stations, *Georg von Neumayer (GvN)* and *Neumayer II (NM II)* were operated from 1981-1992 and 1992-2008, respectively. The stations are named after *Georg von Neumayer (1826-1909)*, a promoter and manager of science - in particular of the first International Polar Year (1882/83) and the first German Antarctic expedition in 1901 (Gernandt et al., 2007).

The station has two main purposes - (1) a wintering crew runs the permanent long-term observatories (geophysics, meteorology, air chemistry) and (2) during the research season in Antarctic summer, the station serves as a logistics hub and point of entry for field parties to the interior of the Antarctic continent (Wesche et al., 2016). In addition to the core observatories, there are other long-term installations investigating underwater acoustics and calls of marine mammals, the group behaviour of an Empire penguin colony close to the station, and an infra-sound station operated on behalf of the Comprehensive Test Ban Treaty Organisation (CTBTO) monitors the global compliance with the ban on atmospheric tests of nuclear weapons.

From late October until end of March the station can be reached via aircraft equipped with skids that are able to land on a groomed snow runway. Depending on sea ice conditions, supply by ship is possible from December until March.

4.1.1 Location

NM III station is located on the *Ekström* ice shelf in the Atlantic sector of coastal Antarctica at approximately 70°40' S, 8°16' W (see Fig. 4.1 left panel). Since the 240 m thick ice shelf is moving north at about 160 m per year, its position is not fixed. The closest ice shelf edge is about 6 km to the north-east. However, the shelf is grounded in this area and hence stabilized. In northerly direction, the distance to the shelf edge is about 18 km. Here, supplies can be unloaded from ice-breaking ships and dragged to the station. The distance to the closest grounding line - the location where the ice sheet flowing from the continent looses ground contact and becomes an ice shelf floating on the ocean - is about 23 km to the south-east (Matsuoka et al., 2018). Measured from the farthest grounding line 117 km south of the station, the Ekström ice shelf is about 135 km long.

The closest neighbouring station is the South African base SANAE IV 225 km to the south-east (see Fig. 4.1, left panel). The British station Halley VI, the only other in Antarctica located on an ice shelf (Schiermeier, 2004), is about 800 km south to south west of NM III (blue star on the insert map in left panel of Fig. 4.1.)

[1] The first-ever German station in Antarctica was Georg Forster station built 1976 by the German Democratic Republic (GDR) in the Schirmacher Oasis at 70°46' S, 11°41' E in the vicinity of the Soviet (now Russian) station Novolazarevskaya. It was operated until 1993 (Gernandt et al., 2007).

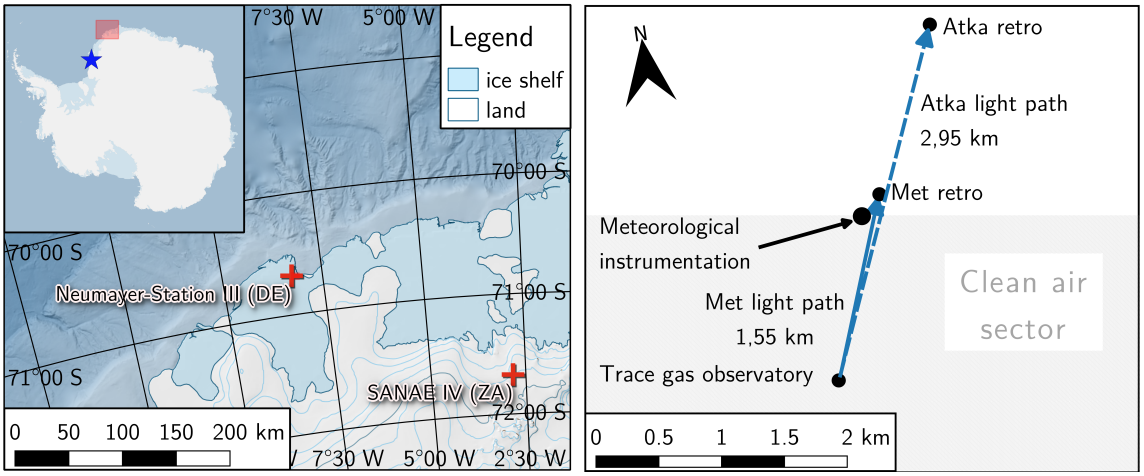

Figure 4.1: Location of Neumayer III station on the Ekström ice shelf (left panel) and overview of the installations in the vicinity of the station (right panel). (maps created with Quantarctica and data sets therein - Matsuoka et al., 2018)

As a coastal site in the north-eastern Weddell sea, NM III is subject to regular influence of low pressure systems circling the Antarctic continent (for a description of the general meteorological conditions see Sec. 6). During the fairly regular storms that these synoptic conditions induce, winds from easterly directions dominate and snow, mostly advected by the wind, leads to a yearly accumulation of about 80 cm. Therefore all installations, including the main station itself, have to be elevated on a regular basis to prevent them from being buried under the snow.

4.1.2 Meteorological observatory

Given the few permanently inhabited locations in Antarctica and the climatological importance of the Antarctic continent for global weather predictions, meteorological observations from this remote region of the globe are extremely valuable (König-Langlo and Loose, 2007). The meteorological observatory of NM III station has been operated since the commission of the GvN station in 1981.

Since then, three-hourly synoptic observations, daily upper air soundings and weekly ozone sonde launches are performed and have been complemented by a range of additional observations. The observatory is part of several networks including the Global Telecommunication System (GTS), the Global Climate Observatory System (GCOS), the Global Atmospheric Watch (GAW), the Network for Detection of Atmospheric Composition Change (NDACC) and the Baseline Surface Radiation Network (BSRN).

The following descriptions of the instrumentation and available data are based on König-Langlo and Loose (2007), which discusses the observatories of GvN and NM II stations. Due to the importance of continuity in long-term monitoring, most procedures and descriptions also apply to the observatory of NM III.

Parameter	Temperature		Wind speed		Wind direction		Pressure	Relative humidity
Short name (altitude)	T10 10 m	T2 2 m	FF10 10 m	FF2 2 m	DD10 10 m	DD2 2 m	Pout 0 m	RH 2 m
Method	ventilated Pt100		cup anemometer		wind vane		quartz barometer	dewpoint hygrometer
Uncertainty	± 0.1 K		± 0.4 m s^{-1}		± 1.5°		± 0.5 mbar*	± 1%
Instrument	Thies Clima 2.1265.xx.000		Thies Clima 4.3324.32.000				Paroscientific Digiquartz 6000-16B	Vaisala HMP337

Table 4.1: Overview of basic meteorological parameters and related instrumentation at Neumayer III. Altitudes indicate elevation above the snow surface. (*) The accuracy of the barometer is indicated as ± 0.08 mbar but due to the tidal movement of the ice shelf and its isostatic movement by snow accumulation and ice shelf basal melting, König-Langlo and Loose (2007) indicate the uncertainty of the altitude determination for sea level pressure correction to be the dominant source of uncertainty.

Basic meteorological parameters

The three-hourly synoptic observations rely on continuous measurements of basic meteorological quantities. To ensure that these measurements are undisturbed by the influence of the main station and other installations (e.g through shadowing, aerodynamic influence on wind speed, direction of snow accumulation patterns), most of the instrumentation is located at a measurement site a few hundred metres south-east of the station (see right panel in Fig. 4.1). The available parameters, accuracies, measurement principles as well as instrument types can be found in Tab. 4.1.

The available data sets on PANGEA contain 1-minute averages of all parameters. The data used for this thesis were provided by König-Langlo (2016b) and König-Langlo (2017b) for the period from January 2016 until January 2017 and by Schmithüsen and Schulz (2018b) from February 2017 until January 2018. The data from February 2018 until August 2018 was obtained through personal communication from Schmithüsen and Müller (2019b) and will be made available on Pangea in the course of 2019.

Radiation measurements

Radiation measurements at NM III are carried out according to the guidelines of the Baseline Surface Radiation Network (BSRN) (König-Langlo et al., 2013). Instruments directed both upwards and downwards allow to determine net energy balances in different spectral ranges. All sensors are ventilated with pre-heated air to prevent hoar frost formation and are exchanged yearly with sensors recently calibrated at the World Radiation Centre in Davos, Switzerland (König-Langlo and Loose, 2007). The available temporal resolutions are 1-min averages. For the period from January 2016 until January 2017 the data is provided by König-Langlo (2016a) and König-Langlo (2017a), for February 2017 until January 2018 by Schmithüsen and Schulz (2018a). The period from February until August 2018 is

Radiation type	Short-wave downward	Short-wave upward	Diffuse	Direct	Long-wave downward	Long-wave upward
Short name	SWD	SWU	DIFF	DIR	LWD	LWU
Spectral range [nm]	250 - 3500	250 - 3500	250 - 3500	200 - 4000	4000 - 50000	4000 - 50000
Method	Pyranometer			Pyrheliom.	Pyrgeometer	
Uncertainty	< 1%	< 1%	< 1%	< 1%	5 $W m^{-2}$	5 $W m^{-2}$
Dir. response (up to 80° at 1000 W)	<5 $W m^{-2}$	<5 $W m^{-2}$	<5 $W m^{-2}$	-	-	-
Instrument	Kipp & Zonen CMP 22	Kipp & Zonen CMP 22	Kipp & Zonen CMP 22	Kipp & Zonen CHP 1	Eppley PIR	Eppley PIR

Table 4.2: Overview of radiation measurement instrumentation at Neumayer III operating to the specifications of the Baseline Surface Radiation Network (BSRN). For details see König-Langlo et al. (2013).

not yet published and was obtained through personal communication from Schmithüsen and Müller (2019a).

In addition to the BSRN parameters, which are listed in Tab. 4.2, additional, non-standard radiation measurements are performed e.g. with instrumentation equipped with long-pass filters. An overview of these parameters can be found in Tab. 4.3.

Radiosondes and ozone sounding

Daily radiosondes are launched from the roof of NM III station to obtain vertical profiles of air pressure, temperature, relative humidity and, through data on lateral displacement obtained via GPS, the wind vector. The sonde used is a Vaisala RS92-SGP (Vaisala, 2013). Temperatures are measured with a capacitive wire in 0.1 °C resolution with an uncertainty of ±0.5 °C. Relative humidity is determined with a thin-film capacitor heated twin sensor with 1% resolution and ±5% uncertainty. Atmospheric pressure is measured with a silicon sensor with 0.1 hPa resolution and ±1 hPa uncertainty from 1080 to 100 hPa and ±0.6 hPa from 100 to 3 hPa ambient pressure. The positioning through GPS is estimated to be precise to ±10 m horizontally and ±20 m vertically. The wind vector determined from the changing GPS position has an accuracy of ±0.15 $m s^{-1}$ and ±2 °. The sonde is carried by a TOTEX rubber ballon that is heated before the launch and typically bursts between 27 km and 37 km altitude (König-Langlo and Loose, 2007).

The radio sonde launches are usually performed daily at 11:00 UTC. If, due to high wind speeds, a first launch attempt fails, a second sonde is prepared. If that is unsuccessful as well, the next attempt is made 6 hours later. Data from the sonde is transferred to a ground module and the full resolution raw data is published on PANGEA. The data used for this thesis was provided by König-Langlo (2016c), König-Langlo (2017c), and Schmithüsen and Schulz (2018c). Data for 2018 is not yet published and was obtained through personal communication from Schmithüsen and Müller (2019c).

Once a week the radio sonde is complemented by an ozone sonde. For this, the RS92-SGP has an interface for a 6A ECC ozonesonde produced by Science Pump Corporation

Radiation type	Short-wave downward with OG1 filter	Short-wave downward with RG8 filter	Ultra Violet	Sunshine duration*
Short name	SWD OG1	SWD RG8	UV	SSD
Spectral range [nm]	525 - 2800	696 - 2800	295 - 385	400 - 1100
Method	Pyranometer		Total UV Radiometer	Photodiodes
Uncertainty	< 1%	< 1%	< 1%	< 10%
Instrument	Kipp & Zonen CM11	Kipp & Zonen CM11	Eppley TUVR	Kipp & Zonen CSD3

Table 4.3: Overview of additional radiation measurement instrumentation at Neumayer III. (*) Sunshine is defined by the World Meteorological Organisation (WMO) as direct radiation at $> 120\,\mathrm{W\,m^{-2}}$. For details see König-Langlo and Loose (2007).

(SPC, 1999). The measurement principle relies on the release of electrons in a redox reaction of ozone in an iodide solution through which the ambient air is pumped. The manufacturer does not indicate the accuracy in the manual but references performance review literature (e.g. Beekmann et al., 1995; Deshler et al., 2008). In these publications the biases compared to other measurement techniques (both co-located in-situ and ground-based) were determined to be about 25% (Beekmann et al., 1995) and 10-15% (Deshler et al., 2008). However, this strongly depends on the correct preparation of the iodide solution to the manufacturer's specifications. The ozone vertical profiles are part of the radio sonde data sets mentioned above.

With regard to the vertical sounding it should be noted that the launches take place from the roof of NM III station (18 m from the base plate). Due to snow accumulation, the station itself furthermore sits on a hill of snow of about 10 m altitude above the surrounding snow surface (determined by laser altimetry -Köhler (2018), personal communication). Therefore, the first 30 m above the ground are not covered by the sondes.

Ceilometer

Ceilometers use the backscatter signal from short laser pulses sent out in vertical direction into the atmosphere to continuously determine the vertical structure of the atmosphere. The pulses are scattered by molecules, aerosols, precipitation as well as cloud droplets. The strength of the backscatter signal from a certain altitude, which is determined through the runtime of the pulse, depends on size, concentration, and optical properties of the different scatterers.

At Neumayer, a Vaisala CL-51 ceilometer is installed on the station's roof.It is mainly used to determine the cloud base height both for the meteorological observatory and the aviation weather forecast. It is designed to detect high cirrus clouds (up to 13 km at a total vertical range of 15 km) even through intermediate cloud layers at lower altitudes (Vaisala, 2010). It operates at 910±10 nm laser wavelength with a pulse repetition rate of 6.5 kHz.

One measurement takes 6 s and the vertical resolution is 10 m with profiles starting at 40 m above ground level. Since the raw backscatter profiles are recorded in addition to cloud layer heights, this data can be used for different purposes related to the vertical structure of the atmosphere and meteorology. Gossart et al. (2017) for example used the ceilometer at NM III for blowing snow detection, others have investigated the possibility to determine the height of the planetary boundary layer from ceilometer profiles at other locations (Caicedo et al., 2017; Escobar Castells, 2018).

4.1.3 Trace gas observatory

The remote location of the Antarctic continent and its pristine troposphere (see Sec. 2.2.2) make NM III and other Antarctic research facilities ideal locations to study a background atmosphere with only minor anthropogenic and, due to the almost ubiquitous ice and snow cover, also little terrestrial influence. Compared to both polluted and pristine regions in lower latitudes, there are only very few sources of aerosols and trace gases in Antarctica and long range transport or sources in the surrounding Southern ocean dominate (Weller et al., 2007).

Atmospheric composition in Antarctica can serve as a backdrop against which other regions can be compared. Due to the distance from most sources and the transport-related delay of mixing, the signal of short-term variations and local sources is drastically reduced. This allows to determine global trends in trace gas concentrations (e.g. SF_6 or ^{14}C, Levin et al., 2010a; Levin et al., 2010b). Furthermore, understanding composition, processes like aerosol formation (Minikin et al., 1998), or isotopic fractionation (Wagenbach et al., 1998; Elsässer et al., 2011) and, based on that, regional and global transport (Weller et al., 2002; Weller et al., 2014) is key for the interpretation of climate records contained in the ice sheets on the continent and global atmospheric circulation.

The trace gas observatory at NM III station serves both these purposes - (1) as a background station for the current atmosphere its instruments are part of the Global Atmosphere Watch (GAW) network and (2) to facilitate the interpretation of signals in ice cores drilled on the plateau further inland (e.g. at Kohnen station 553 km south of NM III - EPICA community et al., 2004).

To obtain representative measurements and samples of Antarctic background composition, a potential influence of the station or vehicles must be prevented. Therefore, the observatory is located about 1.5 km south of the station in the so-called clean air sector (see Fig. 4.1 right panel) that must not be entered by vehicles with an internal combustion engine (unless precautions are taken beforehand). Dominant wind directions are east to south (see Chapter 6 for details) and northerly winds are very rare so that an influence of exhaust produced by activities at the station can be excluded most of the time. At the observatory, wind direction, wind speed and particle concentrations are constantly monitored and sampling is stopped when threshold values are exceeded.

Based on past experience (Weller et al., 2007), winds from a 330° - 30° sector, wind speeds below $2\,m\,s^{-1}$ or above $17.5\,m\,s^{-1}$ or condensation particle concentrations exceeding $2500\,cm^{-3}$ (summer), $800\,cm^{-3}$ (spring and autumn) and $400\,cm^{-3}$ (winter) respectively interrupt sampling and the data is flagged as potentially polluted. Excluding the high wind speed condition, throughout the year this applies to about 2% of the data (Weller et al., 2007). To prevent a local source of pollution, the electricity for the instrumentation in the observatory is provided via cable from the main station.

The observations in the long-term measurement program can be roughly divided into (1) high volume aerosol sampling on cellulose filters (sampled volumes between 20000 and 40000 m^3), which are analysed in a laboratory in Germany for ionic compounds and radio-isotopes, (2) in-situ measurements of trace gases and aerosol particle concentrations, optical properties or size distributions and (3) air samples taken to analyse greenhouse gas concentrations and isotopic signature (e.g. CO_2, CH_4, N_2O) and tracers of anthropogenic origin (e.g. SF_6, ^{85}Kr).

A detailed overview of available measurements can be found on the observatory's website, and in Weller et al. (2007) and Tables 1 and 2 therein. The discussion of the instrumentation in the following two sections will focus on the data sets used in this work. These are available on PANGEA (Weller, 2017; Weller, 2018a; Weller, 2018b) or have been obtained through personal communication (Weller, 2019a; Weller, 2019b) and will be made available on PANGEA in the course of 2019.

Aerosol measurements

The high volume filter sampling yields mass concentrations of ionic compounds in aerosols (in ng m^{-3}) including methane sulfonic acid (MSA^-), chloride (Cl^-), nitrate (NO_3^-), sulfate ($[SO_4]^{2-}$), sodium (Na^+), with an uncertainty of ±10% to ±15% and bromide (Br^-), ammonium (NH_4^+), potassium (K^+), magnesium (Mg^+) and calcium (Ca^+) with an uncertainty of ±20% to ±30% (e.g. Weller, 2017). The filters are usually exchanged on a daily basis. Further details and a discussion of long-term trends of several of these ionic compounds can be found in Weller et al. (2011b).

In addition to aerosol composition, a number of instruments measure further aerosol properties. A TSI Model 3563 integrating nephelometer (TSI, 2002) measures total and backscatter extinction at wavelengths of 450 nm (blue), 550 nm (green), and 700 nm (red). The measured scattering coefficients ϵ are the average extinction by scattering per distance caused by the composition of aerosol particles i with scattering cross-sections $\sigma_{i,\mathrm{aer}}(\lambda)$ in the sample. The sensitivity is $\pm 2.0 \cdot 10^{-7}\,\mathrm{m}^{-1}$ for an averaging time of 60 s for the red and green channels and $\pm 3.0 \cdot 10^{-7}\,\mathrm{m}^{-1}$ for the blue channel. From this measurement of the total scattering coefficient $\mu_{\mathrm{tot}}(\lambda)$, the Ångström coefficient α (see Sec. 3.2), and with the backscatter coefficient $\mu_{\mathrm{back}}(\lambda)$, the backscatter ratio β can be calculated:

$$\alpha_{\lambda_1,\lambda_2} = -\frac{\log(\epsilon_{\mathrm{tot}}(\lambda_1)/\epsilon_{\mathrm{tot}}(\lambda_2))}{\log(\lambda_1/\lambda_2)} \tag{4.1}$$

$$\beta = \epsilon_{\mathrm{back}}(\lambda)/\epsilon_{\mathrm{tot}}(\lambda) \tag{4.2}$$

Black carbon aerosols, important for the global radiation due to their high absorptivity, are measured with absorption photometers where transmission through a filter impacted by the aerosols is compared to a clean section of the same material. At NM III, a Multi-Angle Absorption Photometer (MAAP) model 5012 by Thermo Electron Corp. (now Thermo Fisher Scientific) is installed (TFS, 2009). Aerosols are collected on a glass filter tape with an air flow of 1 $m^3\,h^{-1}$. When a transmission reduction of 20% is reached, the tape is automatically transported forward. Absorption is measured at a wavelength of 670 nm (TFS, 2009) and the detection limit for 10-min averages is < 50 ng m^{-3} (for details see Weller et al., 2013). Since the exhaust of internal combustion engines contains high

concentrations of black carbon in the form of soot, the MAAP can be used to check for contaminations by the station or vehicles.

The concentration of aerosols is continuously measured by a Condensation Particle Counter (CPC) at a 1-min temporal resolution. The model used at NM III is a TSI Model 3022A (TSI, 1999) that can detect particles with diameter of 7 nm and above. After entering the instrument, the aerosols pass through a heated area that supersaturates the air flow in butanol vapour. The flow is then cooled and the butanol condenses on the particles in the flow. After the condensation, the butanol droplets are large enough to be detected optically. Depending on the particle concentration, individual particles are counted ($c_{part} < 10^4\,cm^{-3}$) or the scattered light in the detection volume is measured (TSI, 1999). Details on the particle concentration measurements and long-term trends at NM III can be found in Weller et al. (2011a).

From February until December 2017, a Scanning Mobility Particle Sizer (SMPS) was operated continuously at the trace gas observatory. In this setup, a variable electrical field separates particles that have been brought into a charge equilibrium into different sizes by making use of the different electrical mobility caused by their mass differences. This classifier unit (here a TSI model 3080, TSI, 2009) is coupled to a CPC that thus sequentially determines particle concentrations in the different size bins. The setup is able to detect particles with diameters >16 nm up to 947.5 nm (with size bins increasing from 0.6 nm to about 32 nm). In Weller et al. (2015) aerosol size distributions and new particle formation events have been investigated at NM III and details on SMPS measurements with the setup described above can be found.

Trace gas measurements

In addition to the flask sampling of stable trace and greenhouse gases mentioned above, the trace gas observatory is equipped with a UV absorption O_3 monitor (Ansysco O341M ANSYCO, 2000). It measures sample air and O_3-filtered air in alternating 10 s intervals using a mercury lamp at 253.7 nm as light source (with the measurement principle of classical absorption spectroscopy described in Sec. 3.1). Temperature and pressure are corrected to standard conditions and calibrations using an internal ozone generator are performed on a regular basis. A detection limit of 1 ppb is achieved at a temporal resolution of 1 minute.

4.2 Long-Path DOAS

For the investigations in this thesis, a new Long-Path (LP) DOAS setup was purpose-built for operation under Polar conditions. Its observations complement the long-term measurements described above as well as MAX-DOAS measurements that are running at the trace gas observatory since 2003 (Frieß, 2018) and that briefly will be discussed in Sec. 4.3 below. [2]

As a remote sensing technique, active long-path path differential absorption spectroscopy (LP-DOAS) is well established. It was introduced with the first applications of the DOAS principle by Platt et al. (1979), Platt and Perner (1980), Platt et al. (1980), and Platt and Perner (1983). Since then the technique has been constantly developed further and was applied in a large variety of scientific investigations. It was used to study urban air quality and horizontal (Pöhler, 2010) as well as vertical distribution of pollutants (Volkamer et al., 2005; S. Wang et al., 2006; K. L. Chan et al., 2012), volcanic emissions (Kern et al., 2009), atmospheric halogen chemistry in coastal areas, deserts (Holla et al., 2015; Schmitt, 2016) and polar regions (Hausmann and Platt, 1994; Hönninger et al., 2004; Pöhler et al., 2010; Frieß et al., 2011; Stutz et al., 2011; Zielcke, 2015).

This section will introduce the LP-DOAS measurement principle and then discuss the different components of the new instrument at NM III. A number of improvements incorporated in this setup were developed prior to this thesis project in the group for Remote Sensing and Atmospheric Chemistry at the Institute of Environmental Physics at Heidelberg University and are described in detail in Eger (2014) and Nasse et al. (2019).

4.2.1 Measurement principle

LP-DOAS is an *active* DOAS technique that uses an artificial light source to provide the measurement signal (in contrast to passive techniques like MAX-DOAS or satellite instruments, which use sun light that was scattered in the atmosphere and/or reflected from the Earth's surface).

The radiation from the LP-DOAS light source is sent through the atmosphere where trace gases absorb it. At the end of the atmospheric path, it is collected and analysed based on the DOAS principle (see Sec. 3.3). First LP-DOAS setups were bi-static with separate telescopes for sending and receiving. The application of corner cube retro reflector elements (for optical properties see Rityn, 1967; Eckhardt, 1971) allowed the introduction of mono-static setups (Axelsson et al., 1990), where the sending telescope also receives the light that returns from a retro-reflector array.

In addition to a reduced technical complexity of alignment and operation, this doubles the atmospheric light path within the same air mass. Typical distances between telescope and reflectors in these setups range between a couple of 100 m up to 10 km. Light transmission between the light source and telescope (for sending) and telescope and spectrometer (for receiving) can be realised with mirror optics (requiring a coaxial or Newton type telescope) or with optical fibres. The latter was introduced by Merten et al. (2011) and has advantages for both total transmission of the setup and handling of the optics. The setup used for this thesis is based on this concept but integrates a number of changes introduced by Eger (2014).

[2] From 1999-2003, a zenith sky scattered light DOAS was operated on the station.

The investigation of the performance improvements of these modifications were published in Nasse et al. (2019). Here, only the resulting setup will be described. A schematic depiction of the setup is shown in Fig. 4.2.

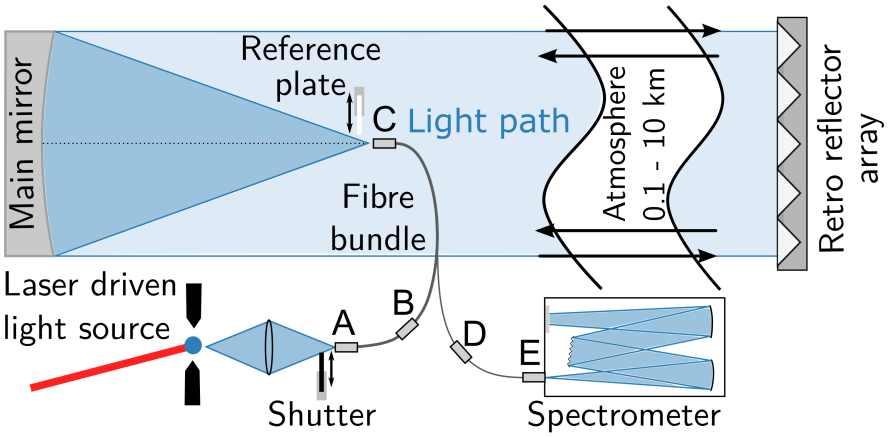

Figure 4.2: Schematic depiction of the LP-DOAS setup. Adapted from Sihler (2007).

Radiation from a laser-driven xenon lamp is coupled into the central fibre of a y-shaped optical fibre bundle (at A in Fig. 4.2, see Sec. 4.2.3 and Fig. 4.7 for details on the fibre bundle configuration). This sending fibre leads to the focal point of the telescope (B) that sends the light through the atmosphere onto an array of retro-reflectors. There, the radiation is reflected, traverses the atmosphere a second time, and re-enters the telescope. To collect this light for analysis, it has to reach a ring of optical fibres located around the sending fibre (see Fig. 4.7). Therefore, the image of the sending fibre has to be blurred.

There are a number of effects that in principle induce this: (a) the comatic aberration of the main mirror for an incident beam that is parallel but not paraxial, (b) diffraction at the apertures of telescope (typical diameters 30-45 cm) and retro-reflectors (common elements have a 62.5 mm diameter with open apertures between 50 and 58 mm), (c) surface faults of mirror and retro-reflectors, (d) the spherical aberration of a spherical main mirror in combination with the lateral offset induced by the retro-reflector elements (see Rityn, 1967; Eckhardt, 1971), and (e) atmospheric turbulence. In addition to these effects, which are either fixed by the choice of components or depend on the state of the atmosphere, the fibre can be moved slightly out of focus to optimize transmission (f).

Merten et al. (2011) estimated the influence of all the effects above and found (a) to (c) to be negligible. Given a fixed effect of the spherical aberration (d), the defocussing (f) has to be adapted taking into account the influence of the atmosphere. There are two local maxima for the transmission (Merten et al., 2011), one for a negative translation of the fibre bundle (i.e. towards the main mirror) and one for positive translations (away from the main mirror). Which of these positions yields the higher total transmission is determined by the size of the image of the sending fibre at the distance of the retro-reflector array in relation to the array's size.

The light collected at (B) is then coupled from the fibre ring to a single, larger diameter mono fibre at (C) from where it enters the spectrometer passing an optical slit at (D). The spectrum created by the diffraction grating is recorded by a CCD camera. To obtain an absorption-free spectrum of the light source ($I_0(\lambda)$ in Eq. 3.5), a reference plate is moved

into the light path at (B) thus creating a shortcut (SC) for the light. To determine the influence of atmospheric background light, background spectra are recorded by shutting off the light source at (A).

4.2.2 Laser-driven light source

A light source for active DOAS measurements ideally has a spectrally smooth emission spectrum (see Sec. 3.4.2) and a high spectral radiance over a broad wavelength range emitted from a small surface area.

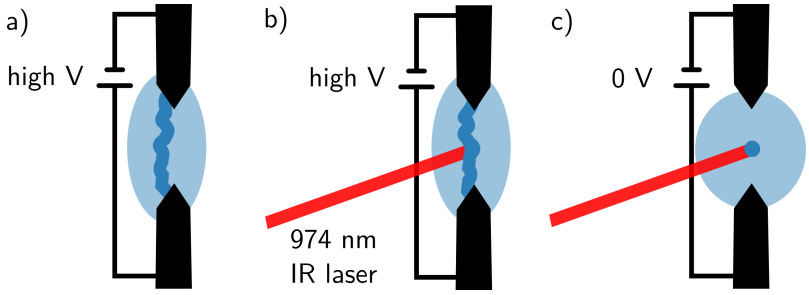

Figure 4.3: Principle of ignition and operation of the laser driven xenon light source.

The LP-DOAS setup at NM III uses a Energetiq EQ-99X Laser Driven Light Source (LDLS) (Energetiq, 2018a). Its functional principle is shown in Fig. 4.3. Like in conventional arc lamps, first a plasma arc is created between two electrodes by applying a high voltage (a)). Then an infra-red, continuous wave laser is focussed onto the plasma providing it with (additional) energy in the small focal point (b)). Finally, the high voltage is switched off and the plasma only persists in the focal point of the laser (c)). The laser used in the EQ-99X operates at a wavelength of 974 nm with a power of 20 W.

Due to the well defined and spatially stable focal point of the laser, the resulting plasma spot is very small (experimentally determined as 63 x 144 µm Full Width at Half Maximum (FWHM), Nasse et al., 2019) and spatially stable. This is a major advantage over conventional xenon lamps where the plasma arc is between 3 to 5 times larger. In these lamps, it is also less stable due to plasma arc instabilities induced by surface irregularities of the electrodes, which over time are enhanced by wear caused by the plasma itself. The LDLS principle and the reduced abrasion of the electrodes furthermore is very favourable for the life time. Conventional xenon lamps typically last between 200 and 2000 h (Kern et al., 2006) whereas the EQ-99X in the NM III setup reached more than 22500 h (the manufacturer indicates life times of at least 10000 h).

The exchange of a light bulb in setups with conventional arc lamps requires a time-consuming realignment of the optics and a skilled operator. The long life-times of the LDLS therefore reduce handling complexity and allow the operation of LP-DOAS setups in low maintenance, long-term applications like the 32-month measurement campaign at NM III. Since the laser can be reused and bulb and optics in the lamp housing of the EQ-99X can be refurbished by the manufacturer, in the long run, operation of LDLS is also cheaper than conventional arc lamps. [3] A detailed description of the LDLS can be found e.g. in Zhu and Blackborow (2011a), Horne et al. (2010), and Islam et al. (2013).

[3] It should be noted that in addition to xenon or other gas discharge lamps, also LEDs have been used as

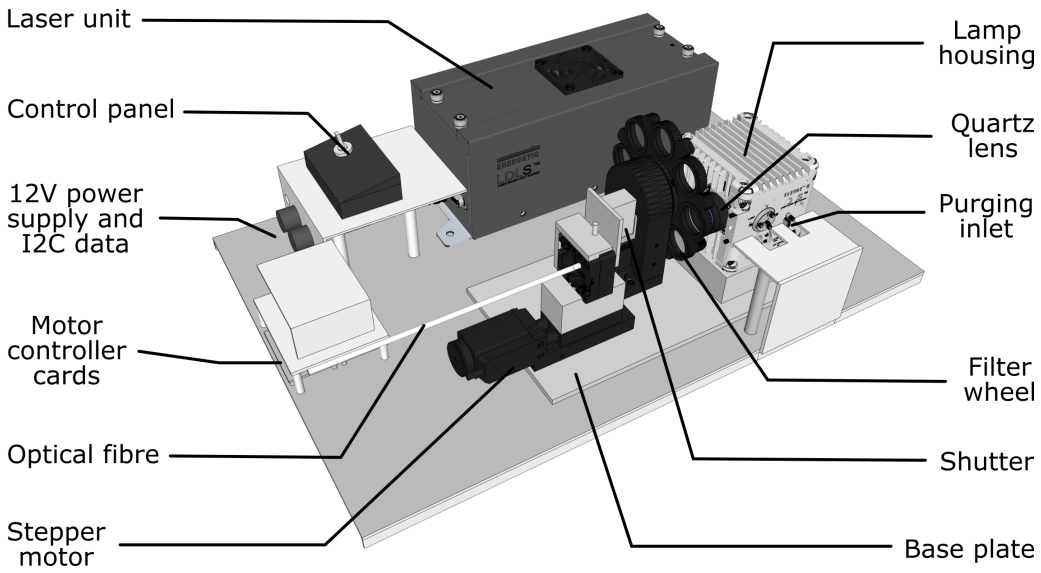

Figure 4.4: Setup of the light source with coupling lens, filter wheel, and shutter on a stepper motor. Lamp housing, filter wheel and stepper motor are mounted on a stable aluminium base plate. This, together with the other components, is fixed on a light-weight plate. During operation filter wheel, light path, and stepper motor with the shutter are covered. See Fig. E.1 in the appendix for a sketch.

The LDLS setup for the NM III LP-DOAS instrument is shown in Fig. 4.4. All components are mounted on a light-weight metal plate. The optical components for coupling into the fibre are additionally fixed on a 5 mm aluminium base plate to ensure stability. A quartz lens with a focal length of $f = 25\,\text{mm}$ is attached to the lamp housing in an optical tube at a distance of 31 mm from the plasma spot. The light passes through the lens and a filter wheel with eight positions (Standa 8MRU-1WA) . It is focussed onto the fibre, which is mounted on a stepper motor (Standa 8MT173-30) that can move along the optical axis. A shutter attached to a magnetic switch can be moved vertically into light path. During operation, filter wheel, light path, and stepper motor with the shutter are covered by an enclosure (see Fig. E.1 in the appendix).

The lamp housing is fitted with a purging inlet that can be connected to a nitrogen gas bottle. Constant purging with N_2 prevents ozone formation inside the housing, which increases irradiances in spectral regions where O_3 absorbs (Zhu and Blackborow, 2011b). In tests, the effect of a constant flow of $1\,\text{l}\,\text{min}^{-1}$ was an increase of the spectral irradiance of about 30% at 255 nm wavelength (Nasse et al., 2019). Furthermore, the slight overpressure created by the gas flow prevents pollutants, in particular organic material, from entering the housing where it can be pyrolysed by the UV radiation. The resulting carbon residue can deposit on light bulb and optics eventually leading to a failure of the light source.

light sources for LP-DOAS measurements (Kern et al., 2006; Sihler et al., 2009). However, the available radiances, in particular in the UV, to date are still much lower than that of xenon lamps. Furthermore, due to the functional principle of LEDs, the spectral coverage of a single LED is relatively narrow and the temperature of the LEDs has to be kept very stable to prevent fluctuations of the spectral radiance. Nevertheless, successful measurements have been performed, in particular in applications with limited power supply (e.g. at a volcano in Kern et al., 2009).

Due to logistical reasons, a constant nitrogen purging was not feasible for the measurements at NM III. To prevent a contamination of the lamp housing, it was purged daily for 30 min with clean air that was created by pumping ambient air through a multi-stage filter system. The air was dried with silica gel, followed by filtering with activated carbon and a particle filter.

Stray-light suppression

A major limitation of DOAS measurement accuracy is light that does not contribute to the measurement signal. In active DOAS applications, one can distinguish between (1) atmospheric background light that enters the light path and the instrument in addition to the measurement signal and (2) spectrometer stray-light caused by undesired deflections of light inside the spectrometer. The former depends on the relative position of the sun to the instrument, the scattering properties of the atmosphere as well as the relation of the telescope's field of view at the retro distance in relation to the retro-reflector array size. To correct it, background spectra of both atmospheric and shortcut measurements are recorded on a regular basis. For this, the light source is shut off with a magnetic switch that moves a plate into the light path (rather than switched off and then re-ignited, which would cause wear on the electrodes). Since during long-term operation, this mechanism failed every so often, a blind insert was added to the filter wheel and was additionally moved into the light path directly behind the lens for background measurements.

Spectrometer stray-light can originate from both atmospheric background light and the measurement signal itself (when e.g. light from the visible spectral range is deflected inside the spectrometer into a measurement in the UV). Nasse et al. (2019) found that for measurements around 300 nm about 90% of internal stray-light originated from the spectral region between 450 and 650 nm for a grating/spectrometer setup commonly used for LP-DOAS. Since typically the irradiance of the measurement signal is at least an order of magnitude higher than from atmospheric background light, the measurement signal itself has the largest potential influence on internal stray-light levels.

To reduce the light source induced stray-light, during the measurement the signal should be limited to the current spectral region of interest as much as possible. In a first step, the light is selectively transmitted through band pass glass filters in the filter wheel (see Tab. 4.4 below). Then the very small and spatially extremely stable plasma spot of the LDLS and the chromatic aberration of the quartz lens are exploited to selectively couple the desired spectral region into the fibre by moving it to the respective focal point with the stepper motor. The principle of this mechanism is shown in Fig. 4.5.

By moving the fibre along the optical axis of the quartz lens, the different foci created by the chromatic aberration of the lens can be reached. All other spectral regions are suppressed.

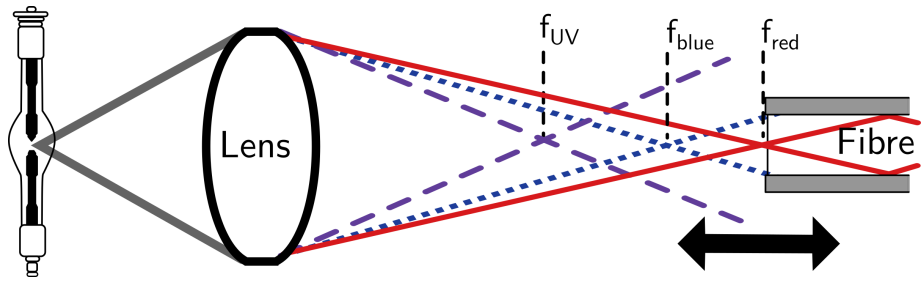

Figure 4.5: Principle of the chromatic aberration filter. The chromatic aberration of the quartz lens leads to separated, aligned foci for the different spectral regions. Relative distances are determined by the respective refractive index. Since that strongly increases in the UV, here a very selective filtering is possible.

Spectral properties

In the spectral range from about 280 nm to 700 nm relevant for measurements in this thesis, the EQ-99X light source offers a high spectral radiance with highest values between 450 nm and 470 nm (see Fig. 4.6). The manufacturer indicates a spectral coverage between 170 nm - 2100 nm, an average spectral radiance of 10 mW mm^{-2} sr^{-1} and a total power of approximately 0.5 W (Energetiq, 2018b). The pressure broadening of xenon emission lines that is induced by the high gas pressure inside the bulb in the LDLS suppresses narrow-band structures that could interfere with the analysis of narrow-band absorption and would require a different treatment of the linearisation of the DOAS equation (Eq. 3.11) (Platt and Stutz, 2008).

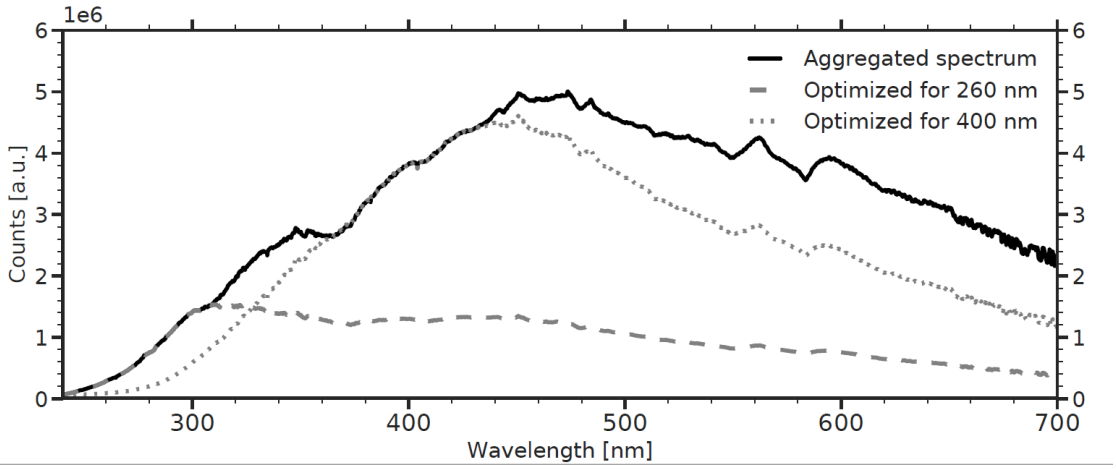

Figure 4.6: Lamp spectra of the LDLS for different coupling configurations. The solid line is the aggregated spectral radiance as recorded by a typical spectrometer used for LP-DOAS. The dashed and dotted lines show the spectral radiances when the position of the fibre is optimized for 260 nm and 400 nm respectively. (adapted from Nasse et al., 2019)

When the spectral radiance of a LDLS is determined with a LP-DOAS setup, the chromatic aberration of the coupling lens described above prevents the recording of the entire spectral radiance spectrum with one light source configuration. The spectral radiance distribution shown in Fig. 4.6 is the aggregated result of measurements for which the

fibre was moved along the foci of several spectral regions as described above (measured by Eger (2014) and adapted from Nasse et al. (2019)). Two of the actually recorded spectra are shown together with the aggregated lamp spectrum and illustrate the principle of the stray-light suppression by using the chromatic aberration.

4.2.3 Optical fibre bundle

The optical fibre bundle in the LP-DOAS setup transmits the light from the LDLS to the telescope and the returning light from the telescope to the spectrometer. The 855 cm long fibre bundle for the NM III LP-DOAS was custom built by Loptek and contains SBUVPI step index, multimode UV fibres. The bundle is covered with a stainless steel tube for improved protection against mechanical stress. For water-tight coupling into the telescope, this tube is equipped with two sealed feed-through cases, which allow to enter the telescope from the front and the back side (see Sec. 4.2.4 for details). The different sections of the fibre bundle with respective cross-sections at the coupling points A to D corresponding to the steps in Sec. 4.2.1 and Fig. 4.2 are sketched in Fig. 4.7. Exact measurements of the different sections are shown in Fig. E.3 in the appendix.

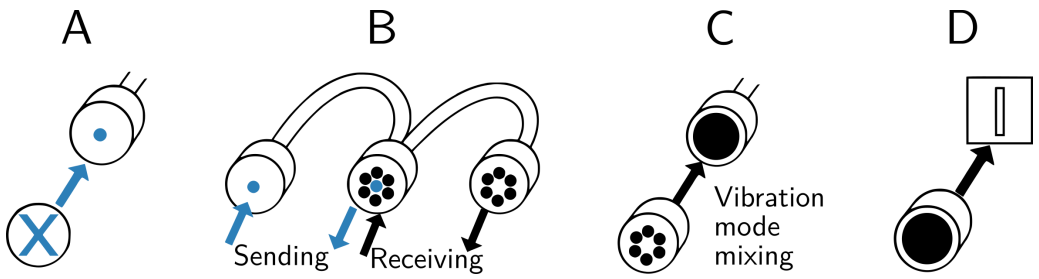

Figure 4.7: Fibre cross sections and configurations in the different segments of the optical fibre bundle. The end face of the mono fibre (D) is roughened with a 5 µm polishing sheet to homogenize the grating illumination in the spectrometer.

Due to the high radiance and small plasma spot of the LDLS, a single 200 µm diameter fibre at the core of the y-shaped bundle is sufficient for coupling into the sending section (A). This core fibre leads to the telescope (B). The receiving section of the fibre is a ring of six 200 µm diameter fibres that collect the light at B and lead towards the spectrometer. At (C) this ring then couples to a single 800 µm diameter fibre that leads to the 200 µm optical slit of the spectrometer.

Fibre modes

Inside an optical fibre, electro-magnetic radiation travels in different distributions, the so-called *modes*. These are a result of the radial symmetry of the fibre and can be described by solving the Helmholtz wave equation for the propagation of the radiation in the fibre core using Maxwell's equations (Kaminow et al., 2013). The possible modes are determined by the dimension of the fibre core, the difference in the refractive index between core and cladding (which determines the numerical aperture of the fibre) as well as the wavelength of the radiation. For a given wavelength λ_0 the number n of modes is proportional to both

numeric aperture N_A and fibre diameter d:

$$n \propto \frac{d \cdot N_A}{\lambda_0} \tag{4.3}$$

For multimode fibres like the ones used here, the number of possible modes increases with with increasing core diameter d, increasing numerical aperture and decreasing wavelength λ. The resulting intensity distribution can be irregular and show interference-like patterns, when only few modes transfer the measurement signal.

In applications with grating spectrometers, this can lead to an irregular and variable illumination of the grating, which in turn can result in spectral structures in the recorded spectra that are very similar to differential absorption signals (Stutz and Platt, 1997). Hence, fibre modes can limit the accuracy of LP-DOAS measurements. To reduce this influence, the coupling of energy from one (dominant) mode to others has to be induced. This coupling happens naturally in fibres due to impurities, irregularities of the core/-cladding surface or the core cross-section, or by mechanical stress induced directly on the fibre or through temperature gradients (Kaminow et al., 2013). When induced on purpose, this coupling is called mode-mixing or mode-scrambling and has been realised by applying pressure on fibres, vibrating them, or by micro-bending (Blake et al., 1986; Stutz and Platt, 1997).

In this setup, fibre modes are mixed with three different measures. Following the investigation of an intentional degradation or roughening of the fibre end faces discussed in Nasse et al. (2019), the fibre bundle was treated with a 5 µm polishing sheet at both fibre ends at the coupling interface (C) as well as the end of the single fibre in front of the optical slit (D). Furthermore, the coupling (C) was attached to a vibrating pump. Lastly, the larger 800 µm diameter of the single fibre leading to the spectrometer is beneficial for mode mixing as more modes are possible.

4.2.4 Telescope

The telescope used for sending and receiving the measurement signal has to withstand the meteorological conditions of Antarctica (while light source and spectrometer are set up inside the trace gas observatory). A sketch of the opened telescope housing is shown in Fig. 4.8. Excluding the wind shield, it is 180 cm long and 52 cm high and wide. The structure of the housing is built from ITEM aluminium profiles that are covered with 3 mm thick plates of a aluminium-polyethylene composite material and, except for a side panel, are sealed with silicone. The edges are reinforced with steel ledges. On the trace gas observatory, it is mounted on a custom made rotary disc that sits on an aluminium profile frame (see also pictures in Figs: E.7 to E.9 in the appendix). Once the orientation of the telescope was adjusted, the disc was blocked. To compensate for the snow accumulation at the NM III site, the entire trace gas observatory has to be elevated regularly. The height of the telescope during the operation was therefore between about 8 m (after the setup) to 5 m (before the raising of the observatory platform) above the snow surface.

The housing is designed for main mirrors with a diameter of 30 cm and a focal length $f = 150$ cm that are held by an adjustable plastic mount in the back (Fig. 4.8 and Fig. E.10 in the appendix). The front opening is a 35 cm diameter quartz window that is tilted against the optical axis of the main mirror by 0.5° to prevent a direct back-reflection of the

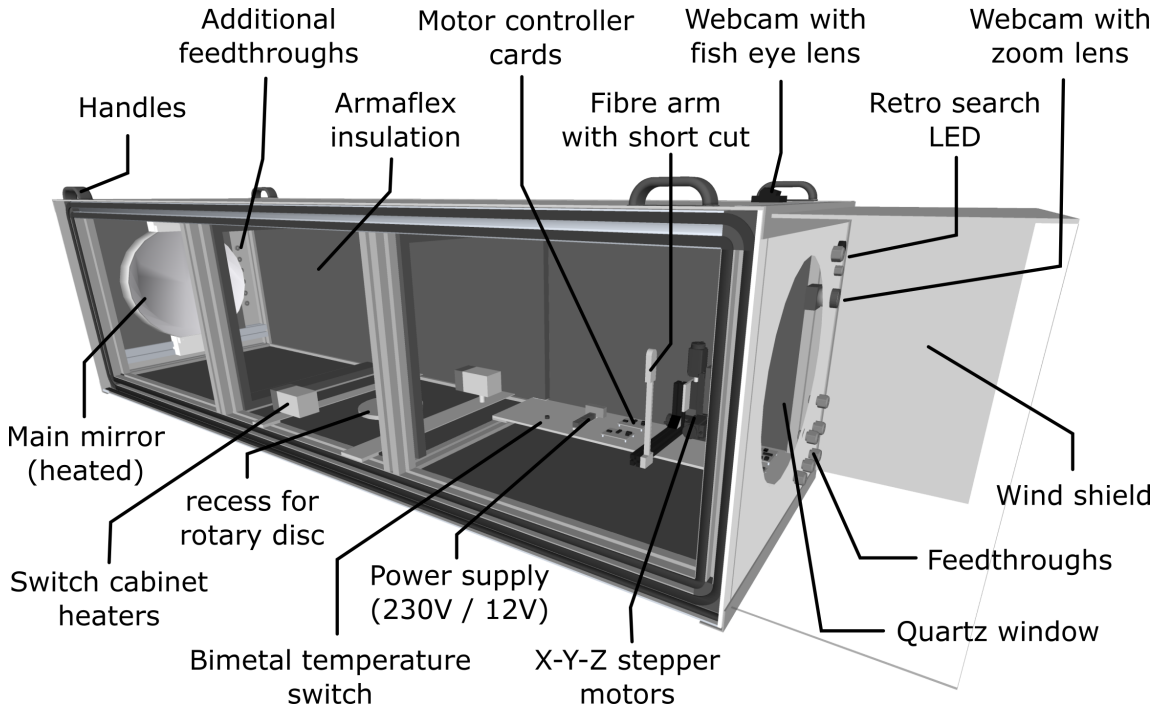

Figure 4.8: Sketch of the open telescope housing. The side panel is screwed to the main body of the telescope when closed. See also Fig. E.6 in the appendix. Cables can be inserted from the front and the back of the telescope.

measurement signal. The front of the instrument is protected by a wind shield to reduce the deposition of blowing snow (see also Fig. E.9).

The fibre bundle is positioned at the focal point of the mirror with an array of three stepper motors (Standa 8MT173-30, minimum resolution 1.25 µm per step) that are connected to cover translations in all three dimensions and move an arm of aluminium profile elements (see also E.10). By moving this stepper motor array in front of the mirror, the light beam created by the mirror can be pivoted by 0.5 ° in every direction to aim for the different retro-reflector arrays. The shortcut, a sandblasted aluminium plate, is mounted on a magnetic switch on this arm and can be moved vertically into light path (see also Fig. E.10).

The stepper motor array as well as all electric components like motor controller cards, a repeater for the I2C microcontroller communication, a hat rail for power distribution of 12 V DC and 230 V AC, and a bi-metal temperature switch are mounted on a 5 mm aluminium plate that is attached to the main structure of the telescope frame to ensure stability of the optical setup.

For temperature regulation inside the telescope, all openings of the telescope frame are filled with 32 mm Armaflex insulation and, where possible, the interior sides of the housing are covered with an additional layer of 19 mm Armaflex. The telescope is equipped for internal heating with three 230 V switch cabinet radiators (2x RS components 415-2969, 1x RS components 415-2981) with a total power of 430 W (upgraded from 200 W after the first year of operation). Furthermore, for the second year of the measurements, a 19 W circular heating film was fixed to the back of the main mirror to prevent misting.

The heating keeps the interior temperature of the telescope about 20-30 K above the exterior temperature (measured outside the front window). With minimum temperatures at NM III of around -40 °C, temperatures inside the telescope (as measured in 25 cm height) never fell below -10 °C (-20 °C in the first year). In laboratory tests before the deployment, a threshold temperature of -20 °C had been determined for a reliable operation of the stepper motors since at lower temperatures, mechanical stress led to blocked mechanics and failures. Temperatures above 20 °C are prevented by a bi-metal switch that stops the radiators.

The telescope is equipped with two webcams. One, with a wide field of view of 178 °, sits on top of the telescope to record atmospheric conditions above the light path. A second webcam, fitted with a zoom lens, is integrated into the front plate and allows to monitor the retro-reflectors. Together with a high power LED spot, visibility and cleanliness of the retro-reflectors can be inspected remotely even in darkness. Exemplary webcam pictures can be found in Fig. E.5. To adapt to spatial conditions of the respective measurement location, all cables and the fibre can be fed into the telescope from the front and the back side (see also Fig. E.9).

The interior of the telescope can be accessed for maintenance from the side where a panel can be removed (see Fig. E.6 for details). This panel is screwed to the main frame and has a three-layer sponge rubber seal that blocks blowing snow. Additionally, the side panel was sealed with aluminium tape during winter periods. Including the rotary disc and mounted on a custom built pallet, the telescope weighs 120 kg (excluding the mirror that is transported separately). A picture of the telescope on the pallet can be found in Fig. E.4 in the appendix.

4.2.5 Retro-reflectors and light paths

For the LP-DOAS measurements from the trace gas observatory, two light paths were available (see Fig. 4.1, right panel), for which two masts with retro-reflector arrays mounted inside of wind shields were set up (see Fig. 4.9). The first one (the "Met" reflector) with 24 reflector elements distributed over an area of 60 cm by 40 cm was located north to north-east from the telescope at 1.55 km distance and about 300 m east of the main station. This allowed to install a 300 meter power supply cable from the reflector array to an outdoor switch cabinet located at the meteorology measurement site south-west of the mast to heat the retro-reflectors.

The second retro-reflector array (the "Atka" reflector - named after the the Atka bay behind it) with a total of 25 reflector elements distributed over an area of 80 cm by 60 cm was located slightly shifted and in extension of the first light path at a distance of 2.95 km. Here, the reflector elements could no be heated. Pictures of both arrays are shown in Fig. 4.9. To compensate for the snow accumulation, the reflector arrays were kept at altitudes between 1.5 to 2 m above the snow surface by regularly moving them up the masts.

For the heated retro-reflector array, boxes holding six corner cube reflector elements were built (see Fig. 4.10). In the box, the single corner cube reflectors are attached to the box cover with a retaining ring and sealed against it with silicon gaskets. The interior of the box is covered with Armaflex thermal insulation on the walls, below the base plate and on the inside of the cover between the elements (the latter is not sketched in Fig. 4.10). Two 230 V 50 W heating resistors are mounted on the base plate. This ensures that the

Figure 4.9: Retro-reflector arrays of the two light paths. The left picture shows the mast with the heated array (Met light path) and the power cable. The middle picture is a close-up of the heated Met array. The right picture shows the retro-reflector array of the Atka light path inside its wind shield. Both arrays were kept between 1.5 - 2 m above the snow surface.

surface of the reflectors stays a couple of K above the exterior temperature to facilitate re-sublimation of ice on the reflectors. A bi-metal temperature switch prevents overheating. Several boxes can be connected to each other in parallel. The resistors inside the boxes can be wired according to heating power requirements. At NM III, available power was limited and therefore 25 W per box were chosen and the resistors were connected in series circuit. In combination with the wind shield, the heating ensured ice-free reflector elements on the Met mast for most of the potential measurement time. The unheated Atka mast occasionally had to be cleaned manually after stronger storms to ensure prompt operability.

4.2.6 Spectrometer

The spectrometer used in the NM III LP-DOAS setup was a Princeton Instruments Acton 300i (Acton, 1996) that is based on the *Czerny-Turner* design (Czerny and A. F. Turner, 1930) (the optical path is sketched on top of the spectrometer in Fig. 4.11). It has a focal length of 300 mm and a revolving grating turret that can hold three different gratings. Different spectral regions can be accessed by turning the grating, which is done by an internal servo-motor. For the measurements, two different gratings were used. During the first year of operation a 1200 gr. mm^{-1} holographic grating was used for all spectral windows (see Sec. 4.2.9 below for details) that, in combination with the 200 µm optical slit, yielded a spectral resolution of 0.54 nm. Due to lamp structures and suspected stray-light issues in the blue spectral range from 400 to 450 nm, for the second year of operation, a second grating was used for this spectral window with 600 gr. mm^{-1} and a 300 nm blaze was used, yielding a resolution of 0.95 nm.

The spectrometer is equipped with a Andor DU440 BU CCD camera with a back illuminated Marconi CCD42-10 chip (York, 2001). It features a 2048 by 512 pixel CCD array with a pixel size of 13.5 µm by 13.5 µm and a resulting image area of 27.6 mm by 6.9 mm (ANDOR, 2005). For the spectral range considered in the measurements in this thesis (280 nm to 680 nm), the minimum quantum efficiency of the chip is at 20% around 280 nm and reaches 80% or higher for wavelengths larger than 350 nm (ANDOR, 2005).

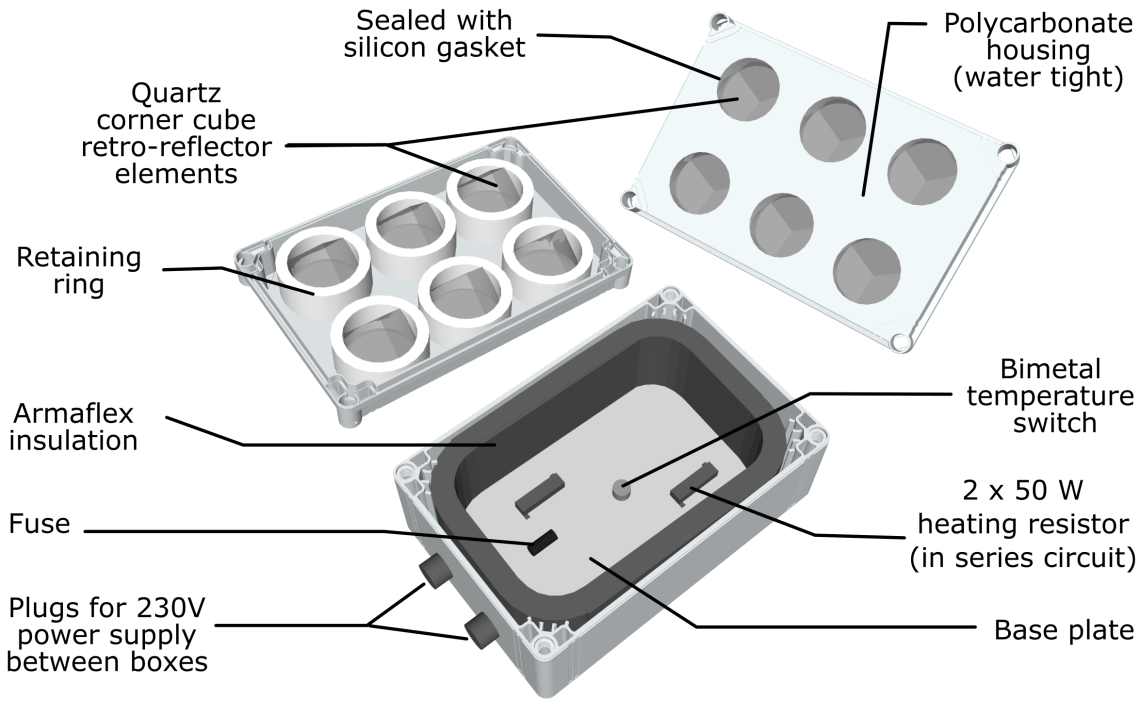

Figure 4.10: Sketch of opened retro-reflector box and two covers.

Due to the 800 µm fibre diameter, only a narrow stripe of about 60 pixels height is illuminated on the CCD array (the optical imaging of the spectrometer is 1:1). To avoid a saturation of the registry during readout, this area is separated into five subsets consisting of 11 pixel lines each that are vertically binned. Due to the chosen readout mode ('random track readout'), the subsets have to be separated by one line of pixels whose signal cannot be used. The five resulting spectra are later binned by the measurement software yielding one spectrum that is saved. The spectral window covered with one grating position is about 65 nm (140 nm for the alternative grating).

To reduce the dark current signal induced by thermal excitation of electrons, the chip of the camera can be cooled and was operated at -30 °C in the Neumayer setup. To prevent negative signals during the readout process, a positive electronic offset is added before each readout. Example spectra for dark current and offset are shown in Fig. 4.12. These spectra were recorded during regular wavelength calibrations. It should be noted, however, that for the analysis of the LP-DOAS measurements no correction by separate dark current or offset spectra is necessary because both are included in the backgrounds used to correct atmospheric and shortcut spectra.

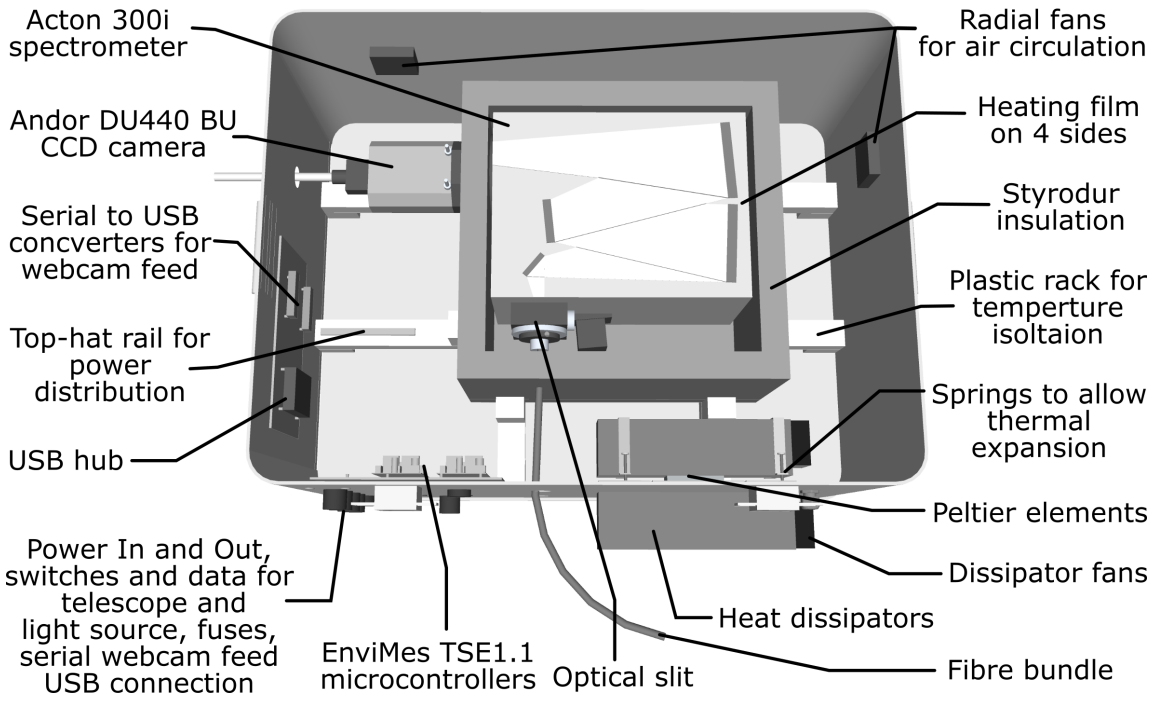

Figure 4.11: Sketch of spectrometer box. It holds the spectrometer and CCD camera but also serves as central controller for 12 V power supply, the operation of stepper motors and other components, and for data acquisition of different sensors (webcams, temperature sensors). The spectrometer is temperature stabilized in a two-stage system with a air to air cooling/heating system for the interior of the box and heating films on the spectrometer inside an insulation. Temperature regulation is done by Arduino micro-controllers on EnviMes TSE 1.1 circuit boards.

Linearity

In the CCD performance protocol (York, 2001), the linearity of the CCD is indicated to be better than 1%. This was verified in a test measurement with gradually increasing integration times and a temperature stabilised LED as proposed in Horbanski (2016). The polynomial fitted to the normalized counts plotted as a function of detector counts shows that the non-linearity from the shortest integration times to saturation varies by less than 0.5% (Fig. 4.13 panel B).

The spectra for the LP-DOAS measurements were recorded with a prescribed target saturations (between 25 and 40% depending on the spectral window) and variable exposure times leading to similar counts in the resulting atmospheric and shortcut spectra. Given this and the small detector non-linearity, no correction was applied to the spectra in the evaluation.

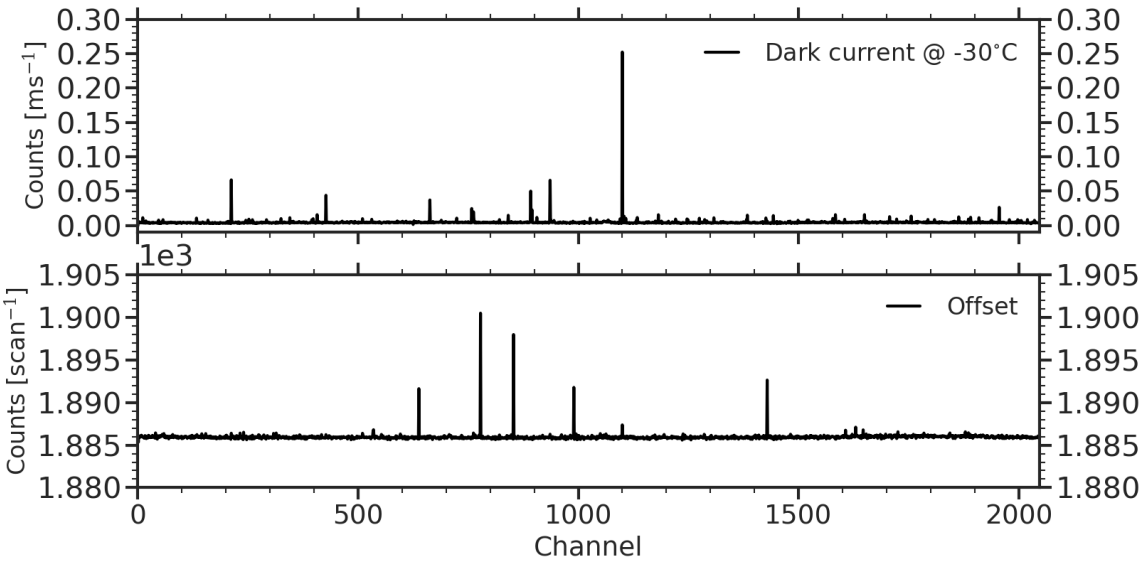

Figure 4.12: Dark current (top) and offset (bottom) of the Andor DU440 BU camera measured on August 1st, 2016. The peaks that are visible are so called hot pixels with an incorrect signal. If necessary, their influence can be corrected in the analysis.

Temperature stability

Optical setups and components respond to changing temperatures with changes of their properties. In spectrometers, this can lead to a shift of the illuminated CCD area or a change of the dispersion, and the instrument function (Platt and Stutz, 2008). An example of this influence is shown in Fig. 4.14 where the temperature of the Acton 300i varied by about 0.8 °C during a test period of new PID parameters for the temperature control. The resulting changes in the shift parameter of a ClO fit are in the order of 0.03 nm (in line with other observations of 0.05 nm K^{-1} Platt and Stutz, 2008).

Even small changes of shift or dispersion can have an influence on the analysis results and therefore the optical bench of spectrometers has to be temperature stabilized. This is often done by thermoregulating the entire spectrometer (e.g. Bobrowski et al., 2003). Although the spectrometer was set up on a heavy duty shelf inside the (heated) container of the trace gas observatory (see E.8), the location next to the door meant regular drops of the lab temperature when it was opened.

To improve the thermal stability, the spectrometer is mounted in a Zarges aluminium transport box (Eurobox 40705, 80 x 60 x 40 cm) and is equipped with a two-stage temperature stabilisation (see Fig. 4.11). The spectrometer case is equipped with heating resistor films (4 films with 12 W power each wired in two pairs in series circuit yielding a total power of 24 W) and covered in 40 mm Styrodur insulation (excluding the CCD camera). Spectrometer and insulation are placed on a plastic rack in the centre of the aluminium box to ensure air circulation around it on all sides. The interior temperature of the box is stabilized with an air to air system based on a heat exchange with two *Peltier* elements with a aluminium block for heat conduction placed between two heat dissipaters that were mounted on the inside and outside of the box.

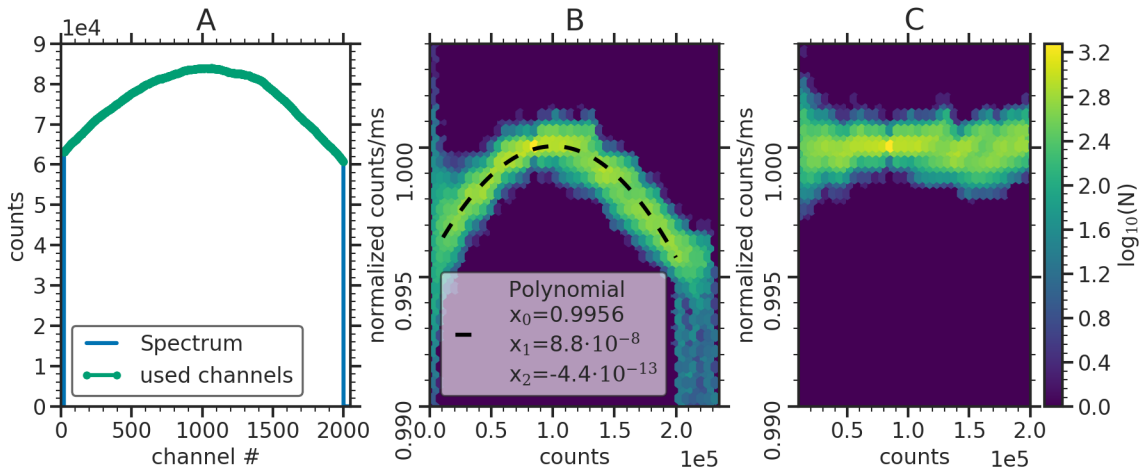

Figure 4.13: Result of the non-linearity test of the ANDOR CCD camera. An example spectrum of the temperature stabilized lamp and the channels considered in the test are plotted in panel (A). Panel (B) shows the the distribution of normalized (to 80 000 counts) counts per milli-second as a function of the detector counts. For high exposures, pixels are saturated and detection efficiency drops drastically. A second-order polynomial was fitted to the data to determine a correction function. In panel (C) the corrected normalized counts per ms to detector counts relation is plotted.

Since the spectrometer can only be heated (and has to cool passively), its target temperature was set to 35 °C and the interior of the box to 25 °C to ensure sufficient heat conduction by the temperature gradient (with lab temperatures varying between 15 and 23 °C).

The air inside the box is circulated around the spectrometer by the fan of the interior heat dissipater and two radial fans on the walls of the box. Since the two Peltier elements are not sufficient to transport all the heat produced inside the box, only top and bottom of the Zarges box are insulated. Thus heat can dissipate via the walls and the air to air regulation only dampens external temperature fluctuations. Both temperature stabilization stages are regulated by Proportional–Integral–Derivative (PID) controllers on two EnviMes TSI 1.1 circuit boards equipped with Arduino Nano 328 micro controllers.

The histograms of spectrometer and spectrometer box temperatures shown in Fig. 4.15, illustrate the resulting temperature stability. For the spectrometer, a median deviation from the target temperature of 0.03 °C is attained (at a resolution of 0.01 °C of the temperature sensors used). It should be noted that this value is an upper limit for the instability as it includes the long response times of the spectrometer after start ups of the measurement system due to its considerable heat capacity. The median deviation of the interior temperature of the box from the target was 0.01 °C. Here it should be noted that this is not representative for the entire box but rather the left side under the CCD camera where the temperature sensor was placed on the top-hat rail. A second sensor on the opposite side of the spectrometer regularly showed systematic deviations of up to 2 °C from the target temperature depending on the lab temperature.

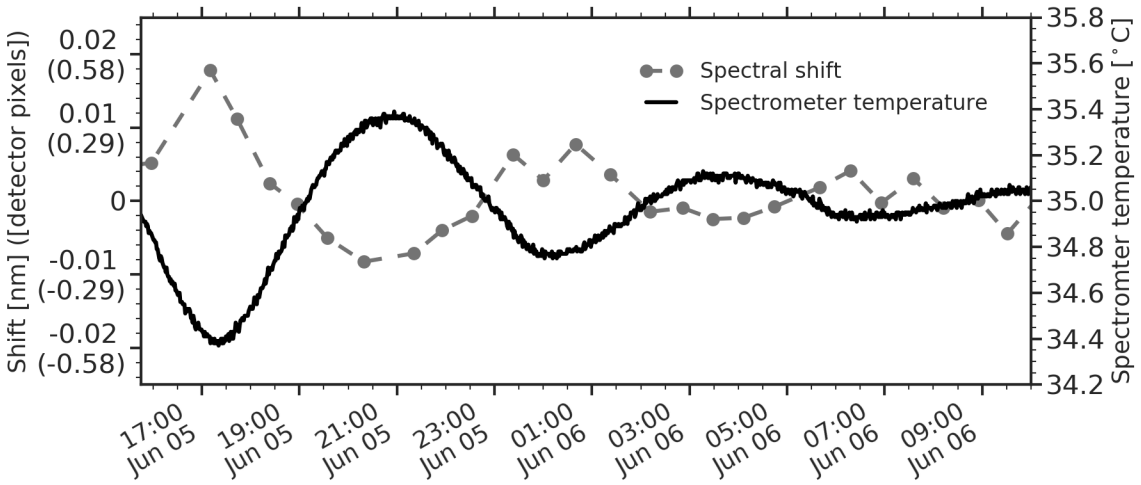

Figure 4.14: Influence of the spectrometer temperature on the shift in a O_3 fit. The period shows the temperature variations of the spectrometer following a re-start of the measurement system with unsuited PID parameters (black curve). The resulting variations of the shift parameter in a O_3 fit are plotted in grey.

4.2.7 System optics

The light throughput of a LP-DOAS system determined by its optical design affects temporal resolution of the measurements, signal to noise ratio, and achievable detection limits. Maximising it requires consideration of all optical components of the system. A useful quantity in the assessment of optical components in general, is the *étendue* G (e.g. Welford and Winston, 1978; Markvart, 2007). For systems in which light propagates unobstructed in a clear and transparent medium, it is an invariant. In a geometric optics description of an optical system, it can be interpreted as a measure of the number of rays transmitted and its invariance means that this number can only be conserved or reduced but never increased, regardless of the optics used. It can be linked to the concept of entropy (Markvart, 2007) that, according to the second law of thermodynamics, can only be conserved or increase.

The étendue is the product of the refractive index n of the medium, a relevant area A and the solid angle Ω subtended at this area by an object.

$$G = n^2 A\Omega \tag{4.4}$$

Which area is relevant depends on the component considered. For the étendue of a light source for example, A could be the size of the emitter and Ω the solid angle around it that is covered by the light collecting optics. For an optical fibre, A could be the core area and Ω the acceptance angle determined by the difference of the refractive index between core and cladding.

The étendue links the radiant flux or radiant power Φ through an optical system with transmittance τ to the radiance R of the light source:

$$\Phi = \tau RG \tag{4.5}$$

The radiant flux Φ through an optical system is limited by the component with the

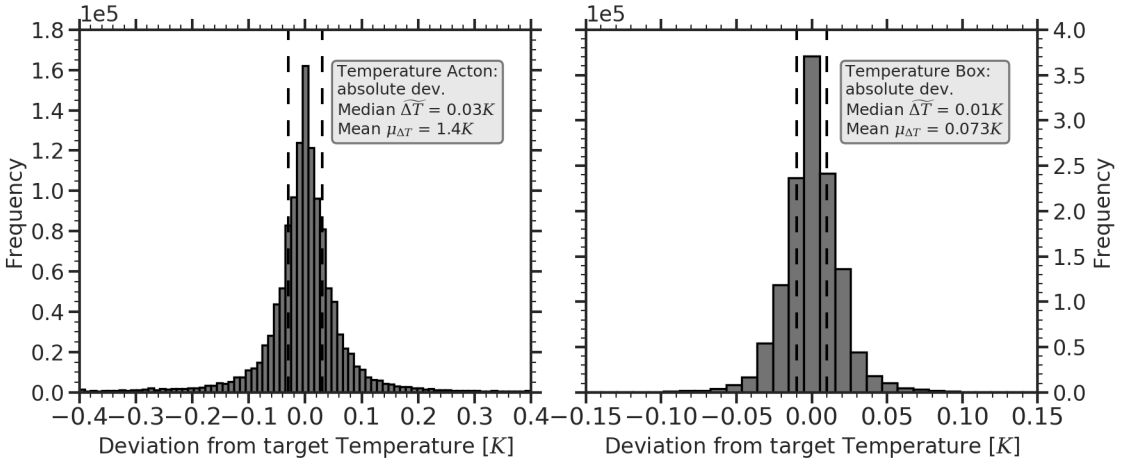

Figure 4.15: Temperature stability of spectrometer (left) and spectrometer box (right).

smallest étendue G_{lim}. For an optimal overall throughput, the limiting étendue should be maximised and the étendues of all components should match as closely as possible.

In the LP-DOAS setup used for the observations in this thesis (see Fig. 4.16), the limiting component is the telescope. Here, A is the surface of the sending (core) fibre of the bundle and Ω is defined by the solid angle captured by the 30 cm diameter main mirror at $f = 150\,\text{cm}$ distance. Increasing the telescope's étendue could be achieved by using larger fibres, a larger main mirror, or by decreasing its focal length. Larger diameter fibres would require a larger single fibre between the bundle and the spectrometer increasing relative light losses at the optical slit. Increasing the mirror diameter would increase the dimensions of the telescope and would require a larger front window, potentially more heating power, and would make the telescope even bulkier.

As for the focal length of the telescope, in addition to the étendue, the field of view and the required reflector surface size associated with it have to be considered. The exact calculation of the fields of view of the ring and the core fibres would require a convolution of the image of the fibres in a focussed telescope with the point spread function associated to the required defocussing of the telescope (Merten et al., 2011). For a telescope in focus, the image size of the fibres in the bundle can be estimated using the lens equation for the object O with object distance o, image I with image distance i, focal length f ($\ll i$), and an intercept theorem.

$$I = \frac{i}{o} \cdot O = i \cdot \left(\frac{1}{f} - \frac{1}{i}\right) \cdot O = \left(\frac{i}{f} - 1\right) \cdot O \approx \frac{i}{f} \cdot O \tag{4.6}$$

For the dimension of the field of view F_{FOV} at the reflectors, the diameter D of the main mirror has to be added.

$$F_{\text{FOV}} = \frac{i}{f} \cdot O + D \tag{4.7}$$

Using the fibre diameter of 200 µm of the central fibre (respectively 700 µm for the ring), the focal length of 150 cm, the field of view is at least 51 cm in diameter (1.02 cm for the ring) at a reflector distance of 1550 m (Met reflector) and 69 cm (1.68 cm) at a reflector distance of 2950 m (Atka reflector). However, usable light only returns from the area,

where the actual fields of view of core and ring resulting from the defocussing overlap and that, at the same time, is covered by reflector elements.

Decreasing the focal length of the telescope to increase the étendue, with Eq. 4.7 would increase the field of view and would hence require even larger reflector array dimensions. As with the setup used at NM III, the field of view is already larger than the available reflector surfaces, increasing the telescope's étendue would not increase overall throughput.

Consequently, the coupling optics from the LDLS into the fibre bundle was set up so that the foci of the UV spectral range that are closer to the lens in the LDLS (and hence achieve a larger solid angle) have a slightly larger and the foci of the visible spectral range achieve a matching étendue with respect to the telescope. For a detailed calculation of the étendues refer to Sec. D.1.2 in the appendix.

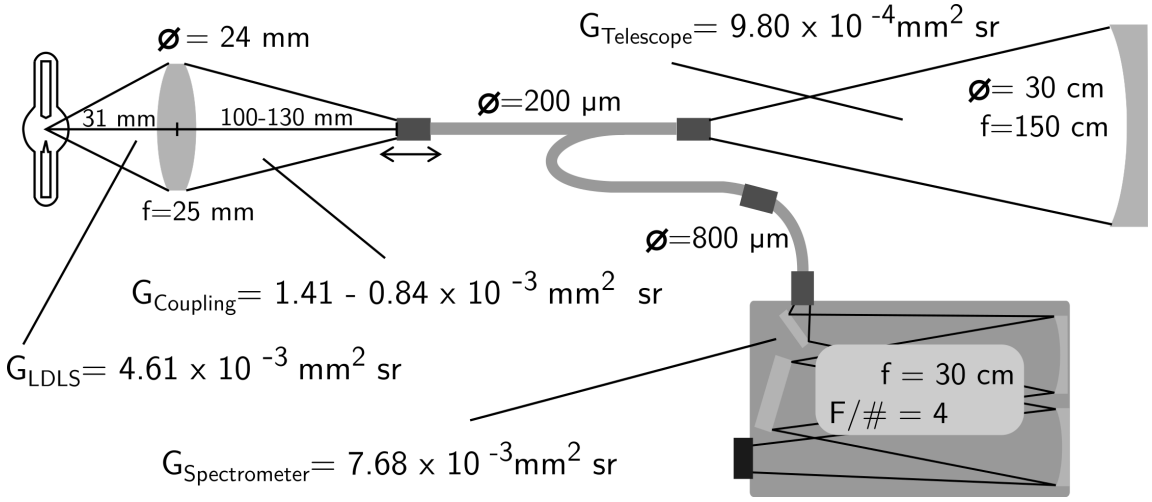

Figure 4.16: Optical components with respective étendues (for detailed calculations see Sec. D.1.2). Since the fibre is moved along the optical axis in front of the lens coupling the light from the light source into the fibre, the étendue here is variable. The limiting étendue of the measurement system is that of the telescope.

4.2.8 Instrument controls

Connection of components

In addition to housing the spectrometer, the spectrometer box also serves as the central hub for the entire LP-DOAS instrument (see also Fig. E.12). A 12 V DC 20 A power supply is connected to the box from where the power is provided to the different components in the light source and the telescope.

The two EnviMes TSE 1.1 circuit boards not only regulate temperatures but also record temperature signals from four sensors inside the spectrometer box (two for regulation, two for monitoring) as well as sensors inside and on the front side of the telescope, and inside the observatory. Furthermore, all stepper motors' and the filter wheel's controller cards (three in the telescope, two in the light source), the shutter and the shortcut magnetic switches, and the relay for the spotlight LED on the telescope are operated by the two boards via the I2C serial protocol. To ensure signal quality between the box and the telescope via the 10 m data cable, a repeater is installed inside the telescope. Two video

converters inside the spectrometer box receive the serial video feed from the two webcams and turn it into a USB signal.

Both EnviMes TSE 1.1 boards and the two video converters are connected to the measurement PC via a USB Hub inside the spectrometer box. The PC also contains a controller card for reading the CCD camera's signal and communicates with the spectrometer via serial COM port. It has two 1 TB hard drives that mirror the acquired data. On NM III, the system was also included in the station's backup system and new data was transferred to a ftp server in Germany on a daily basis.

MS-DOAS acquisition software

All parts of the LP-DOAS measurement system are controlled by MS-DOAS (Frieß, 2013), a Multi-tasking Software for DOAS systems. It allows the parallel operation of several devices be it motors, temperature controllers, or spectrometers. It furthermore provides an environment for the development of measurement routines based on a straight-forward, proprietary, object-oriented script language.

The individual components are integrated in a project and their functionalities can be called either manually in the graphical user interface (GUI) or via measurement scripts. The general structure of the MS-DOAS GUI is shown in Fig. 4.17.

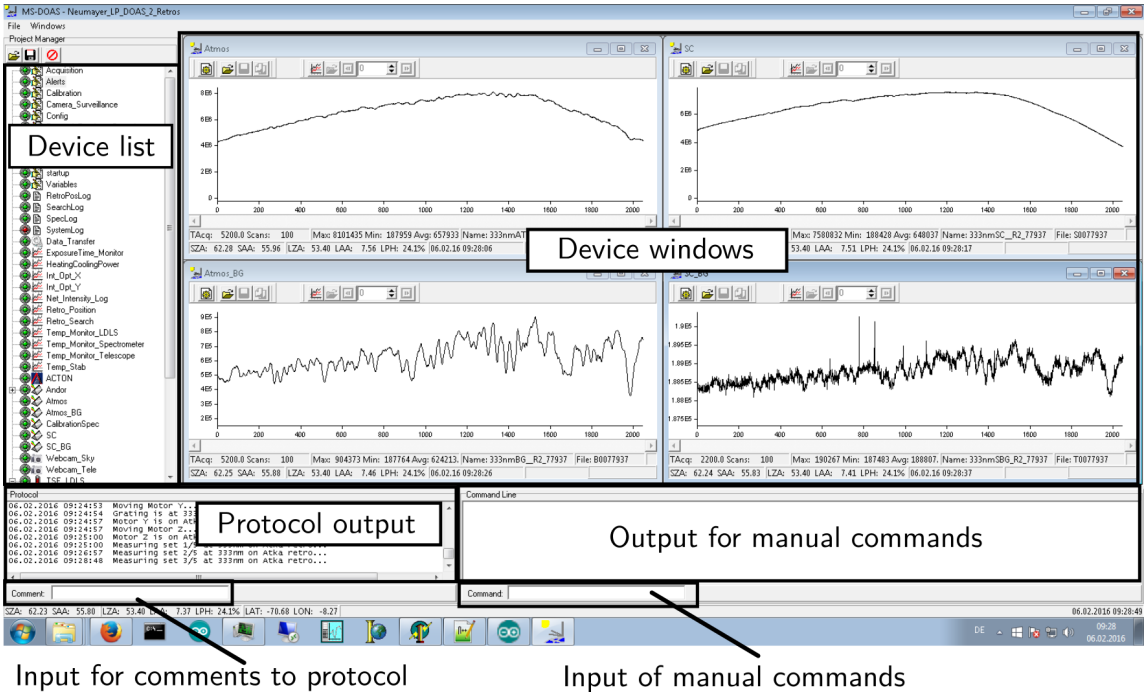

Figure 4.17: The MS-DOAS Graphical User Interface (GUI). On the left side, all integrated devices are listed and a marker displays their current status (idle/busy). When a device is selected, its window opens in the device window area and its setting can be accessed. In the lower left corner, the last messages of a general activities/status log are displayed. Manual notes can be added to the log with an input window. With the command input on the lower right side, commands can be entered, information about a device or the status of a variable can be prompted manually. The script language generally follows a simple *Device_A.command* logic.

Since MS-DOAS previously had not been used with LP-DOAS instruments, the measurement routine was newly implemented. The basic structure of the scripts used to control the measurement system is sketched in Fig. 4.18.

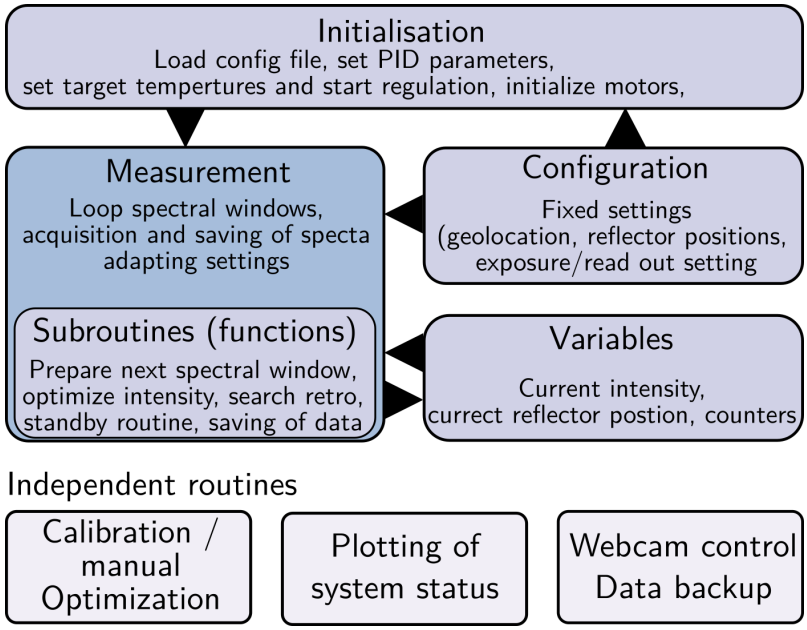

Figure 4.18: Structure of scripts in the MS-DOAS project. Arrows indicate the exchange of values between the scripts. Fixed settings of the setup are defined in the configuration script whereas variable values are stored in the variables script. Independent routines are running in parallel (like the diagnostics plotting) or can be run manually when the measurement is stopped.

The core measurement routine is implemented in four scripts. The initialisation only contains steps that have to be performed once after a start-up of the measurement system (e.g. loading the configuration data, setting the temperatures and PID parameters, initialising the temperature stabilisation, initialising the motors). Then the measurement script is started. After an initial test if the light source is running, the main measurement loop is started. Here the behaviour of the instrument with respect to retro-reflector selection, retro-reflector position optimization and search or standby behaviour during a storm is determined (see Sec. 4.2.9).

Single operations like the reflector search or the optimization routine are called from subroutines (similar to functions) within this script. Fixed settings of the measurement setup (like the readout settings of the CCD camera, the geolocation, number of spectral windows, etc.) are defined in a Configuration script that can be called by the measurement script. Temporary values (like the last position of the reflectors, current measurement intensities, counters for regular optimisation) are stored in a Variables script and can be called and altered by the measurement script.

Peripheral routines like plotting diagnosis data to visualise the current status of the instrument, regular backing up and copying of the data and the acquiring of webcam pictures is done by independent scripts that run simultaneously with the main measurement routine. Other scripts like a calibration routine with step-by-step instructions for the operator or scripts for the semi-automatic alignment of telescope and light source optics have to be started manually after the measurement routine is stopped.

The project records several Logs. In the MiniMax log, all status and other messages that appear in the protocol output window (or are added manually) are recorded. The system log saves all system parameters like current temperatures, positions of grating, motors, and filter wheel, or voltages at the micro-controller boards in 1-minute time resolution. A spectra log contains information on each recorded spectrum (current number, average intensity, exposure time, type of spectrum, reflector it was measured on as well as system parameters at the time of acquisition, etc.). A retro position log stores the positions of the reflectors in steps of the stepper motors. In a RetroSearch log, searched stepper motor positions and the associated signal are recorded.

4.2.9 Implementation of the measurement routine

A central goal in the design of the LP-DOAS system for the NM III measurements was a maximum degree of automation to reduce the supervision requirements for the wintering scientist running the trace gas observatory. Concurrently, the available observation time should be used as efficiently as possible to ensure a high temporal coverage of the atmospheric composition measurements. Except for infrequent problem shooting and repairs of smaller malfunctions, the operation of the LP-DOAS system only required calibration measurements in a monthly to bimonthly interval, a cleaning of the telescope front window every three to six months, occasionally the restart of the LDLS when maintenance requirements in the observatory had required the door to stay open for extended periods. The ensuing drop in lab temperature to close to freezing induced a shutdown of the LDLS' laser. After strong storms, unheated Atka reflector array had to be cleared of snow and ice.

Atmospheric dynamics and horizontal visibility

Atmospheric dynamics that affect visibility had the largest influence on the temporal coverage of the measurements. Evidently, the LP-DOAS principle only works when light sent out into the atmosphere can reach the reflectors and return with a sufficient irradiance. On the ice shelf at the NM III site, two distinctly different meteorological conditions can limit atmospheric visibility. When wind speeds are high enough, blowing snow conditions interrupt measurements (see Sec. 2.2.3).

Since the light path of the instrument is below an altitude of 10 m, already drifting snow limits visibility. During these conditions, measurements with a reduced intensity occasionally were possible, however only on the shorter Met light path. During blowing snow episodes, measurements were regularly interrupted. In addition to snow induced drops of the visibility, fog days, which on average occur on 34 d of the year (Schulz, 2017 - personal communication), hinder measurements.

Furthermore, LP-DOAS observations can be affected in relatively calm meteorological conditions. There are a number of optical effects that influence light propagation in the atmosphere. Turbulent fluctuation of atmospheric density for instance causes diffraction and refraction that lead to a fluctuation of the irradiance, apparent position, size, and sometimes colour of an object (Ryznar, 1963). Irradiance fluctuations are called optical scintillation and are mostly due to temperature variations in the atmosphere causing changes of density and hence in the index of refraction along the light path (Andrews et al., 1999). In atmospheric remote sensing, scintillation can be exploited to infer information

about wind speed, turbulence, and even fluxes of heat, momentum, and moisture (see e.g. Lawrence et al., 1972; Wyngaard and Clifford, 1978; Hill, 1992; Yee et al., 2015).

For LP-DOAS measurements however, scintillation reduces the irradiance from the retro-reflectors and the apparent change of the array's position can lead to a total loss of the measurement signal. The intensity of scintillation increases with stronger local differences of the index of refraction and hence the strength of local temperature gradients. At NM III, during periods with clear skies, radiative cooling of air directly above the surface leads to a regular formation of surface temperature inversions (König-Langlo et al., 1998) that can exceed $2\,\mathrm{K\,m^{-1}}$ - more than two-hundred times(!) the dry adiabatic lapse rate (see statistics of the occurrence of temperature inversions in 6.2 in Chapter 6). The refraction effects of these surface inversions can strongly influence light paths through the atmosphere and the apparent position of objects.[4]

For the relatively close reflector arrays (1.55 km and 2.95 km), most of the time optical scintillation was the dominant effect. When the stable layering of surface temperature inversions is disturbed, the density fluctuations and hence scintillation can become very strong and substantially influence even light paths of a few hundred meters. Ryznar (1963) found that the resolution of a distant object over a snow surface is worst under clear skies with inversion conditions in turbulent flow sufficient to disturb the stratification but weak enough to prevent complete turbulent mixing (i.e. at light wind speeds). Interruptions of the LP-DOAS measurements at NM III due to this phenomenon cannot be tied to particular thresholds for the strength of the surface inversion or wind speeds since conditions vary on short time scales and horizontally are not homogeneous as the two webcam pictures with mirages in Fig. 4.19 illustrate. Reduced irradiances could be observed regularly and for both light paths. In particular the Atka retro-reflector occasionally was lost.

Light path selection

The measurement routine that was implemented for the LP-DOAS measurements at NM III is adapted to deal with the visibility conditions described in the previous section by selecting the appropriate light path.

Additionally, the sequence of spectral windows can be modified based on external factors. At NM III, in spectral windows where photolabile molecules absorb, measurements were only performed for SZAs larger than a predefined threshold to limit observations to the night/low solar irradiance conditions (see Tab. 4.4).

The flow diagram of the measurement script is shown in Fig. 4.20. The two available light paths have a hierarchical relationship. The Met retro-reflector path serves as main path. The Atka retro-reflector array is used for opportunistic measurements if the atmospheric visibility is sufficient. After the initialisation of the instrument (see Fig. 4.18),

[4] For distant objects (see rows of containers and icebergs in Fig 4.19) and dynamically stable conditions, the strong refraction induced by these gradients leads to impressive optical phenomena like *looming* (the visibility of parts of an object that normally are below the horizon, *sinking* (reduced vertical visibility), *stooping* and *towering* (the vertical compression and elongation of an object) and *inferior* and *superior mirages* (the former is the reflection of the sky on warmer air above the surface (hot road); the latter is the visibility of two or more images of an object above each other in alternating orientation). These are common to polar regions and have already been described by Wegener (1918). See also the series of papers on these phenomena by Young et al. (1997), Young and Kattawar (1998), Young (2000), and Young (2004)

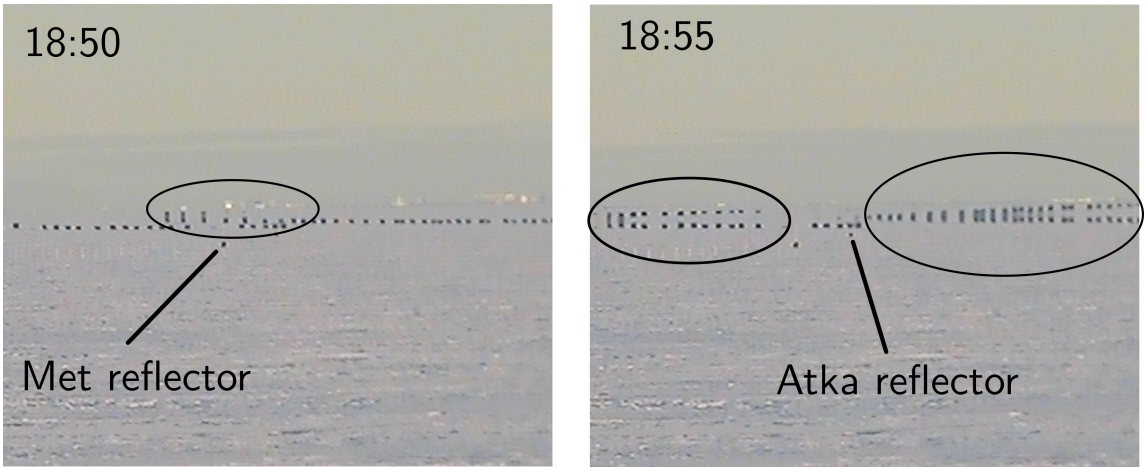

Figure 4.19: Examples of mirages (see footnote 3) observed with the telescope webcam of the LP-DOAS instrument at an interval of 5 minutes. The rows of containers (the summer storage of NM III) that show the mirage effects are about 10 km away.

it operates in one of three states (a) good visibility, (b) poor visibility, and (c) storm/-drift conditions (which includes times when the reflectors are not detectable due to optical scintillation/mirages as well as fog).

The script continuously iterates over a list of spectral windows and corresponding lists with indicators on which light path, under which visibility conditions (only in good, only in bad or regardless) and for which SZAs the respective window should be measured. This is checked in a loop prior to the actual measurement routine (upper part of Fig. 4.20). If the instrument is in poor visibility mode, measurements on the Atka light path are skipped but the visibility on this reflector array is checked and it is searched on a regular basis to return to the good visibility mode if conditions improve. The Atka retro can also be blocked manually by the operator e.g. when the unheated Atka reflector array cannot be kept snow free.

Acquisition routine

If the verification yields that the current spectral window is to be measured, the measurement routine is initiated (lower part of Fig. 4.20). First, the instrument is prepared for the spectral window. In the light source, the corresponding filter is set and the stepper motor moves the fibre to the respective focal distance from the lens. In the telescope, if necessary, the stepper motors move the fibre to the last position of the respective reflector array and adjust the defocussing. If necessary, the grating is changed and turned to the correct spectral position. The CCD readout settings are adjusted to the respective grating.

Then the measurement routine records a series of sets of spectra in the current spectral window. One of these sets consists of five SC spectra interleaved with four atmospheric measurements followed by one atmospheric background and one SC background. This alternating acquisition ensures short time intervals between the spectrum types to limit the influence of changes in atmospheric stray light and of instrument drifts. For the first SC and atmospheric spectra in the first set of a series, exposure times to reach a predefined saturation are determined before the actual measurements. All spectra (including the

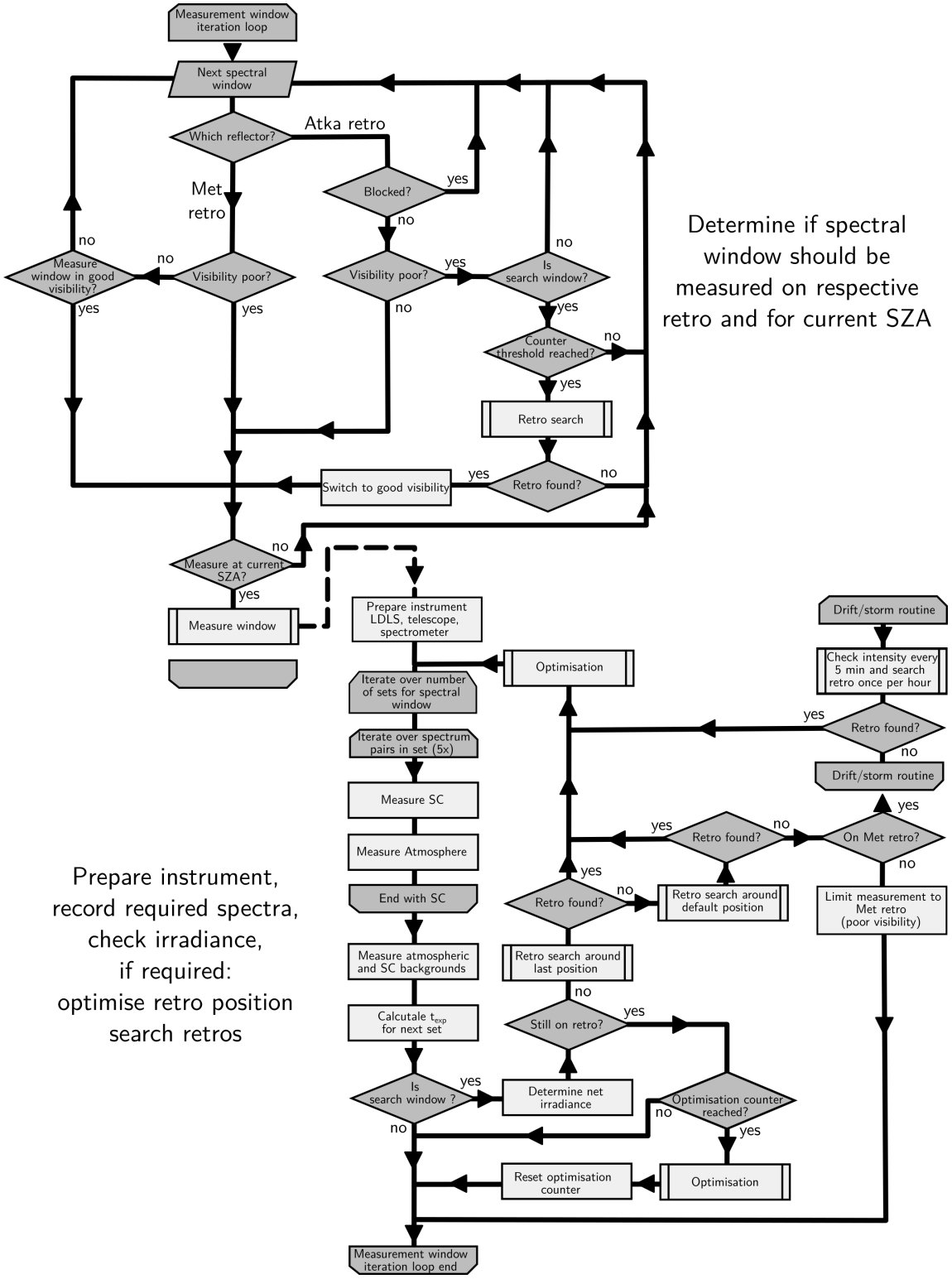

Figure 4.20: LP-DOAS measurement algorithms. The measurement script iterates over a list of spectral windows. First it decides whether the window should be measured currently (based on a number of conditions). Then the measurement routine iterates over the number of sets the respective window is to be measured and deals with intensity optimisation and retro search.

backgrounds) are then measured with these fixed exposure times (either t_{SC} or t_{Atmos}). For the following set in the series, exposure times are calculated and, if necessary, adjusted based on the saturation of the spectra in the previous set.

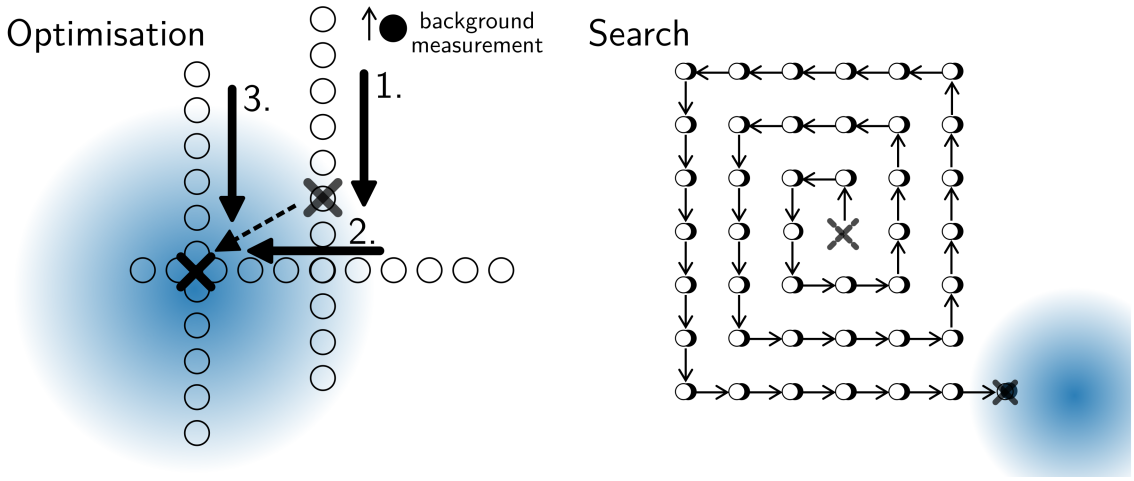

Figure 4.21: Telescope movement patterns for retro-reflector array position-optimisation and search. In the optimisation, a background measurement is taken at a sufficient distance (black circle) and all irradiances of the vertical and horizontal scans are corrected with it. If the maximum is found at the beginning or end of a scan, it is repeated, shifted towards the maximum. In the search routine, a separate background (black dots) for each measurement point (white dots) is recorded to determine the net irradiance.

Signal optimisation

The measurement routine also controls the regular adjustment of the stepper motors in the telescope to maximise the signal (here referred to as optimisation), the search for the reflector array, and the behaviour under storm/drift conditions when no measurements are possible. One of the spectral windows, ideally where the light source has the highest radiance, is designated as the *search window*. During the measurement, the net irradiances in this window are calculated by subtracting an atmospheric background spectrum from an atmospheric measurement. the results are then used for monitoring. To prevent erratic instrument behaviour based on single measurements, a number of counters are used. As soon as a threshold of a counter is reached, a subroutine (e.g. the optimisation of the fibre position) is started or the instrument is set to a different status (e.g. from good visibility to poor).

The counter for the optimisation routine C_{opt} ensures that the position of the reflector array is adjusted on a regular basis. It triggers the optimisation routine once a certain threshold is reached. Ideally, this adjustment is done rarely when intensities are good and more frequently when conditions are variable or deteriorating. Every time the measurement routine reaches the search window and the net irradiance is determined, the counter C_{opt} is increased. The amount of this increase depends in the result of the net irradiance calculation, which is compared to a number of different threshold irradiances.

When the net irradiance is above a threshold characteristic for nearly optimal visibility I_{opt} (determined based on experience during the setup of the instrument), it is increased by

1. If the irradiance is below I_{opt}, but above the running mean of the last 10 net irradiances $\bar{I}$, C_{opt} is increased by 2. If the irradiance is below $\bar{I}$ but above I_{limit} where the retro signal reliably can be distinguished from the background, C_{opt} is increased by 3 and a counter C_{poor} for poor visibility conditions is increased by 1. Using the variable measure $\bar{I}$ and the fixed I_{opt} allows the quick correction of the fibre position when irradiances decrease but limits the time lost optimising the position when visibility is optimal or increasing. When the irradiance is below I_{limit} - i.e. the retro reflector seems to be lost, first an optimisation of the fibre position is performed. If this yields an irradiance above the minimum required for measurements I_{min}, measurements resume, otherwise the retro reflector is treated as lost and a search is initiated as follows.

First, the reflector array is searched around the last fibre position. If found (irradiance above I_{limit}), an optimisation is performed and measurements resume. If not found, a second search around the default fibre position of the respective reflector array is performed. If found then, an optimisation follows and the measurements resume. Otherwise, the current state of the instrument is changed. If the lost reflectors are the Atka array, the instrument changes into the poor visibility mode and measurements are limited to the shorter Met light path. This also happens when a threshold of the poor visibility counter C_{poor} is reached to e.g. prevent a measurement attempt on the Atka light path when measurements on the Met reflector array indicate consistently poor visibility (this is not sketched in Fig. 4.20). If it was the Met array that was lost, the instrument changes into the storm/drift routine. Here, the irradiance at the default position is checked every five minutes and once per hour a search is performed. In between the shutter in the light source is closed to limit unnecessary solarisation of optical components.

The optimisation routine consists of (usually) three quick scans preceded by a measurement of the background irradiance (see Fig. 4.21 left panel). The first scan is done vertically around the current fibre position. For the next scan, the position of the highest irradiance in the previous scan is determined and the second, horizontal scan located around it, before a third, vertical scan is performed at the position of the horizonal scan taht gave the best result. If the highest irradiance is found at either end of a scan track, the scan is repeated shifted towards the maximum. After the optimisation, the new net irradiance is compared to the one for the previous fibre position. The new position is only adopted if the irradiance here is higher than at the old.

The search routine follows a pattern of up to five squares of increasing size around the last reflector position (see Fig. 4.21 right side). At each position, the net irradiance is determined with a measurement of atmosphere and background. As soon as the minimum irradiance for measurements I_{min} is detected, an optimisation is performed.

4.2.10 Operation at Neumayer III

Based on the instrument description and general characterisations in the previous sections, this section discusses the settings chosen for the LP-DOAS observations at Neumayer as well as several aspects particular to the relatively long, continuous operation time of the instrument at NM III.

Measurement settings

For the measurements with the two available light paths to the Met and the Atka retro-reflector arrays, five different spectral windows were used. An overview is given in Tab. 4.4.

Spectral window Grating setting	UV I 287 nm	UV II 333 nm	VIS I 406 nm	VIS I-new 406 nm	VIS II 532 nm	VIS III 618 nm
Spectral range [nm]	280-348	327-395	401-467	378-521*	528-596	614-682
Resolution [nm]	0.54	0.54	0.54	0.95	0.54	0.54
Number of sets	5	5	5	5	3**	3**
Measured on	only Met	either	either	either	either	either
SZA limit	no	no	no	no	only when SZA > 85°	
Band pass filter	UG-5	UG-5	BG-25	BG-25	GG-495	RG-610
Filter window [nm] (>50% transm.)	230-400		320-480		495-2700	610-2700
Target species	ClO, O_3 BrO OClO	BrO, OClO NO_2 HONO	NO_2, IO		I_2, Br_2 OBrO OIO	NO_3

Table 4.4: Overview of the spectral windows measured with the LP-DOAS. Due to potential stray-light issues and lamp structure issues in the VIS I window, a second grating was introduced after the first year of observations. The glass filters (both band-pass and long-pass) in the filter wheel and the respective transmission windows are indicated as well

In the first UV window (UV I), target species were ClO, O_3, SO_2, BrO and OClO. Measurements in this spectral range were only performed on the shorter Met light path (1.55 km one-way) because the combined effect of increasing O_3 absorption and Rayleigh scattering towards shorter wavelengths below 300 nm in combination with a diminishing quantum efficiency of the CCD below 350 nm would have yielded insufficient signal to noise ratios for the detection of ClO between 287 nm and 306 nm (see Chapter 5 for details on the evaluations of the different species).

All other spectral windows were measured on either the Met reflector array (when visibility was poor) or the Atka light path (2.95 km one-way). The second UV window contains BrO, NO_2, and OClO as main target species with the potential to detect HONO and formaldehyde (HCHO) if present. With the first window in the visible spectral range (VIS I), IO as well as strong differential absorption bands of NO_2 were targeted and glyoxal ($(CHO)_2$) could be detected if present in sufficient mixing ratios. The two other visible spectral windows contain photolabile absorbers such as I_2, OIO, OBrO, Br_2 (VIS II) and

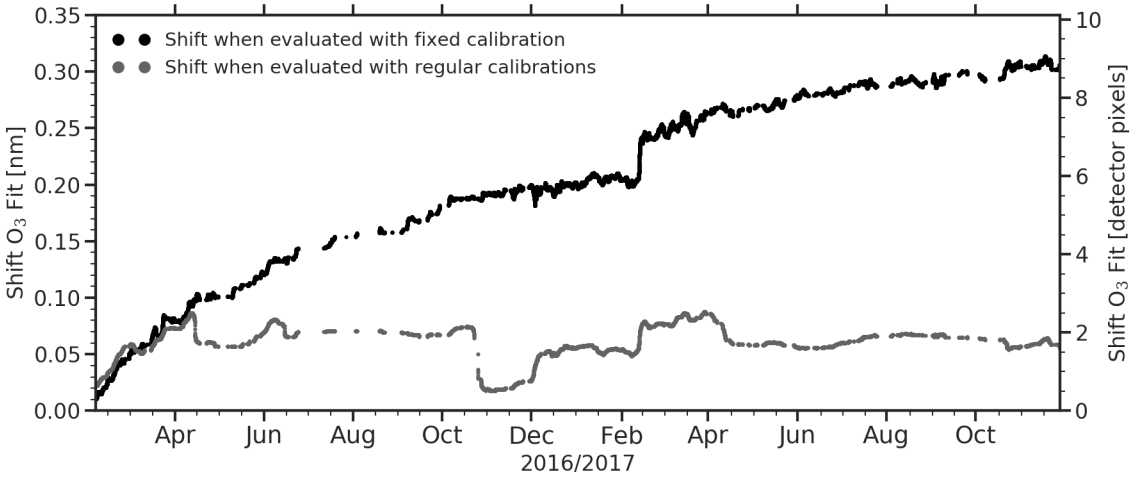

Figure 4.22: Shift of the grating position as determined from O_3 Fits in the wavelength range from 286.5-329.5 nm. The black dots are the rolling median of the spectral shift of an O_3 Fit where the shift was left as an unconstrained parameter. The grey dots are the shift of the same Fit (in terms of absorbers considered, spectra added etc.) but taking the monthly to bi-monthly updated calibrations determined from mercury line spectra.

NO_3 (VIS III). Since these molecules have very short lifetimes during daytime, measurements here were only performed when the SZA was larger than 85°. Furthermore, only 3 sets of spectra pairs (five shortcuts, four atmospheric measurements and one of each background) were recorded.

To reduce the stray-light from adjacent spectral regions (see stray light reduction measures described in Sec. 4.2.2), the filter wheel in the light source was equipped with band-pass and long-pass glass filters matching the spectral windows.

Drift of the grating position

To reach different spectral windows, the grating turret in the spectrometer is sequentially turned to project the respective wavelength range onto the CCD. The DOAS analysis strongly depends on the correct channel-wavelength attribution (see Sec. 3.4.3 and Eq. 3.17). To determine this relationship, known emission line spectra of xenon, neon and mercury lamps were recorded regularly (see examples in Chapter 5 and the appendix). The validity of the calibration spectra for the actual channel-wavelength relationship for a measurement depends on a sufficient reproducibility of the grating position during the iteration through the different spectral windows. During the operation of the spectrometer at NM III from January 2016 until August 2018, the grating was moved about 59 000 times. This led to a gradual shift of the grating position over time. In Fig. 4.22 the shift of a O_3 fit in the UV spectral range is plotted for two different evaluations between February 2016 and November 2017.

First (black dots), a fixed calibration and convolution kernel from the beginning of February 2016 was used. Second (grey dots), regularly updated calibrations and convolution kernels determined from the corresponding mercury line spectra were used. [5]

[5] In the measurement period from mid January 2016 until the beginning of February, different lines of pixels on the CCD were used. In November 2017 the coupling of the light source into the fibre was

Since the spectral window used for this evaluation (287-328 nm) contains very strong O_3 absorption features (in particular between 287 and 300 nm), one can assume that the free shift of the fit reliably counteracts the drifting grating position and hence the steady increase of the shift can be attributed to this drift.

After the first year of operation, the second grating was included in the measurement routine, which probably explains the jump in February 2017 in both curves. For the evaluation with regular updates of the calibration, the shift shows no steady increase. The (remaining) variations could have several explanations. One could be variations of the spectrometer temperature. In particular until May 2016, the temperature regulation parameters were adjusted several times and the variations in Fig. 4.22 are in the same order of magnitude as temperature induced shifts observed in the data (see Fig. 4.14 in the next section). Another reason could be the precision of the wavelength calibration. The dip between November 2016 and March 2017 is caused by different calibrations and the difference of about 0.04 nm is in the same range as the typical error for the constant parameter in the channel-wavelength attribution polynomial (i.e. the wavelength of the first channel of the CCD in a spectral window.)

To correct for this drift in the grating position, the regular calibrations were used in all evaluations. For spectral ranges where background irradiances were sufficient, calibration polynomials were adjusted to the grating drift in between calibration measurements by using the *Fraunhofer* lines in the background light (see Sec. 5.1.1).

Long-term radiance variations

The setup of the LP-DOAS system does not allow to monitor the temporal evolution of the radiance of the LDLS independently from the other optical components. Investigating the average radiance in shortcut spectra can yield information about the combined influence of LDLS, coupling lens, filters, and fibre bundle on the measurements over time. In Fig. 4.23, for the average counts of the five spectral windows per ms, corrected by the respective shortcut backgrounds, weekly medians were calculated.

The relative differences between the different spectral regions approximately correspond to the relative differences of the respective regions in the radiance spectrum of the LDLS (compare to Fig. 4.6). All five spectral regions show similar trends with an overall reduction of the radiances from the start of the measurements. However, the intensive maintenance interventions in January 2017 and November/December 2017 (which included an exchange of the filters and a thorough cleaning of lens and all fibre ends) can be easily discerned and each time seem to have restored radiances more or less to initial levels. Only directly before the final malfunction of the light source in August 2018 a sharp decrease of the radiance is visible.

The variations throughout 2016 between the start of the observations and the first maintenance could be explained by several interventions of the winterer to fix problems with the telescope fibre arm that included a removal of the fibre from the arm and a cleaning of the otherwise inaccessible fibre end. In the second year of the operation, variations during the year are smaller and might be explained by slight differences in the light coupling induced by the regular removal of the 800 µm fibre from the coupling for calibration measurements

adjusted leading to a shift that made the evaluation with a fixed calibration from 2016 unstable. The plot is limited to the period in between.

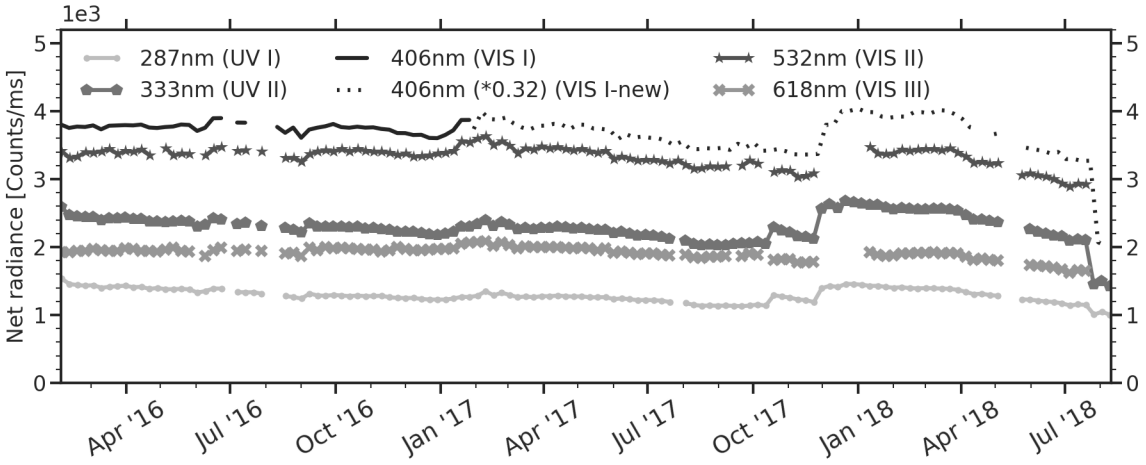

Figure 4.23: Evolution of the net detector signal over time. The average counts over the entire short cut spectra in the different measurement windows was corrected for the short cut background and then weekly medians were calculated. Since in the VIS I window, the grating was changed in February 2017, the recorded radiances (which due to the lower dispersion of the new grating were higher) were adjusted to the first grating (dotted line).

(which also could have been the case in the first year). The only time the telescope was opened and the fibre end cleaned in October 2017 led to a small increase of the radiance.

Based on this analysis, a permanent decrease of the recorded radiance seems to be between less than 1% (VIS II) and 8% (UV I) and still could include a potential solarisation of optical components as well as an actual decrease of the radiance of the LDLS. This indicates a very high long-term temporal stability of the light source, which is further supported by the fact that the position of the fibre in the light source relative to the optical axis of the coupling lens never had to be adjusted throughout the entire operation time.

Temporal coverage

The total observation period at NM III covers 934 days from January 18$^{\text{th}}$ 2016 until August 10$^{\text{th}}$ 2018. There are several longer gaps of more than one week in the data set, which were either caused by instrumental problems, by extended periods of blowing snow during storms, or by a combination of both. On overview of these longer periods and and the cause of the interruption can be found in Tab. 4.5.

The temporal coverage of the LP-DOAS measurements (combining all spectral regions) was calculated on an hourly basis, i.e. if a spectrum was recorded during an hour, this hour is counted towards the measurements. This does not take into consideration the quality of the recorded spectra. The usable portion of the data set for different absorbers will be described in Chapter 5.

Monthly averages of the temporal coverage for the entire observation time are shown in Fig. 4.24. Plots for the single years can be found in Figs. D.25, D.26, and D.27 in the appendix. For periods without measurements, the meteorological data was analysed to determine if blowing snow or strong optical scintillation could explain the gaps. Since

Year	Start		End	Duration	Cause
2016	24.6.	-	11.7.	18 days	2 Storms, measurements did not resume in intermediate calm period from 29.6. until 4.7. due to misting of optical components
	19.7.	-	1.8.	14 days	Storm
	22.8.	-	2.9.	12 days	2 Storms, measurements did not resume in intermediate calm period from 25.8. until 30.8. due to misting of optical components
2017	25.7.	-	2.8.	9 days	Storm
	10.9.	-	19.9.	10 days	Strong storm
	25.9.	-	3.10.	9 days	Storm
	8.10.	-	16.10.	9 days	Storm
	7.12.	-	18.12.	12 days	Storm and reduced telescope window transmissivity
2018	18.4.	-	2.6.	45 days	Problems with telescope stepper motor
	25.6.	-	29.7.	33 days	Problems with telescope and light source stepper motors

Table 4.5: Gaps in the LP-DOAS data set of seven days or longer.

the onset of drifting snow was reported to be at a threshold wind speed of $6\,\mathrm{m\,s^{-1}}$ (König-Langlo and Loose, 2007), a threshold of $8\,\mathrm{m\,s^{-1}}$ hourly mean wind speed was used for a potential influence on the instrument. For the potential influence of optical scintillation (in the absence of high wind speeds), a threshold temperature gradient (hourly mean) of 2 K between 10 m and 2 m altitude was chosen.

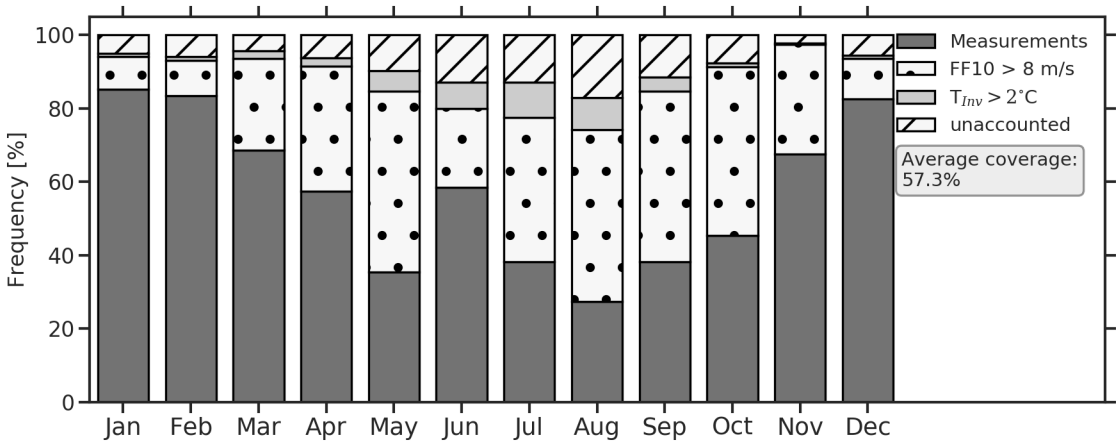

Figure 4.24: Temporal coverage of the LP-DOAS measurements 2016-2018. Percentages are calculated on an hourly basis. For times with no measurements, periods that potentially could have been influenced by blowing snow or strong optical scintillation were marked. However, this does not exclude the possibility that technical problems occurred during these times. The same plot for the separate years can be found in Figs. D.25, D.26, and D.27 in the appendix.

Throughout the year, the average temporal coverage of the observations is 57.3%. Assuming that the selected meteorological criteria sufficiently characterise the limiting atmospheric conditions, only 5 to 10% of the lost observation time cannot be explained directly. In parts, fog episodes, which on average occur on 34 days of the year (Schulz - personal

communication, 2018) could explain this. Times with a blowing snow potential seem to explain most of the gaps, in particular during the windier months from May until October (see also monthly wind speed distributions for the observation period in Fig. 6.6). From May to August, scintillation potentially contributes between 5 and 10% of the inactive time.

4.3 MAX-DOAS

When natural light sources instead of artificial ones are used for DOAS measurements, this is referred to as *passive* DOAS. It can be realised ground-based and from different platforms like ships, aircraft, and even satellites (for overview see Platt and Stutz, 2008). Before the introduction of the DOAS principle, using scattered light for absorption spectroscopy was a long established technique (see e.g. Dobson and Harrison (1926) mentioned in Chapter 3). Other instruments with a zenith sky geometry inferred vertical columns of several trace gases, for example NO_2 (Brewer et al., 1973; Noxon, 1975) and identified the importance of halogen species in the formation of the ozone hole (Solomon et al., 1989).

At NM III, a zenith sky instrument was used to infer the presence of tropospheric iodine monoxide (IO) (Frieß et al., 2001) and study the chemistry of tropospheric ozone depletion events induced by bromine monoxide (BrO) (Frieß et al., 2004) as well as to observe stratospheric trace gases during an ozone hole period (Frieß et al., 2005). A further development in scattered light absorption measurements is the **M**ulti-**AX**is DOAS (MAX-DOAS) (Hönninger and Platt, 2002; Hönninger, 2002; Hönninger et al., 2004; Sinreich et al., 2005).

4.3.1 Measurement principle

MAX-DOAS instruments are equipped with a telescope that can be turned to different elevation angles α (e.g. in Hönninger, 2002, see left panel in Fig. 4.25) or has several individual telescopes fixed in the respective elevations (e.g. in T. Wagner et al., 2004). Light scattered into the instrument from these elevations has traversed the atmosphere on different light paths and hence, depending on the elevation angle, contains a signal from different altitudes. Small elevations close to the horizontal for example, contain a pronounced contribution from absorbers close to the surface. The combination of the information in the separate measurements allows the estimation of vertical profiles of aerosols and trace gases.

The MAX-DOAS instrument at Neumayer consists of a controller and spectrometer unit and a telescope with two channels, one for the UV and the other for the visible spectral range. Spectrometer and controllers have been described in detail in (Ferlemann et al., 2000; Frieß et al., 2001; Frieß et al., 2004). The zenith telescope unit was replaced by a new telescope with two prisms on stepper motors for the two channels and variable elevations (see Fig. 4.25 right panel). Details on the setup can be found in Frieß et al. (2010).

For the DOAS analysis, one elevation, usually the zenith observation, which often has the shortest path through the atmosphere, serves as the references. In the DOAS fit, all other elevations are compared against this reference yielding *differential slant column densities* (dSCDs) i.e. the differences in trace gas mixing rations along the light path between a particular elevation angle and the reference.

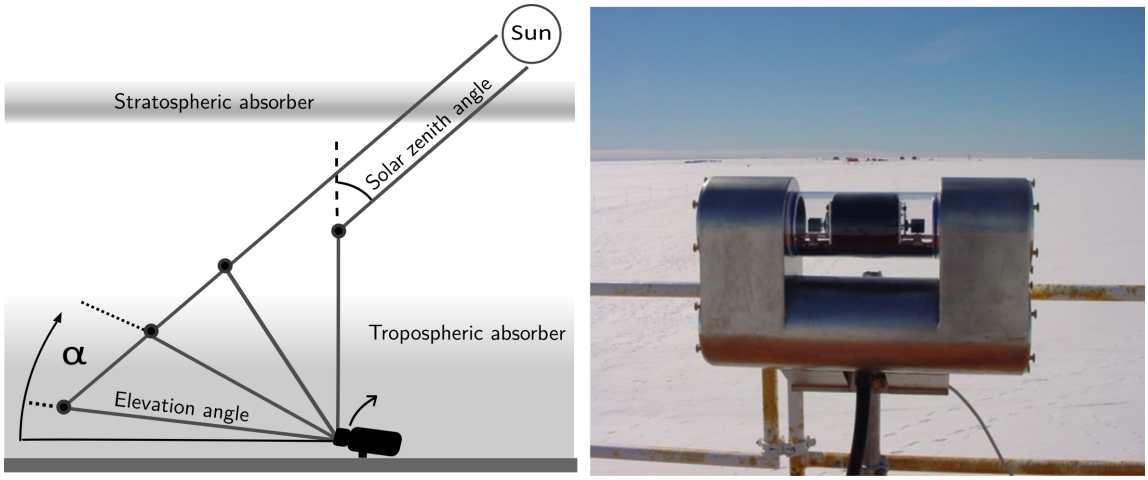

Figure 4.25: Principle of MAX-DOAS measurements and the instrument installed permanently at NM III. The photo shows the telescope unit of the instrument. Spectrometer and controllers are located inside the trace gas observatory. Foto: courtesy of U. Frieß

To calculate vertical columns or mixing ratios, the light path has to be known. Due to Rayleigh- and Mie-scattering, it strongly depends on atmospheric conditions in particular on aerosol extinction along the light path. With radiative transfer simulations, *air mass factors*, the ratio between slant and vertical columns can be estimated to convert the dSCDs (e.g. in T. Wagner et al., 2007).

Another technique is to use the dSCDs of the oxygen collision complex O_4 (T. Wagner et al., 2004; Frieß et al., 2006). For an aerosol-free (Rayleigh-) atmosphere, its vertical distribution is proportional to the square of the oxygen mixing ratio profile in the atmosphere (i.e. the barometric height formula) and hence the expected O_4 signals for different elevations are known. Deviations under conditions with aerosols then are used to infer modified ((often increased, see T. Wagner et al., 2004)) light paths due to (multiple) scattering. With this information, mixing ratio profiles can be estimated.

4.3.2 Profile retrieval

To determine vertical profiles from dSCDs, the optimal estimation method by Rodgers is used (Rodgers, 1990; Rodgers, 2000). An algorithm based on this has been implemented by Yilmaz (2012) and was used Frieß et al. (e.g. in 2011) for profile retrieval in the Arctic. A detailed description and discussion of settings and parameters can be found there.

The retrieval algorithm consists of a two step process (see Fig. 4.26). First, the O_4 dSCDs are used to determine a vertical extinction profile using a radiative transfer model (in this case SCIATRAN2 by Rozanov et al., 2005). Then the dSCDs of a given trace gas are used to determine trace gas vertical profile for which the radiative transfer model takes the influence of the retrieved aerosol extinction profiles on the light paths into account.

MAX-DOAS data used in this thesis for comparison purposes was analysed by Frieß (2018) (both DOAS analysis and profile retrieval). The sequence of elevations as well as the settings of the retrieval algorithm and the properties of the resulting time series and profiles are in Tab. 4.6 below.

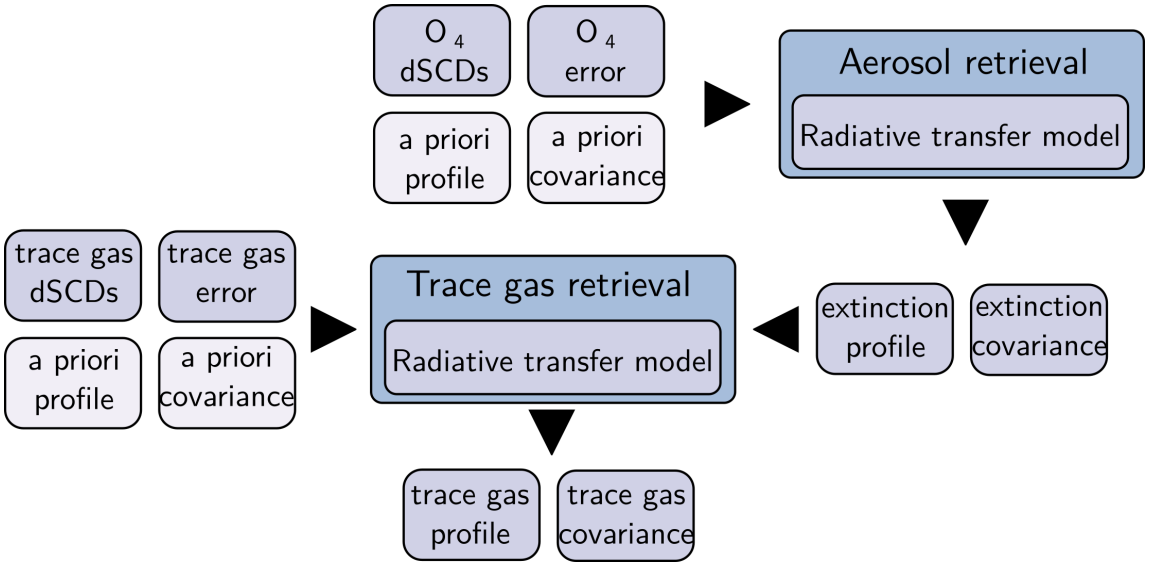

Figure 4.26: Schematic of the two-step retrieval of vertical extinction and trace gas profiles from MAX-DOAS dSCDs.

Retrieval Specifications	
Elevation angles	90, 20, 10, 5, 2, 1, -5, -20
Reference angle	90
Temporal resolution	1 h
Elevation sequences per profile	≈2
Box grid	10 boxes that from the surface exponentially increase in vertical dimension
Surface box height	50 m
Vertical extent of profiles	4 km
A-priori profile	exponentially decreasing
A-priori scale height	0.6 km
A-priori surface mixing ratio	20 ppt
Sensitivity	up to 1.5 - 2 km
Surface albedo	0.98
Additional Information	Vertical structure of the atmosphere from radiosondes
Typical degrees of freedom	3

Table 4.6: Overview of setting used in the MAX-DOAS vertical profile retrieval.

5
Data Analysis

This chapter documents the data analysis of the LP-DOAS observations, assesses the data quality, and, where possible, compares the results to independent observations.

In the first section preparations and prerequisites for the fitting of the spectra are described. Then the models fitted to the observed optical densities in the different spectral intervals are defined and discussed. In the following section 5.2, examples of fits are shown followed by an error analysis. Since the performance of the instrument slightly varied during the relatively long observation period, fit statistics for the entire data set are presented and long-term effects on observed mixing ratios and detection limits are discussed. Based on this, the resulting data was filtered prior to further interpretation. Where the mixing ratios of absorbers could be evaluated in more than one spectral window, the resulting time series were combined after assessing the agreement between them. A summary of the results of the evaluations with e.g. typical levels of uncertainty, detection limits, temporal resolutions and highest observed mixing ratios can be found in Tab. 5.4 at the end of the section.

For two absorbers, O_3 and BrO, independent observations are available. The comparability of the different measurement techniques is discussed and the agreement between LP-DOAS data and the other instruments is investigated in Sec. 5.3.

The storage of the original measurement signal in DOAS spectra allows to adapt the analysis of the data to different research questions. In contrast to many other techniques where either only the time series of an observed quantity is recorded (in this work e.g. by the ozone monitor in the trace gas observatory) or the available quantities of physical samples prevent more than a few different analysis (e.g. the high volume aerosol filter samples), DOAS spectra can be evaluated in numerous ways and as often as required. This allows to flexibly adapt routines to e.g. particular external conditions during the observations or the characteristics of the instrument's components. However, it also means that, within certain limits, there is no entirely standardised evaluation procedure.

5.1 DOAS evaluation

During the observations at NM III from January 14th 2016 until the failure of the LDLS on August 10th 2018, a total of just over 1.3 million measurement spectra were recorded with the LP-DOAS (including short-cuts and backgrounds a total of 3.1 million spectra). This data set was was analysed using the *DOASIS* software package (Kraus, 2006) with an evaluation script originally developed by Pöhler, (2015, personal communication) that was adapted to the output of the MS-DOAS measurement routine and the purposes of this evaluation.

5.1.1 Wavelength calibration and convolution kernels

A prerequisite for the DOAS analysis procedure is the wavelength calibration of the acquired spectra. To determine the channel-wavelength attribution (see Eq. 3.17), spectra of light sources with known emission lines were recorded. During the monthly to bi-monthly calibration routine that was performed at NM III by the respective winterer, emission line spectra of a mercury vapour lamp were used for the UV I (280-348 nm), UV II (327-395 nm) and VIS I (401-467 nm/378-521 nm) spectral windows of the measurement routine (see Tab. 4.4). In the spectral ranges of the VIS II (528-596 nm) and VIS III (614-682 nm) windows, mercury only has a few suitable emission lines and therefore a neon vapour lamp that contained some mercury was used. Additionally, xenon spectra were recorded, which offer a multitude of emission lines for the VIS III window. Examples of all calibration spectra that were used in the evaluation can be found in Fig. 5.1.

Due to the drift of the grating position discussed in Sec. 4.2.10 as well as the limited number of emission lines, on a fortnightly basis the calibrations of the UV II and VIS I spectral windows were corrected using highly-structured Fraunhofer lines (Lampel, 2014). This was only possible when background spectra of sufficient quality were available (i.e. not during polar night).

The spectral resolution as determined from the full width at half maximum (FWHM) of the emission lines was 0.54 nm (0.95 nm for the measurements in the VIS I window after the change of the grating - for details see Sec. 5.2). No variation of the resolution was found using the closely spaced lines of the Ne spectrum between 615 nm and 675 nm (see lowermost panel in Fig. 5.1), Since the shape of the emission lines across the detector changed slightly, for the adaptation of the high-resolution literature absorption cross-sections to the spectrometer resolution (see Sec. 3.4.2), emission lines close to the spectral interval of the respective fit scenario were used as convolution kernels (marked in grey in Fig. 5.1, for fit scenarios see Sec. 5.1.3).

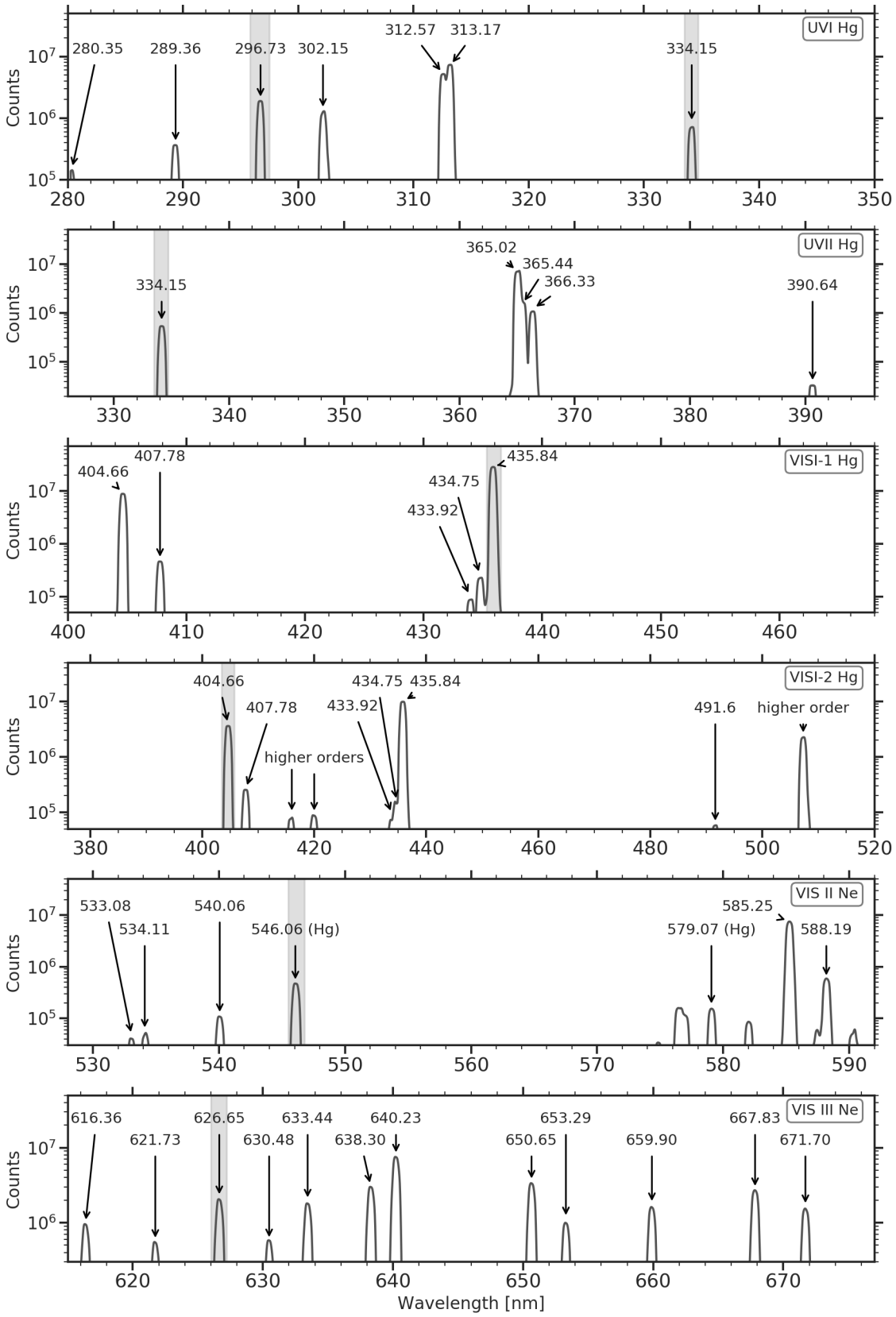

Figure 5.1: Examples of the calibration line emission spectra used for the channel-wavelength attribution and convolution of averaging kernels. The lines used for the convolution are marked for the different fit scenarios.

Scenario		Wavelength interval [nm]	Target species	Considered references	DOAS polyn.	Filter
UVI	1	287.0 - 306.0	ClO SO_2	BrO^2, ClO^4, $HCHO^6$, $NO_2{}^{10}$, $O_3{}^{13}$, $OClO^{17}$, $SO_2{}^{19}$, SC*, BG*	3	HP 1000**
	2	286.5 - 329.5	O_3	BrO^2, ClO^4, $HCHO^6$, $HONO^7$, $NO_2{}^{10}$, $O_3{}^{13}$, $OClO^{17}$, $SO_2{}^{19}$, SC*, BG*	3	HP 1000**
	3	301.7 - 346.4	BrO OClO	BrO^2, ClO^3, $HCHO^5$, $HONO^6$, $NO_2{}^{10}$, $O_3{}^{14}$, $O_4{}^{15}$, $OClO^{17}$, $SO_2{}^{19}$, SC*, BG*	3	HP 4000**
UVII	1	332.5 - 370.5	BrO OClO	BrO^2, $HCHO^5$, $HONO^6$, $NO_2{}^{10}$, $O_3{}^{14}$, $O_4{}^{15}$, $OClO^{17}$, SC*, BG*	3	HP 4000**
	2	352.5 - 386.5	NO_2 HONO	BrO^1, $HCHO^5$, $HONO^6$, $NO_2{}^9$, $O_3{}^{12}$, $O_4{}^{13}$, $OClO^{17}$, SC*, BG*	3	HP 4000**
VISI	1	424.3 - 451.3 (411 - 438)	NO_2 IO	$NO_2{}^{10}$, $O_3{}^{14}$, $O_4{}^{15}$, H_2O^5 Gyoxal $(OCHCHO)^{20}$, IO^9, SC*, BG*	3	-
VISII	1	532.5 - 549	I_2, Br_2 OBrO OIO	$NO_2{}^10$, $O_3{}^{14}$, $O_4{}^{15}$, H_2O^5, OIO^{18}, $I_2{}^8$, $NO_3{}^{11}$, $Br_2{}^1$, $OBrO^{16}$, SC*, BG*	3	-
VISIII	1	616.5 - 1078 + 660.5 - 673.2	NO_3	$NO_2{}^{10}$, $O_3{}^{14}$, H_2O^5, $O_2{}^{12}$, $NO_3{}^{11}$, SC*, BG*	3	-

1:Br_2(Schneider and von Helden, 1997) 2:BrO(Wilmouth et al., 1999) 3:BrO(Fleischmann et al., 2004)
4:ClO(S. P. Sander and Friedl, 1989) 5:H_2O(Rothman et al., 2010; Lampel et al., 2015b)
6:HCHO(Meller and Moortgat, 2000) 7:HONO(Stutz et al., 2000) 8:I_2(Spietz et al., 2006)
9:IO(Spietz et al., 2005) 10:NO_2(Voigt et al., 2002) 11:NO_3(Yokelson et al., 1994)
12:O_2(Rothman et al., 2010) 13:O_3(Burrows et al., 1999) 14:O_3(Serdyuchenko et al., 2014)
15:O_4(Thalman and Volkamer, 2013) 16:OBrO(Fleischmann and Burrows, 2002) 17:OClO(Wahner et al., 1987)
18:OIO(Spietz et al., 2005) 19:SO_2(Bogumil et al., 2003) 20:Glyoxal(Volkamer et al., 2005)

Table 5.1: Overview of the different fit scenarios and literature cross-sections used. A table with spectral resolutions and coverages of the references can be found in Tab. D.1.3. Most literature cross-sections were retrieved from the MPI-Mainz UV/Vis spectral atlas (Keller-Rudek et al., 2013) and web-links therein.(*) Reference and background spectra were retrieved from the current measurement. (**) Binomial high-pass filter iterations for broad-band removal (in addition to the polynomial). The filter is defined inversely: smaller number → stronger filtering.

5.1.2 Correction of atmospheric background and instrumental contributions

After each set of measurement spectra (five short-cut spectra interleaved with four atmospheric spectra), a background spectrum was recorded for both atmospheric and reference (short-cut) spectra with the light source blocked (see Fig. 5.2). For both types of background spectra the same fixed exposure time as in the respective measurement spectrum was used. At the beginning of a fit, these backgrounds are subtracted from the atmospheric/reference spectra, which accounts for atmospheric background light and at the same time removes the instrumental contributions of the dark current signal from the CCD and the electronic offset added to prevent negative signals when converting the electronic signal (see Sec. 3.4.1 and Sec. 4.2.6).

5.1.3 Fit Scenarios

To retrieve the column densities of the different trace gases, suitable sub-sections of the measurement windows (see Tab. 4.4) were selected and fit scenarios were compiled that contain relevant absorbers and other spectral contributions. In Tab. 5.1 an overview of the different fit scenarios with the respective target species and other included absorbers and the references of the utilised literature cross-sections is given. Where available, cross-sections adapted to polar conditions were selected by using a version recorded at a temperature similar to typical air temperatures at NM III (in most cases recorded around 253 K). A separate list with these literature cross sections containing information on the original resolution, spectral coverage, recording technique, and, were applicable, the temperature version used, can be found in Tab. D.2 in the appendix.

For fit scenarios in the lower end of the UV I spectral window, separate references for BrO and O_3 had to be used compared to the other scenarios. For BrO, the cross-section by Fleischmann et al. (2004), which was used in the scenarios targeting BrO, does not cover the entire fitting ranges of the UV I-1 and UV I-2 fit scenarios. Instead Wilmouth et al. (1999) was used.

For the O_3 cross-section by Serdyuchenko et al. (2014), Eger (2014) found systematic deviations when used in the UV below 300 nm, which could be confirmed in tests for this instrument. Below 310 nm, this cross-section was recorded with an Echelle spectrograph plus ICCD camera whereas above, a Fourier transform spectrometer was used (Serdyuchenko et al., 2014). Evaluating O_3 in spectral windows that contain large parts of the transition zone where both cross-sections were patched together seems to create problems. Therefore, for fits that include wavelengths below 300 nm, the cross-section by Burrows et al. (1999) was used (fit scenarios UVI-1 and UVI-2).

In addition to absorber cross-sections, in all fit scenarios a logarithmised short-cut spectrum taken from the currently evaluated set of spectra was added. Two important assumptions in using short-cut spectra as reference are that the signal reflected by a sand-blasted aluminium surface is equivalent to an atmospheric spectrum apart from atmospheric absorption and that the light source has a sufficient temporal stability. The SC spectrum added to the fit compensates a potential influence of systematic differences between SC and atmospheric spectra e.g. due to a slightly different illumination of the grating caused by a difference in the angular signal distribution of the atmospheric signal compared to that from the reference plate as well as potential fluctuations in the light source output.

Furthermore, a logarithmised background spectrum that was recorded after the measurement sequence was added to account for differences between the actual background signals of the atmospheric spectra during recording and the time when the background spectrum was acquired, which can cause an over- or under-compensation of the atmospheric spectra introducing differential structures. The interleaved recording aims at minimising this (see Fig. 5.2), however, when visibility conditions change quickly, it still can be insufficient.

5.1.4 Spectral averaging and temporal resolution

In order to improve the signal to noise ratio, individual short-cut and atmospheric spectra can be summed up after background correction. The resulting optical density spectrum τ is then used in the fitting routine:

$$\tau = \sum_{l} \left(\frac{\sum_{k=1}^{4} (A_{k,l} - A_{B,l})}{\sum_{k=1}^{5} (R_{k,l} - R_{B,l})} \right) \tag{5.1}$$

$\mathrm{R}_{k,l}$ are the k short-cut spectra in a set l, $\mathrm{A}_{k,l}$ are the $k-1$ atmospheric spectra of sequence l, and $\mathrm{R}_{B,l}$ and $\mathrm{A}_{B,l}$ the respective background spectra of set l (see Fig. 5.2). Depending on the the target signal-to-noise ratio for a trace species, which e.g. depends on the strength of the absorption, radiance of the light source in the respective spectral window, or expected mixing ratios, several spectra from one set or even across sets can be used in this summation.

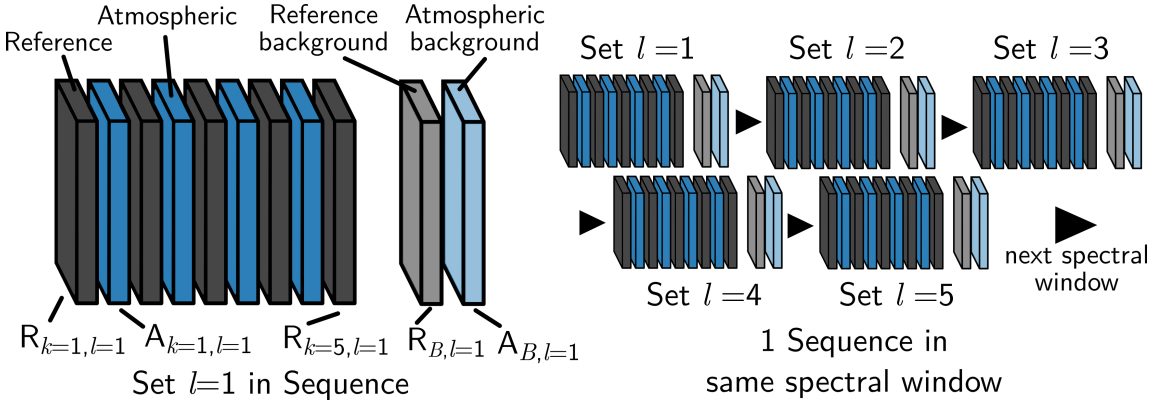

Figure 5.2: Structure of measurements sets and spectral sequences.

Both due to the chosen acquisition settings with exposure times adapted to yield target saturations (and therefore changing with atmospheric visibility conditions), and because spectra can be summed up, LP-DOAS measurements generally do not have a regular, fixed temporal resolution. For a specific fit scenario, the frequency of data points depends on the number of spectra in one set, the exposure times of the spectra, the number of sets measured in the considered spectral window and all other windows, and lastly on the number of summed up spectra.

To investigate the potential improvements of the residuals and the temporal stability of the instrument when different numbers of spectra are summed up and to select appropriate settings for the different absorbers, the fitting routine was performed with several summation settings for evaluations in the UVI, UVII, and VISI spectral windows. The

number of summations were varied from individual to up to 80 atmospheric spectra. This represents average temporal resolutions between about 30 s to 3 h respectively.

The decrease of residuals with increasing summation is shown in Figs. 5.3, 5.4, and 5.5. Comparing the three figures, when only few spectra are summed up and hence the residual is dominated by photon noise, the differences of the average residual RMS values for the three spectral windows reflect the spectral radiance of the LDLS in the three spectral intervals (Fig. 4.6). From the UVI to the VISI spectral window, the spectral radiance of the LDLS increases and accordingly residuals decrease.

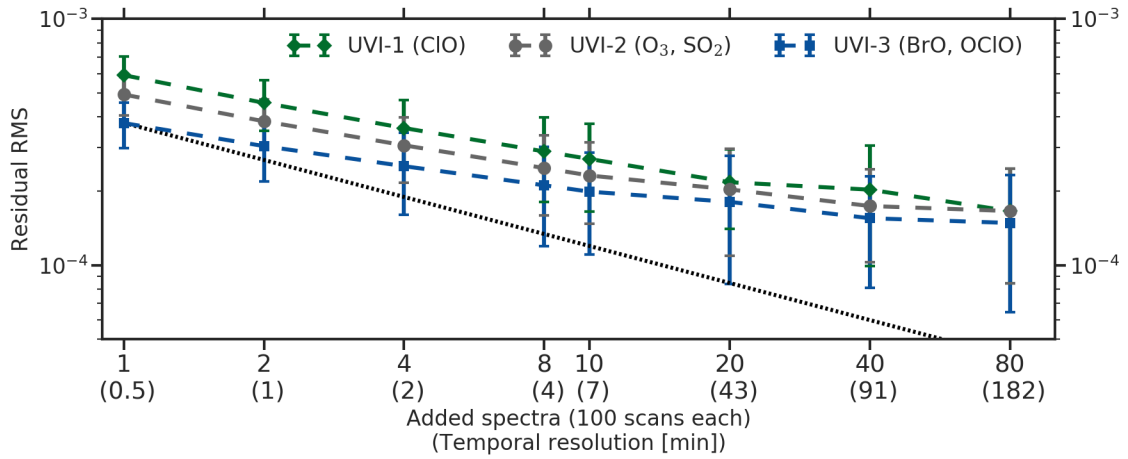

Figure 5.3: Mean residual RMS of different spectra summations/temporal resolutions for the UVI spectral window. The black dotted line marks the decrease of the RMS for pure photon noise.

For the UVI spectral window in Fig. 5.3, when only few spectra (1-8) are summed up, average residual RMS values differ and decrease from the UV1-1 fit scenario (287-306 nm, see Tab. 5.1), over the UVI-2 scenario (286.5-329.5 nm) to the UVI-3 fit scenario (301.7-346.4 nm). This is in agreement with the differences in radiance in the respective intervals that increase from 280 nm to 330 nm (see also spectral radiance distribution for the different spectral windows in Fig. D.4 in the appendix). When about 10 or more spectra are summed up, the differences between the three fit scenarios start to disappear. Here the evaluations no longer seem to be influenced by photon noise and instrumental noise dominates the residuals.

For the UVII spectral window (Fig. 5.4), also for few summed up spectra both fit scenarios show an almost identical evolution of residual RMS values with increased summation, which is expectable given the quasi constant spectral radiance in the UVII window (see Fig. D.4).

For the VISI spectral window, residual RMS values were plotted separately for the two gratings that were used here throughout the course of the measurement campaign. For the measurements with the 1200 gr. mm^{-1} holographic grating that also was used in all other spectral windows, average residuals are only comparable to those in the UVII spectral window, despite the higher radiances the LDLS offers in this spectral region. As will be discussed below, this is due to residual structures probably introduced by the grating when in the position for the VISI spectral window. Therefore, from mid-February 2017, measurements in the VISI spectral window were performed with a 600 gr. mm^{-1} grating. The clear improvement of the residuals of about a factor of 1.5, in addition

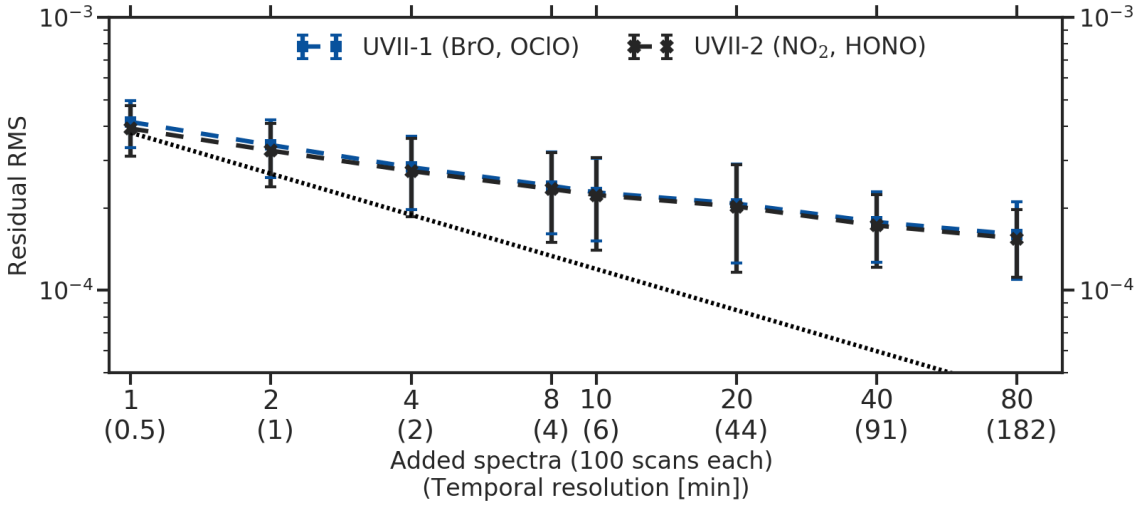

Figure 5.4: Mean residual RMS of different spectra summations/temporal resolutions for the UVII spectral window. The black dotted line marks the decrease of the RMS for pure photon noise.

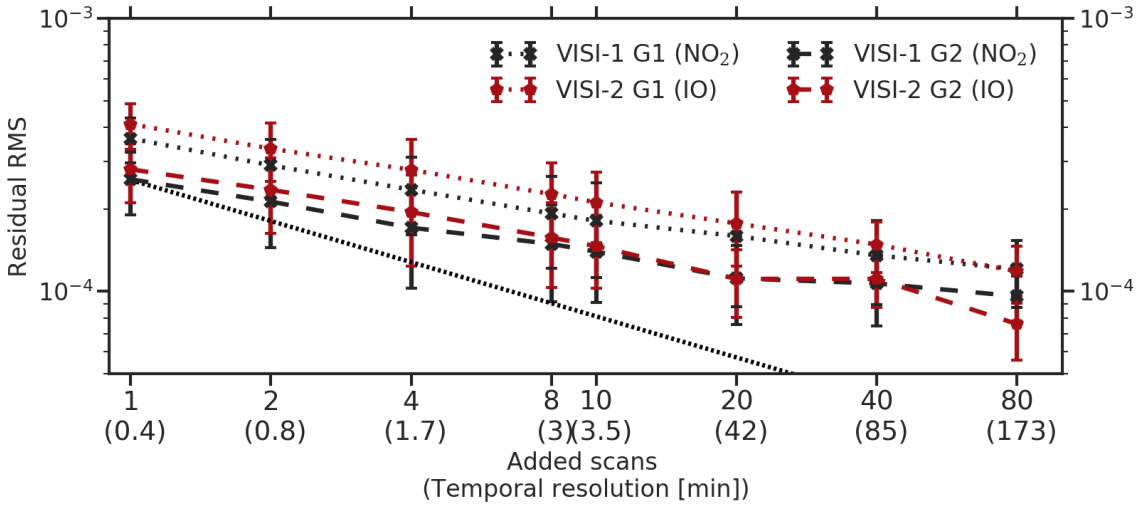

Figure 5.5: Mean residual RMS of different spectra summations/temporal resolutions for the VISI spectral window. The points connected by the dotted curves indicate the average residual RMS values for the 1200 gr. mm^{-1} grating used until February 2017. The dashed lines connect the average residual RMS for the 600 gr. mm^{-1} grating used after that date. The black dotted line marks the decrease of the RMS for pure photon noise.

to the removal of the systematic residual structures previously visible, is largely caused by an improved photon statistics. Due to the smaller dispersion of the new grating, a single pixel on the detector receives more photons even though the received irradiance per wavelength interval does not change. Since in the blue spectral region the received signals under optimal atmospheric visibility were so high that often the technically shortest possible integration times of the detector were reached or even undercut (leading to an oversaturation), compared to the operation with the 1200 gr. mm^{-1}, higher fixed saturation targets had to be set (from 30% to 60%) thus roughly doubling the number recorded photons per saved spectrum. For this higher saturation, the detector linearity is still very good, but the shortest integration times were no longer reached. A doubling in photon numbers should improve the residual RMS by a factor of $\sqrt{2} = 1.41$, which accounts for almost the entire difference between RMS values for single scans.

Based on this analysis, except for the evaluations of BrO, NO_2, NO_3, I_2, Br_2, OIO, and OBrO, a summation of 20 spectra was selected in the data evaluation. This corresponds to a summation of all five sets of spectra measured in a sequence in the respective spectral window (see Fig. 5.2) and yields temporal resolutions between 20 and 50 min depending on the atmospheric visibility. For NO_3, I_2, Br_2, OIO, and OBrO, 12 spectra were summed up since in these spectral windows only three sets per sequence were recorded.

For BrO and NO_2, evaluations with 4 summed up spectra were used. Due to the sufficient detection limits achieved with this configuration (see overview in Tab. 5.4), the higher temporal resolution of about 2 min within a sequence and on average 30 min between sequences was favoured since the observed temporal evolutions of both trace gases were relatively fast (mixing ratio increases of several orders of magnitude within few hours). In particular in the case of NO_2, summing more spectra would have smoothed out spikes in the times series e.g. from short term emissions from vehicles or gusts with air originating from the station.

Most of the ancillary data sets from the observatories of NM III station are available in one-minute temporal resolution. For comparison with the LP-DOAS, these time series were converted to the irregular temporal resolution of the different fit scenarios. For this, the times of acquisition of the first and last spectrum summed up for one DOAS fit/data point were determined. Continuous time series like basic meteorological parameters were averaged within this time period. Non-continuous parameters related to instrument performance e.g. the maximum number of counts in atmospheric and short-cut spectra were averaged for the respective spectrum type within the time period. Since the meteorological data is needed for the conversion of column densities to mixing ratios (see following Sec. 5.2.3), for gaps up to 20 min length in the meteorological data set, missing data points were linearly interpolated between last and next available values assuming that on this time scale no drastic fluctuations of pressure and temperature occur.

5.2 Data quality

5.2.1 Example fits

In the following figures, fit examples for those fit scenarios are shown, where trace gases above the detection limit were detected. Fit statistics for all fit scenarios regarding the fit quality and its temporal evolution is presented in the following section 5.2.4. In the plots, absorbers that were accounted for in the fit scenarios but only had a negligible contribution in the particular fit shown, are not plotted.

Chlorine monoxide (ClO) and sulphur dioxide (SO_2) - UVI-1

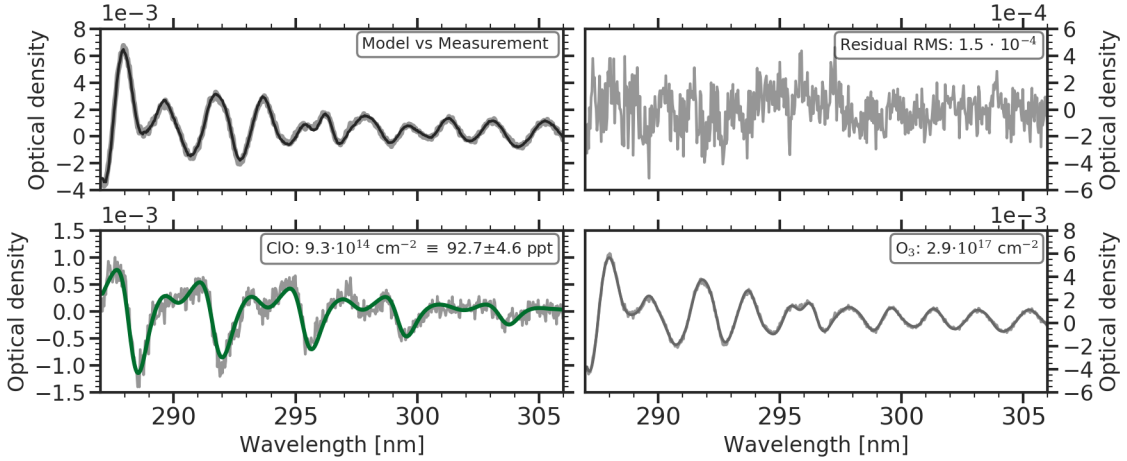

Figure 5.6: Example fit for ClO on March 18th, 2016 10:54 UTC. Fit components with negligible contributions not plotted: BrO, HCHO, NO_2, OClO, SO_2, SC, BG

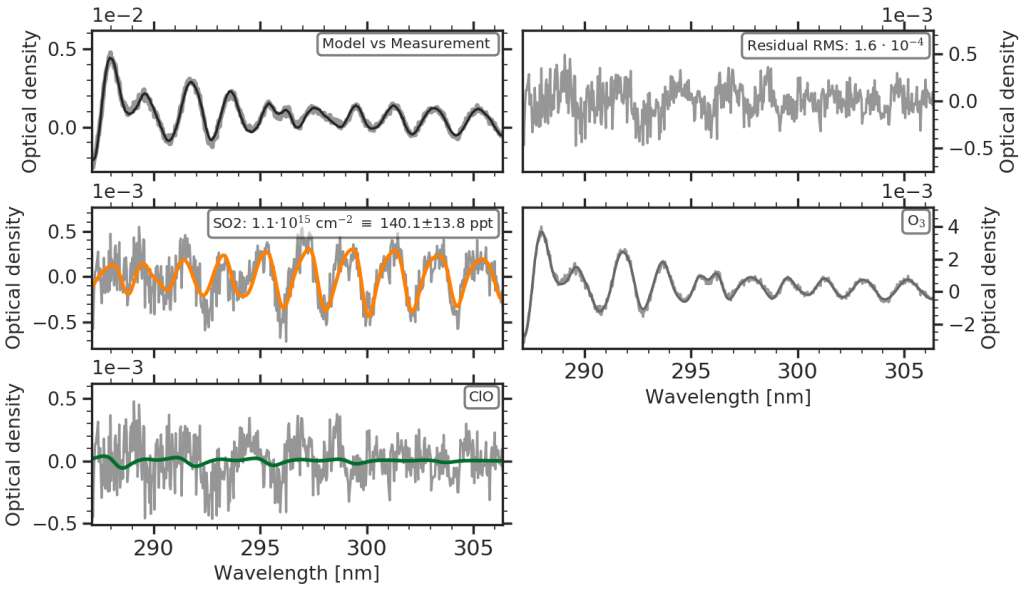

Figure 5.7: Example fit for SO_2 on January 17th, 2018 17:21 UTC. Fit components with negligible contributions not plotted: BrO, HCHO, NO_2, OClO, SC, BG

Ozone (O_3) - UVI-2

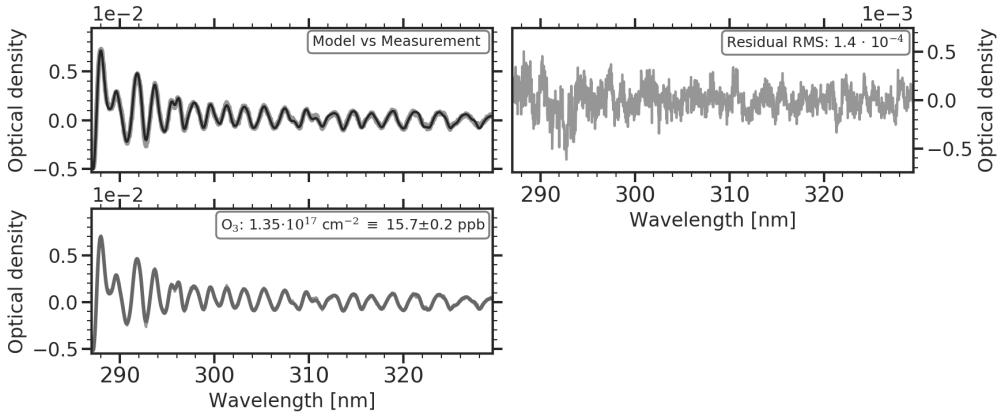

Figure 5.8: Example fit for O_3 on January 25th, 2016 20:48 UTC. Fit components with negligible contributions not plotted: BrO, ClO, HCHO, HONO, NO_2, OClO, SC, BG

Bromine monoxide (BrO) and chlorine dioxide (OClO) - UVI-3

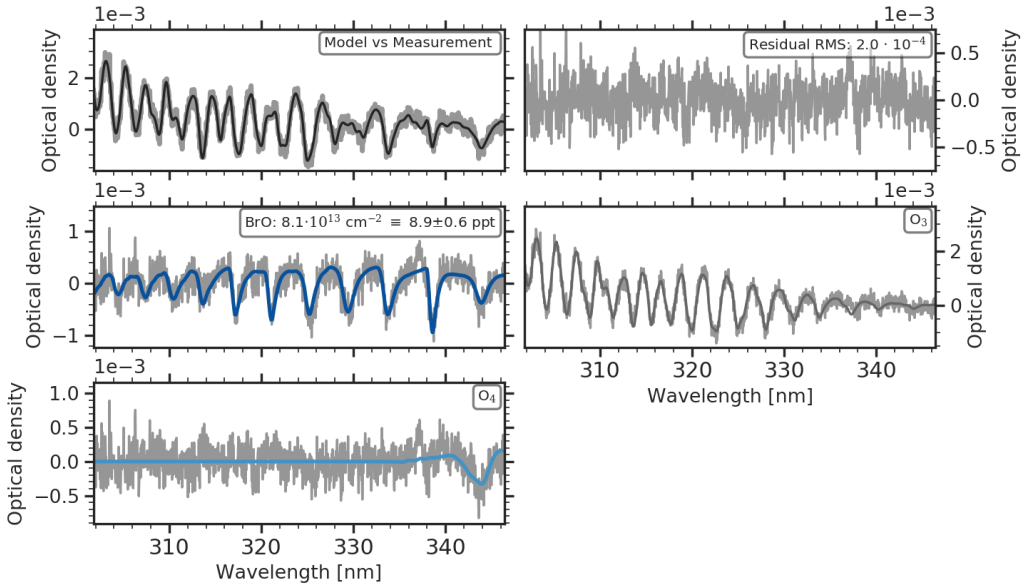

Figure 5.9: Example fit for BrO on May 26th, 2016 12:22 UTC. Fit components with negligible contributions not plotted: ClO, HCHO, HONO, NO_2, OClO, SC, BG

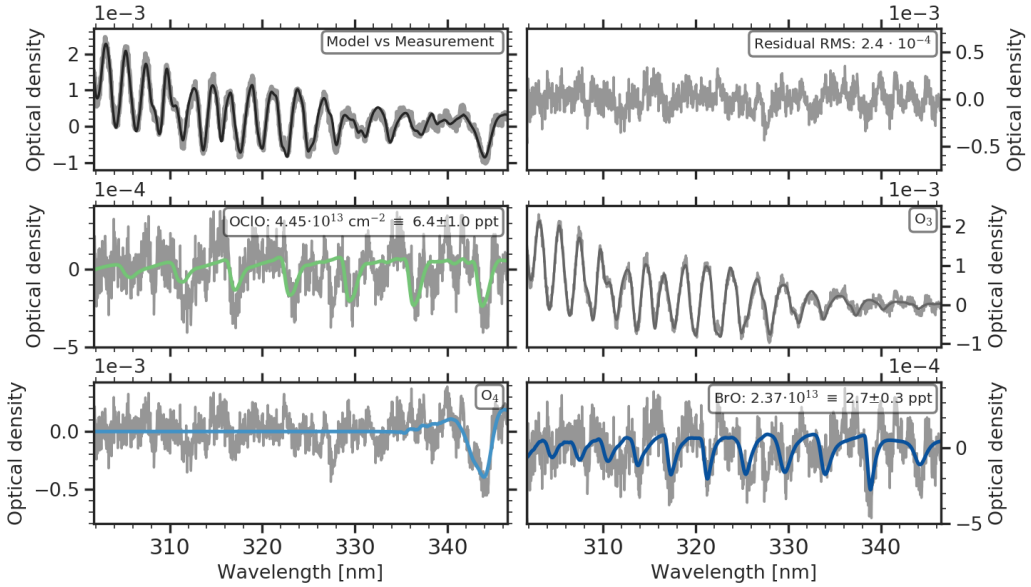

Figure 5.10: Example fit for OClO on May 11th, 2016 17:06 UTC. Fit components with negligible contributions not plotted: ClO, HCHO, HONO, NO_2, SC, BG

Bromine monoxide (BrO) and chlorine dioxide (OClO) - UV2-1

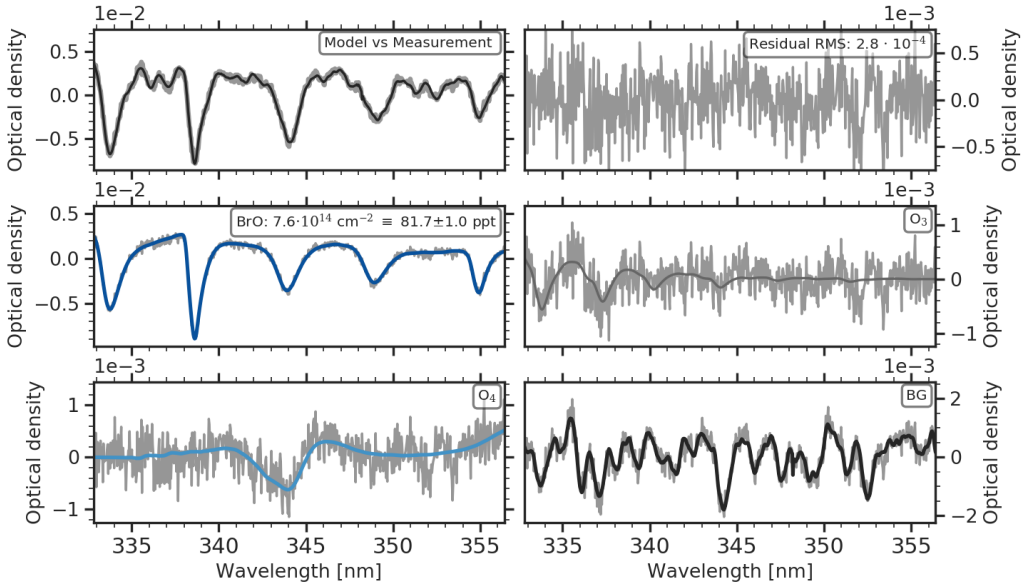

Figure 5.11: Example fit for BrO on November 8th, 2017 11:47 UTC. Fit components with negligible contributions not plotted: OClO, HCHO, HONO, NO_2, SC, BG

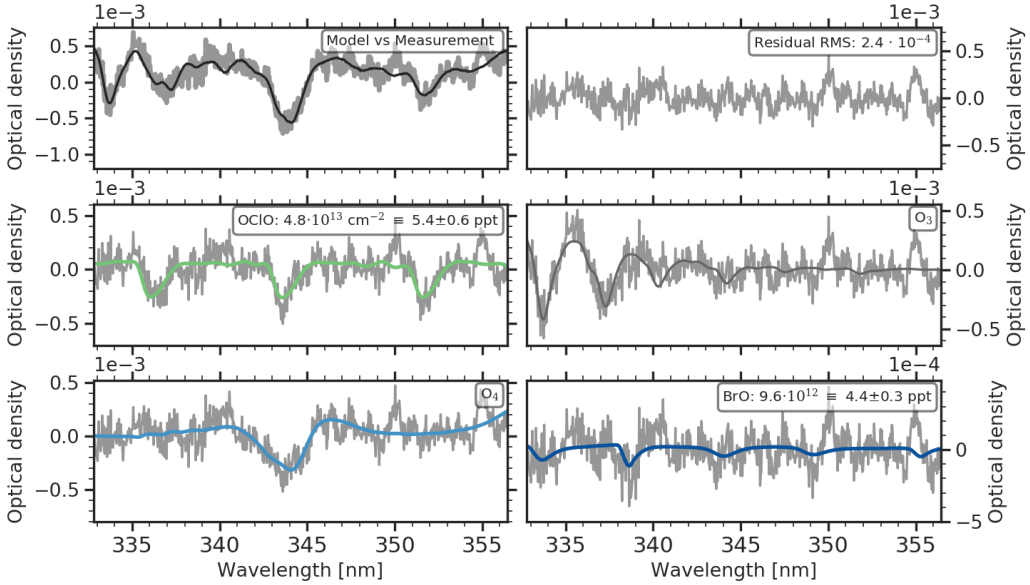

Figure 5.12: Example fit for OClO on April 10th, 2016 19:17 UTC. Fit components with negligible contributions not plotted: HCHO, HONO, NO_2, SC, BG

Nitrogen dioxide (NO_2) - UVII-2

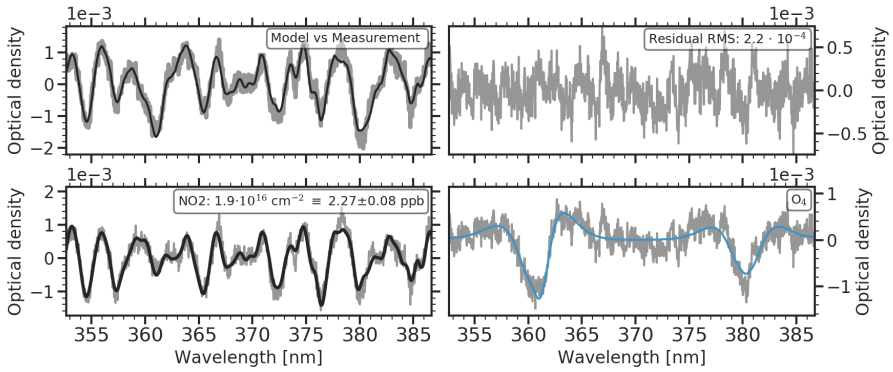

Figure 5.13: Example fit for NO_2 on September 21th, 2016 9:21 UTC. Fit components with negligible contributions not plotted: BrO, HCHO, HONO, O_3, SC, BG

Nitrogen dioxide (NO_2) - VISI-1

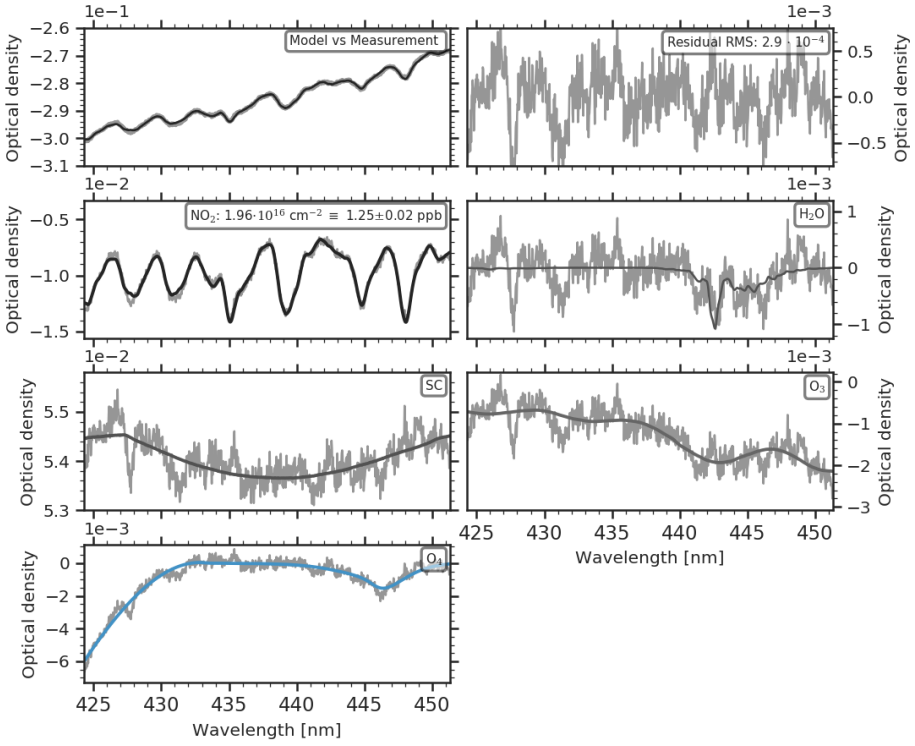

Figure 5.14: Example fit for NO_2 on April 27th, 2016 20:09 UTC. Fit components with negligible contributions not plotted: IO, Glyoxal, BG

Iodine monoxide (IO) - VISI-2

The evaluation of iodine monoxide (IO) column densities proved to be less straight-forward than for the other absorbers and therefore will be discussed in more detail. With the 1200 gr. mm^{-1} holographic grating that initially was used for all spectral windows during the first year of operation, the fitting routine for the evaluation of IO was relatively unstable.

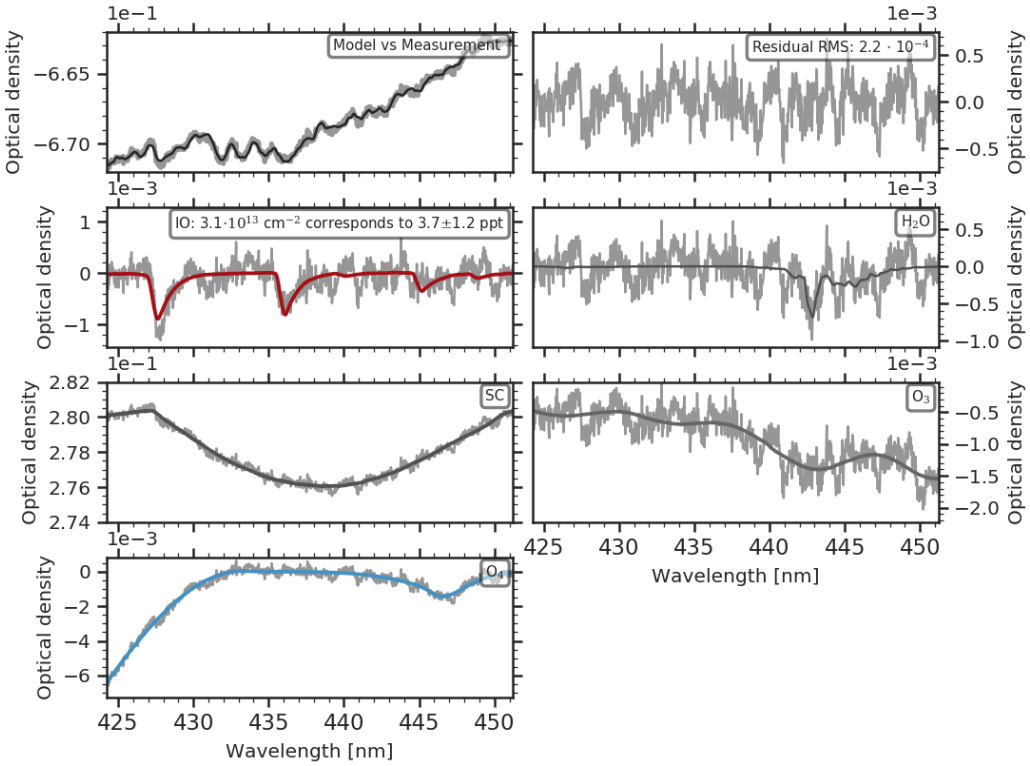

Figure 5.15: Example fit for IO with grating G1 on February 16th, 2016 16:18 UTC. Fit components with negligible contributions not plotted: NO_2 ,Glyoxal, BG

A suitable spectral interval for the evaluation of IO is between 415 nm and 439 nm (see e.g. Zielcke, 2015). This spectral range includes four strong IO absorption bands but avoids strong water absorption lines around 444 nm. When evaluated here, the fit was very unstable. Due to the absence of other strong absorbers apart form water, which at polar temperatures also has small mixing ratios, the shift and squeeze of the fit varied considerably for subsequent spectra (with frequent linear shifts of more than 1 nm when the shift was not limited). At the same time, the instability of the grating position required a certain flexibility for shift and squeeze (see Sec. 4.2.6).

Therefore water absorption lines around 444 nm were deliberately included in the spectral interval fitted, which has been done in other DOAS evaluations (e.g. Frieß et al., 2010). This however, can affect the fit residual. Water absorption cross-sections usually are produced from theoretically calculated absorption line catalogues such as HITRAN (Rothman et al., 2010). As was shown in Lampel et al. (2015b), the choice of the catalogue(-version) has a considerable influence on fit results and the relative strengths of absorption line systems in different spectral regions might have to be scaled for optimal results.

With the fitting range extended to include the water absorption around 444 nm, the shift could be stabilised and was limited to ±0.2 nm. Nevertheless, the resulting mixing ratios exhibited a large scattering. A potential cause for this was identified in the spectral shape of the VISI spectral window.

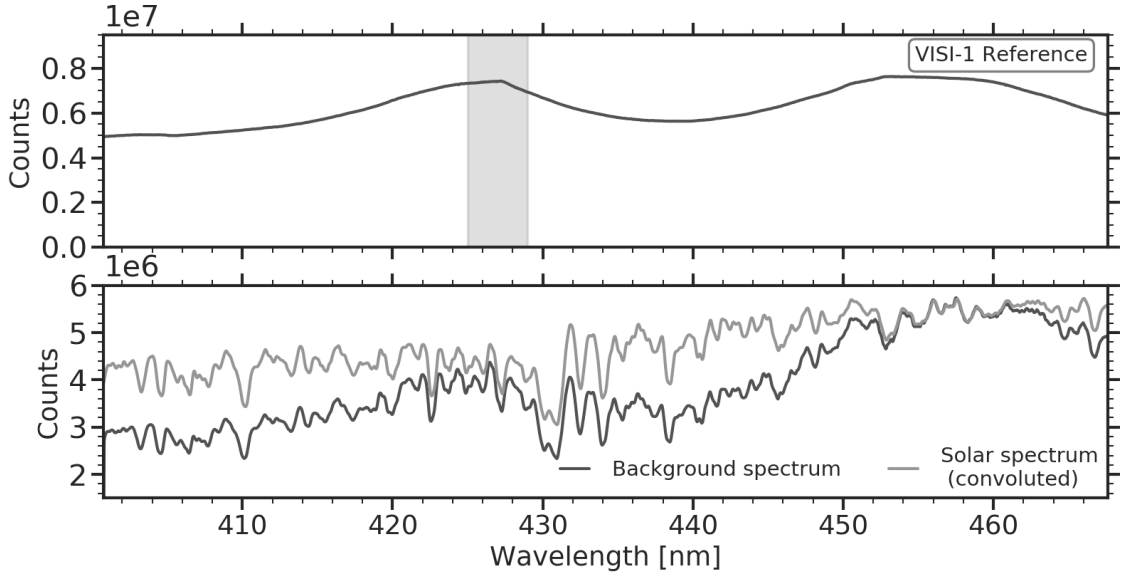

Figure 5.16: Examples of short-cut (top panel) and atmospheric background spectra (dark grey in bottom panel) for the VISI spectral window with the 1200 gr. mm^{-1} holographic grating. For comparison, a high resolution solar spectrum (Kurucz, 2006) was convoluted to spectrometer resolution and scaled to the atmospheric background spectrum around 460 nm.

As can be seen Fig. 5.16, the spectral distribution of the short-cut spectrum is U-shaped between 427 and 452 nm with distinct edges. This shape also modulates atmospheric background spectra as can be seen by comparison with a high-resolution solar spectrum in the lower panel of Fig. 5.16.[1] This spectral shape therefore cannot be caused by the light source. A different sensitivity of the CCD in this spectral range also can be excluded because no comparable structure is observed with the alternative grating.

When the grating is turned, the structure moves accordingly, which indicates that the grating or a stray-light phenomenon caused by it could be the origin of the spectral shape. The holographic grating is blazed for a spectral range between 190 and 400 nm just below the edge at 427 nm, the causal relationship between grating and the structure however, could not be identified. Since it was after the spectrometer was installed at NM III when the implications of this spectral structure became apparent, the possibilities for a detailed investigation were limited.

Generally, the DOAS approach has the advantage that the broad-band shape of spectra is not essential, however, the edges associated with the spectral shape could not reliably compensated for by either the polynomial or high-pass filtering.

While many fits are not affected by this (see fit example in Fig. 5.15), in others the differential structure associated with the edge leads to erroneous IO column densities since

[1] The solar spectrum does not include the effect of atmospheric scattering, which would lead to an additional reduction of the spectral radiance towards shorter wavelengths but cannot explain the U-shaped atmospheric background spectrum.

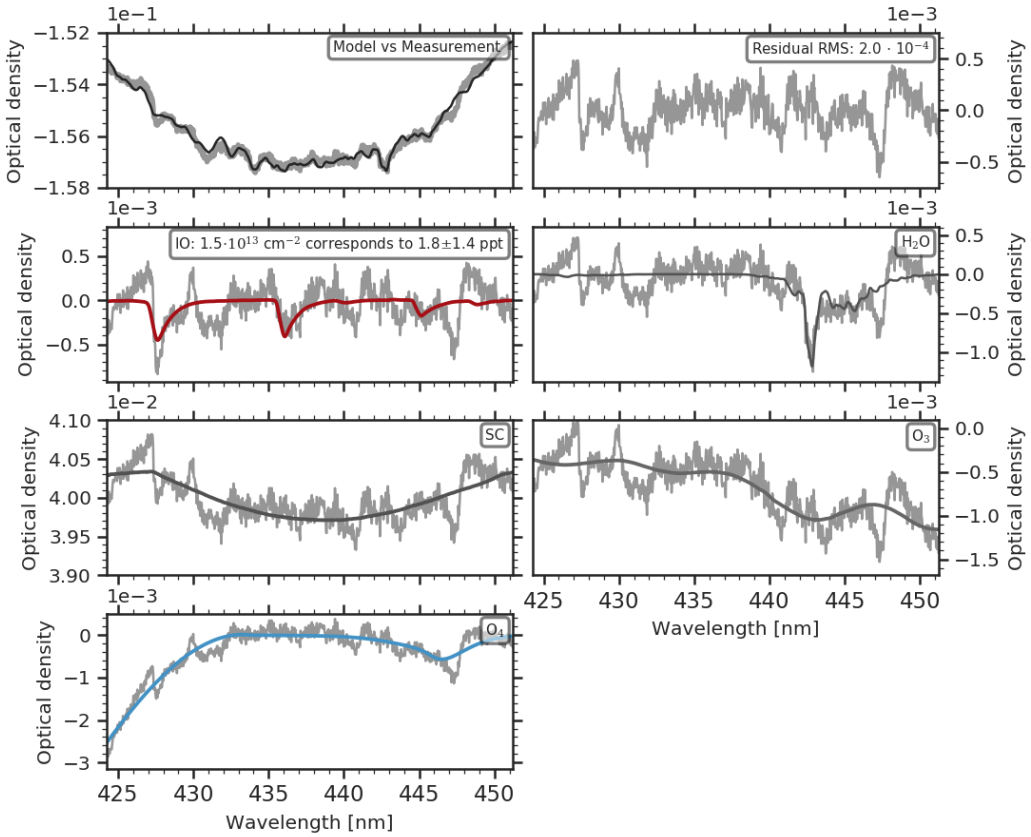

Figure 5.17: Example fit for IO with grating G1 on February 16th, 2016 17:43 UTC. Fit components with negligible contributions not plotted: NO_2, Glyoxal, BG

it coincides with the IO absorption band at 427 nm. An example of this can be seen in Fig. 5.17. This occurs more frequently for high atmospheric intensities when in the VISI spectral window, the CCD operated close to the minimum integration time. Such short integration times can cause an overexposure of the atmospheric spectra compared to the short-cut. The default saturation for measurements in this spectral window was 40%. At a minimum integration time of 5 ms per scan (with 100 scans in a single spectrum) and frequent atmospheric integration times of 7 ms, every additional ms increases to the saturation by 5%. While absolute intensities do not have to agree for atmospheric and reference spectra, a difference in saturations might introduce differential structures comparable to the differential absorption of e.g. IO. This can increase residuals and lead to an overestimation column densities.

To improve the measurement performance in the VISI spectral window a 600 gr. mm^{-1} grating was used for the VISI spectral window from February 15th 2017. An example fit with this new grating is shown in Fig. 5.18. The residual in this fit still contains considerable structures. The overall stability, however, was drastically improved by the new grating.

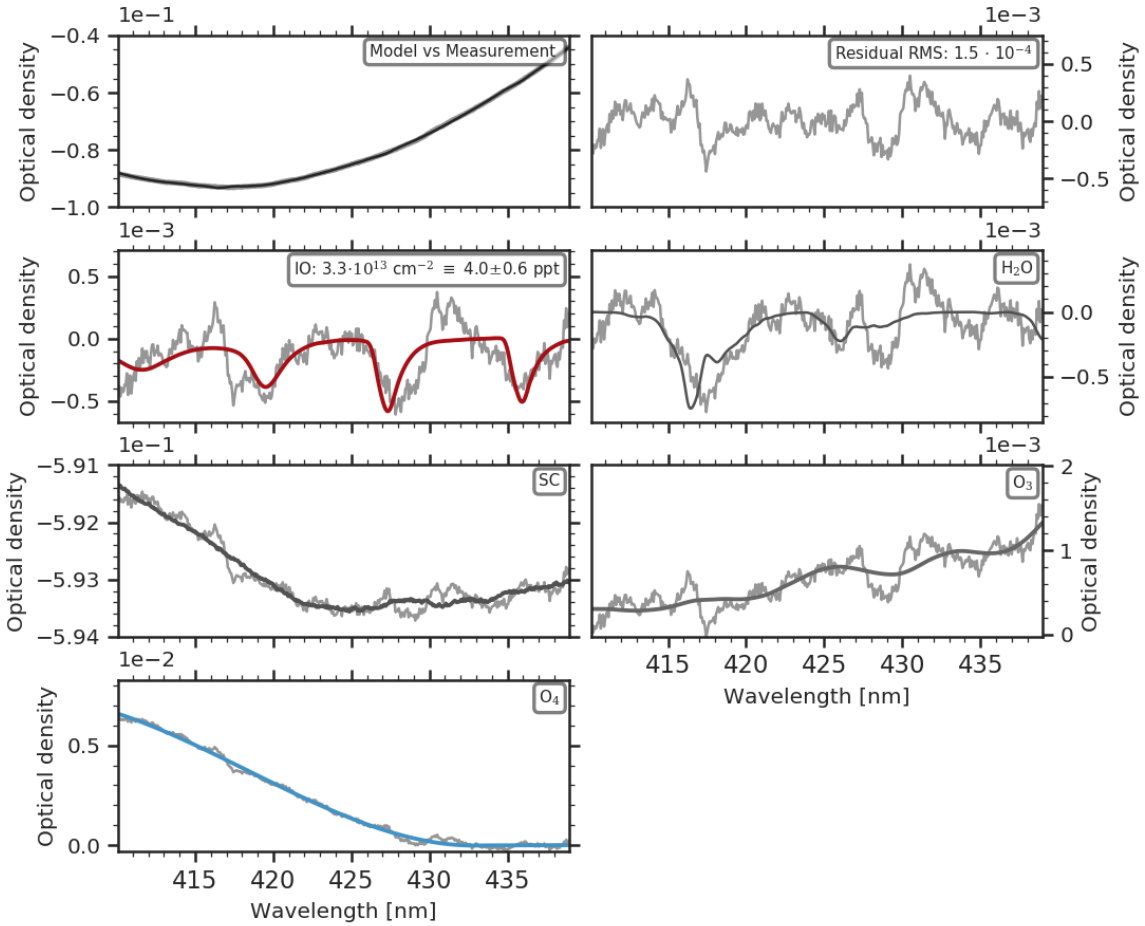

Figure 5.18: Example fit for IO on March 6th, 2018 16:12 UTC with 600 gr.mm^{-1} grating. Fit components with negligible contributions not plotted: NO_2, Glyoxal, BG

5.2.2 Error calculation

The total error, resulting from the error of the linear fit and the error introduced by the uncertainty of shift and squeeze (contribution of the non-linear fitting step) was calculated for all evaluated fit scenarios according to the approach discussed in Sec. 3.6.1. The increase of the fit error by quadratic summation of the linear error ΔS_j and the alignment error $\Delta S_{j,\text{align}}$ from the non-linear fit (see Eq. 3.27) was calculated for all absorbers in all fit scenarios. The contribution varies strongly between the different spectral windows, fit scenarios, and absorbers. Table 5.2 gives an overview of the increase of the total error $\Delta S_{j,\text{tot}}$ compared to the linear error ΔS_j (calculated via $\Delta S_{j,\text{tot}}/\Delta S_j$-1; increases are given in [%]).

For most absorbers, the increase of the total error compared to the linear error alone is below 10%. In several of fit scenarios, absorbers that are accounted for but do not have strong absorption bands exhibit an strong increase by more than a factor of two (e.g. NO_2 in the VIII-1 and VISIII-1 fit scenarios). For a few scenarios the respective target species exhibits a strong increase e.g. BrO in the UVII-1 scenario with 4 summed up spectra or IO in the VISI-1 and VISI-2 fit scenarios. In both cases, linear errors are small (0.4 ppt

Scenario		Spectra	Absorber Increase of the total error ($\Delta S_{j,\mathrm{tot}}/\Delta S_j$ - 1)								
UVI	1	20	BrO 8.4%	**ClO** 21.8%	HCHO 4.9%	NO_2 3.7%	O_3 1.3%	OClO 3.9%	**SO_2** 18.4%		
	2	20	BrO 1.1%	ClO 11.8%	HCHO 0.9%	HONO 0.9%	NO_2 6.9%	**O_3** 0.7%	O_4 4.3%	**OClO** 0.7%	SO_2 6.7%
	3	4	**BrO** 5.7%	ClO 3.8%	HCHO 4.4%	HONO 5.0%	NO_2 9.3%	O_3 4.3%	O_4 2.8%	OClO 3.4%	
	3	20	BrO 4.9%	ClO 2.9%	HCHO 3.5%	HONO 3.8%	NO_2 8.3	O_3 2.6%	O_4 2.3%	**OClO** 2.9%	
UVII	1	4	**BrO** 124.2%	HCHO 117.4%	HONO 4.2%	NO_2 195.2%	O_3 86.1%	O_4 88.7%	OClO 135.7%		
	1	20	BrO 3.3%	HCHO 1.7%	HONO 5.7%	NO_2 6.3%	O_3 11.5%	O_4 1.7%	**OClO** 13.4%		
	2	4	BrO 3.7%	HCHO 1.9%	HONO 6.2%	**NO_2** 7.1%	O_3 11.8%	O_4 1.8%	OClO 13.5%		
	2	20	BrO 3.3%	HCHO 1.7%	**HONO** 5.7%	NO_2 6.3%	O_3 11.4%	O_4 1.7%	OClO 13.4%		
VISI	1	4	**NO_2** 39.0%	O_3 47.5%	O_4 61.3%	H_2O 28.7%	IO 44.0%	Gyoxal 36.9%			
	1	20	NO_2 69.7%	O_3 78.7%	O_4 111.0%	H_2O 41.5%	**IO** 77.1%	Gyoxal 65.4%			
VISII	2	12	NO_2 197.1%	O_3 61.6%	O_4 310.6%	H_2O 156.1%	**I2** 131.7%	**OIO** 218.3%	**Br_2** 171.8%	**OBrO** 49.4%	**NO_3** 289.0%
VISIII	1	12	NO_2 167.9%	O_3 51.8%	H_2O 49.8%	O_2 25.3%	**NO_3** 27.5%				

Table 5.2: Influence of alignment uncertainty on the total measurement error. The percentages indicate the increase of the total error $\Delta S_{j,\mathrm{tot}}$ compared to the error determined in the linear fit (calculated via $\Delta S_{j,\mathrm{tot}}/\Delta S_j$-1). Target absorbers of the respective fit scenario are printed bold.

for BrO and 0.15 ppt for the two IO fit scenarios) and therefore the absolute increase of the error is smaller than the percentages suggest.

As discussed in Sec. 3.6.1, due to the correlation of neighbouring pixels, the total error resulting from linear fit and the contribution of the alignment uncertainty has to be scaled by a factor c_D. These correlations can be introduced by systematic structures in the residual, but also when a high-pass filter is applied to improve the removal of broad-band structures compared to a sole fitting of a polynomial (as is the case for UV evaluations in this analysis).

For species, for which photochemical properties allow to assume a clear diurnal cycle and an immediate relationship to the actinic flux, the factor $c_{\mathrm{D},j}$ was determined following Tuckermann et al. (1997) and Alicke et al. (2002). For absorbers expected to only be present under solar irradiation (BrO, ClO, IO) and below the detection limit of the LP-DOAS during the night, mean μ_j and standard deviation σ_j of retrieved mixing ratios at times when the short-wave downwelling radiation (SWD, see Tab. 4.2) was below 0.5 W m^{-2} were calculated. This corresponds to SZAs above 100°. The correction factor c_D then was obtained by scaling the total error $\Delta S_{j,\mathrm{tot}}$ to match the standard deviation

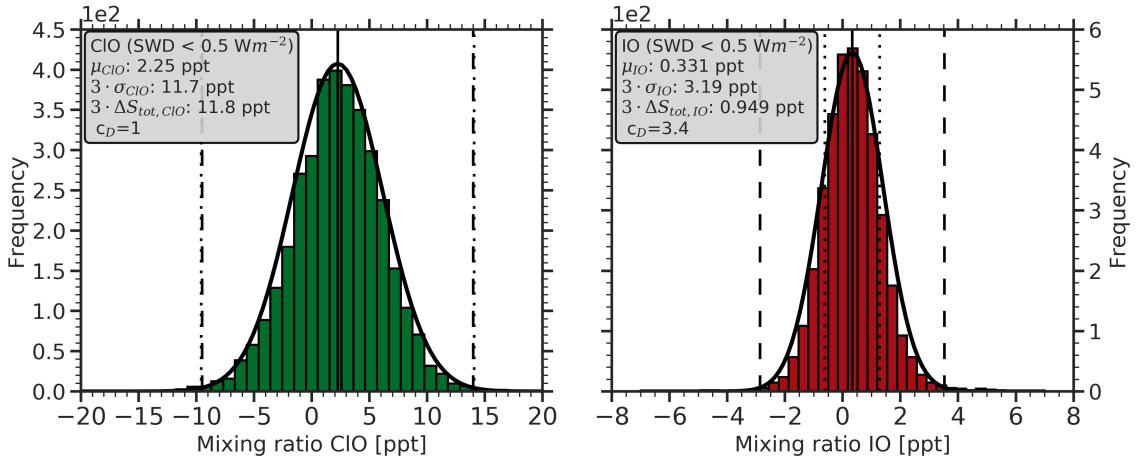

Figure 5.19: Determination of error correction factor for ClO and IO (grating G2). For both absorbers the distribution of mixing ratios is plotted for times when the short-wave downwelling radiation was below 0.5 W m^{-2}. The vertical solid black line marks the mean, the dotted lines mark the ±3-σ interval based on the the total error $\Delta S_{j,\mathrm{tot}}$ of the DOAS fit, the dashed lines mark the ±3-σ interval of the standard deviation of the distribution. The envelope is the Gaussian distribution with the indicated parameters.

σ_j.

$$c_{\mathrm{D},j} = \frac{\sigma_j}{\Delta S_{j,\mathrm{tot}}} \tag{5.2}$$

Examples of the distributions of retrieved mixing ratios of ClO and IO under this selection criterion are shown in Fig. 5.19. In the case of ClO the total error $\Delta S_{\mathrm{ClO,tot}}$ corresponds to the standard deviation of mixing ratios when no ClO would be expected resulting in $c_{\mathrm{D,ClO}} = 1$. For IO, the scattering of mixing ratios is larger than reflected by the total error resulting in $c_{\mathrm{D,IO}} = 3.4$. The correction factors thus determined together with the statistics of the respective distributions can be found in Tab. 5.3.

For photolabile species (OBrO, Br_2, OClO, OIO, I_2, and NO_3), the distributions corresponding to times when mixing ratios are expected to be below the instrumental detection limit were determined by selecting periods when the short-wave downwelling radiation was more than 100 W m^{-2}, which at NM III typically corresponds to SZAs below 80°. Correction factors were determined as before (results see Tab. 5.3). All correction factors thus determined are between 1 and 5.5 with most between 3 and 4, which corresponds to the range factors determined with artificial spectra in Stutz and Platt (1996).

Absorber	Fit Scenario	Average μ [ppt]	Standard deviation σ [ppt]	Total fit error $\Delta S_{j,\mathrm{tot}}$ [ppt]	Correction factor c_D
BrO	UVI-3	0.92	0.74	0.31	2.4
	UVII-1	0.45	1.25	1,05	1.2
OBrO	VISII-1	1	4.5	1.02	4.5
Br_2	VISII-1	591	1718	422	4
ClO	UVI-1	2.25	3.93	3.9	1
OClO	UVI-3	-1.4	1.27	0.39	3.3
	UVII-1	-0.05	1.48	0.85	1.7
IO	VISI-1 G1	0.32	1.55	0.30	5.2
	VISI-1 G2	0.33	1.06	0.31	3.4
OIO	VISII-1	-1	6.10	1.45	4.2
I_2	VISII-1	3.12	24.6	4.48	5.5
NO_3	VISIII-1	-1.65	3.39	0.87	3.9

Table 5.3: Correction factors for the total errors. For BrO, ClO, and IO, periods with less than 0.5 W downwelling short-wave radiation were selected for the calculation of the statistics. For all other absorbers, periods with more than 100 W were used.

5.2.3 Conversion of retrieved slant columns to mixing ratios

The result of the DOAS fit are column densities S_j (in cm^{-2}) of absorbers j (see Eq. 3.7). For further analysis, these column densities were converted into mixing ratios r_j using the ideal gas law and the known light path L to the reflector-array.

$$r_j = \frac{S_j}{2 \cdot L} \cdot \frac{k_B \cdot T_{2\mathrm{m}}}{p} \tag{5.3}$$

For the conversion, the temperature in 2 m altitude ($T_{2\mathrm{m}}$) at the meteorological measurement site (see Fig. 4.1, right panel) and the atmospheric pressure p measured at the main station were used. The factor k_B is the *Boltzmann* constant.

5.2.4 Fit statistics and detection limits

The RMS of the residual is a good measure for fit quality, since the residual represents the part of the measured optical density τ that is not accounted for by the model consisting of polynomial and narrow-band absorption (see Eq. 3.24). To assess the quality of the data set for the observation period, fit statistics were calculated for all fit scenarios (see Tab. 5.1) and the the selected spectra summation settings (see Sec. 5.1.4). Histograms of the residual RMS and the detection limits based on the error calculation above can be found in this section for selected absorbers and in Sec. D.1.6 in the appendix for all other evaluations. Median residual RMS values and detection limits for all absorbers are listed in the data analysis summary in Tab. 5.4. For the three main spectral windows UVI, UVII, and VISI in addition to histograms, time series of residual RMS and detection limits for selected absorbers were plotted and can be found in Fig. 5.20. Fig. 5.21, and Fig. 5.23.

In all three spectral windows residual RMS and detection limits exhibit a considerable variation even though the majority of data points lies within a relatively confined range

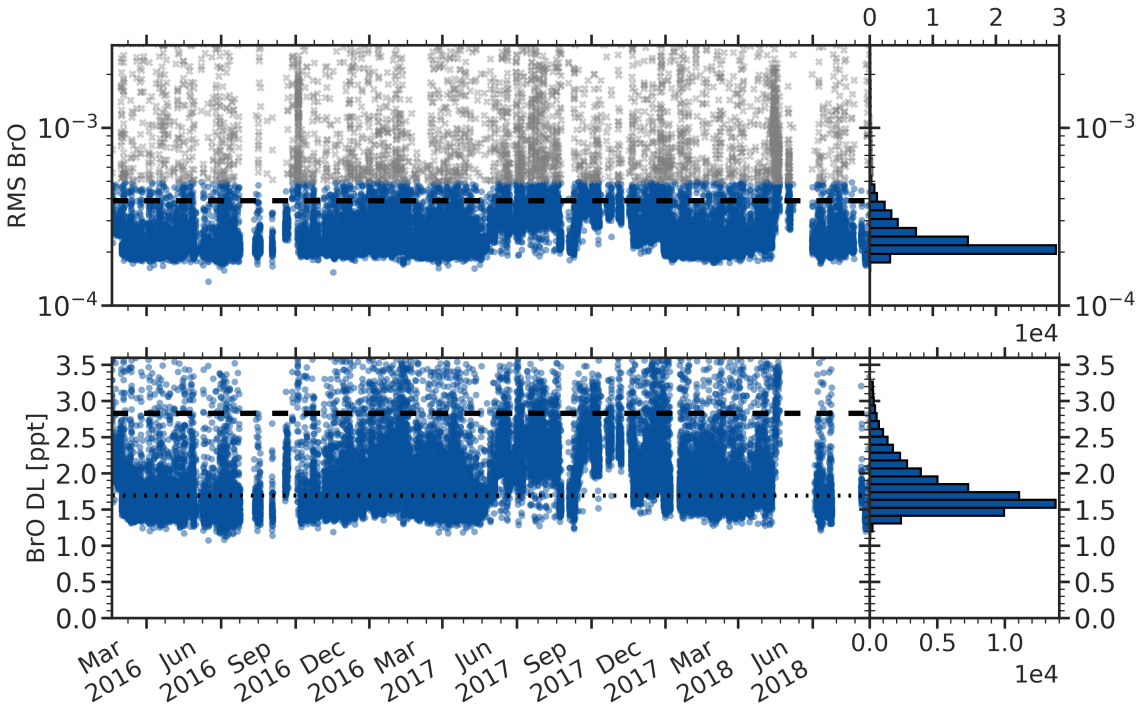

Figure 5.20: Residual and detection limit time series for BrO evaluated in the UVI-3 fit scenario. Dotted lines indicate the respective median. Dashed lines mark the 9th quantile of the distributions. The residual RMS of excluded fits is marked in light grey.

of values (see histograms of the time series in the panels on the right hand side of the plots). Increases of residual RMS and detection limits are the result of decreases of the measurement signal mostly due to (temporary) reductions of atmospheric visibility. All plots show longer gaps in the time series associated with instrumental problems.

In 2016, at the end of June a failure of the shut-off mechanism in the LDLS prevented measurements as signal optimisation and the reflector search routine (see Fig. 4.21) both rely on a comparison of the current atmospheric background signal to the measurement signal. In August 2016 the telescope interior temperatures were too low leading to a frequent mist-up of the front window.

In a third period at the end of August 2016, a problem with one of the stepper motors inside the telescope caused a frequent loss of the measurement signal and, due to harsh meteorological conditions during that part of the year, could not be fixed promptly. During the second year of operation, gaps in the time series are shorter probably due to the increased heating power in the telescope that reduced the misting of optical components.

Larger gaps in the measurements occurred again in April 2018 when successively, probably due to long-term wear, different stepper motors, both in the telescope and the light source broke irreparably. Necessary adjustments to the measurement routine required frequent interventions by the winterer which, depending on the meteorological conditions, could not always be performed immediately and replacing the functionality of the respective motors required some experimenting. Measurements could resume for two periods in June and August 2018 with a reduced functionality but a measurement performance

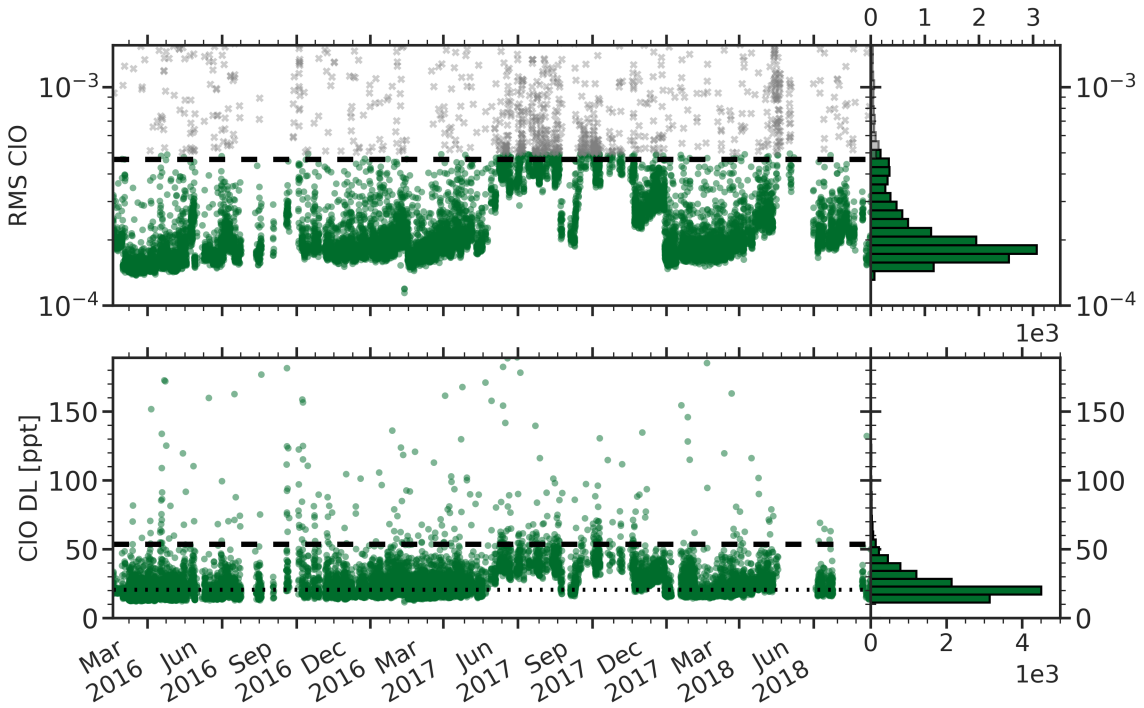

Figure 5.21: Residual and detection limit time series for ClO evaluated in the UVI-1 fit scenario. Dotted lines indicate the respective median. Dashed lines mark the 9$^{\text{th}}$ quantile of the distributions. The residual RMS of excluded fits is marked in light grey.

more or less comparable to the prior observation periods. The break down of the LDLS in August 2018 ended the operation of the instrument.

For the lower limit of residual RMS time series and detection limits, depending on the spectral window, different mid-term variations are visible even though no clear overall trend in the performance from start to end of the measurements can be discerned. In spectral regions with lower spectral radiances, in particular in the UVI-1 fit scenario plotted in Fig. 5.21, the variations of the lower limit of the residual RMS reflect the major maintenance interventions in early 2017 and again late 2017 that restored the transmissivity of optical components with a steady but limited increase of the residuals in between. The influence of these small increases on detection limits, however, is negligible.

In 2017, starting at the end of April, a period with increased residuals and detection limits is apparent in all spectral windows with the largest influence on the UVI window. The reason for this was a contamination of the telescope front window (and probably other optical components) by a residue likely originating from the Armaflex insulation. Despite being marketed as temperature resistant and UV durable, it had started to become brittle causing the deposition of dust like powder inside the telescope. This degradation might have been increased by the fact that for exterior temperatures above 250 K, the heating in the telescope was periodically switched on and off by the bi-metal temperature switch, which might have caused additional wear of the insulation material. In combination with the increased heating power installed at the beginning of 2017, where one radiator had been placed close to the front window to reduce misting, this deposition of residue and

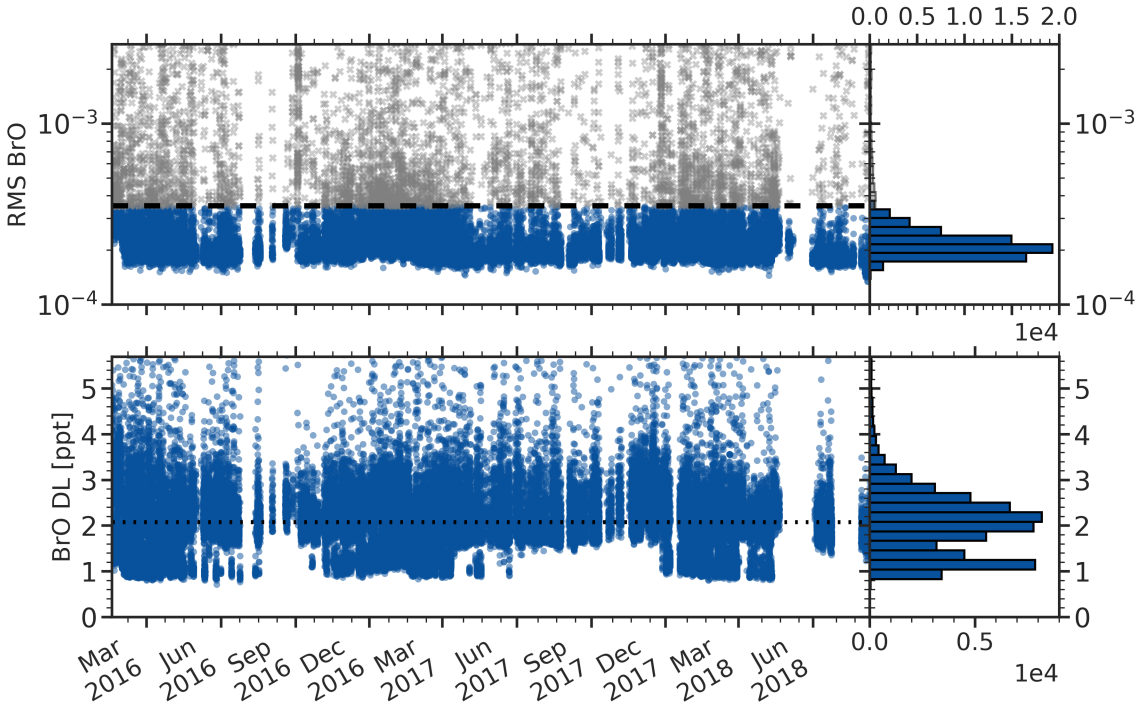

Figure 5.22: Residual and detection limit time series for BrO evaluated in the UVII-1 fit scenario. Dotted lines indicate the respective median. Dashed lines mark the 9th quantile of the distributions. The residual RMS of excluded fits is marked in light grey.

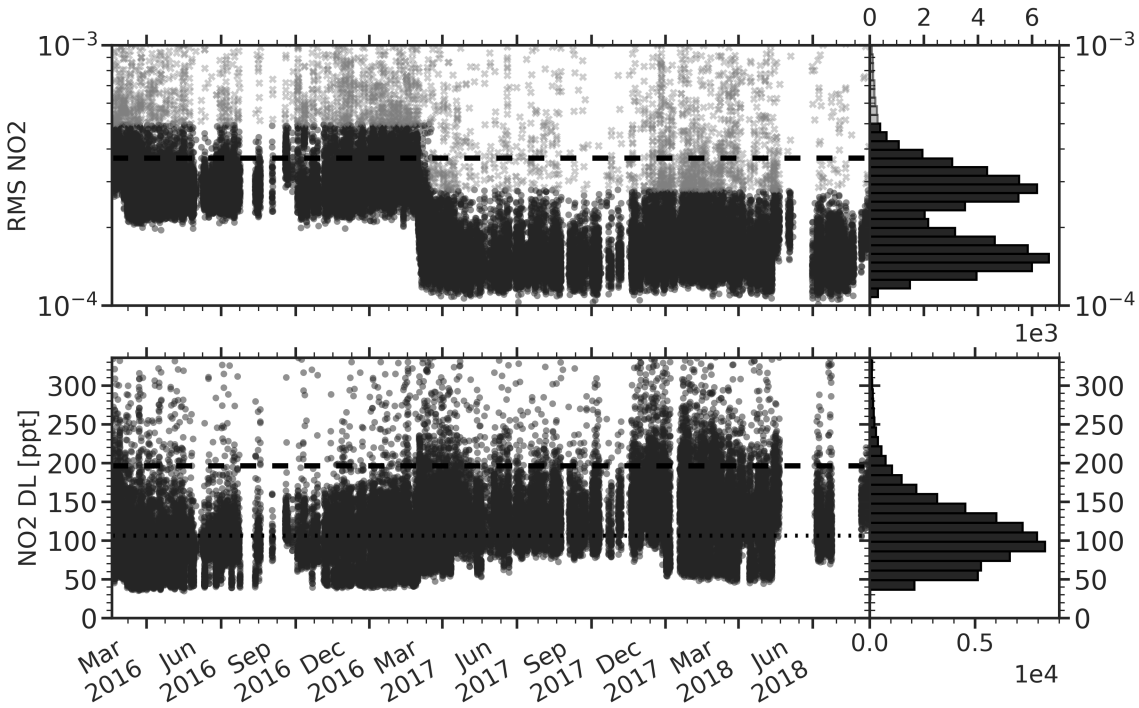

Figure 5.23: Residual and detection limit time series for NO_2 evaluated in the VISI-1 fit scenario. Dotted lines indicate the respective median. Dashed lines mark the 9th quantile of the distributions. The residual RMS of excluded fits is marked in light grey.

subsequent heating on the front window reduced its transmissivity (background-corrected atmospheric signals decreased by about a factor of 2-3).

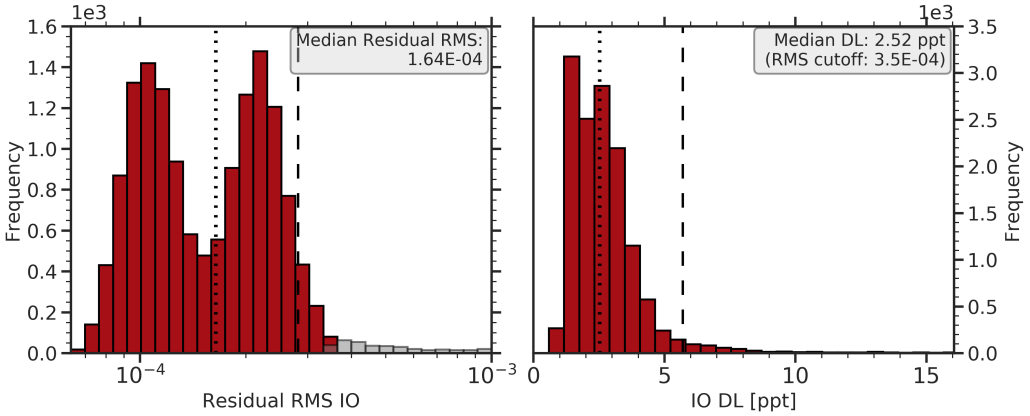

Figure 5.24: Residual and detection limit statistics for IO evaluated in the VISI-1 fit scenarios. Dotted vertical lines indicate the respective median. Dashed lines mark the 9th quantile of the distributions. The residual RMS of excluded fits is marked in light grey.

The debris on the window could be removed mechanically. However, due to the prevalent meteorological conditions at the end of winter, this could only be done at the beginning of August and at the end of October. During the second major maintenance in mid-December 2017, a thorough cleaning of the window and all optical components, and a removal of dust and brittle pieces of the insulation material could restore the transmissivity and regular precautionary cleaning when weather permitted could prevent a similar deposition for the remainder of the observations. The increase of the detection limits during the period of reduced front window transmissivity mainly affects the UVI spectral window and in particular the ClO evaluation where detection limits increased by a factor of about 2-3.

In the spectral windows where measurements were performed on both retro reflectors (both in the UVII - Fig. 5.22 and VISI - Fig. 5.23), the influence of the longer light path is visible in the minimum values of the detection limits. During periods when visibility allowed the frequent utilisation of the second retro-reflector array, detection limits are almost halved in agreement with the roughly two times longer absorption path. In the BrO evaluation UVII spectral window this even leads to a bi-modal distribution of detection limits (see Fig. 5.22).

The temporal evolution of the residual RMS in the VISI spectral window (Fig. 5.23) reflects the changes to the measurement settings, which were discussed in detail in Sec. 5.2.1. The change of the grating reduced the residual RMS by a factor of about 2 leading to the bi-modal distribution of the residual RMS. For NO_2, detection limits did not change considerably by this.

For the evaluation of IO, in the VISI-1 fit scenario, the change of the grating led to a decrease of the detection limit from about 2.9 ppt to 1.6 ppt (see Fig. 5.24 as well as the separate histograms for the two gratings in Fig. D.18 and Fig. D.19 in the appendix).

Due to the effects described above, the detection limits determined for IO observations in this thesis (see following section) are higher than in recent LP-DOAS studies (e.g. Zielcke, 2015) but comparable to previous LP-DOAS observations reported e.g. by Saiz-Lopez et al. (2007a) and Seitz et al. (2009).

5.2.5 Data filtering

All retrieved data sets were filtered before interpretation. The evaluation routine was set up with a pre-filtering mechanism. Over- and under exposed spectra were not considered in the summations for the optical density τ (with limits of $N_{max} = 22000\,\text{counts}\,\text{scan}^{-1}$ and $N_{min} = 200\,\text{counts}\,\text{scan}^{-1}$ respectively). To prevent a summation over gaps in the observations, which would average spectra recorded in potentially very different atmospheric conditions, a maximum temporal offset of one hour between first and last spectrum in a summation was allowed. Furthermore, only fit results with a residual RMS of less than 0.1 were saved, which is an extreme high values that mainly filters out fits that did not converge properly.

For the different evaluations then limits for the residual RMS values for individual fits were set weighing temporal coverage and data quality. Applying stricter limits lower the scattering of data points but reduce temporal coverage and vice versa. The selected RMS limits lie between $2{\cdot}10^{-4}$ and $12{\cdot}10^{-4}$ and can be found in Tab. 5.4. For all data sets the loss of data due to the RMS filtering of the fit results was less than 10% (exact percentages are indicated in Tab. 5.4 as well).

5.2.6 Combination of data sets

The data sets of those species that could be evaluated in two different spectral windows (BrO, OClO, and NO_2), were combined for the data interpretation. By this the temporal coverage is improved. Before data sets were merged, for BrO and NO_2 the agreement between the two time series was investigated. For OClO, there were not enough data points above the detection limit for a meaningful comparison.

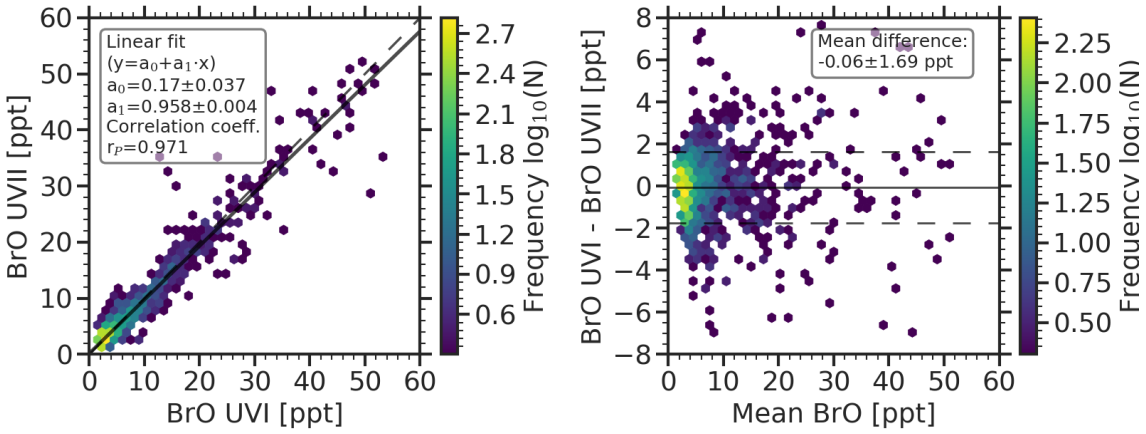

Figure 5.25: Comparison of BrO observations from UVI and UVII spectral windows of the LP-DOAS instrument. The linear fit was done with a weighted orthogonal distance regression that takes into account the errors of both instruments (Boggs et al., 1992). For the correlation the *Pearson* coefficient was calculated. The horizontal line in the right panel indicates the average difference between the two data sets, the dashed lines are the standard deviation.

Different techniques were used to assess the agreement between the data sets from the two spectral windows. To make the consecutively recorded measurements comparable, the time series were resampled to a 30 min temporal resolution. Mixing ratios within one of these 30 min sections, were averaged. Then only intervals containing data from both

evaluations were compared. For periods when the temporal gradients of mixing ratios and the temporal difference between observations from the two spectral windows are large, only a limited agreement can be expected with this approach. Since on several days fast increases of BrO mixing ratios were observed that led to considerable differences between the measurements with a sequence of a single spectral window, this limitation should be kept in mind when assessing the agreement (for details see Chapter 7.1.3).

For data points above the detection limit, the *Pearson* correlation coefficient was calculated. Furthermore, a linear regression was performed. Since errors for the mixing ratios from both spectral windows are known, an orthogonal distance regression was used that weighs errors in both dimensions (Boggs et al., 1987; Boggs and Rogers, 1990).

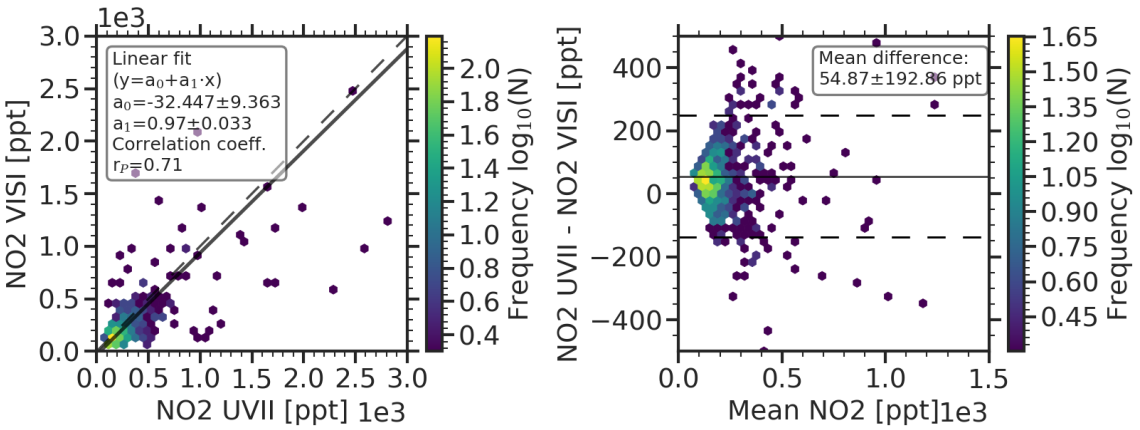

Figure 5.26: Comparison of BrO observations from UVII and VISI spectral windows of the LP-DOAS instrument. The linear fir was done with a weighted orthogonal distance regression that takes into account the errors of both instruments (Boggs et al., 1992). For the correlation the *Pearson* coefficient was calculated. The horizontal line in the right panel indicates the average difference between the two data sets, the dashed lines are the standard deviation.

The correlation coefficient cannot entirely capture systematic offsets between two time series when used for comparison purposes. A regression can yield an acceptable gradient and axis intercepts even when the scatter in the correlation plot is high. Therefore, following the approach by Altman and Bland (1983), additionally the difference between the two times series as a function of the mean mixing ratio was determined. The results for the BrO evaluations are plotted in Fig. 5.25. The comparison of NO_2 time series is shown in Fig. 5.26.

For BrO, both time series are highly correlated with c_p=0.964. The axis intersect of the regression indicates a slightly positive offset (0.17 ppt) of the BrO values from the UVII spectral window. Comparing the differences between corresponding data point of the time series, a difference of only 0.12 ppt is found, however with a standard deviation larger than the respective average error of the two data sets. The higher differences between both time series for larger mixing ratios might at least partly be explained by the fast increases and decreases of the mixing ratios mentioned before. In combination with the resampling, under such conditions a certain difference between the two time series could be expected.

For NO_2, the agreement based on all three methods is not as high as for BrO. The correlation coefficient is only c_p=0.732 and the slope of the regression indicates systematically higher values from the UVII evaluation. Even though the average difference between the

two data sets is only 16.44 ppt, the variation of the difference is large. Compared to BrO, episodes with clearly elevated NO_2 mixing ratios are rare and less persistent which might explain the larger differences especially for higher values. For most of the time NO_2 mixing ratios also are close to the detection limit and exhibit a larger scatter than the BrO data.

Examples of the difference between the two evaluations for both absorbers are shown in Fig. 5.27

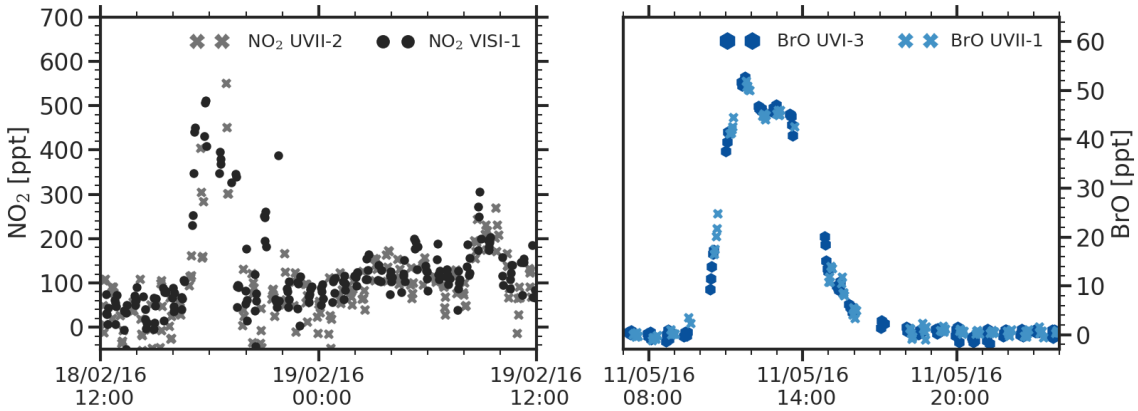

Figure 5.27: Agreement of NO_2 and BrO time series from different spectral windows/fit scenarios.

	Absorber	Added spec.	Temp. res.* [min]	Residual RMS $\cdot 10^{-4}$	Residual RMS limit $\cdot 10^{-4}$	Valid data [%]	Total** error (1σ) [ppt]	Non-lin. err. contrib. [%]	Correction factor c_{D}	Detection limit (3σ) [ppt]	Detected maximum [ppt]
UVI	ClO	20	30	1.9	0.5	92	3.18	21.8	1	9.35	104±4
	O_3	20	30	1.7	0.4	92	0.13 ppb	0.7	2	0.75 ppb	37.0±0.3 ppb
	BrO	4	4/30	2.2	4	90	0.29	5.7	2.4	2.0	110.0±0.7
	OClO	20	30	1.5	3.5	92	0.34	2.9	3.3	3.4	7.5±1.6
	SO_2	20	30	1.9	5	92	7.87	18.4	2	46.3	210±16
UVII	BrO	4	4/30	2.2	3.5	90	0.6	124.2	1.2	2.1	102.0±0.7
	OClO	20	30	1.4	2.5	92	0.41	13.4	1.7	1.96	7.7±0.7
	NO_2	4	4/30	2.1	3.5	90	31.77	7,1	2	185	3.66±0.05 ppb
	HONO	20	30	1.4	3	93	14.8	5.7	3.9	168	<DL
VISI	NO_2 (G1/G2)	4	4/30	3/1.6	5/2.8	93/94	18.1	39.0	2	91/122	3.76±0.07 ppb
	IO (G1/G2)	20	30	2.2/1.1	3.5/2	93/92	0.19	77.1	4.6	2.93/1.6	4.7±1.1
	IO***	20	30	1.4	3.5	94	0.16	127.9	3.4	1.6	3.8±0.8
VISII	I_2	12	25	2.2	4	92	4.57	131.7	5.5	71.6	<DL
	Br_2	12	25	2.2	4	92	309.9	171.8	4	3.6 ppb	<DL
	OIO	12	25	2.2	4	92	0.93	218.3	4.2	11.2	<DL
	OBrO	12	25	2.2	4	92	0.82	49.4	4.5	10.7	<DL
VISIII	NO_3	12	25	7.5	12	90	0.61	27.5	3.9	7.1	<DL

Table 5.4: Overview LP-DOAS data analysis results. All averaged values are medians. (*) If two time resolutions are indicated, the first is the time between data points within a sequence and second the time between sequences.(**) This is the total fit error without correction factor (***) Results when night-time spectrum is added to fit.

5.3 Comparison with co-located instruments

A comparison of LP-DOAS measurements with co-located instruments allows a verification of the results through independent observations. Different measurement geometries (e.g. the point measurements of the ozone monitor versus integrating geometries like in LP-DOAS or MAX-DOAS measurements) to a certain extent, allow conclusions about vertical and horizontal distributions of mixing ratios in the atmosphere.

5.3.1 MAX-DOAS

For the comparison of BrO observations of the LP-DOAS with the vertical trace gas mixing ratio profiles retrieved from measurements of the co-located MAX-DOAS instrument, a data set from mid-January 2016 until mid-May 2018 was used (Frieß 2018 - personal communication). Due to the measurement principle of MAX-DOAS that relies on scattered sun light, no observations during the night as well as during polar night between mid-May and early August are available. In terms of the vertical sensitivity of the MAX-DOAS instrument below its horizontal line of sight where the LP-DOAS light path is located, the sequence of elevation angles considered in the optimal estimation algorithm (see Sec. 4.3), includes two negative elevation angles (-5° and -20°) in addition to the positive elevations of 2°, 5°, 10°, 20°, and 90°. Furthermore, high surface albedos of the snow on the ice shelf at NM III lead to large contribution of reflected light to the total radiation (compare e.g. downwelling and upwelling short-wave radiation in Fig. 6.1). With upwelling radiation frequently contributing up to 45% of total radiation, even elevations above the horizontal are sensitive to mixing ratios below the instrument's altitude. A detailed study of the particular measurement geometry of the NM III MAX-DOAS instrument and modelled box airmass factors can be found in Frieß et al. (2010).

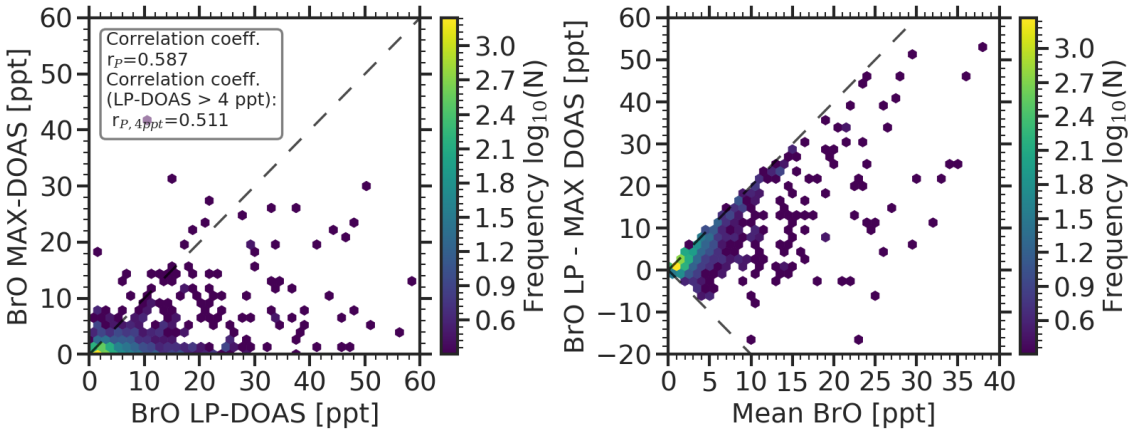

Figure 5.28: Comparison of BrO mixing ratios as measured by the LP-DOAS instrument and retrieved from MAX-DOAS observations for the lowermost profile box. The linear fit was done with a weighted orthogonal distance regression that takes into account the errors of both instruments (Boggs et al., 1992). For the correlation the *Pearson* coefficient was calculated.

The vertical profiles that the retrieval of the MAX-DOAS data yields are available at a temporal resolution of one hour. For the quantitative comparison of the two instruments, the LP-DOAS BrO time series was resampled to match the hourly temporal resolution of

the MAX-DOAS averaging the data in between. When the different comparison techniques used above are applied, the two BrO time series show only a weak agreement. A regression with meaningful results was not possible and only the correlation coefficient for both the entire comparable data set as well as all values for which LP-DOAS observations are above 4 ppt were calculated. The resulting correlation coefficients are r_P=0.587 and r_P=0.511 respectively. Both the correlation plot and the difference of the two time series as function of the mean value (see Fig. 5.28) indicate that mixing ratios from the MAX-DOAS most of the time are below that of the LP-DOAS. The dashed lines added to the right panel of Fig. 5.29 correspond to data points for which the mixing ratio of one of the two time series is zero. For positive differences the LP-DOAS detected BrO while the MAX-DOAS retrieval did not and vice versa for negative differences. A considerable number of data points lies on this line for positive differences and the majority of the points in the upper part of the plot.

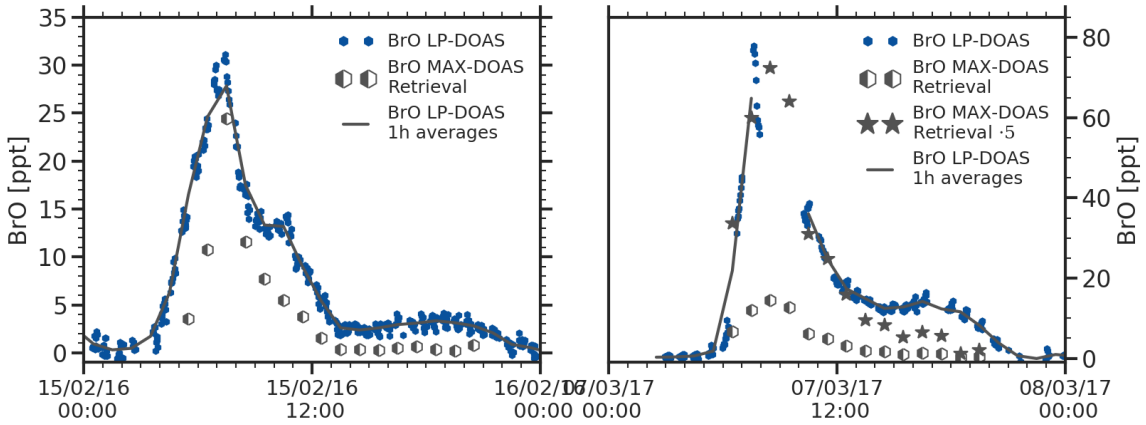

Figure 5.29: Comparison of BrO observations from the MAX-DOAS and LP-DOAS instruments

When individual days are compared, the agreement between both instruments occasionally is much better than the quantitative comparisons suggest. An example for this can be found in the left panel of Fig. 5.29. Both the daily evolution as well as the absolute mixing ratios of BrO agree fairly well on this day, in particular when the LP-DOAS data is averaged to match the hourly temporal resolution of the MAX-DOAS data. On other days (see right panel in Fig. 5.29), the temporal evolution in both time series is similar but the MAX-DOAS retrieval underestimates the surface mixing ratios.

Two aspects of the MAX-DOAS technique and the profile retrieval can potentially contribute to this. When the absorber is assumed to be present in a shallow layer close to the ground (e.g. due to a combination of a surface source and a short atmospheric life time or because of a vertical stratification of the atmosphere caused by temperature inversions) despite the high surface albedo and negative elevations, the MAX-DOAS might only have limited sensitivity towards such a surface layer resulting in weaker absorption signals and ultimately lower retrieved mixing ratios. Additionally, the optimal estimation retrieval algorithm operates on a vertical grid with exponentially increasing vertical spacing. The lowest layer has a height of 50 meter. In the estimation of the vertical absorber profile, mixing ratios within layers are assumed to be constant. A particular surface mixing ratio in the retrieval's atmosphere therefore would correspond to a 50 m thick layer of this mixing ratio. As studies of the vertical structure of ozone depletion events and the vertical

distributions of BrO have shown, surface inversions frequently lead to very shallow layers with elevated absorber mixing ratios of few tens of meters (A. E. Jones et al., 2010). Under such conditions the vertical layer spacing of the retrieval could lead to a 'dilution' of the mixing ratios through attribution of the BrO signal to a much thicker atmospheric layer than actually present in the atmosphere.

For the example in the right panel of Fig. 5.29, a scaling by a factor of five would lead to a much better agreement. If a reduced sensitivity of the MAX-DOAS instrument towards surface layers is omitted, this would mean that the BrO is located in the first 10 m above the surface. While this might be an extreme assumption, at NM III temperature inversions as measured between 2 m and 10 m frequently exceed several K, which might lead to such shallow layers (see Fig. 6.2 in the following section). Furthermore, for several other days that were investigated, the ratio between LP-DOAS and MAX-DOAS data is smaller than 5.

5.3.2 Ozone monitor

Ozone mixing ratios determined in the UVI-2 fit scenario with the LP-DOAS instrument can be compared to the ozone monitor in the trace gas observatory. Figure 5.30 shows a correlation-density plot for the entire data set and the results for the different comparison techniques discussed above.

For the ozone monitor, the uncertainty is not indicated directly (ANSYCO, 2000). The detection limit of 1 ppb stated in the manual was assumed to be a 2σ limit and hence 0.5 ppb was used as uncertainty. Since the ozone data from the monitor is available at a 1 min temporal resolution, it was averaged on the acquisition periods of the single measurements of the LP-DOAS instrument.

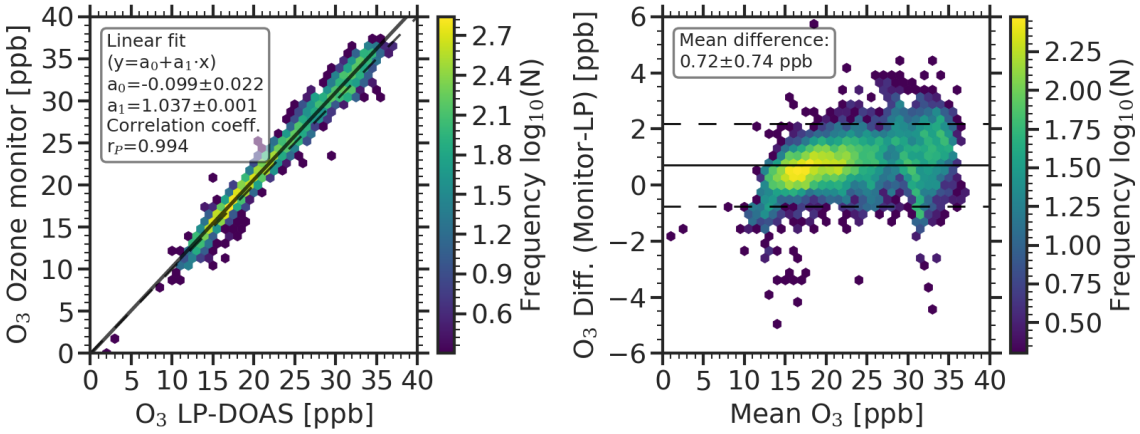

Figure 5.30: Comparison of O_3 mixing ratios as measured by the ozone monitor and the LP-DOAS instrument. The linear fir was done with a weighted orthogonal distance regression that takes into account the errors of both instruments (Boggs et al., 1992). For the correlation the *Pearson* coefficient was calculated.

The regression with a negligible axis intersect and a gradient close to unity, and the correlation coefficient of r_P=0.99 indicate a very good agreement between both data sets. The analysis of the difference between corresponding values as a function of the average ozone mixing ratios, however, reveals a systematic offset between both instruments of

0.72 ppb. One reason could be that both instruments use different absorption cross-section. At ozone mixing ratios of 30 ppb the offset of 0.72 ppb is about 2.5% of the measurement signal, comparable to the known differences between literature cross sections of ozone (Gorshelev et al., 2014). Also the ozone monitor relies on absolute absorption measurement in a very narrow spectral window compared the broad fitting window of the LP-DOAS and thus is susceptible to cross-sensitivities. Also an inaccurate conversion of measurement signals into mixing ratios could contribute. The ozone monitor uses internal temperature and pressure sensors for this, whereas the LP-DOAS data was converted using the meteorological instrumentation of the station's observatory. However to cause the observed differences, a overestimation of 6 K by the ozone monitor would be required to explain the observed difference.

6

Meteorology, atmospheric dynamics and composition at Neumayer III

The long time series of trace gas mixing ratios recorded with the LP-DOAS instrument at NM III allows to study halogen chemistry on an annual time scale with the, albeit limited, possibility to assess inter-annual variability. Furthermore, different aspects of halogen release and atmospheric reactions can be investigated in case studies with high temporal resolution.

For the interpretation of the data set both on the annual and shorter time scales, an understanding of the physical and chemical state of the atmospheric boundary layer at the time of the measurements is necessary. In this chapter, relevant atmospheric quantities recorded by the meteorological- and air chemistry observatories at NM III, as well as observations of non halogen containing trace gases with the LP-DOAS are presented. Furthermore, the potential influence of anthropogenic activities around the station on the LP-DOAS observations is discussed.[1]

An overview of the seasonality of parameters during the observation period will be given and, where possible, observations will be compared to previous publications that have studied the respective quantities at NM III in detail. In Sec 6.1, the influence of solar radiation on the atmosphere will be discussed. In the following section 6.2, annual cycles of meteorological parameters are presented and the origin of characteristic meteorological phenomena, namely the frequency and strength of storms and the development of strong surface temperature inversions are discussed. Section 6.3 gives a brief overview of the seasonal variation of aerosol concentrations and composition. In Sec. 6.4 trace-gas mixing ratios of ozone, both form the trace gas observatory and the LP-DOAS, as well as the NO_2 and SO_2 observations of the LP-DOAS are discussed before concluding with an assessment of the influence of anthropogenic activities around the station on the local composition of the boundary layer and hence halogen observations discussed in the following chapter 7.

[1] If not stated otherwise, data was acquired by the meteorological observatory (see Sec. 4.1.2 for instrumentation and data set references) and the air chemistry observatory (see Sec. 4.1.3 for instruments and data set references).

6.1 Radiation

6.1.1 Annual radiation cycle

The annual variations of several meteorological parameters in Antarctica are strongly influenced by the seasonality in insolation.

Figure 6.1 shows the monthly averages of down- and upwelling short- and long-wave radiation and the resulting surface energy balance on the ice shelf (for spectral ranges covered by the respective instruments see Tab. 4.2 in Sec. 4.1.2). The short-wave downwelling radiation (SWD) is commonly referred to as *global radiation* (American Meteorological Society, 2013) and reflects the annual cycle of solar elevation angles. From May to July, around the (southern) winter solstice, virtually no short wave radiation reaches the ground. During polar day on the other hand, continuous insolation leads to average downwelling fluxes per day comparable to the average irradiance at the equator (Roedel and T. Wagner, 2011). As mentioned in Sec. 2.1.2, snow and ice surfaces have high surface albedos which leads to a large portion of the down-welling radiation being reflected (SWU in Fig. 6.1).

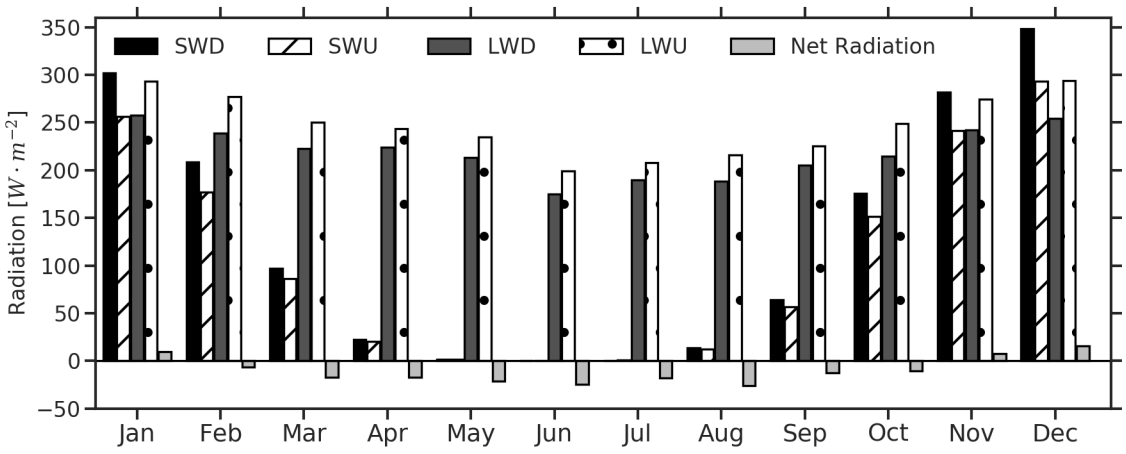

Figure 6.1: Monthly averages of downwelling and upwelling short wave (SWD, SWU) and long-wave (LWD, LWU) radiation as well as the net radiation balance for the observation period from January 2016 until December 2017. See Tab. 4.2 for details on the instruments and covered spectral ranges. Plotted as in König-Langlo et al. (1998).

Long-wave downwelling radiation also varies throughout the year with a minimum in June/July. Since it is predominantly thermal emission of the overlying atmosphere, long-wave downwelling radiation depends much more on the temperature of the atmosphere at the effective altitude from where it originates than on the SZA. The presence of (relatively warm) clouds drastically increases the down-welling fraction of long wave radiation. Equally, the upwelling long-wave radiation is determined by the surface emissivity in the infrared and the temperature of the surface.

Considering the total surface radiation, the monthly energy balance at the surface is negative throughout the year except for the months between November and January (around the southern summer solstice). Compared to the monthly average radiation balance in König-Langlo et al. (1998), the data from 2016 and 2017 in Fig. 6.1 does not exhibit any anomalies apart from a slightly smaller radiation deficit in July compared to 1993.

6.1.2 Radiation balance and atmospheric stability

The negative net surface energy balances throughout most of the year lead to a frequent development of surface temperature inversions. Since the stable stratification of the atmosphere resulting from this limits the vertical transport of trace gases, these conditions can have an important influence on trace gas mixing ratios close to the surface (see also Sec. 2.2.2). Fig. 6.2 shows the occurrence and strength of temperature differences between 2 m and 10 m altitude as measured by the sensors on the pole at the meteorological measurement site.

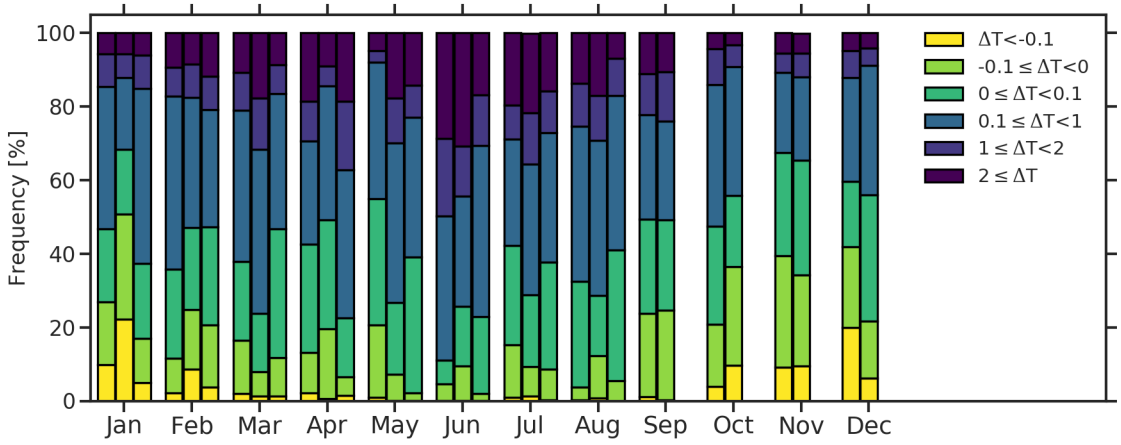

Figure 6.2: Frequency of surface temperature inversions at NM III per month for the observation period from January 2016 until August 2018. The colour code indicates the temperature difference between the 10 m and 2 m sensors at the meteorological measurement site.

Negative temperature gradients allowing convective mixing occur up to 40% of the time in late spring and summer and less than 10% in June. Temperature inversions of 0.1 K or more are present between 50% of the time in summer and up to 80% in June. Since turbulent mixing generally decreases temperature gradients, prevailing average wind speeds have an influence on frequency and strength of temperature inversions and the dominance of strong positive temperature gradients in June is the result of distinctly lower average wind speeds than in April/May and July/August, which will be discussed in the following section.

The net surface radiation balance not only has a distinct annual cycle, but also strongly varies on daily time scales. In Fig. 6.3, global radiation, air temperatures, wind speed, as well as temperature- and radiation balance are plotted for an exemplary period in February 2016, during the transition from positive to negative monthly net radiation balances. It illustrates the main mechanisms that can influence vertical stability of the atmosphere close to the surface.

On the first day shown, the smooth shape of the global radiation curve indicates clear-sky conditions (except for a short period in the morning). The radiation balance is negative for most part of the day except for about six hours around local noon. Under clear-sky conditions and low wind speeds, a temperature inversion with differences of up to 5 K between 2 m and 10 m develops during the night from the 14th to the 15th of February. At around 11 AM on the 15th, clouds reduce the global radiation for the remainder of

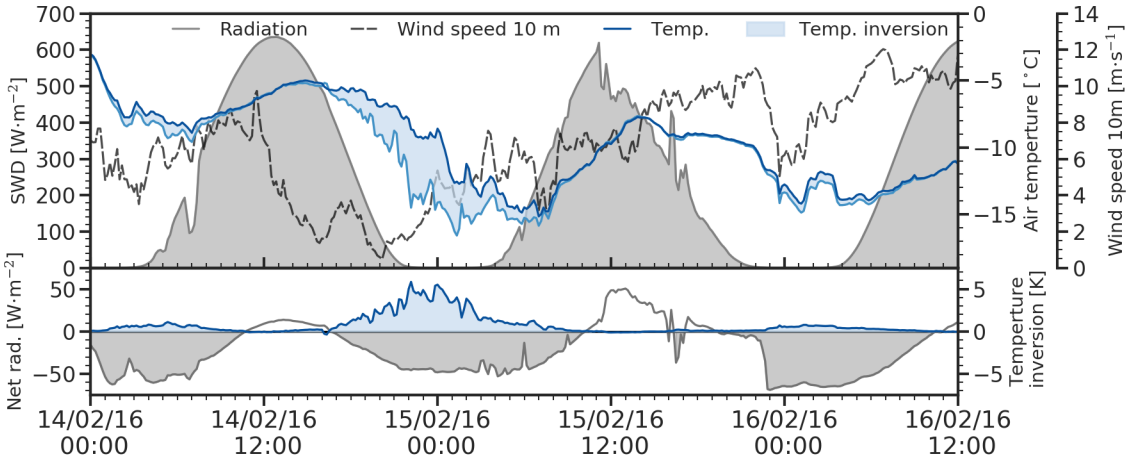

Figure 6.3: Example for the interplay of the net surface energy balance and temperature inversions. In top panel global radiation (shaded in grey), wind speed (grey dashed line), and the temperature in 10 m (dark blue) and 2 m (light blue) altitude are shown. Differences of more than 0.25 K between the two are marked with blue shading. In the lower panel the net surface energy budget (net short-wave radiation plus net long-wave radiation, see Tab. 4.2) is shown. Periods with a negative balance are marked by grey shading. The blue line is the temperature difference with surface temperture inversions marked by blue shading.

the day (with a brief cloud-free period in the afternoon). At the same time, the cloud cover leads to an increase in downwelling long-wave radiation which is reflected in the larger positive net radiation around noon compared to the 14$^{\text{th}}$. The development of the temperature inversion in the afternoon is delayed by this higher long-wave downwelling radiation. When the clouds disperse around 11 PM, the radiation balance quickly becomes negative. However, the development of a temperature inversion is limited by higher wind speeds compared to the previous night. Atmospheric stability and hence the extent of vertical mixing thus can strongly depend on this interplay of the radiation balance, cloud cover and synoptic conditions.

The vertical extent of the surface temperature inversion layer can vary and most of the time is probably larger than covered by the 10 m pole at the meteorological measurement site. The daily radiosonde, launched at 11 UTC offers some insight into the vertical structure of the atmosphere, however only at one point in time. For the interpretation of surface mixing ratios of trace gases and particle concentrations, the comparison of 2 m and 10 m temperatures has been identified as an important measure that is highly correlated with temporal variations of the mixing ratios observed with the LP-DOAS.

6.2 Seasonality of meteorological parameters at NMIII

Another important factor of the meteorology at NM III, in addition to the solar radiation, are the regional synoptic conditions and in particular the cyclonic activity over the Southern ocean.

6.2.1 Cyclonic activity

Low pressure systems around Antarctica often form around 60° S and then drift polewards circling the continent in easterly direction (D. A. Jones and Simmonds, 1993; Roedel and T. Wagner, 2011). The left panel in Fig. 6.4 shows such a situation with five low pressure systems over the Southern ocean around the continent. In the southern hemisphere, circulation around cyclones is clockwise thus leading to westerly winds at the northern edge of the lows and easterly wind directions at the southern as illustrated in the right panel in Fig. 6.4. Meteorological dynamics at NM III are characterised by an alternation of cyclonic and anti-cyclonic episodes created by the movement of the low pressure systems. Due to its location south of this cyclone track, during the cyclones, easterly wind directions and high wind speeds dominate. Anti-cyclonic conditions are characterised by katabatic circulation (induced by cold, dense air masses from the high centre of the continent flowing northwards and accelerating along the slopes of the ice sheet). For NM III, the velocities reached by these southerly winds are moderate compared to other locations in Antarctica and rarely exceed $10\,\mathrm{m\,s^{-1}}$ (König-Langlo et al., 1998, see also wind rose in Fig. 6.8 for times when the LP-DOAS instrument could measure).

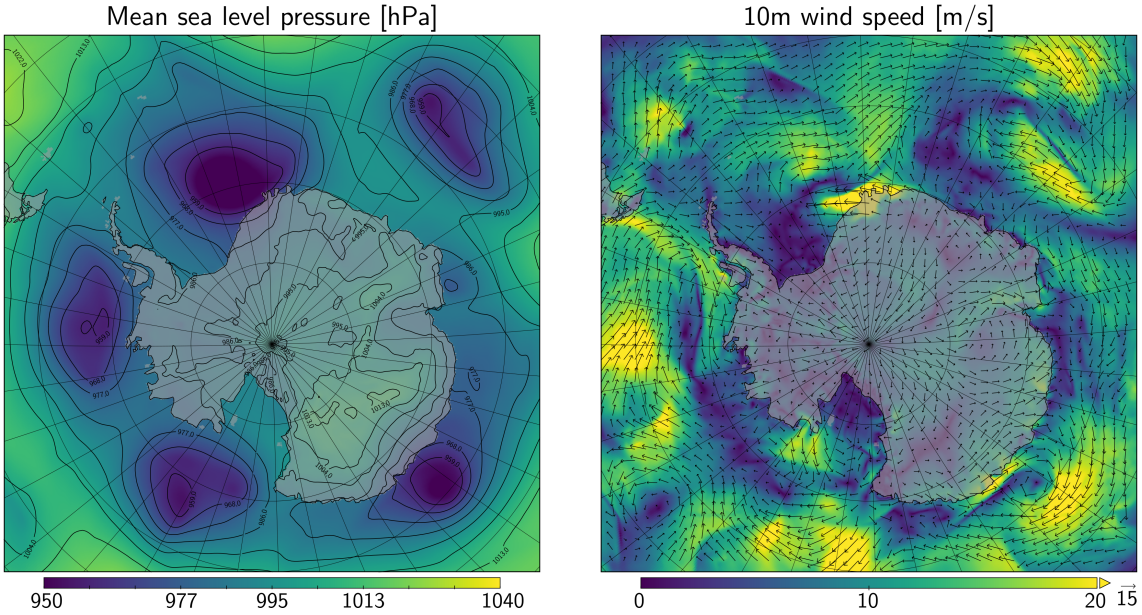

Figure 6.4: Mean sea level pressure and 10 m wind speeds around Antarctica for March, 19, 2016 at 18:00 UTC. Generated using Copernicus Climate Change Service (C3S) (2017) information and *Panoply* by Schmunk (2018).

6.2.2 Temperature and atmospheric pressure

The annual monthly mean temperature at NM III is the result of the annual insolation cycle (see Fig. 6.5) modulated by the advection of air masses of different origin, depending on synoptic conditions. The maximum temperature is reached in December/January and a minimum in July (July-August in König-Langlo et al., 1998). Compared to latitudes without polar night, at NM III there is no clear insolation-related temperature minimum because the decrease of temperatures through net radiative cooling continues after the onset of the polar night until the return of sunlight (van Loon, 1967).

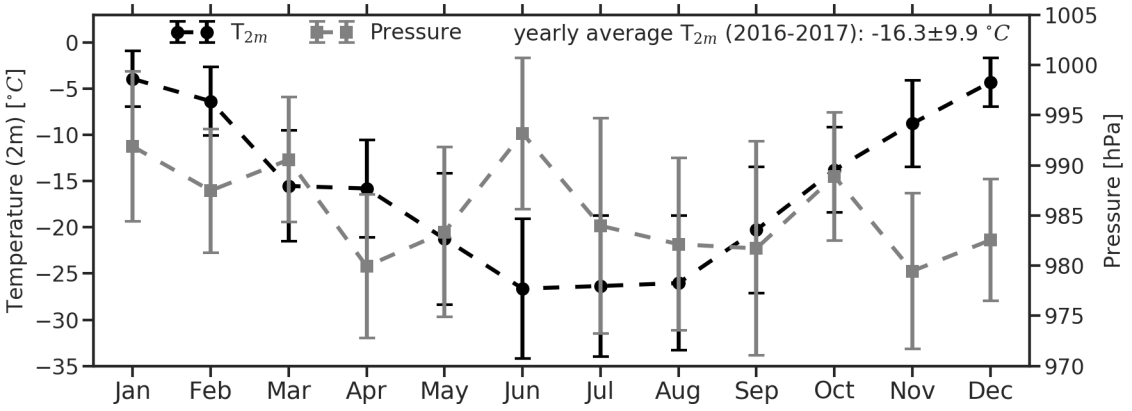

Figure 6.5: Monthly averages of 2m temperature and atmospheric pressure. See Tab. 4.1 for details on the instruments. The station pressure was reduced to sea level using the recommendations in WMO-CIMO (2012). Error bars indicate the standard deviation.

Compared to the average temperatures between 1991 and 1995 presented in König-Langlo et al. (1998), the data from 2016 and 2017 agrees within the standard deviation with the largest difference in the average June temperatures, which are about 5 K lower in 2016-17. The yearly average temperatures from both periods agree within 0.2 °C.

Short term (hours to days) variations of the temperature are linked to the cyclonic activity. Under the influence of cyclones, comparably warm air masses are advected clockwise from the northern edge around the low pressure systems. Increases in temperatures are reinforced by the insulating effect of cloud cover often associated with the cyclonic activity. Under anti-cyclonic conditions, cold air from the interior of the continent decreases temperatures and frequent clear skies lead to an additional radiative cooling.

The annual cycle of the surface pressure at NM III shows two maxima in January and June. These are the result of large scale atmospheric patterns around the Antarctic continent. The cyclones circling over the Southern ocean lead to a region between 55° and 70° S, referred to as Circumpolar Trough (CPT), where atmospheric surface pressures on average have a meridional minimum (D. A. Jones and Simmonds, 1993).

Location and strength of this trough depend on the meridional temperature gradient in the lower troposphere between mid- and high latitudes (between 50° S and 65° S at a pressure level of 500 hPa; van Loon, 1967). This gradient has two yearly maxima around the equinoxes in March and September. The latter one more or less coincides with the surface temperature minimum in August/September. The former in March is the result of different cooling rates of the atmosphere between mid- and high latitudes (for details see

van Loon, 1967). Maxima in the meridional temperature gradient lead to a higher cyclonic intensity and a poleward shift of the CPT. The periodic variation of strength and location of the trough is called Semi-annual Oscillation (SAO). The minima in surface pressure in March/April and September coincide with higher frequencies of elevated wind speeds in March/April and September when the CPT is closer to NM III and the cyclonic activity around the continent is strongest (Fig. 6.6).

Compared to the period from 1991-1995 in König-Langlo et al. (1998), sea level surface pressures[2] from 2016-2017 agree within the standard deviation with slightly lower average pressures for the early springs of 1991-1995 and a later drop of the pressure in autumn (in April rather than March).

6.2.3 Wind speed and direction

The alternating influence of cyclonic and anti-cyclonic conditions is clearly visible in the daily average wind speeds at 10 m altitude plotted in Fig. 6.6. Areas in grey indicate stormy periods with average wind speeds above $15\,\mathrm{m\,s^{-1}}$ or more in 6 h averages. This corresponds to about 7 on the Beaufort scale ("high wind, moderate gale"). Such conditions on average occur every 10.1±10.2 d at NM III and last 2.8±2.0 d. The variations of storminess due to the SAO is clearly visible with calmer periods from December until mid-February as well as in June.

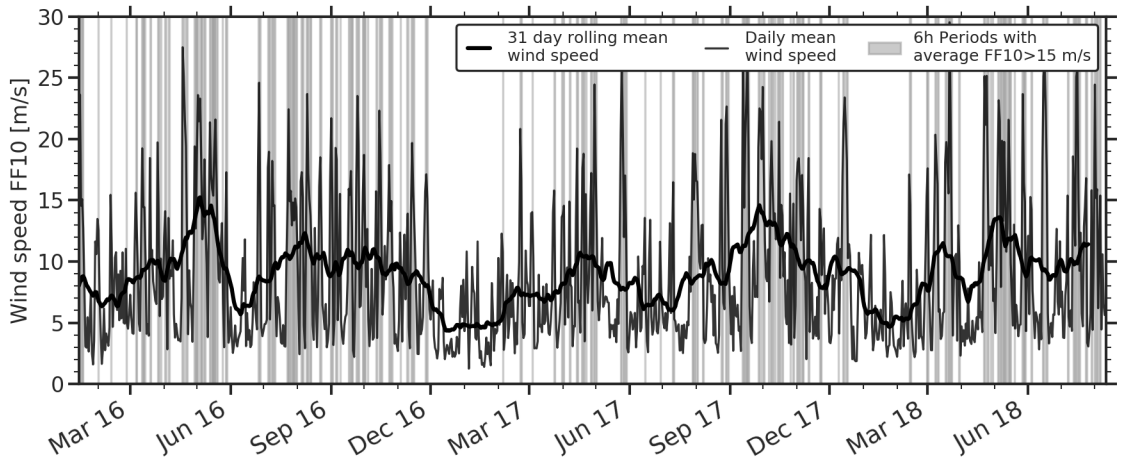

Figure 6.6: Monthly wind speed distributions for the observation period (FF10 = measured in 10 m altitude in $\mathrm{m\,s^{-1}}$)

The distribution of wind speeds and directions shown in Fig. 6.7 also reflects the alternating synoptic regimes. The highest wind speeds occurring under the influence of strong low pressure systems north of NM III are exclusively associated with winds from easterly directions. When only those periods are considered, when the LP-DOAS could measure, easterly directions still dominate followed by katabatic winds from southern to south-western directions. Overall, winds almost exclusively come from a 180° sector between 60°

[2] reduced from the station pressure using the recommendations in WMO-CIMO (2012)

and 240°.[3] This is in very good agreement with the distribution of wind directions from 1991-1995 (König-Langlo et al., 1998).

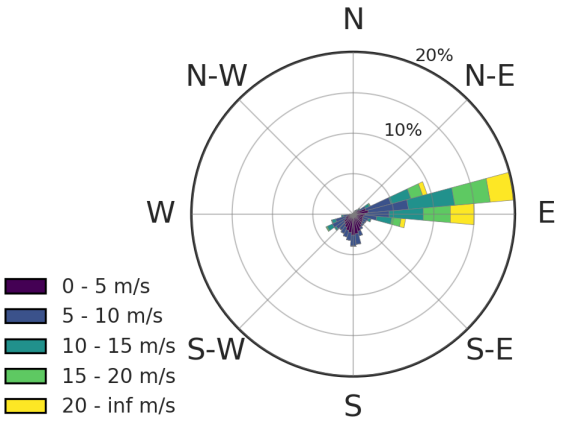

Figure 6.7: Wind conditions in 2016 and 2017 (10 min averages). Data from 2018 was omitted for plot to be representative of the annual cycle. The same plot for the entire measurement period can be found in Fig. D.28 in the appendix.

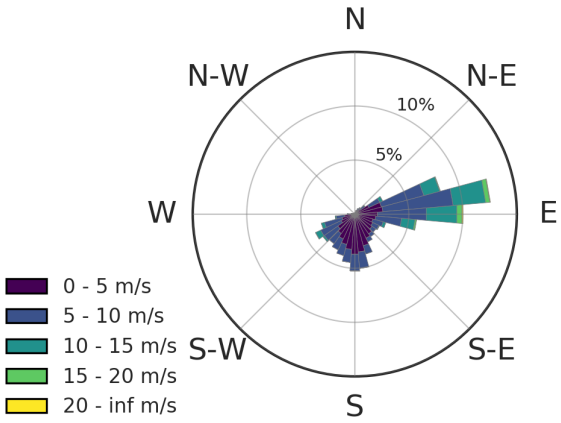

Figure 6.8: Wind conditions when the LP-DOAS instrument recorded spectra in 2016 and 2017. Data from 2018 was omitted for plot to be representative of the annual cycle. For entire observation period see Fig. D.29 in the appendix.

6.3 Aerosol concentration and composition

The available instrumentation for aerosol observations and characterisation in the trace gas observatory at NM III is extensive (see overview in Sec. 4.1.3). A detailed discussion of all parameters would be beyond the scope of this thesis. Therefore only particle concentrations and aerosol composition with relevance for halogen chemistry will be covered here. Where necessary, additional data will be included in the case studies below. For a detailed discussion of aerosols at NM III, the interested reader is referred to the following publications:

Trace element composition of aerosols and its seasonal variability was investigated in a five year mass spectrometer study in Weller et al. (2008). Ionic composition and optical properties were studied in Weller and Lampert (2008). Variations of condensation particle concentrations on inter-annual, seasonal, and daily time scales are discussed in Weller et al. (2011a). The link between climate indices and ionic composition (Weller et al., 2011b) and radio-nuclides (Elsässer et al., 2011) as well as the long-term variations of black carbon (Weller et al., 2013) has been investigated. Teinilä et al. (2014) described the chemsitry of sea salt aerosol and Weller et al. (2015) reported frequent natural new particle formation events in late summer/autumn and spring.

The concentration of condensation particles shows a very distinct annual cycle that varies over about one order of magnitude throughout the year (see Fig. 6.9 top panel; details on the instrumentation can be found in Sec. 4.1.3). Maximum concentrations are reached in March with around 1000 cm^{-3} for clean air conditions. The annual minimum is in June when particle concentrations frequently fall below 100 cm^{-3}.

[3] The location of the LP-DOAS light paths west of NM III station (see Fig. 4.1) therefore ensures the smallest possible influence by the station and activities in its surroundings.

Aerosol measurements at the trace gas observatory occasionally can be affected by the station or, in particular during the summer research season, by the exhaust of vehicles in the vicinity of the station. This influence can be excluded by applying a filter of wind directions and speeds (in Weller et al. (2011a) a sector between 330° and 30° and wind speeds below 2.2 m s^{-1} are excluded - this was not applied in Fig. 6.9)

A detailed study by Weller et al. (2011a) including thermodenuder measurements to determine the volatility of aerosol components attributed the annual cycle in condensation particle concentrations largely to the seasonality of the source strength of aerosol precursors from biogenic sources in the Southern ocean (see DMS chemistry in Sec. 2.5.3) reflected in the signal of methanesulfonic acid (MSA) and non-sea-salt SO_4^{2-} in aerosols collected daily on filters (see dotted and dashed green lines in the top panel in Fig. 6.9).

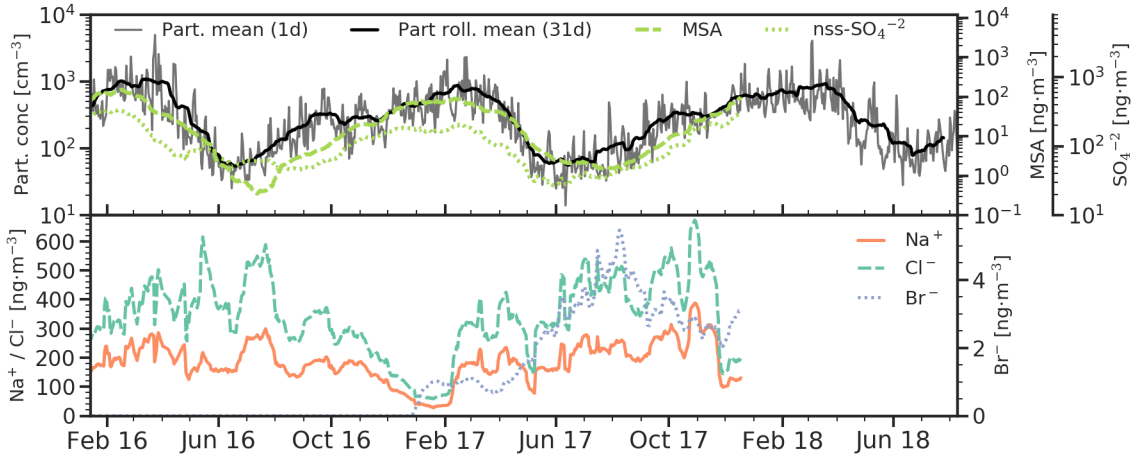

Figure 6.9: Annual cycle of condensation particle concentrations and ionic aerosol composition. In the top panel the solid grey line are daily means of condensation particle concentrations and the solid black line the corresponding 31-day rolling mean. The green lines are mass concentrations of methanesulfonic acid (MSA - dashed line) and non-sea-salt SO_4^{2-} (dotted line) from aerosol filter samples collected on a daily basis. The lower panel shows mass concentrations of sea salt aerosol related ions from the aerosol filter samples (Na^+ - solid red, Cl^- - dashed green, Br^- - dotted blue; only available for 2017). All ion abundances are 31-day rolling means.

When comparing the annual cycle of condensation particles and MSA, systematic deviations in late winter and late summer are apparent, a phenomenon also reported by Weller et al. (2011a) who attributed the excess in condensation particles to natural new particle formation events potentially induced by halogen chemistry (without specifying a concrete mechanism). In Weller et al. (2015) several new particle formation events for the period from February to April as well as from mid-August to the end of September could be identified and the observed particle growth could not be explained solely based on sulfate compounds but required another low volatility trace gas.

For ionic aerosol composition related to sea salt aerosol (sodium, chloride, and bromide), the annual cycles more or less irror that of particle concentrations and ions of biogenic origin (see lower panel in Fig. 6.9). Since the production of sea salt aerosols both from the open ocean and sea ice surfaces increases with wind speed, the contribution of sodium, chloride, and bromide to aerosol composition resembles the seasonality of wind speeds at

NM III (even though for the production rates of advected sea salt aerosols, wind speeds in the source region are the relevant quantity).

On a daily time scale, the variations of sea salt-related ions are not always clearly associated with higher (local) wind speeds and elevated mass concentrations can be the result of transport. On the other hand, local meteorology can directly influence ion mass concentrations through local production of sea salt aerosols. Since distances from the source region to NM III in this case are shorter, larger particles can reach the station. This potentially leads to increased mass concentrations of sodium, chloride, and bromide in local aerosols compared to to particles advected through long range transport.

A detailed study of sea salt chemistry by Teinilä et al. (2014) could identify the isotopic signals of open ocean as well as sea ice surface related aerosol production. A clear connection to the seasonal variation and hence importance of sea ice surfaces throughout the year, however, could not be clearly established which might be explained by the influence of local sea salt aerosol production (see also Weller et al., 2011a).

6.4 Non-halogen trace gases

In addition to the ozone monitor data (see Sec. 4.1.3), the evaluation of LP-DOAS observations yields time series of O_3, NO_2, and SO_2. The data of the entire observation period are shown in Fig. 6.11 and will be discussed in the following sections.

6.4.1 Ozone

Surface ozone mixing ratios at NM III exhibit a very pronounced annual cycle (see Fig. 6.11 for the LP-DOAS data and Fig. 6.10 for the annual cycle of 2017 as observed by the ozone monitor, data for 2016 and the part of 2018 considered in this thesis can be found in Sec. D.2.2 in the Appendix in figures D.30 and D.31).

The causes of the long-term seasonality of O_3 were discussed in detail in Sec. 2.3. Compared to the monthly means in Fig. 2.7 in Sec. 2.3.2, Fig. 6.10 contains hourly means showing the short term variations of ozone, in particular the ozone depletions in spring. The chemistry of these ODEs was discussed in detail in Sec. 2.4. Examples are discussed in Sec. 7.1. Short-term increases of ozone mixing ratios can also be discerned which are usually associated with a change of air masses by advection.

The onset of the ODE period at NM III for the three winters included in this thesis varied from early July (2018), over mid-July (2017) to late July/early August (2016) and lasted until November. For the remainder of the year, with one exception in 2016, no larger depletion events occurred.

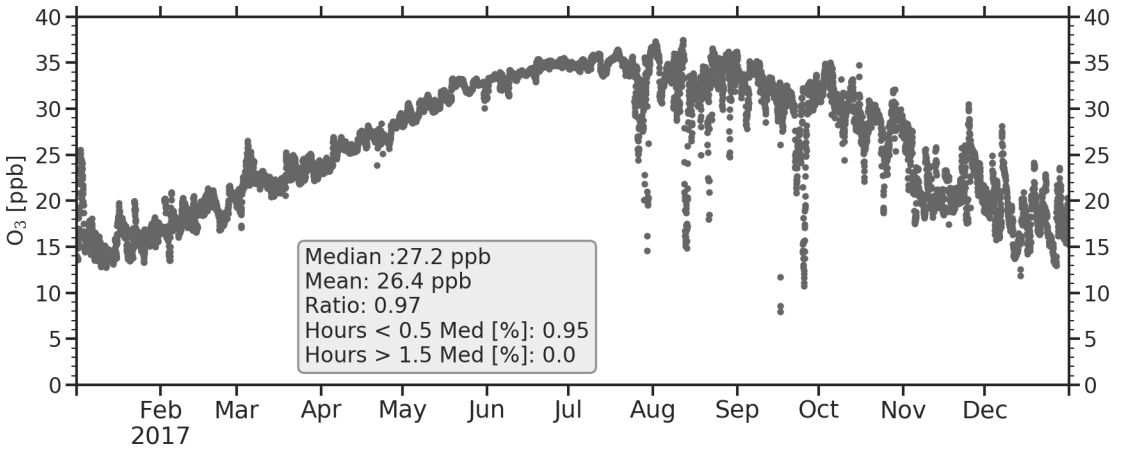

Figure 6.10: Annual cycle of hourly averages of surface ozone mixing ratios at Neumayer III in 2017 as measured by the UV absorption spectroscopy instrument (see 4.1.3) in the trace gas observatory. Statistics was calculated as in Helmig et al. (2007).

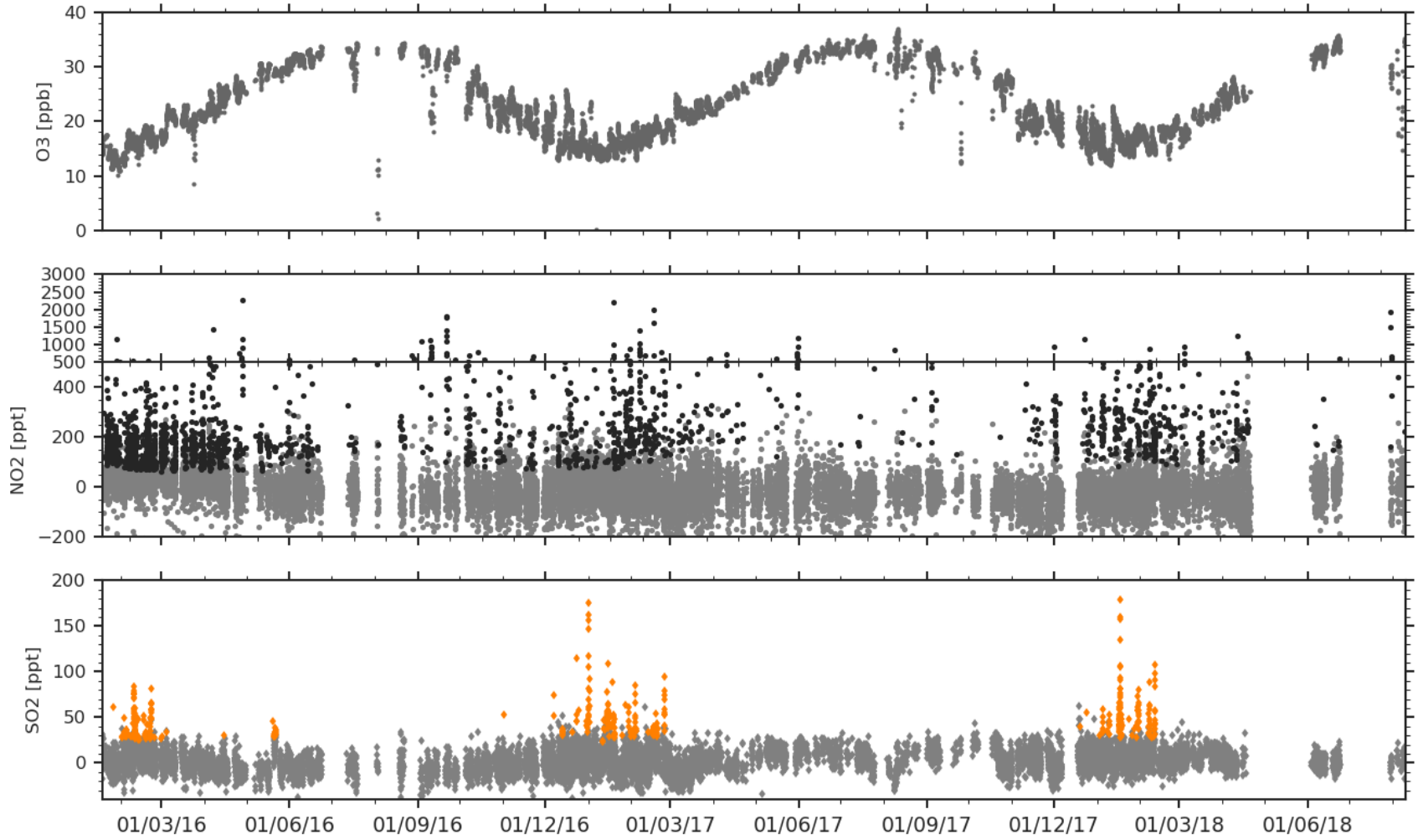

Figure 6.11: Overview of LP-DOASdata sets of O_3 (top), NO_2 (middle), and SO_2 (bottom) for the entire observation period. The plotted data are 30 min averages. Data points above the respective detection limit are coloured. Data below the detection limit is marked in grey. Note that for a better assessment of smaller mixing ratios as well as maximum values, for NO_2 the plot is split in two with different linear ordinate axes.

The ozone data from the observation period in this thesis can be compared to the O_3 data set from NM III from 1992 to 2015. For this, the approach in the review of annual O_3 cycles in polar regions by Helmig et al. (2007) was reproduced and yearly means and medians of O_3 mixing ratios were calculated. The ratio of both values can serve as a measure for the influence of large amplitude short-term variations of the ozone mixing ratio as the mean is more influenced by extreme values than the median. Furthermore, the percentage of time when ozone was below half of the yearly median was calculated with data sets from Weller (2005a) to Weller (2018a) - see bibliography for all data sets in between. The results can be found in Tab. 6.1.

	1992 - 2015	2016	2017
Median O_3 [ppb]	25.0 ± 1.0	25.6	27.2
Mean O_3 [ppb]	24.5 ± 1.0	25.1	26.4
Ratio Mean/Median	0.98	0.98	0.97
$O_3 < 0.5$ Median [%]	3.4 ± 1.9	2.9	1.0

Table 6.1: Average ozone mixing ratios at NMIII for the period between 1992 and 2015 as well as 2016 and 2017, the two years fully covered by LP-DOAS observations. Mean and median ozone mixing ratio were calculated for data sets from 1992 until 2017 reproducing the approach in Helmig et al. (2007). For data set references see Weller (2005a) to Weller (2018a) in the bibliography.

Comparing 2016 and 2017 to the averages from 1992 to 2015, 2016 seems to be representative for the ozone seasonality at NM III both with respect to mean and median values but also with regard to the fraction of low O_3 periods. For 2017, mean and median are higher than on average during the previous 24 years and the fraction of low O_3 hours is considerably smaller. Comparable values, however, were observed previously in 1992.

Since the LP-DOAS ozone observations and the ozone monitor agree well, except for a small constant offset (see Sec. 5.3.2), in the following analysis mostly the higher resolution ozone monitor data will be used.

6.4.2 Nitrogen dioxide

The NO_2 mixing ratios measured at NM III exhibit a fairly pronounced seasonality (see Fig. 6.11). A majority of observations above the detection limit falls between the end of November and the end of March. This can also be seen in the histograms of hourly mean mixing ratios of the four seasons based on the two complete years of observations 2016 and 2017. The fewest observations of NO_2 above the detection limit occur in Winter (June, July, and August). Spring and Autumn show comparable distributions.

When the daily maxima are considered (see Fig. 6.13), a difference in the seasonality of mixing ratios above and below 500 ppt can be discerned. While the former are observed more or less every month on 1 to 5 days, from January to April days with NO_2 between the detection limit and 500 ppt occur more frequently. The highest mixing ratios that were detected from 2016 to 2018 are around 3.5 ppb.

To investigate the relation between NO_2 mixing ratios from the LP-DOAS observations and atmospheric parameters, correlations can be analysed (see Fig. 6.14). For this, the relevant parameters were averaged to the temporal resolution of the NO_2 measurements.

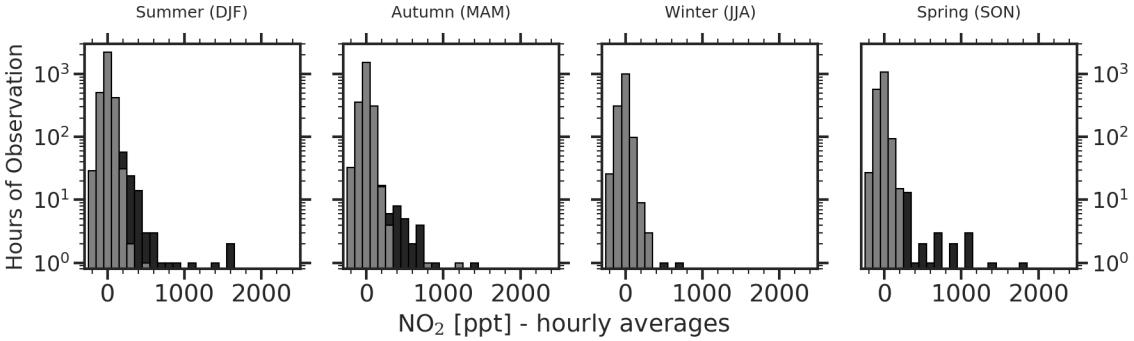

Figure 6.12: Seasonal distribution of elevated NO_2. For the histograms only hourly averaged data from January 2016 until December 2017 was taken into account to prevent a distortion by the additional observations from January until August 2018. Values above the detection limit are coloured, values below the detection limit are plotted in grey.

For ozone mixing ratios as well as atmospheric pressure, de-trended times series were calculated. For the ozone data, a three-week running median was calculated and subtracted from the time series. For the atmospheric pressure for which short-term variations on time scale of days are much larger than the yearly variation, a 90-day running mean was calculated and subtracted from the pressure data which for large parts removes the long-term variations due to the SAO (see Sec. 6.2.2 above) and allows to assess correlations with the alternating high- and low pressure conditions induced by the cyclones circling the continent.

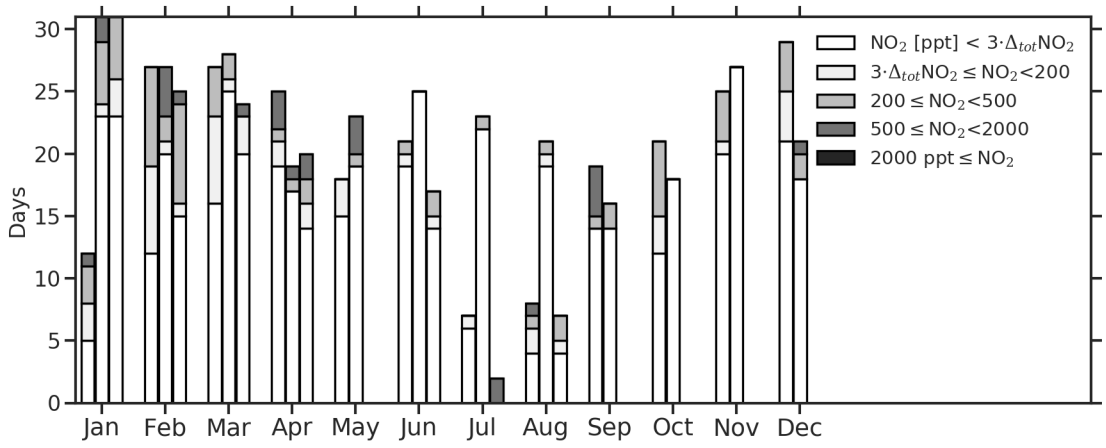

Figure 6.13: Distribution of daily maxima of NO_2 mixing ratios throughout the observation period. For the individual months the left bar represents the year 2016, the middle bar the year 2017, and the right bar the year 2018. The total length of the bars corresponds to the available data in the respective month in days. The colour code marks the daily maximum mixing ratio. The maximum was determined from a time series of hourly medians to limit the influence of single outliers. Only values above 4σ of the total error were taken into account in the colour coding.

The most important factor for elevated NO_2 mixing ratios seems to be atmospheric stability. NO_2 above 500 ppt is almost exclusively associated with low wind speeds.[4] There are practically no observations with wind speeds above 10 $m\,s^{-1}$ and mixing ratios above 500 ppt only occur for wind speeds below 5 $m\,s^{-1}$. Furthermore, peak NO_2 mixing ratios above 500 ppt are associated with strongly positive to neutral temperature differences between 2 m and 10 m altitude indicating a stratification of the lowermost atmosphere. When considering the correlation of NO_2 with *Richardson* numbers many high mixing ratios are close to the critical threshold of 0.25, however both below and above. At higher values a flow is stable and laminar. For Richardson numbers below, turbulence can develop, i.e. the wind shear is strong enough to counteract buoyancy forces of a temperature stratification. For negative values, there is static instability i.e. convection develops turbulence independent of wind shear. Flow close to the critical number can be complex with residual turbulence surviving for higher Ri and at the same time still decoupled flows can exist e.g. in different altitudes for values below 0.25 (Anderson and Neff, 2008).

The correlation with absolute temperatures reflects the occurrence of elevated NO_2 mostly from end of November to end of April when temperatures rarely fall much below -25 °C. Mixing ratios above 1 ppb are only observed for global radiation below 400 $W\,m^{-2}$. This could be the result of photochemistry where for high short-wave radiation the *Leighton* ratio shifts towards NO. At the same time, local atmospheric stability has to be considered. Since the increasing insolation often leads to positive surface energy balances just before noon (see Fig. 6.3), the stable stratification of the atmosphere could be broken up by convection before the maximum in the radiation is reached.

Fewer observations of elevated NO_2 around noon are also found when considering mixing ratios in relation to the hour of the day. This agrees with the occurrence of lower mixing ratios for SZAs below 60 °, which at NM III is undershot at noon from end of October until mid-February - the period with the highest frequency of NO_2 observations. For the remainder of the day, there is no clear cycle as would be expected by a photolytic source of the NO_2. When the correlation with excess respectively deficient ozone is considered, there is no apparent correlation with ozone mixing ratios which could be suspected for a release of NO that locally would titrate O_3 forming NO_2. The only elevated NO_2 values for ozone deficiencies of more than 5 ppb can be linked to elevated NO_2 during ODE periods but in all cases only occurred after ozone mixing ratios had already dropped.

The correlation of NO_2 with pressure shows a mostly positive relation in agreement with the central role of a stably stratified lower boundary layer, which develops in calm, anti-cyclonic periods. The few periods of elevated mixing ratios that occurred under lower than average pressure can be linked to the time after particularly strong cyclones when pressures were already rising again and conditions hence calm but the pressure was still considerably lower than the running average.

[4] It should be kept in mind, that the onset of blowing snow for wind speeds between 12 to 15 $m\,s^{-1}$, depending on surface snow characteristics limits LP-DOAS observations which could introduce a bias.

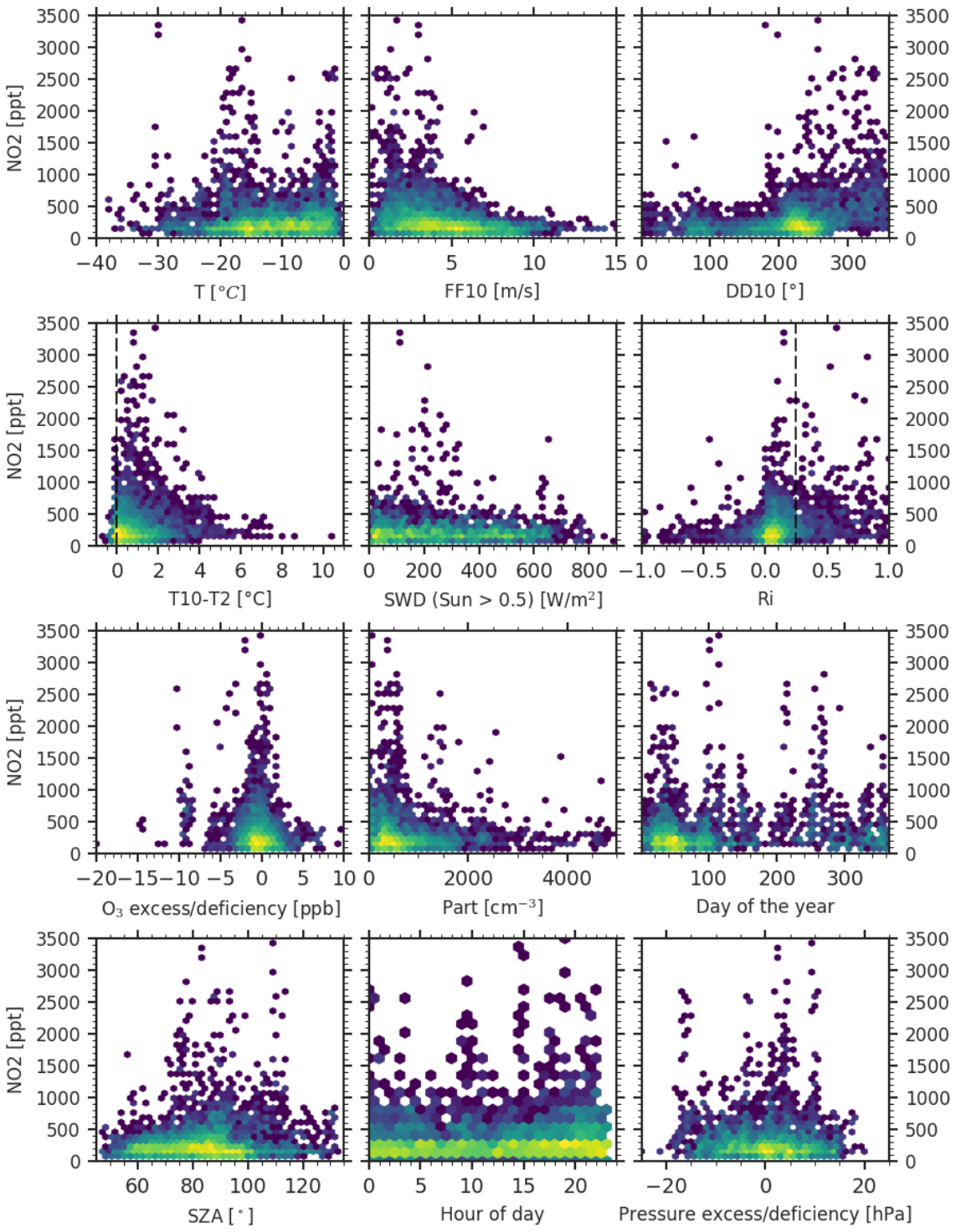

Figure 6.14: Correlation of NO_2 mixing ratios above the detection limit with other atmospheric parameters. The colour code marks the density of values. For the temperature, measurements in 2 m altitude were used, FF10 and DD10 are wind speed and direction in 10 m altitude. SWD is the short wave downwelling radiation and Ri is the Richardson number (see Eq. 2.3).The deficiency and excess of O_3 was determined by subtracting a 21-day rolling average from the ozone monitor time series. Part is the the particle concentration.

NO_2 source attribution

Even though the snow surfaces at NM III are sources of NO_X (e.g. A. E. Jones et al., 2000; A. E. Jones et al., 2001, see Sec. 2.3.3 for details), the reported mixing ratios of up to 40 ppt in the interstitial air of the snow pack and up to 20 ppt in the atmosphere directly above the snow are clearly below the detection limit for NO_2 achieved with the LP-DOAS (about 100 ppt in the VISI analysis and about 180 ppt in the UVII analysis respectively).

The most likely source of the observed NO_2 mixing ratio therefore is the exhaust of internal combustion engines operated in and around the station. For power and heat supply, NM III station is equipped with 4 diesel-powered block-type thermal power stations which can each deliver 160 kW electrical and 190 kW thermal energy (Gernandt and Huch, 2009). Typically, three stations are operated in rotation while the fourth serves as security reserve. When wind conditions permit, up to 30 kW of the power demand can be met with a wind generator operated next to the main station. The smoke stack for the generators is located on the roof of the station, about 30 m above the snow surface not affected by accumulation around the station.

Further sources of nitrogen oxides throughout the entire year include Pistenbully-snow groomers which are used for transport and the movement of snow around the station as well as snowmobiles used for personal transport. From late October until mid-March a groomed snow runway north-west of the station is used for scientific and logistic flight operations between the research stations located in Dronning Maud Land.

The shorter, Met-light path of the LP-DOAS instrument is largely located inside the clean air sector south of the main station (see location overview in Fig. 4.1, right panel), which vehicles enter only exceptionally and after precautions for the sampling instrumentation in the trace gas observatory have been taken to prevent or minimize contamination. However, during the summer research season (from November until February), and in particular from December to February, this can happen several times a month and is logged in the monthly reports of the trace gas observatory together with flight operations (if applicable).

The longer Atka light-path from the Met reflector array extends another 1.4 km to the north-north east. Vehicle operations around the station and displacements to the north are not logged. In particular the distribution of accumulated snow with the groomers is performed regularly after longer periods of blowing snow to prevent an excessive snow accumulation in the direct vicinity of the station. When the snow is moved around, often two snow groomers operate constantly for eight hours straight in a radius of about 300 m around the station. In preparation of the upcoming winter season, these activities tend to be intensified in summer.

While all these activities can lead to elevated NO_2 mixing ratios, a clear attribution of particular operations to observed increases is not straight forward. The operation of the LP-DOAS instrument on two different light paths allows an investigation of the origin of NO_2 emissions. When NO_2 observations from both the UVII-2 and the VISI-1 evaluation are combined and resampled to an hourly time scale, for the entire observation period from January 18th 2016 until August 10th 2018, 10829 h of valid observations are available. For 8091 h or 75% of that observation time, measurements were performed on the Met light path (1.55 km one way), the remaining 3556 h or 25% of the time measurements were performed on the Atka light path (2.95 km one way). For the Met light path in 590 h of the observation time at least one data point was above the NO_2 detection limit corresponding

to 7.2% of the observation time on the Met light path or 5.5% of the total observation time. For the measurements on the Atka light path at least one observation of NO_2 above the detection limit per hour was observed in 927 h or 26% of the observation time on this retro reflector array corresponding to 8.5% of the total observation time. In total 14% of the total hours of valid observations are affected by elevated NO_2 mixing ratios.

In Fig. 6.15 and Fig. 6.16 windroses for NO_2 observations above the detection limit separated into the observations on the two light paths are shown.

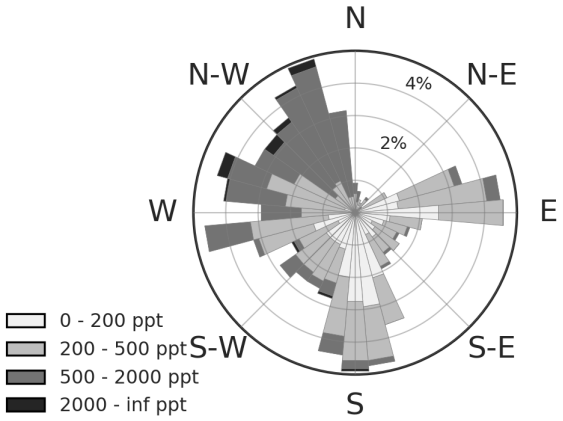

Figure 6.15: Distribution of NO_2 mixing ratios above the detection limit as a function of wind direction for measurements on the (shorter) Met-retro reflector array. The colour code marks the the mixing ratio. For the respective wind direction the colour code indicates the mixing ratios and the length of the cones their frequency. Data in the original temporal resolution of the LP-DOAS was used.

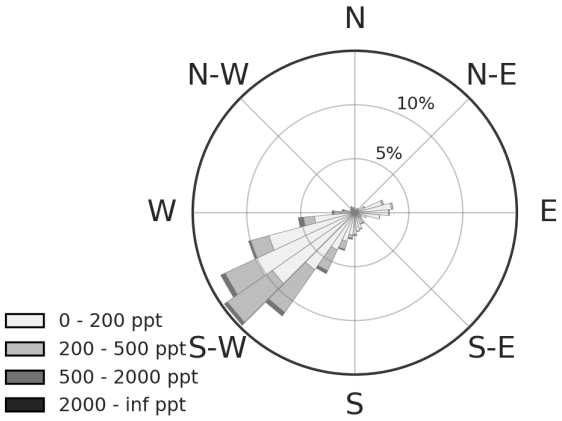

Figure 6.16: Distribution of NO_2 mixing ratios above the detection limit as a function of wind direction for measurements on the (longer) Atka-retro reflector array. The colour code marks the the mixing ratio. For the respective wind direction the colour code indicates the mixing ratios and the length of the cones their frequency. Data in the original temporal resolution of the LP-DOAS was used.

For the Met light path (Fig. 6.15) a clear relationship between winds from the sector from 270° to 360° and high mixing ratios is visible. NO_2 above the detection limit is observed about 50% of the time when wind directions come from this sector, which throughout the entire observation period very rarely is the case (compare to Fig. 6.8). The source of these NO_2 emissions could be the station itself or the snow clearing activities in its vicinity. Either source could explain the fact that elevated mixing ratios are not always observed when winds come from these directions. For times with a sufficient convection the presumably constant emissions of NO_x from the station, could be 'invisible' to the LP-DOAS because the exhaust plume passes above the LP-DOAS light path and is not mixed down to the surface level on the short distance between smoke stack and light path (roughly 400-600 m depending on the wind direction). For a very shallow inversion layer, the light paths could be even shielded when the exhaust is emitted above the layer. If rather Pistenbully operations are the source, the irregular nature of these emissions could explain the observed percentages.

For the sector from 60° to 270°, also elevated NO_2 can be observed. While for wind directions from 180° to 270° occasional Pistenbully and snowmobile traffic to other scientific installations south-west of the trace gas observatory could be a potential source, no obvious source of emissions exists east of the light paths. Most observations from this 60° to 270° are

at times with very low wind speeds. For wind speeds below 2.2 m s^{-1}, observations at the trace gas observatory are routinely flagged as potentially contaminated since occasionally a transport against the current wind direction could be observed for such calm conditions (see e.g. Weller et al., 2007)

For the periods of elevated NO_2 mixing ratios for measurements on the Atka light path, wind directions between 190° and 260° dominate and again indicate the station or activities in its immediate vicinity as the source. Observed mixing ratios on average are smaller than for the direct influence from the station on the shorter light path, probably due to the fact that the station generators or vehicles in its vicinity constitute a point source whose exhaust plume for these wind directions only affects the remoter half of the Atka light path behind the Met reflector array east of the station (as seen from the telescope). The mixing ratio determined with the LP-DOAS, however, is the average along the entire light path, which for inhomogeneous distributions on the scale of the path length leads to an underestimation of absorber mixing ratios inside the plume. Similar to the influence of the station on the Met light path, elevated mixing ratios occur about 50% of the time when winds are coming from the 190° to 260° sector.

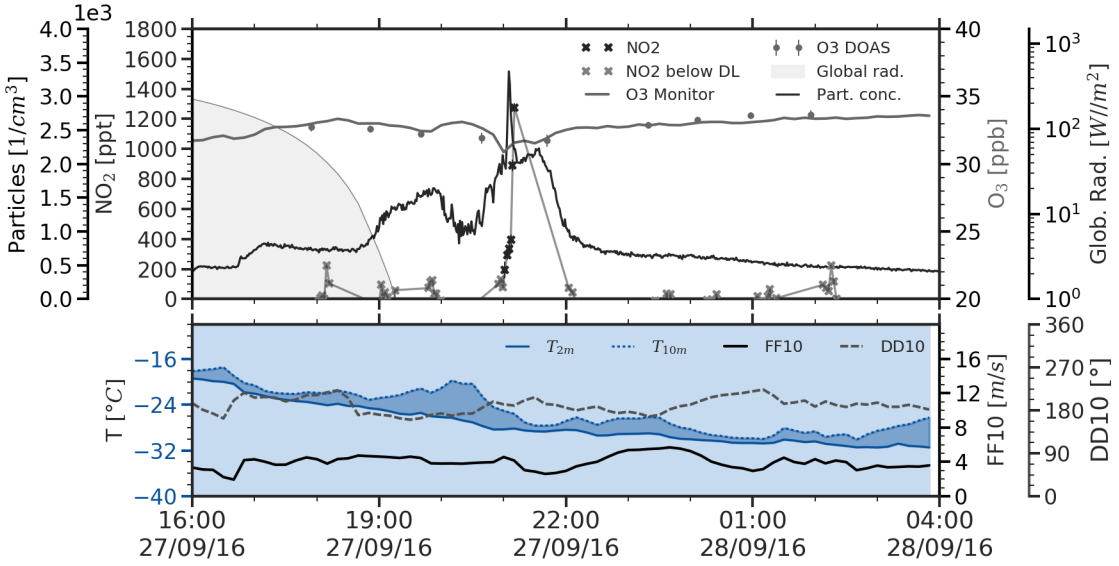

Figure 6.17: Example of the influence of a Pistenbully traverse on NO_2, O_3 and particle concentrations. The period shows the arrival of a traverse (Pistenbully and two heavy sledges) from the south under low wind speeds and continuous temperature inversion conditions passing west of the trace gas observatory and light paths.

An illustration of the influence of a single vehicle on NO_2 mixing ratios as well as particle concentrations and ozone can be found in Fig. 6.17. The depicted period shows the arrival of a traverse (one Pistenbully and two sledges, one with a heavy habitation module) from the south-south west on September 27th 2016. Within a period of 10 min a dip of ozone mixing ratios by about 2 ppb (due to reaction of emitted NO with O_3, see R. 15) is followed by a spike in particle concentrations and a coincident increase in NO_2 mixing ratios. Peak NO_2 mixing ratios are reached about six minutes after the peak in particles (and 10 min after the drop in ozone). During the episode, LP-DOAS measurements were performed on the short light path and the time difference between ozone and particle concentration

signals and the peak of NO_2 agrees remarkably well with the time it takes to cover the 1550 m of the Met light path from the trace gas observatory to the reflectors at the observed wind speed of 2.8 m s^{-1} (about 9 min).

Another period showing a likely influence of the station's generators on NO_2 mixing ratios during polar night is depicted in Fig. 6.18.

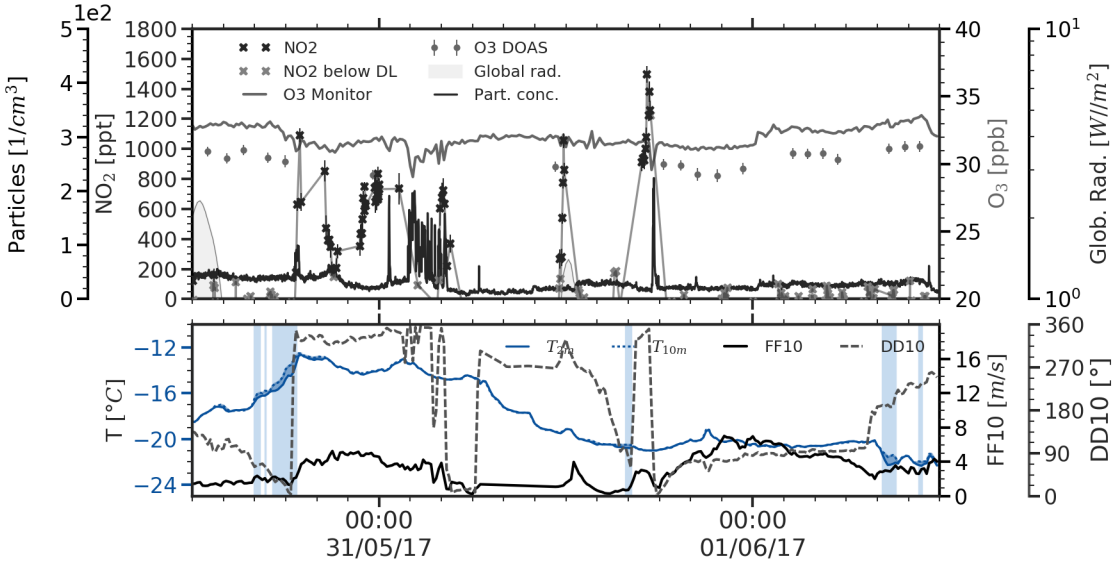

Figure 6.18: Example of the influence NMIII station on NO_2, O_3 and particle concentrations for a two-day period during polar night

For a two-day period, characterised by very low wind speed from variable but mostly northerly directions (see grey dashed line in lower panel of Fig. 6.18) elevated NO_2 mixing ratios were observed. Despite the calm conditions, no temperature inversion developed except for short periods. As soon as the wind direction turned to 280° to 360°, increases in NO_2 mixing ratios are observed which coincide with peaks in particle concentrations and titration induced short-term drops of the ozone mixing ratios. Since no vehicle operation was reported during the two days and elevated NO_2 around midnight on May 31st are not very likely to correspond to activities of the wintering crew, the source in this case probably is the station generator.

For the two examples discussed, an identification of the origin of elevated NO_2 mixing ratios in the LP-DOAS light paths was possible because operations on the station are greatly reduced during the wintering from end of March until October. During the summer research season more personnel and more activities on the station complicate the situation and explain the higher frequencies of elevated NO_2 observed from November to February.

6.4.3 Sulphur dioxide

The SO_2 mixing ratios above the detection limit show a clear seasonality (see Fig. 6.11). Elevated SO_2 observations almost exclusively fall into a period from December until late February with highest values in late December/early January. The peak mixing ratio detected was 230 ppt on December 23rd, 2016. The short period of elevated mixing ratios is also found when daily maxima are considered (see Fig. 6.19), as well as in the seasonal histograms of hourly means for the years 2016 and 2017 shown in Fig. 6.20.

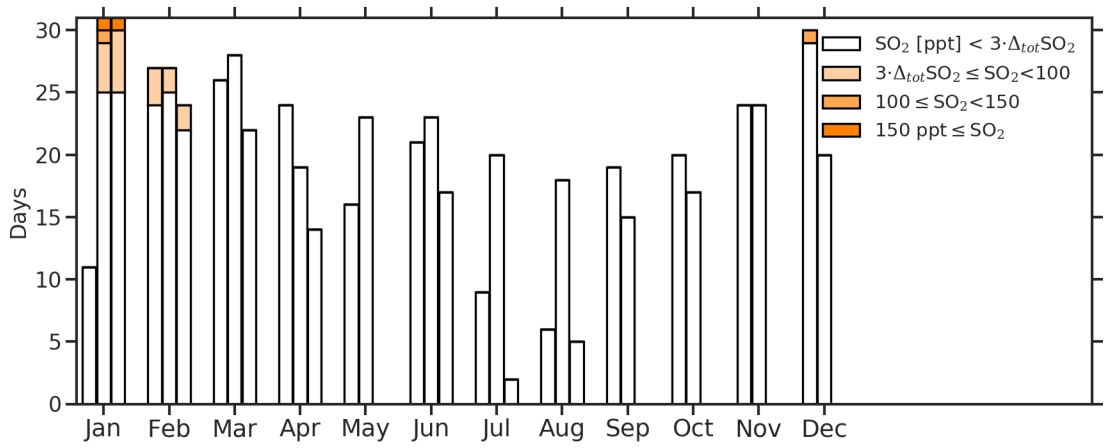

Figure 6.19: Distribution of daily maxima of SO_2 mixing ratios throughout the observation period. For the individual months the left bar represents the year 2016, the middle bar the year 2017, and the right bar the year 2018. The total length of the bars corresponds to the available data in the respective month in days. The colour code marks the daily maximum mixing ratio. The maximum was determined from a time series of hourly medians to limit the influence of single outliers. Only values above 4σ of the total error were taken into account.

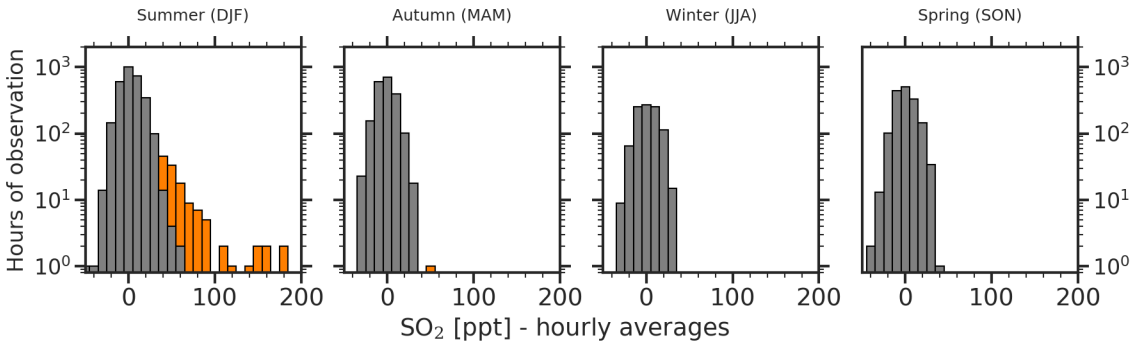

Figure 6.20: Seasonal distribution of elevated SO_2. For the histograms only hourly averaged data from January 2016 until December 2017 was taken into account to prevent a distortion by the additional observations from January until August 2018. Values above the detection limit are coloured, values below the detection limit are plotted in grey. The data set with night-time reference was used.

The summer distribution of SO_2 mixing ratios (Fig. 6.20, left panel) shows that, except for a few peak values, mixing rations most of the time are below 100 ppt.

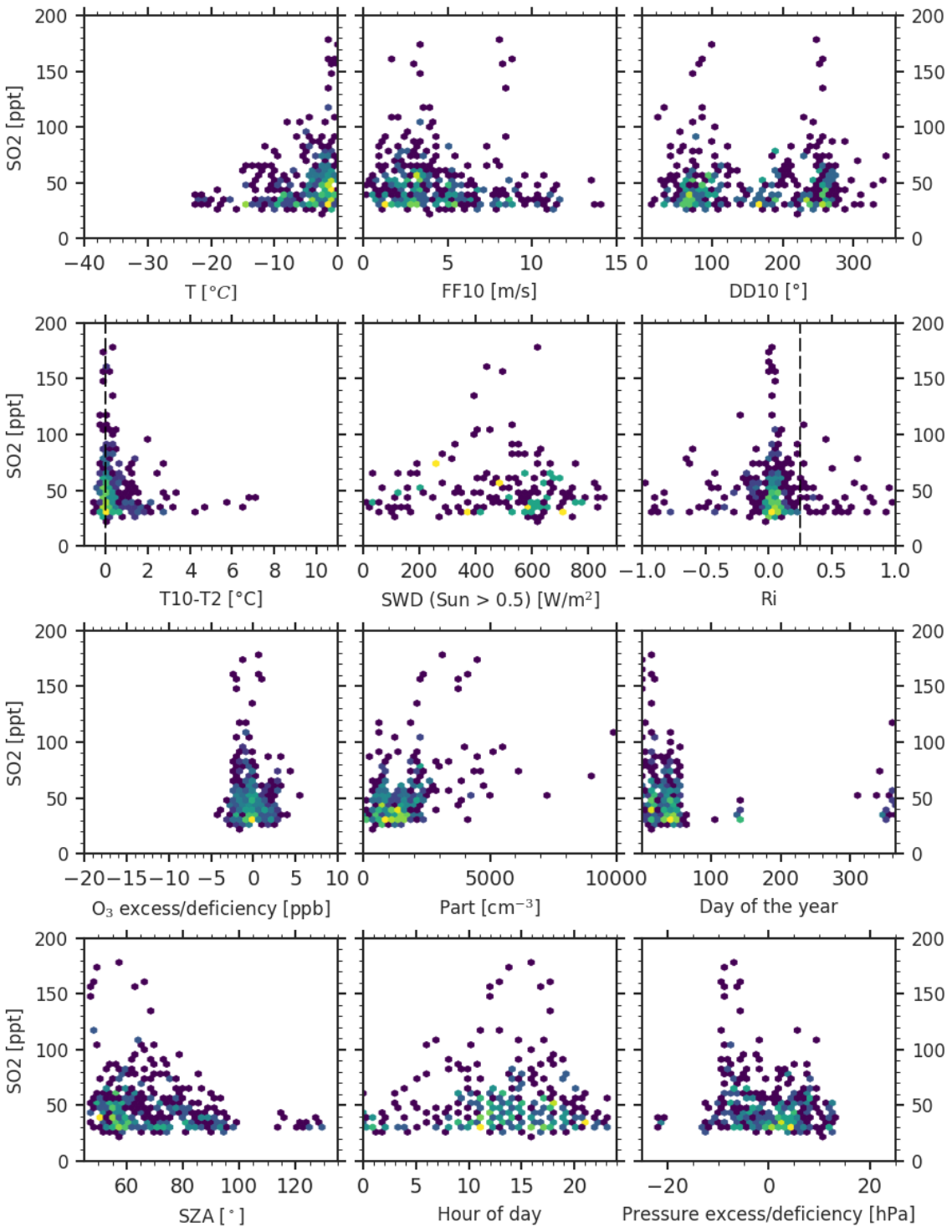

Figure 6.21: Correlation of SO_2 mixing ratios above the detection limit with other atmospheric parameters. The colour code marks the density of values. For the temperature, measurements in $2\,\mathrm{m}$ altitude were used, FF10 and DD10 are wind speed and direction in $10\,\mathrm{m}$ altitude. SWD is the short wave downwelling radiation and Ri is the Richardson number (see Eq. 2.3).The deficiency and excess of O_3 was determined by subtracting a 21-day rolling average from the ozone monitor time series. Part is the the particle concentration.

When the correlations with other atmospheric parameters are considered (see Fig. 6.21), periods of elevated SO_2 are characterised by high air temperatures close to 0 °C, typical for calm conditions during polar day, low to moderate wind speeds (no observations above 8 m s^{-1}) and both winds from easterly and south-westerly directions. Atmospheric stability does not seem to be an important prerequisite for elevated SO_2 values with mostly weak or inexistent temperature inversions and Richardson numbers mostly below the threshold of 0.2 for turbulent mixing for the highest mixing ratios.

There is a positive correlation of global radiation and SO_2 peaks which is also reflected in the occurrence of the highest detected signals for small SZAs between 60° and 40° and between 10am and 6pm. Ozone mixing ratios during periods with elevated SO_2 mostly do not deviate from the current average. A few SO_2 data points are associated with slightly increased ozone mixing ratios. There is a correlation of SO_2 with particle concentrations, however, two regimes seem to exist. For SO_2 mixing ratios above 100 ppt, particle concentrations never exceed 5 000 cm^{-3}, while for mixing ratios below 100 ppt, maximum particle concentrations reach 10 000 cm^{-3}.

The correlation of SO_2 with lower than average atmospheric pressures (about 10 hPa) is associated with lower than average but increasing atmospheric pressure and thus improving meteorological conditions.

SO_2 source attribution

Similar to NO_2, there are both anthropogenic and natural sources of SO_2 in the boundary layer of coastal Antarctica. SO_2 is a by-product of the combustion of fossil fuels, which at NM III are used for heating and power generation as well as vehicle and aircraft operation. When regulations of the sulphur content were not as strict as to date, considerable mixing ratios related to local pollution were reported around stations in Antarctica (e.g. peaks of more than 60 ppb in particular related to ship operations at McMurdo by Lugar, 1993), and in a study on emission inventories based on fuel consumption data from 2004 and 2005, Shirsat and Graf (2009) estimated a combined SO_2 flux of 158 Mg·year^{-1} from power generation and heating on all stations in Antarctica. Even though current European regulations require diesel fuel to contain a sulphur mass fraction of less than 0.001% (*EN590, Directive 2009/30/EC* 2009), the remaining sulphur fraction can influence observations.

The most important natural source of sulphur in coastal Antarctica around NM III are biogenic DMS emissions from the open ocean. Release and atmospheric reaction pathways are discussed in Sec. 2.5.3. The release of DMS from the ocean peaks with biologic activity in summer, in polar regions additionally modulated by sea ice cover (Read et al., 2008), which reaches its minimum in February (see Sec. 2.2.1). [5]

Observed average DMS mixing ratios during the summer months range from 46 ppt at

[5] An additional source of non-sea salt sulphur that has been reported is the release of sulphur containing compounds from penguin excrements. Xie et al. (2002) observed the release of dimethyl trisulfide (DMTS), dimethyl tetrasulfide (DMTTS), and dimethyl pentasulfide (DMPS) from penguin droppings and even estimated a contribution $5.5{\cdot}10^{-5}$ nmol m^{-3} per penguin downwind of a colony. At NM III there is a colony of emperor penguins (*Aptenodytes forsteri*) on the sea ice about 8 km north east of NM III station that in summer consists of about 10 000 adult animals (S. Richter et al., 2018). When the estimates by Xie et al. (2002) are applied to the colony at NM III, neglecting samples were taken from (smaller) Adélie (*Pygoscelis adelia*), Gentoo (*Pygoscelis papua*), and Chinstrap penguins (*Pygoscelis antarcticus*) on the Antarctic peninsula, their estimates would correspond to 10 ppt of sulphur, which is below the detection limit of the LP-DOAS instrument even if all sulphur would be converted to SO_2.

Halley to 170 ppt at Dumont D'Urville (Read et al., 2008). Model estimates yield mixing ratios between a fifth and a tenth of these values for average SO_2 from DMS oxidation (Marelle et al., 2017).

During the investigation of the origin of the observed SO_2 peaks, an unpublished data set of filter SO_2 measurements likely in combination with an ion chromatography analysis routine that were acquired at NM III from 1997 until 1998 could be obtained through private communication from Weller and Minikin, 2019. The seasonality of these weekly filter samples and the LP-DOAS observations agree well. Unfortunately, no additional information about details ob measurement and uncertainties could be obtained. Therefore, the comparison is only included in the appendix (Fig. D.32).

One approach to distinguish the source of SO_2 is based on considerations of atmospheric sulphur chemistry. SO_2 from DMS is the product of the abstraction reaction pathway (R 65) that eventually yields sulphuric acid, which is detected as non-sea-salt SO_4^{2-} in aerosol collected on filters in the trace gas observatory. A product of the addition pathways of DMS (R 66 and R 67) is methylsulfonic acid (MSA), which is also measured in the aerosol collected at NM III (see Fig. 6.9, upper panel for annual cycles of both ions). SO_2 from DMS chemistry therefore should correlate with both ions whereas anthropogenic SO_2 emissions from combustion should only increase the nss-SO_4^{2-} in the aerosol. In principle, the ratio of MSA to nss-SO_4^{2-} in aerosol collected during periods of elevated SO_2 could serve as a way to distinguish sources. However, as discussed in detail in Legrand and Pasteur (1998), this ratio can be influenced by other effects such as a different affinity for condensation onto larger aerosol particles between the two ions. Furthermore, when an air mass containing MSA, SO_2, and nss-SO_4^{2-} no longer is in contact with DMS-emitting sea surfaces, the MSA to nss-SO_4^{2-} ratio with time shifts towards the latter as gradually the SO_2 is converted into nss-SO_4^{2-} but no 'fresh' MSA is added.

When MSA and nss-SO_4^{2-} content on the aerosol filters is compared to the observed SO_2 mixing ratios, a clear correlation of increased mass concentrations of both ions and SO_2 is visible. Furthermore, for filter samples corresponding to the highest SO_2 mixing ratios, the MSA to nss-SO_4^{2-} generally increases, in line with a biogenic origin of the SO_2. This can be seen for an example period in Fig. 6.22.

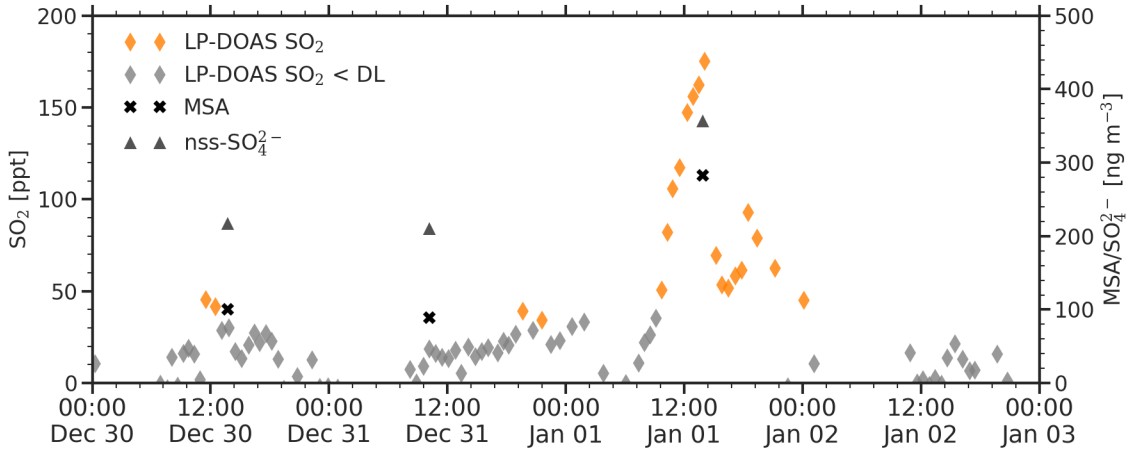

Figure 6.22: Comparison of LP-DOAS SO_2 with ions from aerosols for example period.

Taking into account the observations of NO_2 and its clear relation to a station or vehicle influence, NO_2 can also be used to assess the origin of SO_2. Assuming that on the time scale of minutes it takes the air at typical wind speeds to reach the LP-DOAS light paths or the trace gas observatory from the station or a vehicle in its vicinity, an exhaust plume should still contain both NO_x and SO_2. While several instances of both NO_2 and SO_2 above but close to the detection limit could be identified in the data set, all days with peak SO_2 above 50 ppt show no correlation of SO_2 with NO_2 mixing ratios. An example period of elevated SO_2 and simultaneously observed NO_2 is shown in Fig. 6.23.

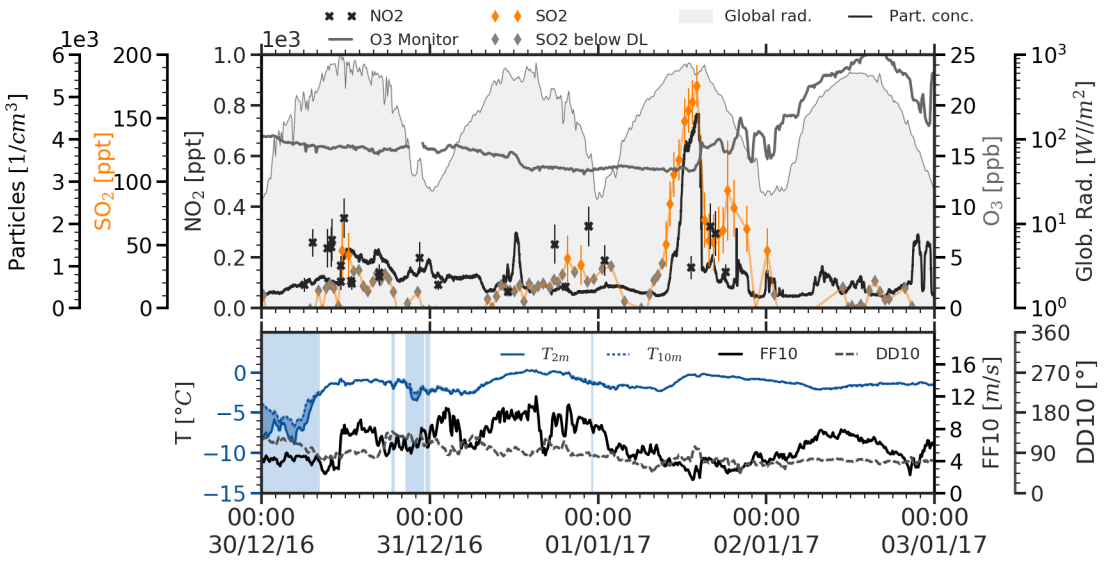

Figure 6.23: Example period with elevated SO_2. Please note that for clarity NO_2 data below the detection limit was not plotted. In addition to SO_2 and NO_2, ozone mixing ratios as well as particle concentrations and meteorological parameters are shown.

While on December 30th 2016, the elevated mixing ratios of SO_2 and NO_2 coincide and the SO_2 could be of anthropogenic origin, during the clear peak of SO_2 on the January 2nd 2017, no comparable NO_2 peak is visible and only few data points are above the detection limit.

Considering the comparison to filter SO_2 measurements, ion mass concentrations detected in filtered aerosol, and the comparison with NO_2 mixing ratios strongly point to the conclusion that the majority of observed SO_2 signals is of biogenic origin. This is supported by the very pronounced SO_2 seasonality and the fact that it was not observed above the detection limit outside the summer period despite the documented instances of NO_2 contamination throughout the entire year. Furthermore, SO_2 mixing ratios correlate with solar radiation, and peak around noon, which would be expected for the formation via reaction with photochemistry-dependent OH but were not observed during the night, despite an independence from photochemistry of SO_2 formation in combustion processes.

6.5 Anthropogenic influences

6.5.1 Influence on atmospheric mixing ratios

For atmospheric measurements that aim at the observation of natural conditions and processes, a potential interference from anthropogenic activities has to be considered. Coastal Antarctica, on a global scale, offers extremely pristine conditions. However, the hostile environmental conditions throughout large parts of the year require considerable logistical efforts to support a human presence and the operation of scientific instrumentation. As was discussed in Sec. 6.4.2, the generation of power and heat on NM III station as well as vehicle traffic potentially influence the observed mixing ratios. Based on the observed NO_2 mixing ratios, which for the attained detection limits of the LP-DOAS instrument with a high certainty can be attributed to anthropogenic activities, in about 14% of the observation time measurements were potentially contaminated. Most of the highest observed mixing ratios and periods of sustained NO_2 mixing ratios above the detection limit could be attributed to the station's exhaust or vehicle activity in its immediate vicinity. Based on previous experience, periods of potential contaminations can be masked in the data set by the application of filters based on meteorological parameters like wind direction and speed (see e.g. Weller et al., 2007; Weller et al., 2011a). The filtering parameters that are typically used for point observations at the trace gas observatory to flag data as potentially contaminated or, depending on the instrument, stop the data acquisition, exclude wind from a sector between 330 and 30°, observations at wind speeds below $2.2\,\mathrm{m\,s^{-1}}$ as well as particle concentration thresholds adapted to the annual cycle of particle concentrations.

Due to the orientation of the light paths of the LP-DOAS instrument (see Fig. 4.1) and based on the analysis of the relationship between wind direction and observed NO_2 mixing ratios, an adapted filter was determined. For measurements on the longer Atka retro-reflector, winds between 180 and 30° were excluded, whereas observations on the shorter Met light path were filtered for wind directions between 270 and 30°. The filtering based on particle concentrations was not used. The result of these filtering conditions on the NO_2 mixing ratios above the detection limit can be seen in Figure 6.24.

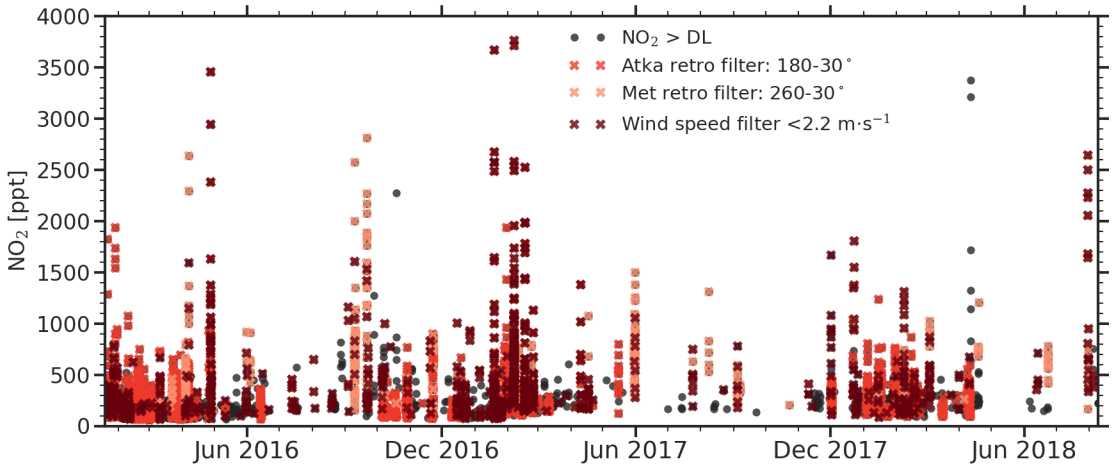

Figure 6.24: Effect of a contamination filter based on wind wind speed and direction on observed NO_2 mixing ratios.

Except for one period with mixing ratios up to 3.5 ppb in April 2018, the majority of NO_2 observations could be linked to meteorological parameters. Applying these filter conditions to the entire LP-DOAS data set calculated on an hourly basis would flag 86 to 88% of observations on the Met light path as uncontaminated and 61% of observations on the Atka light path. For absorbers that were detected in spectral windows that operated on both light paths (all except UVI), this would yield a total of 81% of uncontaminated observations.

When correlating NO_2 observations with the time series of BrO and ClO (the discussion of the data follows in the next chapter), it can be seen that high mixing ratios of both halogen species never coincided with high NO_2 values (Fig. 6.25).

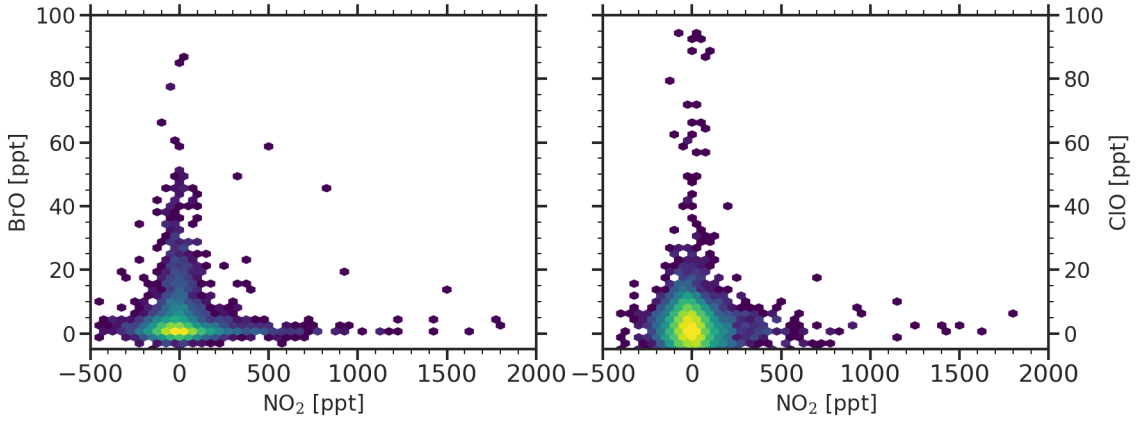

Figure 6.25: Correlation plots for BrO and ClO mixing ratios with NO_2 mixing ratios. Due to the different acquisition times of the three data sets, 30 min averages were calculated and corresponding periods were correlated.

Regarding this plot, it should however be kept in mind, that both halogen (families) react with NO_x (cf. R 41 to R 43). An absent overlap of elevated mixing ratios therefore could simply mean that pollution from the station always deactivated halogen species. In the entire time series no clear example for a pollution induced drop in halogen species mixing ratios of an ongoing activation period could be identified.

For the further analysis, data sets were not filtered with these parameters by default. Overviews of time series contain the entire observation period. In the halogen chemistry case studies discussed below, a potential anthropogenic influence during observations was checked using NO_2 mixing ratios as a marker.

6.5.2 Indirect influence via snow surfaces

Snow surfaces can play a crucial role in the release of halogen trace gases (see Sec. 2.4.7). In addition to an influence of exhaust on current atmospheric mixing ratios, it is conceivable that if the observed trace gas abundances and chemical processes are the result of local chemistry, the contamination of local snow surfaces can indirectly affect the observations. For instance the formation of dihalogens in the surface layer in the bromine explosion reaction cycle requires a proton and hence an acidic surface (R 49). As sea water is alkaline, surfaces have to be acidified for heterogeneous halogen release to occur (see Sec. 2.4.7). Since the pristine atmosphere of Antarctica has only few natural sources of acidity

(R. Sander et al., 2006), acid production from exhaust related to nitrogen oxides or sulphur contained in the fuel could change the surface pH of the snow when deposited.

An assessment of such an influence is not straightforward and would require a detailed study of surface properties, emission fluxes, deposition time, adsoption or reaction on snow surfaces and much more. However, it can be argued that even if anthropogenic emissions alter the composition or chemical properties of the snow, for large parts of the year this can be neglected because of the regular renewal of the local surface snow during storms. Fig. 6.26 shows an exemplary period from March 2016 with 10 m wind speeds and the snow height just behind the trace gas observatory as measured by a laser distance instrument.

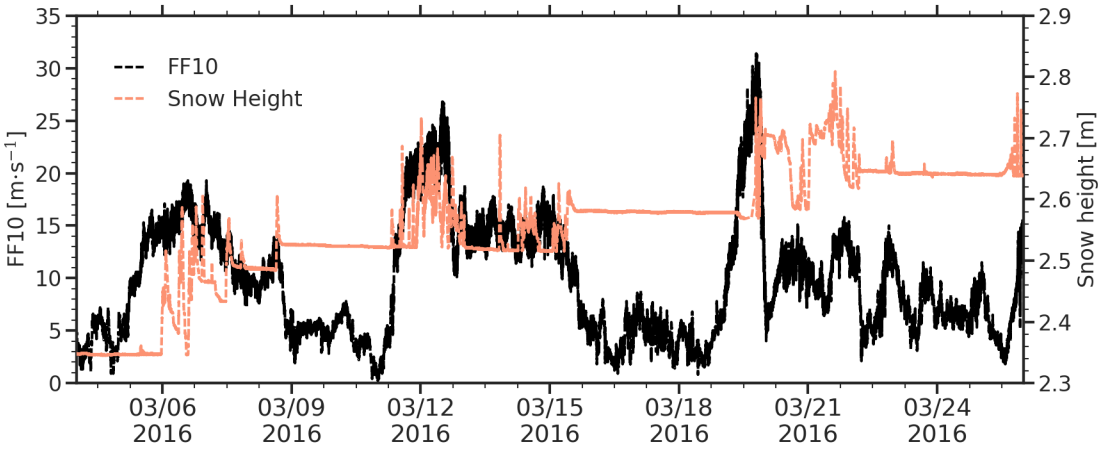

Figure 6.26: Example period that shows how storms influence snow height at NMIII. The snow height data was measured by a laser distance instrument in the immediate vicinity. The wind speed data was acquired at the meteorological measurement site at 10 m altitude. Snow height data obtained via personal communication from König-Langlo, 2016.

During the period, three storms with increasing peak wind speeds occurred. The resulting depositions of new snow is clearly visible between the single storm episodes. During the the storms the detected snow height varied between 10 and 20 cm indicating an constant interplay between wind erosion and deposition. Therefore, at least briefly after a storm/blowing snow period, it can be assumed that the snow surfaces around NM III station are not altered by anthropogenic influence. For longer periods between storms, the (past) observed NO_2 mixing ratios can be used as a marker to assess a potential anthropogenic influence on atmospheric observations and surfaces.

7
Halogen observations

In this chapter, the time series of observed halogen species are discussed. An overview of the available data sets is given and the interplay of relevant atmospheric parameters with the respective trace gas is investigated.

In Sec. 7.1 to Sec. 7.3, the observations of bromine, chlorine and iodine compounds are presented and discussed. For the entire observation period, the occurrence, frequency, and seasonality of elevated mixing ratios is investigated using the long temporal coverage of the LP-DOAS observations. To elucidate the prerequisites for episodes of elevated mixing ratios of the respective species, the influence of atmospheric parameters as well as the potential influence of halogens on other atmospheric processes, mixing ratios were correlated with selected atmospheric parameters and other trace gases.

Based on this overview, identified influence factors and processes are then analysed in detail using case studies of suitable observation periods to verify hypothesis regarding the prerequisites for a halogen release, the dominant atmospheric factors during episodes of elevated mixing ratios, and the fate of halogen compounds after the release into the atmosphere.

Since for several of the observed episodes of elevated halogen radical mixing ratios, a clear depletions of ozone comparable to those usually observed in springtime ODEs (Oltmans, 1981) seems to be absent, expected depletion rates based on the observed halogen mixing ratios were estimated for different days and absorber combinations and then compared to observed ozone abundances.

Lastly, a coincidence of elevated bromine monoxide and likely natural new particle formation events is discussed, which was observed on several occasions. While the possibilities of a detailed study of the particle formation and growth mechanisms were limited owing to a lack of suitable instrumentation, in Sec. 7.4 the observed episodes are described, the available data is analysed and hypothesis regarding proposed particle formation mechanisms are discussed.

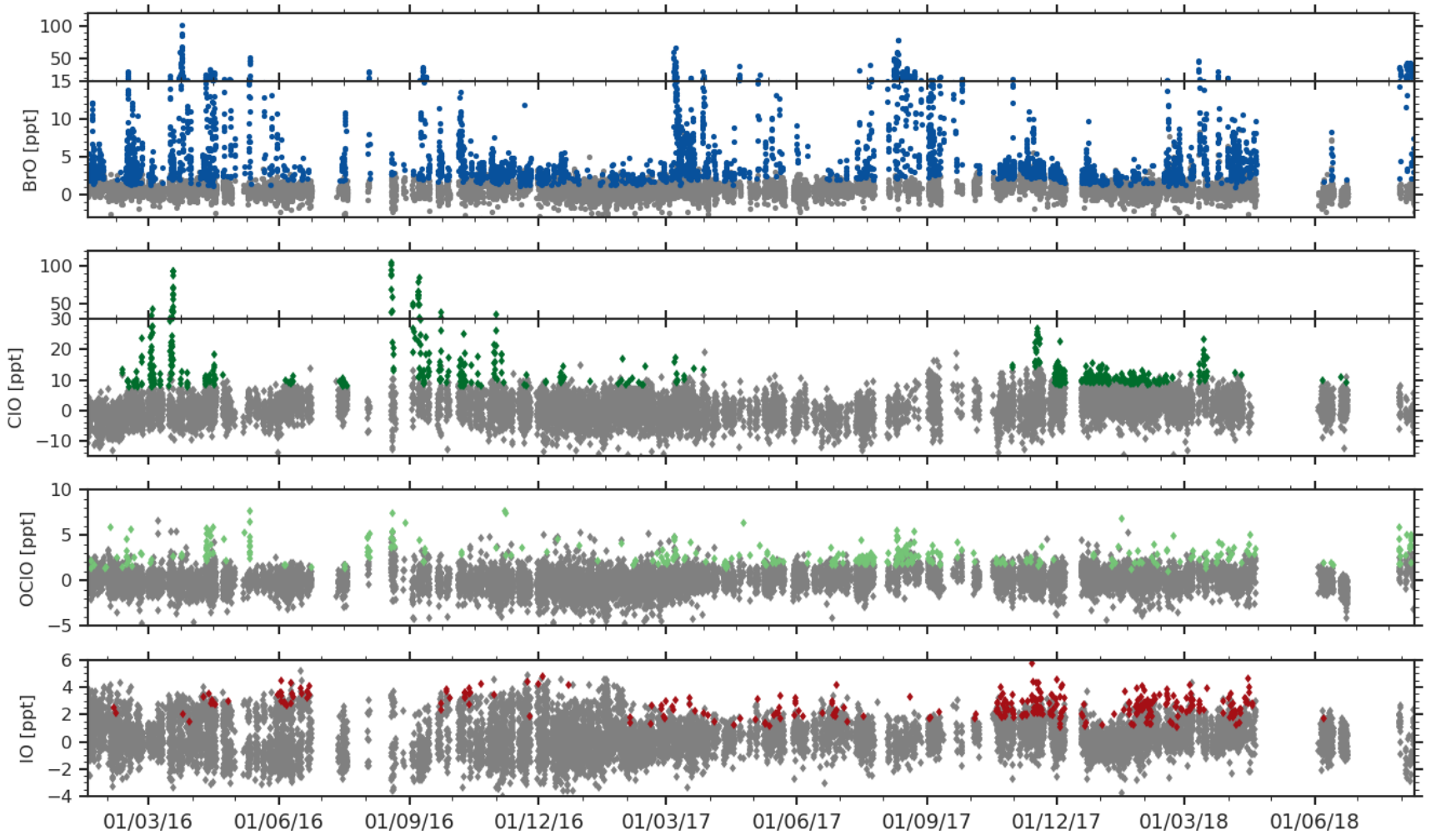

Figure 7.1: Overview of data sets of BrO (top panel), ClO (upper middle panel), OClO (lower middle panel), and IO (lower panel) for the entire observation period. The plotted data are 30 min averages. Data points above the respective detection limit are coloured. Data below the detection limit are marked in grey. Note that for a better assessment of smaller mixing ratios as well as maximum values, for BrO and ClO plots are split in two with different linear ordinate axes.

Fig. 7.1 shows 30 min averages of the entire time series of all halogen species that were observed above their respective detection limits. To accommodate the wide range of observed mixing ratios of BrO and ClO in the figure, for these absorbers two linear axis plots were combined. As discussed in Sec. 5.2.4 and Sec. 4.2.9, there are 10 gaps of more than a week in the data sets which are also visible in the halogen trace gas time series (see also Tab. 4.5). Additionally, there are shorter interruptions, mostly due to the visibility conditions in the atmosphere during regular episodes of blowing snow at NM III (see Fig. 6.6). The annual average temporal coverage of the measurements was 57% and is discussed in detail in Sec. 4.2.10.

7.1 Bromine

Among the bromine compounds that absorb in the spectral ranges covered by the LP-DOAS instrument and that, in principle, could be measured, only BrO was observed above the detection limit (median detection limits of 2 ppt with lowest limits between 0.3 ppt and 0.4 ppt for measurements in the UVII spectral window on the longer Atka light path). Upper limits for Br_2 and OBrO, based on median detection limits during the observation period, are 3.6 ppb and 10.7 ppt respectively (see overview in Tab: 5.4). The BrO observations are discussed in the following sections.

7.1.1 Overview of bromine monoxide observations

When comparing the BrO time series with the selection of previously reported BrO observations in Tab. 2.1, the most striking feature are the attained peak mixing ratios during the 32 months of observations at NM III. The highest value of 110 ppt is almost a factor of three higher than the highest values so far reported (45 ppt) by Zielcke (2015) from the Weddell sea and 41 ppt by Pöhler et al. (2010) from the Amundsen Gulf in the Arctic. Peak mixing ratios of 30 ppt or more, which are frequently reported as observed maximum values, were detected on 32 days during the entire observation campaign.

Taking the BrO peak mixing ratios in Fig. 7.1, a seasonality with two periods of high BrO activity and the highest peak mixing ratios is discernible - one from February to April and one in August and September. To investigate this further, the distribution of daily maxima throughout the 32 months of observations was determined. For this, hourly averages of the BrO mixing ratios were calculated and for the resulting time series the daily maxima were determined. The distributions of daily maxima for all months of the observation period is shown in Fig. 7.2.

The two periods with a frequent occurrence of mixing ratios above the detection limit and high daily maxima are also visible here. One begins in February, in late (Antarctic) summer and continues into May just before the beginning of polar night (May 21st). In March the highest number of days with maximum mixing ratios above 20 ppt during this period was observed. In June, only on a few days BrO above the detection limit was detected. The second period of frequent BrO observations begins after the end of polar night (July 22nd) in late July/early August - depending on the year considered. Even though only in 2017 more than 10 days of observations are available during these two months due to frequent storms at this time of the year, the distributions for both months on the remaining days with observations show an increased frequency and higher mixing ratios than in June.

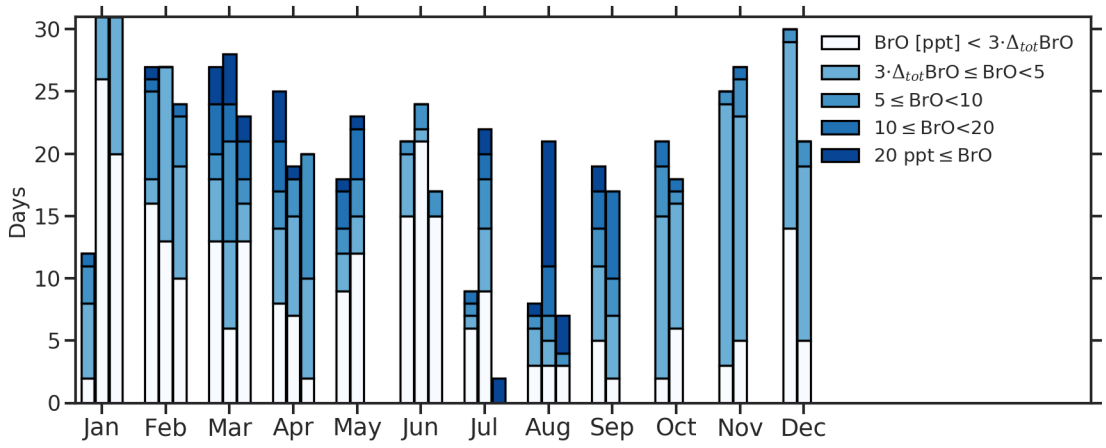

Figure 7.2: Distribution of daily maxima of BrO mixing ratios throughout the observation period. For the individual months the left bar represents the year 2016, the middle bar the year 2017, and the right bar the year 2018. The total length of the bars corresponds to the available data in the respective month in days. The colour code marks the daily maximum mixing ratio. The maximum was determined from a time series of hourly means to limit the influence of single outliers.

From September until December, due to the failure of the light source in the LP-DOAS instrument in August 2018, only observations from 2016 and 2017 are available. While mixing ratios above 20 ppt are only observed in September, from October to December mixing ratios up to 5 ppt are very frequent and in October as well as November, only on a minority of days no BrO above the detection limit was observed. A second minimum in BrO activity is reached in January when on most of the days in 2017 and 2018 no BrO above the detection limit is observed. Since the operation of the instrument only started on January 18$^{\text{th}}$ 2016, January data from this year represent the second half of the month and show BrO above the detection limit on most days, likely caused by an earlier onset of the activation period in autumn, which is also visible in the occurrence of higher mixing ratios in February 2016 compared to the same month in 2017 and 2018.

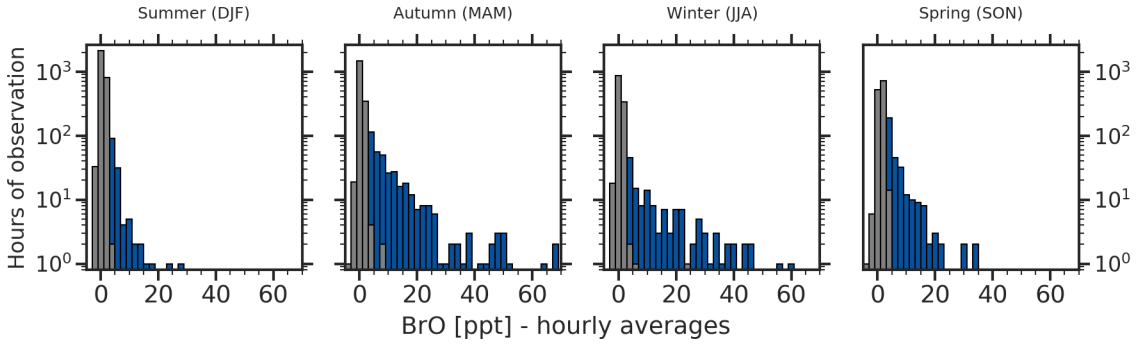

Figure 7.3: Seasonal distribution of elevated BrO. For the histograms only hourly averaged data from January 2016 until December 2017 was taken into account to prevent a distortion by the additional observations from January until August 2018. Values above the detection limit are coloured, values below the detection limit are plotted in grey. Note the logarithmic scale.

When histograms of hourly averages of BrO mixing ratios for the four seasons are considered, a similar picture emerges (see Fig. 7.3). To prevent a distortion of the histograms due to the incomplete observations from 2018, only data from January 18$^{\text{th}}$ 2016 until January 17$^{\text{th}}$ 2018 was considered.

In the Antarctic summer (December to February), the fewest observations above the detection limit relative to the observation time and the lowest mixing ratios are found. Mixing ratios above 10 ppt mostly fall into the month of February. BrO above the detection limit is only observed for 349 h or 12% of the valid observation time (i.e. the time when LP-DOAS data for BrO is available), even though the instrument has the best temporal coverage during this time of the year. The absorber specific absolute temporal coverage of BrO in summer (defined as the total number of hours during which at least one observation of BrO mixing ratios is available divided by the total number of hours) is 77%. Note that this is lower than the overall temporal coverage of the LP-DOAS instrument discussed in Sec. 4.2.10 and shown in Fig. 4.24. This is because for the absorber specific temporal coverage only valid DOAS fits and the times when the instrument was measuring in either the UVI or UVII spectral windows are considered, whereas the absolute temporal coverage discussed in Sec. 4.2.10 combines all spectral windows and considers all times when spectra were recorded - regardless of their quality.

In autumn (March to May), BrO is detected during 478 h corresponding to 26% of the observation time. As can be seen in Fig. 7.2, the highest maximum mixing ratios are reached during this season with a few hourly averages even surpassing 60 ppt and a considerable number of observations between 10 ppt and 30 ppt. The absolute temporal coverage for BrO for this part of the year is 53%.

Even though mixing ratios above 20 ppt are reached on several days in winter (June to August), BrO above the detection limit is only detected during 172 h corresponding to 14% of the observation time which for July and August 2016 was very limited due to meteorological conditions. An absolute temporal coverage of only 32% for BrO was reached in winter. In spring (September to November), BrO is observed during 548 h which corresponds to 43% of the valid measurement time, the highest value for all seasons. Due to the high storm activity, the absolute temporal coverage, however, is only 41%. As can be seen in the corresponding histogram, most of the observations in spring are below 10 ppt and mixing ratios above 15 ppt are rarely reached.

7.1.2 Influence of atmospheric parameters on BrO

In previous observations, elevated BrO mixing ratios often were observed under specific atmospheric and meteorological conditions. These can be linked to physical and chemical processes which are prerequisites for or at least favourable to halogen activation. With the comprehensive data set available for this thesis, the large variations of atmospheric conditions and parameters at NM III throughout the year allow to test these prerequisites. For this, correlations of selected parameters with the observed BrO mixing ratios can be analysed. The basis for this are the individual observations of BrO from the combined evaluations of the UVI and UVII spectral windows that are above the detection limit. The parameters against which the BrO mixing ratios are compared were averaged between the first and last measurement spectrum of each BrO data point in the time series. For

O_3 mixing ratios and atmospheric pressure, which both exhibit an annual variation, detrended time series were calculated by subtracting an 30-day and 90-day running mean respectively. The correlations can be found in Fig. 7.4.

Temperature dependence

In the correlation between BrO mixing ratios and the 2 m air temperature (Fig. 7.4, left panel in the first row) two clusters can be identified which are a result of the combined influence of the annual temperature cycle and the influence of synoptic conditions on air temperatures on shorter time scales.

As was discussed above, during storms air is advected from the Southern ocean flowing around the low pressure system before arriving at NM III (see Sec. 6.2). Anti-cyclonic periods are frequently characterised by a calm, cloud free atmosphere and the longer these conditions last, the stronger temperatures decrease through radiative cooling. Independent of the time of year, the observed temperature differences between stormy and calm periods are roughly 20 K. The elevated mixing ratios up to 110 ppt for temperatures between -15 °C and -25 °C therefore correspond to BrO activation in autumn when such temperatures are typically reached a couple of days after a storm. At the same time, this temperature range also corresponds to stormy conditions in late winter and spring, the second period of increased BrO abundances and hence to BrO mixing ratios directly after a storm before the radiative cooling during ant-cyclonic conditions. A second cluster of elevated mixing ratios is visible for temperatures between -35 °C and -40 °C, close to the minimum temperatures at NM III, which corresponds to observations under anti-cyclonic conditions in late winter.

Temperatures of -20 °C and below were often reported during the observation of springtime ozone depletion events (Simpson et al., 2007, and references therin). An influence of temperature on halogen release can be linked to several precipitation processes in the surface layer on sea ice and the quasi-liquid layer on aerosols and snow that enables or increases bromine release. At 270 K, carbonates start to precipitate and according to R. Sander et al. (2006) at 265 K 90% of carbonates are removed from the surface layer thus eliminating the carbonate buffer of sea water. This allows the surfaces to get acidified, which is a prerequisite for the heterogeneous reactions of the bromine explosion (see R 49). This is particularly relevant for sea ice surfaces but since in particular fresh marine aerosols are also alkaline and at least partly carbonate buffered (Pszenny et al., 2004), it might also be important for release from fresh aerosols or even snow surfaces affected by the deposition of fresh sea salt aerosols. Other temperature thresholds that also apply to surface layers of aerosol and snow grains are those for mirabilite ($Na_2SO_4{\cdot}H_2O$) precipitation at -8 °C and hydrohalite ($NaCl{\cdot}2H_2O$) precipitation at -20 °C both leading to a relative enhancement of bromide in the surface layer (see also Sec. 2.4.7).

When investigating these threshold temperatures with the observed BrO mixing ratios, it has to be considered that the available temperature measurements at 2 m altitude not necessarily reflect the temperature of the surface layer in which the precipitation takes place. Furthermore, temperatures in the source regions of the BrO mixing ratios might not be the same as measured at NM III when advected air masses rather than local chemsitry was observed. This applies in particular to carbonate precipitation in sea ice surface layers.

For temperatures above -10 °C, the majority of observations is between the detection limit and 5 ppt with few values between 5 and 10 ppt. Higher mixing ratios are only observed below -10 °C, which would agree with the threshold temperature for carbonate

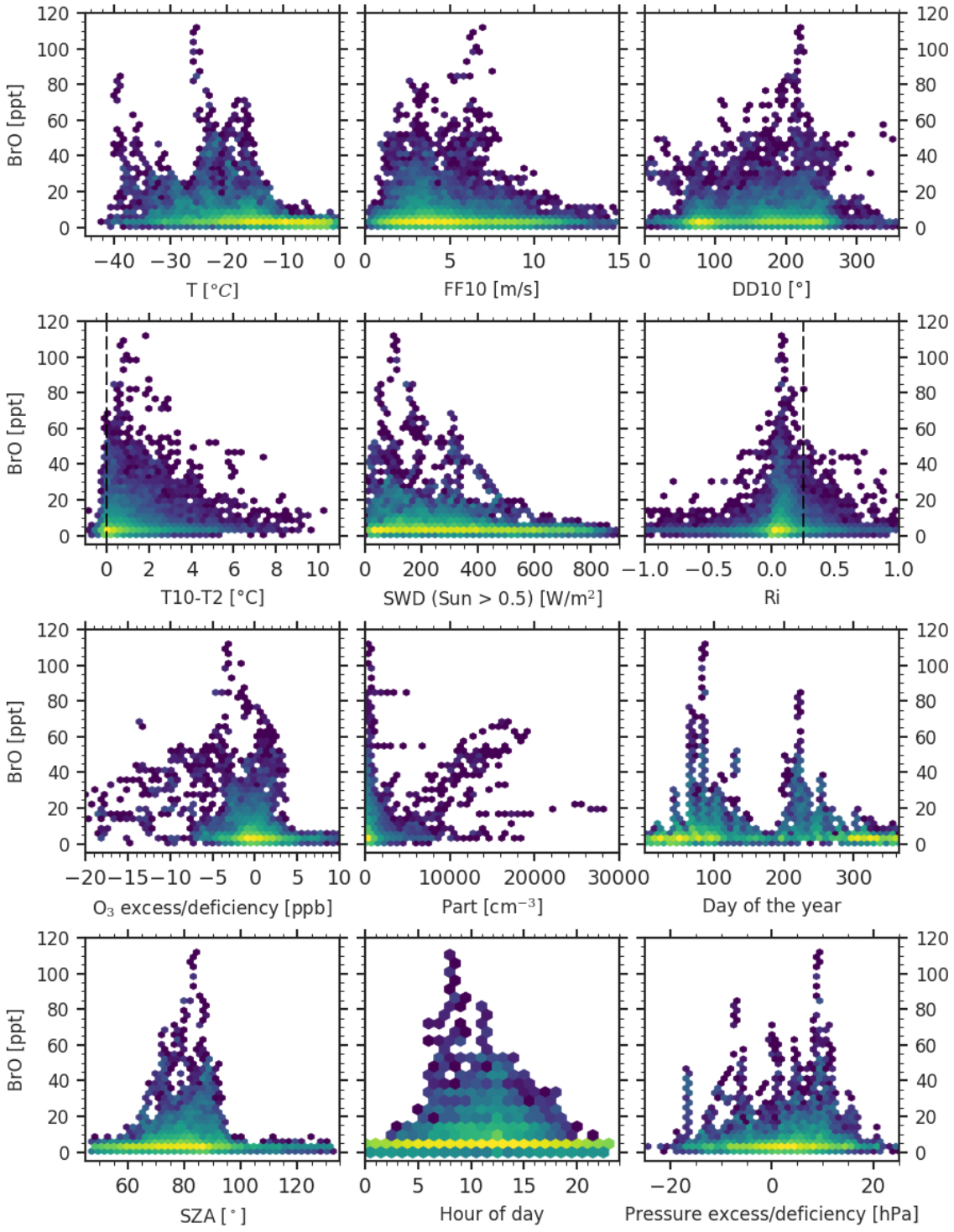

Figure 7.4: Correlation of BrO mixing ratios above the detection limit with other atmospheric parameters. The colour code marks the density of values. For the temperature, measurements in 2 m altitude were used, FF10 and DD10 are wind speed and direction in 10 m altitude. SWD is the short wave downwelling radiation and Ri is the Richardson number (see Eq. 2.3).The deficiency and excess of O_3 was determined by subtracting a 21-day rolling average from the ozone monitor time series. Part is the the particle concentration.

precipitation. The overall highest mixing ratios are only observed around -25 °C, which is below the threshold temperature of hydrohalite precipitation. For even lower temperatures Koop et al. (2000) determined that through further precipitation processes, the ratio of bromide to chloride in the surface layer further increases favouring a release of bromine over chlorine. Furthermore, salty surfaces are expected to remain liquid and thus chemically active down to temperatures of -43 °C for which indeed elevated BrO mixing ratios were observed.

In conclusion, the observed correlation of BrO mixing ratios with air temperature generally agrees with various threshold temperatures assuming that the 2 m air temperatures used here are representative for the surface layer. The precipitation of carbonates already starts at -2 °C, however, it is not clear if precipitation rates at these temperatures are sufficient to remove the carbonate buffer. One explanation for the observation of elevated BrO mixing ratios above -10 °C could be that the bromine is released from surface layers that no longer posses sea water characteristics e.g. when carbonate buffer was removed prior to a transport to surfaces at NM III.

Wind speed and direction

The correlation of BrO mixing ratios with wind speed (Fig. 7.4, centre panel in the first row) shows an anti-correlation of mixing ratios and 10 m wind velocities with most observations below $7\,\mathrm{m\,s^{-1}}$. No mixing ratios above 30 ppt are observed above $8\,\mathrm{m\,s^{-1}}$ and for wind speeds above $12\,\mathrm{m\,s^{-1}}$, the threshold values for drifting and blowing snow conditions at NM III, only a few observations at mixing ratios below 10 ppt are found. Blowing snow conditions have been reported to be an alternative release pathway for reactive bromine from the lofted snow particles (Yang et al., 2008; A. E. Jones et al., 2009; Yang et al., 2010; Frieß et al., 2011). The potential to investigate this with the LP-DOAS observations however, is limited. Due to the measurement principle, the fact that observations at wind speeds up to $15\,\mathrm{m\,s^{-1}}$ are available signifies that drifting and blowing snow only can have had a limited (vertical) extent since obviously the visibility was sufficient for measurements.

For most periods of elevated BrO, the wind came from easterly or south-westerly winds. This is further illustrated in the windrose for BrO mixing ratios in Fig. 7.5. Interestingly, all observations with mixing ratios of 70 ppt or more are associated with wind from south-south west (200°). This is the prevailing wind directions during anti-cyclonic periods. For directions between 300 and 360° only few observations above the detection limit exist and mixing ratios are generally low. This could be due to the rare occurrence of winds from these directions (see Fig. 6.7). Alternatively, these wind directions very often are associated with a NO_2 contamination from NM III station (see Sec. 6.4.2). Since high NO_x can act as a sink for BrO (see R 43 and R 42), this could explain the low mixing ratios.

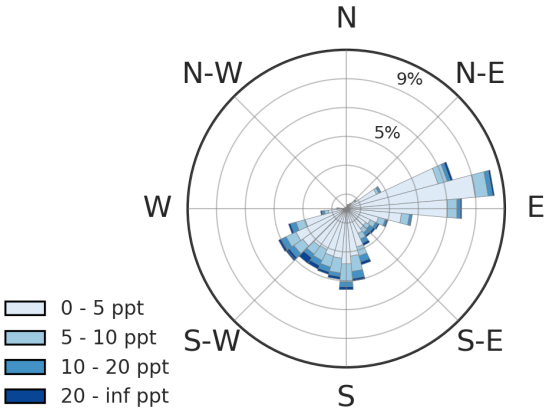

Figure 7.5: Distribution of BrO mixing ratios above the detection limit as a function of wind direction. The colour code marks the the mixing ratio. For the respective wind direction the cones show the distribution of mixing ratios and the colour code indicated the mixing ratio. Data in the original temporal resolution of the LP-DOAS was used.

Atmospheric pressure

To investigate the relationship between the synoptic situation and BrO mixing ratios, a de-trended times series of atmospheric pressure on the station altitude was calculated by subtracting a 90-day running average from the atmospheric pressure data to remove the long-term pressure variations due to the SAO (see Sec. 6.2.2). For BrO, there seems to be a slightly positive correlation with excess atmospheric pressure (i.e. calm, anti-cyclonic conditions) and the highest mixing ratios were detected at about +10 hPa (see Fig. 7.4 last row right panel). Most of the observations above 20 ppt that are associated with a pressure deficiency could be identified as elevated mixing ratios after passage of particularly developed low pressure systems when atmospheric pressure was rising again and hence conditions calm but it was still below the long-term average. This correlation with elevated or at least increasing atmospheric pressure associated with calm conditions after a storm hints towards an importance of atmospheric stability for BrO observations.

Atmospheric stability

Atmospheric stability and calm conditions also characterise many of the previously reported observations of elevated BrO mixing ratios (Simpson et al., 2007; Saiz-Lopez and von Glasow, 2012, and references therin). To assess the stability of the atmosphere at NM III, both the gradient *Richardson* number for the first 10 m (see Eq. 2.3 in Sec. 2.2.2) and the temperature difference between 10 m and 2 m altitude were calculated and then correlated with BrO mixing ratios (see Fig. 7.4 second row the right and left panel respectively).

For the temperature difference, positive values signify a surface temperature inversion with warmer air above colder air at the surface. This situation is associated with a reduced vertical mixing and, depending on the life time of a species, can influence observed mixing ratios acting as a 'lid' (for details see Sec. 2.2.2). For a presumed constant source flux within the inversion layer, mixing ratios would be increased in the limited volume thus created (Anderson and Bauguitte, 2007; Anderson and Neff, 2008).

For the correlation between mixing ratios and the temperature difference, a clear association of elevated BrO mixing ratios with positive differences i.e. inversion conditions is visible. Only very few and low mixing ratios were observed for a negative temperature difference, prerequisite for vertical mixing through convection.

In addition to the vertical temperature profile of the atmosphere, the *Richardson* number also considers the influence of mixing through wind-induced turbulence. For negative Richardson numbers static instability occurs, i.e. turbulence develops through convection independent of wind shear. Between 0 and a critical value of 0.25, the atmospheric flow is turbulent, even though close to the critical threshold, decoupling of layers in the flow and other complex flow situations can develop (Anderson and Neff, 2008). For values above 0.25, the flow is stably stratified and laminar. The correlation of BrO shows the highest mixing ratios for turbulent conditions - although mostly for positive Richardson numbers. As will be seen in the discussions of the case studies, many days with elevated halogen mixing ratios show a highly dynamic daily cycle. Often mixing ratios start to build up under stable conditions and then decline once turbulence leads to a sufficiently strong mixing. The peak mixing ratios therefore often coincide with turbulent atmospheric conditions that limit further increases. A number of data points lie even at negative *Richardson* numbers indicating convective mixing, however, mostly below 30 ppt.

Combing the correlations with both measures, the significance of atmospheric stability for elevated mixing ratios is clear. As will be discussed in detail in a case study in Sec. 7.1.3, the development of temperature inversions is not only a prerequisite for most observations of elevated Bro mixing ratios at NM III but the strength of the inversion also correlates with the temporal variation of mixing ratios.

Solar radiation, SZA, and daily cycle

Considering the correlation of BrO with global radiation (Fig. 7.4 second row centre panel), mixing ratios up to 10 ppt are observed for the entire range of irradiances between close to 0 and 850 $\mathrm{W\,m^{-2}}$. For higher mixing ratio,s an anti-correlation between global radiation values and BrO is visible with the highest mixing ratio reached at around 100 $\mathrm{W\,m^{-2}}$. Combing the correlation with SZA and the distribution of mixing ratios as a function of the hour of the day, the highest mixing ratios occur in the early morning starting at SZAs of 95° i.e. already before sunrise. In the daily cycle (Fig. 7.4 last row centre panel), even though mixing ratios up to 60 ppt are distributed around noon, the highest peaks of BrO mixing ratios are only observed in the morning.

A causal link between the influence of solar radiation, the level of the sun, and BrO mixing ratio could be both direct via photochemistry or indirect via an influence on atmospheric structure and dynamics (or a combination of both). This interplay and the observed daily cycles are investigated and discussed in detail in Sec. 7.1.3 .

Seasonal cycle

When plotted as a function of the day of the year (Fig. 7.4 third row right panel), the annual cycle of BrO mixing ratios already discussed above is clearly visible. Even though for BrO very high mixing ratios were observed throughout the entire observation period, highest mixing ratios in this correlation form two surprisingly dense peaks. From late spring well into summer, the high numbers of observations just above the detection limit are visible. These predominantly occur during Polar day when almost constantly radiation for photolysis reactions is available and hence often no night-time drops of BrO mixing ratios are observed. For an example period see Fig. 7.17.

Ozone

The correlation of BrO with deviations from the current average ozone mixing ratios shows the influence of BrO on ozone. O_3 deficiencies from -5 to -20 ppb are associated with BrO mixing ratios up to 60 ppt. For O_3 excess, only small mixing ratios, mostly below 5 ppt, were observed. Maybe surprisingly, the highest mixing BrO ratios coincided with no or only small ozone decreases. As will be argued below, these episodes of high BrO mixing ratios were likely the result of a recent and local release and the time between this release and the observation of the air mass was not sufficient to lead to considerable ozone destruction. Atmospheric conditions during these episodes are described and discussed in Sec. 7.1.3. The expected ozone destruction for different halogen presences is investigated in Sec. 7.1.4.

Particle concentrations

For the correlation of condensation particle concentrations to BrO mixing ratios, two clusters of values seem to exist. In one, the entire range of observed mixing ratios is associated with particle concentrations below 1000 cm^{-3}. When this is compared to the annual cycle of particle concentrations in Fig. 6.9, it becomes clear that the average background particle concentrations has its peak around 1000 cm^{-3} and hence this first cluster represents BrO for normal background conditions, depending on the season. With this the second cluster that seems to indicate a positive correlation between BrO mixing ratios up to 70 ppt and particle concentrations are observations under extraordinarily high particle concentrations. These could either be of anthropogenic origin, since vehicles and the exhaust of NM III station contain soot and other particles, or it could be correlation with natural new particle formation events that typically characterised by high concentrations of very small particles. The relationship between particle concentrations and BrO was investigated in detail in Sec. 7.4.

7.1.3 Characteristics of BrO activation periods

As discussed in Sec. 2.2.2, the temporal variations of the boundary layer mixing ratios observed in a particular location can be the product of multiple causes. Either the signal is a result of an inhomogeneous distribution of mixing ratios being advected past the instruments. In the context of elevated BrO mixing ratios and depleted ozone, this would be the case for an air mass into which bromine had been released and ozone destructed somewhere upstream prior to the observation. The temporal gradients of the observed quantities in this case would be determined by horizontal transport and, for depleted air masses not at the same altitude as observations, possibly vertical mixing dynamics.

In the extreme, in such a case instruments would only record the result of processes that occurred in the past and whose characteristics are not necessarily related to those at the measurement location in terms of local atmospheric and environmental conditions. Hence it is difficult or impossible to infer these conditions solely based on the observed variation of mixing ratios. For such measurements, typically air mass back-trajectories are calculated and correlated with factors that are relevant for investigated processes such as surface contact time with sea ice surfaces, properties of these surfaces along the trajectory, or exposure to cumulative amounts of solar radiation (e.g. in Saiz-Lopez et al., 2007a; Frieß et al., 2011; Mastromonaco et al., 2016). While such episodes allow to assess the broader influence of halogen chemistry on the boundary layer or a potential export of halogens to the free troposphere following a release episode, it is difficult to study the actual release mechanisms with such observations.

In the other extreme, observed mixing ratios in a static atmosphere could be the result of purely local processes, similar to studying a reaction chamber experiment. In the real atmosphere this hardly ever occurs, since it would require practically absent vertical mixing and horizontal transport. The temporal variations of mixing ratios observed in such a case then would be determined by both physical and chemical source and sink mechanisms such as reactions between compounds, photolysis rates, or deposition as well as the mixing on the spatial scales of the contained volume, depending on the distances between sources and the measurement.

When wind speeds and hence horizontal transport are not negligible, which generally is the case at NM III, an observation of quasi-local processes would still be possible, if the relevant conditions upstream would be the same as in the measurement location. Assuming a typical wind speed of $5\,\mathrm{m\,s^{-1}}$, as was often the case when elevated BrO mixing ratios were observed, and that air flow is only horizontal (i.e. no mixing with air from higher altitudes), a 12 h observation period corresponds to a catchment area radius of 216 km. For observations in many locations, homogeneity of e.g. surface properties on such scales is not a reasonable assumption. However over the open ocean or the sea ice region, it could be argued that conditions are similar on the scale of several hundreds of kilometres. For air masses in the coastal region of the Antarctic continent, homogeneity still might be assumed for trajectories that pass over snow surfaces with comparable properties, with respect to halogen chemistry e.g. at a constant distance to the coast and hence comparable influence of the ocean (the sea ice) on the surfaces e.g. in terms of sea salt aerosol deposition or irradiation.

In reality, observations are most likely to be a combination of both processes with one being dominant. In Hausmann and Platt (1994), where similar scenarios were discussed, model estimates for the temporal evolution of the transition zone between an air mass

depleted in ozone and the surrounding air masses can be found. Assuming an initial plume containing ozone depleted and BrO enriched air, they describe the broadening of the transition zone caused by turbulent diffusion. Thus the observed temporal variation of ozone and BrO in a fixed measurement location would depend on the degree of smoothing and hence turbulent diffusion. In the following it will be argued, that for the LP-DOAS observations at NM III, while containing examples that come very close to both idealised cases discussed above, in the majority of cases the local effects dominated and for selected periods the temporal variations of mixing ratios can be described by chemical processes. In the following, example periods for both situations will be presented and compared.

BrO during ozone depletion events

The lack of coverage by LP-DOAS observations due to meteorological conditions in late winter and early spring was already discussed in Sec. 6.4.1. When comparing the available measurements to the data by the ozone monitor, several of the most pronounced ODEs are missing in the LP-DOAS data set. The BrO observations during these periods obviously suffer from the same lack sufficient visibility conditions. Therefore, during typical ODEs, the phenomenon that initially drew the attention to polar halogen chemistry, the LP-DOAS setup at NM III is relatively 'blind'. Fig. 7.6 shows one of the few periods with a considerable decrease in O_3 and simultaneous LP-DOAS measurements.

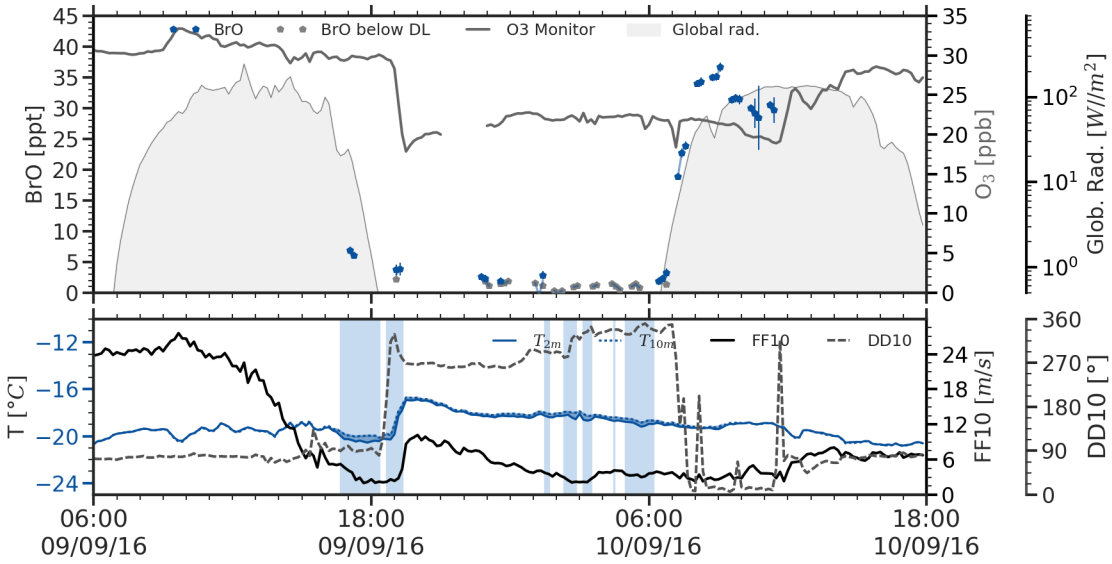

Figure 7.6: Example period for an observation of elevated BrO during an ozone depletion event (ODE). The detection of BrO follows the advection of an air mass that prior had been subjected to halogen induced ozone destruction and thus contains lower ozone mixing ratios and bromine compounds that react to BrO upon illumination.

The top panel shows O_3 and BrO mixing ratios together with global radiation (on a logarithmic scale) and the lower panel core meteorological data. Areas shaded in blue indicate times with surface inversions when the difference between the 10 m (dotted blue) and the 2 m temperature (solid blue) is larger than +0.25 K. Wind speeds in 10 m altitude

(FF10) are plotted in a black solid line, wind direction in 10 m altitude (DD10) are plotted in dashed grey.

At the beginning of the depicted period, wind speeds are very high with directions from the north east, typical conditions during a storm induced by a low pressure system north west of NM III (see Fig. 6.4 and Sec. 6.2.1). Temperatures are around -20 °C and the absence of a temperature difference between the two altitudes indicates a well mixed boundary layer.

At around noon on September 9th, wind speeds start to decrease and fall below 5 m s^{-1}. A surface temperature inversion starts to form. Between 6 pm and 7 pm, wind directions turn from 90° via 300° to 280°. Simultaneously wind speed picks up to 11 m s^{-1} and the temperature quickly rises by 3 K indicating a change of air mass. With this change of air mass, ozone mixing ratios drop from around 29 ppb to 18 ppb within 40 min (i.e. at a rate of -16.5 ppb h^{-1}). This high rate and the fact that no solar radiation is available indicate that this change in ozone mixing ratios cannot be induced by photolytic halogen chemistry.

Throughout the night, ozone mixing ratios increase slightly and the wind slowly turns to northerly directions. Immediately at sunrise, at a global radiation of less than 10 W m^{-2}, BrO mixing ratios increase to around 35 ppt within 90 min (+21.6 ppt h^{-1}), showing that the air mass advected the previous evening contained bromine species, either in the form of a reservoir species or on aerosol surfaces that now are photolysed respectively released. At BrO mixing ratios around 35 ppt the ozone mixing ratio decreases by about 3 ppb in 5 h (-0.6 ppb h^{-1}) before around noon the wind starts to change to easterly directions and picks up causing a loss of the LP-DOAS measurement signal and an abrupt increase of ozone mixing ratios by 6 ppb in just 20 min (+18 ppb h^{-1}), indicating another change of the observed air mass.

BrO during local bromine release

Rather than being induced by transport, the majority of days with observations of elevated BrO at NM III are characterised by conditions that very likely are dominated by local (or resorting to the argument of the great horizontal homogeneity in coastal Antarctica) quasi-local processes. One example for such a period is shown in Fig. 7.7. The depicted period starts on February 13th at wind speeds around 12 m s^{-1} from easterly directions and blowing snow conditions that prevented LP-DOAS measurements. Due to the time of the year these stormy conditions are associated with high temperatures just below 0 °C. In the late afternoon of the 13th wind speeds start to decrease. The reduced vertical mixing and a negative surface temperature budget lead to the formation of surface temperature inversion.

At sunrise on the 14th, a modest increase of BrO mixing ratios from below the detection limit to 3.5 ppt in 5 h (+0.7 ppt h^{-1}) is visible. When the net energy balance of the surface turns positive just before noon (compare also Fig. 6.3 that contains a part of the period shown in Fig. 7.7), the temperature inversion vanishes and mixing ratios decrease. When the inversion reforms in the afternoon, BrO rises from a minimum of around 2 ppt to 7 ppt in 6 h (+0.8 ppt h^{-1}). During this period ozone mixing ratios show a very small decrease of roughly 0.5 ppb, below the uncertainty of the ozone monitor.

Due to low wind speeds and hence reduced vertical mixing through turbulence from the 14th to the 15th, a stronger temperature inversion than in the previous night develops. At sunrise, BrO mixing ratios quickly increase from below the detection limit to 29 ppt from

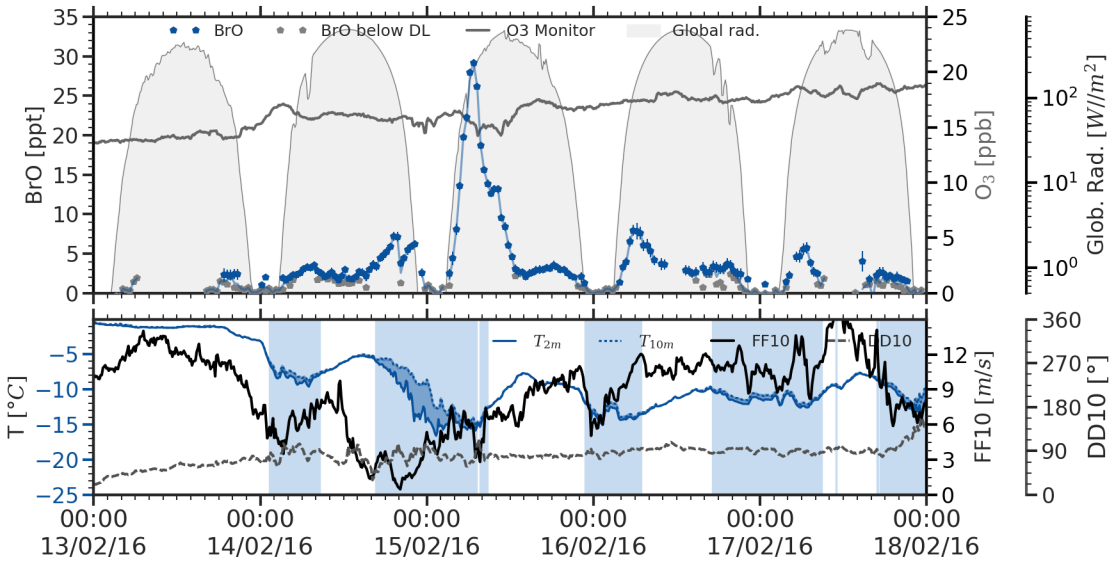

Figure 7.7: Example period of elevated BrO mixing ratios attributed local release processes. The period is characterised by a preceding storm followed by an initial day of low BrO mixing ratios before repeated, fast releases of BrO are observed.

3:15 until 6:45 (+8.3 ppt h^{-1}). This increase in BrO is associated with a decrease of O_3 mixing ratios from 16.5 ppb to 14.5 ppb (-0.4 ppb h^{-1}).

The increasing solar radiation reduces the temperature inversion an eventually leads to increased vertical mixing. Probably due to this, at around 7:00 BrO mixing ratios quickly drop by 16 ppt in two and a half hours (-6.5 ppt h^{-1}). An additional effect that has to be considered here is the increase of HO_2 mixing ratios with increasing solar radiation (formation via reactions R 1 to R 3), which reacts with BrO and thus decreases mixing ratios (R 52). When the resulting HOBr, however, reaches a surface containing bromide, it can form Br_2 (R 50) and subsequent release and photolysis (R 50) can lead to an increase of active bromine in the atmosphere.

Wind speeds around 9 m s^{-1} and cloud cover in the afternoon of the 15th probably limit the formation of a temperature inversion, which in turn limits the increase of BrO mixing ratios which stay around 2-3 ppt for the rest of the sunlit day.

During the night a weak temperature inversion develops and on the following day with increasing radiation another increase of BrO mixing ratios to 8 ppt within two and a half hours (+3.2 ppt h^{-1}) is visible. With a break up of the surface inversion the daily cycle of the previous day is repeated. Despite the lower peak mixing ratio in the morning, afternoon BrO mixing ratios reach levels around 3 ppt comparable to the previous afternoon. This might be due to an earlier formation of the temperature inversion. On the 17th the daily cycles again is repeated, however with further decreased peak mixing ratios of 5 ppt attained in the morning. Wind speeds at 13 m s^{-1} around noon briefly interrupt LP-DOAS observations. In the afternoon BrO mixing ratios of 2 ppt are reached.

An interesting observation during this period is the evolution of the peak mixing ratios attained on the different days. There are different ways to interpret this. The peak mixing ratios either could be determined by the atmosphere with higher mixing ratios for lower wind speeds and stronger surface inversions (i.e. smaller vertical mixing). Alternatively,

the 14th could be interpreted as the build up bromine compounds that led to a strong release on the 15th which might have depleted the reservoir of bromide on surfaces. Consequently, the peak mixing ratios on the following days steadily decrease. This question and the potential source of the bromine compounds for this local release is discussed in detail on the basis of another example period in Sec. 7.1.5.

7.1.4 Comparison of local release and transport induced episodes

Depending on the available instrumentation, the are different ways to assess whether an observed bromine trace gas signal was induced by transport or local chemistry. One that was already used above and has been used before (e.g. in Hausmann and Platt, 1994) is to determine the change rate of ozone mixing ratios and compare them to measured trace gas mixing ratios or model output based on suspected mixing ratios . Another way of distinguishing (quasi-) local chemistry from advection is to investigate the vertical structure of the atmosphere. Assuming that the halogen activation is linked to ground surfaces, a local release should be limited in vertical extent (however depending on the local convection and turbulent diffusion). The profile retrieval algorithm with MAX-DOAS observations of slant column densities yield an optimal estimation of the vertical distribution BrO mixing ratios (see Sec. 4.3). Both approaches will be tested in the following with selected examples from the NM III time series.

Observed ozone depletion rates

When the data from the ozone monitor at NM III is used, also the strong ozone depletion events can be included in the analysis, which were not accessible by LP-DOAS due to frequent blowing snow conditions they were associated with. Based on their estimates and the BrO observations available by that time, Hausmann and Platt (1994) concluded that for O_3 loss rates in excess of -1.5 ppb h^{-1} it is unlikely that BrO-catalysed local destruction of ozone can explain the observed ozone temporal gradients. With a threshold of 3 ppb absolute decrease in O_3 ratios, on 29 days rapid decreases of ozone could be identified during the observations at NM III. The associated loss rates range from -0.6 ppb h^{-1} (on August 4th 2016) to -134.4 ppb h^{-1} when O_3 mixing ratios dropped from 32,3 ppb to 11.1 ppb within only 5 min on July 29th 2017. The average loss rate was -13.6 $\pm$ 25.0 ppb h^{-1} and in most cases well above the threshold given by Hausmann and Platt (1994). In a number of cases, similar to the example in Fig. 7.6, a clear indication for the transport related nature of the O_3 decrease was an onset of the depletion in darkness. For most other episodes, clear indication in the corresponding meteorological data was seen when mixing ratios started to decrease.

For a few cases ongoing halogen chemistry in an air mass already depleted in ozone could be observed. An example of such a case of a combined influence of advection and chemistry within the air mass can be seen in Fig. 7.8

In this case, ozone mixing ratios start to decrease before sunrise and decline throughout the day. After sunrise the BrO mixing ratio initially increases to 40 ppt and during the day varied in anti-correlation with O_3 mixing ratios reaching up to 50 ppt. These short term variations probably are caused by either horizontal or, given the frequent occurrence of complex structured layers in the polar atmosphere (see Sec. 2.2.2), more likely vertical inhomogeneities in the air mass advected past the instruments at NM III. This is also

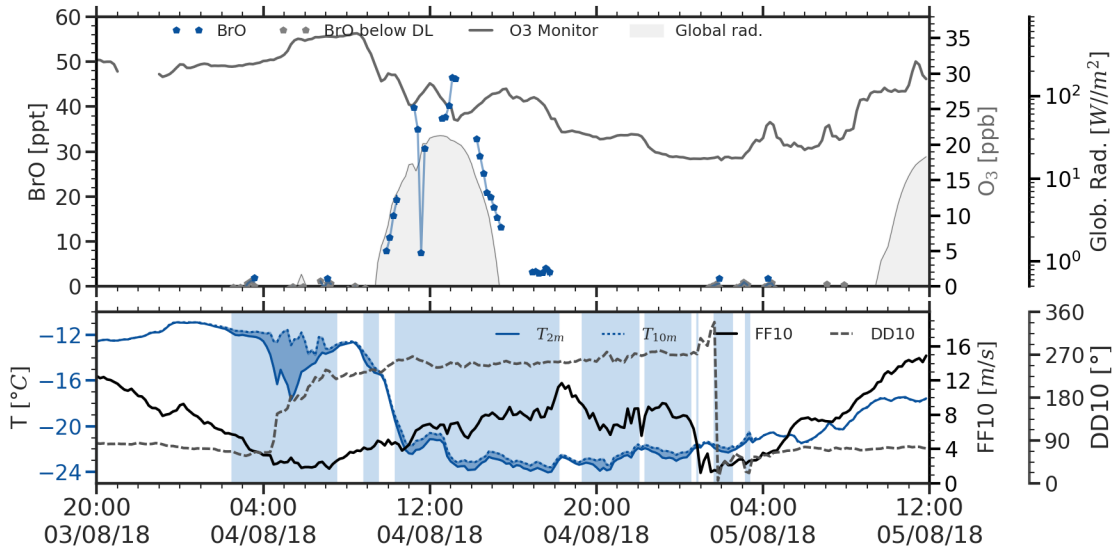

Figure 7.8: Example period with an observed decrease of ozone mixing ratios resulting from a combination of advection and local chemsitry. Ozone mixing ratios drop before, during the day, elevated BrO mixing ratios are observed that contribute to a further depletion of ozone in the air mass.

supported by almost continuous surface temperature inversion during the episode. After sunset, ozone mixing ratios continue to decrease until winds turn to easterly directions and pick up inducing rising O_3 mixing ratios.

Note the low levels of global radiation (with a peak around 35 W m^{-2}) in this episode. A recent point of discussion in the scientific community were the required irradiance levels for a formation of BrO. For instance Mastromonaco et al. (2016) proposed a night-time depletion of gaseous mercury through reaction with molecular bromine (rather than reaction with BrO - see Sec. 2.5.2) based on the analysis that an observed air mass had only been subjected 6-7 W which they argued to be insufficient for BrO formation. Similarly S. Brooks et al. (2011) argued that on the Greenland ice sheet SZAs of 85° and below would be required to observe BrO induced mercury depletion. In this episode however, BrO mixing ratios of up to 20 ppt were measured in the morning of the 4$^{\text{th}}$ of August at an irradiance of just 8 W m^{-2} at an SZA of 91.2° which suggests that already very low light levels before sunrise are sufficient for BrO formation.

Estimating ozone depletion during local halogen activation episodes

For the example period for potentially local bromine chemistry discussed above, the measured ozone depletions for the majority of days with elevated BrO mixing ratios in the NM III data set are small (<1 ppb h^{-1}). If these small decreases of ozone are exclusively caused by local chemistry, the observed loss of ozone should be explainable solely based on locally observed halogen mixing ratios. This was investigated using a very simplified description of reaction rates.

It was assumed that the observed ozone loss is solely caused by the self reaction of BrO, providing a lower limit for the ozone destruction rate. The self reaction pathways introduced above for generic combinations of halogens (R 28 to 31) are shown below in

reaction set R 68 for the BrO-BrO reaction with according rate constants calculated for T=250 K:

	at 250 K	
$BrO + BrO \longrightarrow Br_2 + O_2$	$k_1 = 2.7 \cdot 10^{-12} cm^3 s^{-1}$	(R 28 revis.)
$\longrightarrow Br + Br + O_2$	$k_2 = 7.1 \cdot 10^{-13} cm^3 s^{-1}$	(R 29 revis.)
$\longrightarrow OBrO + Br$	negligible	(R 30 revis.)
$+ M \longrightarrow X_2O_2 + M$	negligible	(R 31 revis.)
	Rates: (R. Atkinson et al., 2007)	(R 68)

For a description of the ozone destruction only reactions R 28 revis. and R 29 revis. in R 68 have to be considered. In addition to a negligible branching ratio in the possible reactions of the BrO-BrO self reaction, the formation of OBrO would not lead to a net ozone destruction as is would quickly be photolysed and the resulting oxygen atom would react back to ozone. The bromine molecule formed in 28 revis. during the day is also quickly photolysed.

$Br_2 + h\nu \longrightarrow 2\,Br$	$j_1 = 4.4 \cdot 10^{-2}\,s^{-1}$	(R 24 revis.)
	(C. R. Thompson et al., 2015)	(R 69)

The bromine atoms (either formed in R 29 revis. or in R 69) then destroy ozone:

$Br + O_3 \longrightarrow BrO + O_2$	$k_3 = 6.3 \cdot 10^{-13} cm^3 s^{-1}$	(R 25 revis.)
	(R. Atkinson et al., 2007)	(R 70)

In this catalytic cycle, the self reaction(s) (R 68) are the rate limiting step (Hausmann and Platt, 1994). The temporal evolution of the ozone mixing ratio therefore can be described by the following equation:

$$\frac{d[O_3]}{dt} = -\frac{d[Br]}{dt} = -2 \cdot (k_1 + k_2) \cdot [BrO]^2 \tag{7.1}$$

For the comparison between between observed ozone mixing ratios and those thus estimated, the cumulative destruction of ozone over the entire day based on the observed mixing ratios of BrO was calculated. The starting O_3 mixing ratios was selected at a time before sunrise. Observed increases of ozone mixing ratios through the course of the day (e.g. through vertical mixing) were not considered. Calculated and observed O_3 mixing ratios therefore can only expected to agree as long as the variation of ozone is controlled by local chemistry. In Fig. 7.9 the results of this calculation for one day of the example period in Fig. 7.7, February 15th, 2016 is shown. In Fig. 7.10 results for the day with the highest observed BrO mixing ratio throughout the entire observation period is shown. For both examples, as long as BrO mixing ratios monotonically increase, there is a good agreement between estimated and observed ozone mixing ratios. A soon as BrO mixing ratios vary on short time scales (indicating the influence of a separate air mass or mixing) or start to decline when the morning temperature inversions disappear, as expected, the estimated values start to deviate from the observations. The ozone depletion rates for the periods of

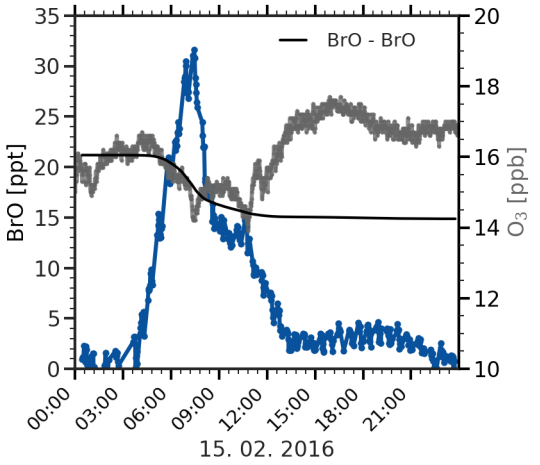

Figure 7.9: Estimation of ozone destruction by BrO on February 15th 2016 based on the BrO BrO self reaction

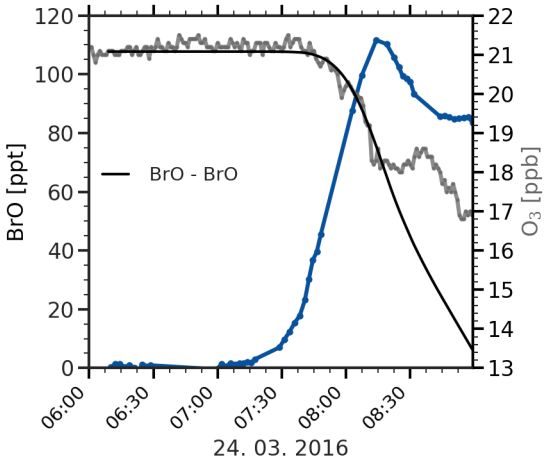

Figure 7.10: Estimation of ozone destruction by BrO on March 24th 2016 based on the BrO BrO self reaction

good agreement between the estimate and the observation are -0.26 ppb h^{-1} for February 15th, 2016 and -2.44 ppb h^{-1} for March 24th, 2016 respectively. When the entire day of the 24th is considered (Fig. 7.11), it becomes clear that these extraordinarily high BrO mixing ratios could deplete the background ozone mixing ratios of around 20 ppb during that time of the year within six and a half hours corresponding to a loss rate of 3.1 $ppbh^{-1}$ (see intersect of grey dashed lines in Fig. 7.11).

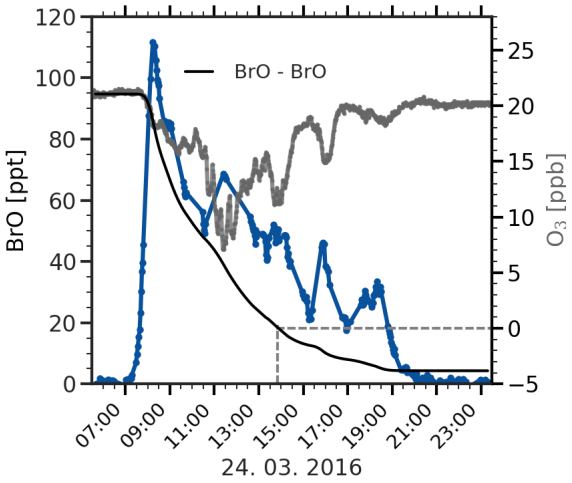

Figure 7.11: Estimation of ozone destruction by BrO on March 24th 2016 based on the BrO-BrO self reaction calculated for the entire day of observations.

For a proper assessment of the chemistry resulting in the observed mixing ratios, an actual chemistry model would be required. In particular loss processes of BrO are not considered in the simple estimates presented above. However, it could be argued that the uncertainty introduced by this is greatly reduced when, as was done here, the actual evolution of BrO mixing ratios is used to estimate the ozone depletion rather than running

the calculation with a fixed starting mixing ratio for both ozone and BrO. Given the simplicity of the approach, the agreement between estimates and observations is surprisingly good. Regarding this approach, it should be noted that, while the central role of the self reaction together with the bromine explosion was assumed to be the dominant mechanism in many publications (e.g. Hausmann and Platt, 1994; Le Bras and Platt, 1995; Simpson et al., 2007; Cao et al., 2014; Cao et al., 2016b), recent observations high mixing ratios of dihalogens (Pratt et al., 2013; Liao et al., 2014; Custard et al., 2016; Custard et al., 2017; S. Wang and Pratt, 2017) have put the role of the photolysis of snow sourced dihalogens in the depletion of ozone into focus. C. R. Thompson et al. (2017), based on a modelling study, argue that the photolysis of released dihalogens is comparable and under certain conditions even dominant over the recycling of bromine atoms via the self reaction.

Vertical distribution

Investigating the vertical distribution of BrO mixing ratios can help the interpretation of surface based observations such as LP-DOAS measurements, in particular when short term fluctuations are observed, which could be the result of mixing between atmospheric layers with different mixing ratios (see e.g. Fig. 7.11).

Simultaneous observations of elevated atmospheric extinction related to aerosols and activated bromine potentially contain information on recycling and transport of reactive bromine (Simpson et al., 2017). Also for estimating the overall impact of halogen chemistry on the troposphere or for a comparison of ground-based and satellite observations, information about the vertical distribution of halogen mixing ratios is valuable.

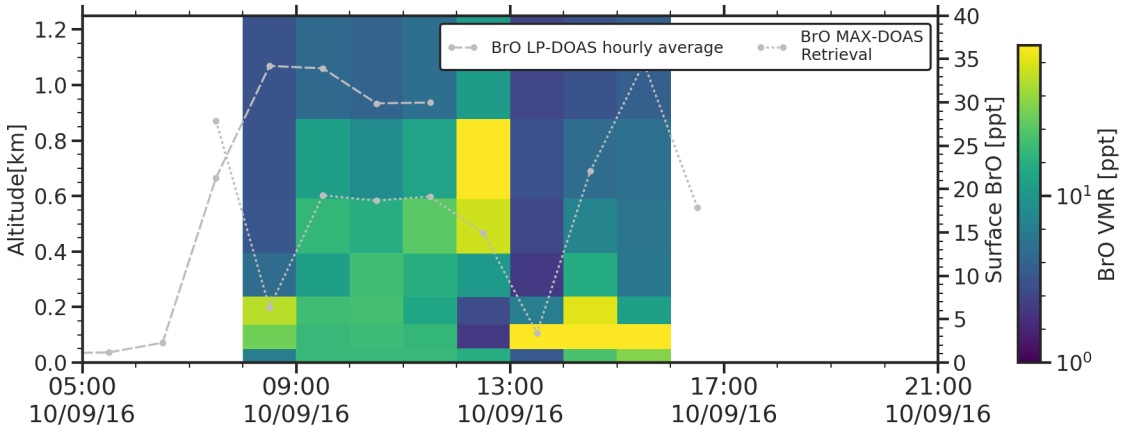

Figure 7.12: Vertical distribution and surface mixing ratios of BrO on September 19th as determined from the MAX-DOAS retrieval (colour code and dotted grey line) and measured by the LP-DOAS 8dashed grey line.

While a systematic analysis of the profile retrieval results of the co-located MAX-DOAS instrument would go beyond the scope of this thesis, results corresponding to the two example periods already discussed in Sec. 7.1.3 will be briefly presented in the following to illustrate the differences in spatial distribution for advection induced and local released BrO mixing ratios. Analysis of the slant columns and the retrieval of the vertical profiles was performed by U. Frieß (personal communication, 2018) and the resulting data were kindly provided for this thesis. For a more detailed discussion of vertical distributions of

BrO in polar regions, the interested reader is referred to recent publications (e.g. A. E. Jones et al., 2010; Frieß et al., 2011; Peterson et al., 2015; Peterson et al., 2017; Simpson et al., 2017; Peterson et al., 2018; Prados-Roman et al., 2018).

The two examples of vertical distributions discussed in the following correspond to selected days during the two example periods discussed above (Fig. 7.6 and Fig. 7.7). The temporal coverage of the MAX-DOAS observations during these two days reflects the availability of solar radiation of sufficient intensity for measurements. For comparison with the surface observations in Fig. 7.6 and Fig. 7.7, the LP-DOAS BrO mixing ratios and the results for the surface box of the MAX-DOAS retrieval were plotted together with the vertical profiles. Even though, these profiles are determined up to 4 km altitude, based on the averaging kernels, a measure for vertical sensitivity of the observations, the vertical extent of the retrieval results was limited.

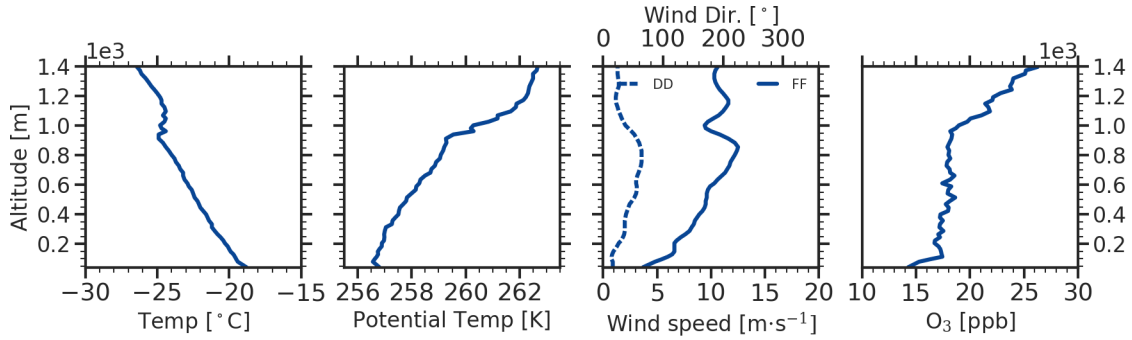

Figure 7.13: Vertical profiles of temperature, potential temperature, wind speed and direction at 10:53 on September 10th, 2016

For the profiles of September 10th 2016, the example for a transport induced period of depleted ozone and elevated BrO mixing ratios, in the first half of the day, an increase of the mixing height of elevated BrO from the first three boxes up to 250 m at 9:30 to the first six boxes at 12:30 is visible (corresponding to an altitude of about 900 m). As can be seen in Fig. 7.13 in the vertical profiles of temperature, potential temperature, and O_3 partial pressure of a radiosonde launched at 10:53, this altitude corresponds to the boundary layer height at that time. The radiosonde data thus still covers the period of depleted ozone from the evening of September 9th to the 10th around noon (compare to Fig. 7.6).

The vertical distribution of both BrO in the MAX-DOAS profiles and the radiosonde ozone data support the interpretation of this episode being the result of advection of an air mass with previous bromine activity. Similar to the argumentation in the comparison of MAX-DOAS and LP-DOAS surface mixing ratio observations in Sec. 5.3.1, the higher BrO surface mixing ratios observed with LP-DOAS indicate vertical gradient with higher mixing ratios close to the ground. The signal of this distribution is attributed the the entire lowermost box in the MAX-DOAS retrieval leading to lower mixing ratios. Based on the ratio of both mixing ratios, signals of both instruments would agree for vertical extent of 35 m for the layer of elevated BrO.

Reduced ozone levels around 18 ppb observed in the vertical profile in Fig. 7.13 between 60 m and 900 m above sea level (NM III station is at 43 m above sea level) probably are the result of the previous ozone destruction while the shallow layer in immediate contact with the surface shows an additional depletion. It is probably the result of ozone destruction by

the elevated BrO mixing ratios observed on September 10th with both MAX-DOAS and LP-DOAS. The stronger destruction at the surface could indicate an additional input of bromine via heterogeneous or other surface related activations mechanisms thus sustaining levels of active bromine in the air mass.

The MAX-DOAS vertical profiles for the remainder of the day from 13:30 to 15:30 then seem to show an air mass with a different vertical distribution of BrO, limited to the lowermost 200 m. Unfortunately no LP-DOAS observations from this period are available. The retrieved peak in BrO surface mixing ratios of around 35 ppt at 15:30 coincides with a smaller dip in ozone mixing ratios of about 2 ppb (see Fig. 7.6) indicating that also in this new air mass bromine chemistry was active prior to advection. It also illustrates how the complex vertical structure of the polar atmosphere during halogen activation episodes influences surface observations (for a detailed discussion see also A. E. Jones et al., 2010).

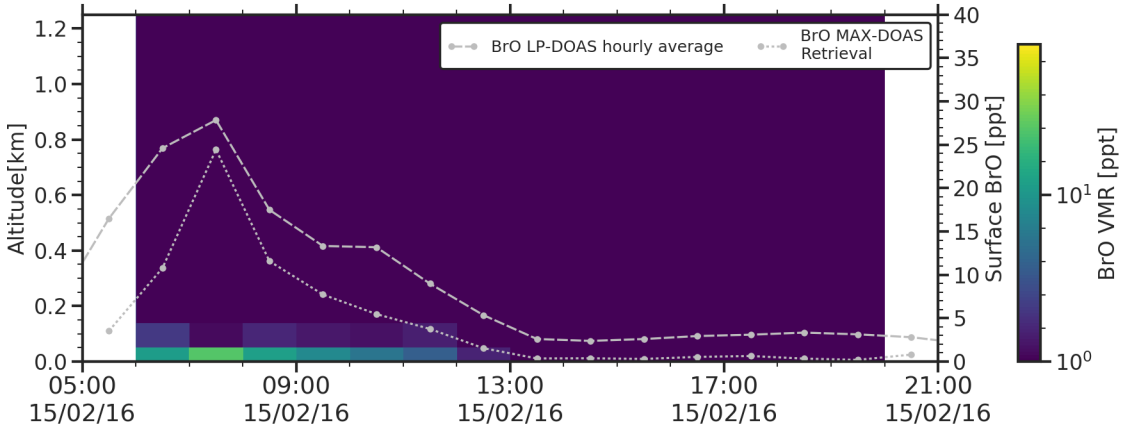

Figure 7.14: Comparison of retrieved MAX-DOAS vertical profiles and surface mixing ratios of BrO with LP-DOAS observations on February 15th, 2016. Mixing ratios in the profiles are confined to the lowermost boxes of the retrieval grid and disappear with the onset of turbulent mixing around noon.

The vertical profiles for the example period of local halogen release on February 15th, 2016 contrast the previous case (see Fig. 7.14). The profiles retrieved from the MAX-DOAS observations show that the presence of BrO is clearly limited to the lowermost layers of the atmosphere on February 15th. Build up, peak and decrease of surface mixing ratios from both DOAS instruments agree fairly well with the LP-DOAS mixing ratios again about 30% higher, pointing to avertical gradient. The box height for an equivalent MAX-DOAS signal would be between 20 to 30 m. The vertical profiles of temperature, potential temperature, and wind conditions (see Fig. 7.15 - unfortunately no ozone sonde was launched on this day) still show a very shallow surface inversion layer that immediately after the launch at 10:49 started to disappear and with it BrO mixing ratios decreased (compare also to Fig. 7.7). Correcting for the station altitude, the vertical extent of this layer is between 100 m and 150 m and thus in agreement with the retrieved BrO vertical distributions. In conclusion, the analysis of vertical distributions of bromine monoxide and ozone mixing ratios supports the interpretation of the dynamics of the two types of activation periods based on the combined information of the available surface sensors

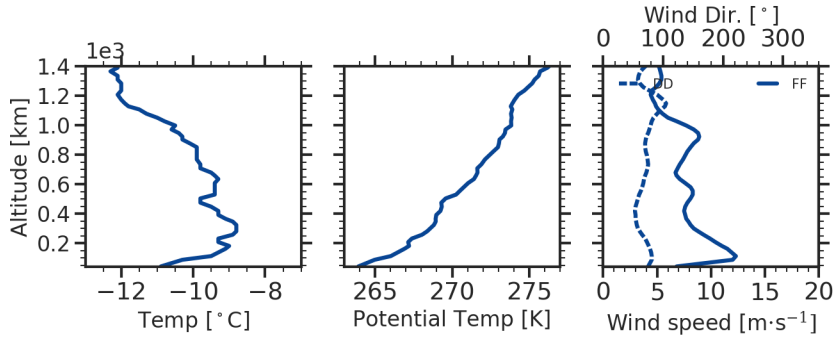

Figure 7.15: Vertical profiles of temperature, potential temperature, wind speed and direction from a radiosonde launched at 10:49 on February 15th, 2016

Local bromine release in spring

In the period of increased bromine activity from late summer to autumn, the lack major ozone depletion events (except for one episode on March 24th, 2016 when the maximum BrO mixing ratios of the entire observation period were detected, see e.g. Fig. 7.11) and the simultaneous occurrence of very high BrO mixing ratios suggests that most events are dominated by local processes. The local bromine activation is however not limited to this time of the year. Also during the late winter and spring period of increased activity, local release during calm conditions can be observed. In many cases a stormy period associated with the advection of an air mass containing bromine seems to initiate local release. An example for such an episode is shown in Fig. 7.16 Following a storm on August 7th, the

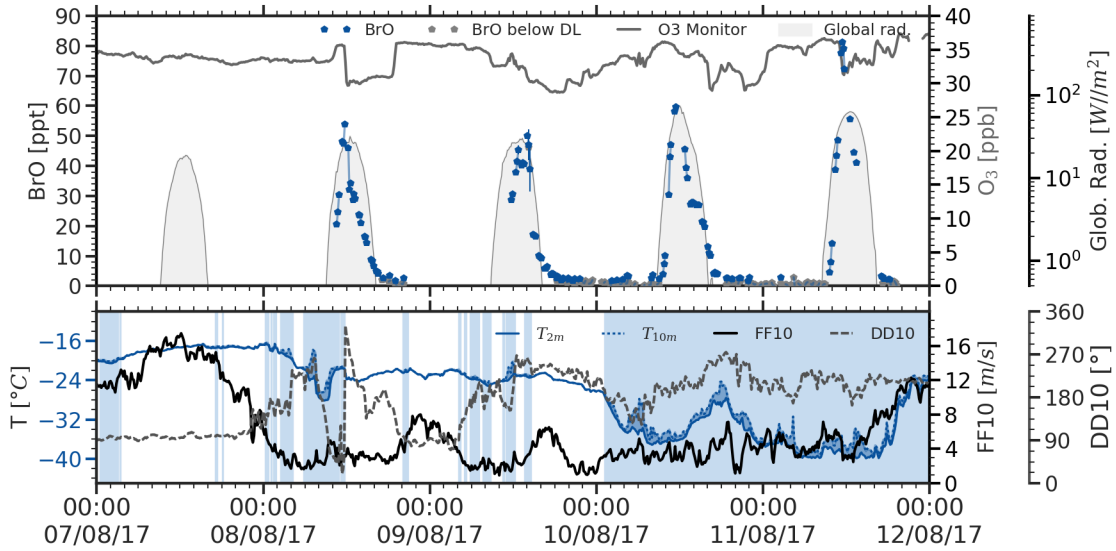

Figure 7.16: Example period with elevated BrO mixing ratios from a local release event from August 7th to 11th, 2017.

following day a change of wind directions coincides with a sudden drop in ozone and the detection of BrO by the LP-DOAS. Over the following days wind speeds lie between 2 and 7 $\mathrm{m\,s^{-1}}$ and wind directions from south-westerly directions dominate. Under these

increasingly calm conditions temperatures drop from around -20 °C to just over -40 °C on the 11th. From the 10th onwards a constant surface temperature inversion is visible as the global radiation is not strong enough to break it up around noon as was observed e.g. in Fig. 7.7. From the 8th to 11th BrO peak mixing ratios from 50 up to 80 ppt are observed. Due to reduced or absent convection, in particular on the latter two days the daily cycles seems to follow the global radiation. Judging from the variations of O_3 mixing ratios that during the period of constant surface temperature inversion show decreases not linked to bromine mixing ratios, probably vertical mixing between previously separated air masses or vertical layers additionally influences the observed time series.

Local bromine chemsitry during Polar day

In contrast to the dark winter months, from October into December just before or during Polar day, radiation almost continuously is available. In the seasonal histogram for BrO (Fig. 7.2), this time of the year is characterised by frequent activation but low levels of bromine monoxide. The cause for this can be seen in an example period in Fig. 7.17 starting at the first day of polar day at NM III (November 15th, 2017).

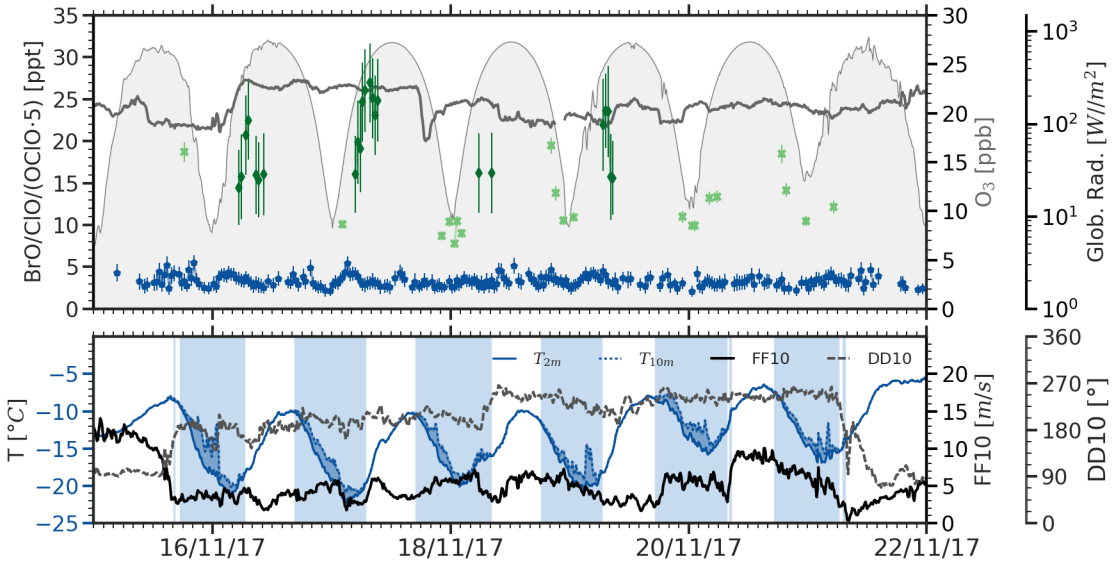

Figure 7.17: Example of continuous presence of BrO (blue) during polar day from November 15th to November 21st, 2017. Additionally mixing ratios of ClO (dark green) and OClO (light green) are shown. Note that clarity only observations above the detection limit were plotted.

During the entire period, wind speeds range between 2 and 5 m s^{-1} with occasional increases to 7 m s^{-1}. Winds constantly come from southerly to south-westerly direction. Under these conditions, the daily temperature cycle shows radiation-induced amplitudes between about -10 °C and -20 °C. Every night a surface temperature inversion forms and modulates measured BrO mixing ratios until the daily breakup of the inversion. Ozone mixing ratios during the episode vary slightly, but show no major impact of BrO induced local production. The observations of ClO and OClO, also plotted in Fig.7.17 will be discussed in the following sections.

Despite the constant availability of solar radiation, only mixing ratios of 2-5 ppt, very

close to the detection limit, were observed. This could either be because under consonantly available global radiation trace gases for bromine sink reactions are efficiently produced (e.g. HO_x - see 37). Surprisingly, the large variation of atmospheric stability with a frequent occurrence of convective mixing around noon is not really reflected in the temporal evolution BrO mixing ratios. In particular the break up of the surface temperature inversion that seems to strongly influence the ClO mixing ratios observed simultaneously does not lead to a convective dilution of BrO mixing ratios below the detection limit. Considering the alternative release pathway of dihalogens via photolytic production of OH in the surface layer (see Sec. 2.4.5 and R 60 to R 64), a peak production via this pathway around noon (J. L. Thomas et al., 2011) might counteract the loss through convection.

7.1.5 The role of the snow surface

Considering the observed annual cycle of bromine activity at NM III, the frequent and high mixing ratios from February to May pose the question of the relevant surface(s) for the observed halogen release. The onset of the autumn period of frequent BrO presence coincides with the minimum in sea ice extent around the Antarctic continent (see 2.4). Even though smaller patches of ice along the coast persist through summer and in the Weddell sea east of the base of the Antarctic peninsula multi-year sea ice exists, large areas of the Southern ocean are ice free in February.

In recent years, a potential role of snow surfaces both on sea ice and land in the release halogens has come into focus (e.g. J. L. Thomas et al., 2011; J. L. Thomas et al., 2012; Pratt et al., 2013; S. Wang and Pratt, 2017; Peterson et al., 2018). The vast snow surfaces on the ice shelves and the ice shield of coastal Antarctica constitute potentially very large source surfaces.

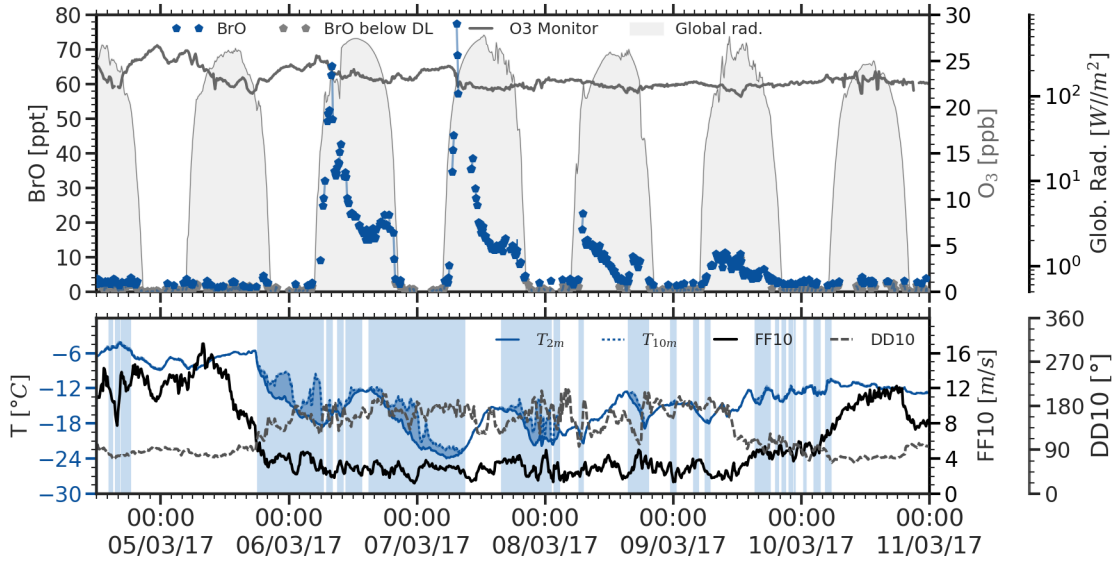

Figure 7.18: Example period for steadily decreasing BrO peak mixing ratios on a local release episode.

Several of the observations discussed above point to a central role of local snow surfaces for halogen chemistry. (1) Even during transport induced O_3 depletion events, the lowest detected ozone mixing ratios were measured close to the surface (see ozone sonde data

in Fig. 7.13). (2) Under the conditions observable by LP-DOAS measurements, surface temperature inversions are a prerequisite for elevated halogen mixing ratios. With limited vertical mixing, the source of activated bromine therefore has to be located inside the inversion layer. (3) The systematic difference between surface mixing ratios retrieved from MAX-DOAS observations and the measurements with the LP-DOAS indicate a strong vertical gradient with highest mixing ratios close to the ground. (4) If aerosol surfaces would be the dominant source, a correlation of peak BrO mixing ratios with particle concentrations might be expected. The absence of a clear correlation of BrO with particle concentrations might point to a central role of the snow surface. However, it should be stated, that detailed information about these particles is available, in particular no size distribution. The lack of correlation therefore probably should not be over-interpreted.

Evolution of a local bromine activation episode

Assuming the snow surface as the relevant source, the development and evolution during a local release episode, could proceed in the following steps (see Fig. 7.18).

(1) During storms regularly observed prior to the observations of local bromine activation, sea salt, either from sea ice surfaces or the open ocean, is transported and partly deposited on the snow surfaces in coastal Antarctica. Depending on the chemical properties of the aerosol (e.g. regarding surface pH, chloride to bromide ratio), after the storm, surfaces either might have to get acidified before becoming active for halogen release, or, e.g. when aerosols are older and already have a lower pH (Finlayson-Pitts and Hemminger, 2000), surfaces might directly contribute to an activation. For some episodes (e.g. the example in February 2016, Fig. 7.7), a day with smaller mixing ratios is observed between the end of the windy period and the first strong activation. In other cases (e.g. the example period in Fig. 7.18), the activation more or less immediately follows the drop in wind speeds (see March 5th and 6th, 2018 in Fig. 7.18).

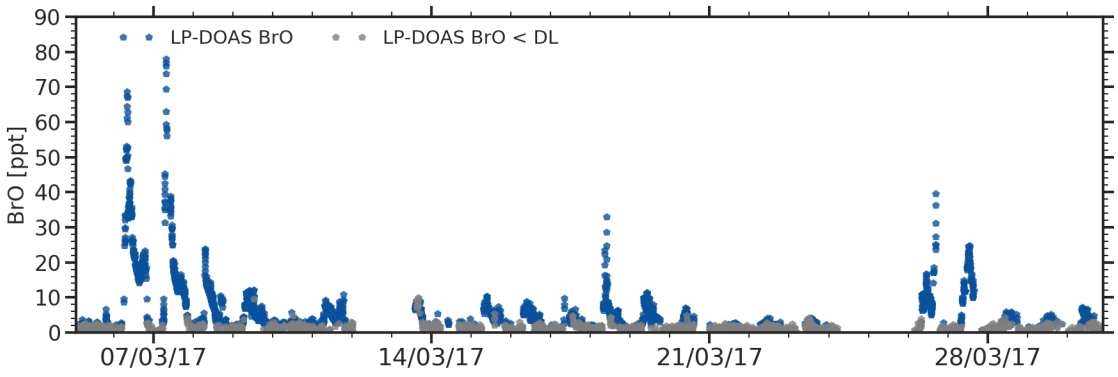

Figure 7.19: BrO mixing ratios as observed by the LP-DOAS throughout March 2017.

(2) Under calm meteorological conditions, bromine then is activated through release from the sea salt freshly deposited on the snow surface or from aerosol surfaces present within the surface inversion layer. The daily cycle of BrO mixing ratios is modulated by formation and build-up of surface temperature inversions as discussed above. With the break up of the inversion around noon, an export of bromine to higher atmospheric layer is possible.

(3) Continued release of bromine from the salty snow surfaces then leads to a depletion of the available bromide leading to increasingly smaller activation rates and observed mixing ratios of BrO on the days following the initial activation.

(4) The episode ends due to insufficient bromide in the snow surface layer or the next storm replenishes the salt and the next release episode starts. This dynamic can be seen e.g. throughout the entire month of March 2017 following the episode in Fig. 7.18 (see Fig. 7.19)

Analysing the ionic composition supports the hypothesis, that salt is transported to NM III during storms or episodes with elevated wind speeds. Fig. 7.20 shows the BrO mixing ratios from March 4th to 10th, 2017 together with mass concentrations of sodium ions, chloride, and bromide detected on aerosol filter samples. The sampling time is the interval prior to the respective data point.

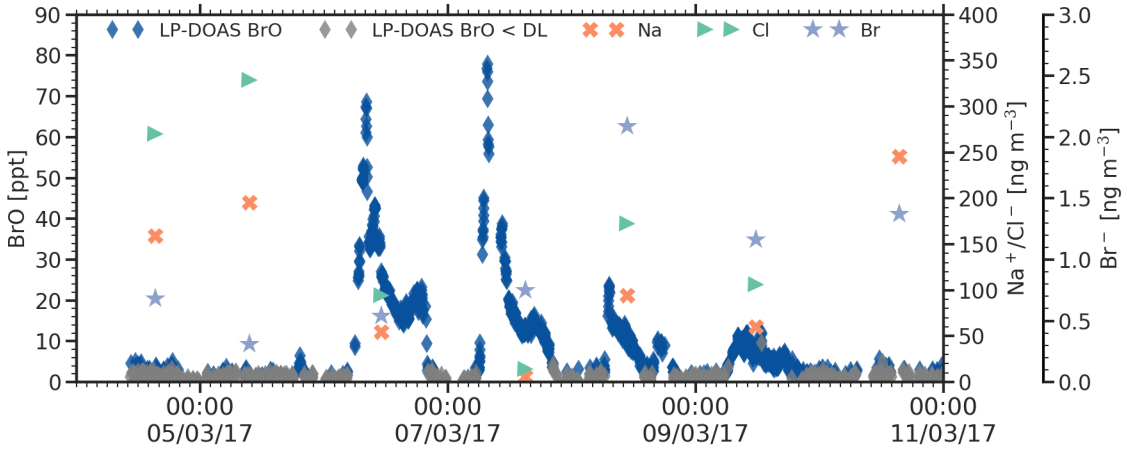

Figure 7.20: Relationship between aerosol ion mass concentrations and BrO mixing ratios for the example period in Fig. 7.18.

At higher wind speeds on March 4th and 5th, sodium and chloride mass concentrations are high (150-200 ng m^{-3} and 300-350 ng m^{-3} respectively), indicating a high salt content of the aerosols. At lower wind speeds on the 6th also ion mass concentrations drop and stay relatively low before increasing again with increasing wind speeds on the 10th. Interestingly, bromide mass concentrations show a slightly different behaviour. While sodium and chloride concentrations stay lower than on the first two days of the episode, bromide shows a very high concentration immediately after the second day of high BrO mixing ratios. Given the low winds speeds and limited advection, this might be due to an uptake of bromine species (e.g. HOBr) by local aerosols following the high mixing rations on the 7th.

As discussed previously, the variation of peak mixing ratios can be strongly influenced by the vertical atmospheric structure and dynamics. To investigate whether the observed continuous decrease of (peak) mixing ratios actually can be linked to a depletion of bromide on reactive surfaces, the vertical profile of the atmosphere for the 6th to the 9th was investigated.

The profiles of the potential temperature, shown in Fig. 7.21, indicate that the extent of the inversion layer reached very similar heights when the radiosondes were launched at around 11am on the four days. While this obviously only constitutes a single measurement

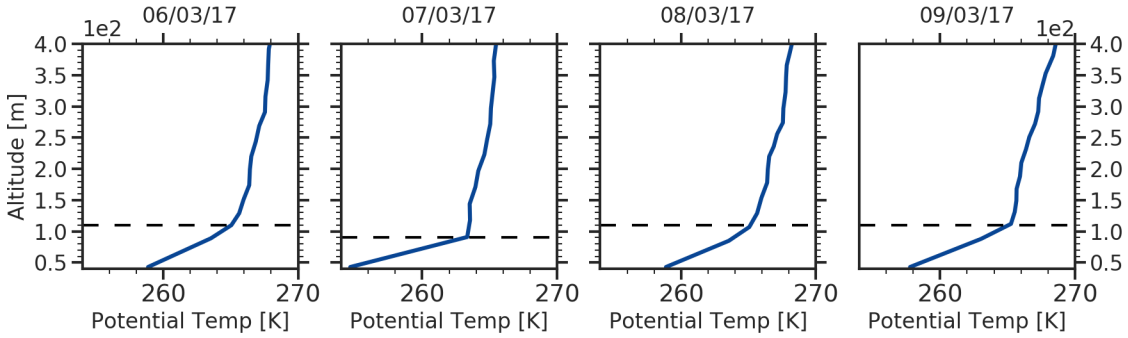

Figure 7.21: Comparison of potential temperature profiles from radiosondes from March 6th to 9th, 2017.

point for the entire day and a highly dynamic system, in combination with the similar meteorological conditions on the four days, a similar vertical extent of the surface layer might be assumed. The slightly higher mixing ratio on March 7th compared to the previous day could be the result of the slightly lower inversion layer or a stronger vertical temperature gradient (Fig. 7.21, second panel). The observed decrease in BrO mixing ratios with time after the start of an activation period therefore is probably not modulated by atmospheric dynamics (in contrast to the daily cycle) but indicates a permanent loss of bromine from the surface-lower boundary layer system. While deposition to local snow or aerosol surfaces would allow a later reactivation, a permanent removal could occur through convective transport out of the inversion layer followed e.g. by advection in higher altitudes.

When inspecting the MAX-DOAS vertical profiles for the three days with the highest BrO values during the period (March 6th to 8th, 2017), on the 7th 2 h before noon vertical mixing heights starts to increase from the lowermost 50 m to 140 m (i.e. the first two boxes of the retrieval grid). After noon on both the 7th and the 8th, elevated layers of BrO between 200-400 m and 1.2 km are discernible. Given that the increase of the mixing height and the occurrence of the elevated layers coincide with the sudden drop in the mixing ratios observed by the LP-DOAS, this suggests a vertical export of air masses with elevated BrO mixing ratios to higher altitudes of the boundary layer.

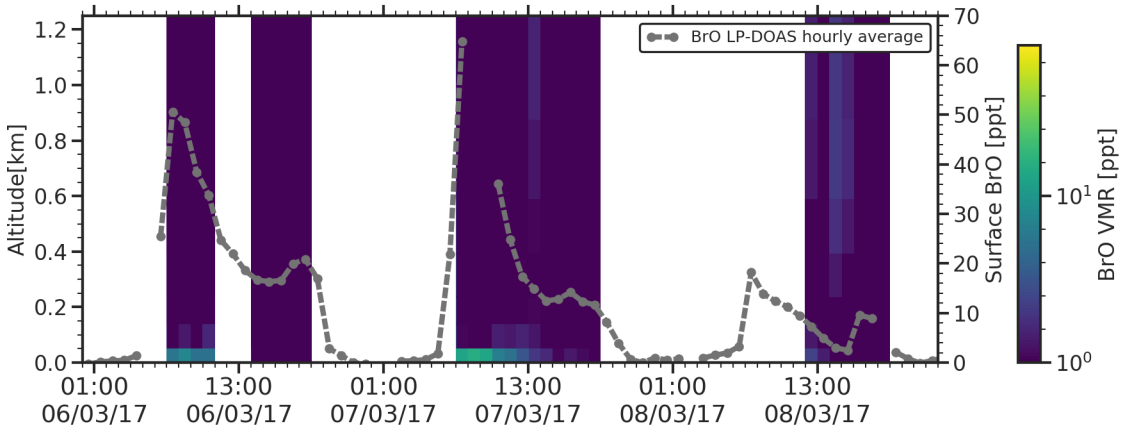

Figure 7.22: Vertical BrO distributions from MAX-DOAS observations for the beginning of March 2017. Additionally the surface mixing ratios observed by the LP-DOAS was plotted (grey dashed line).

Comparison to similar observations

Results of BrO observations at NM III can be compared to other observations on daily and on the annual time scale. From a vast number of publications on BrO observations two were selected that investigate aspects of particularly relevance to the observations described above.

In a study investigating the halogen chemistry over snow surfaces at Summit on the Greenland ice sheet (72.6° N, 38.5° W), J. L. Thomas et al. (2011) observed daily cycles very similar to those discussed here (see also the associated publications: Stutz et al., 2011; J. L. Thomas et al., 2012). Even though the measured BrO mixing ratios were much lower at Summit (in the order of a few ppt), the observed and modelled daily variation of atmospheric mixing ratios of BrO (additionally NO, NO_2, and O_3 were modelled) is very similar to that observed at NM III (see Fig. 7.23). As assumed for days with elevated BrO mixing ratios under calm conditions at NM III, J. L. Thomas et al. (2011) find that a daily cycle with higher mixing ratios in the morning and a second peak in the afternoon are the result of surface temperature inversions and boundary layer dynamics.

One of the central findings of the modelling results in J. L. Thomas et al. (2011) is the observation that observed BrO mixing ratios could only be reproduced, when in addition to the bromine explosion reaction mechanism, photolysis induced OH formation and subsequent release of dihalogens was enabled. This release pathway contributed about 50% of the active bromine in the atmosphere.

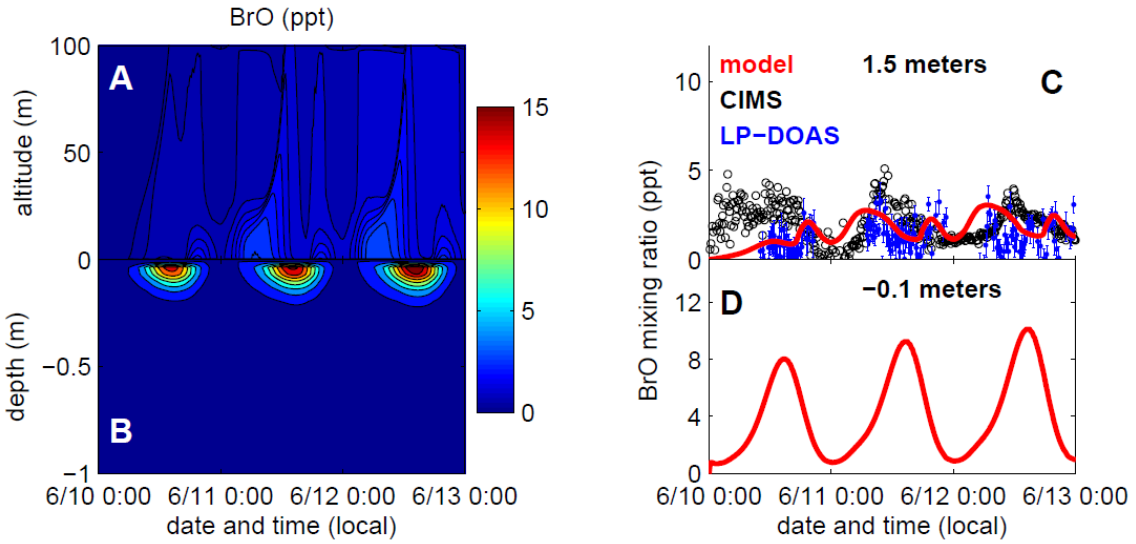

Figure 7.23: Modelled BrO mixing ratios in the atmosphere (A) and interstitial air (B) for Summit, Greenland. Modelled mixing ratios in the atmosphere at an altitude of 1.5m above the snowpack are compared with both CIMS and LP-DOAS measurements in panel (C). Predicted interstitial air mixing ratios 10 cm below the snow surface are shown in (D). Reproduced from J. L. Thomas et al. (2011) under CC 3.0

The great distance to the coast and as well as the high altitude of about 3200 m obviously limit the potential for a more detailed comparison, the results however illustrate, which aspects of halogen chemistry could be addressed with the LP-DOAS observations in combination with an atmospheric chemistry model.

In terms of long-term observations in Antarctica, there are in generally only a few data sets available (an overview of instruments and published observations can be found in Prados-Roman et al., 2018). Among these observations there is only one other LP-DOAS measurement by Saiz-Lopez et al. (2007a), who operated an instrument for 13 months on Halley Station (UK). The annual observations from this campaign are reproduced in Fig. 7.24. In Fig. 7.25, the corresponding time period from February 2017 to January 2018 from NM III is plotted. Daily averages and the running average were calculate as in Saiz-Lopez et al. (2007a). The year 2017 was selected for the comparison because temporal coverage in spring was better than in 2016.

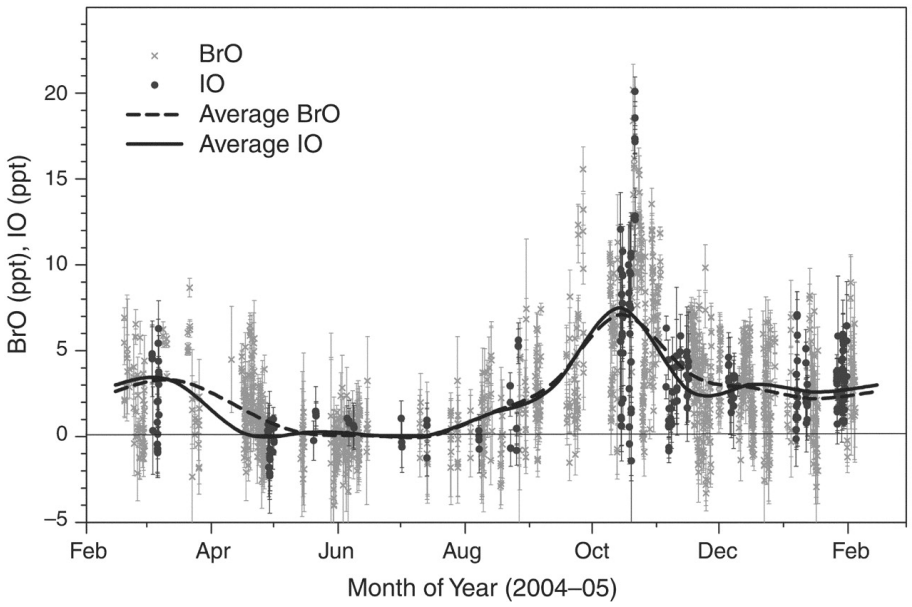

Figure 7.24: Annual variation of the halogen oxides measured at Halley Station. The 10-day moving averages of BrO and IO are indicated by a dashed line and a solid line, respectively. The maximum IO and BrO mixing ratios occurred in spring (October), whereas during winter (May to August) the radicals were consistently below the detection limit. A second smaller peak in the annual halogen mixing ratio cycle may also be present during autumn (March to April). Reproduced from Saiz-Lopez et al. (2007a) with permission from AAAS, 2019

Even though daily averages show considerable variations in both data sets due to the episodic nature of elevated BrO mixing ratios, the order of magnitude of values is comparable throughout the year. Both running means show two periods of increased activity. Comparing the maxima of the two periods, BrO values at NM III generally seem to be higher than at Halley (about 3-4 ppt for both peaks). The autumn periods at both stations in March more or less coincide, while the peak of the spring activation periods shows a marked difference. The beginning of the activation period at NM III seems be at the beginning of August, reaches a first peak in mid-August, then a second, smaller maximum in mid-September and lasts until the beginning of October. This period agrees with the occurrence of ODEs in the ozone data from NM III (see Figs. D.30, 6.10, and D.31). In the observations by Saiz-Lopez et al. (2007a), the running mean shows a slow increase starting from mid-August and reaches the highest values in mid-October.

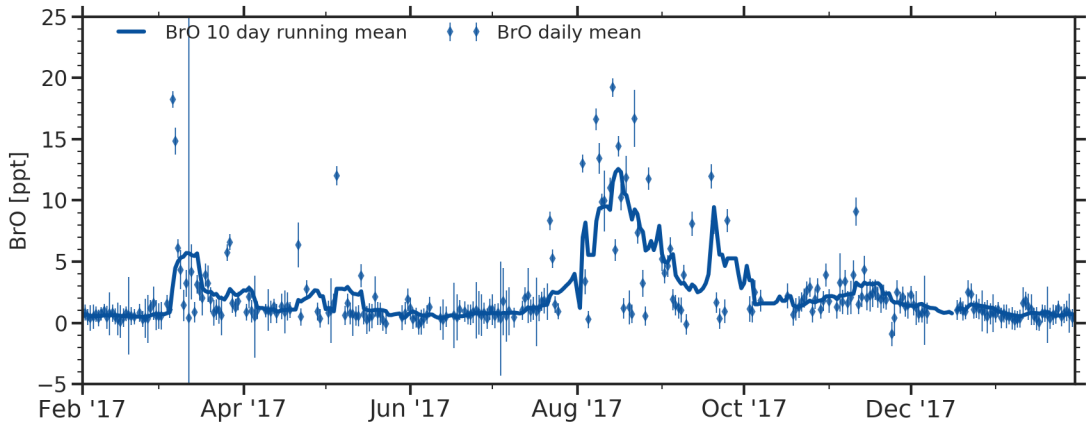

Figure 7.25: Daily averages of BrO observations from Neumayer III for period from February 2017 to January 2018. Values were calculated as in Saiz-Lopez et al. (2007a). Diamonds represent daily averages with the corresponding errors. The blue line is a 10-day running mean. The year 2017 was selected because of the best temporal coverage of polar spring. The equivalent time period as in 7.24 is plotted for easier comparison.

An explanation for this difference could be the location of the two stations. Halley is located about 800 km south west of NM III at -75.6° S, -26.2° W (see insert map in Fig. 4.1). Polar night at Halley lasts about three weeks longer than at NM III (end at NM III: July 22$^{\text{nd}}$, end at Halley: August 13$^{\text{th}}$). However, this is not sufficient to explain the time difference of almost two months between the first peak at NM III and that at Halley. Another explanation could be a different exposure to low pressure systems that circle the continent. NM III is closer to the average track of low pressure systems leading to a long term average wind speed of 8.9 m s^{-1} compared to only 6.2 m s^{-1} at Halley (König-Langlo et al., 1998). A higher exposure to storms and hence long range transport from the sea ice region in the Weddell sea, one of the most active regions in terms bromine activation (Schönhardt et al., 2012), could result in an earlier onset longer duration of the ODE season at NM III.

7.2 Chlorine

The LP-DOAS data set contains frequent observations of the chlorine species ClO and OClO. Similar to the structure of the previous section, in the following the data sets of both absorbers will be described and relevant aspects discussed based on case studies.

7.2.1 Overview of chlorine observations

ClO above the detection limit was observed on 162 days of the observation period at NM III at a median detection limit of 9.4 ppt. This corresponds to 17% percent of days of the observation period or 26% of the days when spectra are in the UVI spectral range are available. Similar to BrO, very high mixing ratios of up to 104±4 ppt were observed, which exceeds recently reported observations from Alert, Canada (S. Wang and Pratt, 2017) by more than a factor of ten and is about twice as much as during the so far only other observation of ClO in Antarctica by Zielcke (2015).

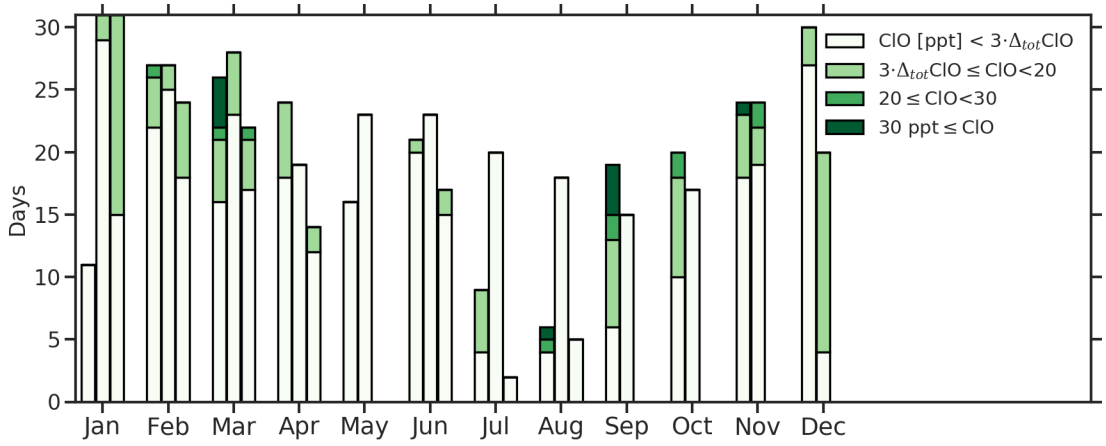

Figure 7.26: Distribution of daily maxima of ClO mixing ratios throughout the observation period. For the individual months the left bar represents the year 2016, the middle bar the year 2017, and the right bar the year 2018. The total length of the bars corresponds to the available data in the respective month in days. The colour code marks the daily maximum mixing ratio. The maximum was determined from a time series of hourly means to limit the influence of single outliers.

When considering the 30 min averages of ClO mixing ratios in Fig. 7.1, in 2016 a similar seasonality than that of BrO is visible, however with fewer observations above the detection limit. High mixing ratios occurred from mid-February to end of April during the late summer/autumn period of high BrO activity. A second period of high ClO activity, again concurrent with the observation of elevated BrO mixing ratios, starts in late August and last until November with occasional observations in December. In contrast to BrO, for which peak values in autumn are higher, peak ClO values in both periods are comparable.

For 2017, this annual cycle of ClO is not as distinct. Except for a few observations above the detection limit in February and March, no ClO was observed until mid-December. As was discussed in Sec. 4.2.10 and is visible in the time series of RMS values in Fig. 5.21, starting in April 2017, the transmissivity of the telescope front window was affected by deposition of an unidentified residue, probably released by the ageing insulation inside the

telescope. Until the front window was properly cleaned during a major maintenance in mid-December 2017, recorded irradiances steadily declined from April to December, with a brief period of improved transmissivity after a cleaning in October. Since the radiances of the LDLS are weakest in the UVI spectral window and within the window, the spectral region where ClO is evaluated (287 nm - 306 nm) has the smallest intensities (see reference spectrum for the UVI spectral window in the top panel in Fig. D.4 in the appendix), it is most affected by the reduced measurement signals.

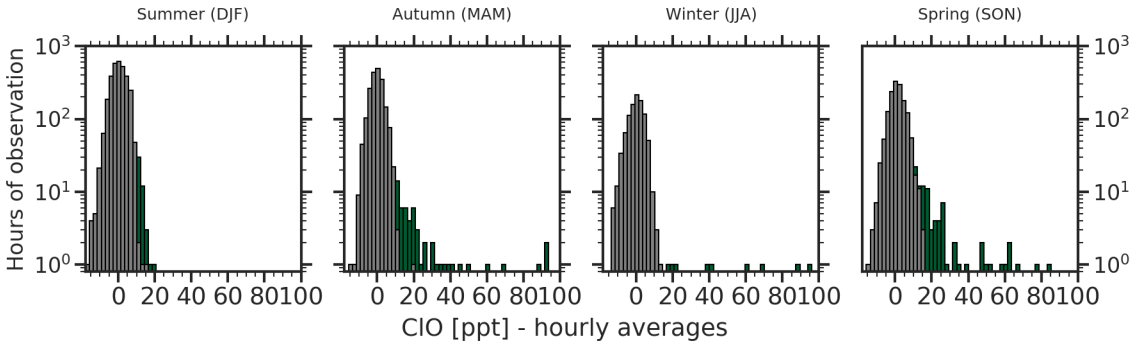

Figure 7.27: Seasonal distribution of elevated ClO. For the histograms only hourly averaged data from January 2016 until December 2017 was taken into account to prevent a distortion by the additional observations from January until August 2018. Values above the detection limit are coloured, values below the detection limit are plotted in grey.

After the intervention, ClO above the detection limit is again observed including elevated mixing ratios in March 2018, before technical problems interrupted the observations.

The seasonality of ClO mixing ratios and the disparity between 2016 and 2017 is also reflected in the histograms of daily maxima for all individual months of the observation period (Fig. 7.26) and the histograms of 30 min averages shown in Fig. 7.27.

In addition to ClO, OClO was detected. Most observed mixing ratios were close to the detection limits (median values of 3.4 ppt for evaluation in the the UVI spectral window and about 2 ppt in the UVII window). Mixing ratios above the detection limit were observed on 306 days or 48% of the days with measurements (which corresponds to 33% of all days during the observation period).

OClO, among others, is a reaction product of a BrO-ClO cross halogen reaction (see detailed reaction pathways in R 73 below). A simultaneous observation with elevated BrO and ClO mixing ratios therefore would be expected. At the same time, OClO is easily photolysed with atmospheric lifetimes in the order of seconds based on observations by Pöhler et al. (2010). The highest OClO mixing ratio of about 7 ppt observed at NM III did not reach the values of 27 ppt reported by Pöhler et al. (2010) but is the only other observation in polar regions reported in literature so far.

In agreement with this formation mechanism, the seasonal cycle of OClO (see Fig. 7.1, third panel) basically follows those of BrO and ClO, however during the months with the highest mixing ratios of BrO and ClO (February to March and September to October), OClO values seem to be low or missing. Since during these months radiation levels are still or already high, atmospheric life times probably are too short for an observation of OClO mixing ratios above the detection limit. Furthermore, high BrO and high ClO mixing ratios rarely occur simultaneously and since the species with lower abundance limits the

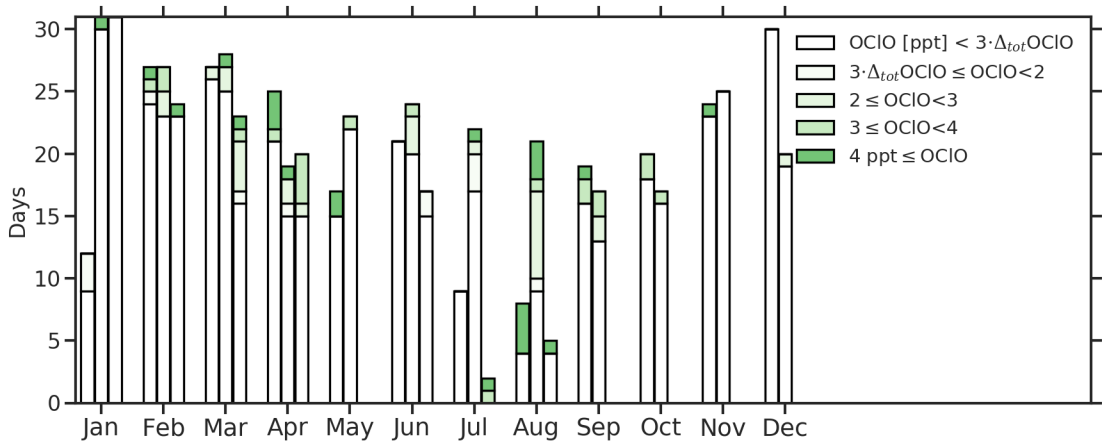

Figure 7.28: Distribution of daily maxima of OClO mixing ratios throughout the observation period. For the individual months the left bar represents the year 2016, the middle bar the year 2017, and the right bar the year 2018. The total length of the bars corresponds to the available data in the respective month in days. The colour code marks the daily maximum mixing ratio. The maximum was determined from a time series of hourly means to limit the influence of single outliers.

formation rate of OClO, mixing ratios can be expected to be lower than those of the limiting species (see Sec. 7.2.5 below for details).

Since OClO was evaluated both in the UVI and UVII spectral window, it was less affected by the reduced transmissivity of the telescope window. The observations of OClO in 2017, in combination with the observed seasonality of BrO, can serve as an indication that periods of active ClO chemistry in fact did occur but were below the temporarily higher detection limits of the LP-DOAS instrument for ClO (15-20 ppt) during that part of the observations .

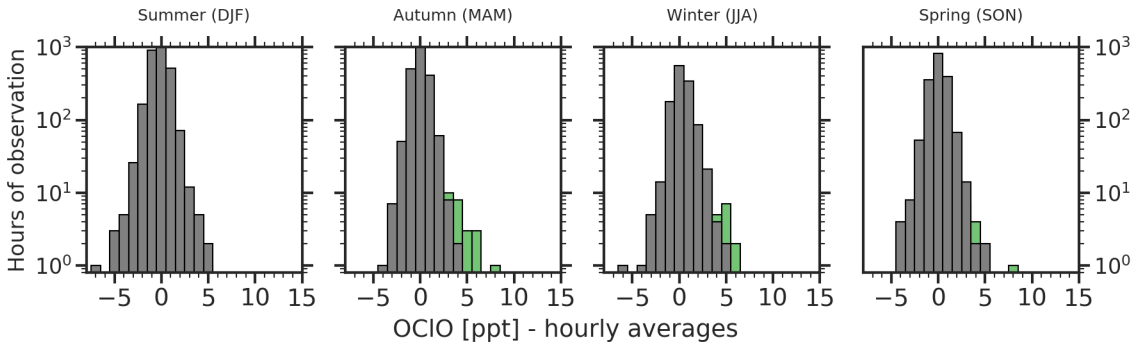

Figure 7.29: Seasonal distribution of elevated OClO. For the histograms only hourly averaged data from January 2016 until December 2017 was taken into account to prevent a distortion by the additional observations from January until August 2018. Values above the detection limit are coloured, values below the detection limit are plotted in grey.

7.2.2 Influence of atmospheric parameters on ClO and OClO

To investigate the relationships between elevated mixing ratios of chlorine species and ambient conditions, correlations with selected atmospheric parameters were analysed. Scatter plots for both species and the different parameters can be found in Fig. 7.30 for ClO and in Fig. 7.31 for OClO. As for the equivalent analysis of BrO mixing ratios, the other parameters were averaged to match the temporal resolution of the LP-DOAS data and O_3 and atmospheric pressure time series were de-trended (see Sec. 7.1.2 for details).

Temperature dependence

The correlation between atmospheric temperatures and ClO mixing ratios (Fig. 7.30, first row left panel) resembles that of BrO. For temperatures between 0 °C and -15 °C, only mixing ratios just above the detection limit are observed. The highest mixing ratios are detected at temperatures around -20 °C, typical for calm conditions in autumn. Interestingly, a number of observations with high mixing ratios exists for temperatures below -30 °C, which is below the threshold temperature for the onset of hydrohalite ($NaCl{\cdot}2H_2O$) precipitation at -20 °C (R. Sander et al., 2006). This indicates that either air temperatures are not representative of the surface layer on snow or aerosols, or that the precipitation does not affect the availability of chloride in surface layer sufficiently to prevent a chlorine release.

Since maximum mixing ratios of OClO did not exhibit a very pronounced cycle, no clear correlation with atmospheric temperatures is visible in Fig. 7.31, first row left panel, and data points are scattered across the entire temperature range from 0 °C to -40 °C.

Wind speed and direction

The correlations of ClO and OClO with wind speeds are very similar (see Fig. 7.30 respectively Fig. 7.31, first row centre panel). The majority of observations above the detection limit is associated with wind speeds below $5\,m\,s^{-1}$ with single measurements for wind speeds up to $10\,m\,s^{-1}$. Both ClO and OClO are only observed for winds from a sector between 70° and 230° which reflects the general distribution of wind directions at NM III (see Fig. 7.30 and Fig. 7.31 first row right panel as well as windroses in Figs. 7.32 and 7.33). The majority of ClO observations above 30 ppt is associated with wind from southerly directions. This is less pronounced in the OClO data (compare wind roses in Fig. 7.32 and Fig. 7.33).

Atmospheric pressure

For ClO, most observations of mixing ratios above 30 ppt occurred at higher than average atmospheric pressure, i.e. under calm, anti-cyclonic conditions which agrees well with the correlation with wind directions, which during such episodes predominantly are from the south to south-west. For OClO, the data is relatively scattered, however a tendency of OClO above the detection limit at higher pressures is also discernible and the majority of observations is associated with excess pressures of 5 hPa or more.

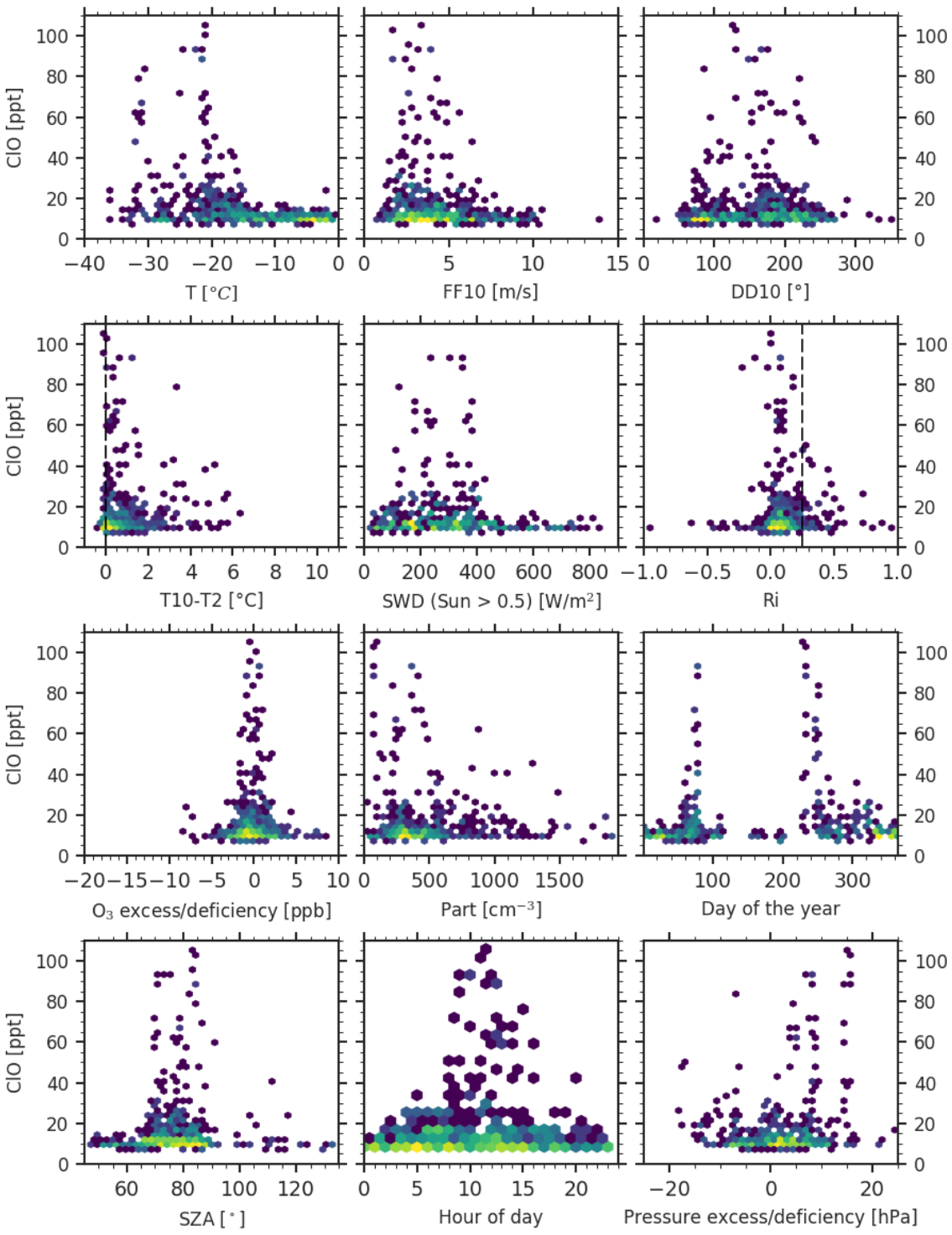

Figure 7.30: Correlation of ClO mixing ratios above the detection limit with other atmospheric parameters. The colour code marks the density of values. For the temperature, measurements in 2 m altitude were used, FF10 and DD10 are wind speed and direction in 10 m altitude. SWD is the short wave downwelling radiation and Ri is the Richardson number (see Eq. 2.3).The deficiency and excess of O_3 was determined by subtracting a 21-day rolling average from the ozone monitor time series. Part is the the particle concentration.

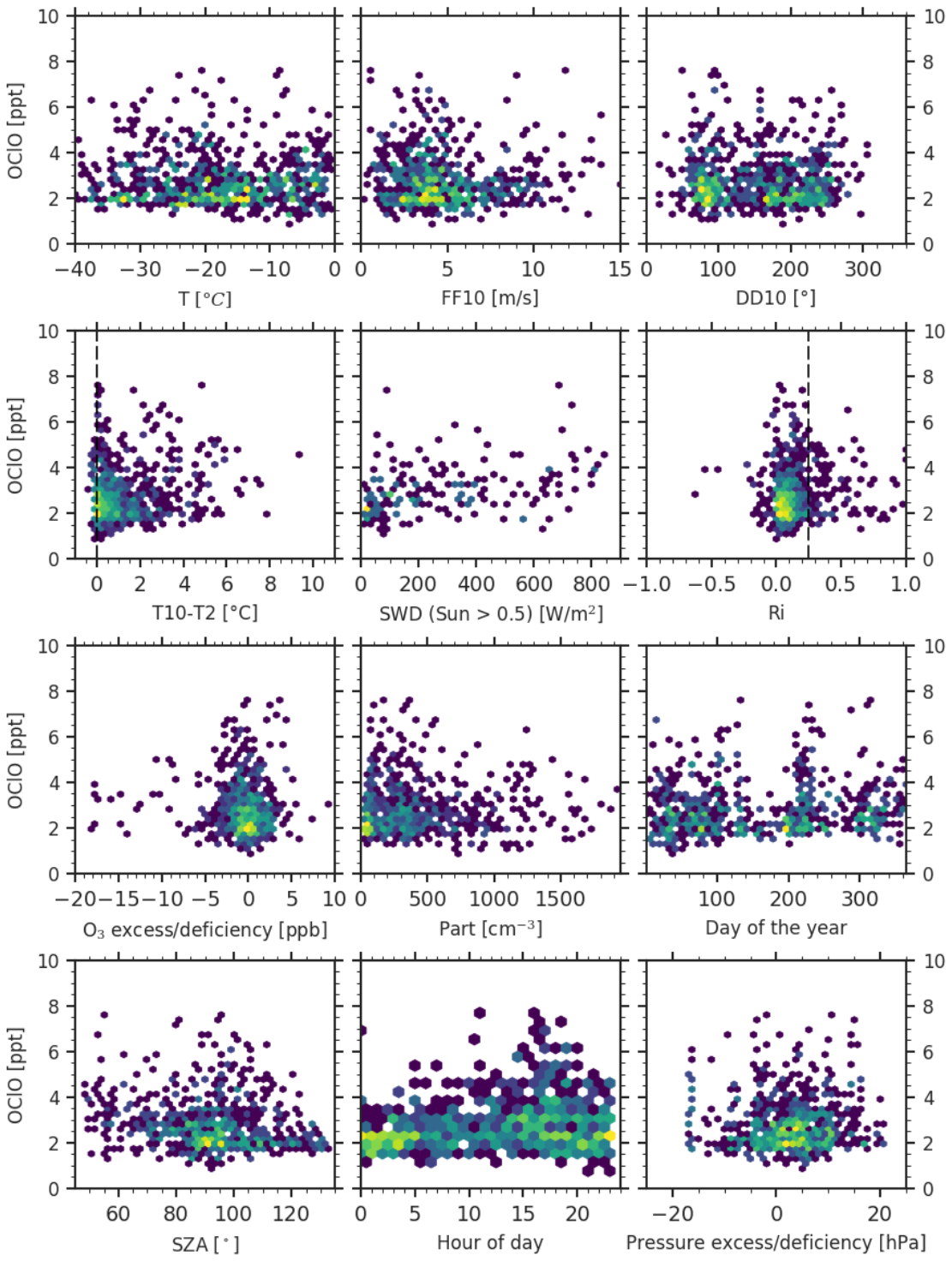

Figure 7.31: Correlation of OClO mixing ratios above the detection limit with other atmospheric parameters. The colour code marks the density of values. For the temperature, measurements in 2 m altitude were used, FF10 and DD10 are wind speed and direction in 10 m altitude. SWD is the short wave downwelling radiation and Ri is the Richardson number (see Eq. 2.3).The deficiency and excess of O_3 was determined by subtracting a 21-day rolling average from the ozone monitor time series. Part is the the particle concentration.

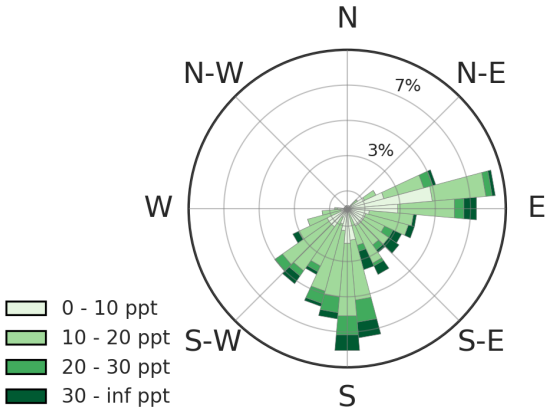

Figure 7.32: Distribution of ClO mixing ratios above the detection in relation to wind directions. The colour code marks the the mixing ratio. For the respective wind direction the cones show the distribution of mixing ratios and the colour code indicated the mixing ratio. Data in the original temporal resolution of the LP-DOAS was used.

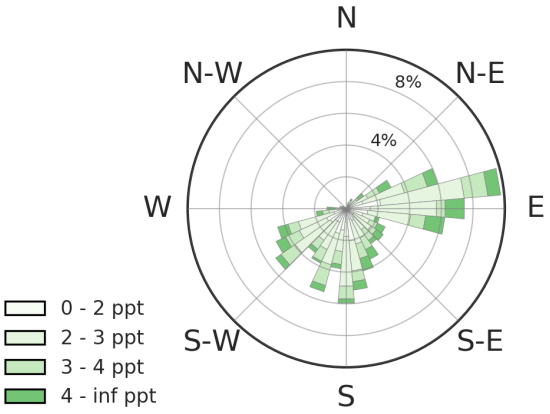

Figure 7.33: Distribution of OClO mixing ratios above the detection in relation to wind directions. The colour code marks the the mixing ratio. For the respective wind direction the cones show the distribution of mixing ratios and the colour code indicated the mixing ratio. Data in the original temporal resolution of the LP-DOAS was used.

Atmospheric stability

Similar to BrO observations during local release episodes, basically all measurements of ClO and OClO coincided with temperature inversion conditions indicating relatively stable atmospheric conditions and reduced mixing (in Figs. 7.30 and 7.31 second row, left panel). This can be seen clustering of observations at positive temperature differences. Similar to BrO, most high mixing ratios ClO and OClO are associated with Richardson numbers below the critical value of 0.25 which often characterise atmospheric conditions that end increases in mixing ratios after a rise under stable conditions through turbulent mixing (in Figs. 7.30 and 7.31 second row, right panel).

Solar radiation, SZA, and daily cycle

Due to their different chemistry, the relationships of ClO and OClO with radiation parameters differ. For ClO, while observations above the detection limit vary from global radiation values of a few $\mathrm{W\,m^{-2}}$ up to $800\,\mathrm{W\,m^{-2}}$, mixing ratios above 20 ppt are limited to a range between 150 and $400\,\mathrm{W\,m^{-2}}$, indicating a dependence of the release on photochemistry (see Fig. 7.30, second row centre panel). This is supported by the correlation with SZAs (see Fig. 7.30, last row left panel), where except for a few values, all observations lie between 90° and 65°. When mixing ratios are plotted as a function of the hour of the day, the daily cycle shows a symmetrical distribution of values around noon, when maxima are observed.

For the photolytically unstable OClO, except for some scattered values across the entire range of global radiation, most observations lie between irradiances of 0 and $200\,\mathrm{W\,m^{-2}}$ (see Fig. 7.31, second row centre panel). This agrees with a clustering of values at SZAs between 85° and 100° (see Fig. 7.31, last row left panel). The distribution of mixing ratios over the hours of the day shows that the daily cycle of OClO is skewed towards the

afternoon/early evening which agrees with a formation from BrO and ClO cross reactions. Naturally, the precursors need to present in the atmosphere, before OClO can be formed (see Fig. 7.31, last row centre panel). Furthermore, a concentration of observations around 2 ppt can be seen from about 4:00 pm to 5:00 am, which for large parts of the year at NM III is night-time. This indicates that OClO formed around sunset seems to survive in darkness until sunrise on the following day, however at slightly lower mixing ratios than immediately after formation .

Seasonal cycle

The seasonal distributions of ClO and OClO in the correlation plots (Figs. 7.30 and 7.31, third row right panel)) agree with the discussion above. For ClO a gap in the observations from May(day 120) until early August (day 210) is visible as well as peak mixing ratios in march (day 60 to 90) and again in August and September (day 220 to 260). From September to February, low but regular occurrences of ClO are visible.

For OClO (Fig. 7.31, third row right panel)), lower mixing ratios between May and end of July, essentially during polar night, are also visible, however more observations are above the detection limit, compared the same period in the ClO data. This suggests that also ClO occasionally might have been present during this time of the year albeit below the detection limit of the LP-DOAS instrument. In August (around day 220) a concentration of elevated OClO mixing ratios can be observed, likely corresponding to the beginning of the spring period of elevated ClO activity, when OClO is already formed but the available radiation levels are still low enough for OClO to persist above the detection limit. For the autumn ClO activity period, a similar peak is not really visible. From October to February OClO mixing ratios between 4 and 6 ppt occurred on several days.

Ozone

Most ClO observations are associated with only minor O_3 deficiencies compared to the long-term average ozone mixing ratios. Values in the respective scatter plot are distributed more or less symmetrically around -1 ppb and even for high ClO mixing ratios, no strong deviations from the average are visible. Considering that typical ODEs are characterised by a marked drop in ozone mixing ratios, this indicates that the chlorine chemsitry observed at NM III is not associated with these, mostly transport induced episodes and very likely a local phenomenon. Since the de-trending leads to a certain variation of ozone mixing ratios attributed to the dependent trace gas mixing ratios in the scatter plots, a possible influence of ClO on ozone is hard to discern with this approach and therefore investigated in detail in Sec. 7.2.4 below.

Even though also for OClO, most mixing ratios are distributed around average ozone mixing ratios, a few more observations under ozone depletion conditions are visible in the scatter plot than for ClO (see Fig. 7.31 third row left panel). These observations might be the signal of chlorine chemistry during ODEs below the ClO detection limit of the LP-DOAS, however, since the detected OClO mixing ratios in these cases are close to their detection limit, some caution is advised in this interpretation. The association with less extreme O_3 deficiencies would agree with a formation of OClO after days with active bromine and chlorine chemistry that probably has led to a certain degree of ozone destruction (see Sec. 7.2.4 for details).

Particle concentrations

Most ClO and OClO mixing ratios above the detection limit were observed at relatively low particle concentrations below $500\,\mathrm{cm}^{-3}$ (see Figs. 7.30 and 7.31 third row centre panel). For ClO even an anti-correlation of very high mixing ratios and particle concentrations seems to be visible. This observation is in line with the occurrence of ClO and (hence) OClO under very calm atmospheric conditions which at NM III generally are associated with lower particle concentrations (except for new particle formation events, see Sec. 7.4)

7.2.3 Chlorine release mechanisms

Despite multiple observations of chlorine species, e.g. ClO (Tuckermann et al., 1997; Zielcke, 2015; Custard et al., 2016), BrCl (Spicer et al., 2002; Pratt et al., 2013; Buys et al., 2013) and more recently Cl_2 (Liao et al., 2014; Custard et al., 2016; S. Wang and Pratt, 2017) the release mechanism(s) governing chlorine activation are still under active debate.

For a long time, a presence of chlorine compounds in the polar boundary was believed to be a by-product of heterogeneous bromine release. As discussed in Sec. 2.4.5, in the dihalogen formation step of the bromine explosion reaction cycle in the surface layer, either Br_2 or, due to typically high chloride to bromide ratios in these surface layers, BrCl forms. Because of a higher polarity, the latter degasses not as quickly as Br_2. Therefore, if bromide concentrations are sufficient, another reaction to Br_2 and subsequent release to the atmosphere the dominant pathway.

When, however, bromide in the surface layer is depleted, BrCl can be emitted to the atmosphere (i.e. the sequence of reactions R 53 to R 55 stops at R 53:

$$\mathrm{HOBr} + \mathrm{Cl^-} + \mathrm{H^+} \xrightarrow{\mathrm{mp}} \mathrm{BrCl} + \mathrm{H_2O} \qquad \text{(R 53 revis.)}$$

(R 71)

This has been observed in laboratory experiments (e.g. with artificial snow with different bromide to chloride ratios Wren et al., 2013). The ClO formed by reaction with ozone in principle can react with HO_2 to form HOCl. Upon uptake by a surface layer containing chloride, this could form Cl_2, which would be the sequence of reactions equivalent to the 'bromine explosion' (see also greyed out reactions in Fig. 2.9). For their laboratory study, Wren et al. (2013) indeed conclude, that the subsequent occurrence of Br_2 release, followed by BrCl and finally Cl_2 can be interpreted as a 'halogen explosion'.

It should be noted, however, that due to the high reactivity of chlorine atoms with hydrocarbons (see R 26), based on the current understanding of the chlorine chemsitry, the activated chlorine atom is not expected to initiate an 'explosion' type of reaction chain in the sense that chlorine is auto-catalytically released with the exponential increase in mixing ratios observed as for bromine release. If ozone and VOCs are present in the atmosphere, modelling studies find that up 70% of the reaction partners of chlorine atoms are organic molecules and only 27% is ozone (C. R. Thompson et al., 2015). Therefore, the 'chlorine explosion' reactions would not be self-enforcing as for bromine because the hydrocarbon sink leads to a net amplification factor smaller than one.

With the recent observation of high abundances of molecular chlorine over Arctic snow packs (Liao et al., 2014; S. Wang and Pratt, 2017; Custard et al., 2016; Custard et al.,

2017), alternative release pathways have come into focus. The proposed mechanisms, in addition to the pathway above include 'chlorine versions' of the alternative pathways discussed in Sec. 2.4.5 above. Liao et al. (2014) propose a 'photochemical formation with O_3 from the snowpack' based on the mechanism proposed Oum et al. (1998a) which leads to a formation of OH in the surface layer, after which reactions R 60 to R 64 occur - only with chlorine. In S. Wang and Pratt (2017), the uptake of $ClONO_2$ and subsequent formation of HOCl in the surface (the chlorine equivalent to R 59) contributes between 51 and 73% to the release of Cl_2 while the remaining contribution is a parametrised 'snow pack emission'. The details of chlorine release chemistry therefore clearly require further research.

Solely based on the observational data from NM III, the details and dominant processes in chlorine release clearly cannot be identified. Therefore in the following, two example episodes with elevated ClO mixing ratios will be discussed and, where possible, connections to the current discussions will be made. For a proper investigation, the LP-DOAS observations would have to be combined with a detailed chemistry model.

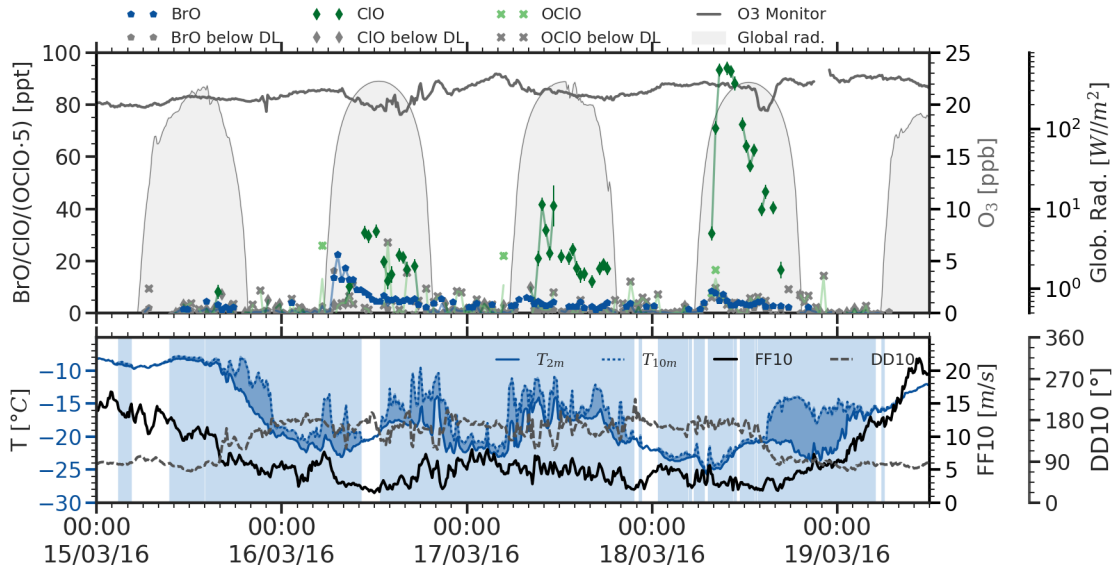

Figure 7.34: Example period with sequential release of bromine and chlorine as observed by BrO and ClO detection. Throughout the episode, ClO peak mixing ratios increase with time.

The first example discussed (Fig. 7.34), is a period between two storms in March 2016. It was characterised by very stable atmospheric conditions and clear skies for almost the entirety of the three days with ClO above the detection limit from March 16th to 16th, 2016. Wind speeds dropped on the 15th and stayed below 5 m s^{-1} for most of time. Except for brief periods, a constant temperature inversion was present. Since during these periods wind speeds were very low, also here only limited mixing can be assumed. Similar to a local emission episode for BrO (see. e.g. Fig. 7.7), on the first day after the storm temperatures drop, a surface inversion forms. Low initial mixing ratios of BrO (<5 ppt) and potentially a single observation of ClO above the detection limit are visible. On the 16th, BrO mixing ratios quickly rise in the morning after sunrise to about 20 ppt and then decline over the rest of the day. About one hour after the BrO peak, ClO mixing ratios rise above the detection limit and reach a maximum just below 30 ppt around noon and

then decline with some short time variations in the afternoon. These variations correspond to short term variations of the extent of the temperature difference of the inversion which could be caused by some limited turbulence induced by variations of wind speeds that are visible during the afternoon.

On the 17th, daily cycles similar to the previous day can be observed with an increase of BrO followed by ClO with peak mixing ratios just before noon. However, the maximum mixing ratio of BrO on this day is just over 5 ppt while ClO briefly reaches values close to 40 ppt. On the 18th, BrO shows a similar daily cycle than on the previous days while ClO reaches mixing ratios of 95 ppt in the morning. It also seems that the temporal offset between the peak mixing ratio of BrO and that of ClO has become smaller.

A crucial property of a source surface for chlorine in all of the proposed release mechanisms is the bromide to chloride ratio since it seems to determine the partitioning between Br_2, BrCl, and Cl_2 release (Wren et al., 2013). The lower the ratio the more the release shifts to towards chlorine. This also seems in agreement with observations in which Br_2 and BrCl release was reported to be much more frequent than that of Cl_2 and in many cases even the only dihalogens detected (Buys et al., 2013; Pratt et al., 2013; Liao et al., 2014).

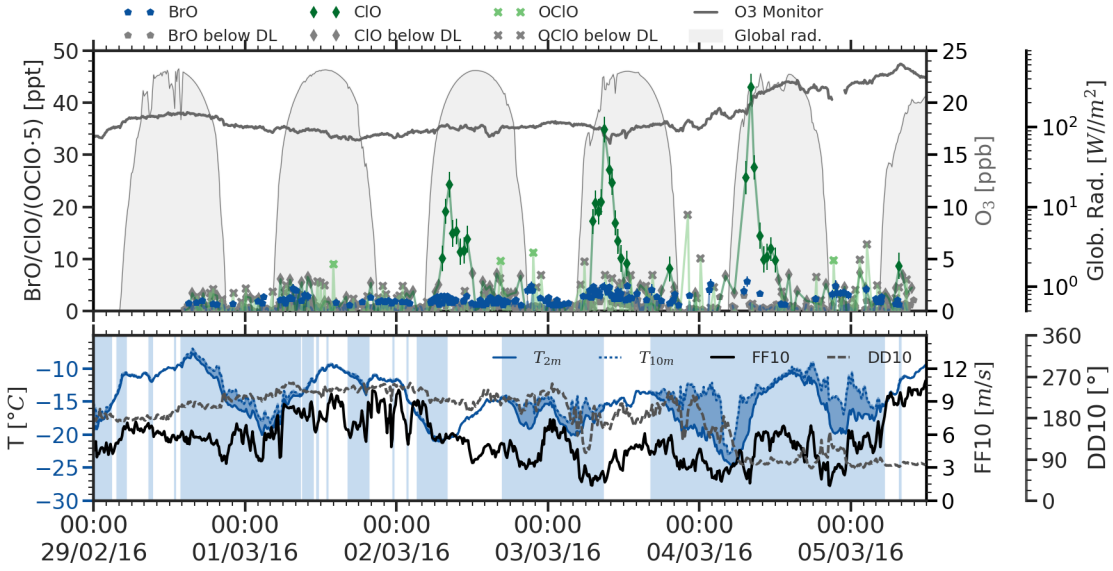

Figure 7.35: Example period from the beginning of March 2016 with weak bromine monoxide activity followed by a chlorine release with increasing ClO peak mixing ratios from day to day.

The period at NM III (presented by in Fig.) could be interpreted a result of the same mechanism. After an initial release of bromine, the depletion of bromide in the surface layer leads to a shift towards chlorine. If the halogen release mechanism at play is the bromine explosion, the shift from Br_2 to BrCl, would prevent a further increase of reactive bromine because each heterogeneous cycle at best would conserve the active bromine in the atmosphere. The slow decline of BrO on the 16th could be explained by this. If the release mechanism is a formation of HOBr through other reactions (e.g. OH formation in the surface layer), the shift towards chlorine would be the result of the previous release and hence surface layer depletion of bromide.

The further shift towards higher ClO observations and shorter temporal differences between BrO and ClO peaks then would be the result of a continuous reduction of surface bromide concentrations that, even if replenished to a certain degree by a probable uptake of reservoir bromine species during the night and potentially snow metamorphism never recovers to the initial values. A decreasing bromide concentration might also explain the increasing peak mixing ratios of ClO as the chlorine release capacity increases with a decreasing probability that a BrCl or Cl_2 molecule in the surface exchanges replace a chlorine atom by reaction with bromide prior to release.

Increasing peak mixing ratios over time are regularly observed in ClO release episodes, e.g. in the second case study in Fig. 7.35. In terms of meteorology this episode is very similar to the previous one. One important difference is that it occurred slightly earlier in the year which might explain that on the days with elevated ClO mixing ratios (March 2nd to 4th, 2016), the break up of the surface temperature inversion around noon modulated both BrO and ClO daily cycles, which here is more pronounced than in the previous example.

In the discussion of declining BrO peak mixing ratios during extended periods of BrO activation (see Sec. 7.1.5 and Fig. 7.19) it was argued that the decreasing peak mixing ratios were a result of a decreasing bromide concentration. In Fig, 7.36 ClO observations are added to the same period as shown in Fig. 7.19

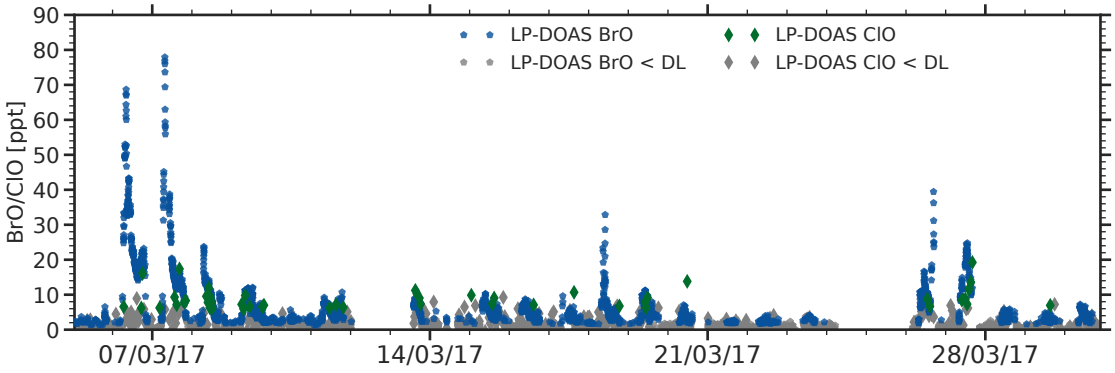

Figure 7.36: BrO and ClO mixing ratios as observed by the LP-DOAS in March 2017.

Even though the chase studies presented here show fast some ClO observations coincide with the initially high BrO mixing ratios, no shift towards a release of chlorine is visible throughout the entire period. It should be noted that during the two gaps in the time series in Fig. 7.36, fresh sea salt aerosol might have been deposited and bromide replenished, which would explain the increased BrO peaks on March 26th and 27th, but in comparison with the example periods for high ClO activity there seems to be a discrepancy.

This leads to the interesting question which factors control whether after a storm elevated BrO or elevated ClO is observed (throughout almost the entire observation period one of the halogen species always dominated while the other exhibited much smaller mixing ratios). Part of an explanation might be the characteristics of halogens or halogen carriers (sea salt aerosols or salty blowing snow) during the individual storm. A difference in the bromide to chloride ratio associated with the deposition after the storms (e.g. deposition of fresh sea salt aerosols with a bromide to chloride ratio close to sea water in one storm versus

advection of aged aerosols that through previous halogen activation might be depleted in bromide in another) could lead to different starting conditions for the halogen activation.

For further investigations into this, a characterisation of salt deposition through aerosols as well as blowing salty snow would be crucial. Since currently aerosol sampling at NM III is partly shut down during blowing snow conditions, the effect of these episodes cannot be assessed properly. Given the observations of active halogen chemistry under blowing snow conditions (Yang et al., 2008; Yang et al., 2010; A. E. Jones et al., 2009; Frieß et al., 2011) this might be an important factor for the episodes discussed in this section and above.

7.2.4 Influence of ClO on ozone destruction

Similar to the estimates of ozone depletion through the BrO-BrO self reaction, for suitable days (i.e. a preferably complete daily cycle of both trace gases), an influence of BrO-ClO cross reactions on ozone mixing ratios observed by the ozone monitor was investigated. For ozone depletion in the troposphere, the ClO self reaction is too slow to contribute substantially to a decrease in ozone and hence can be neglected. (see rate constants in R 72).

		at 250 K	
$ClO + ClO$	$\longrightarrow Cl_2 + O_2$	$k_4 = 1.7 \cdot 10^{-15} cm^3 s^{-1}$	(R 28 revis.)
	$\longrightarrow Cl + Cl + O_2$	$k_5 = 1.6 \cdot 10^{-16} cm^3 s^{-1}$	(R 29 revis.)
	$\longrightarrow Cl + OClO$	$k_6 = 1.5 \cdot 10^{-15} cm^3 s^{-1}$	(R 30 revis.)
		Rates: (R. Atkinson et al., 2007)	(R 72)

The BrO-ClO cross reaction has several pathways, which are listed in R73.

		at 250 K	
$BrO + ClO$	$\longrightarrow Br + OClO$	$k_7 = 8.8 \cdot 10^{-12} cm^3 s^{-1}$	(R 28 revis.)
	$\longrightarrow Br + Cl + O_2$	$k_8 = 5.9 \cdot 10^{-12} cm^3 s^{-1}$	(R 29 revis.)
	$\longrightarrow BrCl + O_2$	$k_9 = 1.5 \cdot 10^{-12} cm^3 s^{-1}$	(R 30 revis.)
	$\longrightarrow Cl + OBrO$	NA	(R 30 revis.)
$+ M$	$\longrightarrow BrOOCl + M$	NA	(R 31 revis.)
		Rates: (R. Atkinson et al., 2007)	(R 73)

For a net destruction of ozone, only those reactions forming a dihalogen or two radicals are relevant (i.e. R 29 revis. and R 30 revis. above). At daytime, halogendioxides are rapidly photolysed (lifetimes in the order of seconds to minutes, C. R. Thompson et al., 2015) and the resulting O(3P) atom quickly reacts with ambient oxygen to reform ozone.

$OClO + h\nu$	$\longrightarrow O + ClO$	$j_2 = 7.6 \cdot 10^{-2}\, s^{-1}$	(R 24 revis.)
		(Pöhler et al., 2010)	

If BrCl is formed in the cross halogen reaction (R 30 revis.), during the day it is quickly photolysed leading to two halogen atoms that can take part in ozone destruction (see 24 revis.).

$$\mathrm{BrCl} + h\nu \longrightarrow \mathrm{Br} + \mathrm{Cl} \qquad j_3 = 1.26 \cdot 10^{-2}\,\mathrm{s}^{-1} \qquad \text{(R 24 revis.)}$$

(C. R. Thompson et al., 2015)

In combination with the influence of the self reaction of BrO (see Eq. 7.1), the temporal evolution of O_3 mixing ratios is then described by Eq. 7.2

$$\frac{d[\mathrm{O_3}]}{dt} = \underbrace{-2 \cdot (k_1 + k_2) \cdot [\mathrm{BrO}]^2}_{\text{BrO self reac.}} \underbrace{-2 \cdot (k_8 + k_9) \cdot [BrO][ClO]}_{\text{BrO-ClO cross reac.}} \tag{7.2}$$

As before, the estimation of the temporal evolution of the ozone mixing ratio is started with a value corresponding to a period without halogen activity above the detection limit. Then ozone mixing ratios at the different time steps are calculated solely based on the observed mixing ratios of BrO and ClO. Two examples for this approach are shown in Fig. 7.37 and Fig. 7.38.

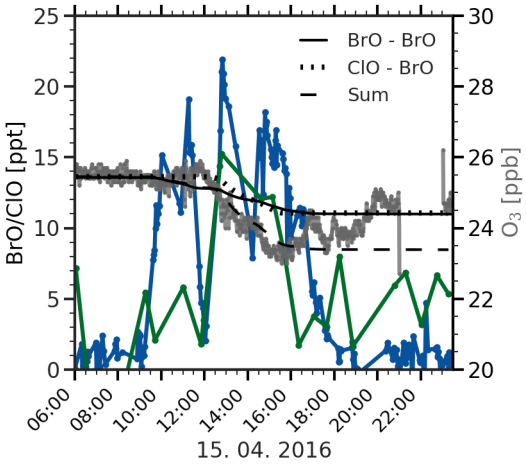

Figure 7.37: Estimation of ozone destruction by cross halogen reactions between BrO and ClO on April 4th 2016.

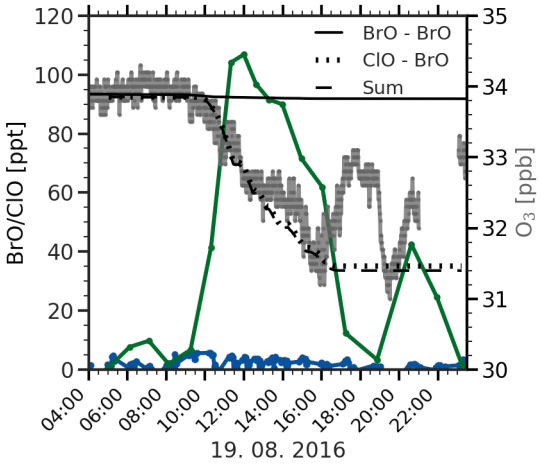

Figure 7.38: Estimation of ozone destruction by cross halogen reactions between BrO and ClO on August 19th 2016.

In Fig. 7.38 an example with comparable mixing ratios of BrO and ClO is shown with peak values around 20 ppt and 15 ppt for BrO and ClO, respectively. Over the day, the largest decrease of ozone is about 2 ppb within 4 hours in the afternoon. As can be seen, the BrO self reaction at the observed mixing ratios only explains a decrease of about 1 ppb while the combination of BrO self and BrO-ClO cross reaction captures the temporal evolution of ozone relatively well.

A more extreme case is shown in Fig. 7.38. On this day, which is part of the case study period in Fig. 7.34 above, ClO mixing ratios reached values of over 100 ppt with BrO mixing ratios around 5 ppt. A maximum decrease of ozone of about 2.6 ppb is observed on this day. While the small BrO mixing ratios via the BrO self reaction have no visible

impact on ozone, the ClO-BrO cross reaction again agrees well with the observed ozone mixing ratios.

In conclusion, a presence ClO increases the ozone depleting influence of BrO. High mixing ratios of ClO alone have no large influence without sufficient levels of BrO. This becomes very clear when comparing the ozone destruction caused by around 100 ppt of BrO (see Fig. 7.11 above) to the impact of a comparable concentration of ClO in combination with low BrO mixing ratios. While the latter leads to ozone destruction rates of about 0.4 ppb h^{-1}, the former causes ozone to drop at about 4 ppb h^{-1} - a factor of 10 faster.

7.2.5 OClO formation

As discussed above, OClO is one of the reaction products of the BrO-ClO cross reaction (see reactions under R 73). Due to the influence of convection on the BrO and ClO daily cycles, mixing ratios of both species tend to be much lower in the afternoon than the peak values reached in the morning respectively around noon, even when the onset of a temperature inversion leads to second peak in mixing ratios. This partly explains why the observed OClO mixing ratios are lower than might be expected from peak mixing ratios of BrO and ClO during the day.

Furthermore, for the large majority of observations, either BrO or ClO is present at much lower mixing ratios than the other species. Since the species with the lower abundance in the BrO-ClO cross reaction limits the attainable OClO mixing ratios, a high activity of one of the two does not result in high abundances of OClO. The case study in Fig. 7.39 therefore shows a relatively rare situation.

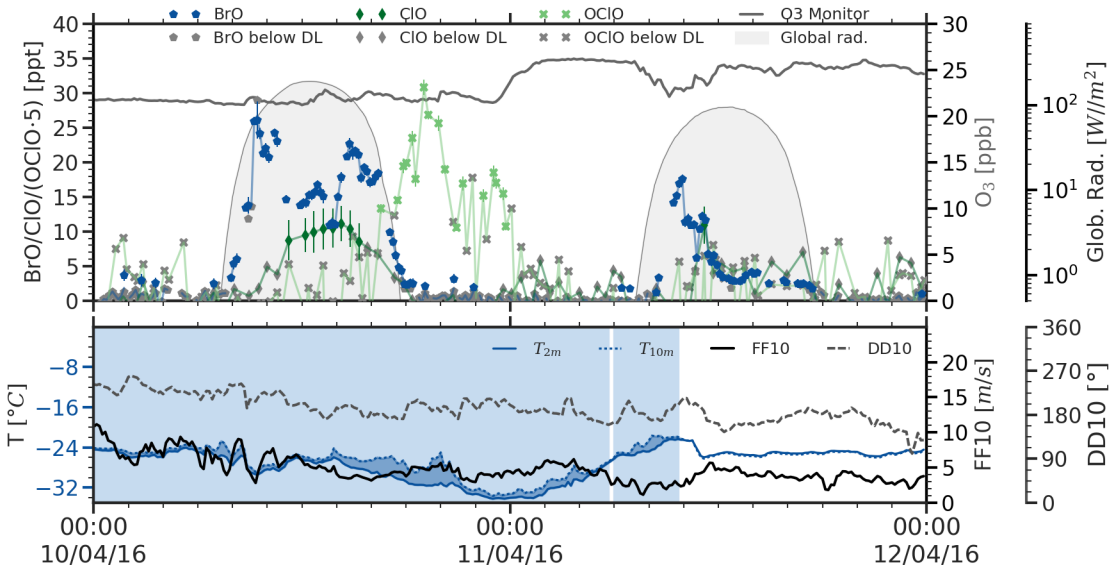

Figure 7.39: Example period with an evening peak of OClO mixing ratios formed from the BrO-ClO cross halogen reaction reaction.

Throughout the 10th of April, 2016, a continuous temperature inversion limited vertical mixing throughout the entire day. BrO mixing ratios show only a minor drop around noon from values around 25 ppt and recover to about 20 ppt in the afternoon. Starting at noon, ClO mixing ratios rise above the detection limit and reach about 10 ppt in the

afternoon when BrO mixing ratios increase back to about 20 ppt. Starting just before sunset, OClO mixing ratios above the detection limit become visible. Note that for better visibility OClO mixing ratios in Fig. 7.39 were multiplied by a factor of 5. After sunset, OClO mixing ratios reach a maximum of about 5-6 ppt before declining when a reduction of the temperature inversion and a simultaneous increase in ozone mixing ratios indicate increased horizontal or vertical mixing or the advection of a different air mass.

Taking the highest simultaneously attained mixing ratios of BrO and ClO (in this case 20 ppt and 10 ppt, respectively), the expected maximum mixing ratio of OClO can be estimated based on the the branching ratio of the rate constants in the reactions in R 73. For the ratio of k_7 to k_{tot} and a temperature of 250 K (almost exactly the air temperature during the case study period), Turnipseed et al. (1991) report $k_7/k_{tot} = 0.51 \pm 0.09$. For the mixing ratios above expected OClO mixing ratios this would correspond to 5.0±0.9 ppt which agrees very well with the observed peak of OClO mixing ratios.

7.3 Iodine

Among the iodine species, which in principle can be detected with the LP-DOAS instrument, only IO was observed above the detection limit (median DL values 2.93 ppt with the grating used in the first year of operations, 1.6 ppt with the grating used for the remainder of the observations.) I_2 and OIO were not observed above their respective detection limits of 71.6 ppt respectively 11.2 ppt. Following the general structure of the previous sections, iodine monoxide observations will be described in the following.

7.3.1 Overview of iodine monoxide observations

Iodine monoxide was detected on 173 days of the observation period which corresponds to 27% of the days with valid measurements or 18% of the entire observation period. The observed mixing ratios generally were very low and often close to the detection limit. The maximum mixing ratio that could be detected was 6 ppt. In the overview of the 30 min averages of the available data set in Fig. 7.1, the influence of the change to the measurement configuration in February 2017 is clearly visible (see Sec. 5.2 for a detailed discussion). The new grating with lower resolution reduced the scatter of mixing ratios by about a factor of 2 which is reflected in a similar improvement of the detection limit.

Due to the instrumental issues, results of spectra acquired during the first year of operation should be considered with caution. The difference in the instrument performance is reflected in the distribution of daily maxima for the individual months of the entire observation period. For most months from January 2016 to 2017 no or only few observations were recorded above the high detection limits. Comparing the months from February 2017 until the end of the observations in 2018, a systematic difference in the frequency of daily maxima is visible. In 2017 fewer observations above the detection limit were recorded. As can be seen in the overview time series (Fig. 7.1), the number of observations above the detection limit increased after the second major maintenance intervention in Mid-December 2017. At that time, the trace gas observatory was raised to counteract snow accumulation. In addition to the cleaning of the misted front window mentioned before, the realignment of the telescope made measurements on the second, longer light path fully operational again. During the time of remote trouble shooting regarding the decreased signal strength and before the full maintenance could be performed, the measurements were frequently limited

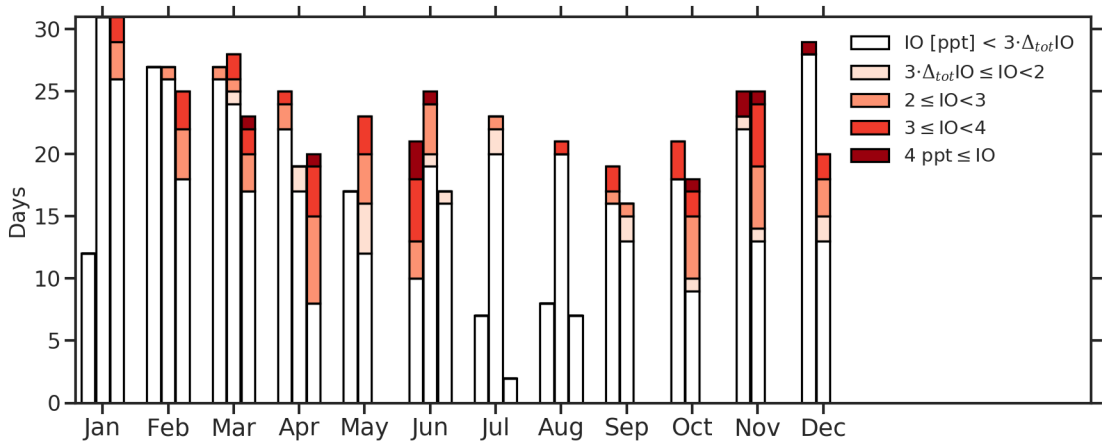

Figure 7.40: Distribution of daily maxima of IO mixing ratios throughout the observation period. For the individual months the left bar represents the year 2016, the middle bar the year 2017, and the right bar the year 2018. The total length of the bars corresponds to the available data in the respective month in days. The colour code marks the daily maximum mixing ratio. The maximum was determined from a time series of hourly means to limit the influence of single outliers.

to the shorter light path by the winterer leading to smaller absorption signals. From June 2017 to mid-December 2017, only 7% of the measurement time the longer light path was used compared to an average of 30% after realignment and cleaning.

For the season histograms for IO hourly observations in Fig. 7.41, differing from the equivalent plots of the other absorbers only observations from August 2017 until July 2018 were considered to minimise (a) the influence of the inferior instrument performance during the first year of operation and (b) reduced sensitivity due to the limitation of measurements to the shorter light path.

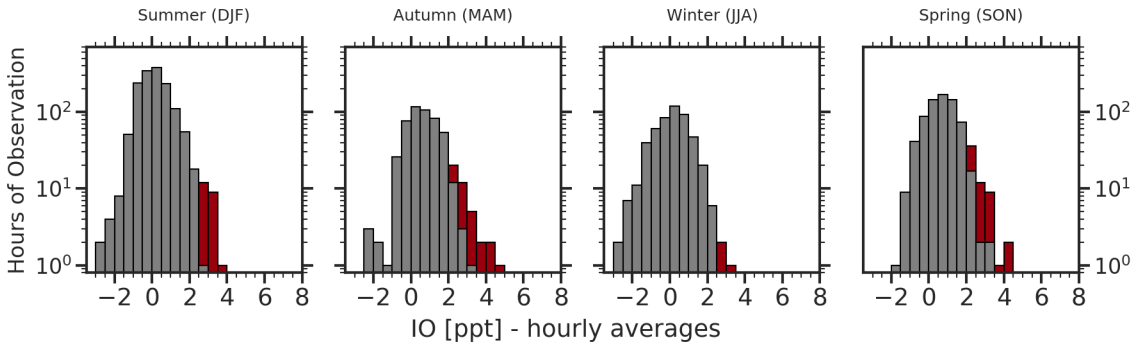

Figure 7.41: Seasonal distribution of elevated IO. For the histograms only hourly averaged data from August 2017 until July 2018 was taken into account to limit an influence of the instrumental issues on the distributions. Values above the detection limit are coloured, values below the detection limit are plotted in grey. The data set with night-time reference was used.

All four histograms again illustrate how close to the detection limit the majority of observations are and how limited the available data base is due to the different issues concerning the VISI spectral window. A seasonality is not discernible except for a minimum of observations above the detection limit in winter. In spring and autumn on few occasions

hourly averages above 4 ppt are observed. In light of the limitations of the instrument, a reliable assessment of the annual cycle of IO probably is not possible. Nevertheless it can be can be assumed that higher IO mixing ratios e.g. comparable of observations of up to 20 ppt at Halley by Saiz-Lopez et al. (2007a), at least after the change of the grating would have been detectable with the LP-DOAS instrument.

7.3.2 Influence of atmospheric parameters on IO

Despite the limitations of the data set, the influence of environmental parameters on the mixing ratios observed above the detection limit was determined as before for the other trace gases. Ambient data sets were averaged to match the temporal resolution of the IO measurements and de-trended time series of ozone and atmospheric pressure were used. Results can be found in Fig. 7.43. For a number of parameters observations are scattered across the entire range of values typically encountered throughout the year. Since these correlations do not allow to draw meaningful conclusions, only correlations where systematic patterns seem to be discernible will be briefly discussed in the following. As in the correlations of the other species, a correlation with temperature inversion conditions can seen in the respective correlation (Fig. 7.43 second row, left panel). The majority of observations is associated with positive temperature differences (i.e. surface temperature inversions). The values of Richardson numbers mostly lie within the turbulent range between 0 and 0.25

Major ozone depletions do not seem to coincide with the observed IO mixing ratios (within the variations of the de-trended time series) with an approximately symmetrical distribution of mixing ratios around the average ozone mixing ratios (see Fig. 7.43 third row left panel). Most observations occurred under particle concentrations below 500 cm^{-3} (Fig. 7.43 third row centre panel). The remaining correlations show no clear structure.

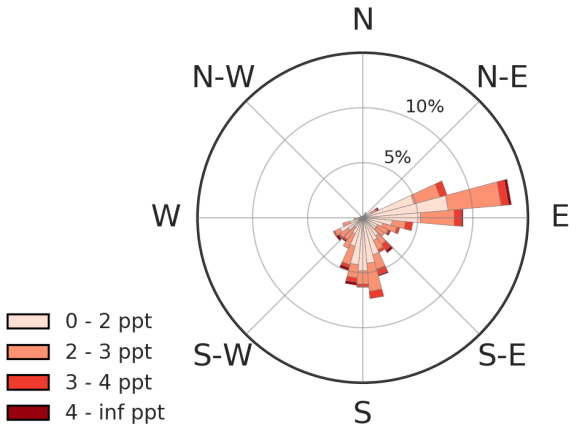

Figure 7.42: Distribution of IO mixing ratios above the detection limit as a function of wind direction. The colour code marks the the mixing ratio. For the respective wind direction the cones show the distribution of mixing ratios and the colour code indicates the mixing ratio. Data in the original temporal resolution of the LP-DOAS was used.

The analysis of observed mixing ratios as a function of wind directions in Fig. 7.42 reflects the dominant wind directions at NM III. Observations are limited to a sector between

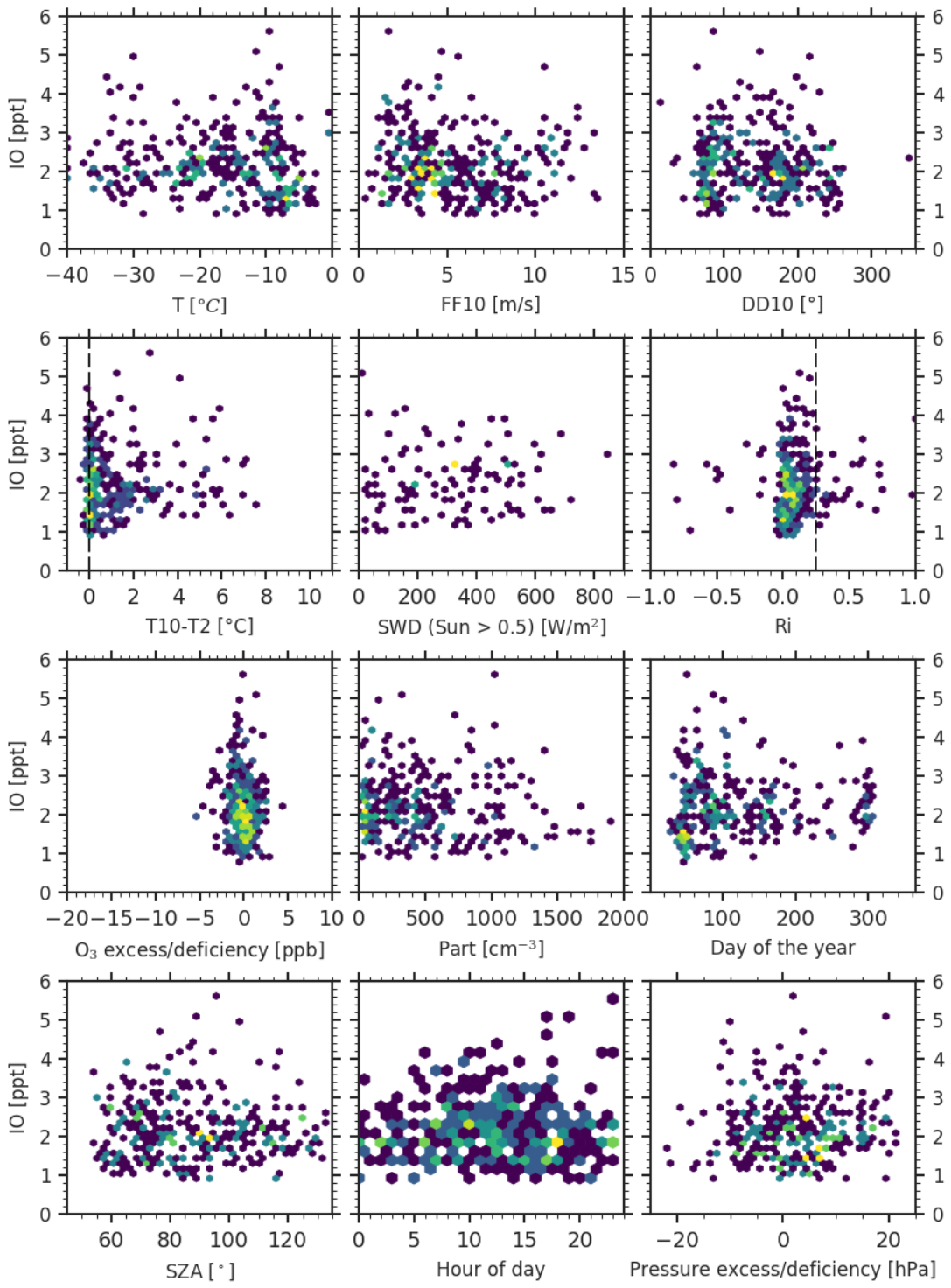

Figure 7.43: Correlation of IO mixing ratios above the detection limit with other atmospheric parameters. The colour code marks the density of values. For the temperature, measurements in 2 m altitude were used, FF10 and DD10 are wind speed and direction in 10 m altitude. SWD is the short wave downwelling radiation and Ri is the Richardson number (see Eq. 2.3).The deficiency and excess of O_3 was determined by subtracting a 21-day rolling average from the ozone monitor time series. Part is the the particle concentration.

60° and 200°, which partly excludes south westerly winds, which frequently characterise the calmest anti-cyclonic conditions on the ice shelf at NM III.

7.3.3 Example periods for IO observations

The lack of reliable (continuous) observations of IO mixing ratios dynamics limits the potential for investigating release and atmospheric reactivity of iodine monoxide. In the first example a two-day period from the beginning of polar day in November 2017 is shown (Fig. 7.44).

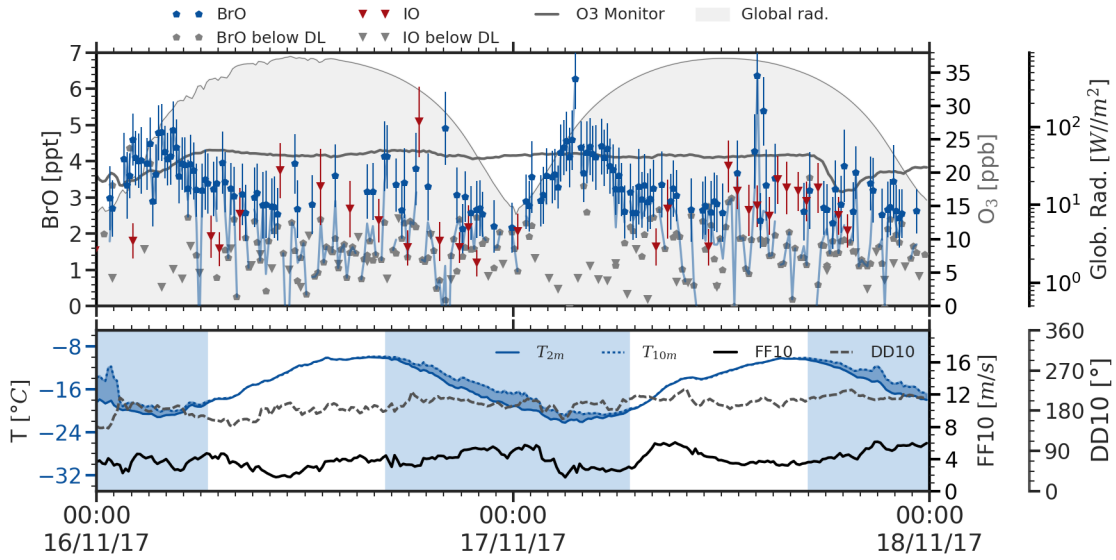

Figure 7.44: Example period with elevated IO mixing ratios at the beginning of polar night. Observations below the respective detection limit are plotted in grey.

The two days are characterised by a highly dynamic atmosphere that periodically oscillated between stable, stratified conditions and turbulent flow around noon. Wind speeds stayed below 7 m s^{-1} and winds constantly came from southerly directions. When comparing the daily cycles of BrO and IO, IO mixing ratios are relatively uninfluenced by breakup and formation of the surface temperature inversions potentially pointing to fundamentally different sources for both species. BrO shows a decline of mixing ratios, however not as abrupt as in daily cycles discussed above. This might indicate that photochemical processes dominate the temporal evolution of both species, for BrO leading to an increased reaction with HO_2 with a peak formation rate around noon while the daily cycle of IO might indicate a photochemical source mechanism that peaks at noon. A similar noon time peak of IO following a morning peak of BrO was also observed by Zielcke (2015) and interpreted as the result of a decreasing sink for IO when BrO mixing ratios decline and the BrO-IO cross reactions becomes less important.

Alternatively the observed daily cycle is linked to a variable source of iodine species. Even though the exact origin of iodine compounds in polar regions is still incompletely understood, biogenic organic and inorganic iodine species are believed to play a central role in the marine polar atmosphere (Saiz-Lopez et al., 2012). Due to their biogenic origin and a very pronounced annual cycle of biological activity in polar regions, a peak of emissions

would be expected during polar day and supported by a minimum sea ice extent. If IO precursors that lead to the observations in Fig. 7.44 are indeed released from the ocean, the correlation of daily IO maxima with increased turbulent flow around noon could signify an increased advection of marine iodine compounds. Fast photolysis around noon would thus explain the observed IO daily cycles.

In a second example of IO observations, a different daily cycle is visible. Fig. 7.45 shows a three day section of a period of about ten days with a regular occurrence of elevated BrO and IO mixing ratios (see Fig. D.34 in the appendix.) The selected days are characterised by calm atmospheric conditions with light winds around $5\,\mathrm{m\,s^{-1}}$ from southerly directions. Atmospheric stability is increased and a continuous surface temperature inversion can be observed.

Bromine monoxide mixing ratios exhibit more or less U-shaped daily cycles, modulated by turbulent mixing and the peak of chemical sinks (e.g. HO_2) around noon. The daily cycles of IO vary between about 2 ppt and 4 ppt. In the morning, coincident with BrO, a slight increase of IO mixing ratios by about 1 ppt can be observed followed by a slow decline of mixing ratios throughout the rest of the day with a slight increase in the afternoon of some days (e.g. on April 4^{th}, 2018). This daily cycle, similar to BrO also modulated by a peak reaction rate with HO_2 around noon agrees with previous MAX-DOAS observations at NM III. Frieß et al. (2010) also reported a U shaped diurnal cycle with peak signals equivalent to about 1.6 ppt, close to the mixing ratios observed with the LP-DOAS during the example period. Over the three day period, mixing ratios of both halogen species do not seem to change drastically and the observed variation of mixing ratios might indicate a cycling of a halogen stock between night-time and day-time species under negligible exchange of air masses -for iodine e.g. via IO self reactions to OIO or I_2O_2, which are rapidly photolysed again even at low radiation level. Similar to observations by Zielcke (2015), IO is occasionally observed apparently before solar radiation is available. At these very low light levels, however, the bias of the pyranometers at high SZAs has to be considered as well as the vicinity of the detection limit to these night-time values.

7.3.4 Influence of IO on ozone

Even though only few suitable days with a more or less continuous daily cycle are available in the IO data set, a potential influence of the BrO-IO cross reaction on ozone mixing ratios was estimated for one example, which can also serve a plausibility check for observed IO levels. Since no days with a simultaneous presence of BrO, ClO, and IO with sufficient data quality could be identified, interactions between three halogen species cannot be investigated.

In contrast to the estimation for ClO, for a presence of elevated IO mixing ratios, the IO-IO self reaction has to be considered. The two possible reaction pathways with rate constants calculated for 250 kelvin can be found in R 74.

	at 250 K	
$\mathrm{IO + IO \longrightarrow I + I + O_2}$	$k_{10} = 1.8 \cdot 10^{-11}\mathrm{cm^3 s^{-1}}$	(R 28 revis.)
$\longrightarrow \mathrm{I + OIO}$	$k_{11} = 4.4 \cdot 10^{-11}\mathrm{cm^3 s^{-1}}$	(R 29 revis.)
	Rates: (R. Atkinson et al., 2007)	(R 74)

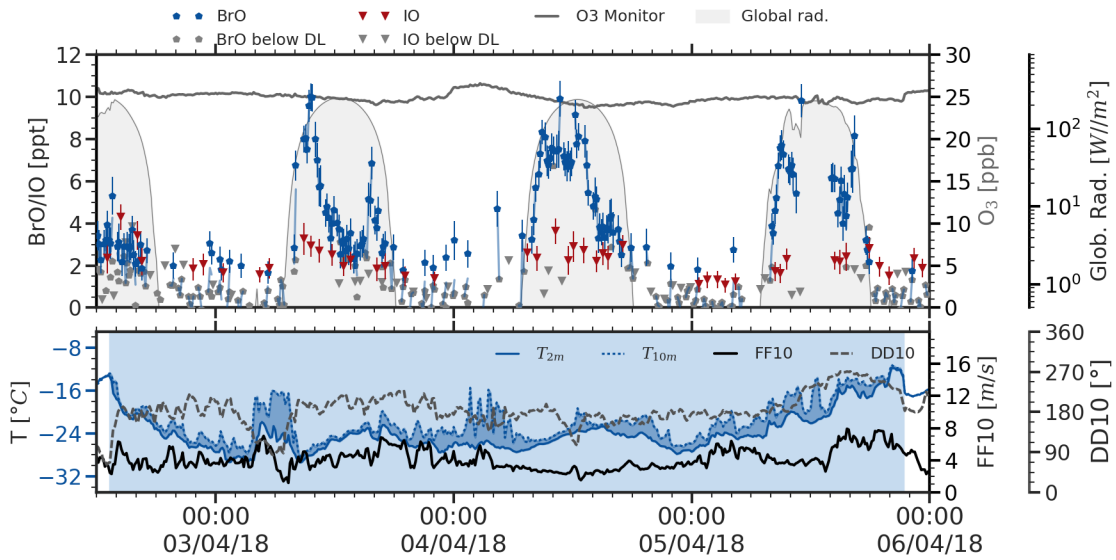

Figure 7.45: Example period with elevated IO mixing ratios observed in August 2018. Observations below the respective detection limit are plotted in grey.

Since OIO is quickly photolysed during the day (with atmospheric life times in the order bezween about 30 s and 10 min depending on the photlysis product; C. R. Thompson et al., 2015), no net ozone destruction occurs via R 29 revis. and only R 28 revis. has to be considered.

$$\mathrm{OIO} + h\nu \longrightarrow \mathrm{O} + \mathrm{ClO} \qquad j_4 = 1.5 \cdot 10^{-3}\,\mathrm{s}^{-1} \qquad \text{(R 24 revis.)}$$

(C. R. Thompson et al., 2015) (R 75)

The reaction pathways and rate constants for the BrO-IO cross halogen reaction are shown in R 76.

$$\begin{aligned} &&&\text{at } 250\,\mathrm{K} \\ \mathrm{BrO} + \mathrm{IO} &\longrightarrow \mathrm{Br} + \mathrm{OIO} && k_{12} = 9.4 \cdot 10^{-11}\mathrm{cm}^3\mathrm{s}^{-1} && \text{(R 28 revis.)} \\ &\longrightarrow \mathrm{Br} + \mathrm{I} + \mathrm{O_2} && k_{13} = 7.2 \cdot 10^{-12}\mathrm{cm}^3\mathrm{s}^{-1} && \text{(R 29 revis.)} \\ &\longrightarrow \mathrm{IBr} + \mathrm{O_2} && k_{14} = 4.3 \cdot 10^{-11}\mathrm{cm}^3\mathrm{s}^{-1} && \text{(R 30 revis.)} \end{aligned}$$

Rates: (R. Atkinson et al., 2007) (R 76)

With the same argument as above, the formation of OIO from the cross halogen reaction can be neglected for the estimation of ozone depletion rates. When two single halogen radicals are formed, both can immediately react with ozone. If IBr is formed it has to be photolysed before leading to ozone destruction. At an atmospheric life time of about 15 s, this reaction is much faster than the formation of the dihalogen and therefore the cross reaction is rate determining step in the reaction sequence.

$$\mathrm{IBr} + h\nu \longrightarrow \mathrm{I} + \mathrm{Br} \qquad j_5 = 6.8 \cdot 10^{-2}\,\mathrm{s}^{-1} \qquad \text{(R 24 revis.)}$$

(C. R. Thompson et al., 2015) (R 77)

With the BrO self reaction, described and discussed in Sec.7.1.4 and R 68, the combined influence of BrO and IO on ozone mixing ratios can be described by Eq. 7.3

$$\frac{d[\mathrm{O_3}]}{dt} = \underbrace{-2 \cdot (k_1 + k_2) \cdot [\mathrm{BrO}]^2}_{\text{BrO self reac.}} \underbrace{-2 \cdot (k_{13} + k_{14}) \cdot [BrO][IO]}_{\text{BrO-IO cross reac.}} \underbrace{-2 \cdot k_{10} \cdot [\mathrm{IO}]^2}_{\text{IO self reac.}} \tag{7.3}$$

The influence of the iodine monoxide presence on ozone mixing ratios was calculated on April 3rd, on one of the days from the example period for IO presence discussed above (see Fig. 7.45)

Ozone mixing ratios on the selected day did not show a clear background value that could be used as initial value for depletion estimation but show some variability just before sunrise which is linked to short time variations of the inversion temperature difference at that time (compare with Fig. 7.45) indicating a dynamic influence rather than an active chemical origin. As starting mixing ratio, the ozone level at 5:00am before sunrise was selected. It should be noted that the initial ozone mixing ratio does not influence the description of the depletion, which generally is appropriate unless ozone mixing ratios fall below 1 ppb (Le Bras and Platt, 1995). Therefore the calculated ozone curves simply could be shifted to another starting mixing ratio of ozone. Both observed and estimated changes

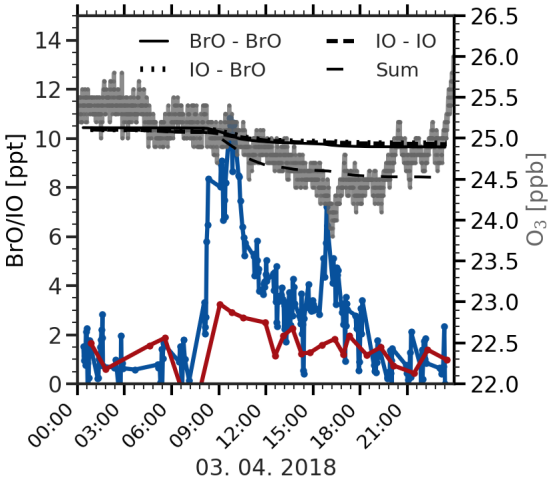

Figure 7.46: Example of ozone destruction by the cumulative effect of BrO self reaction, IO self reaction and the BrO-IO cross halogen reaction.

of ozone mixing ratios are very small. Excluding the probably turbulence-induced drop in mixing ratios at 4:30pm, observed ozone decreases by only 0.5 ppb in 7 h corresponding to a destruction rate of only 0.07 ppb h^{-1}. The estimate based on the observed mixing ratios yields a comparable decrease, but seems to slightly underestimate the destruction. Considering the temporal evolution of ozone mixing ratios before and after the sunlit period, the reduction of observed ozone mixing ratios might be influenced by a trend that is independent of halogen-related destruction, which would explain the difference.

Interestingly, in this combination of mixing ratios, all three destruction pathways seem to have similar influence on ozone mixing ratios. This illustrates how even low levels of iodine monoxide can have a considerable influence on ozone destruction rates.

In conclusion, the IO data set suffers from two independent technical issues that limit

the ability to derive conclusions based on the observations at NM III. For selected days observed mixing ratios and daily cycles, however, seem plausible and in agreement with previous observations, and support the finding that already small (<2 ppt) IO levels can have a significant impact on the ozone budget.

7.4 Contemporaneous observation of elevated BrO and high particle concentrations

The highest mixing ratios of BrO during the entire observation period were observed on March 24th, 2016 and coincided with very untypical atmospheric conditions, namely a particle concentration about a factor of 20 -30 higher than on average during that time of year as well as massive decreases of ozone mixing ratios similar to ODEs in spring. While short peaks of elevated NO_2 mixing ratios were observed on the first days of this episode, an assessment of meteorological conditions and several aerosol parameters suggests that the event had a natural origin.

The high particle concentrations observed on the three days implicate that the episode was a new particle formation event. Such events have been reported for this time of the year at NM III, however not with such extraordinary measurement values (Weller et al., 2015). Unfortunately, a SMPS that is available in the trace gas observatory was not running on the three days when the event occurred.

In March 2018 a similar event could be identified on two days when particle size distribution information is available. Both events will be described and discussed in the following.

Potential new particle formation event?

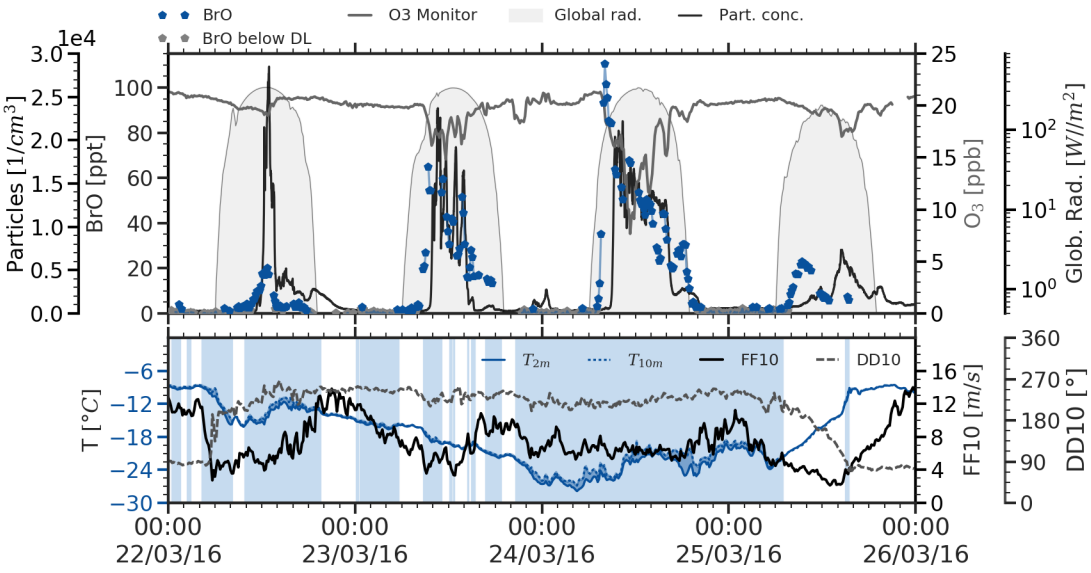

Figure 7.47: Period with extremely high BrO mixing ratios that correlated with extremely high particle concentrations and drops in ozone mixing ratios.

In Fig. 7.47 the entire period during March is shown including the observed particle concentrations. Fig.7.48 to Fig. 7.50 show the individual days in detail.

The episode started after a storm that lasted until the 21st (not shown in Fig. 7.47). Wind speeds dropped in the night of the 22nd, while wind directions turned from east to south west. Already during the night of the 22nd, a constant decrease of ozone mixing ratios is visible indicating that the advected air previously might have been affected by halogen chemistry.

When the detailed presentation of the 22nd in Fig. 7.48 is considered, however no immediate increase of BrO is visible at sunrise as for example in the episode of an ozone decrease by both advection and local chemistry (Fig. 7.16). A number of NO_2 observations slightly above the detection limit are visible. Wind directions and missing titration spikes in the ozone data suggest that if at all, only parts the light paths of the LP-DOAS were affected by this.

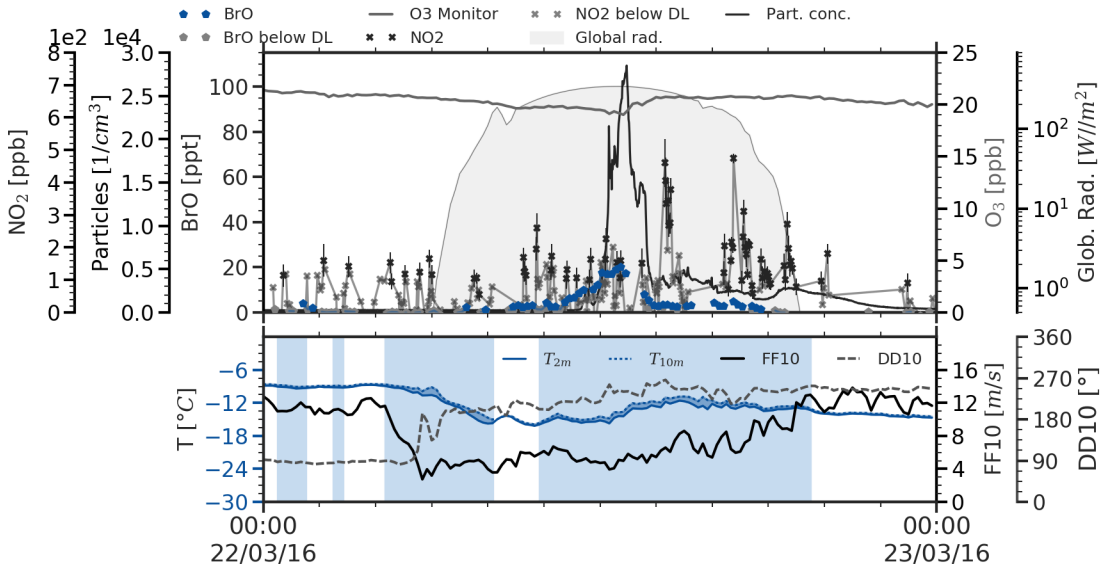

Figure 7.48: Mixing ratios of BrO, O_3, NO_2 as well as particle concentrations and meteorological data March 22nd 2016 during likely new particle formation event.

Around noon and simultaneously with BrO, particle concentrations show a massive increase with a peak of 28 000 cm^{-3}. The threshold concentration for measurements to be flagged as potentially contaminated is 2000 cm^{-3} during that time of the year and the average background concentrations around 1000 cm^{-3} (cf. 6.9). When inspecting the aerosol backscatter signal for the entire period, no increases of the signal at times of high particle concentrations were found. From this it can be concluded that the observed particles were small because high concentrations of large particles would have increased the backscatter signal.

Also the black carbon concentrations, which could indicate e.g. soot aerosols from combustion processes did not increase, ruling out a contamination. Both observations indirectly support the hypothesis that a new particle formation was observed.

After about two hours, particle concentrations quickly decrease together with BrO while O_3 starts to rise.

The increase in wind speeds at that time suggests that this was due to increased mixing.

In the afternoon two short spikes in NO_2 mixing ratios are visible, however both only with a small influence on particle concentrations. With increasing winds towards the evening, particle concentrations return to low background values around midnight and BrO decreases below the detection limit.

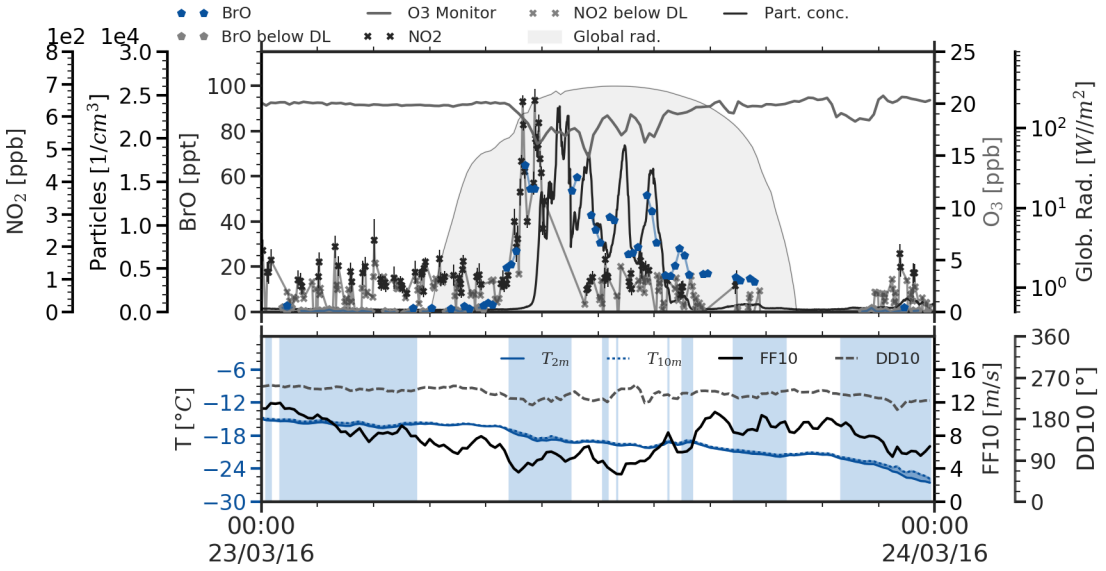

Figure 7.49: Mixing ratios of BrO, O_3, NO_2 as well as particle concentrations and meteorological data March 23rf 2016 during likely new particle formation event.

On the 23rd wind speeds decrease from about $10\,\mathrm{m\,s^{-1}}$ to $4\,\mathrm{m\,s^{-1}}$ around noon. Due to these moderate wind speeds no pronounced temperature inversion develops and it can be assumed that turbulent mixing dominated the boundary layer. The *Richardson* number is around 0.15 throughout the day, below the critical threshold of 0.25 for stable conditions. With the formation a weak temperature inversion around and a coincident drop if wind speeds, around 9:00, a fast increase of BrO mixing ratios from close to the detection limit to over 60 ppt is visible. At the same time, NO_2 mixing ratios increase to about 650 ppt which could be attributed to Pistenbully activities in the vicinity of the station. The high BrO mixing ratios lead to a decrease of O_3 mixing ratios by about 4 ppb. About 90 min after the increase of BrO, particle concentrations start to rise from background values to over $22\,000\,\mathrm{cm^{-3}}$. As this was accompanied by a slight change in wind speed and direction, it could be attributed to mixing phenomena, in the light of temporal offset from the BrO increase, it could be speculated if a photochemical influence involving BrO could have cause the peak in particle concentrations.

For the remainder of the day, particle concentrations, and ozone and BrO mixing ratios vary where particle concentrations and BrO show a striking correlation even on short timescales and ozone is anti-correlated. These fast variations coincide with changes of the wind speed suggesting that the signal is caused by atmospheric dynamics and e.g. is the result of a alternating observation of two decoupled layers in a vertically structured boundary layer, which are frequently observed over ice shelves (cf. Sec. 2.2.2 Anderson and Neff, 2008).

Wind speeds increase to $10\,\mathrm{m\,s^{-1}}$ in the afternoon, the episode ends and all values return to background levels.

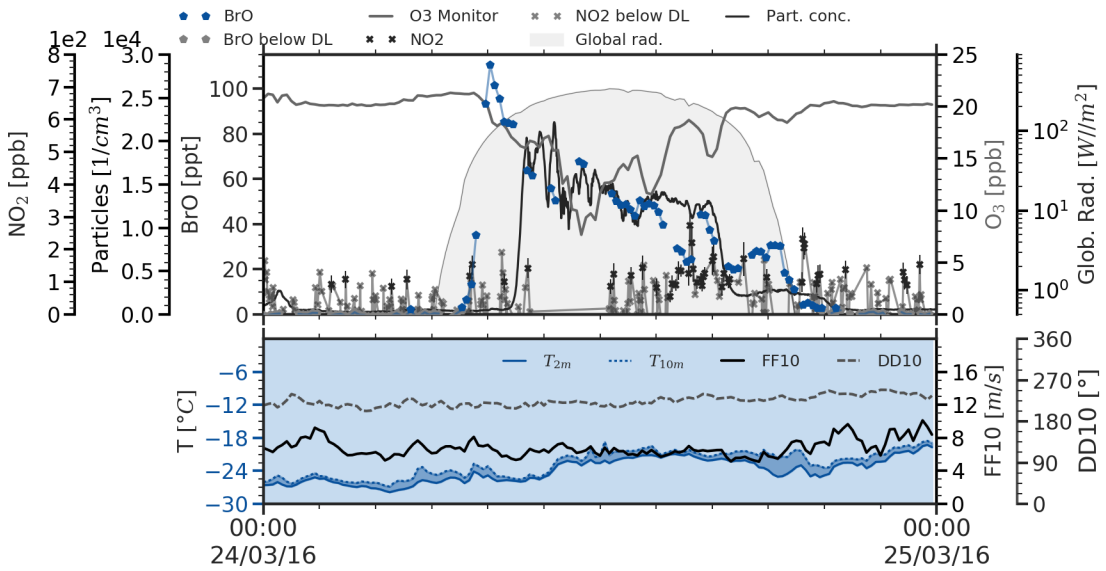

Figure 7.50: Mixing ratios of BrO, O_3, NO_2 as well as particle concentrations and meteorological data March 24th 2016 during likely new particle formation event.

On the 24th (Fig. 7.50), a similar pattern as on the previous day emerges. A continuous temperature inversion is visible, however at moderate wind speeds. Hence the *Richardson* number varies between 0.05 and 0.15 throughout the day. About one hour after sunrise, BrO mixing ratios quickly rise to 111 ppt, the highest values observed in this data set. As the estimate of ozone depletion that was calculated for this day shows (Fig. 7.10 and Fig. 7.11), the coincident decrease of ozone mixing ratios that is visible until the drop in BrO, probably due to mixing, can be entirely explained by the observed BrO levels.

For the remainder of the day, ozone varies anti-correlated to the BrO and particle concentrations. No evident meteorological cause for the end of the episode can be identified, except for slightly increasing wind speeds. After sunset, all values again return to background values. This strong correlation of elevated particle concentrations as well as the high BrO mixing ratios including a symmetry around noon for all three particle concentrations spikes make an involvement of photochemical processes in the phenomenon very likely. However, no particle formation mechanism actively involving bromine species is currently known.

Humphries et al. (2015) recently observed new particle formation over the southern ocean coincident with ozone depletion which they attributed to a presence of BrO. They hypothesised that the particle observed cloud be oxidised mercury. The occurrence of mercury depletion events under elevated BrO is a well known phenomenon and has been observed widely, also at NM III (Ebinghaus et al., 2002; Temme et al., 2003). To explain the observed particle concentrations at NM III, typical mercury levels in the Antarctic boundary layer (1-2 ng m^{-3}; Ebinghaus et al., 2002) are not sufficient when one assumes that all particles form at the cut-off size of the particle counter (10 nm). A formation of smaller droplets followed by growth through other vapours cannot be excluded, however no observations of this could be found in the literature.

Weller et al. (2015) suspect a combination of sulphur and ammonia as the cause for the new particle formation events at NM III. These two compounds in combination have

been observed to be extremely efficient in particle formation (Kirkby et al., 2011). BrO could have an influence in DMS oxidation, which in polar regions is the most important sulphur source (Read et al., 2008). However, following the results of the model study by von Glasow and Crutzen (2004), a presence of BrO would rather decrease the number of small particles (cf. 2.5.3). The question whether and how BrO might e involved in events like the one discussed above therefore clearly needs further research.

New particle formation event and BrO

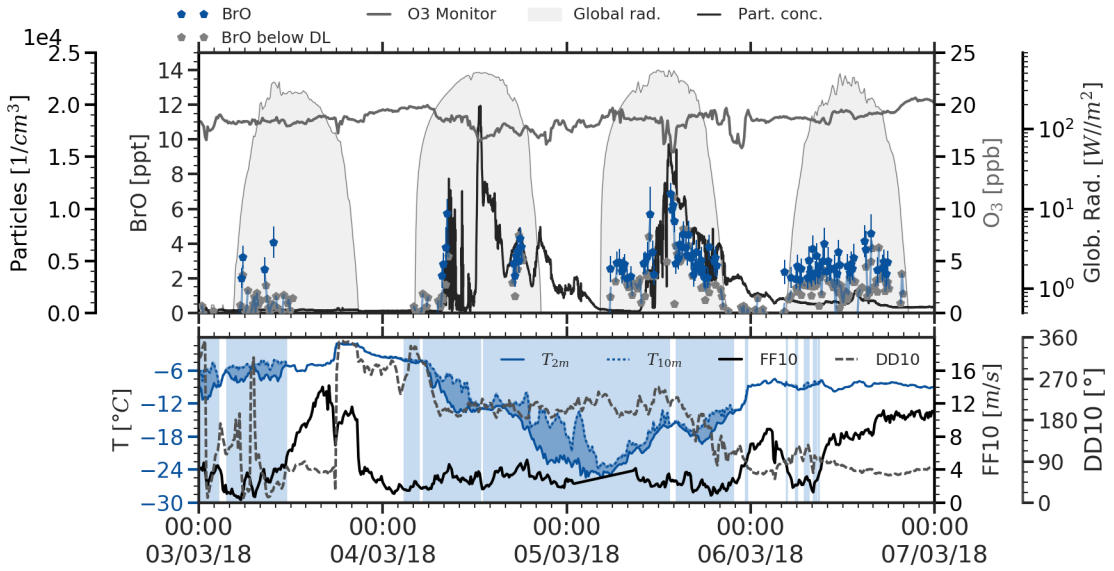

Figure 7.51: Episode from March 2018 that showed elevated BrO and rapid increases of particle concentrations linked to new particle formation on two consecutive days.

The lack of a particle size distribution and hence the missing confirmation of a new particle formation event for the episode in March 2016 to a certain degree limits the potential of further investigation. Additional SMSP data that was obtained from R. Weller (2018 - personal communication) contains two days that were not affected by contamination and showed slightly elevated BrO mixing ratios and increases of the particle concentration similar to the episode from March 2016 (Fig. 7.51).

BrO mixing ratios are obviously much lower than in March 2016 and also seem to coincide with increased particle concentrations rather than precede them, but otherwise conditions and the time of the year are comparable.

In the measured particle size distribution (Fig. 7.52) two particle formation events are clearly visible. Growth rates were determined to be $0.6\,\mathrm{nm\,h^{-1}}$, which is rather slow. Weller (2019 - personal communication) suspects a lack of condensible vapours as the limiting factor.

A detailed analysis of this episode was not possible so far. However, it confirms the simultaneous occurrence of BrO and particle formation events. A possible causal relation between both will have to be investigated in future research.

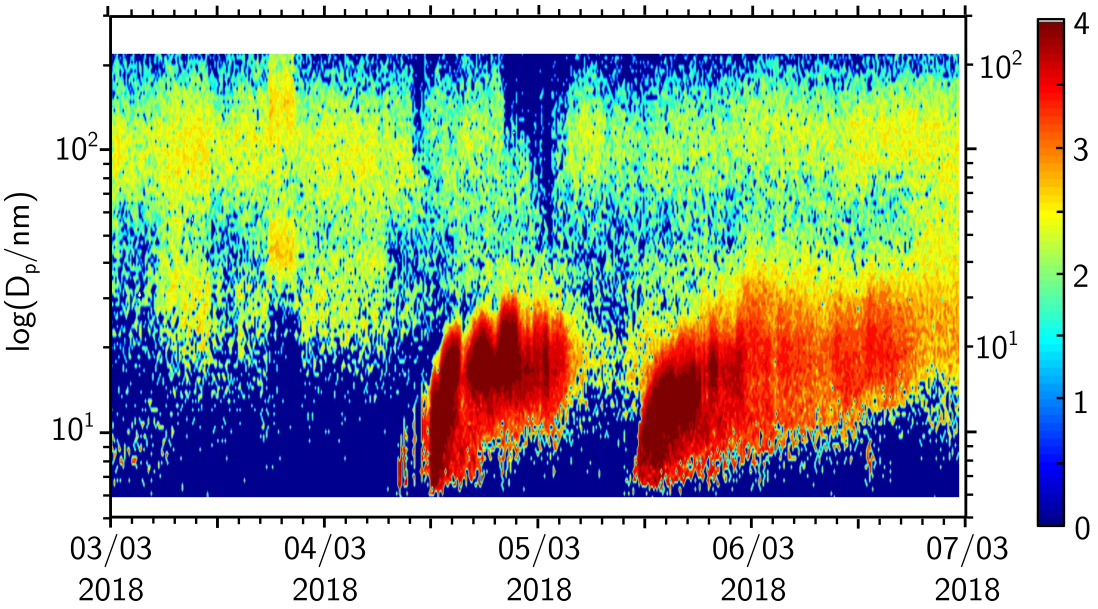

Figure 7.52: Number size distributions of aerosols at NMIII for two days showing new particle formation events. Growth rates were determined to be 0.6 $\mathrm{nm\,h^{-1}}$. Data was evaluated and provided by Weller (2019 - personal communication).

8
Conclusions

This thesis investigates the abundance, release, chemistry, and influence of reactive halogen trace gases in the coastal region of Antarctica on the basis of observations of bromine monoxide (BrO), chlorine monoxide (ClO), chlorine dioxide (OClO), iodine monoxide (IO), nitrogen dioxide (NO_2), sulphur dioxide (SO_2), and ozone (O_3). This data set was acquired at the German Antarctic research station Neumayer III (NMIII) over a time period of 32 months from January 2016 until August 2018. For a number of additional trace gases including molecular iodine (I_2), iodine dioxide (OIO), molecular bromine (Br_2), and bromine dioxide (OBrO) upper limits of abundance during this period were determined.

The central instrument used for this investigation was a newly developed Long-Path Differential Optical Absorption Spectroscopy (LP-DOAS) instrument that was purpose-built for the deployment in Antarctica as part of this thesis project. A key component of the instrument is a laser driven light source (LDLS) that offers a broad-band spectral coverage, high temporal stability, and a very long life time (>20000 h in this application). These properties allowed the design of an instrument with very limited operation and maintenance requirements, and a high reliability. This permitted measurements to be part of the air chemistry observational program of NM III under the supervision of the wintering air chemist.

For the optimal utilisation of the observation time, two absorption light paths were set up in the vicinity of NM III. Depending on atmospheric visibility, the instrument could dynamically adapt its measurement routine and switch between both. When discounting meteorological conditions that made observations impossible (mainly storms with blowing snow conditions) on 95% of the observation time measurements were performed. The overall temporal coverage of the instrument was about 60% and on 644 days of the 935-day operation time observations of trace gas mixing ratios are available. At present, the acquired data set constitutes the longest continuous measurement with a LP-DOAS instrument. These observations yield a comprehensive picture of the short- and long term seasonality of the targeted halogen trace gases over the Ekström ice shelf.

The recorded BrO atmospheric mixing ratios throughout the year show a distinctive bimodal distribution of high activity. The first period starts around the beginning of August and lasts until mid-October with variations of the onset and the termination of about two weeks between the years. It coincides with the well-known period of ozone depletion events (ODE) at NM III. Upon return of sunlight after the polar night, bromine is activated over the vast sea ice areas around the continent and air masses, depleted in ozone and containing active halogen species, are advected to NM III - often under stormy conditions.

The second period of high BrO activity starts in mid-February to March when the first major storms of the year reach the Antarctic coast. Maximum mixing ratios reached up to 111.2±0.7 ppt - the highest values so far reported from the polar regions. BrO activation regularly occurs under calm conditions between these storms until April to mid-May when at NM III the polar night begins. Between these periods, during polar night BrO was detected only occasionally in the short hours of twilight around noon, while during polar day often a constant presence at low mixing ratios could be observed.

During the two periods of high activity, two types of activation events could be identified: Periods under ODE conditions were characterised by a rapid, transport dominated decrease of ozone mixing ratios with decrease rates between 3 to over 100 ppb h^{-1} - depending on meteorological conditions. At daytime, BrO levels between 20 to 60 ppt were detected and an ongoing ozone depletion close to the ground could be observed. The analysis of vertical BrO profiles retrieved from measurements of a Multi-Axis DOAS instrument co-located on the trace gas observatory showed that elevated BrO during these episodes was well mixed within the boundary layer.

During anti-cyclonic periods, BrO activation events were characterised by a build up and an activation phase. During the former, wind speeds were decreasing but still moderately high and low mixing ratios of BrO were detected. This usually lasted a day and was followed by a period of rapid increases of BrO mixing ratios in the morning hours that started slightly before sunrise (at solar zenith angles of about 95°). BrO occasionally reached values of over 100 ppt. Under continued stable atmospheric conditions, these morning increases could be observed continuously over periods of more than a week with decreasing amplitude. Ozone rarely decreased by more than a couple of ppb during these episodes. In estimates of the ozone destruction based on observed BrO mixing ratios, it could be confirmed that local halogen chemistry is sufficient to account for the observed decreases as long as turbulent mixing was weak. MAX-DOAS vertical profiles during these episodes showed very shallow layers of elevated BrO with a vertical extent below 100 m, which agrees with similar findings in other locations.

Based on these observations, it was concluded that activation under calm conditions was dominated by local chemistry with a likely central role of local snow surfaces. Such local events dominated the autumn BrO events but were also observed between storms in spring. Daily cycles of BrO both during transport induced events and under local release were strongly modulated by atmospheric dynamics, which over the ice shelf frequently alternated between stable stratification from afternoon to early morning and turbulent mixing around noon.

The annual cycle of ClO follows that of BrO. However, ClO was only observed under calm atmospheric conditions. ClO mixing ratios during both spring and autumn activity periods reached values comparable to BrO with a maximum mixing ratio of 105±4 ppt. Interestingly, very high peak mixing ratios of BrO were never observed simultaneously with

ClO and vice versa. The reason for this is unclear but might be linked to the bromide to chloride ratio of snow and aerosols advected during the storm prior to the activation events since a reduction of the bromide to chloride ratio in ageing snow surfaces might favour chlorine activation.

As a product of the BrO-ClO cross reaction, OClO was frequently observed up to maximum values of 7.7±0.8 ppt in the evening after days when both halogen species were present. Its annual seasonality thus follows that of the other two halogen compounds. Also the destruction of ozone by BrO-ClO cross halogen reactions could be observed and reproduced in reaction kinetics estimations.

In the light of these observations, the seasonality of the detected bromine and chlorine species could be interpreted as dominated by the availability of saline surfaces. Transport induced events under ODE conditions require sea ice surfaces, either as a direct source of bromine or to produce sea salt aerosols on which bromine can be activated. Under local release, the surrounding snow surfaces act as an efficient reactor that leads to episodic, strong increases of halogen mixing ratios close to the surface. The halogens for this local release are advected to the observation site during the storms preceding a release, either as salty snow or as sea salt aerosol. This is independent of seasonal sea ice extent since the open ocean equally provides sea salt aerosols. For a location like the ice shelf at NM III, as long as there are ice or snow surfaces available, halogen release is only limited by the availability of saline surfaces and solar radiation. During the winter halogen activation minimum, solar radiation and advection are reduced due to low solar zenith angles and the minimum in storm activity due to the semi-annual oscillation (SAO), respectively. During the summer minimum, radiation is available but advection of salt is reduced due to the second minimum in the SAO, resulting in continuous but low level presence of halogens in the boundary layer probably released from the halides remaining on local surfaces.

For IO, due to several technical issues specifically related to the retrieval of this absorber, the base of available observations is small and substantiated conclusions about the annual cycle and overall impact cannot be drawn. Observed ozone depletion during the episodic presence of the very low levels of IO observed throughout the year (maximum mixing ratio: 6.5±1.0 ppt) could be reproduced with estimates based on the observed halogen species mixing ratios, confirming the impact that even low levels of IO can have on ozone.

The detected ozone mixing ratios agreed well with a co-located ozone monitor in the trace gas observatory. Due to the limitation of LP-DOAS measurements under stormy conditions, however, many of the ozone depletion episodes were not detected.

The potential influence of the nearby station and anthropogenic activities in its vicinity was assessed by analysing the observed NO_2 mixing ratios. The difference in light-path averaged NO_2 mixing ratios along both light paths confirms that the sources of NO_2 are emissions from the stations and its immediate surroundings. In total, less than 15% of the observation time was potentially affected by anthropogenic emissions. In the analysis of the different case studies, this could be investigated using NO_2 mixing ratios as a marker for pollution.

During summer, SO_2 mixing ratios of up to 230±17 ppt were observed. Based on analysis of potential NO_2 contamination as well as ionic mass concentrations measured at NM III, this observation could be identified as a very likely natural signal. Its seasonality is in good agreement with the annual cycles of marine di-methyl sulphide emissions. An influence of elevated BrO mixing ratios on the DMS oxidation that has been reported, could not be observed at the achieved detection limits.

A correlation of high particle concentrations likely caused by natural new particle formation events was observed during the first year of observations but not investigated further due to a lack of suitable instrumentation. For a comparable episode in 2018, the simultaneous occurrence of two new particle formation events and elevated BrO mixing ratios could be confirmed. Whether or not a causal relation between both phenomena exists, is currently unclear and requires further investigation.

In conclusion, the data set acquired for this thesis allows an assessment of the seasonal variability of reactive halogen species in the boundary layer of coastal Antarctica. The time series of ClO and OClO are the first long-term observations of these species in both polar regions. In the light of the potential influence of reactive chlorine on other chemical cycles from DMS over volatile organic compounds like methane to NO_x, these observations are a valuable contribution to the understanding of boundary layer chemistry in Antarctica. The high temporal resolution of the LP-DOAS observations was illustrated in the case studies above. It offers the potential of detailed studies of chemical processes over snow surfaces with reliable observational constraints through the combination of the trace gas observations with excellent long-term data sets acquired by the observatories of NM III.

9
Outlook

Based on the experience with the new LP-DOAS instrument during the two and a half years of operation, several technical improvements could be made to further increase the reliability. If insulation of the telescope is required in a future deployment, the Armaflex material currently used should be replaced by an alternative that provides better thermal and UV resistance. This could prevent a contamination of optical components as occurred during the operation at NM III. Alternatively, the interior of the telescope could be lined with an additional layer to reduce the ageing of foam surfaces, which created a fine black powder inside the telescope. Further improvements of the reliability could be achieved by selecting stepper motors with a higher durability and by making the exchange of motors more convenient.

For measurements with an infrastructure of meteorological observations similar to the one at NM III, the coupling of meteorological data (e.g. horizontal visibility) into the decision making of the measurement software of the instrument could further improve the temporal coverage of the observations or improve the quality of the acquired spectra.

The setup of the instrument during operation at NM III was optimised for the UV spectral windows, in terms of light path lengths and number of retro-reflector elements. This lead to very high measurement signals close to the minimum exposure time of the CCD in the spectral range around 450 nm and might have contributed to the worse than expected performance of the instrument in the detection of IO. An increased length of the alternative light path or at least more frequent measurements on it might have improved the results, albeit at the expense of observation time. Even in the setup selected for this work, the longer light path was more affected by blowing snow and scintillation. For future measurements, this should be considered and adapted to the respective target species.

Regarding the halogen chemistry studied in this thesis, several aspects of the available data set could be investigated in more detail:
For the presented case studies of both local and transport induced halogen activations, an air mass back-trajectory analysis should be performed to link observed mixing ratios to source regions or to confirm e.g. the assumption that even at moderate wind speeds

observations during local release episodes correspond to the observation of horizontally homogeneous conditions over the vast snow plains of coastal Antarctica.

Furthermore, the analysis of the SMPS data illustrates that the investigation of the relationship between BrO and particle formation events merits further attention. As a first step, the BrO measurements could be systematically searched for similar occurrences of elevated particle concentrations including episodes with lower BrO mixing ratios. As the example shown above illustrates, particle formation also seems to occur at lower BrO mixing ratios than in the initially identified period. This, however, could also indicate that both phenomena are correlated rather than causally linked.

The simple estimates of ozone destruction rates illustrate the potential of the data set to study halogen release and chemistry in proper atmospheric chemistry models. An interesting question, for example, would be to identify the relative importance of the snow surface compared to aerosol surfaces close to the ground in the local release of halogen species. In addition, the fast increases of mixing ratios in the morning that seem to be correctly described by simple reaction kinetics estimates, potentially allow to investigate which of the proposed mechanisms for dihalogen release govern the observed increases. Equally, the current understanding of chlorine release and chemistry could be tested with the observations from this thesis.

To facilitate the usage of the acquired data for such modelling investigations, a submission of a quality controlled data set to a public data base like PANGEA should be envisaged.

For the investigation of the influence of the vertical structure of the atmosphere on surface observations, a systematic comparison of LP-DOAS results with MAX-DOAS vertical profiles, radio and ozone sondes, and potentially the ceilometer data from NM III should be performed. The use of LP-DOAS data as a-priori constraints in the retrieval of vertical trace gas profiles could be tested to potentially improve the quality of the profiles. For this, the cause of the observed systematic differences between the LP-DOAS data and the surface mixing ratios of the retrieval need to be investigated.

Even though the shallow layers of elevated BrO mixing ratios during local activation might not be visible to satellite instruments due to an insufficient vertical column density, days with high mixing ratios could be compared to satellite observations.

One of the key results of the investigations in this thesis is the potentially important role of local snow surfaces for the release of reactive halogens. A better understanding of the processes governing this highly complex system would be desirable. In relation to questions emerging from this thesis, the halide signature of the snow surfaces at NM III is an important part of the argument made in this thesis but not well known. A collection of snow samples during and after a storm in the autumn activation period would provide important information in that regard.

For an assessment of the potential importance of snow surfaces in (coastal) Antarctica for the overall halogen budget in the region, observations in other locations, preferably at different distances from the coast could help to investigate, how far inland release of halogens similar to the observed episodes is possible. A recent cooperation in the interpretation of MAX-DOAS measurement during surprising ozone depletion episodes at Kohnen station, about 750 km south-east of NM III, might give first insights into this question (Frey et al., 2019).

A

Bibliography - Own contribution

Parts of this thesis have been published in:

Nasse, J.-M., P. G. Eger, D. Pöhler, S. Schmitt, U. Frieß, and U. Platt (2019). "Recent improvements of Long-Path DOAS measurements: impact on accuracy and automated long-term observations". In: *Atmos. Meas. Tech. Discuss.* DOI: 10.5194/amt- 2019-69.

B
Bibliography

Abbatt, J. P. D., N. Oldridge, A. Symington, V. Chukalovskiy, R. McWhinney, S. Sjostedt, and R. Cox (2010). "Release of Gas-Phase Halogens by Photolytic Generation of OH in Frozen Halide-Nitrate Solutions: An Active Halogen Formation Mechanism?" In: *The Journal of Physical Chemistry A* 114.23, pp. 6527–6533. DOI: 10.1021/jp102072t (cit. on pp. 36, 38, 40).

Abbatt, J. P. D., J. L. Thomas, K. Abrahamsson, C. Boxe, A. Granfors, A. E. Jones, M. D. King, A. Saiz-Lopez, P. B. Shepson, J. Sodeau, D. W. Toohey, C. Toubin, R. von Glasow, S. N. Wren, and X. Yang (2012). "Halogen activation via interactions with environmental ice and snow in the polar lower troposphere and other regions". In: *Atmospheric Chemistry and Physics* 12.14, pp. 6237–6271. DOI: 10.5194/acp-12-6237-2012 (cit. on pp. 10, 12, 14, 20, 28, 33, 40).

Abbatt, J. P. D. (1994). "Heterogeneous reaction of HOBr with HBr and HCl on ice surfaces at 228 K". In: *Geophysical Research Letters* 21.8, pp. 665–668. DOI: 10.1029/94gl00775 (cit. on p. 33).

– (1995). "Interactions of HBr, HCl, and HOBr with supercooled sulfuric acid solutions of stratospheric composition". In: *Journal of Geophysical Research* 100.D7, p. 14009. DOI: 10.1029/95jd01367 (cit. on p. 33).

Abbatt, J. P. D., W. R. Leaitch, A. A. Aliabadi, A. K. Bertram, J.-P. Blanchet, A. Boivin-Rioux, H. Bozem, J. Burkart, R. Y. W. Chang, J. Charette, J. P. Chaubey, R. J. Christensen, A. Cirisan, D. B. Collins, B. Croft, J. Dionne, G. J. Evans, C. G. Fletcher, R. Ghahremaninezhad, E. Girard, W. Gong, M. Gosselin, M. Gourdal, S. J. Hanna, H. Hayashida, A. B. Herber, S. Hesaraki, P. Hoor, L. Huang, R. Hussherr, V. E. Irish, S. A. Keita, J. K. Kodros, F. Köllner, F. Kolonjari, D. Kunkel, L. A. Ladino, K. Law, M. Levasseur, Q. Libois, J. Liggio, M. Lizotte, K. M. Macdonald, R. Mahmood, R. V. Martin, R. H. Mason, L. A. Miller, A. Moravek, E. Mortenson, E. L. Mungall, J. G. Murphy, M. Namazi, A.-L. Norman, N. T. O'Neill, J. R. Pierce, L. M. Russell, J. Schneider, H.

Schulz, S. Sharma, M. Si, R. M. Staebler, N. S. Steiner, M. Galí, J. L. Thomas, K. von Salzen, J. J. B. Wentzell, M. D. Willis, G. R. Wentworth, J.-W. Xu, and J. D. Yakobi-Hancock (2018). "New insights into aerosol and climate in the Arctic". In: *Atmospheric Chemistry and Physics Discussions*, pp. 1–60. DOI: 10.5194/acp-2018-995 (cit. on p. 47).

Abbatt, J. P. D., W. R. Leaitch, A. A. Aliabadi, A. K. Bertram, J.-P. Blanchet, A. Boivin-Rioux, H. Bozem, J. Burkart, R. Y. W. Chang, J. Charette, J. P. Chaubey, R. J. Christensen, A. Cirisan, D. B. Collins, B. Croft, J. Dionne, G. J. Evans, C. G. Fletcher, M. Gali, R. Ghahremaninezhad, E. Girard, W. Gong, M. Gosselin, M. Gourdal, S. J. Hanna, H. Hayashida, A. B. Herber, S. Hesaraki, P. Hoor, L. Huang, R. Hussherr, V. E. Irish, S. A. Keita, J. K. Kodros, F. Köllner, F. Kolonjari, D. Kunkel, L. A. Ladino, K. Law, M. Levasseur, Q. Libois, J. Liggio, M. Lizotte, K. M. Macdonald, R. Mahmood, R. V. Martin, R. H. Mason, L. A. Miller, A. Moravek, E. Mortenson, E. L. Mungall, J. G. Murphy, M. Namazi, A.-L. Norman, N. T. O'Neill, J. R. Pierce, L. M. Russell, J. Schneider, H. Schulz, S. Sharma, M. Si, R. M. Staebler, N. S. Steiner, J. L. Thomas, K. von Salzen, J. J. B. Wentzell, M. D. Willis, G. R. Wentworth, J.-W. Xu, and J. D. Yakobi-Hancock (2019). "Overview paper: New insights into aerosol and climate in the Arctic". In: *Atmospheric Chemistry and Physics* 19.4, pp. 2527–2560. DOI: 10.5194/acp-19-2527-2019 (cit. on p. 2).

Acton (1996). *Operating Instructions Acton Research Corporation SpectraPro-300i*. Acton Research Corporation (now Princeton Instruments). URL: ftp://ftp.princetoninstruments.com/public/manuals/Acton/Sp-300i.pdf (cit. on pp. 80, 288).

Adams, J. W., N. S. Holmes, and J. N. Crowley (2002). "Uptake and reaction of HOBr on frozen and dry NaCl/NaBr surfaces between 253 and 233 K". In: *Atmospheric Chemistry and Physics* 2.1, pp. 79–91. DOI: 10.5194/acp-2-79-2002 (cit. on pp. 33, 34).

Aguzzi, A. and M. J. Rossi (2002). "Heterogeneous Hydrolysis and Reaction of BrONO2and Br2O on Pure Ice and Ice Doped with HBr". In: *The Journal of Physical Chemistry A* 106.24, pp. 5891–5901. DOI: 10.1021/jp014383e (cit. on pp. 34, 35).

Alicke, B., U. Platt, and J. Stutz (2002). "Impact of nitrous acid photolysis on the total hydroxyl radical budget during the Limitation of Oxidant Production/Pianura Padana Produzione di Ozono study in Milan". In: *Journal of Geophysical Research* 107.D22. DOI: 10.1029/2000jd000075 (cit. on pp. 60, 123).

Altman, D. G. and J. M. Bland (1983). "Measurement in Medicine: The Analysis of Method Comparison Studies". English. In: *Journal of the Royal Statistical Society. Series D (The Statistician)* 32.3, pp. 307–317. DOI: 10.2307/2987937 (cit. on p. 131).

American Meteorological Society (2013). *The Glossary of Meteorology*. Online Edition. retrieved in 2019. URL: http://glossary.ametsoc.org/wiki/Main_Page (cit. on p. 140).

Amory, C., H. Gallée, F. Naaim-Bouvet, V. Favier, E. Vignon, G. Picard, A. Trouvilliez, L. Piard, C. Genthon, and H. Bellot (2017). "Seasonal Variations in Drag Coefficient

over a Sastrugi-Covered Snowfield in Coastal East Antarctica". In: *Boundary-Layer Meteorology* 164.1, pp. 107–133. DOI: 10.1007/s10546-017-0242-5 (cit. on p. 22).

Anderson, P. S. and S. J.-B. Bauguitte (2007). "Behaviour of tracer diffusion in simple atmospheric boundary layer models". In: *Atmospheric Chemistry and Physics* 7.19, pp. 5147–5158. DOI: 10.5194/acp-7-5147-2007 (cit. on pp. 18, 175).

Anderson, P. S. and W. D. Neff (2008). "Boundary layer physics over snow and ice". In: *Atmospheric Chemistry and Physics* 8.13, pp. 3563–3582. DOI: 10.5194/acp-8-3563-2008 (cit. on pp. 12, 16–18, 21, 22, 153, 175, 176, 223).

ANDOR (2005). *Andor DU440 camera specifications*. Andor Technologies (now part of Oxford Instruments) (cit. on p. 80).

Andrews, L. C., R. L. Phillips, C. Y. Hopen, and M. A. Al-Habash (1999). "Theory of optical scintillation". In: *Journal of the Optical Society of America A* 16.6, p. 1417. DOI: 10.1364/josaa.16.001417 (cit. on p. 90).

Angot, H., A. Dastoor, F. D. Simone, K. Gårdfeldt, C. N. Gencarelli, I. M. Hedgecock, S. Langer, O. Magand, M. N. Mastromonaco, C. Nordstrøm, K. A. Pfaffhuber, N. Pirrone, A. Ryjkov, N. E. Selin, H. Skov, S. Song, F. Sprovieri, A. Steffen, K. Toyota, O. Travnikov, X. Yang, and A. Dommergue (2016). "Chemical cycling and deposition of atmospheric mercury in polar regions: review of recent measurements and comparison with models". In: *Atmospheric Chemistry and Physics* 16.16, pp. 10735–10763. DOI: 10.5194/acp-16-10735-2016 (cit. on pp. 2, 3, 44).

Ångström, A. (1929). "On the Atmospheric Transmission of Sun Radiation and on Dust in the Air". In: *Geografiska Annaler* 11, p. 156. DOI: 10.2307/519399 (cit. on p. 52).

– (1930). "On the Atmospheric Transmission of Sun Radiation. II". In: *Geografiska Annaler* 12, p. 130. DOI: 10.2307/519561 (cit. on p. 52).

ANSYCO (2000). *Ozon Analysator O341M zur Immissions-/MAK-Messung - Spcifications*. Analytische Systeme und Komponenten GmbH. URL: http://epic.awi.de/27245/1/Mer2000a.pdf (cit. on pp. 69, 136).

Artiglia, L., J. Edebeli, F. Orlando, S. Chen, M.-T. Lee, P. C. Arroyo, A. Gilgen, T. Bartels-Rausch, A. Kleibert, M. Vazdar, M. A. Carignano, J. S. Francisco, P. B. Shepson, I. Gladich, and M. Ammann (2017). "A surface-stabilized ozonide triggers bromide oxidation at the aqueous solution-vapour interface". In: *Nature Communications* 8.1. DOI: 10.1038/s41467-017-00823-x (cit. on p. 35).

Asmi, E., A. Frey, A. Virkkula, M. Ehn, H. E. Manninen, H. Timonen, O. Tolonen-Kivimäki, M. Aurela, R. Hillamo, and M. Kulmala (2010). "Hygroscopicity and chemical composition of Antarctic sub-micrometre aerosol particles and observations of new particle formation". In: *Atmospheric Chemistry and Physics* 10.9, pp. 4253–4271. DOI: 10.5194/acp-10-4253-2010 (cit. on p. 47).

Atkinson, H. M., R.-J. Huang, R. Chance, H. K. Roscoe, C. Hughes, B. Davison, A. Schönhardt, A. S. Mahajan, A. Saiz-Lopez, T. Hoffmann, and P. S. Liss (2012). "Iodine emissions from the sea ice of the Weddell Sea". In: *Atmospheric Chemistry and Physics* 12.22, pp. 11229–11244. DOI: 10.5194/acp-12-11229-2012 (cit. on pp. 37, 39).

Atkinson, R., D. L. Baulch, R. A. Cox, J. N. Crowley, R. F. Hampson, R. G. Hynes, M. E. Jenkin, M. J. Rossi, and J. Troe (2007). "Evaluated kinetic and photochemical data for atmospheric chemistry: Volume III - gas phase reactions of inorganic halogens". In: *Atmospheric Chemistry and Physics* 7.4, pp. 981–1191. DOI: 10.5194/acp-7-981-2007 (cit. on pp. 29–31, 184, 210, 218, 219).

Axelsson, H., B. Galle, K. Gustavsson, P. Ragnarsson, and M. Rudi (1990). "A transmitting/receiving telescope for DOAS measurements using retro-reflector technique". In: *Optical Remote Sensing of the Atmosphere, OSA Technical Digest Series* 4, pp. 641–644 (cit. on p. 70).

Barnes, I., J. Hjorth, and N. Mihalopoulos (2006). "Dimethyl sulfide and dimethyl sulfoxide and their oxidation in the atmosphere". English. In: *Chemical reviews* 106.3, pp. 940–975. ISSN: 0009-2665 and 1520-6890. URL: https://pubs.acs.org/doi/10.1021/cr020529%2B (cit. on p. 45).

Barrie, L. A. (1991). "Snow Formation and Processes in the Atmosphere that Influence its Chemical Composition". In: *Seasonal Snowpacks*. Springer Berlin Heidelberg, pp. 1–20. DOI: 10.1007/978-3-642-75112-7_1 (cit. on p. 13).

Barrie, L. A., J. W. Bottenheim, R. C. Schnell, P. J. Crutzen, and R. A. Rasmussen (1988). "Ozone destruction and photochemical reactions at polar sunrise in the lower Arctic atmosphere". In: *Nature* 334.6178, pp. 138–141. DOI: 10.1038/334138a0 (cit. on pp. 2, 28, 29, 38).

Barrie, L. A. (1986). "Arctic air pollution: An overview of current knowledge". In: *Atmospheric Environment* 20.4, pp. 643–663. DOI: 10.1016/0004-6981(86)90180-0 (cit. on p. 47).

Barry, R. G. and T. Y. Gan (2011). *The global cryosphere. past, present, and future*. 1st. Cambridge: Cambridge Univ. Press, XV, 472 S. DOI: 10.1017/CBO9780511977947 (cit. on p. 7).

Bartels-Rausch, T., H.-W. Jacobi, T. F. Kahan, J. L. Thomas, E. S. Thomson, J. P. D. Abbatt, M. Ammann, J. R. Blackford, H. Bluhm, C. Boxe, F. Domine, M. M. Frey, I. Gladich, M. I. Guzmán, D. Heger, T. Huthwelker, P. Klán, W. F. Kuhs, M. H. Kuo, S. Maus, S. G. Moussa, V. F. McNeill, J. T. Newberg, J. B. C. Pettersson, M. Roeselová, and J. R. Sodeau (2014). "A review of air–ice chemical and physical interactions (AICI): liquids, quasi-liquids, and solids in snow". In: *Atmospheric Chemistry and Physics* 14.3, pp. 1587–1633. DOI: 10.5194/acp-14-1587-2014 (cit. on pp. 3, 13, 14, 28, 33).

Bauguitte, S. J.-B., W. J. Bloss, M. J. Evans, R. A. Salmon, P. S. Anderson, A. E. Jones, J. D. Lee, A. Saiz-Lopez, H. K. Roscoe, E. W. Wolff, and J. M. C. Plane (2012). "Summertime NOx measurements during the CHABLIS campaign: can source and sink estimates unravel observed diurnal cycles?" In: *Atmospheric Chemistry and Physics* 12.2, pp. 989–1002. DOI: 10.5194/acp-12-989-2012 (cit. on p. 29).

Beekmann, M., G. Ancellet, D. Martin, C. Abonnel, G. Duverneuil, F. Eideliman, P. Bessemoulin, N. Fritz, and E. Gizard (1995). "Intercomparison of tropospheric ozone profiles obtained by electrochemical sondes, a ground based lidar and an airborne UV-photometer". In: *Atmospheric Environment* 29.9, pp. 1027–1042. DOI: 10.1016/1352-2310(94)00336-j (cit. on p. 66).

Begoin, M., A. Richter, M. Weber, L. Kaleschke, X. Tian-Kunze, A. Stohl, N. Theys, and J. P. Burrows (2010). "Satellite observations of long range transport of a large BrO plume in the Arctic". In: *Atmospheric Chemistry and Physics* 10.14, pp. 6515–6526. DOI: 10.5194/acp-10-6515-2010 (cit. on p. 42).

Bevington, P. R. (1969). *Data reduction and error analysis for the physical sciences*. 1st. McGraw-Hill Education (cit. on p. 58).

Blake, J. N., B. Y. Kim, and H. J. Shaw (1986). "Fiber-optic modal coupler using periodic microbending". In: *Optics Letters* 11.3, p. 177. DOI: 10.1364/ol.11.000177 (cit. on p. 77).

Blechschmidt, A.-M., A. Richter, J. P. Burrows, L. Kaleschke, K. Strong, N. Theys, M. Weber, X. Zhao, and A. Zien (2016). "An exemplary case of a bromine explosion event linked to cyclone development in the Arctic". In: *Atmospheric Chemistry and Physics* 16.3, pp. 1773–1788. DOI: 10.5194/acp-16-1773-2016 (cit. on pp. 3, 42).

Bloss, W. J., M. Camredon, J. D. Lee, D. E. Heard, J. M. C. Plane, A. Saiz-Lopez, S. J.-B. Bauguitte, R. A. Salmon, and A. E. Jones (2010). "Coupling of HOx, NOx and halogen chemistry in the antarctic boundary layer". In: *Atmospheric Chemistry and Physics* 10.21, pp. 10187–10209. DOI: 10.5194/acp-10-10187-2010 (cit. on p. 3).

Bobrowski, N., G. Hönninger, B. Galle, and U. Platt (2003). "Detection of bromine monoxide in a volcanic plume". In: *Nature* 423.6937, pp. 273–276. DOI: 10.1038/nature01625 (cit. on p. 83).

Boggs, P. T. and J. E. Rogers (1990). "Orthogonal Distance Regression". In: *Statistical analysis of measurement error models and applications*. Ed. by P. J. Brown and W. A. Fuller. Vol. 112. Contemporary mathematics. Joint Summer Research Conference in the Mathematical Sciences on Statistical Analysis of Measurement Error Models and Applications Jun10-16 1989, Arcata, Calif. Providence, RI: American Mathematical Society. ISBN: 978-0-8218-5117-3. URL: https://bookstore.ams.org/conm-112/1 (cit. on p. 131).

Boggs, P. T., R. H. Byrd, J. E. Rogers, and R. B. Schnabel (1992). *User's Reference Guide for ODRPACK Version 2.01 Software for Weighted Orthogonal Distance Regression*. U.S. DEPARTMENT OF COMMERCE - Technology Administration - National Institute of

Standards and Technology. Gaithersburg, MD 20899. URL: https://docs.scipy.org/doc/external/odrpack_guide.pdf (cit. on pp. 130, 131, 134, 136).

Boggs, P. T., R. H. Byrd, and R. B. Schnabel (1987). "A Stable and Efficient Algorithm for Nonlinear Orthogonal Distance Regression". In: *Society for Industrial and Applied Mathematics. SIAM Journal on Scientific and Statistical Computing* 8.6, pp. 1052–1078. ISSN: 0196-5204 and 2168-3417. DOI: 10.1137/0908085 (cit. on p. 131).

Bogumil, K., J. Orphal, T. Homann, S. Voigt, P. Spietz, O. C. Fleischmann, A. Vogel, M. Hartmann, H. Kromminga, H. Bovensmann, J. Frerick, and J. P. Burrows (2003). "Measurements of molecular absorption spectra with the SCIAMACHY pre-flight model: instrument characterization and reference data for atmospheric remote-sensing in the 230-2380 nm region". In: *Journal of Photochemistry and Photobiology A: Chemistry* 157.2-3, pp. 167–184. DOI: 10.1016/s1010-6030(03)00062-5 (cit. on pp. 52, 108, 289).

Bottenheim, J. W. and E. Chan (2006). "A trajectory study into the origin of spring time Arctic boundary layer ozone depletion". In: *Journal of Geophysical Research* 111.D19. DOI: 10.1029/2006jd007055 (cit. on p. 18).

Bottenheim, J. W., A. G. Gallant, and K. A. Brice (1986). "Measurements of NOy species and O3 at 82° N latitude". In: *Geophysical Research Letters* 13.2, pp. 113–116. DOI: 10.1029/gl013i002p00113 (cit. on p. 28).

Brandt, R. E., S. G. Warren, A. P. Worby, and T. C. Grenfell (2005). "Surface Albedo of the Antarctic Sea Ice Zone". In: *Journal of Climate* 18.17, pp. 3606–3622. DOI: 10.1175/jcli3489.1 (cit. on p. 8).

Brasseur, G. P., R. G. Prinn, and A. A. P. Psezenny, eds. (2003). *Atmospheric Chemistry in a Changing World*. Springer Berlin Heidelberg. 316 pp. ISBN: 3540430504. DOI: 10.1007/978-3-642-18984-5 (cit. on pp. 23, 24).

Breider, T. J., M. P. Chipperfield, G. W. Mann, M. T. Woodhouse, and K. S. Carslaw (2014). "Suppression of CCN formation by bromine chemistry in the remote marine atmosphere". In: *Atmospheric Science Letters* 16.2, pp. 141–147. DOI: 10.1002/asl2.539 (cit. on p. 45).

Brewer, A. W., C. T. McElroy, and J. B. Kerr (1973). "Nitrogen dioxide concentrations in the atmosphere". In: *Nature* 246.5429, pp. 129–133. DOI: 10.1038/246129a0 (cit. on p. 101).

Brooks, S., C. Moore, D. Lew, B. Lefer, G. Huey, and D. Tanner (2011). "Temperature and sunlight controls of mercury oxidation and deposition atop the Greenland ice sheet". In: *Atmospheric Chemistry and Physics* 11.16, pp. 8295–8306. DOI: 10.5194/acp-11-8295-2011 (cit. on p. 183).

Brooks, S. B., A. Saiz-Lopez, H. Skov, S. E. Lindberg, J. M. C. Plane, and M. E. Goodsite (2006). "The mass balance of mercury in the springtime arctic environment". In: *Geophysical Research Letters* 33.13. DOI: 10.1029/2005gl025525 (cit. on p. 44).

Burrows, J. P., A. Richter, A. Dehn, B. Deters, S. Himmelmann, S. Voigt, and J. Orphal (1999). "Atmospheric remote-sensing reference data from GOME: Part 2. Temperature-dependent absorption cross-sections of O3 in the 231-794 nm range". In: *Journal of Quantitative Spectroscopy and Radiative Transfer* 61.4, pp. 509–517. DOI: 10.1016/s0022-4073(98)00037-5 (cit. on pp. 108, 109, 289).

Buys, Z., N. Brough, L. G. Huey, D. J. Tanner, R. von Glasow, and A. E. Jones (2013). "High temporal resolution Br_2, BrCl and BrO observations in coastal Antarctica". In: *Atmospheric Chemistry and Physics* 13.3, pp. 1329–1343. DOI: 10.5194/acp-13-1329-2013 (cit. on pp. 2, 37–39, 206, 208).

Caicedo, V., B. Rappenglück, B. Lefer, G. Morris, D. Toledo, and R. Delgado (2017). "Comparison of aerosol lidar retrieval methods for boundary layer height detection using ceilometer aerosol backscatter data". In: *Atmospheric Measurement Techniques* 10.4, pp. 1609–1622. DOI: 10.5194/amt-10-1609-2017 (cit. on p. 67).

Cao, L., U. Platt, and E. Gutheil (2016a). "Role of the boundary layer in the occurrence and termination of the tropospheric ozone depletion events in polar spring". In: *Atmospheric Environment* 132, pp. 98–110. DOI: 10.1016/j.atmosenv.2016.02.034 (cit. on p. 29).

Cao, L., H. Sihler, U. Platt, and E. Gutheil (2014). "Numerical analysis of the chemical kinetic mechanisms of ozone depletion and halogen release in the polar troposphere". In: *Atmospheric Chemistry and Physics* 14.7, pp. 3771–3787. DOI: 10.5194/acp-14-3771-2014 (cit. on pp. 29, 32, 35, 47, 186).

Cao, L., M. He, H. Jiang, H. Grosshans, and N. Cao (2016b). "Sensitivity of the Reaction Mechanism of the Ozone Depletion Events during the Arctic Spring on the Initial Atmospheric Composition of the Troposphere". In: *Atmosphere* 7.10, p. 124. DOI: 10.3390/atmos7100124 (cit. on p. 186).

Chambers, S. D., S. Preunkert, R. Weller, S.-B. Hong, R. S. Humphries, L. Tositti, H. Angot, M. Legrand, A. G. Williams, A. D. Griffiths, J. Crawford, J. Simmons, T. J. Choi, P. B. Krummel, S. Molloy, Z. Loh, I. Galbally, S. Wilson, O. Magand, F. Sprovieri, N. Pirrone, and A. Dommergue (2018). "Characterizing Atmospheric Transport Pathways to Antarctica and the Remote Southern Ocean Using Radon-222". In: *Frontiers in Earth Science* 6. DOI: 10.3389/feart.2018.00190 (cit. on p. 19).

Chan, K. L., D. Pöhler, and U. Platt (2012). "Long term NO2 measurements in Hong Kong using LED based long path differential optical absorption spectroscopy". eng. In: *Atmospheric measurement techniques* 5.5, pp. 901–912. ISSN: 1867-8548. DOI: 10.5194/amt-5-901-2012 (cit. on p. 70).

Chen, Q., T. Sherwen, M. Evans, and B. Alexander (2018). "DMS oxidation and sulfur aerosol formation in the marine troposphere: a focus on reactive halogen and multiphase chemistry". In: *Atmospheric Chemistry and Physics* 18.18, pp. 13617–13637. DOI: 10.5194/acp-18-13617-2018 (cit. on pp. 2, 3).

Christopherson, R. W. and G. H. Birkeland (2015). *Geosystems. An introduction to physical geography.* 9. ed., global ed. Always learning. Boston ; Munich [u.a.]: Pearson, 647, [36] S. ISBN: 978-1-292-05775-0 (cit. on p. 5).

Commane, R., K. Seitz, J. Buxmann, U. Platt, and D. Pöhler (2011). "Iodine monoxide at a clean marine coastal site. observations of high frequency variations and inhomogeneous distributions". eng. In: *Atmospheric chemistry and physics* 11.13, pp. 6721–6733. ISSN: 1680-7324. DOI: 10.5194/acp-11-6721-2011 (cit. on pp. 30, 35, 55).

Copernicus Climate Change Service (C3S) (2017). *ERA5: Fifth generation of ECMWF atmospheric reanalyses of the global climate.* Copernicus Climate Change Service Climate Data Store (CDS). Retrieved 2018-12-14. URL: https://cds.climate.copernicus.eu/cdsapp#!/home (cit. on p. 143).

Crutzen, P. J. (1974). "A Review of Upper Atmospheric Photochemistry". In: *Canadian Journal of Chemistry* 52.8, pp. 1569–1581. DOI: 10.1139/v74-229 (cit. on pp. 2, 28).

– (1986). *Is the Detergent of the Atmosphere Decreasing? Importance of Methane for the OH Radical Concentration and Atmospheric Photochemistry.* Tech. rep. Batiment Jean Monnet, Luxembourg: Commission of the European Communities. URL: https://publications.europa.eu/en/publication-detail/-/publication/99c7dbe1-e543-4bfb-9547-a808ecf9581c (cit. on p. 1).

Cunningham, R. W. (1993). "Comparison of three methods for determining fit parameter uncertainties for the Marquardt Compromise". In: *Computers in Physics* 7.5, p. 570. DOI: 10.1063/1.168470 (cit. on p. 58).

Custard, K. D., A. R. W. Raso, P. B. Shepson, R. M. Staebler, and K. A. Pratt (2017). "Production and Release of Molecular Bromine and Chlorine from the Arctic Coastal Snowpack". In: *ACS Earth and Space Chemistry* 1.3, pp. 142–151. DOI: 10.1021/acsearthspacechem.7b00014 (cit. on pp. 2, 35, 39, 186, 206).

Custard, K. D., C. R. Thompson, K. A. Pratt, P. B. Shepson, J. Liao, L. G. Huey, J. J. Orlando, A. J. Weinheimer, E. Apel, S. R. Hall, F. Flocke, L. Mauldin, R. S. Hornbrook, D. Pöhler, S. General, J. Zielcke, W. R. Simpson, U. Platt, A. Fried, P. Weibring, B. C. Sive, K. Ullmann, C. Cantrell, D. J. Knapp, and D. D. Montzka (2015). "The NOx dependence of bromine chemistry in the Arctic atmospheric boundary layer". In: *Atmospheric Chemistry and Physics* 15.18, pp. 10799–10809. DOI: 10.5194/acp-15-10799-2015 (cit. on p. 32).

Custard, K. D., K. A. Pratt, S. Wang, and P. B. Shepson (2016). "Constraints on Arctic Atmospheric Chlorine Production through Measurements and Simulations of Cl2 and ClO". In: *Environmental Science & Technology* 50.22, pp. 12394–12400. DOI: 10.1021/acs.est.6b03909 (cit. on pp. 186, 206).

Czerny, M. and A. F. Turner (1930). "Über den Astigmatismus bei Spiegelspektrometern". In: *Zeitschrift für Physik* 61.11-12, pp. 792–797. DOI: 10.1007/bf01340206 (cit. on p. 80).

Dacey, J. W. H. and S. G. Wakeham (1986). "Oceanic Dimethylsulfide: Production During Zooplankton Grazing on Phytoplankton". In: *Science* 233.4770, pp. 1314–1316. DOI: 10.1126/science.233.4770.1314 (cit. on p. 45).

Davis, D., G. Chen, M. Buhr, J. Crawford, D. Lenschow, B. Lefer, R. Shetter, F. Eisele, L. Mauldin, and A. Hogan (2004). "South Pole NOx Chemistry: an assessment of factors controlling variability and absolute levels". In: *Atmospheric Environment* 38.32, pp. 5375–5388. DOI: 10.1016/j.atmosenv.2004.04.039 (cit. on pp. 18, 27).

Deshler, T., J. L. Mercer, H. G. J. Smit, R. Stubi, G. Levrat, B. J. Johnson, S. J. Oltmans, R. Kivi, A. M. Thompson, J. Witte, J. Davies, F. J. Schmidlin, G. Brothers, and T. Sasaki (2008). "Atmospheric comparison of electrochemical cell ozonesondes from different manufacturers, and with different cathode solution strengths: The Balloon Experiment on Standards for Ozonesondes". In: *Journal of Geophysical Research* 113.D4. DOI: 10.1029/2007jd008975 (cit. on p. 66).

Dobson, G. M. B. and D. N. Harrison (1926). "Measurements of the Amount of Ozone in the Earth's Atmosphere and Its Relation to Other Geophysical Conditions". In: *Proceedings of the Royal Society A: Mathematical, Physical and Engineering Sciences* 110.756, pp. 660–693. DOI: 10.1098/rspa.1926.0040 (cit. on pp. 50, 101).

Dominé, F., M. Albert, T. Huthwelker, H.-W. Jacobi, A. A. Kokhanovsky, M. Lehning, G. Picard, and W. R. Simpson (2008). "Snow physics as relevant to snow photochemistry". In: *Atmospheric Chemistry and Physics* 8.2, pp. 171–208. DOI: 10.5194/acp-8-171-2008 (cit. on pp. 13, 14).

Dominé, F. and P. B. Shepson (2002). "Air-Snow Interactions and Atmospheric Chemistry". In: *Science* 297.5586, pp. 1506–1510. DOI: 10.1126/science.1074610 (cit. on pp. 13, 14).

Dominé, F. and E. Thibert (1995). "Biogeochemistry of Seasonally Snow-Covered Catchments (Proceedings of a Boulder Symposium, July 1995)". In: 228. IAHS PubI. Chap. Relationship between atmospheric composition and snow composition for HCl and HNO3, pp. 3–10. ISBN: 0-947571-44-2 (cit. on p. 13).

Dommergue, A., F. Sprovieri, N. Pirrone, R. Ebinghaus, S. Brooks, J. Courteaud, and C. P. Ferrari (2010). "Overview of mercury measurements in the Antarctic troposphere". In: *Atmospheric Chemistry and Physics* 10.7, pp. 3309–3319. DOI: 10.5194/acp-10-3309-2010 (cit. on p. 44).

Douglas, T. A., L. L. Loseto, R. W. Macdonald, P. Outridge, A. Dommergue, A. Poulain, M. Amyot, T. Barkay, T. Berg, J. Chételat, P. Constant, M. Evans, C. Ferrari, N. Gantner, M. S. Johnson, J. Kirk, N. Kroer, C. Larose, D. Lean, T. G. Nielsen, L. Poissant, S. Rognerud, H. Skov, S. Sørensen, F. Wang, S. Wilson, and C. M. Zdanowicz (2012). "The fate of mercury in Arctic terrestrial and aquatic ecosystems, a review". In: *Environmental Chemistry* 9.4, p. 321. DOI: 10.1071/en11140 (cit. on p. 44).

Ebinghaus, R., H. H. Kock, C. Temme, J. W. Einax, A. G. Löwe, A. Richter, J. P. Burrows, and W. H. Schroeder (2002). "Antarctic Springtime Depletion of Atmospheric Mercury".

In: *Environmental Science & Technology* 36.6, pp. 1238–1244. DOI: 10.1021/es015710z (cit. on pp. 44, 224).

Eckhardt, H. D. (1971). "Simple Model of Corner Reflector Phenomena". In: *Applied Optics* 10.7, p. 1559. DOI: 10.1364/ao.10.001559 (cit. on pp. 70, 71).

Eger, P. (2014). "Improving Long-Path DOAS measurements with a Laser Driven Light Source and a new fibre configuration". MA thesis. Combined Faculties for Natural Sciences and for Mathematics of the Ruperto-Carola University of Heidelberg, Germany (cit. on pp. 70, 76, 109).

Ehn, J. K., B. J. Hwang, R. Galley, and D. G. Barber (2007). "Investigations of newly formed sea ice in the Cape Bathurst polynya: 1. Structural, physical, and optical properties". In: *Journal of Geophysical Research* 112.C5. DOI: 10.1029/2006jc003702 (cit. on p. 10).

Elsässer, C., D. Wagenbach, R. Weller, M. Auer, A. Wallner, and M. Christl (2011). "Continuous 25-yr aerosol records at coastal Antarctica – II: variability of the radionuclides 7Be, 10Be and 210Pb." In: *Tellus B: Chemical and Physical Meteorology* 63.5, pp. 920–934. DOI: 10.1111/j.1600-0889.2011.00543.x (cit. on pp. 67, 146).

EN590, Directive 2009/30/EC (2009). European Standards Organization (CEN). URL: https://eur-lex.europa.eu/legal-content/EN/ALL/?uri=CELEX:32009L0030 (cit. on p. 161).

Energetiq (2018a). *EQ-99X LDLS Data sheet*. 1-18. Energetiq Technology, Inc. URL: https://www.energetiq.com/DataSheets/EQ99X-Data-Sheet.pdf (cit. on p. 72).

– (2018b). *LDLS frequently Asked Questions*. Website. URL: https://www.energetiq.com/faq.php (cit. on p. 75).

EPICA community, L. Augustin, C. Barbante, P. R. F. Barnes, J. M. Barnola, M. Bigler, E. Castellano, O. Cattani, J. Chappellaz, D. Dahl-Jensen, B. Delmonte, G. Dreyfus, G. Durand, S. Falourd, H. Fischer, J. Flückiger, M. E. Hansson, P. Huybrechts, G. Jugie, S. J. Johnsen, J. Jouzel, P. Kaufmann, J. Kipfstuhl, F. Lambert, V. Y. Lipenkov, G. C. Littot, A. Longinelli, R. Lorrain, V. Maggi, V. Masson-Delmotte, H. Miller, R. Mulvaney, J. Oerlemans, H. Oerter, G. Orombelli, F. Parrenin, D. A. Peel, J.-R. Petit, D. Raynaud, C. Ritz, U. Ruth, J. Schwander, U. Siegenthaler, R. Souchez, B. Stauffer, J. P. Steffensen, B. Stenni, T. F. Stocker, I. E. Tabacco, R. Udisti, R. S. W. van de Wal, M. van den Broeke, J. Weiss, F. Wilhelms, J.-G. Winther, E. W. Wolff, and M. Zucchelli (2004). "Eight glacial cycles from an Antarctic ice core". In: *Nature* 429.6992, pp. 623–628. DOI: 10.1038/nature02599 (cit. on p. 67).

Escobar Castells, I. (2018). "Boundary layer dynamics and meteorology at the Antarctic research station Neumayer". MSc. thesis. Imperial College London - Ruprecht-Karls universit/"at Heidelberg (cit. on p. 67).

EUMETSAT Ocean and Sea Ice Satellite Application Facility (2015). "Global sea ice concentration climate data records 1978-2015". In: *Copernicus climate change service (C3S)*.

Version 1.2, 2015. Retrieved 2018-12-14. Norwegian and Danish Meteorological Institutes. URL: https://cds.climate.copernicus.eu/cdsapp#!/dataset/satellite-sea-ice?tab=overview (cit. on p. 11).

Fan, S.-M. and D. J. Jacob (1992). "Surface ozone depletion in Arctic spring sustained by bromine reactions on aerosols". In: *Nature* 359.6395, pp. 522–524. DOI: 10.1038/359522a0 (cit. on pp. 28, 33).

Farman, J. C., B. G. Gardiner, and J. D. Shanklin (1985). "Large losses of total ozone in Antarctica reveal seasonal ClO x /NO x interaction". In: *Nature* 315.6016, pp. 207–210. DOI: 10.1038/315207a0 (cit. on pp. 2, 28, 50).

Ferlemann, F., N. Bauer, R. Fitzenberger, H. Harder, H. Osterkamp, D. Perner, U. Platt, M. Schneider, P. Vradelis, and K. Pfeilsticker (2000). "Differential optical absorption spectroscopy instrument for stratospheric balloonborne trace-gas studies". In: *Applied Optics* 39.15, p. 2377. DOI: 10.1364/ao.39.002377 (cit. on p. 101).

Fickert, S., J. W. Adams, and J. N. Crowley (1999). "Activation of Br2and BrCl via uptake of HOBr onto aqueous salt solutions". In: *Journal of Geophysical Research: Atmospheres* 104.D19, pp. 23719–23727. DOI: 10.1029/1999jd900359 (cit. on p. 33).

Finlayson-Pitts, B. J., F. E. Livingston, and H. N. Berko (1990). "Ozone destruction and bromine photochemistry at ground level in the Arctic spring". In: *Nature* 343.6259, pp. 622–625. DOI: 10.1038/343622a0 (cit. on p. 29).

Finlayson-Pitts, B. J. and J. C. Hemminger (2000). "Physical Chemistry of Airborne Sea Salt Particles and Their Components". In: *The Journal of Physical Chemistry A* 104.49, pp. 11463–11477. DOI: 10.1021/jp002968n (cit. on p. 192).

Fleischmann, O. C. and J. P. Burrows (2002). "Absorption measurements using a Fourier transform spectrometer;spectral resolution 5 cm^{-1}". Institute of Environmental Physics (IUP), Institute of Remote Sensing (IFE), University of Bremen. URL: http://www.iup.physik.uni-bremen.de/gruppen/molspec/index.html (cit. on pp. 52, 108, 289).

Fleischmann, O. C., M. Hartmann, J. P. Burrows, and J. Orphal (2004). "New ultraviolet absorption cross-sections of BrO at atmospheric temperatures measured by time-windowing Fourier transform spectroscopy". In: *Journal of Photochemistry and Photobiology A: Chemistry* 168.1-2, pp. 117–132. DOI: 10.1016/j.jphotochem.2004.03.026 (cit. on pp. 108, 109, 289).

Foster, K. L. (2001). "The Role of Br2 and BrCl in Surface Ozone Destruction at Polar Sunrise". In: *Science* 291.5503, pp. 471–474. DOI: 10.1126/science.291.5503.471 (cit. on p. 37).

Frey, M., H. Winton, N. Brough, J.-M. Nasse, U. Frieß, J. Savarino, and R. Weller (2019). "New insights into the atmospheric oxidising capacity above the Antarctic Plateau". In: *Geophysical Research Abstracts*. Vol. 21. EGU2019-10516. European Geoscience Union. EGU General Assembly 2019. URL: https://meetingorganizer.copernicus.org/EGU2019/EGU2019-10516.pdf (cit. on p. 232).

Frieß, U. (2013). *MS-DOAS: Muli-tasking Software for DOAS Systems*. Institute of Environmental Physics - Heidelberg University (cit. on p. 88).

– (2018). "MAX-DOAS Observations at Neumayer III/Antartica 2001-2018 - Slant columns and retrieved profiles". Personal Communication (cit. on pp. 61, 70, 102).

Frieß, U., T. Deutschmann, B. S. Gilfedder, R. Weller, and U. Platt (2010). "Iodine monoxide in the Antarctic snowpack". In: *Atmospheric Chemistry and Physics* 10.5, pp. 2439–2456. DOI: 10.5194/acp-10-2439-2010 (cit. on pp. 2, 37, 39, 101, 119, 134, 218).

Frieß, U., J. Hollwedel, G. König-Langlo, T. Wagner, and U. Platt (2004). "Dynamics and chemistry of tropospheric bromine explosion events in the Antarctic coastal region". In: *Journal of Geophysical Research: Atmospheres* 109.D6, n/a–n/a. DOI: 10.1029/2003jd004133 (cit. on pp. 37, 38, 42, 101).

Frieß, U., K. Kreher, P. V. Johnston, and U. Platt (2005). "Ground-Based DOAS Measurements of Stratospheric Trace Gases at Two Antarctic Stations during the 2002 Ozone Hole Period". In: *Journal of the Atmospheric Sciences* 62.3, pp. 765–777. DOI: 10.1175/jas-3319.1 (cit. on p. 101).

Frieß, U., P. S. Monks, J. J. Remedios, A. Rozanov, R. Sinreich, T. Wagner, and U. Platt (2006). "MAX-DOAS O4measurements: A new technique to derive information on atmospheric aerosols: 2. Modeling studies". In: *Journal of Geophysical Research* 111.D14. DOI: 10.1029/2005jd006618 (cit. on p. 102).

Frieß, U., H. Sihler, R. Sander, D. Pöhler, S. Yilmaz, and U. Platt (2011). "The vertical distribution of BrO and aerosols in the Arctic: Measurements by active and passive differential optical absorption spectroscopy". In: *Journal of Geophysical Research* 116. DOI: 10.1029/2011jd015938 (cit. on pp. 37, 42, 70, 102, 174, 178, 187, 210).

Frieß, U., T. Wagner, I. Pundt, K. Pfeilsticker, and U. Platt (2001). "Spectroscopic measurements of tropospheric iodine oxide at Neumayer Station, Antarctica". In: *Geophysical Research Letters* 28.10, pp. 1941–1944. DOI: 10.1029/2000gl012784 (cit. on pp. 2, 37, 39, 101).

George, I. J. and C. Anastasio (2007). "Release of gaseous bromine from the photolysis of nitrate and hydrogen peroxide in simulated sea-salt solutions". In: *Atmospheric Environment* 41.3, pp. 543–553. DOI: 10.1016/j.atmosenv.2006.08.022 (cit. on p. 36).

Gernandt, H., S. E. D. El Naggar, J. Janneck, T. Matz, and C. Drücker (2007). "From Georg Forster Station to Neumayer Station III - a Sustainable Replacement at Atka Bay for Future". In: *Polarforschung, Bremerhaven, Alfred Wegener Institute for Polar and Marine Research & German Society of Polar Research* 76.(1/2), pp. 59–85 (cit. on p. 62).

Gernandt, H. and M. Huch (2009). "Neumayer-Station III - die neue Forschungsplattform in der Antarktis". In: *Polarforschung, Bremerhaven, Alfred Wegener Institute for Polar and Marine Research & German Society of Polar Research* 78.3, pp. 133–136 (cit. on p. 155).

Giglio, D. and G. C. Johnson (2016). "Subantarctic and Polar Fronts of the Antarctic Circumpolar Current and Southern Ocean Heat and Freshwater Content Variability: A View from Argo". In: *Journal of Physical Oceanography* 46.3, pp. 749–768. DOI: 10.1175/jpo-d-15-0131.1 (cit. on p. 6).

Gilman, J. B., J. F. Burkhart, B. M. Lerner, E. J. Williams, W. C. Kuster, P. D. Goldan, P. C. Murphy, C. Warneke, C. Fowler, S. A. Montzka, B. R. Miller, L. Miller, S. J. Oltmans, T. B. Ryerson, O. R. Cooper, A. Stohl, and J. A. de Gouw (2010). "Ozone variability and halogen oxidation within the Arctic and sub-Arctic springtime boundary layer". In: *Atmospheric Chemistry and Physics* 10.21, pp. 10223–10236. DOI: 10.5194/acp-10-10223-2010 (cit. on p. 46).

Gorshelev, V., A. Serdyuchenko, M. Weber, W. Chehade, and J. P. Burrows (2014). "High spectral resolution ozone absorption cross-sections Part 1: Measurements, data analysis and comparison with previous measurements around 293 K". In: *Atmospheric Measurement Techniques* 7.2, pp. 609–624. DOI: 10.5194/amt-7-609-2014 (cit. on p. 137).

Gossart, A., N. Souverijns, I. V. Gorodetskaya, S. Lhermitte, J. T. M. Lenaerts, J. H. Schween, A. Mangold, Q. Laffineur, and N. P. M. van Lipzig (2017). "Blowing snow detection from ground-based ceilometers: application to East Antarctica". In: *The Cryosphere* 11.6, pp. 2755–2772. DOI: 10.5194/tc-11-2755-2017 (cit. on pp. 22, 67).

Grainger, J. F. and J. Ring (1962). "Anomalous Fraunhofer Line Profiles". In: *Nature* 193.4817, pp. 762–762. DOI: 10.1038/193762a0 (cit. on p. 52).

Grannas, A. M., A. E. Jones, J. Dibb, M. Ammann, C. Anastasio, H. J. Beine, M. Bergin, J. Bottenheim, C. S. Boxe, G. Carver, G. Chen, J. H. Crawford, F. Dominé, M. M. Frey, M. I. Guzmán, D. E. Heard, D. Helmig, M. R. Hoffmann, R. E. Honrath, L. G. Huey, M. Hutterli, H. W. Jacobi, P. Klán, B. Lefer, J. McConnell, J. Plane, R. Sander, J. Savarino, P. B. Shepson, W. R. Simpson, J. R. Sodeau, R. von Glasow, R. Weller, E. W. Wolff, and T. Zhu (2007). "An overview of snow photochemistry: evidence, mechanisms and impacts". In: *Atmospheric Chemistry and Physics* 7.16, pp. 4329–4373. DOI: 10.5194/acp-7-4329-2007 (cit. on pp. 8, 21, 26–28, 40).

Greenaway, K. R. (1950). "Experiences with Arctic flying weather". In: *Canadian Branch Royal. Met. Soc.,1(9)*. URL: http://cmosarchives.ca/RMS/r0109.pdf (cit. on p. 47).

Grenfell, T. C. and D. K. Perovich (2004). "Seasonal and spatial evolution of albedo in a snow-ice-land-ocean environment". In: *Journal of Geophysical Research* 109.C1. DOI: 10.1029/2003jc001866 (cit. on pp. 8, 10).

Grenfell, T. C., S. G. Warren, and P. C. Mullen (1994). "Reflection of solar radiation by the Antarctic snow surface at ultraviolet, visible, and near-infrared wavelengths". In: *Journal of Geophysical Research* 99.D9, p. 18669. DOI: 10.1029/94jd01484 (cit. on p. 8).

Haas, C. (2017). “Sea ice thickness distribution”. In: *Sea ice*. Ed. by D. N. Thomas. Third edition. Chichester, UK ; Hoboken, NJ: Wiley Blackwell. Chap. 2, 652 p. ISBN: 978-1-118-77838-8. URL: https://www.wiley.com/en-us/Sea+Ice%2C+3rd+Edition-p-9781118778388 (cit. on p. 12).

Hausmann, M. and U. Platt (1994). “Spectroscopic measurement of bromine oxide and ozone in the high Arctic during Polar Sunrise Experiment 1992”. In: *Journal of Geophysical Research* 99.D12, p. 25399. DOI: 10.1029/94jd01314 (cit. on pp. 2, 18, 28, 42, 55, 70, 178, 182, 184, 186).

Hausmann, M., U. Brandenburger, T. Brauers, and H.-P. Dorn (1999). “Simple Monte Carlo methods to estimate the spectra evaluation error in differential-optical-absorption spectroscopy”. In: *Applied Optics* 38.3, p. 462. DOI: 10.1364/ao.38.000462 (cit. on p. 60).

Helmig, D., B. Johnson, S. J. Oltmans, W. Neff, F. Eisele, and D. Davis (2008). “Elevated ozone in the boundary layer at South Pole”. In: *Atmospheric Environment* 42.12, pp. 2788–2803. DOI: 10.1016/j.atmosenv.2006.12.032 (cit. on p. 27).

Helmig, D., S. J. Oltmans, D. Carlson, J.-F. Lamarque, A. E. Jones, C. Labuschagne, K. Anlauf, and K. Hayden (2007). “A review of surface ozone in the polar regions”. In: *Atmospheric Environment* 41.24, pp. 5138–5161. DOI: 10.1016/j.atmosenv.2006.09.053 (cit. on pp. 25, 26, 149, 151, 306).

Hill, R. J. (1992). “Review of optical scintillation methods of measuring the refractive-index spectrum, inner scale and surface fluxes”. In: *Waves in Random Media* 2.3, pp. 179–201. DOI: 10.1088/0959-7174/2/3/001 (cit. on p. 91).

Hoffmann, T., C. D. O’Dowd, and J. H. Seinfeld (2001). “Iodine oxide homogeneous nucleation: An explanation for coastal new particle production”. In: *Geophysical Research Letters* 28.10, pp. 1949–1952. DOI: 10.1029/2000gl012399 (cit. on p. 30).

Holla, R., S. Schmitt, U. Frieß, D. Pöhler, J. Zingler, U. Corsmeier, and U. Platt (2015). “Vertical distribution of BrO in the boundary layer at the Dead Sea”. In: *Environmental Chemistry* 12.4, p. 438. DOI: 10.1071/en14224 (cit. on p. 70).

Hollwedel, J., M. Wenig, S. Beirle, S. Kraus, S. Kühl, W. Wilms-Grabe, U. Platt, and T. Wagner (2004). “Year-to-year variations of spring time polar tropospheric BrO as seen by GOME”. In: *Advances in Space Research* 34.4, pp. 804–808. DOI: 10.1016/j.asr.2003.08.060 (cit. on p. 38).

Hönninger, G., C. von Friedeburg, and U. Platt (2004). “Multi axis differential optical absorption spectroscopy (MAX-DOAS)”. In: *Atmospheric Chemistry and Physics* 4.1, pp. 231–254. DOI: 10.5194/acp-4-231-2004 (cit. on pp. 37, 70, 101).

Hönninger, G. and U. Platt (2002). “Observations of BrO and its vertical distribution during surface ozone depletion at Alert”. In: *Atmospheric Environment* 36.15-16, pp. 2481–2489. DOI: 10.1016/s1352-2310(02)00104-8 (cit. on pp. 28, 29, 42, 101).

Hönninger, G. (2002). "Halogen Oxide Studies in the Boundary Layer by Multi Axis Differential Optical Absorption Spectroscopy and Active Longpath-DOAS". PhD thesis. Heidelberg University. DOI: 10.11588/heidok.00001940 (cit. on p. 101).

Honrath, R. E., M. C. Peterson, S. Guo, J. E. Dibb, P. B. Shepson, and B. Campbell (1999). "Evidence of NOx production within or upon ice particles in the Greenland snowpack". In: *Geophysical Research Letters* 26.6, pp. 695–698. DOI: 10.1029/1999gl900077 (cit. on p. 26).

Horbanski, M. (2016). "Emissions and Distribution of Reactive Iodine from Seaweed in Coastal Regions - Investigations using new mobile and in-situ DOAS techniques". PhD thesis. Combined Faculties for Natural Sciences and for Mathematics of the Ruperto-Carola University of Heidelberg, Germany. DOI: 10.11588/heidok.00020106 (cit. on p. 82).

Horne, S., D. Smith, M. Besen, M. Partlow, D. Stolyarov, H. Zhu, and W. Holber (2010). "A novel high-brightness broadband light-source technology from the VUV to the IR". In: *Next-Generation Spectroscopic Technologies III*. Ed. by M. A. Druy, C. D. Brown, and R. A. Crocombe. SPIE. DOI: 10.1117/12.850269 (cit. on p. 72).

Huff, A. K. and J. P. D. Abbatt (2002). "Kinetics and Product Yields in the Heterogeneous Reactions of HOBr with Ice Surfaces Containing NaBr and NaCl". In: *The Journal of Physical Chemistry A* 106.21, pp. 5279–5287. DOI: 10.1021/jp014296m (cit. on p. 33).

Huff, A. K. and J. P. D. Abbatt (2000). "Gas-Phase Br2Production in Heterogeneous Reactions of Cl2, HOCl, and BrCl with Halide-Ice Surfaces". In: *The Journal of Physical Chemistry A* 104.31, pp. 7284–7293. DOI: 10.1021/jp001155w (cit. on p. 33).

Humphries, R. S., R. Schofield, M. D. Keywood, J. Ward, J. R. Pierce, C. M. Gionfriddo, M. T. Tate, D. P. Krabbenhoft, I. E. Galbally, S. B. Molloy, A. R. Klekociuk, P. V. Johnston, K. Kreher, A. J. Thomas, A. D. Robinson, N. R. P. Harris, R. Johnson, and S. R. Wilson (2015). "Boundary layer new particle formation over East Antarctic sea ice - possible Hg-driven nucleation?" In: *Atmospheric Chemistry and Physics* 15.23, pp. 13339–13364. DOI: 10.5194/acp-15-13339-2015 (cit. on pp. 47, 224).

Huntington, H. P., J. H. Mosli, and V. Shustov (1998). "Peoples of the Arctic: Characteristics of Human Populations Relevant to Pollution Issues". In: *AMAP Assessment Report: Arctic Pollution Issues*. Ed. by H. P. Huntington. Oslo, Norway: Arctic Monitoring and Assessment Programme (AMAP), xii+859 pp. (Cit. on p. 6).

Impey, G. A., P. B. Shepson, D. R. Hastie, L. A. Barrie, and K. G. Anlauf (1997). "Measurements of photolyzable chlorine and bromine during the Polar Sunrise Experiment 1995". In: *Journal of Geophysical Research: Atmospheres* 102.D13, pp. 16005–16010. DOI: 10.1029/97jd00851 (cit. on p. 38).

Impey, G., C. Mihele, K. Anlauf, L. Barrie, D. Hastie, and P. Shepson (1999). "Measurements of Photolyzable Halogen Compounds and Bromine Radicals During the Polar Sunrise Experiment 1997". In: *Journal of Atmospheric Chemistry* 34.1, pp. 21–37. DOI: 10.1023/a:1006264912394 (cit. on p. 37).

Islam, M., L. Ciaffoni, G. Hancock, and G. A. D. Ritchie (2013). "Demonstration of a novel laser-driven light source for broadband spectroscopy between 170 nm and 2.1 micrometer". In: *The Analyst* 138.17, p. 4741. DOI: 10.1039/c3an01020a (cit. on p. 72).

ISO 21348 (2007). International Organization for Standardization ISO - Space environment (natural and artificial) — Process for determining solar irradiances. URL: https://www.iso.org/standard/39911.html (cit. on p. 8).

Jacob, D. (1999). *Introduction to Atmospheric Chemistry*. Princeton University Press. 280 pp. ISBN: 0691001855 (cit. on p. 28).

Järvinen, E., A. Virkkula, T. Nieminen, P. P. Aalto, E. Asmi, C. Lanconelli, M. Busetto, A. Lupi, R. Schioppo, V. Vitale, M. Mazzola, T. Petäjä, V.-M. Kerminen, and M. Kulmala (2013). "Seasonal cycle and modal structure of particle number size distribution at Dome C, Antarctica". In: *Atmospheric Chemistry and Physics* 13.15, pp. 7473–7487. DOI: 10.5194/acp-13-7473-2013 (cit. on p. 47).

Jobson, B. T., H. Niki, Y. Yokouchi, J. Bottenheim, F. Hopper, and R. Leaitch (1994). "Measurements of C2-C6hydrocarbons during the Polar Sunrise1992 Experiment: Evidence for Cl atom and Br atom chemistry". In: *Journal of Geophysical Research* 99.D12, p. 25355. DOI: 10.1029/94jd01243 (cit. on pp. 28, 39, 46).

Jones, A. E., P. S. Anderson, M. Begoin, N. Brough, M. A. Hutterli, G. J. Marshall, A. Richter, H. K. Roscoe, and E. W. Wolff (2009). "BrO, blizzards, and drivers of polar tropospheric ozone depletion events". In: *Atmospheric Chemistry and Physics* 9.14, pp. 4639–4652. DOI: 10.5194/acp-9-4639-2009 (cit. on pp. 2, 22, 29, 42, 174, 210).

Jones, A. E., P. S. Anderson, E. W. Wolff, H. K. Roscoe, G. J. Marshall, A. Richter, N. Brough, and S. R. Colwell (2010). "Vertical structure of Antarctic tropospheric ozone depletion events: characteristics and broader implications". In: *Atmospheric Chemistry and Physics* 10.16, pp. 7775–7794. DOI: 10.5194/acp-10-7775-2010 (cit. on pp. 136, 187, 188).

Jones, A. E., P. S. Anderson, E. W. Wolff, J. Turner, A. M. Rankin, and S. R. Colwell (2006). "A role for newly forming sea ice in springtime polar tropospheric ozone loss? Observational evidence from Halley station, Antarctica". In: *Journal of Geophysical Research* 111.D8. DOI: 10.1029/2005jd006566 (cit. on pp. 18, 42).

Jones, A. E., R. Weller, P. S. Anderson, H.-W. Jacobi, E. W. Wolff, O. Schrems, and H. Miller (2001). "Measurements of NO_x emissions from the Antarctic snowpack". In: *Geophysical Research Letters* 28.8, pp. 1499–1502. DOI: 10.1029/2000gl011956 (cit. on pp. 18, 26, 27, 155).

Jones, A. E., R. Weller, A. Minikin, E. W. Wolff, W. T. Sturges, H. P. McIntyre, S. R. Leonard, O. Schrems, and S. Bauguitte (1999). "Oxidized nitrogen chemistry and speciation in the Antarctic troposphere". In: *Journal of Geophysical Research: Atmospheres* 104.D17, pp. 21355–21366. DOI: 10.1029/1999jd900362 (cit. on pp. 26, 27).

Jones, A. E., R. Weller, E. W. Wolff, and H.-W. Jacobi (2000). "Speciation and rate of photochemical NO and NO2 production in Antarctic snow". In: *Geophysical Research Letters* 27.3, pp. 345–348. DOI: 10.1029/1999gl010885 (cit. on pp. 26, 27, 155).

Jones, D. A. and I. Simmonds (1993). "A climatology of Southern Hemisphere extratropical cyclones". In: *Climate Dynamics* 9.3, pp. 131–145. DOI: 10.1007/bf00209750 (cit. on pp. 143, 144).

Jourdain, B., S. Preunkert, O. Cerri, H. Castebrunet, R. Udisti, and M. Legrand (2008). "Year-round record of size-segregated aerosol composition in central Antarctica (Concordia station): Implications for the degree of fractionation of sea-salt particles". In: *Journal of Geophysical Research* 113.D14. DOI: 10.1029/2007jd009584 (cit. on p. 21).

Kaleschke, L. (2004). "Frost flowers on sea ice as a source of sea salt and their influence on tropospheric halogen chemistry". In: *Geophysical Research Letters* 31.16. DOI: 10.1029/2004gl020655 (cit. on pp. 2, 40).

Kalnajs, L. E. and L. M. Avallone (2006). "Frost flower influence on springtime boundary-layer ozone depletion events and atmospheric bromine levels". In: *Geophysical Research Letters* 33.10, n/a–n/a. DOI: 10.1029/2006gl025809 (cit. on p. 41).

Kaminow, I. P., T. Li, and A. E. Willner (2013). *Optical Fiber Telecommunications*. 6th. Vol. VIA. Oxford, UK: Elsevier Science. 794 pp. ISBN: 9780123969583 (cit. on pp. 76, 77).

Keller-Rudek, H., G. K. Moortgat, R. Sander, and R. Sörensen (2013). "The MPI-Mainz UV/VIS Spectral Atlas of Gaseous Molecules of Atmospheric Interest". In: *Earth System Science Data* 5.2, pp. 365–373. DOI: 10.5194/essd-5-365-2013 (cit. on pp. 53, 108, 289).

Kern, C., H. Sihler, L. Vogel, C. Rivera, M. Herrera, and U. Platt (2009). "Halogen oxide measurements at Masaya Volcano, Nicaragua using active long path differential optical absorption spectroscopy". English. In: *Bulletin of Volcanology* 71.6, pp. 659–670. ISSN: 0258-8900 and 1432-0819. DOI: 10.1007/s00445-008-0252-8 (cit. on pp. 70, 73).

Kern, C., S. Trick, B. Rippel, and U. Platt (2006). "Applicability of light-emitting diodes as light sources for active differential optical absorption spectroscopy measurements". In: *Applied Optics* 45.9, p. 2077. DOI: 10.1364/ao.45.002077 (cit. on pp. 72, 73).

Kirkby, J., J. Curtius, J. Almeida, E. Dunne, J. Duplissy, S. Ehrhart, A. Franchin, S. Gagné, L. Ickes, A. Kürten, A. Kupc, A. Metzger, F. Riccobono, L. Rondo, S. Schobesberger, G. Tsagkogeorgas, D. Wimmer, A. Amorim, F. Bianchi, M. Breitenlechner, A. David, J. Dommen, A. Downard, M. Ehn, R. C. Flagan, S. Haider, A. Hansel, D. Hauser, W. Jud, H. Junninen, F. Kreissl, A. Kvashin, A. Laaksonen, K. Lehtipalo, J. Lima, E. R. Lovejoy, V. Makhmutov, S. Mathot, J. Mikkilä, P. Minginette, S. Mogo, T. Nieminen, A. Onnela, P. Pereira, T. Petäjä, R. Schnitzhofer, J. H. Seinfeld, M. Sipilä, Y. Stozhkov, F. Stratmann, A. Tomé, J. Vanhanen, Y. Viisanen, A. Vrtala, P. E. Wagner, H. Walther, E. Weingartner, H. Wex, P. M. Winkler, K. S. Carslaw, D. R. Worsnop, U. Baltensperger, and M. Kulmala (2011). "Role of sulphuric acid, ammonia and galactic

cosmic rays in atmospheric aerosol nucleation". In: *Nature* 476.7361, pp. 429–433. DOI: 10.1038/nature10343 (cit. on p. 225).

Klonecki, A., P. Hess, L. Emmons, L. Smith, J. Orlando, and D. Blake (2003). "Seasonal changes in the transport of pollutants into the Arctic troposphere-model study". In: *Journal of Geophysical Research* 108.D4. DOI: 10.1029/2002jd002199 (cit. on p. 22).

König-Langlo, G., J. C. King, and P. Pettré (1998). "Climatology of the three coastal Antarctic stations Dumont d'Urville, Neumayer, and Halley". In: *Journal of Geophysical Research: Atmospheres* 103.D9, pp. 10935–10946. DOI: 10.1029/97jd00527 (cit. on pp. 19, 91, 140, 143–146, 197).

König-Langlo, G. and B. Loose (2007). "The Meteorological Observatory at Neumayer Stations (GvN and NM-II) Antarctica". en. In: *Polarforschung; 76; 25-38*. DOI: 10.2312/polarforschung.76.1-2.25 (cit. on pp. 22, 63–66, 100).

König-Langlo, G., R. Sieger, H. Schmithüsen, A. Bücker, F. Richter, and D. E.G. (2013). *The Baseline Surface Radiation Network and its World Radiation Monitoring Centre at the Alfred Wegener Institute*. Tech. rep. 174. GCOS. URL: http://bsrn.awi.de/fileadmin/user_upload/bsrn.awi.de/Publications/gcos-174.pdf (cit. on pp. 64, 65).

König-Langlo, G. (2016a). *Basic and other measurements of radiation at Neumayer Station 2016*. PANGEA data sets. URL: https://www.pangaea.de/ (cit. on p. 64).
Radiation NMIII (2016-01). DOI: 10.1594/pangaea.858856.

– (2016b). *Continuous meteorological observations at Neumayer station 2016*. PANGEA data sets. URL: https://www.pangaea.de/ (cit. on p. 64).
Meteorology NMIII (2016-01). DOI: 10.1594/PANGAEA.858916.

– (2016c). *Radiosonde measurements from Neumayer Station 2016/2017*. PANGEA data sets. URL: https://www.pangaea.de/ (cit. on p. 65).
Radiosondes NMIII (2016-01). DOI: 10.1594/pangaea.858858.

– (2017a). *Basic and other measurements of radiation at Neumayer Station 2016/2017*. PANGEA data sets. URL: https://www.pangaea.de/ (cit. on p. 64).
Radiation NMIII (2016-02). DOI: 10.1594/pangaea.874512.
Radiation NMIII (2016-03). DOI: 10.1594/pangaea.874517.
Radiation NMIII (2016-04). DOI: 10.1594/pangaea.874522.
Radiation NMIII (2016-05). DOI: 10.1594/pangaea.874527.
Radiation NMIII (2016-06). DOI: 10.1594/pangaea.874532.
Radiation NMIII (2016-07). DOI: 10.1594/pangaea.874537.
Radiation NMIII (2016-08). DOI: 10.1594/pangaea.874542.
Radiation NMIII (2016-09). DOI: 10.1594/pangaea.874547.
Radiation NMIII (2016-10). DOI: 10.1594/pangaea.874552.
Radiation NMIII (2016-11). DOI: 10.1594/pangaea.874557.
Radiation NMIII (2016-12). DOI: 10.1594/pangaea.874562.
Radiation NMIII (2017-01). DOI: 10.1594/pangaea.874567.

– (2017b). *Continuous meteorological observations at Neumayer station 2016/2017*. PANGEA data sets. URL: https://www.pangaea.de/ (cit. on p. 64).
Meteorology NMIII (2016-02). DOI: 10.1594/pangaea.874574.
Meteorology NMIII (2016-03). DOI: 10.1594/pangaea.874575.
Meteorology NMIII (2016-04). DOI: 10.1594/pangaea.874576.
Meteorology NMIII (2016-05). DOI: 10.1594/pangaea.874577.
Meteorology NMIII (2016-06). DOI: 10.1594/pangaea.874578.
Meteorology NMIII (2016-07). DOI: 10.1594/pangaea.874579.
Meteorology NMIII (2016-08). DOI: 10.1594/pangaea.874580.
Meteorology NMIII (2016-09). DOI: 10.1594/pangaea.874581.
Meteorology NMIII (2016-10). DOI: 10.1594/pangaea.874582.
Meteorology NMIII (2016-11). DOI: 10.1594/pangaea.874583.
Meteorology NMIII (2016-12). DOI: 10.1594/pangaea.874584.
Meteorology NMIII (2017-01). DOI: 10.1594/pangaea.874585.

– (2017c). *Radiosonde measurements from Neumayer Station 2016*. PANGEA data sets. URL: https://www.pangaea.de/ (cit. on p. 65).
Radiosondes NMIII (2016-02). DOI: 10.1594/pangaea.874514.
Radiosondes NMIII (2016-03). DOI: 10.1594/pangaea.874519.
Radiosondes NMIII (2016-04). DOI: 10.1594/pangaea.874524.
Radiosondes NMIII (2016-05). DOI: 10.1594/pangaea.874529.
Radiosondes NMIII (2016-06). DOI: 10.1594/pangaea.874534.
Radiosondes NMIII (2016-07). DOI: 10.1594/pangaea.874539.
Radiosondes NMIII (2016-08). DOI: 10.1594/pangaea.874544.
Radiosondes NMIII (2016-09). DOI: 10.1594/pangaea.874549.
Radiosondes NMIII (2016-10). DOI: 10.1594/pangaea.874554.
Radiosondes NMIII (2016-11). DOI: 10.1594/pangaea.874559.
Radiosondes NMIII (2016-12). DOI: 10.1594/pangaea.874564.
Radiosondes NMIII (2017-01). DOI: 10.1594/pangaea.874569.

Koop, T., A. Kapilashrami, L. T. Molina, and M. J. Molina (2000). "Phase transitions of sea-salt/water mixtures at low temperatures: Implications for ozone chemistry in the polar marine boundary layer". In: *Journal of Geophysical Research: Atmospheres* 105.D21, pp. 26393–26402. DOI: 10.1029/2000jd900413 (cit. on pp. 41, 174).

Koponen, I. K. (2003). "Number size distributions and concentrations of the continental summer aerosols in Queen Maud Land, Antarctica". In: *Journal of Geophysical Research* 108.D18. DOI: 10.1029/2003jd003614 (cit. on p. 47).

Kottmeier, C. and B. Fay (1998). "Trajectories in the Antarctic lower troposphere". In: *Journal of Geophysical Research: Atmospheres* 103.D9, pp. 10947–10959. DOI: 10.1029/97jd00768 (cit. on p. 19).

Kraus, S. (2006). *DOASIS – A Framework Design for DOAS*. 1st Edition. Shaker Verlag. ISBN: 978-3-8322-5452-0 (cit. on pp. 58, 106).

Kreher, K., P. V. Johnston, S. W. Wood, B. Nardi, and U. Platt (1997). "Ground-based measurements of tropospheric and stratospheric BrO at Arrival Heights, Antarctica". In:

Geophysical Research Letters 24.23, pp. 3021–3024. DOI: 10.1029/97gl02997 (cit. on pp. 28, 37).

Kreher, K., J. G. Keys, P. V. Johnston, U. Platt, and X. Liu (1996). "Ground-based measurements of OClO and HCl in austral spring 1993 at Arrival Heights, Antarctica". In: *Geophysical Research Letters* 23.12, pp. 1545–1548. DOI: 10.1029/96gl01318 (cit. on pp. 2, 28).

Kulmala, M., J. Kontkanen, H. Junninen, K. Lehtipalo, H. E. Manninen, T. Nieminen, T. Petaja, M. Sipila, S. Schobesberger, P. Rantala, A. Franchin, T. Jokinen, E. Jarvinen, M. Aijala, J. Kangasluoma, J. Hakala, P. P. Aalto, P. Paasonen, J. Mikkila, J. Vanhanen, J. Aalto, H. Hakola, U. Makkonen, T. Ruuskanen, R. L. Mauldin, J. Duplissy, H. Vehkamaki, J. Back, A. Kortelainen, I. Riipinen, T. Kurten, M. V. Johnston, J. N. Smith, M. Ehn, T. F. Mentel, K. E. J. Lehtinen, A. Laaksonen, V.-M. Kerminen, and D. R. Worsnop (2013). "Direct Observations of Atmospheric Aerosol Nucleation". In: *Science* 339.6122, pp. 943–946. DOI: 10.1126/science.1227385 (cit. on p. 2).

Kurucz, R. L. (2006). "High Resolution Irradiance Spectrum from 300 to 1000 nm". In: *arXiv*. arXiv: astro-ph/0605029v1 [astro-ph] (cit. on p. 120).

Kyrö, E.-M., V.-M. Kerminen, A. Virkkula, M. D. Maso, J. Parshintsev, J. Ruíz-Jimenez, L. Forsström, H. E. Manninen, M.-L. Riekkola, P. Heinonen, and M. Kulmala (2013). "Antarctic new particle formation from continental biogenic precursors". In: *Atmospheric Chemistry and Physics* 13.7, pp. 3527–3546. DOI: 10.5194/acp-13-3527-2013 (cit. on p. 47).

Lampel, J., U. Frieß, and U. Platt (2015a). "The impact of vibrational Raman scattering of air on DOAS measurements of atmospheric trace gases". In: *Atmospheric Measurement Techniques* 8.9, pp. 3767–3787. DOI: 10.5194/amt-8-3767-2015 (cit. on p. 52).

Lampel, J., D. Pöhler, J. Tschritter, U. Frieß, and U. Platt (2015b). "On the relative absorption strengths of water vapour in the blue wavelength range". In: *Atmospheric Measurement Techniques* 8.10, pp. 4329–4346. DOI: 10.5194/amt-8-4329-2015 (cit. on pp. 108, 119, 289).

Lampel, J. (2014). "Measurements of reactive trace gases in the marine boundary layer using novel DOAS methods". PhD thesis. Combined Faculties for Natural Sciences and for Mathematics of the Ruperto-Carola University of Heidelberg, Germany. DOI: 10.11588/heidok.00017394 (cit. on p. 106).

Larsen, J., O. Anisimov, A. Constable, A. Hollowed, N. Maynard, P. Prestrud, T. Prowse, and J. Stone (2014). "Polar Regions". In: *Climate Change 2014: Impacts, Adaptation and Vulnerability*. Ed. by V. R. Barros, C. B. Field, D. J. Dokken, M. D. Mastrandrea, and K. J. Mach. Cambridge University Press. Chap. 28, pp. 1567–1612. DOI: 10.1017/cbo9781107415386.008 (cit. on p. 6).

Law, K. S. and A. Stohl (2007). "Arctic Air Pollution: Origins and Impacts". In: *Science* 315.5818, pp. 1537–1540. DOI: 10.1126/science.1137695 (cit. on pp. 22, 32).

Lawrence, R. S., G. R. Ochs, and S. F. Clifford (1972). "Use of Scintillations to Measure Average Wind Across a Light Beam". In: *Applied Optics* 11.2, p. 239. DOI: 10.1364/ao.11.000239 (cit. on p. 91).

Le Bras, G. and U. Platt (1995). "A possible mechanism for combined chlorine and bromine catalyzed destruction of tropospheric ozone in the Arctic". In: *Geophysical Research Letters* 22.5, pp. 599–602. DOI: 10.1029/94gl03334 (cit. on pp. 29, 186, 220).

Legrand, M., S. Preunkert, J. Savarino, M. M. Frey, A. Kukui, D. Helmig, B. Jourdain, A. E. Jones, R. Weller, N. Brough, and H. Gallée (2016). "Inter-annual variability of surface ozone at coastal (Dumont d'Urville, 2004–2014) and inland (Concordia, 2007–2014) sites in East Antarctica". In: *Atmospheric Chemistry and Physics* 16.12, pp. 8053–8069. DOI: 10.5194/acp-16-8053-2016 (cit. on pp. 26, 27).

Legrand, M. and E. C. Pasteur (1998). "Methane sulfonic acid to non-sea-salt sulfate ratio in coastal Antarctic aerosol and surface snow". In: *Journal of Geophysical Research: Atmospheres* 103.D9, pp. 10991–11006. DOI: 10.1029/98jd00929 (cit. on p. 162).

Leighton, P. A. (1961). *Photochemistry of air pollution*. eng. Physical chemistry ARRAY(0x5626d2ca3280). New York [u.a.]: Academic Press, IX, 300 S. (Cit. on p. 24).

Lemke, P., J. Ren, R. Alley, I. Allison, J. Carrasco, G. Flato, Y. Fujii, G. Kaser, P. Mote, R. Thomas, and T. Zhang (2007). "Observations: Changes in Snow, Ice and Frozen Ground." In: *Climate Change 2007: The Physical Science Basis. Contribution of Working Group I to the Fourth Assessment Report of the Intergovernmental Panel on Climate Change*. Ed. by S. Solomon, D. Qin, M. Manning, Z. Chen, M. Marquis, K. Averyt, M. Tignor, and H. Miller. Cambridge University Pres. URL: https://www.ipcc.ch/publications_and_data/ar4/wg1/en/ch4.html (cit. on pp. 1, 9).

Leonard, K. C., L.-B. Tremblay, J. E. Thom, and D. R. MacAyeal (2012). "Drifting snow threshold measurements near McMurdo station, Antarctica: A sensor comparison study". In: *Cold Regions Science and Technology* 70, pp. 71–80. DOI: 10.1016/j.coldregions.2011.08.001 (cit. on p. 22).

Levenberg, K. (1944). "A method for the solution of certain non-linear problems in least squares". In: *Quarterly of Applied Mathematics* 2.2, pp. 164–168. ISSN: 0033569X, 15524485. URL: http://www.jstor.org/stable/43633451 (cit. on p. 58).

Levin, I., T. Naegler, R. Heinz, D. Osusko, E. Cuevas, A. Engel, J. Ilmberger, R. L. Langenfelds, B. Neininger, C. v. Rohden, L. P. Steele, R. Weller, D. E. Worthy, and S. A. Zimov (2010a). "The global SF6 source inferred from long-term high precision atmospheric measurements and its comparison with emission inventories". In: *Atmospheric Chemistry and Physics* 10.6, pp. 2655–2662. DOI: 10.5194/acp-10-2655-2010 (cit. on p. 67).

Levin, I., T. Naegler, B. Kromer, M. Diehl, R. Francey, A. Gomez-Pelaez, P. Steele, D. Wagenbach, R. Weller, and D. Worthy (2010b). "Observations and modelling of the global distribution and long-term trend of atmospheric 14CO2". In: *Tellus B: Chemical*

and Physical Meteorology 62.1, pp. 26–46. DOI: 10.1111/j.1600-0889.2009.00446.x (cit. on p. 67).

Li, L. and J. W. Pomeroy (1997). "Estimates of Threshold Wind Speeds for Snow Transport Using Meteorological Data". In: *Journal of Applied Meteorology* 36.3, pp. 205–213. DOI: 10.1175/1520-0450(1997)036<0205:eotwsf>2.0.co;2 (cit. on p. 22).

Liao, J., L. G. Huey, D. J. Tanner, F. M. Flocke, J. J. Orlando, J. A. Neuman, J. B. Nowak, A. J. Weinheimer, S. R. Hall, J. N. Smith, A. Fried, R. M. Staebler, Y. Wang, J.-H. Koo, C. A. Cantrell, P. Weibring, J. Walega, D. J. Knapp, P. B. Shepson, and C. R. Stephens (2012). "Observations of inorganic bromine (HOBr, BrO, and Br2) speciation at Barrow, Alaska, in spring 2009". In: *Journal of Geophysical Research: Atmospheres* 117.D14, n/a–n/a. DOI: 10.1029/2011jd016641 (cit. on pp. 37, 38).

Liao, J., H. Sihler, L. G. Huey, J. A. Neuman, D. J. Tanner, U. Friess, U. Platt, F. M. Flocke, J. J. Orlando, P. B. Shepson, H. J. Beine, A. J. Weinheimer, S. J. Sjostedt, J. B. Nowak, D. J. Knapp, R. M. Staebler, W. Zheng, R. Sander, S. R. Hall, and K. Ullmann (2011). "A comparison of Arctic BrO measurements by chemical ionization mass spectrometry and long path-differential optical absorption spectroscopy". In: *Journal of Geophysical Research* 116. DOI: 10.1029/2010jd014788 (cit. on p. 38).

Liao, J., L. G. Huey, Z. Liu, D. J. Tanner, C. A. Cantrell, J. J. Orlando, F. M. Flocke, P. B. Shepson, A. J. Weinheimer, S. R. Hall, K. Ullmann, H. J. Beine, Y. Wang, E. D. Ingall, C. R. Stephens, R. S. Hornbrook, E. C. Apel, D. Riemer, A. Fried, R. L. Mauldin, J. N. Smith, R. M. Staebler, J. A. Neuman, and J. B. Nowak (2014). "High levels of molecular chlorine in the Arctic atmosphere". In: *Nature Geoscience* 7.2, pp. 91–94. DOI: 10.1038/ngeo2046 (cit. on pp. 2, 35, 37, 39, 46, 186, 206–208).

Lugar, R. M. (1993). *Results of SO_2, NO_x, and CO monitoring at McMurdo Station, Antarctica*. Tech. rep. EG&H Idaho, Inc. - Environmental Technology Unit. URL: https://www.osti.gov/servlets/purl/10192136 (cit. on p. 161).

Lutgens, F. K. and E. J. Tarbuck (2016). *The atmosphere. An introduction to meteorology*. 13. ed. Hoboken, NJ: Pearson Education. ISBN: 978-0-321-98462-3. URL: https://www.pearson.com/us/higher-education/product/Lutgens-Atmosphere-The-An-Introduction-to-Meteorology-13th-Edition/9780321984623.html (cit. on p. 15).

Macdonald, R. W. and L. L. Loseto (2010). "Are Arctic Ocean ecosystems exceptionally vulnerable to global emissions of mercury? A call for emphasised research on methylation and the consequences of climate change". In: *Environmental Chemistry* 7.2, p. 133. DOI: 10.1071/en09127 (cit. on p. 44).

Madronich, S., R. L. McKenzie, M. M. Caldwell, and L. O. Björn (1995). "Changes in Ultraviolet Radiation Reaching the Earths Surface". In: *Ambio* 24.3, pp. 143–152. URL: http://www.jstor.org/stable/4314320 (cit. on p. 8).

Mahajan, A. S., H. Oetjen, A. Saiz-Lopez, J. D. Lee, G. B. McFiggans, and J. M. C. Plane (2009). "Reactive iodine species in a semi-polluted environment". In: *Geophysical Research Letters* 36.16. DOI: 10.1029/2009gl038018 (cit. on pp. 37, 39).

Mandel, L. and E. Wolf (2008). *Optical coherence and quantum optics*. Repr. with corr. Cambridge: Cambridge University Press, XXVI, 1166 Seiten. ISBN: 978-0-521-41711-2 (cit. on p. 52).

Marelle, L., J.-C. Raut, K. S. Law, L. K. Berg, J. D. Fast, R. C. Easter, M. Shrivastava, and J. L. Thomas (2017). "Improvements to the WRF-Chem 3.5.1 model for quasi-hemispheric simulations of aerosols and ozone in the Arctic". In: *Geoscientific Model Development* 10.10, pp. 3661–3677. DOI: 10.5194/gmd-10-3661-2017 (cit. on p. 162).

Markvart, T. (2007). "The thermodynamics of optical étendue". In: *Journal of Optics A: Pure and Applied Optics* 10.1, p. 015008. DOI: 10.1088/1464-4258/10/01/015008 (cit. on p. 85).

Marquardt, D. W. (1963). "An Algorithm for Least-Squares Estimation of Nonlinear Parameters". In: *Journal of the Society for Industrial and Applied Mathematics* 11.2, pp. 431–441. DOI: 10.1137/0111030 (cit. on p. 58).

Masclin, S., M. M. Frey, W. F. Rogge, and R. C. Bales (2013). "Atmospheric nitric oxide and ozone at the WAIS Divide deep coring site: a discussion of local sources and transport in West Antarctica". In: *Atmospheric Chemistry and Physics* 13.17, pp. 8857–8877. DOI: 10.5194/acp-13-8857-2013 (cit. on p. 27).

Mastromonaco, M. N., K. Gårdfeldt, B. Jourdain, K. Abrahamsson, A. Granfors, M. Ahnoff, A. Dommergue, G. Méjean, and H.-W. Jacobi (2016). "Antarctic winter mercury and ozone depletion events over sea ice". In: *Atmospheric Environment* 129, pp. 125–132. DOI: 10.1016/j.atmosenv.2016.01.023 (cit. on pp. 44, 178, 183).

Matsuoka, K., A. Skoglund, G. Roth, S. Tronstad, and Y. Melær (2018). *Quantartica - A free GIS package for Antarctica*. Norwegian Polar Institute. URL: http://quantarctica.npolar.no/ (cit. on pp. 62, 63).
SCAR Antarctic Digital Database Version 6.0. Scientific Committee on Antarctic Research (SCAR). 2014. URL: https://www.add.scar.org/.
SCAR Antarctic Digital Database Version 7.0. Scientific Committee on Antarctic Research (SCAR). 2017. URL: https://www.add.scar.org/.
COMNAP Antarctic Facilities List. The Council of Managers of National Antarctic Programs (COMNAP). 2017. URL: https://www.comnap.aq/Members/SitePages/Home.aspx.

McConnell, J. C., G. S. Henderson, L. Barrie, J. Bottenheim, H. Niki, C. H. Langford, and E. M. J. Templeton (1992). "Photochemical bromine production implicated in Arctic boundary-layer ozone depletion". In: *Nature* 355.6356, pp. 150–152. DOI: 10.1038/355150a0 (cit. on pp. 28, 33, 36, 40).

Meller, R. and G. K. Moortgat (2000). "Temperature dependence of the absorption cross sections of formaldehyde between 223 and 323 K in the wavelength range 225-375 nm". In: *Journal of Geophysical Research: Atmospheres* 105.D6, pp. 7089–7101. DOI: 10.1029/1999jd901074 (cit. on pp. 108, 289).

Merten, A., J. Tschritter, and U. Platt (2011). "Design of differential optical absorption spectroscopy long-path telescopes based on fiber optics". In: *Applied Optics* 50.5, p. 738. DOI: 10.1364/ao.50.000738 (cit. on pp. 70, 71, 86).

Mie, G. (1908). "Beiträge zur Optik trüber Medien, speziell kolloidaler Metallösungen". In: *Annalen der Physik* 330.3, pp. 377–445. DOI: 10.1002/andp.19083300302 (cit. on p. 52).

Minikin, A., M. Legrand, J. Hall, D. Wagenbach, C. Kleefeld, E. Wolff, E. C. Pasteur, and F. Ducroz (1998). "Sulfur-containing species (sulfate and methanesulfonate) in coastal Antarctic aerosol and precipitation". In: *Journal of Geophysical Research: Atmospheres* 103.D9, pp. 10975–10990. DOI: 10.1029/98jd00249 (cit. on p. 67).

Mishchenko, M., J. Hovenier, and L. Travis, eds. (1999). *Light Scattering by Nonspherical Particles*. 1st. Elsevier. ISBN: 9780124986602 (cit. on p. 52).

Molina, M. J. and F. S. Rowland (1974). "Stratospheric sink for chlorofluoromethanes: chlorine atom-catalysed destruction of ozone". In: *Nature* 249.5460, pp. 810–812. DOI: 10.1038/249810a0 (cit. on pp. 2, 28).

Murray, B. J., D. O'Sullivan, J. D. Atkinson, and M. E. Webb (2012). "Ice nucleation by particles immersed in supercooled cloud droplets". In: *Chemical Society Reviews* 41.19, p. 6519. DOI: 10.1039/c2cs35200a (cit. on p. 12).

Murray, J. L., L. Hacquebord, D. J. Gregor, and H. Loeng (1998). "Physical/Geographical Characteristics of the Arctic". In: *AMAP Assessment Report: Arctic Pollution Issues*. Ed. by J. L. Murray. Oslo, Norway: Arctic Monitoring and Assessment Programme (AMAP), xii+859 pp. (Cit. on pp. 5, 6).

Murray, L. T., L. J. Mickley, J. O. Kaplan, E. D. Sofen, M. Pfeiffer, and B. Alexander (2014). "Factors controlling variability in the oxidative capacity of the troposphere since the Last Glacial Maximum". In: *Atmospheric Chemistry and Physics* 14.7, pp. 3589–3622. DOI: 10.5194/acp-14-3589-2014 (cit. on pp. 23, 24).

Myhre, G., N. Bellouin, T. F. Berglen, T. K. Berntsen, O. Boucher, A. Grini, S. A. M. Ivar, I. Johnsrud, I. M. Michael, F. Stordal, and D. TanréE (2007). "Comparison of the radiative properties and direct radiative effect of aerosols from a global aerosol model and remote sensing data over ocean". In: *Tellus B: Chemical and Physical Meteorology* 59.1, pp. 115–129. DOI: 10.1111/j.1600-0889.2006.00238.x (cit. on p. 22).

Nasse, J.-M., P. G. Eger, D. Pöhler, S. Schmitt, U. Frieß, and U. Platt (2019). "Recent improvements of Long-Path DOAS measurements: impact on accuracy and automated long-term observations". In: *Atmos. Meas. Tech. Discuss.* in review. DOI: 10.5194/amt-2019-69 (cit. on pp. 3, 54, 70–77).

US-Naval-Observatory, A. A. D. (2018). *Rise, Set, and Twilight Definitions*. Website. retrieved 2 July, 2018. URL: http://aa.usno.navy.mil/faq/docs/RST_defs.php (cit. on p. 8).

Neff, W. D., D. Helmig, A. Grachev, and D. Davis (2008). "A study of boundary layer behavior associated with high NO concentrations at the South Pole using a minisodar, tethered balloon, and sonic anemometer". In: *Atmospheric Environment* 42.12, pp. 2762–2779. DOI: 10.1016/j.atmosenv.2007.01.033 (cit. on pp. 16, 18).

Neuman, J. A., J. B. Nowak, L. G. Huey, J. B. Burkholder, J. E. Dibb, J. S. Holloway, J. Liao, J. Peischl, J. M. Roberts, T. B. Ryerson, E. Scheuer, H. Stark, R. E. Stickel, D. J. Tanner, and A. Weinheimer (2010). "Bromine measurements in ozone depleted air over the Arctic Ocean". In: *Atmospheric Chemistry and Physics* 10.14, pp. 6503–6514. DOI: 10.5194/acp-10-6503-2010 (cit. on p. 38).

Nič, M., J. Jirát, B. Košata, A. Jenkins, and A. McNaught, eds. (2009). *IUPAC Compendium of Chemical Terminology*. IUPAC. DOI: 10.1351/goldbook (cit. on pp. 23, 60).

Noxon, J. F. (1975). "Nitrogen dioxide in the stratosphere and troposphere measured by ground-based absorption spectroscopy". In: *Science* 189.4202, pp. 547–549. DOI: 10.1126/science.189.4202.547 (cit. on p. 101).

Obbard, R. W., H. K. Roscoe, E. W. Wolff, and H. M. Atkinson (2009). "Frost flower surface area and chemistry as a function of salinity and temperature". In: *Journal of Geophysical Research* 114.D20. DOI: 10.1029/2009jd012481 (cit. on p. 40).

Obrist, D., Y. Agnan, M. Jiskra, C. L. Olson, D. P. Colegrove, J. Hueber, C. W. Moore, J. E. Sonke, and D. Helmig (2017). "Tundra uptake of atmospheric elemental mercury drives Arctic mercury pollution". In: *Nature* 547.7662, pp. 201–204. DOI: 10.1038/nature22997 (cit. on p. 44).

Oltmans, S. J., R. Schnell, P. Sheridan, R. Peterson, S.-M. Li, J. Winchester, P. Tans, W. Sturges, J. Kahl, and L. Barrie (1989). "Seasonal surface ozone and filterable bromine relationship in the high Arctic". In: *Atmospheric Environment (1967)* 23.11, pp. 2431–2441. DOI: 10.1016/0004-6981(89)90254-0 (cit. on pp. 2, 28).

Oltmans, S. J. (1981). "Surface ozone measurements in clean air". In: *Journal of Geophysical Research* 86.C2, p. 1174. DOI: 10.1029/jc086ic02p01174 (cit. on pp. 2, 25, 167).

Oltmans, S. J. and W. D. Komhyr (1986). "Surface ozone distributions and variations from 1973–1984: Measurements at the NOAA Geophysical Monitoring for Climatic Change Baseline Observatories". In: *Journal of Geophysical Research* 91.D4, p. 5229. DOI: 10.1029/jd091id04p05229 (cit. on p. 28).

Oum, K. W., M. J. Lakin, D. O. D. andT. Brauers, and B. J. Finlayson-Pitts (1998a). "Formation of Molecular Chlorine from the Photolysis of Ozone and Aqueous Sea-Salt Particles". In: *Science* 279.5347, pp. 74–76. DOI: 10.1126/science.279.5347.74 (cit. on p. 207).

Oum, K. W., M. J. Lakin, and B. J. Finlayson-Pitts (1998b). "Bromine activation in the troposphere by the dark reaction of O3 with seawater ice". In: *Geophysical Research Letters* 25.21, pp. 3923–3926. DOI: 10.1029/1998gl900078 (cit. on pp. 34, 35, 40).

PANGAEA - Data Publisher for Earth & Environmental Science (2018). Alfred Wegener Institute, Helmholtz Center for Polar, Marine Research (AWI), and the Center for Marine Environmental Sciences, University of Bremen (MARUM). URL: https://www.pangaea.de/ (cit. on p. 61).

Perner, D., D. H. Ehhalt, H. W. Pätz, U. Platt, E. P. Röth, and A. Volz (1976). "OH - Radicals in the lower troposphere". In: *Geophysical Research Letters* 3.8, pp. 466–468. DOI: 10.1029/gl003i008p00466 (cit. on p. 50).

Peterson, P. K., W. R. Simpson, K. A. Pratt, P. B. Shepson, U. Frieß, J. Zielcke, U. Platt, S. J. Walsh, and S. V. Nghiem (2015). "Dependence of the vertical distribution of bromine monoxide in the lower troposphere on meteorological factors such as wind speed and stability". In: *Atmospheric Chemistry and Physics* 15.4, pp. 2119–2137. DOI: 10.5194/acp-15-2119-2015 (cit. on p. 187).

Peterson, P. K., D. Pöhler, H. Sihler, J. Zielcke, S. General, U. Frieß, U. Platt, W. R. Simpson, S. V. Nghiem, P. B. Shepson, B. H. Stirm, S. Dhaniyala, T. Wagner, D. R. Caulton, J. D. Fuentes, and K. A. Pratt (2017). "Observations of bromine monoxide transport in the Arctic sustained on aerosol particles". In: *Atmospheric Chemistry and Physics* 17.12, pp. 7567–7579. DOI: 10.5194/acp-17-7567-2017 (cit. on pp. 38, 187).

Peterson, P. K., D. Pöhler, J. Zielcke, S. General, U. Frieß, U. Platt, W. R. Simpson, S. V. Nghiem, P. B. Shepson, B. H. Stirm, and K. A. Pratt (2018). "Springtime Bromine Activation over Coastal and Inland Arctic Snowpacks". In: *ACS Earth and Space Chemistry* 2.10, pp. 1075–1086. DOI: 10.1021/acsearthspacechem.8b00083 (cit. on pp. 2, 187, 191).

Petrich, C. and H. Eicken (2017). "Overview of sea ice growth and properties". In: *Sea ice*. Ed. by D. N. Thomas. Third edition. Chichester, UK ; Hoboken, NJ: Wiley Blackwell. Chap. 1, 652 p. ISBN: 978-1-118-77838-8. URL: https://www.wiley.com/en-us/Sea+Ice%2C+3rd+Edition-p-9781118778388 (cit. on p. 10).

"IPCC, 2013: Annex III: Glossary" (2013). In: *Climate Change 2013: The Physical Science Basis. Contribution of Working Group I to the Fifth Assessment Report of the Intergovernmental Panel on Climate Change*. Ed. by S. Planton. Cambridge, United Kingdom and New York, NY, USA: Cambridge University Press, pp. 1447–1465. DOI: 10.1017/CBO9781107415324.031. URL: www.climatechange2013.org (cit. on p. 9).

Platt, U. (2000). "Reactive Halogen Species in the Mid-Latitude Troposphere — Recent Discoveries". In: *Water, Air, and Soil Pollution* 123.1/4, pp. 229–244. DOI: 10.1023/a:1005267321567 (cit. on p. 28).

Platt, U., W. Allan, and D. Lowe (2004). "Hemispheric average Cl atom concentration from $^{13}C/^{12}C$ ratios in atmospheric methane". In: *Atmospheric Chemistry and Physics* 4.9/10, pp. 2393–2399. DOI: 10.5194/acp-4-2393-2004 (cit. on pp. 34, 46).

Platt, U. and G. Hönninger (2003). "The role of halogen species in the troposphere". In: *Chemosphere* 52.2, pp. 325–338. DOI: 10.1016/s0045-6535(03)00216-9 (cit. on p. 28).

Platt, U. and E. (Lehrer (1996). *Arctic tropospheric ozone chemistry: Arctoc*. Research rep. European Commission (cit. on pp. 2, 33).

Platt, U. and D. Perner (1980). "Direct measurements of atmospheric CH2O, HNO2, O3, NO2, and SO2by differential optical absorption in the near UV". In: *Journal of Geophysical Research: Oceans* 85.C12, pp. 7453–7458. DOI: 10.1029/jc085ic12p07453 (cit. on pp. 50, 55, 70).

– (1983). "Measurements of Atmospheric Trace Gases by Long Path Differential UV/Visible Absorption Spectroscopy". English. In: *Optical and Laser Remote Sensing*. Ed. by A. L. Schawlow, D. K. Killinger, and A. Mooradian. 1st ed. Springer Series in Optical Sciences. Berlin/Heidelberg: Springer. DOI: 10.1007/978-3-540-39552-2 (cit. on pp. 50, 70).

Platt, U., D. Perner, and H. W. Pätz (1979). "Simultaneous measurement of atmospheric CH_2O, O_3, and NO_2 by differential optical absorption". In: *Journal of Geophysical Research* 84.C10, p. 6329. DOI: 10.1029/jc084ic10p06329 (cit. on pp. 50, 55, 70).

Platt, U. and J. Stutz (2008). *Differential Optical Absorption Spectroscopy. Principles and Applications*. Ed. by Springer. Springer Berlin Heidelberg. ISBN: 978-3-642-05946-9. DOI: 10.1007/978-3-540-75776-4 (cit. on pp. 49, 55–57, 59, 75, 83, 101).

Platt, U. and T. Wagner (1998). "Satellite mapping of enhanced BrO concentrations in the troposphere". In: *Nature* 395.6701, pp. 486–490. DOI: 10.1038/26723 (cit. on p. 38).

Platt, U. and C. Janssen (1995). "Observation and role of the free radicals NO3, ClO, BrO and IO in the troposphere". In: *Faraday Discussions* 100, p. 175. DOI: 10.1039/fd9950000175 (cit. on pp. 2, 33).

Platt, U., D. Perner, A. M. Winer, G. W. Harris, and J. N. Pitts (1980). "Detection of NO3 in the polluted troposphere by differential optical absorption". In: *Geophysical Research Letters* 7.1, pp. 89–92. DOI: 10.1029/gl007i001p00089 (cit. on pp. 55, 70).

Platt, U., K. Pfeilsticker, and M. Vollmer (2007). "Radiation and Optics in the Atmosphere". In: *Springer Handbook of Lasers and Optics*. Ed. by F. Träger. Springer New York, pp. 1165–1203. DOI: 10.1007/978-0-387-30420-5_19 (cit. on p. 51).

Pöhler, D., L. Vogel, U. Frieß, and U. Platt (2010). "Observation of halogen species in the Amundsen Gulf, Arctic, by active long-path differential optical absorption spectroscopy". In: *Proceedings of the National Academy of Sciences* 107.15, pp. 6582–6587. DOI: 10.1073/pnas.0912231107 (cit. on pp. 2, 37, 39, 70, 169, 199, 210).

Pöhler, D. (2010). "Determination of two dimensional trace gas distributions using tomographic LP-DOAS measurements in the city of Heidelberg, Germany". PhD thesis. Combined Faculties for Natural Sciences and for Mathematics of the Ruperto-Carola University of Heidelberg, Germany. DOI: 10.11588/heidok.00010996 (cit. on p. 70).

Prados-Roman, C., L. Gómez-Martín, O. Puentedura, M. Navarro-Comas, J. Iglesias, J. R. de Mingo, M. Pérez, H. Ochoa, M. E. Barlasina, G. Carbajal, and M. Yela (2018). "Reactive bromine in the low troposphere of Antarctica: estimations at two research sites". In: *Atmospheric Chemistry and Physics* 18.12, pp. 8549–8570. DOI: 10.5194/acp-18-8549-2018 (cit. on pp. 37, 187, 196).

Prandtl, L. (1905). "Über Flüssigkeitsbewegung bei sehr kleiner Reibung". In: *Verhandlungen des 3. Internationalen Mathematiker-Kongresses in Heidelberg vom 8. bis 13. August 1904*. Ed. by A. Krazer. Nendeln, X, 755 S. (Cit. on p. 16).

Pratt, K. A., K. D. Custard, P. B. Shepson, T. A. Douglas, D. Pöhler, S. General, J. Zielcke, W. R. Simpson, U. Platt, D. J. Tanner, L. G. Huey, M. Carlsen, and B. H. Stirm (2013). "Photochemical production of molecular bromine in Arctic surface snowpacks". In: *Nature Geoscience* 6.5, pp. 351–356. DOI: 10.1038/ngeo1779 (cit. on pp. 2, 35, 36, 38, 40, 41, 186, 191, 206, 208).

Pruppacher, H. R. and J. D. Klett (2010). *Microphysics of clouds and precipitation*. 2., rev. and enl. ed., [repr.] Atmospheric and oceanographic sciences library. Dordrecht: Springer Netherlands, XX, 954 S. DOI: 10.1007/978-0-306-48100-0 (cit. on pp. 12, 13).

Pszenny, A. A. P., J. Moldanová, W. C. Keene, R. Sander, J. R. Maben, M. Martinez, P. J. Crutzen, D. Perner, and R. G. Prinn (2004). "Halogen cycling and aerosol pH in the Hawaiian marine boundary layer". In: *Atmospheric Chemistry and Physics* 4.1, pp. 147–168. DOI: 10.5194/acp-4-147-2004 (cit. on p. 172).

Raman, C. V. and K. S. Krishnan (1928). "A New Type of Secondary Radiation". In: *Nature* 121.3048, pp. 501–502. DOI: 10.1038/121501c0 (cit. on p. 51).

Rankin, A. M., E. W. Wolff, and S. Martin (2002). "Frost flowers: Implications for tropospheric chemistry and ice core interpretation". In: *Journal of Geophysical Research: Atmospheres* 107.D23, AAC 4–1–AAC 4–15. DOI: 10.1029/2002jd002492 (cit. on pp. 10, 21, 40).

Read, K. A., A. C. Lewis, S. Bauguitte, A. M. Rankin, R. A. Salmon, E. W. Wolff, A. Saiz-Lopez, W. J. Bloss, D. E. Heard, J. D. Lee, and J. M. C. Plane (2008). "DMS and MSA measurements in the Antarctic Boundary Layer: impact of BrO on MSA production". In: *Atmospheric Chemistry and Physics* 8.11, pp. 2985–2997. DOI: 10.5194/acp-8-2985-2008 (cit. on pp. 2, 45, 161, 162, 225).

Richter, A., F. Wittrock, M. Eisinger, and J. P. Burrows (1998). "GOME observations of tropospheric BrO in northern hemispheric spring and summer 1997". In: *Geophysical Research Letters* 25.14, pp. 2683–2686. DOI: 10.1029/98gl52016 (cit. on p. 38).

Richter, S., R. C. Gerum, W. Schneider, B. Fabry, C. L. Bohec, and D. P. Zitterbart (2018). "A remote-controlled observatory for behavioural and ecological research: A case study on emperor penguins". In: *Methods in Ecology and Evolution* 9.5, pp. 1168–1178. DOI: 10.1111/2041-210x.12971 (cit. on p. 161).

Rityn, N. E. (1967). “Optics of corner cube reflectors”. In: *Sov. J. Opt. Technol.* 34, pp. 198–201 (cit. on pp. 70, 71).

Rodgers, C. D. (1990). “Characterization and error analysis of profiles retrieved from remote sounding measurements”. In: *Journal of Geophysical Research* 95.D5, p. 5587. DOI: 10.1029/jd095id05p05587 (cit. on p. 102).

Rodgers, C. D. (2000). *Inverse Methods for Atmospheric Sounding*. WORLD SCIENTIFIC. DOI: 10.1142/3171 (cit. on p. 102).

Roedel, W. and T. Wagner (2011). *Physik unserer Umwelt: Die Atmosphäre*. Springer Berlin Heidelberg. DOI: 10.1007/978-3-642-15729-5 (cit. on pp. 15, 16, 18, 20, 21, 52, 140, 143).

Roscoe, H. K., B. Brooks, A. V. Jackson, M. H. Smith, S. J. Walker, R. W. Obbard, and E. W. Wolff (2011). “Frost flowers in the laboratory: Growth, characteristics, aerosol, and the underlying sea ice”. In: *Journal of Geophysical Research* 116.D12. DOI: 10.1029/2010jd015144 (cit. on p. 40).

Röthlisberger, R., M. A. Hutterli, E. W. Wolff, R. Mulvaney, H. Fischer, M. Bigler, K. Goto-Azuma, M. E. Hansson, U. Ruth, M.-L. Siggaard-Andersen, and J. P. Steffensen (2002). “Nitrate in Greenland and Antarctic ice cores: a detailed description of post-depositional processes”. In: *Annals of Glaciology* 35, pp. 209–216. DOI: 10.3189/172756402781817220 (cit. on p. 46).

Rothman, L., I. Gordon, R. Barber, H. Dothe, R. Gamache, A. Goldman, V. Perevalov, S. Tashkun, and J. Tennyson (2010). “HITEMP, the high-temperature molecular spectroscopic database”. In: *Journal of Quantitative Spectroscopy and Radiative Transfer* 111.15, pp. 2139–2150. DOI: 10.1016/j.jqsrt.2010.05.001 (cit. on pp. 108, 119, 289).

Rozanov, A., V. Rozanov, M. Buchwitz, A. Kokhanovsky, and J. P. Burrows (2005). “SCIATRAN 2.0 – A new radiative transfer model for geophysical applications in the 175–2400nm spectral region”. In: *Advances in Space Research* 36.5, pp. 1015–1019. DOI: 10.1016/j.asr.2005.03.012 (cit. on p. 102).

Ryznar, E. (1963). “Visual Resolution and Optical Scintillation in Stable Stratification over Snow”. In: *Journal of Applied Meteorology* 2.4, pp. 526–530. DOI: 10.1175/1520-0450(1963)002<0526:vraosi>2.0.co;2 (cit. on pp. 90, 91).

Saiz-Lopez, A., A. S. Mahajan, R. A. Salmon, S. J.-B. Bauguitte, A. E. Jones, H. K. Roscoe, and J. M. C. Plane (2007a). “Boundary Layer Halogens in Coastal Antarctica”. In: *Science* 317.5836, pp. 348–351. DOI: 10.1126/science.1141408 (cit. on pp. 2, 37, 39, 129, 178, 196, 197, 215).

Saiz-Lopez, A., K. Chance, X. Liu, T. P. Kurosu, and S. P. Sander (2007b). “First observations of iodine oxide from space”. In: *Geophysical Research Letters* 34.12. DOI: 10.1029/2007gl030111 (cit. on p. 39).

Saiz-Lopez, A., J. M. C. Plane, A. R. Baker, L. J. Carpenter, R. von Glasow, J. C. G. Martin, G. McFiggans, and R. W. Saunders (2012). "Atmospheric Chemistry of Iodine". In: *Chemical Reviews* 112.3, pp. 1773–1804. DOI: 10.1021/cr200029u (cit. on pp. 30, 35, 47, 217).

Saiz-Lopez, A. and R. von Glasow (2012). "Reactive halogen chemistry in the troposphere". In: *Chemical Society Reviews* 41.19, p. 6448. DOI: 10.1039/c2cs35208g (cit. on pp. 2, 28–31, 35–38, 42, 175).

Sander, R., J. P. Burrows, and L. Kaleschke (2006). "Carbonate precipitation in brine - a potential trigger for tropospheric ozone depletion events". In: *Atmospheric Chemistry and Physics* 6.12, pp. 4653–4658. DOI: 10.5194/acp-6-4653-2006 (cit. on pp. 14, 41, 166, 172, 201).

Sander, S. P. and R. R. Friedl (1989). "Kinetics and product studies of the reaction chlorine monoxide + bromine monoxide using flash photolysis-ultraviolet absorption". In: *The Journal of Physical Chemistry* 93.12, pp. 4764–4771. DOI: 10.1021/j100349a017 (cit. on pp. 108, 289).

Schiermeier, Q. (2004). "Cold comfort". In: *Nature* 431.7010, pp. 734–735. DOI: 10.1038/431734a (cit. on p. 62).

Schmithüsen, H. and H. Müller (2019a). "Basic and other measurements of radiation at Neumayer Station 2018/2019". unpublished - to be published on PANGEA. URL: https://www.pangaea.de/ (cit. on p. 65).

– (2019b). "Continuous meteorological observations at Neumayer station 2018/2019". unpublished - to be published on PANGEA. URL: https://www.pangaea.de/ (cit. on p. 64).

– (2019c). "Radiosonde raw data from Neumayer Station 2018/2019, links to files". unpublished - to be published on PANGEA. URL: https://www.pangaea.de/ (cit. on p. 65).

Schmithüsen, H. and H. Schulz (2018a). *Basic and other measurements of radiation at Neumayer Station 2017/2018*. PANGEA data sets. URL: https://www.pangaea.de/ (cit. on p. 64).
Radiation NMIII (2017-02). DOI: 10.1594/pangaea.887515.
Radiation NMIII (2017-03). DOI: 10.1594/pangaea.887516.
Radiation NMIII (2017-04). DOI: 10.1594/pangaea.887517.
Radiation NMIII (2017-05). DOI: 10.1594/pangaea.887519.
Radiation NMIII (2017-06). DOI: 10.1594/pangaea.887520.
Radiation NMIII (2017-07). DOI: 10.1594/pangaea.887521.
Radiation NMIII (2017-08). DOI: 10.1594/pangaea.887522.
Radiation NMIII (2017-09). DOI: 10.1594/pangaea.887523.
Radiation NMIII (2017-10). DOI: 10.1594/pangaea.887524.
Radiation NMIII (2017-11). DOI: 10.1594/pangaea.887525.
Radiation NMIII (2017-12). DOI: 10.1594/pangaea.887526.
Radiation NMIII (2018-01). DOI: 10.1594/pangaea.887527.

– (2018b). *Continuous meteorological observations at Neumayer station 2017/2018*. PANGEA data sets. URL: https://www.pangaea.de/ (cit. on p. 64).
Meteorology NMIII (2017-02). DOI: 10.1594/pangaea.887742.
Meteorology NMIII (2017-03). DOI: 10.1594/pangaea.887743.
Meteorology NMIII (2017-04). DOI: 10.1594/pangaea.887744.
Meteorology NMIII (2017-05). DOI: 10.1594/pangaea.887745.
Meteorology NMIII (2017-06). DOI: 10.1594/pangaea.887746.
Meteorology NMIII (2017-07). DOI: 10.1594/pangaea.887747.
Meteorology NMIII (2017-08). DOI: 10.1594/pangaea.887748.
Meteorology NMIII (2017-09). DOI: 10.1594/pangaea.887749.
Meteorology NMIII (2017-10). DOI: 10.1594/pangaea.887750.
Meteorology NMIII (2017-11). DOI: 10.1594/pangaea.887751.
Meteorology NMIII (2017-12). DOI: 10.1594/pangaea.887752.
Meteorology NMIII (2018-01). DOI: 10.1594/pangaea.887753.

– (2018c). *Radiosonde raw data from Neumayer Station 2017/2018, links to files*. PANGEA data sets. URL: https://www.pangaea.de/ (cit. on p. 65).
Radiosondes NMIII (2017-02). DOI: 10.1594/pangaea.887455.
Radiosondes NMIII (2017-03). DOI: 10.1594/pangaea.887456.
Radiosondes NMIII (2017-04). DOI: 10.1594/pangaea.887457.
Radiosondes NMIII (2017-05). DOI: 10.1594/pangaea.887458.
Radiosondes NMIII (2017-06). DOI: 10.1594/pangaea.887459.
Radiosondes NMIII (2017-07). DOI: 10.1594/pangaea.887460.
Radiosondes NMIII (2017-08). DOI: 10.1594/pangaea.887461.
Radiosondes NMIII (2017-09). DOI: 10.1594/pangaea.887462.
Radiosondes NMIII (2017-10). DOI: 10.1594/pangaea.887463.
Radiosondes NMIII (2017-11). DOI: 10.1594/pangaea.887464.
Radiosondes NMIII (2017-12). DOI: 10.1594/pangaea.887465.
Radiosondes NMIII (2018-01). DOI: 10.1594/pangaea.887466.

Schmitt, S. (2016). "The Dynamics of Reactive Halogen Species at the Dead Sea Valley". PhD thesis. Combined Faculties for Natural Sciences and for Mathematics of the Ruperto-Carola University of Heidelberg, Germany. DOI: 10.11588/heidok.00020245 (cit. on p. 70).

Schmunk, R. (2018). *Panoply netCDF, HDF and GRIB Data Viewer*. NASA Goddard Institute for Space Studies, 2880 Broadway, New York, NY 10025 USA. URL: https://www.giss.nasa.gov/tools/panoply/ (cit. on pp. 11, 143).

Schneider, W. and G. von Helden (1997). "Br2 absorption cross-section at 294K". In: *Berichte des Forschungszentums Jülich*. 3340. personal communication. E.-P. Röth, R. Ruhnke, G. Moortgat, R. Meller, and W. Schneider (cit. on p. 108).

Schönhardt, A., M. Begoin, A. Richter, F. Wittrock, L. Kaleschke, J. C. G. Martín, and J. P. Burrows (2012). "Simultaneous satellite observations of IO and BrO over Antarctica". In: *Atmospheric Chemistry and Physics* 12.14, pp. 6565–6580. DOI: 10.5194/acp-12-6565-2012 (cit. on pp. 38, 39, 197).

Schönhardt, A., A. Richter, F. Wittrock, H. Kirk, H. Oetjen, H. K. Roscoe, and J. P. Burrows (2008). "Observations of iodine monoxide columns from satellite". In: *Atmospheric Chemistry and Physics* 8.3, pp. 637–653. DOI: 10.5194/acp-8-637-2008 (cit. on p. 39).

Schottky, W. (1918). "Über spontane Stromschwankungen in verschiedenen Elektrizitätsleitern". In: *Annalen der Physik* 362.23, pp. 541–567. DOI: 10.1002/andp.19183622304 (cit. on p. 52).

Seinfeld, J. H. and S. N. Pandis (2016). *Atmospheric Chemistry and Physics*. 3rd Edition. John Wiley+ Sons. ISBN: 1118947401. URL: https://www.wiley.com/en-us/Atmospheric+Chemistry+and+Physics%3A+From+Air+Pollution+to+Climate+Change%2C+3rd+Edition-p-9781119221173 (cit. on pp. 20, 23–25).

Seitz, K., J. Buxmann, D. Pöhler, T. Sommer, J. Tschritter, C. O'Dowd, and U. Platt (2009). "The spatial distribution of the reactive iodine species IO from simultaneous active and passive DOAS observations". In: *Atmospheric Chemistry and Physics Discussions* 9.5, pp. 21371–21398. DOI: 10.5194/acpd-9-21371-2009 (cit. on pp. 30, 129).

Selin, N. E. (2009). "Global Biogeochemical Cycling of Mercury: A Review". In: *Annual Review of Environment and Resources* 34.1, pp. 43–63. DOI: 10.1146/annurev.environ.051308.084314 (cit. on p. 44).

Serdyuchenko, A., V. Gorshelev, M. Weber, W. Chehade, and J. P. Burrows (2014). "High spectral resolution ozone absorption cross-sections - Part 2: Temperature dependence". In: *Atmospheric Measurement Techniques* 7.2, pp. 625–636. DOI: 10.5194/amt-7-625-2014 (cit. on pp. 108, 109, 289).

Shirsat, S. V. and H. F. Graf (2009). "An emission inventory of sulfur from anthropogenic sources in Antarctica". In: *Atmospheric Chemistry and Physics* 9.10, pp. 3397–3408. DOI: 10.5194/acp-9-3397-2009 (cit. on p. 161).

Sihler, H. (2007). "Light-Emitting Diodes as Light Sources in Spectroscopic Measurements of Atmospheric Trace Gases". Diploma thesis. Friedrich-Schiller-Universität Jena - Physikalisch-Astronomische Fakult"at (cit. on p. 71).

– (2012). "Halogen Activation in the Polar Troposphere". PhD thesis. Combined Faculties for Natural Sciences and for Mathematics of the Ruperto-Carola University of Heidelberg, Germany. DOI: 10.11588/heidok.00013663 (cit. on p. 42).

Sihler, H., U. Platt, S. Beirle, T. Marbach, S. Kühl, S. Dörner, J. Verschaeve, U. Frieß, D. Pöhler, L. Vogel, R. Sander, and T. Wagner (2012). "Tropospheric BrO column densities in the Arctic derived from satellite: retrieval and comparison to ground-based measurements". In: *Atmospheric Measurement Techniques* 5.11, pp. 2779–2807. DOI: 10.5194/amt-5-2779-2012 (cit. on pp. 38, 47).

Sihler, H., C. Kern, D. Pöhler, and U. Platt (2009). "Applying light-emitting diodes with narrowband emission features in differential spectroscopy". In: *Opt. Lett.* 34.23, pp. 3716–3718. DOI: 10.1364/OL.34.003716 (cit. on p. 73).

Simpson, W. R., R. von Glasow, K. Riedel, P. Anderson, P. Ariya, J. Bottenheim, J. P. Burrows, L. J. Carpenter, U. Frieß, M. E. Goodsite, D. Heard, M. Hutterli, H.-W. Jacobi, L. Kaleschke, W. D. Neff, J. Plane, U. Platt, A. Richter, H. Roscoe, R. Sander, P. Shepson, J. Sodeau, A. Steffen, T. Wagner, and E. Wolff (2007). "Halogens and their role in polar boundary-layer ozone depletion". In: *Atmospheric Chemistry and Physics* 7.16, pp. 4375–4418. DOI: 10.5194/acp-7-4375-2007 (cit. on pp. 20, 28, 29, 31, 40–42, 47, 172, 175, 186).

Simpson, W. R., S. S. Brown, A. Saiz-Lopez, J. A. Thornton, and R. von Glasow (2015). "Tropospheric Halogen Chemistry: Sources, Cycling, and Impacts". In: *Chemical Reviews* 115.10, pp. 4035–4062. DOI: 10.1021/cr5006638 (cit. on pp. 3, 28–30, 33–35, 40, 41, 43, 46).

Simpson, W. R., P. K. Peterson, U. Frieß, H. Sihler, J. Lampel, U. Platt, C. Moore, K. Pratt, P. Shepson, J. Halfacre, and S. V. Nghiem (2017). "Horizontal and vertical structure of reactive bromine events probed by bromine monoxide MAX-DOAS". In: *Atmospheric Chemistry and Physics* 17.15, pp. 9291–9309. DOI: 10.5194/acp-17-9291-2017 (cit. on pp. 186, 187).

Sinreich, R., U. Frieß, T. Wagner, and U. Platt (2005). "Multi axis differential optical absorption spectroscopy (MAX-DOAS) of gas and aerosol distributions". In: *Faraday discussions* 130, pp. 153–164. DOI: 10.1039/B419274P (cit. on p. 101).

Sipilä, M., N. Sarnela, T. Jokinen, H. Henschel, H. Junninen, J. Kontkanen, S. Richters, J. Kangasluoma, A. Franchin, O. Peräkylrä, M. P. Rissanen, M. Ehn, H. Vehkamräki, T. Kurten, T. Berndt, T. Peträjrä, D. Worsnop, D. Ceburnis, V.-M. Kerminen, M. Kulmala, and C. O'Dowd (2016). "Molecular-scale evidence of aerosol particle formation via sequential addition of HIO3". In: *Nature* 537.7621, pp. 532–534. DOI: 10.1038/nature19314 (cit. on p. 30).

Sjostedt, S. J. and J. P. D. Abbatt (2008). "Release of gas-phase halogens from sodium halide substrates: heterogeneous oxidation of frozen solutions and desiccated salts by hydroxyl radicals". In: *Environmental Research Letters* 3.4, p. 045007. DOI: 10.1088/1748-9326/3/4/045007 (cit. on pp. 36, 40).

Solomon, S., R. W. Portmann, and D. W. J. Thompson (2007). "Contrasts between Antarctic and Arctic ozone depletion". In: *Proceedings of the National Academy of Sciences* 104.2, pp. 445–449. DOI: 10.1073/pnas.0604895104 (cit. on p. 8).

Solomon, S., R. W. Sanders, M. A. Carroll, and A. L. Schmeltekopf (1989). "Visible and near-ultraviolet spectroscopy at McMurdo Station, Antarctica: 5. Observations of the diurnal variations of BrO and OClO". In: *Journal of Geophysical Research* 94, pp. 11393–11403. URL: http://onlinelibrary.wiley.com/doi/10.1029/JD094iD09p11393/full (cit. on p. 101).

Solomon, S., R. R. Garcia, F. S. Rowland, and D. J. Wuebbles (1986). "On the depletion of Antarctic ozone". In: *Nature* 321.6072, pp. 755–758. DOI: 10.1038/321755a0 (cit. on p. 2).

SPC (1999). *Operator's Manual Model 6A ECC ozonesonde*. Science Pump Corporation. URL: http://isr.sri.com/mirror/summit/ftp/science/ICECAPS/radiosondes/reference/Manuals_Use_Link_Below/TSC-1%20Manual_Feb2002.pdf (cit. on p. 66).

Spicer, C. W., R. A. Plastridge, K. L. Foster, B. J. Finlayson-Pitts, J. W. Bottenheim, A. M. Grannas, and P. B. Shepson (2002). "Molecular halogens before and during ozone depletion events in the Arctic at polar sunrise: concentrations and sources". In: *Atmospheric Environment* 36.15-16, pp. 2721–2731. DOI: 10.1016/s1352-2310(02)00125-5 (cit. on p. 206).

Spietz, P., J. C. Gómez Martín, and J. P. Burrows (2005). "Spectroscopic studies of the I2/O3 photochemistry". In: *Journal of Photochemistry and Photobiology A: Chemistry* 176.1-3, pp. 50–67. DOI: 10.1016/j.jphotochem.2005.08.023 (cit. on pp. 108, 289).

– (2006). "Effects of column density on I_2 spectroscopy and a determination of I_2 absorption cross section at 500 nm". In: *Atmospheric Chemistry and Physics* 6.8, pp. 2177–2191. DOI: 10.5194/acp-6-2177-2006 (cit. on pp. 108, 289).

Spolaor, A., T. Opel, J. R. McConnell, O. J. Maselli, G. Spreen, C. Varin, T. Kirchgeorg, D. Fritzsche, A. Saiz-Lopez, and P. Vallelonga (2016a). "Halogen-based reconstruction of Russian Arctic sea ice area from the Akademii Nauk ice core (Severnaya Zemlya)". In: *The Cryosphere* 10.1, pp. 245–256. DOI: 10.5194/tc-10-245-2016 (cit. on p. 47).

Spolaor, A., P. Vallelonga, J. Gabrieli, T. Martma, M. P. Björkman, E. Isaksson, G. Cozzi, C. Turetta, H. A. Kjær, M. A. J. Curran, A. D. Moy, A. Schönhardt, A.-M. Blechschmidt, J. P. Burrows, J. M. C. Plane, and C. Barbante (2014). "Seasonality of halogen deposition in polar snow and ice". In: *Atmospheric Chemistry and Physics* 14.18, pp. 9613–9622. DOI: 10.5194/acp-14-9613-2014 (cit. on pp. 46, 47).

Spolaor, A., P. Vallelonga, J. M. C. Plane, N. Kehrwald, J. Gabrieli, C. Varin, C. Turetta, G. Cozzi, R. Kumar, C. Boutron, and C. Barbante (2013). "Halogen species record Antarctic sea ice extent over glacial–interglacial periods". In: *Atmospheric Chemistry and Physics* 13.13, pp. 6623–6635. DOI: 10.5194/acp-13-6623-2013 (cit. on pp. 2, 46).

Spolaor, A., P. Vallelonga, C. Turetta, N. Maffezzoli, G. Cozzi, J. Gabrieli, C. Barbante, K. Goto-Azuma, A. Saiz-Lopez, C. A. Cuevas, and D. Dahl-Jensen (2016b). "Canadian Arctic sea ice reconstructed from bromine in the Greenland NEEM ice core". In: *Scientific Reports* 6.1. DOI: 10.1038/srep33925 (cit. on p. 47).

Spreen, G., L. Kaleschke, and G. Heygster (2008). "Sea ice remote sensing using AMSR-E 89-GHz channels". In: *Journal of Geophysical Research* 113.C2. Data retrieved from https://seaice.uni-bremen.de/sea-ice-concentration/time-series/ - Dec 2018. DOI: 10.1029/2005jc003384 (cit. on pp. 10, 12).

Steen, A. O., T. Berg, A. P. Dastoor, D. A. Durnford, L. R. Hole, and K. A. Pfaffhuber (2009). "Dynamic exchange of gaseous elemental mercury during polar night and day". In: *Atmospheric Environment* 43.35, pp. 5604–5610. DOI: 10.1016/j.atmosenv.2009.07.069 (cit. on p. 44).

Stohl, A. (2006). “Characteristics of atmospheric transport into the Arctic troposphere”. In: *Journal of Geophysical Research* 111.D11. DOI: 10.1029/2005jd006888 (cit. on p. 32).

Stohl, A. and H. Sodemann (2010). “Characteristics of atmospheric transport into the Antarctic troposphere”. In: *Journal of Geophysical Research* 115.D2. DOI: 10.1029/2009jd012536 (cit. on p. 19).

Strutt (Lord Rayleigh), J. W. (1881). “X. On the electromagnetic theory of light”. In: *The London, Edinburgh, and Dublin Philosophical Magazine and Journal of Science* 12.73, pp. 81–101. DOI: 10.1080/14786448108627074 (cit. on p. 51).

– (1899). “XXXIV. On the transmission of light through an atmosphere containing small particles in suspension, and on the origin of the blue of the sky”. In: *The London, Edinburgh, and Dublin Philosophical Magazine and Journal of Science* 47.287, pp. 375–384. DOI: 10.1080/14786449908621276 (cit. on p. 51).

Stull, R. B. (1994). *An introduction to boundary layer meteorology*. eng. Repr. Atmospheric sciences library. Dordrecht [u.a.]: Kluwer, XII, 666 S. DOI: 10.1007/978-94-009-3027-8 (cit. on p. 16).

Sturm, M. and R. A. Massom (2017). “Snow in the sea ice system: friend or foe?” In: *Sea ice*. Ed. by D. N. Thomas. Third edition. Chichester, UK ; Hoboken, NJ: Wiley Blackwell. Chap. 3, 652 p. ISBN: 978-1-118-77838-8. URL: https://www.wiley.com/en-us/Sea+Ice%2C+3rd+Edition-p-9781118778388 (cit. on pp. 10, 12).

Stutz, J., E. S. Kim, U. Platt, P. Bruno, C. Perrino, and A. Febo (2000). “UV-visible absorption cross sections of nitrous acid”. In: *Journal of Geophysical Research: Atmospheres* 105.D11, pp. 14585–14592. DOI: 10.1029/2000jd900003 (cit. on pp. 108, 289).

Stutz, J., J. L. Thomas, S. C. Hurlock, M. Schneider, R. von Glasow, M. Piot, K. Gorham, J. F. Burkhart, L. Ziemba, J. E. Dibb, and B. L. Lefer (2011). “Longpath DOAS observations of surface BrO at Summit, Greenland”. In: *Atmospheric Chemistry and Physics* 11.18, pp. 9899–9910. DOI: 10.5194/acp-11-9899-2011 (cit. on pp. 37, 55, 70, 195).

Stutz, J. and U. Platt (1996). “Numerical analysis and estimation of the statistical error of differential optical absorption spectroscopy measurements with least-squares methods”. In: *Applied Optics* 35.30, p. 6041. DOI: 10.1364/ao.35.006041 (cit. on pp. 58–60, 124).

Stutz, J. and U. Platt (1997). “Improving long-path differential optical absorption spectroscopy with a quartz-fiber mode mixer”. English. In: *Applied Optics* 36.6, p. 1105. ISSN: 0003-6935 and 1539-4522. DOI: 10.1364/AO.36.001105 (cit. on pp. 56, 77).

Teinilä, K., A. Frey, R. Hillamo, H. Tülp, and R. Weller (2014). “A study of the sea-salt chemistry using size-segregated aerosol measurements at coastal Antarctic station Neumayer”. In: *Atmospheric Environment* 96, pp. 11–19. DOI: 10.1016/j.atmosenv.2014.07.025 (cit. on pp. 146, 148).

Temme, C., F. Slemr, R. Ebinghaus, and J. Einax (2003). "Distribution of mercury over the Atlantic Ocean in 1996 and 1999–2001". In: *Atmospheric Environment* 37.14, pp. 1889–1897. DOI: 10.1016/s1352-2310(03)00069-4 (cit. on pp. 44, 224).

TFS (2009). *Model 5012 Instruction Manual Multi Angle Absorption Photometer (MAAP)*. Thermo Fisher Scientific Inc. URL: https://assets.thermofisher.com/TFS-Assets/LSG/manuals/EPM-manual-Model%205012%20MAAP.pdf (cit. on p. 68).

Thalman, R. and R. Volkamer (2013). "Temperature dependent absorption cross-sections of O2-O2 collision pairs between 340 and 630 nm and at atmospherically relevant pressure". In: *Physical Chemistry Chemical Physics* 15.37, p. 15371. DOI: 10.1039/c3cp50968k (cit. on pp. 108, 289).

The Antarctic Treaty (1959). 402 U.N.T.S. 71. URL: https://treaties.un.org/pages/showDetails.aspx?objid=0800000280136dbc (cit. on pp. 6, 7).

Thibert, E. and F. Dominé (1997). "Thermodynamics and Kinetics of the Solid Solution of HCl in Ice". In: *The Journal of Physical Chemistry B* 101.18, pp. 3554–3565. DOI: 10.1021/jp962115o (cit. on p. 13).

Thomas, D. N., ed. (2017). *Sea ice*. eng. Third edition. Chichester, UK ; Hoboken, NJ: Wiley Blackwell, xii, 652 Seiten. ISBN: 978-1-118-77838-8. URL: https://www.wiley.com/en-us/Sea+Ice%2C+3rd+Edition-p-9781118778388.

Thomas, J. L., J. E. Dibb, L. G. Huey, J. Liao, D. Tanner, B. Lefer, R. von Glasow, and J. Stutz (2012). "Modeling chemistry in and above snow at Summit, Greenland – Part 2: Impact of snowpack chemistry on the oxidation capacity of the boundary layer". In: *Atmospheric Chemistry and Physics* 12.14, pp. 6537–6554. DOI: 10.5194/acp-12-6537-2012 (cit. on pp. 191, 195).

Thomas, J. L., J. Stutz, B. Lefer, L. G. Huey, K. Toyota, J. E. Dibb, and R. von Glasow (2011). "Modeling chemistry in and above snow at Summit, Greenland – Part 1: Model description and results". In: *Atmospheric Chemistry and Physics* 11.10, pp. 4899–4914. DOI: 10.5194/acp-11-4899-2011 (cit. on pp. 191, 195).

Thompson, A. M. (1992). "The Oxidizing Capacity of the Earth's Atmosphere: Probable Past and Future Changes". In: *Science* 256.5060, pp. 1157–1165. DOI: 10.1126/science.256.5060.1157 (cit. on pp. 1, 23).

Thompson, C. R., P. B. Shepson, J. Liao, L. G. Huey, E. C. Apel, C. A. Cantrell, F. Flocke, J. Orlando, A. Fried, S. R. Hall, R. S. Hornbrook, D. J. Knapp, R. L. M. III, D. D. Montzka, B. C. Sive, K. Ullmann, P. Weibring, and A. Weinheimer (2015). "Interactions of bromine, chlorine, and iodine photochemistry during ozone depletions in Barrow, Alaska". In: *Atmospheric Chemistry and Physics* 15.16, pp. 9651–9679. DOI: 10.5194/acp-15-9651-2015 (cit. on pp. 29, 30, 32, 34, 39, 46, 184, 206, 210, 211, 219).

Thompson, C. R., P. B. Shepson, J. Liao, L. G. Huey, C. Cantrell, F. Flocke, and J. Orlando (2017). "Bromine atom production and chain propagation during springtime Arctic

ozone depletion events in Barrow, Alaska". In: *Atmospheric Chemistry and Physics* 17.5, pp. 3401–3421. DOI: 10.5194/acp-17-3401-2017 (cit. on pp. 3, 186).

Tie, X. (2003). "Effect of clouds on photolysis and oxidants in the troposphere". In: *Journal of Geophysical Research* 108.D20. DOI: 10.1029/2003jd003659 (cit. on p. 29).

Toyota, K., J. C. McConnell, A. Lupu, L. Neary, C. A. McLinden, A. Richter, R. Kwok, K. Semeniuk, J. W. Kaminski, S.-L. Gong, J. Jarosz, M. P. Chipperfield, and C. E. Sioris (2011). "Analysis of reactive bromine production and ozone depletion in the Arctic boundary layer using 3-D simulations with GEM-AQ: inference from synoptic-scale patterns". In: *Atmospheric Chemistry and Physics* 11.8, pp. 3949–3979. DOI: 10.5194/acp-11-3949-2011 (cit. on p. 29).

TSI (1999). *Model 3022A Condensation Particle Counter - Specifications*. TSI Incorporated. URL: http://epic.awi.de/27246/1/TSI1999a.pdf (cit. on p. 69).

– (2002). *Model 3563 Integrating Nephelometer - Specifications*. TSI Incorporated. URL: http://epic.awi.de/27247/1/TSI2002a.pdf (cit. on p. 68).

– (2009). *Series 3080 Electrostatic classifier*. TSI Incorporated. URL: http://tsi.com/electrostatic-classifier-3080n/ (cit. on p. 69).

Tuckermann, M., R. Ackermann, C. Golz, H. Lornezen-Schmidt, T. Senne, J. Stutz, B. Trost, W. Unold, and U. Platt (1997). "DOAS-observation of halogen radical-catalysed arctic boundary layer ozone destruction during the ARCTOC-campaigns 1995 and 1996 in Ny-Alesund, Spitsbergen". In: *Tellus B* 49.5, pp. 533–555. DOI: 10.1034/j.1600-0889.49.issue5.9.x (cit. on pp. 37, 39, 60, 123, 206).

Turner, J. and S. Pendlebury, eds. (2004). *The international Antarctic weather forecasting handbook*. British Antarctic Survey. URL: http://nora.nerc.ac.uk/id/eprint/17324/ (cit. on p. 22).

Turnipseed, A. A., J. W. Birks, and J. G. Calvert (1991). "Kinetics and temperature dependence of the bromine monoxide plus chlorine monoxide reaction". In: *The Journal of Physical Chemistry* 95.11, pp. 4356–4364. DOI: 10.1021/j100164a035 (cit. on p. 213).

Vaisala (2010). *USER'S GUIDE Vaisala Ceilomter CL51*. Vaisala Corporation. URL: https://www.vaisala.com/sites/default/files/documents/CL51-Datasheet-B210861EN.pdf (cit. on p. 66).

– (2013). *Vaisala Radiosonde RS92-SGP - Manual*. Vaisala Corporation. URL: https://www.vaisala.com/en/file/8226/download?token=CkC5AXlB (cit. on p. 65).

Vallelonga, P., N. Maffezzoli, A. D. Moy, M. A. J. Curran, T. R. Vance, R. Edwards, G. Hughes, E. Barker, G. Spreen, A. Saiz-Lopez, J. P. Corella, C. A. Cuevas, and A. Spolaor (2017). "Sea-ice-related halogen enrichment at Law Dome, coastal East Antarctica". In: *Climate of the Past* 13.2, pp. 171–184. DOI: 10.5194/cp-13-171-2017 (cit. on p. 47).

van Loon, H. (1967). "The Half-Yearly Oscillations in Middle and High Southern Latitudes and the Coreless Winter". In: *Journal of the Atmospheric Sciences* 24.5, pp. 472–486. DOI: 10.1175/1520-0469(1967)024<0472:thyoim>2.0.co;2 (cit. on p. 144).

Vaughan, D., J. Comiso, I. Allison, J. Carrasco, G. Kaser, R. Kwok, P. Mote, T. Murray, F. Paul, J. Ren, E. Rignot, O. Solomina, K. Steffen, and T. Zhang (2013). "Observations: Cryosphere". In: *Climate Change 2013: The Physical Science Basis. Contribution of Working Group I to the Fifth Assessment Report of the Intergovernmental Panel on Climate Change*. Ed. by T. Stocker, D. Qin, G.-K. Plattner, M. Tignor, S. Allen, J. Boschung, A. Nauels, Y. Xia, V. Bex, and P. Midgley. Cambridge, United Kingdom and New York, NY, USA: Cambridge University Press. Chap. 4, pp. 317–382. DOI: 10.1017/CBO9781107415324.012. URL: www.climatechange2013.org (cit. on pp. 9, 10, 12).

Vingarzan, R. (2004). "A review of surface ozone background levels and trends". In: *Atmospheric Environment* 38.21, pp. 3431–3442. DOI: 10.1016/j.atmosenv.2004.03.030 (cit. on p. 26).

Vinogradova, A. A. and Y. A. Ivanova (2018). "Transport of Air Masses and Pollutants to the Russian Arctic Islands (1986–2016): Long-Term, Interannual, and Seasonal Variations". In: *Izvestiya, Atmospheric and Oceanic Physics* 54.7, pp. 688–699. DOI: 10.1134/s0001433818070174 (cit. on p. 22).

Voigt, S., J. Orphal, and J. P. Burrows (2002). "The temperature and pressure dependence of the absorption cross-sections of NO2 in the 250-800 nm region measured by Fourier-transform spectroscopy". In: *Journal of Photochemistry and Photobiology A: Chemistry* 149.1-3, pp. 1–7. DOI: 10.1016/s1010-6030(01)00650-5 (cit. on pp. 108, 289).

Volkamer, R., L. T. Molina, M. J. Molina, T. Shirley, and W. H. Brune (2005). "DOAS measurement of glyoxal as an indicator for fast VOC chemistry in urban air". In: *Geophysical Research Letters* 32.8. DOI: 10.1029/2005gl022616 (cit. on pp. 70, 108).

von Glasow, R. and P. J. Crutzen (2003). "Tropospheric Halogen Chemistry". In: *Treatise on Geochemistry*. Elsevier, pp. 1–67. DOI: 10.1016/b0-08-043751-6/04141-4 (cit. on p. 28).

– (2004). "Model study of multiphase DMS oxidation with a focus on halogens". In: *Atmospheric Chemistry and Physics* 4.3, pp. 589–608. DOI: 10.5194/acp-4-589-2004 (cit. on pp. 2, 45, 225).

Voosen, P. (2017). "2.7-million-year-old ice opens window on past". In: *Science* 357.6352, pp. 630–631. DOI: 10.1126/science.357.6352.630 (cit. on p. 1).

– (2018). "Outer space may have just gotten a bit closer". In: *Science*. DOI: 10.1126/science.aau8822 (cit. on p. 15).

Wagenbach, D., M. Legrand, H. Fischer, F. Pichlmayer, and E. W. Wolff (1998). "Atmospheric near-surface nitrate at coastal Antarctic sites". In: *Journal of Geophysical*

Research: Atmospheres 103.D9, pp. 11007–11020. DOI: 10.1029/97jd03364 (cit. on p. 67).

Wagner, T., B. Dix, C. v. Friedeburg, U. Frieß, S. Sanghavi, R. Sinreich, and U. Platt (2004). "MAX-DOAS O 4 measurements: A new technique to derive information on atmospheric aerosols—Principles and information content". In: *Journal of Geophysical Research* 109.D22205, p. 19. ISSN: 0148-0227. DOI: 10.1029/2004JD004904 (cit. on pp. 101, 102).

Wagner, T., O. Ibrahim, R. Sinreich, U. Frieß, R. von Glasow, and U. Platt (2007). "Enhanced tropospheric BrO over Antarctic sea ice in mid winter observed by MAX-DOAS on board the research vessel Polarstern". In: *Atmospheric Chemistry and Physics* 7.12, pp. 3129–3142. DOI: 10.5194/acp-7-3129-2007 (cit. on pp. 37, 38, 102).

Wagner, T., C. Leue, M. Wenig, K. Pfeilsticker, and U. Platt (2001). "Spatial and temporal distribution of enhanced boundary layer BrO concentrations measured by the GOME instrument aboard ERS-2". In: *Journal of Geophysical Research: Atmospheres* 106.D20, pp. 24225–24235. DOI: 10.1029/2000jd000201 (cit. on p. 42).

Wagner, W. and A. Pruß (2002). "The IAPWS Formulation 1995 for the Thermodynamic Properties of Ordinary Water Substance for General and Scientific Use". In: *Journal of Physical and Chemical Reference Data* 31.2, pp. 387–535. DOI: 10.1063/1.1461829 (cit. on p. 25).

Wahner, A., G. S. Tyndall, and A. R. Ravishankara (1987). "Absorption cross sections for symmetric chlorine dioxide as a function of temperature in the wavelength range 240-480nm". In: *The Journal of Physical Chemistry* 91.11, pp. 2734–2738. DOI: 10.1021/j100295a018 (cit. on pp. 108, 289).

Wang, S., R. Ackermann, and J. Stutz (2006). "Vertical profiles of O3 and NOx chemistry in the polluted nocturnal boundary layer in Phoenix, AZ: I. Field observations by long-path DOAS". In: *Atmospheric Chemistry and Physics* 6.9, pp. 2671–2693. DOI: 10.5194/acp-6-2671-2006 (cit. on p. 70).

Wang, S. and K. A. Pratt (2017). "Molecular Halogens Above the Arctic Snowpack: Emissions, Diurnal Variations, and Recycling Mechanisms". In: *Journal of Geophysical Research: Atmospheres* 122.21, pp. 11, 991–12, 007. DOI: 10.1002/2017jd027175 (cit. on pp. 2, 37, 39, 186, 191, 198, 206, 207).

Wang, X., D. J. Jacob, S. D. Eastham, M. P. Sulprizio, L. Zhu, Q. Chen, B. Alexander, T. Sherwen, M. J. Evans, B. H. Lee, J. D. Haskins, F. D. Lopez-Hilfiker, J. A. Thornton, G. L. Huey, and H. Liao (2018). "The role of chlorine in tropospheric chemistry". In: *Atmospheric Chemistry and Physics Discussions*, pp. 1–40. DOI: 10.5194/acp-2018-1088 (cit. on p. 39).

Wegener, A. (1918). "Elementare Theorie der atmosphärischen Spiegelungen". In: *Annalen der Physik* 362.19, pp. 203–230. DOI: 10.1002/andp.19183621904 (cit. on p. 91).

Welford, W. T. (T. and (. a. Winston Roland (1978). *The optics of nonimaging concentrators : light and solar energy*. English. Includes index. New York : Academic Press. ISBN: 0127453504 (cit. on p. 85).

Weller, R. (2019a). "Airchemistry at Neumayer station, Antarctica during the year 2018". unpublished - to be published on PANGEA. URL: https://www.pangaea.de/ (cit. on pp. 25, 68).

– (2019b). "Black carbon concentration measurements at the coastal Antarctic site Neumayer 2016-2018". unpublished - Private communication (cit. on p. 68).

Weller, R., A. E. Jones, A. Wille, H.-W. Jacobi, H. P. McIntyre, W. T. Sturges, M. Huke, and D. Wagenbach (2002). "Seasonality of reactive nitrogen oxides (NOy) at Neumayer Station, Antarctica". In: *Journal of Geophysical Research: Atmospheres* 107.D23, ACH 2–1–ACH 2–11. DOI: 10.1029/2002jd002495 (cit. on p. 67).

Weller, R., I. Levin, D. Schmithüsen, M. Nachbar, J. Asseng, and D. Wagenbach (2014). "On the variability of atmospheric 222Rn activity concentrations measured at Neumayer, coastal Antarctica". In: *Atmospheric Chemistry and Physics* 14.8, pp. 3843–3853. DOI: 10.5194/acp-14-3843-2014 (cit. on pp. 19, 67).

Weller, R., I. Levin, D. Wagenbach, and A. Minikin (2007). "The air chemistry observatory at Neumayer Stations (GvN and NM-II) Antarctica". In: *Polarforschung, Bremerhaven, Alfred Wegener Institute for Polar and Marine Research & German Society of Polar Research* 76.1, pp. 39–46 (cit. on pp. 67, 68, 157, 164).

Weller, R., A. Minikin, A. Petzold, D. Wagenbach, and G. König-Langlo (2013). "Characterization of long-term and seasonal variations of black carbon (BC) concentrations at Neumayer, Antarctica". In: *Atmospheric Chemistry and Physics* 13.3, pp. 1579–1590. DOI: 10.5194/acp-13-1579-2013 (cit. on pp. 68, 146).

Weller, R., A. Minikin, D. Wagenbach, and V. Dreiling (2011a). "Characterization of the inter-annual, seasonal, and diurnal variations of condensation particle concentrations at Neumayer, Antarctica". In: *Atmospheric Chemistry and Physics* 11.24, pp. 13243–13257. DOI: 10.5194/acp-11-13243-2011 (cit. on pp. 21, 69, 146–148, 164).

Weller, R., K. Schmidt, K. Teinilä, and R. Hillamo (2015). "Natural new particle formation at the coastal Antarctic site Neumayer". In: *Atmospheric Chemistry and Physics* 15.19, pp. 11399–11410. DOI: 10.5194/acp-15-11399-2015 (cit. on pp. 2, 47, 69, 146, 147, 221, 224).

Weller, R. (2005a). *Airchemistry at Neumayer Station, Antarctica during the year 1992*. PANGEA data set. DOI: 10.1594/pangaea.271526 (cit. on p. 151).

– (2005b). *Airchemistry at Neumayer Station, Antarctica during the year 1993*. PANGEA data set. DOI: 10.1594/pangaea.271527.

– (2005c). *Airchemistry at Neumayer Station, Antarctica during the year 1994*. PANGEA data set. DOI: 10.1594/pangaea.271528.

– (2005d). *Airchemistry at Neumayer Station, Antarctica during the year 1995*. PANGEA data set. DOI: 10.1594/pangaea.271529.

– (2005e). *Airchemistry at Neumayer Station, Antarctica during the year 1996*. PANGEA data set. DOI: 10.1594/pangaea.271530.

– (2005f). *Airchemistry at Neumayer Station, Antarctica during the year 1997*. PANGEA data set. DOI: 10.1594/pangaea.271531.

– (2005g). *Airchemistry at Neumayer Station, Antarctica during the year 1998*. PANGEA data set. DOI: 10.1594/pangaea.271533.

– (2005h). *Airchemistry at Neumayer Station, Antarctica during the year 1999*. PANGEA data set. DOI: 10.1594/pangaea.271525.

– (2005i). *Airchemistry at Neumayer Station, Antarctica during the year 2000*. PANGEA data set. DOI: 10.1594/pangaea.269833.

– (2005j). *Airchemistry at Neumayer Station, Antarctica during the year 2001*. PANGEA data set. DOI: 10.1594/pangaea.271115.

– (2005k). *Airchemistry at Neumayer Station, Antarctica during the year 2002*. PANGEA data set. DOI: 10.1594/pangaea.271114.

– (2005l). *Airchemistry at Neumayer Station, Antarctica during the year 2003*. PANGEA data set. DOI: 10.1594/pangaea.269662.

– (2005m). *Airchemistry at Neumayer Station, Antarctica during the year 2004*. PANGEA data set. DOI: 10.1594/pangaea.338937.

– (2006). *Airchemistry at Neumayer Station, Antarctica during the year 2005*. PANGEA data set. DOI: 10.1594/pangaea.475935.

– (2007). *Airchemistry at Neumayer station, Antarctica during the year 2006*. PANGEA data set. DOI: 10.1594/pangaea.652740.

– (2008). *Airchemistry at Neumayer station, Antarctica during the year 2007*. PANGEA data set. DOI: 10.1594/pangaea.701890.

– (2009). *Airchemistry at Neumayer station, Antarctica during the year 2008*. PANGEA data set. DOI: 10.1594/pangaea.722916.

– (2010). *Airchemistry at Neumayer station, Antarctica during the year 2009*. PANGEA data set. DOI: 10.1594/pangaea.754568.

– (2011). *Airchemistry at Neumayer station, Antarctica during the year 2010*. PANGEA data set. DOI: 10.1594/pangaea.761799.

– (2012). *Airchemistry at Neumayer station, Antarctica during the year 2011*. PANGEA data set. DOI: 10.1594/pangaea.787837.

Weller, R. (2013). *Airchemistry at Neumayer station, Antarctica during the year 2012*. PANGEA data set. DOI: 10.1594/pangaea.815285.

– (2014). *Airchemistry at Neumayer station, Antarctica during the year 2013*. PANGEA data set. DOI: 10.1594/pangaea.833109.

– (2016a). *Airchemistry at Neumayer station, Antarctica during the year 2014*. PANGEA data set. DOI: 10.1594/pangaea.860936.

– (2016b). *Airchemistry at Neumayer station, Antarctica during the year 2015*. PANGEA data set. DOI: 10.1594/pangaea.860939.

– (2017). *Airchemistry at Neumayer station, Antarctica during the year 2016*. PANGEA data set. DOI: 10.1594/pangaea.882136 (cit. on pp. 25, 28, 68).

– (2018a). *Airchemistry at Neumayer station, Antarctica during the year 2017*. PANGEA data set. DOI: 10.1594/pangaea.893176 (cit. on pp. 25, 68, 151).

– (2018b). *Year-round particle size distribution measurements at the coastal Antarctic site Neumayer*. PANGEA data sets. DOI: 10.1594/pangaea.887414 (cit. on p. 68).

Weller, R. and A. Lampert (2008). "Optical properties and sulfate scattering efficiency of boundary layer aerosol at coastal Neumayer Station, Antarctica". In: *Journal of Geophysical Research* 113.D16. DOI: 10.1029/2008jd009962 (cit. on p. 146).

Weller, R., D. Wagenbach, M. Legrand, C. Elsässer, X. Tian-Kunze, and G. König-Langlo (2011b). "Continuous 25-yr aerosol records at coastal Antarctica – I: inter-annual variability of ionic compounds and links to climate indices". In: *Tellus B: Chemical and Physical Meteorology* 63.5, pp. 901–919. DOI: 10.1111/j.1600-0889.2011.00542.x (cit. on pp. 21, 68, 146).

Weller, R., J. Wöltjen, C. Piel, R. Resenberg, D. Wagenbach, G. König-Langlo, and M. Kriews (2008). "Seasonal variability of crustal and marine trace elements in the aerosol at Neumayer station, Antarctica". In: *Tellus B: Chemical and Physical Meteorology* 60.5, pp. 742–752. DOI: 10.1111/j.1600-0889.2008.00372.x (cit. on pp. 20, 21, 146).

Wennberg, P. (1999). "Bromine explosion". In: *Nature* 397.6717, pp. 299–301. DOI: 10.1038/16805 (cit. on pp. 2, 33).

Wesche, C., R. Weller, G. König-Langlo, T. Fromm, A. Eckstaller, U. Nixdorf, and E. Kohlberg (2016). "Neumayer III and Kohnen Station in Antarctica operated by the Alfred Wegener Institute". In: *Journal of large-scale research facilities JLSRF* 2. DOI: 10.17815/jlsrf-2-152 (cit. on p. 62).

Wilmouth, D. M., T. F. Hanisco, N. M. Donahue, and J. G. Anderson (1999). "Fourier transform ultraviolet spectroscopy of the $A^2\Pi_{3/2} \leftarrow X^2\Pi_{3/2}$ transition of BrO". In: *Journall of Physical Chemistry A* 103.45, pp. 8935–8945. DOI: 10.1021/jp991651o (cit. on pp. 108, 109, 289).

Witschas, B. (2012). "Light Scattering on Molecules in the Atmosphere". In: *Atmospheric Physics*. Ed. by U. Schumann. Springer Berlin Heidelberg, pp. 69–83. DOI: 10.1007/978-3-642-30183-4_5 (cit. on p. 51).

WMO-CIMO (2012). *Pressure Reduction Formula*. Tech. rep. Geneva, Switzerland: World Meteorological Organisation - Commission for Instruments and Methods of Observation. URL: https://www.wmo.int/pages/prog/www/IMOP/meetings/SI/ET-Stand-1/Doc-10_Pressure-red.pdf (cit. on pp. 144, 145).

Wolff, E. W., M. A. Hutterli, and A. E. Jones (2007). "Past atmospheric composition and chemistry from ice cores - progress and prospects". In: *Environmental Chemistry* 4.4, p. 211. DOI: 10.1071/en07031 (cit. on pp. 2, 46).

Wren, S. N., D. J. Donaldson, and J. P. D. Abbatt (2013). "Photochemical chlorine and bromine activation from artificial saline snow". In: *Atmospheric Chemistry and Physics* 13.19, pp. 9789–9800. DOI: 10.5194/acpd-13-14163-2013 (cit. on pp. 2, 34, 35, 38, 40, 41, 206, 208).

Wyngaard, J. C. and S. F. Clifford (1978). "Estimating Momentum, Heat and Moisture Fluxes from Structure Parameters". In: *Journal of the Atmospheric Sciences* 35.7, pp. 1204–1211. DOI: 10.1175/1520-0469(1978)035<1204:emhamf>2.0.co;2 (cit. on p. 91).

Xie, Z.-Q., L. Sun, J. Wang, and B. Liu (2002). "A potential source of atmospheric sulfur from penguin colony emissions". In: *Journal of Geophysical Research* 107.D22. DOI: 10.1029/2002jd002114 (cit. on p. 161).

Yang, X., J. A. Pyle, R. A. Cox, N. Theys, and M. V. Roozendael (2010). "Snow-sourced bromine and its implications for polar tropospheric ozone". In: *Atmospheric Chemistry and Physics* 10.16, pp. 7763–7773. DOI: 10.5194/acp-10-7763-2010 (cit. on pp. 2, 22, 29, 42, 174, 210).

Yang, X., V. Neděla, J. Runštuk, G. Ondrušková, J. Krausko, Ľ. Vetráková, and D. Heger (2017). "Evaporating brine from frost flowers with electron microscopy and implications for atmospheric chemistry and sea-salt aerosol formation". In: *Atmospheric Chemistry and Physics* 17.10, pp. 6291–6303. DOI: 10.5194/acp-17-6291-2017 (cit. on p. 40).

Yang, X., J. A. Pyle, and R. A. Cox (2008). "Sea salt aerosol production and bromine release: Role of snow on sea ice". In: *Geophysical Research Letters* 35.16. DOI: 10.1029/2008gl034536 (cit. on pp. 2, 10, 21, 22, 174, 210).

Yee, M. S., V. R. Pauwels, E. Daly, J. Beringer, C. Rüdiger, M. F. McCabe, and J. P. Walker (2015). "A comparison of optical and microwave scintillometers with eddy covariance derived surface heat fluxes". In: *Agricultural and Forest Meteorology* 213, pp. 226–239. DOI: 10.1016/j.agrformet.2015.07.004 (cit. on p. 91).

Yilmaz, S. (2012). "Retrieval of Atmospheric Aerosol and Trace Gas Vertical Profiles using Multi-Axis Differential Optical Absorption Spectroscopy". PhD thesis. Combined

Faculties for Natural Sciences and for Mathematics of the Ruperto-Carola University of Heidelberg, Germany. DOI: 10.11588/heidok.00013128 (cit. on p. 102).

Yokelson, R. J., J. B. Burkholder, R. W. Fox, R. K. Talukdar, and A. R. Ravishankara (1994). "Temperature Dependence of the NO_3 Absorption Spectrum". In: *The Journal of Physical Chemistry* 98.50, pp. 13144–13150. DOI: 10.1021/j100101a009 (cit. on pp. 108, 289).

York, J. M. (2001). "CCD Perfomance Protocol Andor DU440 BU - CCD Serial No. 2521" (cit. on pp. 80, 82).

Young, A. T. (1981). "Rayleigh scattering". In: *Applied Optics* 20.4, p. 533. DOI: 10.1364/ao.20.000533 (cit. on p. 51).

– (2000). "Sunset science III Visual adaptation and green flashes". In: *Journal of the Optical Society of America A* 17.12, p. 2129. DOI: 10.1364/josaa.17.002129 (cit. on p. 91).

– (2004). "Sunset Science. IV. Low-Altitude Refraction". In: *The Astronomical Journal* 127.6, pp. 3622–3637. DOI: 10.1086/420806 (cit. on p. 91).

Young, A. T. and G. W. Kattawar (1998). "Sunset science II A useful diagram". In: *Applied Optics* 37.18, p. 3785. DOI: 10.1364/ao.37.003785 (cit. on p. 91).

Young, A. T., G. W. Kattawar, and P. Parviainen (1997). "Sunset science I The mock mirage". In: *Applied Optics* 36.12, p. 2689. DOI: 10.1364/ao.36.002689 (cit. on p. 91).

Zhu, H. and P. Blackborow (2011a). "LDLS sheds light on analytical-sciences applications". English. In: *Laser Focus World* 47.12, pp. 53–53. ISSN: 1043-8092 (cit. on p. 72).

– (2011b). *Operation of Laser-Driven Light Sources below 300nm: Ozone Mitigation.* Tech. rep. Energetiq. URL: https://www.energetiq.com/Operation-of-Laser-Driven-Light-Sources-below-300nm-Ozone-Mitigation.php (cit. on p. 73).

Zielcke, J. (2015). "Observations of reactive bromine, iodine and chlorine species in the Arctic and Antarctic with Differential Optical Absorption Spectroscopy". PhD thesis. Combined Faculties for Natural Sciences and for Mathematics of the Ruperto-Carola University of Heidelberg, Germany. DOI: 10.11588/heidok.00018932 (cit. on pp. 2, 32, 37, 39, 70, 119, 129, 169, 198, 206, 217, 218).

C
Lists

List of Figures

List of Tables

D
Additional Data

D.1 LP-DOAS instrument

D.1.1 System specifications

LP-DOAS System
Neumayer III

Light source		EQ-99X (2015)
Fibre bundle	sending bundle length	8.55 m
	receiving bundle length	7.55 m + 1 m
	sending fibre diameters	1x200 µm
	receiving fibre diameters	6x200 µm+1x800 µm
	treatment (spectrometer end)	5 µm coarse polished
Telescope	focal length	1.5 m
	mirror diameter	30 cm
	Numerical aperture	0.1
Light path	(one way)	1.55 km/(2.95 km)
Retroreflector	No. of 2 ” elements	24 (heated)/(32)
	target size (H x W)	60 x 40 cm/(140 x 80 cm)
Spectrometer	Model	Acton 300i
	Focal length	300 mm
	f-number	3.1
	Numerical aperture	0.12
	Optical slit	200 µm
	Grating	1200 gr.mm^{-1} / 600 gr.mm^{-1} holograph./300 nm blaze
	CCD	Andor DU440 BU
	Spectral resolution	0.54 nm/(0.95 nm)
	Spectral window	65 nm/140 nm

Table D.1: Overview of all components of the Neumayer III LP-DOAS system

D.1.2 Calculation of étendues

As stated in Eq. 4.4, the étendue is defined as:

$$G = n^2 A\Omega \tag{D.1}$$

where n is the refractive index of the medium the radiation is traversing, A the emitting/receiving surface, and Ω the solid angle the radiation is emitted to/received from.

For optical components there are several measures to describe the acceptance angle of radiation that can enter it. One is the numerical aperture NA:

$$NA = n\sin(\alpha) \tag{D.2}$$

Here, n is again the refractive index and α is half of the plane angle of acceptance. Another measure is the f-number that links the aperture D to the focal length f:

$$F/\# = \frac{D}{f} \tag{D.3}$$

The f-number is linked to the angle α by:

$$F/\# = \frac{1}{2 \cdot \tan(\alpha)} \tag{D.4}$$

The solid angle Ω and the half angle α are linked by:

$$\Omega = 2\pi \cdot (1 - \cos(\alpha)) \tag{D.5}$$

For the solid angle subtended by a lens or mirror with aperture/diameter D and object distance b, Ω is calculated by:

$$\Omega = 2\pi \cdot (1 - \cos(\arctan\left(\frac{D}{2 \cdot b}\right))) \tag{D.6}$$

For a given NA, Ω is calculated by:

$$\Omega = 2\pi \cdot (1 - \cos(\arcsin(N_\mathrm{A}))) \tag{D.7}$$

For a given f-number, Ω is calculated by:

$$\Omega = 2\pi \cdot (1 - \cos(\arctan\left(\frac{1}{2 \cdot F/\#}\right))) \tag{D.8}$$

For the calculation of the étendues in the light source (Fig. D.1), the FWHM dimensions of the light source (see Sec. 4.2.2) and the surface of an ellipse were used to calculated the relevant area A. For the lens with 25 mm focal length a free aperture of 24 mm was used.

The étendue of the spectrometer (Fig. D.3) can be influenced by the selection of the optical slit. In the fibre configuration chosen in this setup (with a 800 µm single fibre in front of the slit), the width of the slit determines the étendue of the spectrometer (the f-number is fixed).

The area of the circular fibre cross-section that is not blocked by the slit is calculated

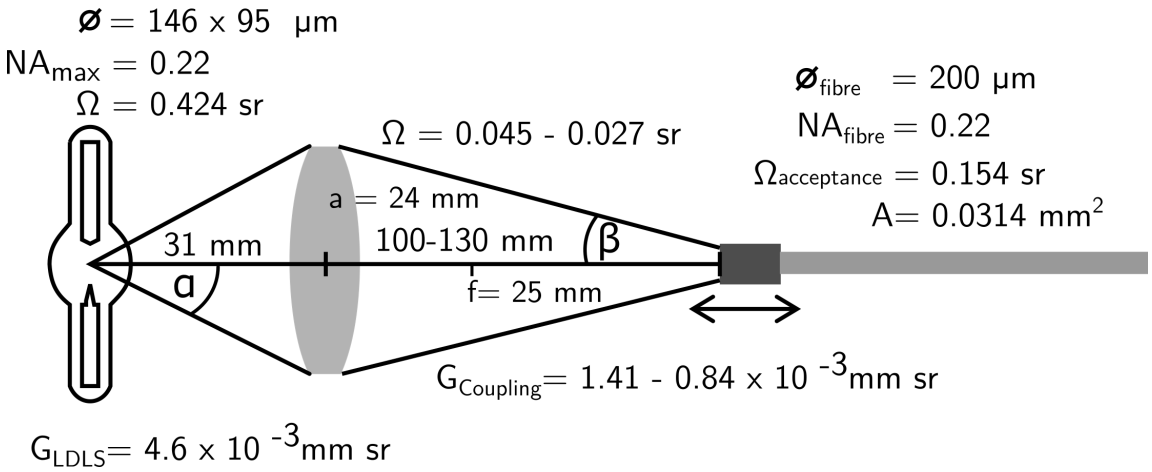

Figure D.1: Calculation of the étendues in the light source. For the étendue of the LDLS, the dimension of the plasma spot and the solid angle defined by free aperture a of the lens are considered. For the coupling into the fibre, the cross-section of the fibre and the solid angle defined by the free aperture of the lens are considered. The latter is the characteristic étendue (rather than the acceptance angle of the fibre defined by its numerical aperture of 0.22), because it is smaller. The distance of fibre end from the lens is determined by the distance from plasma spot to lens. The variation of this distance is the result of the chromatic aberration stray-light filter.

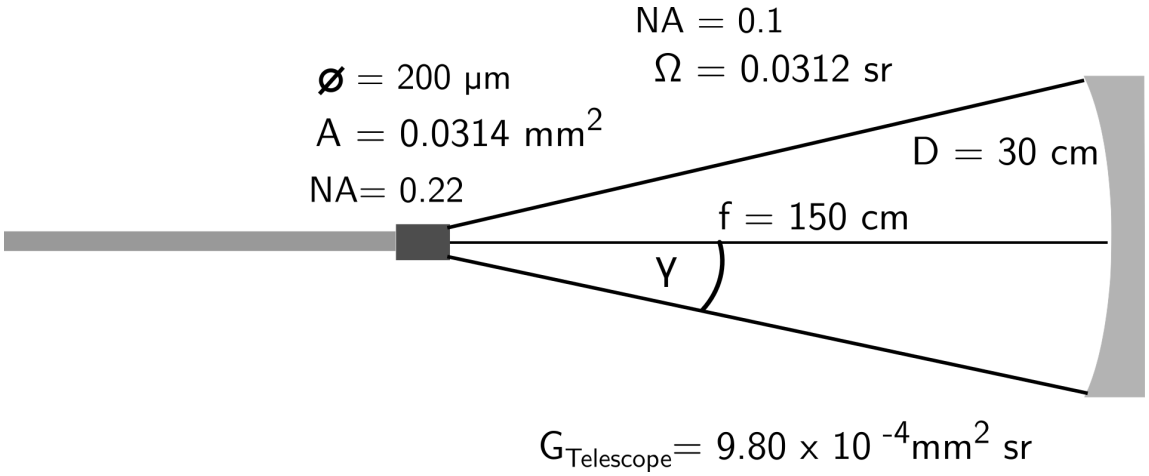

Figure D.2: Calculation of the étendue of the telescope. As the relevant emitting area, the cross-section of the central sending fibre was used. The solid angle is defined by the diameter D of the main mirror and its focal length f. The étendue of the receiving ring of fibres is larger than that of the sending fibre and light that misses the mirror when sending it out never reaches the reflectors. Therefore it is not relevant for radiant flux considerations.

by:

$$A = \pi \cdot r^2 \cdot \left(\frac{s \cdot \sqrt{(r^2 - (\frac{s}{2})^2)}}{\pi \cdot r^2} + 4 \cdot \frac{\arcsin\left(\frac{s}{2r}\right)}{2\pi} \right) \tag{D.9}$$

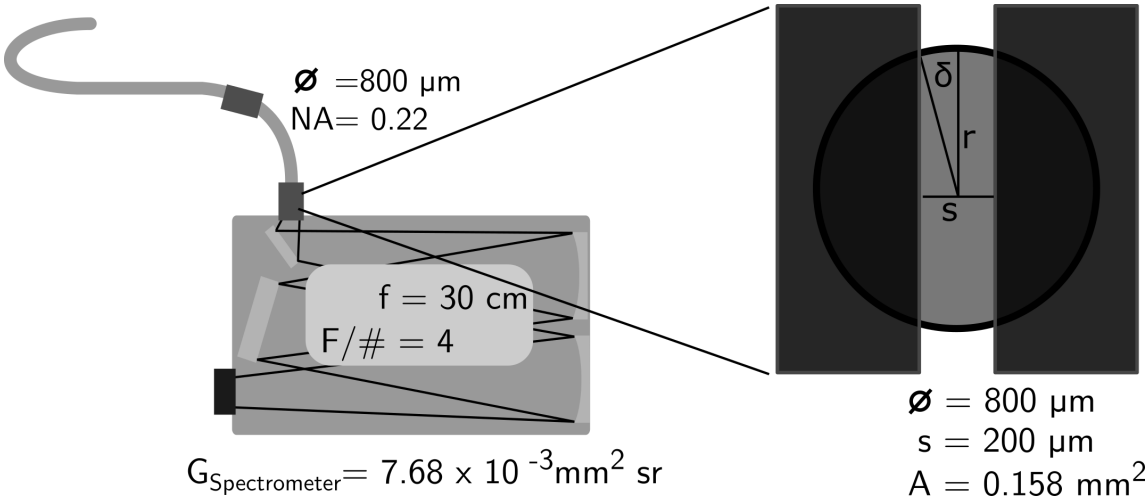

Figure D.3: Calculation of the étendue of the spectrometer. The f-number of the Acton 300i is indicated in Acton (1996). The free surface of the single fibre can be calculated using Eq. D.9.

D.1.3 Overview of references

Molecule/spectral component	Reference	Temp. [K]	Spec. cov. [nm]	Res. [nm]
BrO	Wilmouth et al. (1999)	298	285-386	0.07*
	Fleischmann et al. (2004)	243	300-385	0.04*
ClO	S. P. Sander and Friedl (1989)	298	244-317	0.07*
H_2O	(Rothman et al., 2010; Lampel et al., 2015b)	293	300-800	calculated
HCHO	Meller and Moortgat (2000)	298	224-376	0.04*
HONO	Stutz et al. (2000)	298	291-404	0.08
I_2	Spietz et al. (2006)	298	543-578	0.25
IO	Spietz et al. (2005)	298	408-474	0.07*
NO_2	Voigt et al. (2002)	246	436-800	0.01*
NO_3	Yokelson et al. (1994)	240	440-694	0.10
O_3	Burrows et al. (1999)	241	230-794	0.2
	Serdyuchenko et al. (2014)	263	213-1100	0.04*
O_4	Thalman and Volkamer (2013)	253	335-596	0.3
OBrO	Fleischmann and Burrows (2002)	298	384-616	0.05*
OClO	Wahner et al. (1987)	298	242-476	0.07*
OIO	Spietz et al. (2006)	298	532-568	36
SO2	Bogumil et al. (2003)	243	239-395	0.21
Atmospheric BG Short-cut BG	measured			
SC spectrum BG spectrum	measured			
Reciprocal lamp spectrum	calculated from measurement			
Atmospheric night-time spectrum	measured			

Table D.2: Overview of chosen literature cross-sections and other spectral components used in the DOAS fit. Cross-section files were retrieved from the MPI-Mainz UV/Vis spectral atlas (Keller-Rudek et al., 2013) and web-links therein. (*) These cross-sections were recorded with Fourier-transform spectrometers. Therefore the resolution in wavelengths varies; representative values were chosen.

D.1.4 Example reference spectra

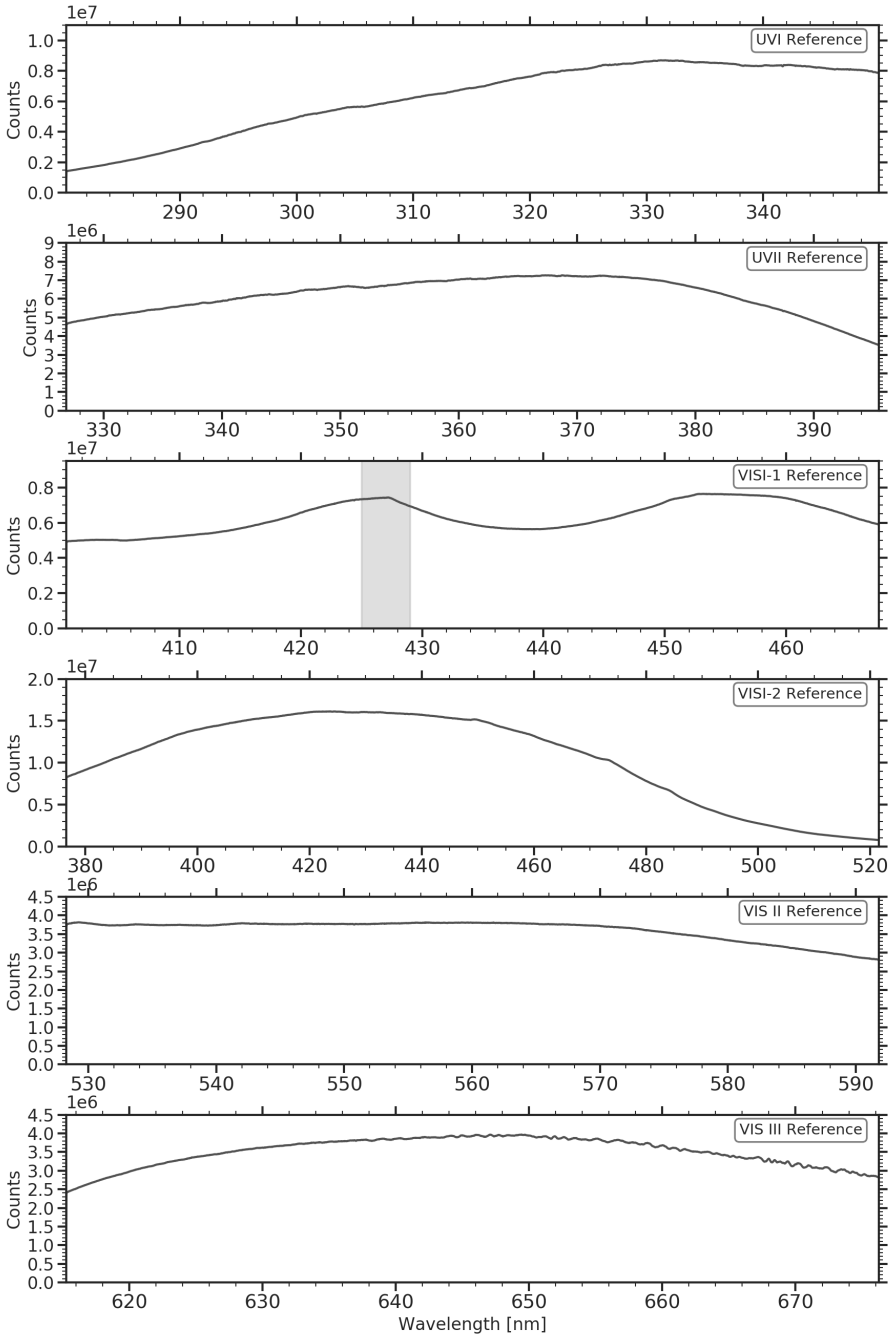

Figure D.4: Example reference spectra for spectral windows. For the VISI spectral window, spectra for both of the gratings used during the observations are shown.

D.1.5 Example fits

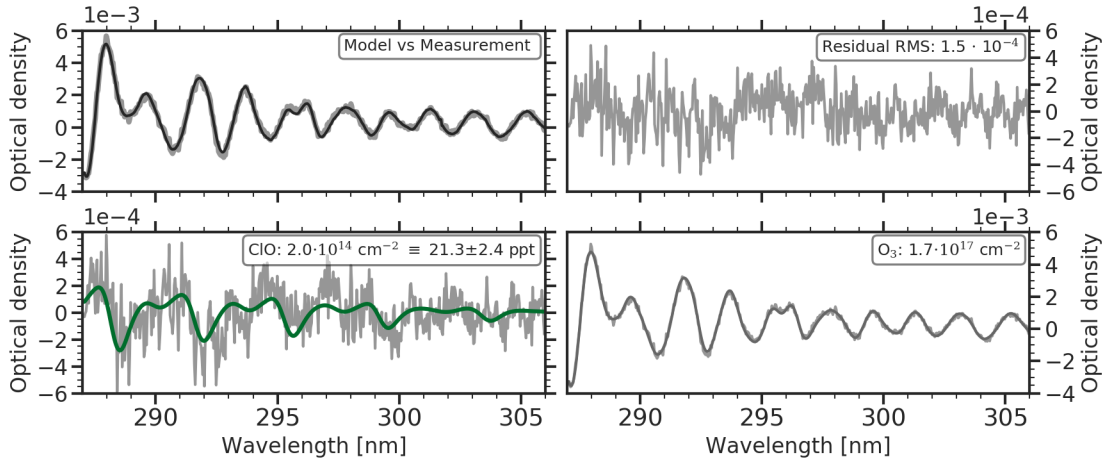

Figure D.5: Example fit for ClO on March 16th, 2016 16:08 UTC. Fit components with negligible contributions not plotted: BrO, HCHO, NO_2, OClO, SO_2, SC, BG

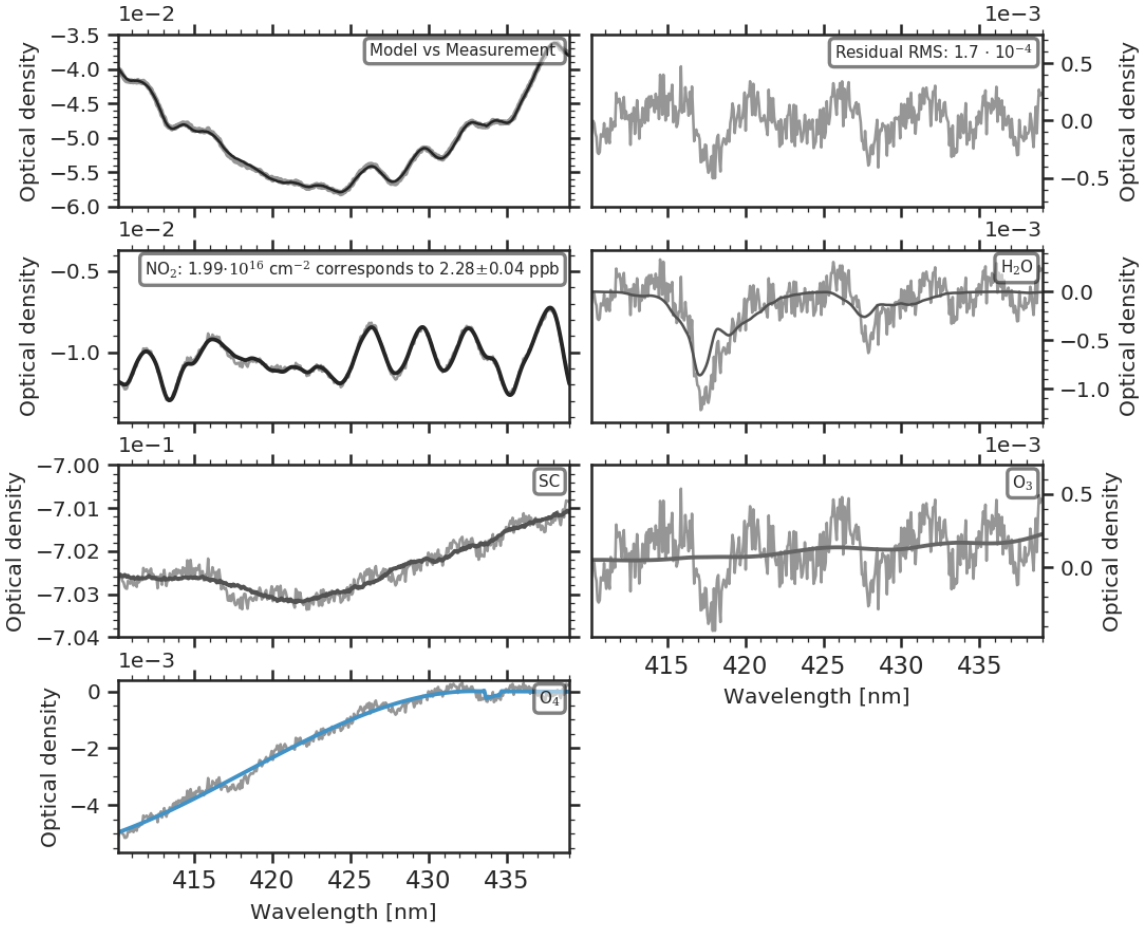

Figure D.6: Example fit for NO_2 evaluated in the VISI-1 fit scenario with the new 600 gr. mm^{-1} grating. Fit components with negligible contributions not plotted: IO, Glyoxal, BG

D.1.6 Fit statistics

UVI-1

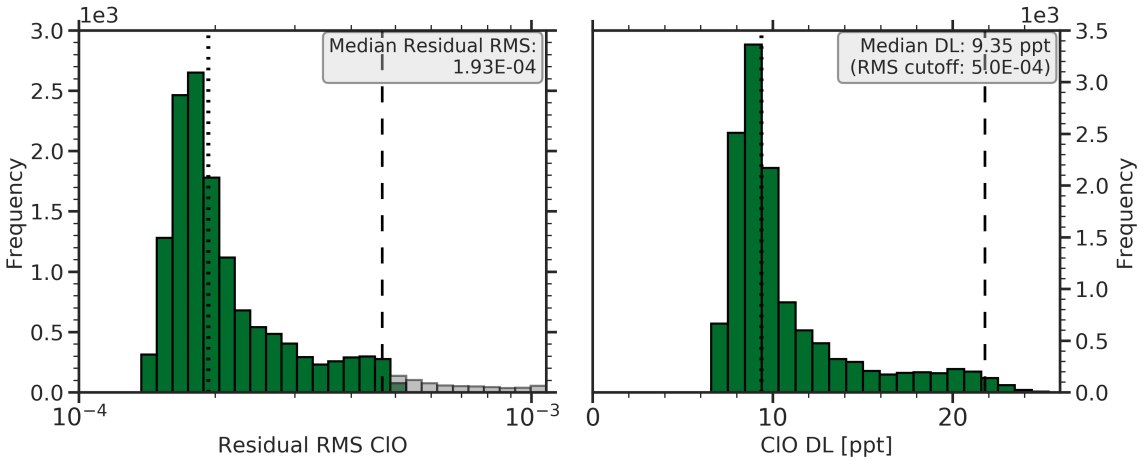

Figure D.7: Residual and detection limit statistics for ClO evaluated in the UVI-1 fit scenarios. Dotted vertical lines indicate the respective median. Dashed lines mark the 9th quantile. The residual RMS of excluded fits is marked in light grey.

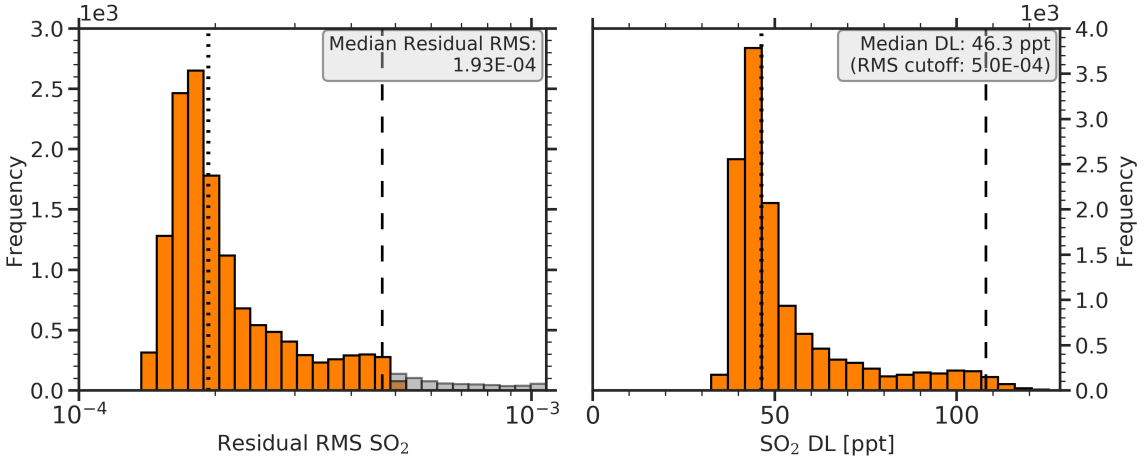

Figure D.8: Residual and detection limit statistics for SO_2 evaluated in the UVI-1 fit scenario. Dotted vertical lines indicate the respective median. Dashed lines mark the 9th quantile of the distributions. The residual RMS of excluded fits is marked in light grey.

UVI-2

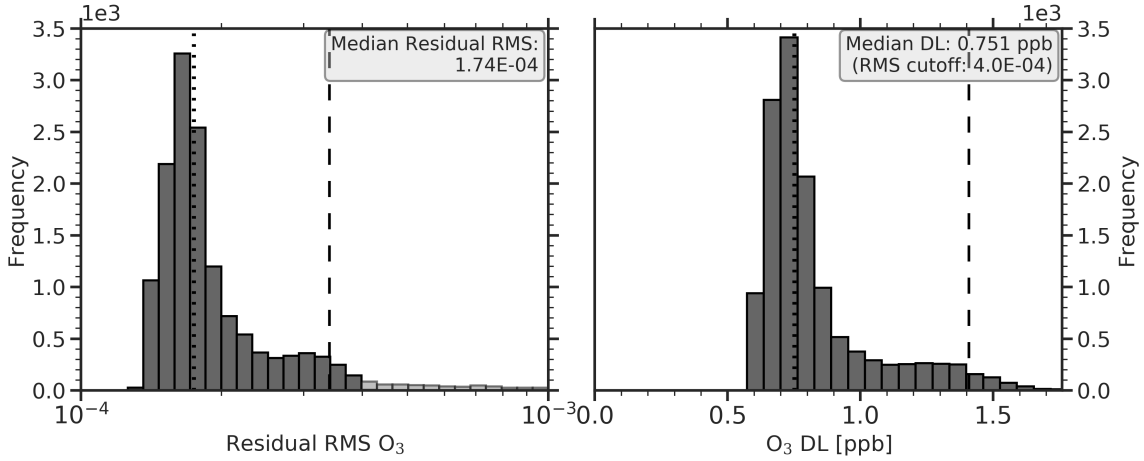

Figure D.9: Residual and detection limit statistics for O_3 evaluated in the UVI-2 fit scenarios. Dotted vertical lines indicate the respective median. Dashed lines mark the 9th quantile of the distributions. The residual RMS of excluded fits is marked in light grey.

UVI-3

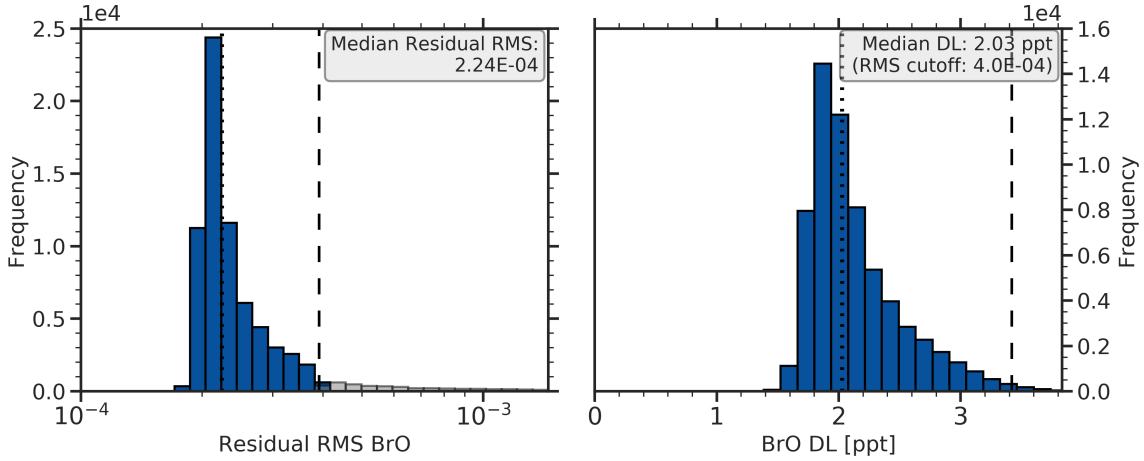

Figure D.10: Residual and detection limit statistics for BrO evaluated in the UVI-3 fit scenarios. Dotted vertical lines indicate the respective median. Dashed lines mark the 9th quantile of the distributions. The residual RMS of excluded fits is marked in light grey.

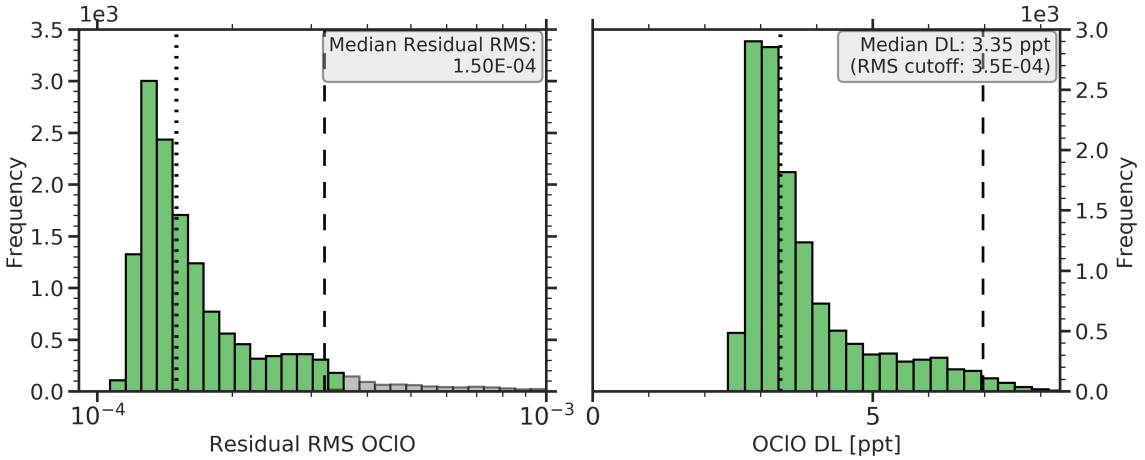

Figure D.11: Residual and detection limit statistics for OClO evaluated in the UVI-3 fit scenarios. Dotted vertical lines indicate the respective median. Dashed lines mark the 9th quantile of the distributions. The residual RMS of excluded fits is marked in light grey.

UVII-1

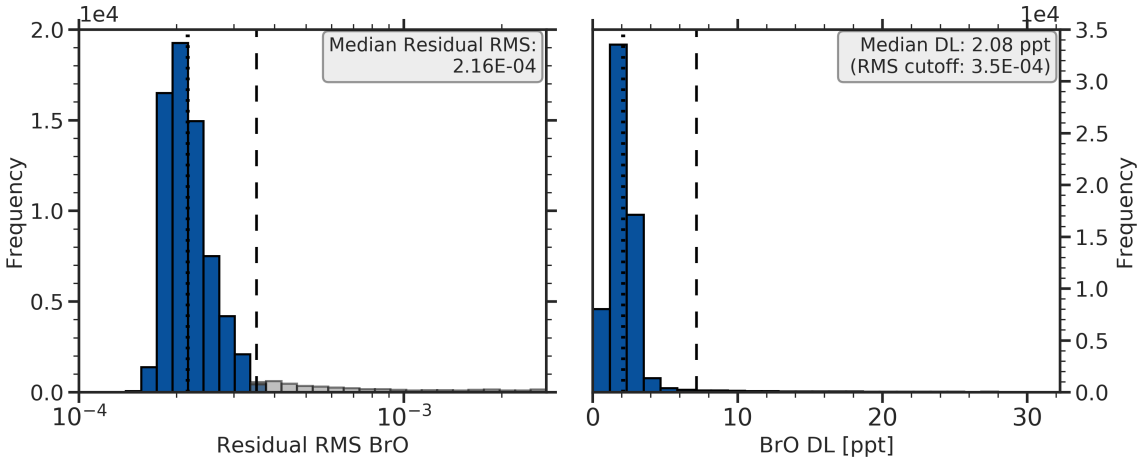

Figure D.12: Residual and detection limit statistics for BrO evaluated in the UVII-2 fit scenario. Dotted vertical lines indicate the respective median. Dashed lines mark the 9th quantile of the distributions.The residual RMS of excluded fits is marked in light grey.

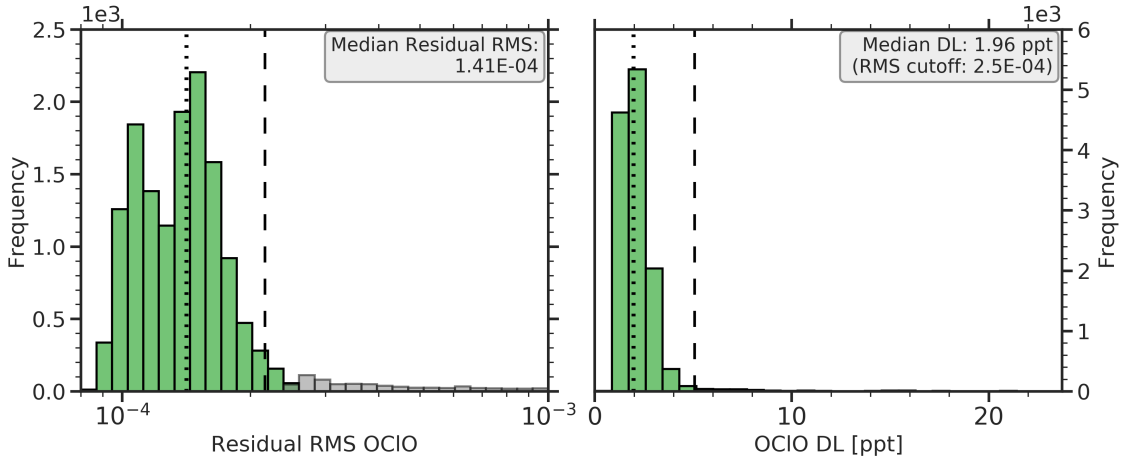

Figure D.13: Residual and detection limit statistics for HONO evaluated in the UVII-2 fit scenario. Dotted vertical lines indicate the respective median. Dashed lines mark the 9th quantile of the distributions. The residual RMS of excluded fits is marked in light grey.

UVII-2

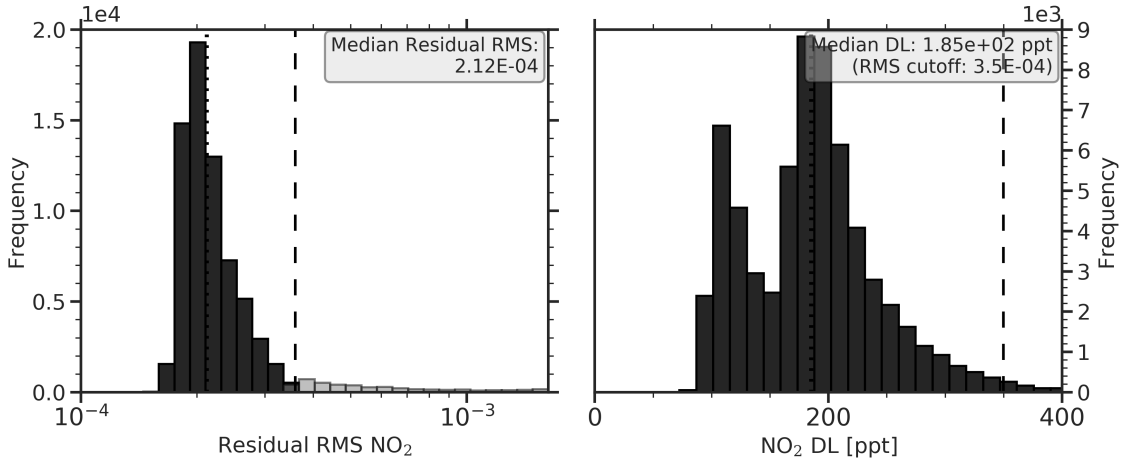

Figure D.14: Residual and detection limit statistics for NO_2 evaluated in the UVII-2 fit scenario. Dotted vertical lines indicate the respective median. Dashed lines mark the 9th quantile of the distributions. The residual RMS of excluded fits is marked in light grey.

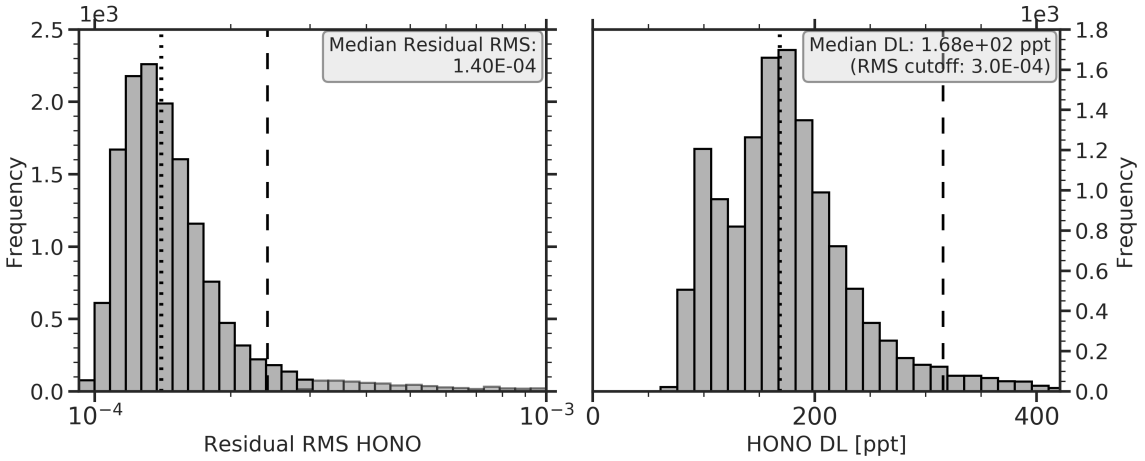

Figure D.15: Residual and detection limit statistics for HONO evaluated in the UVII-2 fit scenario. Dotted vertical lines indicate the respective median. Dashed lines mark the 9th quantile of the distributions. The residual RMS of excluded fits is marked in light grey.

VISI-1

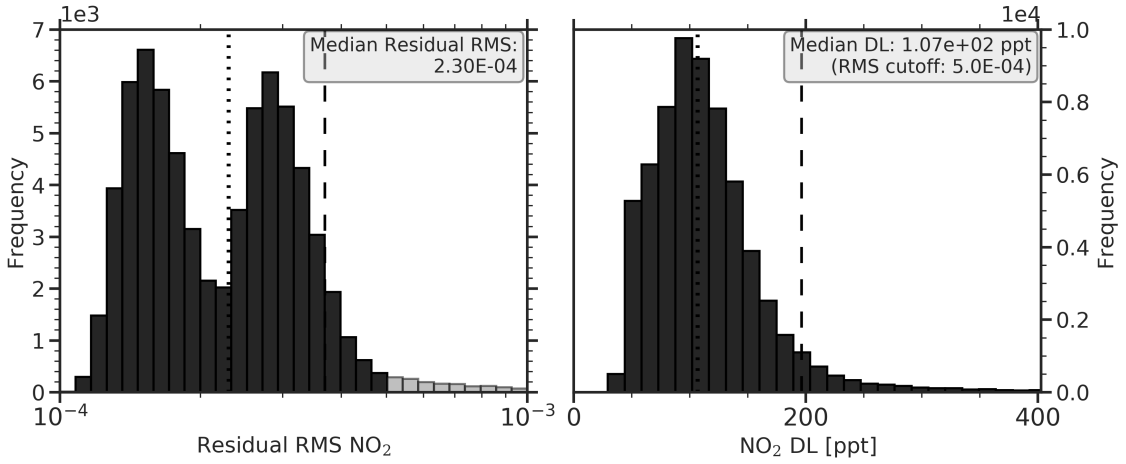

Figure D.16: Residual and detection limit statistics for NO_2 evaluated in the VISI-1 fit scenarios. Dotted vertical lines indicate the respective median. Dashed lines mark the 9th quantile of the distributions. The residual RMS of excluded fits is marked in light grey.

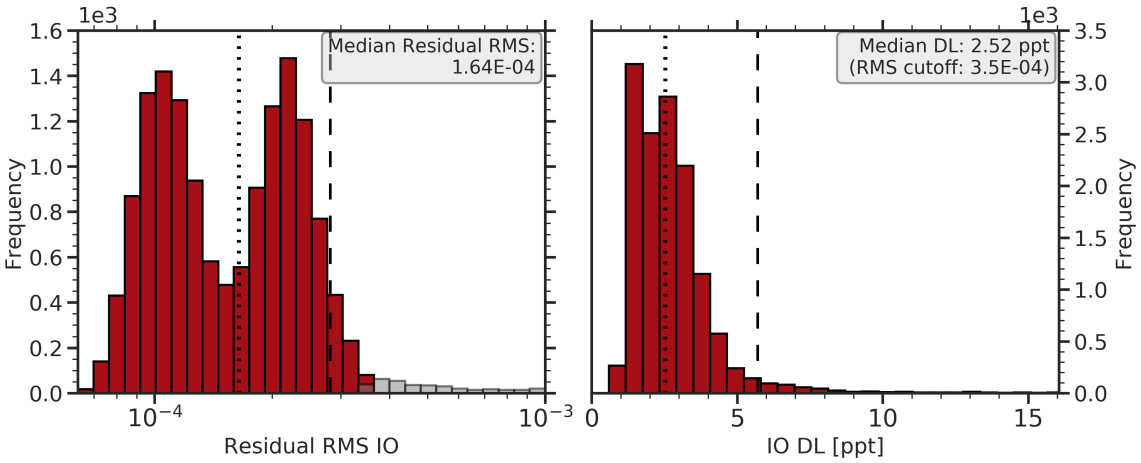

Figure D.17: Residual and detection limit statistics for IO evaluated in the VISI-1 fit scenarios. Dotted vertical lines indicate the respective median. Dashed lines mark the 9$^{\text{th}}$ quantile of the distributions. The residual RMS of excluded fits is marked in light grey.

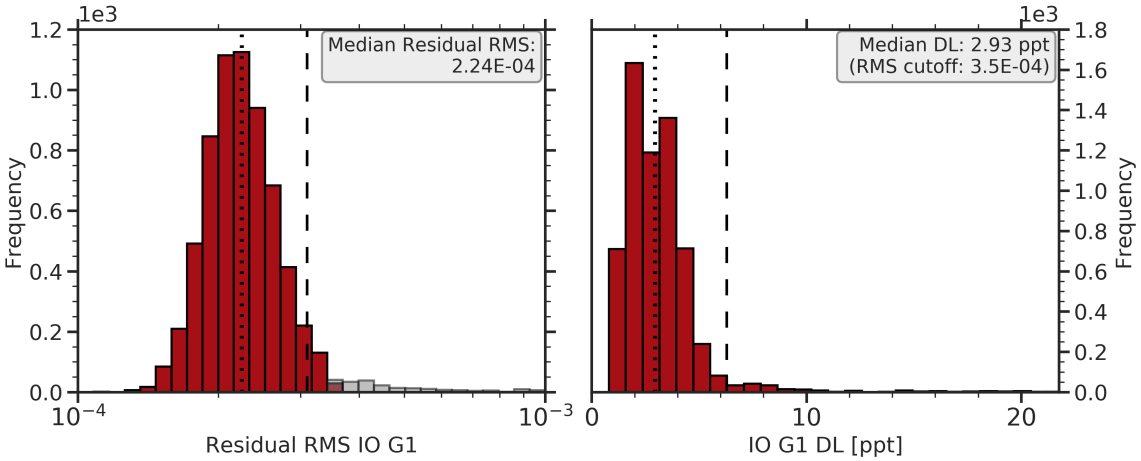

Figure D.18: Residual and detection limit statistics for IO evaluated in the VISI-1 fit scenarios measured with grating G1 (1200 gr. mm^{-1}) until February 15$^{\text{th}}$ 2017. Dotted vertical lines indicate the respective median. Dashed lines mark the 9$^{\text{th}}$ quantile of the distributions. The residual RMS of excluded fits is marked in light grey.

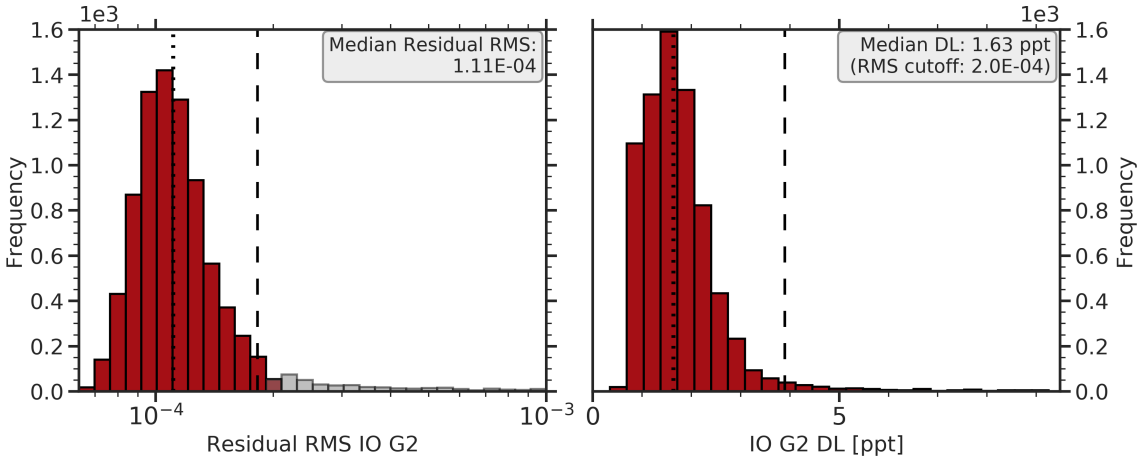

Figure D.19: Residual and detection limit statistics for IO evaluated in the VISI-1 fit scenarios measured with grating G2 (600 gr. mm^{-1}) from February 15$^{\text{th}}$ 2017 onwards. Dotted vertical lines indicate the respective median. Dashed lines mark the 9$^{\text{th}}$ quantile of the distributions. The residual RMS of excluded fits is marked in light grey.

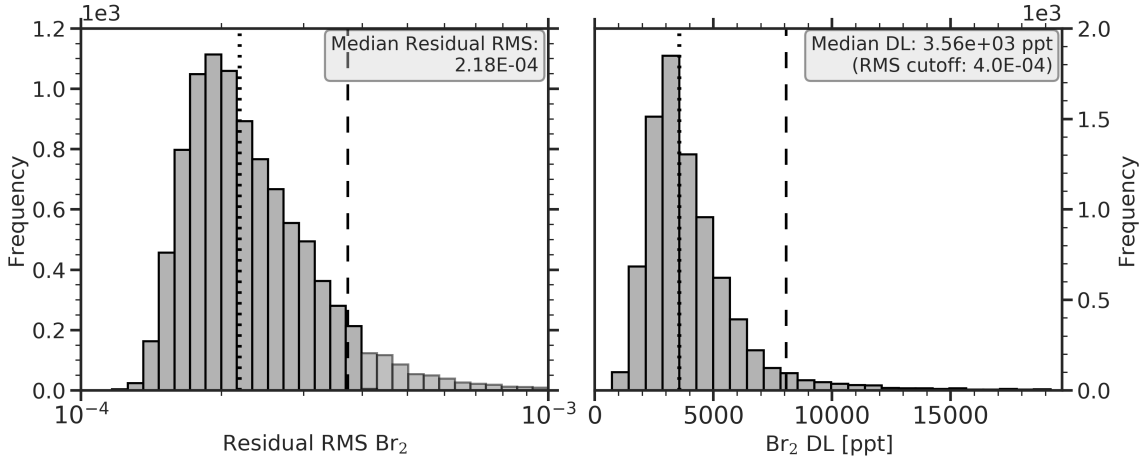

Figure D.20: Residual and detection limit statistics for Br_2 evaluated in the VISII-1 fit scenario. Dotted vertical lines indicate the respective median. Dashed lines mark the 9th quantile of the distributions. The residual RMS of excluded fits is marked in light grey.

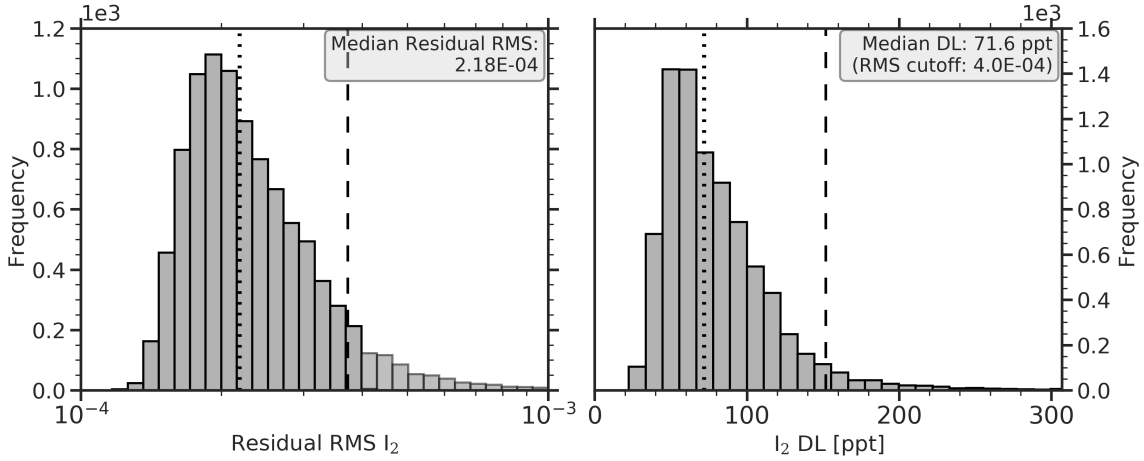

Figure D.21: Residual and detection limit statistics for I_2 evaluated in the VISII-1 fit scenario. Dotted vertical lines indicate the respective median. Dashed lines mark the 9th quantile of the distributions. The residual RMS of excluded fits is marked in light grey.

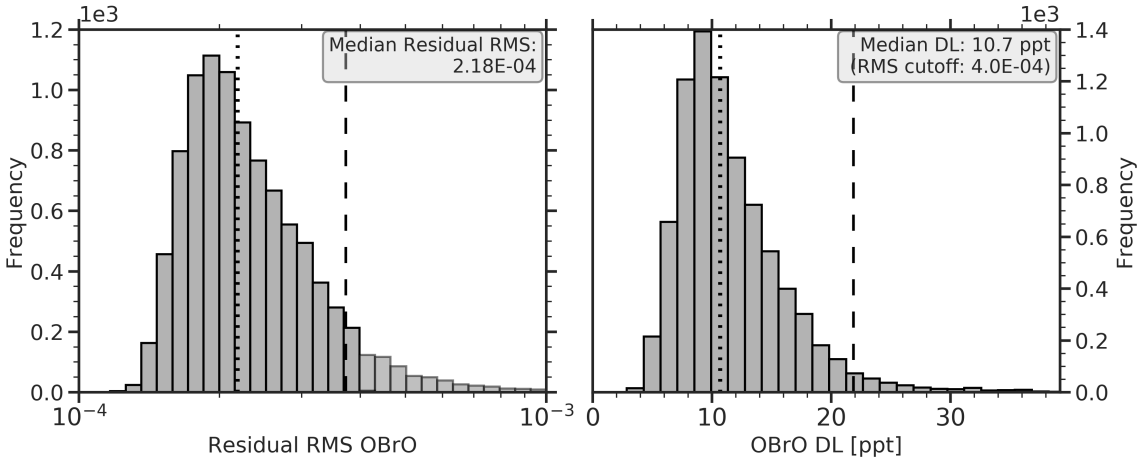

Figure D.22: Residual and detection limit statistics for OBrO evaluated in the VISII-1 fit scenario. Dotted vertical lines indicate the respective median. Dashed lines mark the 9th quantile of the distributions. The residual RMS of excluded fits is marked in light grey.

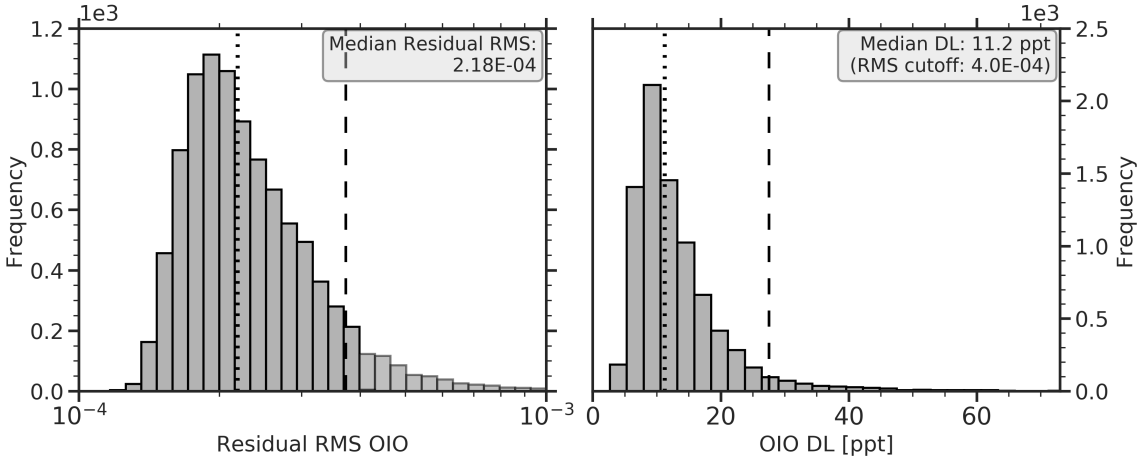

Figure D.23: Residual and detection limit statistics for OIO evaluated in the VISII-1 fit scenario. Dotted vertical lines indicate the respective median. Dashed lines mark the 9th quantile of the distributions. The residual RMS of excluded fits is marked in light grey.

VISIII-1

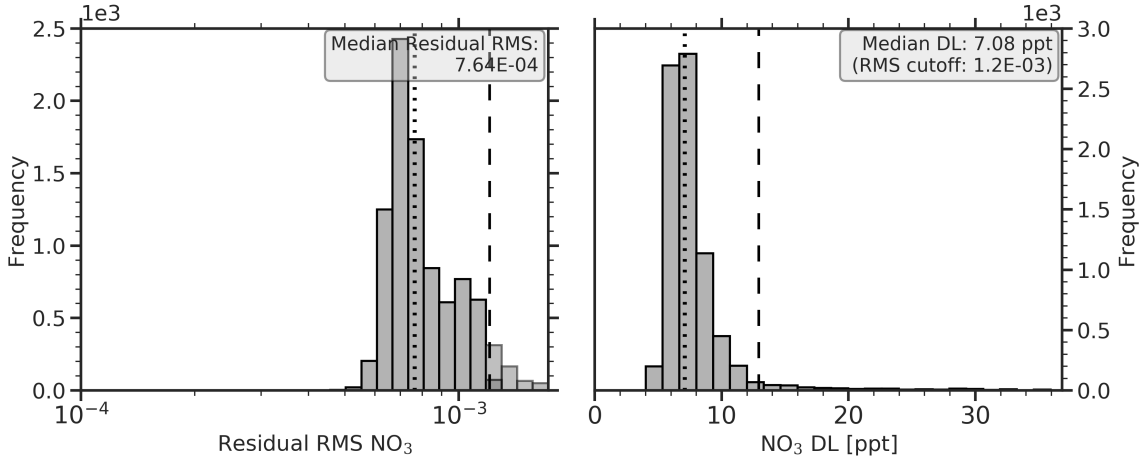

Figure D.24: Residual and detection limit statistics for NO_3 evaluated in the VISIII-1 fit scenarios. Dotted vertical lines indicate the respective median. Dashed lines mark the 9^{th} quantile of the distributions. The residual RMS of excluded fits is marked in light grey.

D.1.7 Temporal coverage of observations by year

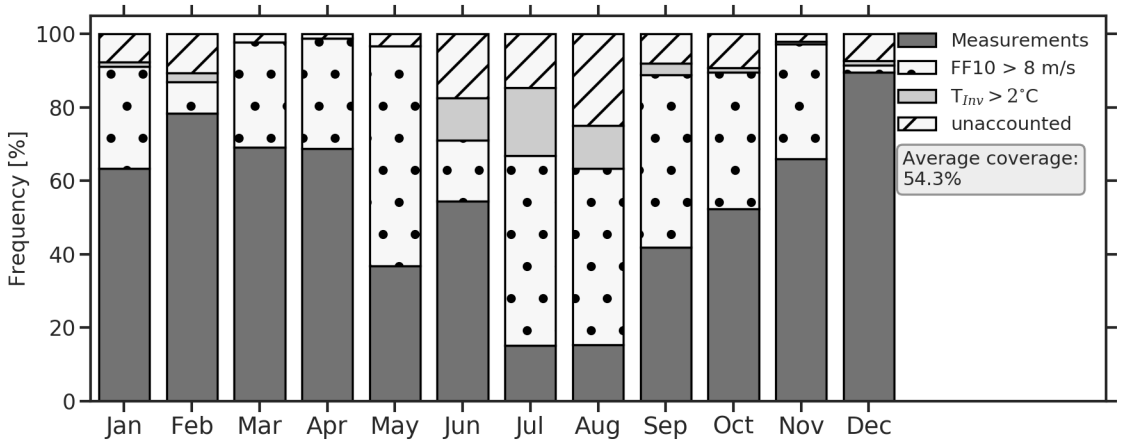

Figure D.25: Temporal coverage of the LP-DOAS measurements in 2016. Percentages are calculated on an hourly basis. For times with no measurements, periods that potentially could have been influenced by blowing snow or strong optical scintillation were marked. However, this does not exclude the possibility that technical problems occurred during these times.

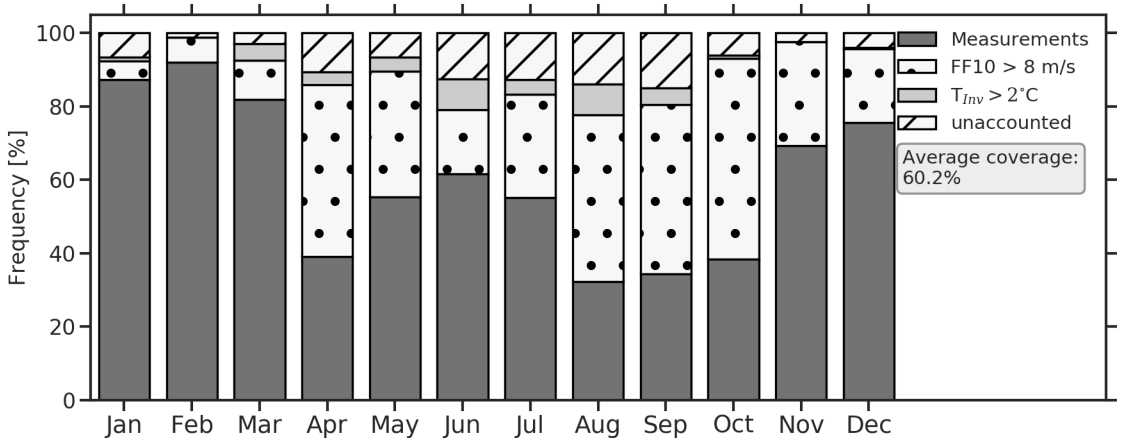

Figure D.26: Temporal coverage of the LP-DOAS measurement in 2017. Percentages are calculated on an hourly basis. For times with no measurements, periods that potentially could have been influenced by blowing snow or strong optical scintillation were marked. However, this does not exclude the possibility that technical problems occurred during these times.

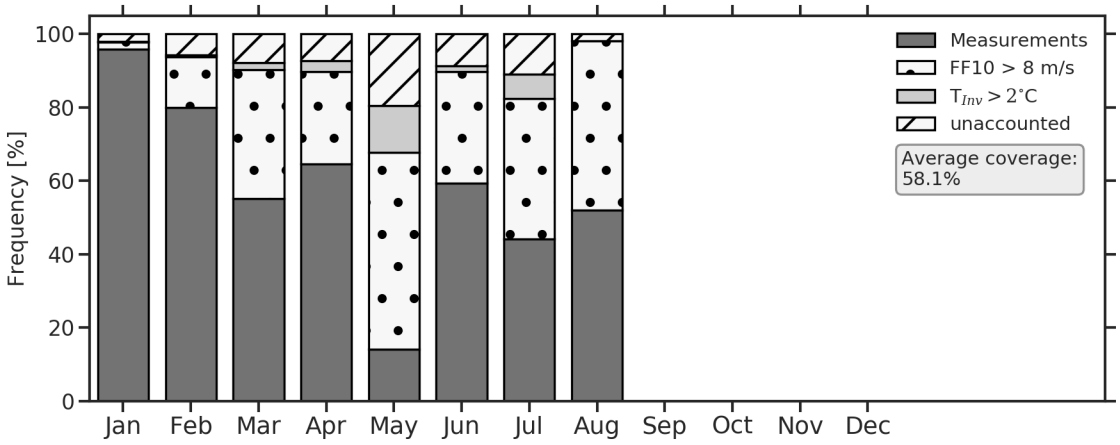

Figure D.27: Temporal coverage of the LP-DOAS measurements in 2018. Percentages are calculated on an hourly basis. For times with no measurements, periods that potentially could have been influenced by blowing snow or strong optical scintillation were marked. However, this does not exclude the possibility that technical problems occurred during these times.

D.2 Additional data

D.2.1 Wind data entire observation period

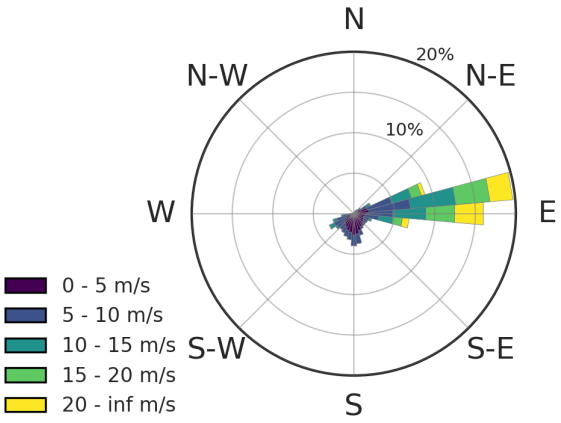

Figure D.28: Wind conditions during the entire measurement period (10 min averages).

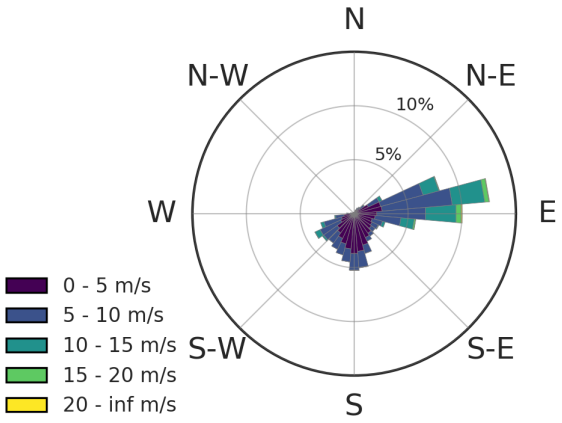

Figure D.29: Wind conditions when the LP-DOAS instrument recorded during the entire measurement period (10 min averages).

D.2.2 Ozone annual cycles

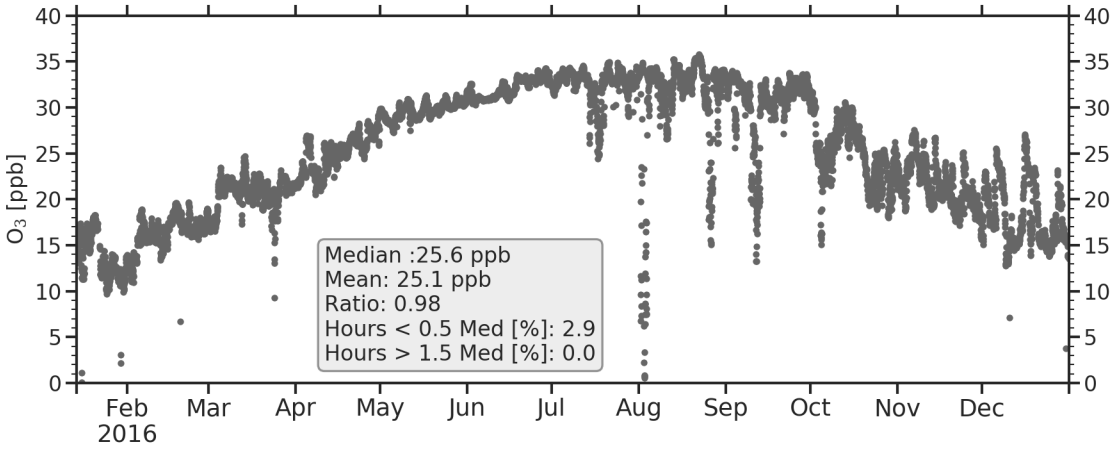

Figure D.30: Annual cycle of hourly surface ozone mixing ratios at Neumayer III in 2016 as measured by the UV absorption spectroscopy instrument (see 4.1.3) in the trace gas observatory. Statistics was calculated as in Helmig et al. (2007).

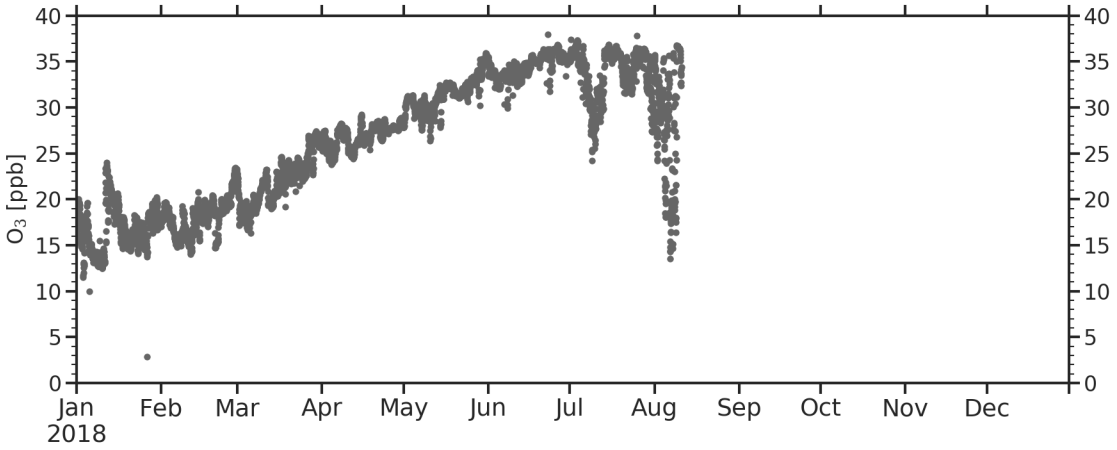

Figure D.31: Annual cycle of hourly surface ozone mixing ratios at Neumayer III in 2018 (for the part of the year that is considered in this thesis) as measured by the UV absorption spectroscopy instrument (see 4.1.3) in the trace gas observatory.

D.2.3 SO_2 observations at NMIII from filter and LP-DOAS measurements

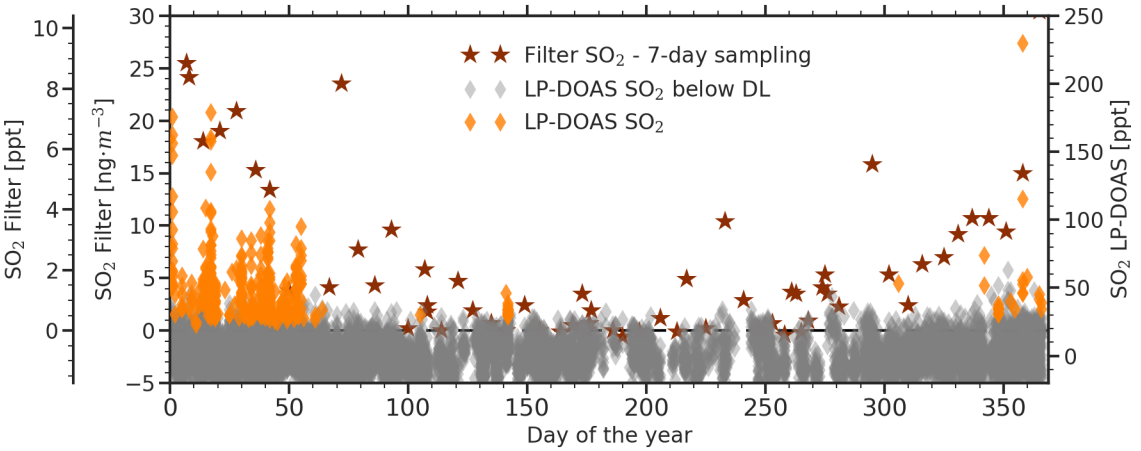

Figure D.32: Comparison of SO_2 observations from filter and LP-DOAS measurements. No specifics on the exact measurement technique used could be obtained in addition to the data set. For the conversion of the filter measurements to ppt, a temperature of 263 K and an atmospheric pressure of 985 hPa was used.

D.2.4 Histogram of hourly averages of IO mixing ratios for entire data set

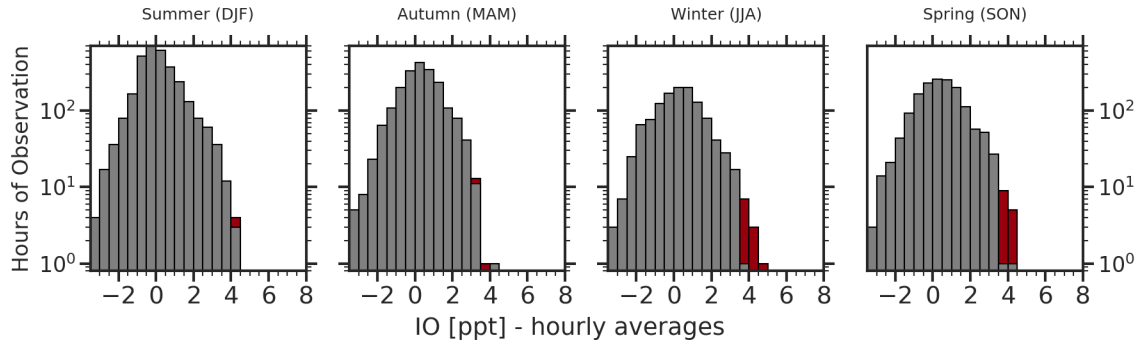

Figure D.33: Seasonal histograms of IO mixing ratios for the entire data set including first year of operation before the change of gratings.

D.2.5 Additional case studies

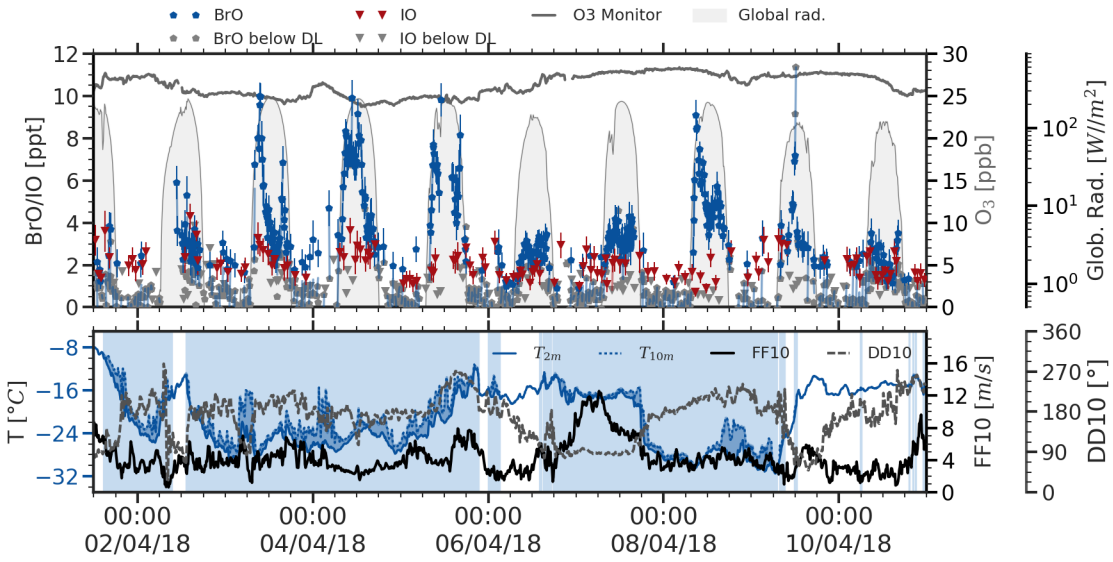

Figure D.34: Example period with elevated BrO and IO mixing ratios from April 2018.

E

Sketches and pictures of Neumayer LP-DOAS instrument

E.1 Laser driven light source

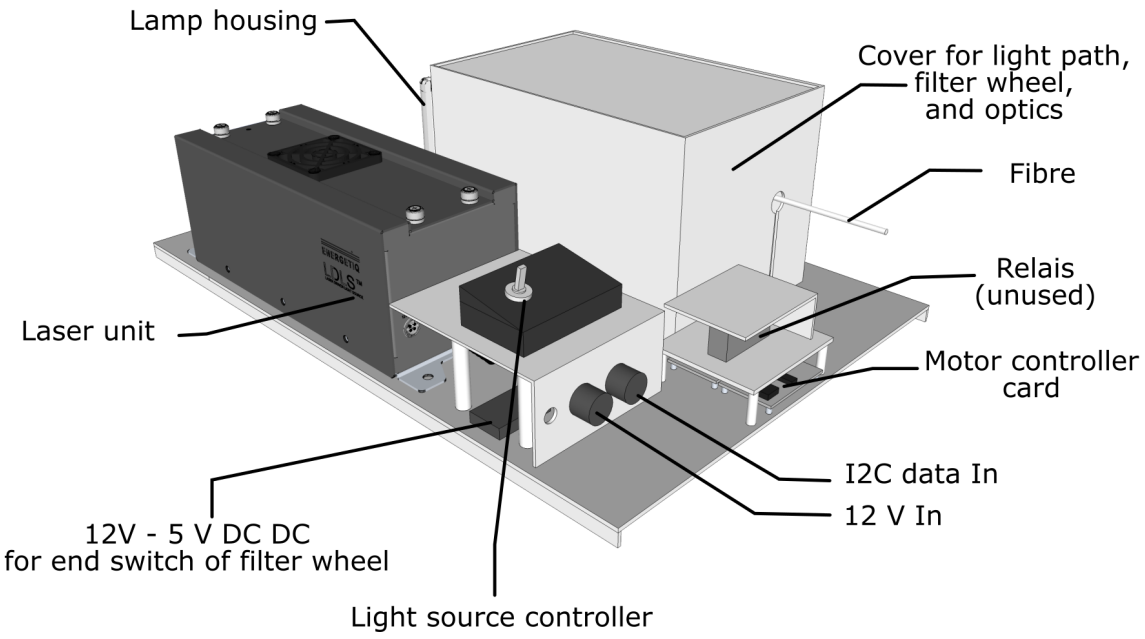

Figure E.1: Sketch of LDLS setup with covered light path and optics. The cover reduces stray-light, in particular when the light source is shut off for background spectra recording. Furthermore it protects surroundings from UV radiation from light source.

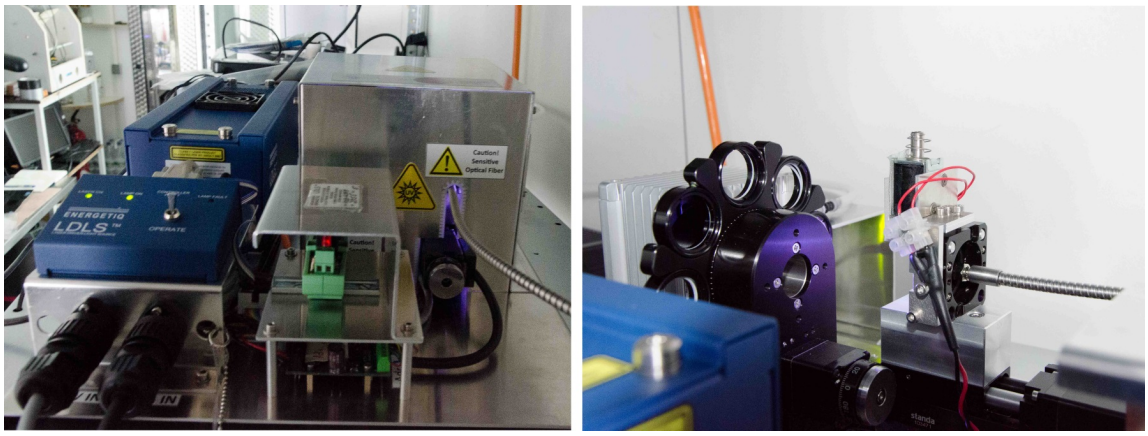

Figure E.2: Photos of LDLS setup with covered optics (left) and detail of filter wheel and shutter mechanism (right).

E.2 Optical fibre bundle

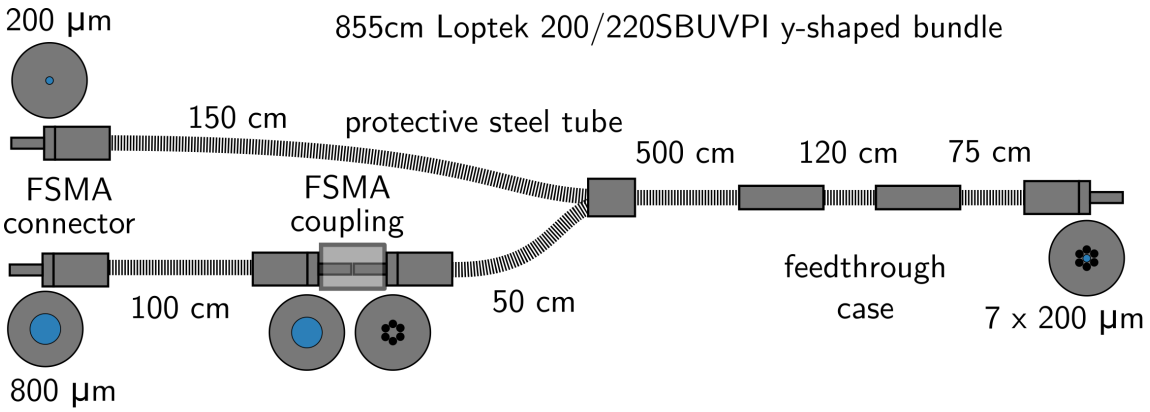

Figure E.3: Fibre bundle assembly for operation of LP-DOAS on the trace gas observatory. The two feedthrough cases are adapted for entering the telescope from the front and the back.

E.3 Telescope

Figure E.4: Telescope and rotary disc on custom made pallet. The front window is further protected by a metal plate.

Figure E.5: Example picture from telescope's webcams. The left shows the wide field of view camera and the right the zoom webcam with a signal coming back from the Atka retro-reflector array (little bright spot).

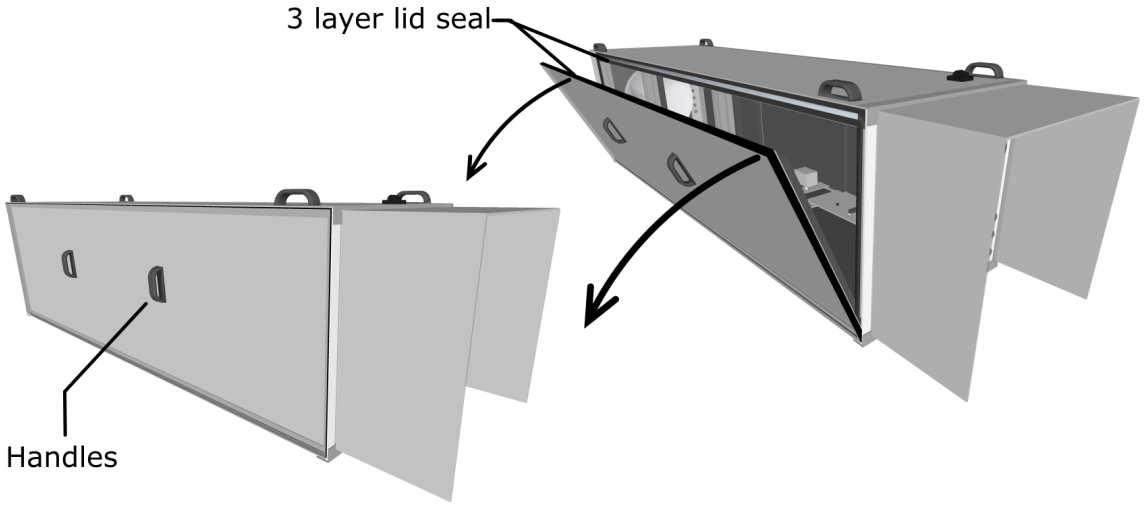

Figure E.6: Sketch of the telescope's side panel that can be removed for maintenance. The panel has three layers of sponge rubber seals to prevent drifting snow from entering. It is screwed to the main body when the telescope is closed.

Figure E.7: Pictures of the telescope set up on the roof of the trace gas observatory container.

Figure E.8: Pictures of telescope on the trace gas observatory container(left and centre) and other components on a heavy duty shelf inside the trace gas observatory.

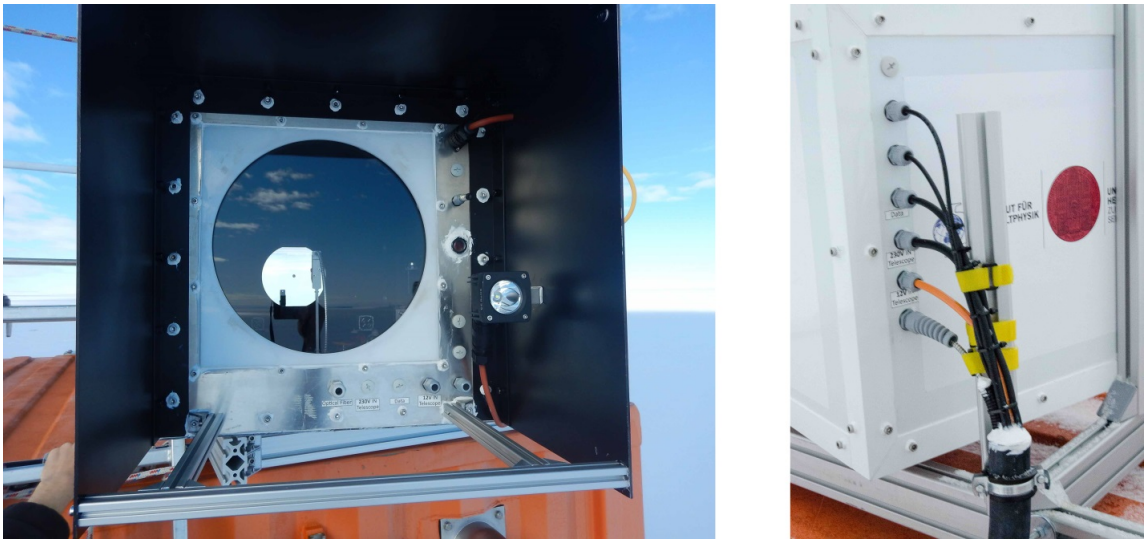

Figure E.9: Pictures of telescope's front (left) and back (right). Power supply, fibre, and data cables can be introduced from the front or backside into the telescope.

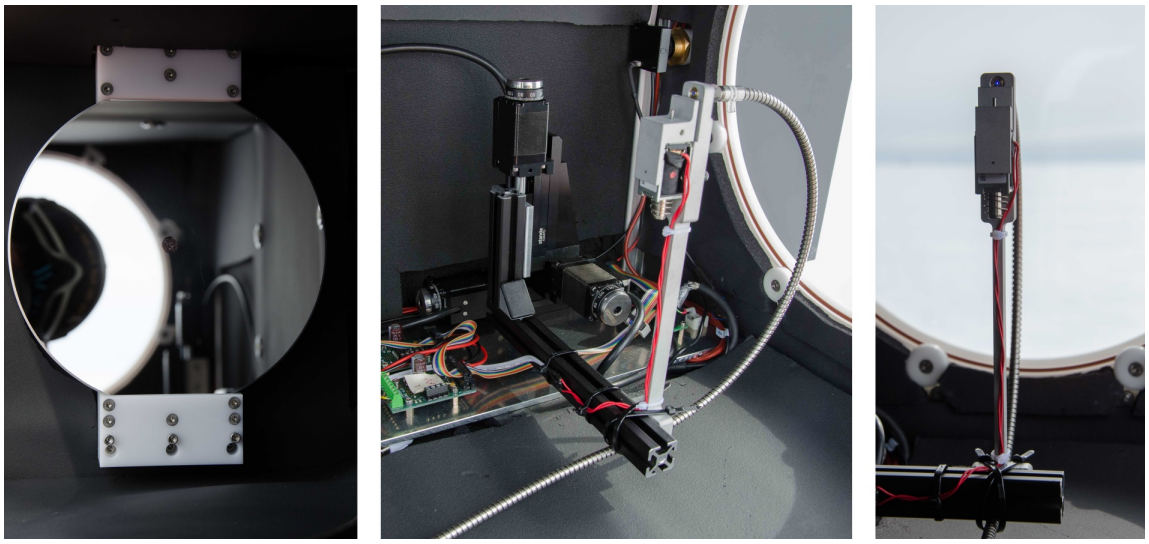

Figure E.10: Pictures of mirror (left), stepper motors (centre), and fibre arm with fibre and short cut (right) inside the telescope.

E.4 Retro-reflector arrays

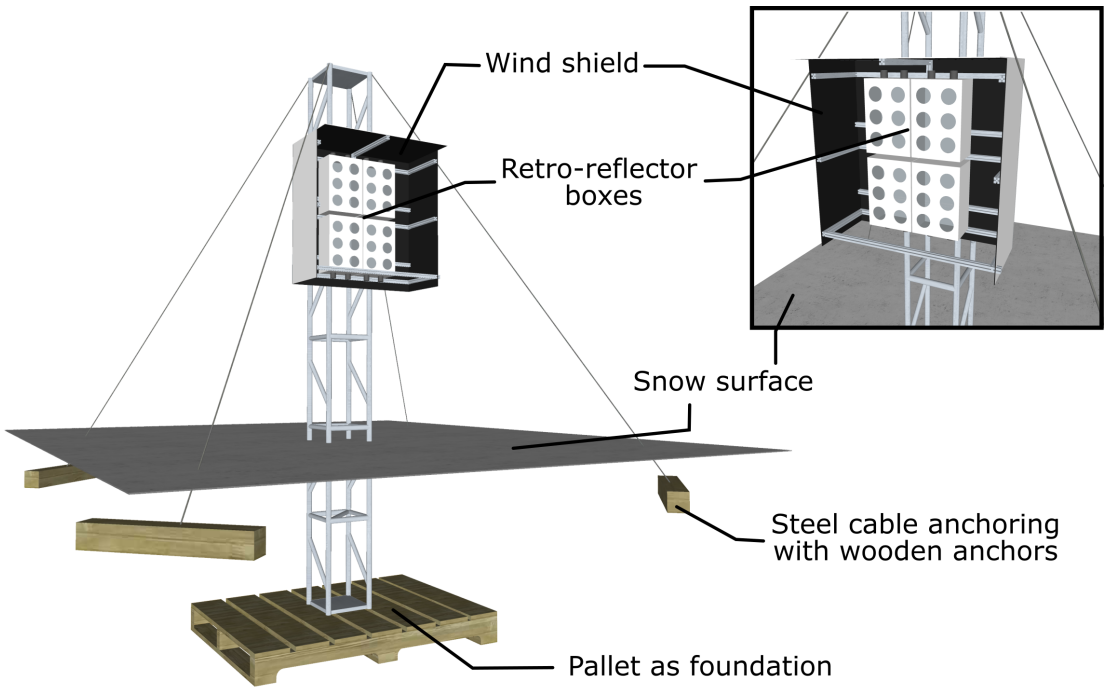

Figure E.11: Sketch of the mast that holds the retro-reflector array. The mast is set on a pallet that is buried in the snow in approximately 1 m depth during the setup. It is then anchored with steel ropes attached to scantlings that are buried as well. When the anchors are frozen in, the mast is secured by the steel cables. The wind shield prevents snow from depositing on the reflector boxes during storms.

E.5 Spectrometer box

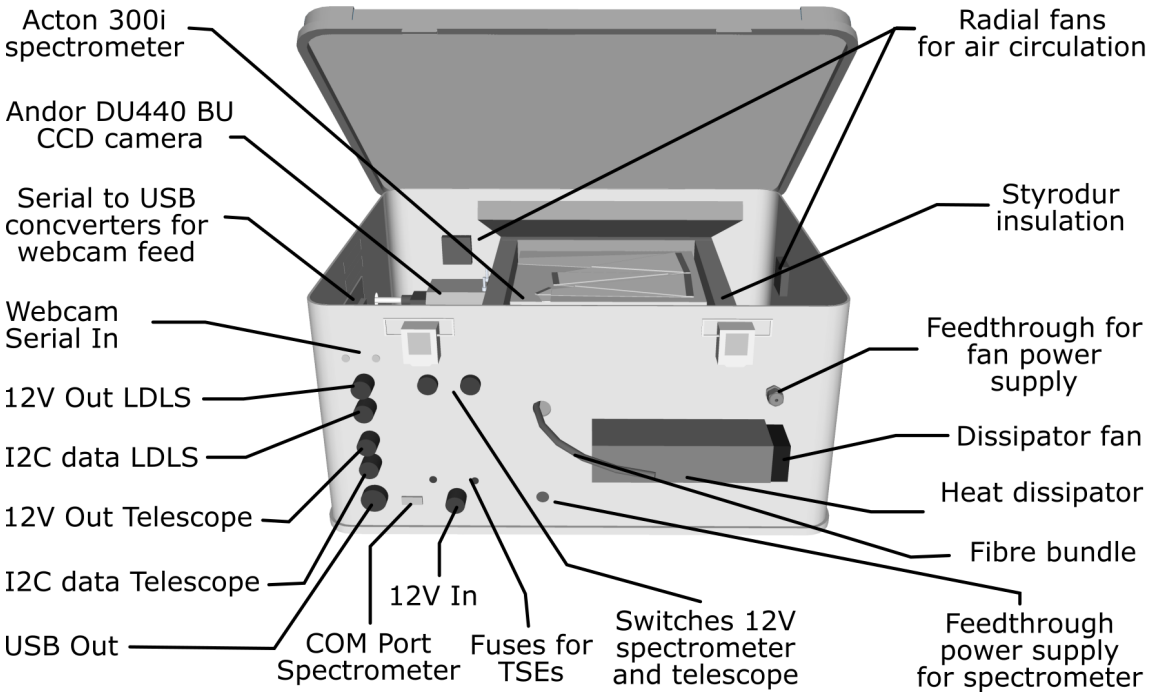

Figure E.12: Sketch of the front side of the spectrometer box with all connector for instrument periphery. During operation the insulation and the lid of the Zarges box are closed.

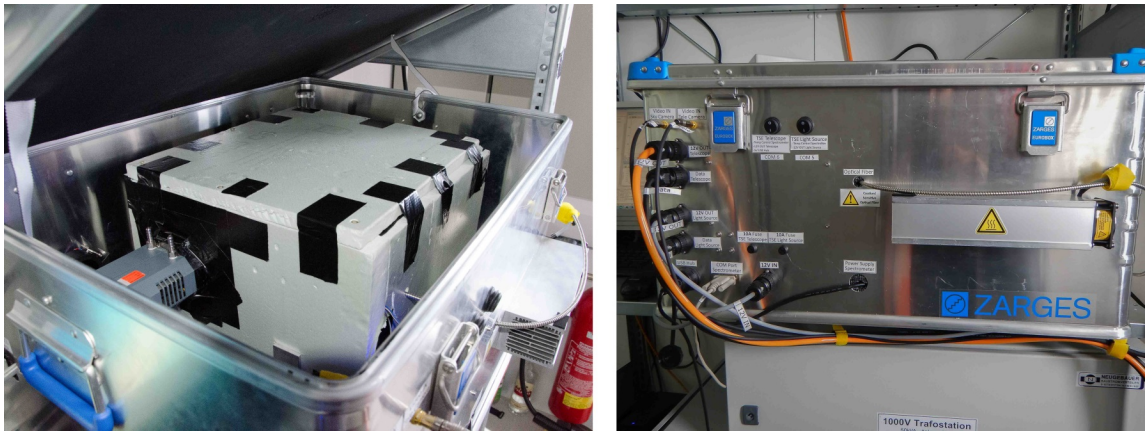

Figure E.13: Pictures of spectrometer inside the spectrometer box (left) and the front side of the spectrometer box. During operation the lid of the Zarges box is closed.

Glossary

AMAP Artic Monitoring and Assessment Program. 5

AMDE Atmospheric Mercury Depletion Event. 44

CCD Charge-Coupled Device - device for the movement of an electrical charge; here used as an electronic light sensor. 55, 56, 80, 120

CCN Cloud Condensation Nuclei. 45

CE-DOAS Cavity-Enhanced Differential Optical Absorption Spectroscopy. 49

CIMS Chemical Ionisation Mass Spectroscopy. 38, 39

CPC Condensation Particle Counter. 69

CPT Circumpolar Trough. 144

DMS Dimethyl sulfide. 45, 147, 161, 162

DOAS Differential Optical Absorption Spectroscopy. 3, 38, 49, 51, 52, 54, 55, 56, 57, 58, 70, 72, 74, 75, 97, 101, 105, 106, 120, 123

FWHM Full Width at Half Maximum. 72, 286

GEM Gaseous Elemental Mercury. 44

GvN Georg von Neumayer. 62, 63

irradiance radiant flux received per area in [$\mathrm{W\,m^{-2}}$]. 58, 90

LDLS Laser Driven Light Source. 72, 76, 106, 111, 126

LP-DOAS Long-Path Differential Optical Absorption Spectroscopy. 3, 39, 54, 56, 61, 70, 72, 74, 75, 76, 79, 80, 81, 82, 85, 87, 88, 90, 91, 98, 99, 105, 106, 110, 123, 129, 130, 131, 134, 135, 136, 139, 142, 145, 149, 150, 151, 152, 155, 156, 157, 158, 162, 164, 167, 169, 171, 174, 178, 179, 180, 181, 182, 186, 187, 188, 189, 191, 192, 194, 195, 198, 200, 201, 204, 205, 207, 209, 213, 214, 215, 218, 222, 229, 230, 231, 232

MAAP Multi-Angle Absorption Photometer. 68

MAX-DOAS Multi-Axis Differential Optical Absorption Spectroscopy. 3, 51, 61, 70, 101, 134, 135, 136, 182, 186, 187, 188, 191, 194, 218, 232

MSA Methane sulfonic acid. 45

NM II Neumayer II. 62, 63

NM III Neumayer III. 3, 8, 16, 17, 18, 19, 20, 21, 22, 25, 26, 28, 36, 44, 47, 61, 62, 63, 64, 65, 66, 67, 68, 69, 70, 72, 73, 76, 77, 78, 79, 80, 87, 88, 90, 91, 95, 97, 99, 101, 106, 109, 113, 120, 124, 134, 136, 139, 141, 143, 144, 145, 146, 145, 147, 148, 149, 151, 153, 155, 161, 162, 164, 166, 169, 171, 172, 174, 175, 176, 177, 178, 179, 180, 182, 183, 187, 190, 191, 193, 195, 196, 197, 198, 199, 201, 204, 205, 206, 207, 208, 210, 215, 218, 220, 221, 224, 227, 228, 229, 230, 231, 232

ODE Ozone Depletion Event. 2, 28, 32, 33, 40, 42, 44, 45, 46, 149, 153, 167, 179, 196, 197, 205, 221

PID Proportional–Integral–Derivative. 84, 89

ppb parts per billion - Mixing ratio of a species (per volume), alternatively: nanomole per mole. 25, 49, 69, 136

ppt parts per trillion - Mixing ratio of a species (per volume), alternatively: picomole per mole. 26, 36, 38, 49

QLL Quasi Liquid Layer. 14, 33, 40

radiance radiant flux per radiating area and solid angle in $[\mathrm{W\,m^{-2}\,sr^{-1}}]$. 50, 51, 53, 56, 76

RMS Root Mean Square. 58, 125, 130

SAO Semi-annual Oscillation. 144, 145, 151, 175

SMPS Scanning Mobility Particle Sizer. 69, 221

spectral radiance radiance per unit wavelength in $[\mathrm{W\,m^{-2}\,nm^{-1}\,sr^{-1}}]$. 50, 55, 72, 75

SSA specific surface area. 13

SZA solar zenith angle. 8, 23, 26, 29, 91, 92, 96, 123, 124, 140, 153, 161, 176, 183, 204, 218

UV ultraviolet radiation. 51, 52, 109

UV-A Ultraviolet radiation between 315 and 400 nm wavelength. 8

UV-B Ultraviolet radiation between 280 and 315 nm wavelength. 8

UV-C Ultraviolet radiation between 100 and 280 nm wavelength. 8

VIS visble radition. 51, 52

VOC Volatile Organic Compound. 46, 206

WMO World Meteorological Organisation. 65

Acknowledgements - Danksagung

Meine Arbeit an diesem Projekt wurde sowohl von der deutschen Forschungsgemeinschaft (DFG), als auch durch ein Promotionsstipendium des Evangelischen Studienwerks Villigst unterstützt. Die Auslandsförderung durch das Studienwerk ermöglichte mir auch zwei Aufenthalte beim British Antarctic Survey (BAS) und im St. Catharine's College der Universität Cambridge in Großbritannien, wo ich sehr freundlich aufgenommen wurde. Neben dem Promotionsstipendium des Evangelischen Studienwerks Villigst durfte ich auch die ideelle Promotionsförderung der Studienstiftung des deutschen Volkes in Anspruch nehmen. Während der Promotionszeit war ich Mitglied der Heidelberg Graduate School of Fundamental Physics (HGSFP) durch deren Unterstützung ich an einer fünfwöchigen Winter School zu Atmosphärenforschung in Grenoble teilnehmen konnte.
Der Aufbau des neuen Langpfad-DOAS Instruments und die mehr als zwei Jahre andauernden Messungen, sowie die drei dafür notwendigen Kampagnen auf der deutschen Antarktisstation Neumayer III wären ohne die großzügige Unterstützung durch das Alfred Wegener Institut - Helmholtzzentrum für Polar- und Meeresforschung nicht möglich gewesen.
Für diese breite Unterstützung durch die verschiedenen Institutionen bin ich sehr dankbar.

Bei den folgenden Personen möchte ich mich darüber hinaus für ihren Beitrag zu dieser Arbeit persönlich bedanken:

Vielen Dank an meinen Doktorvater, Prof. Ulrich Platt für die Möglichkeit, dieses Thema zu bearbeiten. Während meiner Promotionszeit hatte ich viel Freiheit meine Ideen zu verfolgen und auszuprobieren. Seine Anregungen waren sehr wertvoll für diese Arbeit und haben geholfen, das Ziel nicht aus den Augen zu verlieren. Der Austausch bei der Teilnahme an Workshops und Winter Schools sowie regelmäßige Fahrten zu Konferenzen, die mir ermöglicht wurden, waren ein wichtiger Beitrag für die Arbeit an meinem Projekt.

Vielen Dank an Prof. Werner Aeschbach für die Übernahme der Zweitbegutachtung.

Ein besonderes herzliches Dankeschön an Dr. Udo Frieß für die Möglichkeit, dieses Projekt umsetzen zu dürfen, für das Vertrauen und die Freiheiten bei der Planung und Organisation dabei, die Unterstützung bei Konferenzbesuchen und auf Kampagnen, für Motivation und Ansporn, Anregungen und Hilfestellungen und nicht zuletzt für das fleißige Korrekturlesen.

Einen genauso herzlichen Dank an Dr. Stefan Schmitt für das geduldige Beantworten meiner ganzen Fragen, denen er als mein Schreibtischnachbar nicht entkommen konnte. Die Diskussionen über die Feinheiten von Langpfad-DOAS oder Atmosphärenchemie, die praktischen Tipps und Tricks, und der Ansporn doch noch eine neue Auswertung auszuprobieren haben mich immer wieder motiviert.

Der Bau des neuen Langpfad-DOAS Instruments wäre ohne ganze Reihe von Menschen so nicht möglich gewesen. Dafür zunächst ein großes Dankeschön an Dr. Denis Pöhler für seine Hilfe, das Teilen seiner großen Erfahrung bei Planung und Konstruktion, und den scharfen Blick auf die praktischen Probleme bei der Umsetzung. Vielen Dank an Dr. Johannes Lampel für Unterstützung bei der Steuerung und Temperaturregelung. Vielen Dank an Udo für die Umsetzung immer neue Anforderungen an MS-DOAS.
Danke an Heribert Sommer aus der IUP Werkstatt, der bei einem engen Zeitplan viele Teile des neuen Instruments gebaut hat und mit dem zusammen ich für einige komplizierte Ideen praktikable Lösungen gefunden habe.

Vielen Dank an die Teilnehmer der "Halogenmeetings" für die regen Diskussionen und neue Ideen - neben Prof. Platt, Udo und Stefan auch Dr. Holger Sihler, Max Herrmann und Moritz Schöne

Danke auch an die übrige Arbeitsgruppe für die angenehme Atmosphäre und die interessanten Gespräche sowie an meine Bürokolleginnen Jule Thome und Sabrina Ebenhoch.

Für eifriges Korrekturlesen und hilfreiche Anmerkungen vielen Dank an Jonas Kuhn, Lukas Tirpitz, Holger Sihler, Stefan Schmitt

Ein großes Dankeschön an Dr. Rolf Weller vom AWI für die Unterstützung bei Planung und Umsetzung der Messungen auf Neumayer III von den ersten Skizzen des Instruments, über Hilfe bei Logistik- und Zollfragen bis zum Abbau der Komponenten. Vielen Dank auch an Dr. Eberhard Kohlberg, Dr. Christine Wesche, Bernd Loose, Beate Kuhlmann-Treu und Peter Köhler vom AWI, stellvertretend für die gesamte AWI-Logistik in Bremerhaven

Ein besonderer Dank gilt den Teilnehmerinnen und Teilnehmern der 36., 37., und 38. Neumayer III Überwinterungen, ohne deren herausragende Arbeit in den vergangenen drei Jahren der Betrieb des Langpfad-DOAS nicht möglich gewesen wäre. Dabei mussten sich insbesondere die LuftchemikerInnen, Dr. Thomas Schaefer, Dr. Zsofía Juranyí und Dr. Helene Hoffmann um alle kleinen und großen Problemen des Instruments kümmern und das bei schwierigsten Wetterbedingungen. Vielen Dank auch an Hauke Schulz für das Beantworten all meiner Fragen zum meteorologischen Observatorium der Station. Für die tatkräftige Unterstützung beim Aufbau vor Ort vielen Dank an die Techniker der Sommerbesatzung von Neumayer III.

Für die gemeinsame Zeit auf der Station, Tischkickerduelle, Ausflüge an die Schelfeiskante und auf die Atkabucht oder den Zeitvertreib bei Verzögerungen bei An- und Abreise vielen Dank an Nanna Karlsson, Anna Winter, Lewin Probst, Rick Blenkner, Olaf Eisen, Emma Smith und Judith Neunhäuserer. Merci à Céline Le Bohec pour le jour de stage avec les manchots empereur, une expérience inoubliable.

A big thank you to Dr. Anna Jones who hosted me twice at the British Antarctic Survey in Cambridge. During the time there and the discussions with her and Dr. Xin Yang, Dr. Markus Frey, Dr. Neil Brough as well as many other specialists in all things polar, I learned a lot about atmospheric chemistry and Antarctica. Thanks to Prof. John Pyle from the University of Cambridge I was able to stay in an accommodation of St Catharine's College and could participate in college life as a temporary member of the MCR.

Thank you to my housemates in Barton road and other Catz members, in particular Rosie Maxton, Sophie McManus, Alex Scott, Katrin Daehn and many others for the warm welcome, a wonderful time in Cambridge and an open ear when times were tough.

Vielen Dank an die Menschen, die mich in den vergangenen Jahren begleitet haben und für mich da waren: Therese, Philipp, Marian und Sanam mit Joni für vier tolle Jahre in Heidelberg und Merle und Matthias in der Ferne, Chris for a place to stay in London and for always being up to no good, Stolzi und Chrissi für Spaa in Wien und das übliche EGU Schlafplätzchen. Vielen Dank an Annette und Klaus für die kleinen Fluchten aus Heidelberg und einen besonderen Dank an Jonathan für all seine Unterstützung.

Meinem Vater Dr. Hubert Nasse (1951 - 2016) vielen Dank für die vielen kleinen und großen Momente - und seine Fotos davon, das geduldige Beantworten meiner Fragen, den gelassenen Rückhalt bei allen Flausen und Plänen, und seine Neugier auf die Welt, die ich geerbt habe.

Einen großen Dank an meine Mutter Christel und meine Schwester Laura - dafür, dass sie immer für mich da sind, mich bei allem unterstützt haben, und wir zusammenhalten.

Zuletzt, vielen Dank Paula, dass du da bist, für deine Unterstützung, dass du mich immer wieder hast ziehen lassen, und für deine große Geduld mit mir und dieser Arbeit.